AECL EACL

AECL-11311, COG-95-171

Technical Summary of AECL's Mine-by Experiment Phase 1: Excavation Response

Résumé du rapport technique d'EACL sur l'essai au voisinage de l'excavation Phase 1: Reaction à l'excavation

R.S. Read, C.D. Martin

February 1996 février

AECL

TECHNICAL SUMMARY OF AECL'S MINE-BY EXPERIMENT PHASE 1: EXCAVATION RESPONSE

by

R.S. Read and C.D. Martin

Whiteshell Laboratories
Pinawa, Manitoba R0E 1L0
1996

AECL-11311
COG-95-171

TECHNICAL SUMMARY OF AECL'S MINE-BY EXPERIMENT PHASE 1: EXCAVATION RESPONSE

by

R.S. Read and C.D. Martin

ABSTRACT

The first phase of the Mine-by Experiment was conducted at the 420 Level of the Underground Research Laboratory (URL) to investigate the response induced in the rock mass by excavating a 3.5-m-diameter circular tunnel using a non-explosive technique. The main objective of the experiment was to study the processes involved in progressive failure and the development of excavation-induced damage around underground openings. To this end, state-of-the-art geomechanical and geophysical instrumentation was used to monitor the excavation of the 46-m-long Mine-by Experiment test tunnel. The results from the experiment show that progressive failure in compressive regions around the tunnel initiates at stresses about 50% of the rock strength measured in uniaxial compression tests in the laboratory. The difference between the laboratory and *in situ* behaviour is attributed to complex stress changes that occur during excavation of the tunnel, especially in the vicinity of the advancing face. These effects are not simulated in standard laboratory tests. Numerical modelling and *in situ* characterization studies were conducted to establish the extent and characteristics of the damaged zone around the test tunnel. As part of this study, *in situ* stresses and material properties were established through back analysis of measured displacements and strains. Using these boundary conditions, it was shown that the damaged zone was limited to within 1 m of the original tunnel perimeter. The characteristics of the damaged zone, however, were found to be highly variable around the tunnel, and were dependent on the nature of the stress concentrations, geology, stress magnitudes and orientations and, to a lesser extent, the excavation method and sequence.

AECL
Whiteshell Laboratories
Pinawa, Manitoba R0E 1L0
1996

AECL-11311
COG-95-171

RÉSUMÉ DU RAPPORT TECHNIQUE D'EACL SUR L'ESSAI AU VOISINAGE DE L'EXCAVATION PHASE 1 : RÉACTION À L'EXCAVATION

par

R.S. Read et C.D. Martin

RÉSUMÉ

La première phase de l'Essai au voisinage de l'excavation a été menée au niveau 420 du Laboratoire de recherches souterrain (LRS) en vue d'étudier la réaction induite dans la masse rocheuse en creusant une galerie circulaire de 3,5 m de diamètre au moyen d'un procédé technique sans utilisation d'explosifs. Le but principal de cet essai était d'analyser les processus de rupture progressive mis en jeu et l'évolution des dommages causés par les travaux d'excavation à la périphérie des accès souterrains. On a eu recours, à cette fin, à des instruments de géophysique et de géomécanique d'avant-garde pour surveiller les travaux de forage de la galerie de 46 m de longueur de l'Essai au voisinage de l'excavation. Les résultats de cet essai indiquent que la rupture progressive dans les régions qui subissent des sollicitations en compression autour de la galerie s'amorce à des contraintes d'environ 50 % de la résistance de la roche mesurée par des essais de compression uniaxiale réalisés au laboratoire. La différence de comportement notée entre les résultats obtenus au laboratoire et ceux obtenus *in situ* est attribuée à des modifications de contraintes complexes qui se manifestent au cours du forage de la galerie, en particulier au voisinage du front d'attaque. Dans les essais de laboratoire normaux, ces effets ne sont pas simulés. On a réalisé des études de modélisation numérique et de caractérisation *in situ* en vue d'établir l'étendue et les caractéristiques de la zone endommagée autour de la galerie d'essai. Dans le cadre de cette étude, les contraintes *in situ* et les propriétés des matériaux ont été établies par rétroanalyse des déplacements et des déformations qui ont été mesurés. Il a été démontré, en se fondant sur ces conditions aux limites, que la zone endommagée était limitée à une distance de moins de 1 m du périmètre initial de la galerie. On s'est toutefois rendu compte que les caractéristiques de la zone endommagée étaient très variables à la périphérie de la galerie et qu'elles étaient fonction des concentrations de contraintes, de la géologie, de l'ampleur et de l'orientation des contraintes ainsi que, dans une moindre mesure, de la méthode et de la séquence de réalisation des travaux.

EACL
Laboratoires de Whiteshell
Pinawa (Manitoba) R0E 1L0
1996

AECL-11311
COG-95-171

CONTENTS

continued ...

CONTENTS (continued)

continued ...

CONTENTS (concluded)

EXECUTIVE SUMMARY

Atomic Energy of Canada Limited (AECL) has constructed an Underground Research Laboratory (URL) approximately 120 km northeast of Winnipeg, Manitoba. The URL has been excavated to a depth of 443 m in the Lac du Bonnet granite batholith, with horizontal developments at 240-m depth (240 Level) and 420-m depth (420 Level). These developments provide access to conduct *in situ* multi-disciplinary experiments, such as the Mine-by Experiment, in rock mass conditions that are representative of many granitic plutons within the Canadian Shield.

In 1989, an external Peer Review Panel was selected by AECL to review the experiments planned for the URL. The report from this review stated:

> *The Mine-by Experiment must be conducted on the 420 Level. Failure to experiment at this level could ultimately result in the need to exclude environments at candidate repository sites where similar high horizontal stresses were found, since it would not be possible to argue that the concept had been tested under appropriate conditions deep within plutons. Horizontal stresses might thus limit the depth at which a repository could be developed.*

In light of this recommendation, the rock mass at the 420 Level was characterized to locate a representative site for the Mine-by Experiment. The area chosen for the experiment typifies the 420 Level in terms of geology, geotechnical properties and *in situ* stresses. The high *in situ* stresses and highly anisotropic stress ratios measured in the experiment area represent an upper bound compared to measurements taken at similar depths elsewhere in the Canadian Shield. Under such conditions, three zones are expected around an underground opening: 1) a disturbed zone remote from the opening in which the material behaviour is essentially unchanged, but the stress state is perturbed by the opening; 2) a smaller damaged zone near the tunnel wall characterized by changes in both the pre-excavation stress state and in the material behaviour of the rock mass; and 3) a failed zone defined by a region of slabbing or rock fall-out. The nature and extent of the damaged and failed zones, and the processes responsible for their development, are important in terms of understanding the probability of increased permeability within these regions.

Rock mass behaviour and damage development were monitored around a 3.5-m-diameter test tunnel, excavated using a non-explosive technique involving line-drilling and hydraulic rock splitting. An essential feature of the Mine-by Experiment is that instrumentation was installed and operating prior to excavation of the test tunnel. In this way, it was possible to monitor the complete excavation-induced response of the rock mass, including effects ahead of the advancing tunnel face. Geomechanical and geophysical instruments, including extensometers, convergence arrays, triaxial strain cells and an acoustic emission/microseismic (AE/MS) monitoring system, were installed for the experiment. New instruments, such as the excavation damage extensometer (Ed-ex), were also developed to provide detailed measurements close to the tunnel wall. In total, over 500 data channels were monitored during the main excavation stage of the experiment.

During excavation of the test tunnel, a multi-stage process of progressive brittle failure resulted in the development of 'v-shaped' notches, typical of borehole breakouts, in the areas of compressive stress concentration in the roof and floor. The sequence of events leading to failure was similar to that observed in laboratory tests on block samples containing a central hole. However, the compressive stress at the point of failure on the tunnel wall was only about 50% of the rock strength determined from uniaxial compression tests in the laboratory. The difference between the laboratory and *in situ* strengths is attributed to stress changes that occur slightly ahead of the advancing tunnel face. As the tunnel advances, the magnitudes and orientations of the principal stresses in parts of this region change significantly, causing micro-scale damage which locally weakens, or 'pre-conditions', the rock mass. Upon tunnel advance, the degree of damage is highest at the surface of the opening where confinement is zero and compressive stress concentrations are greatest. Hence, the rock strength is lowest at the tunnel wall and increases away from the opening up to a value comparable to that measured in the laboratory. These effects are not simulated in standard laboratory tests.

Two separate back analyses, using strain and/or displacement measurements from the Mine-by Experiment, were conducted to verify the stress boundary conditions upon which the initial interpretation of the *in situ* failure process was based. The two analyses produced consistent results, constituting an improved estimate of the principal stress orientations and magnitudes at the 420 Level. While this estimate differed somewhat from the stress tensor used in the initial analysis of progressive failure, the results confirmed that the original estimate was sufficient for the purpose of understanding the failure process. The back analyses highlighted the potential difficulties in determining *in situ* stresses in highly-stressed conditions using traditional stress measurement techniques.

The refined estimate of the stress tensor was used to identify regions of non-linear/non-elastic behaviour by comparing the measured rock mass response to the expected elastic response. The comparison showed that the region ahead of the advancing face exhibits essentially linear elastic behaviour, but that the region behind the face is affected by the development of excavation-induced damage. Results from underground characterization, geophysics surveys and numerical modelling indicate that damage is most evident in areas of compressive stress concentration in the roof and floor of the test tunnel, and, to a lesser extent, in areas of tensile stress concentration in the sidewalls. These results also show that the damaged zone associated with the Mine-by Experiment test tunnel is limited to within about 1 m from the original tunnel perimeter. However, the characteristics of the damaged zone are highly variable around the tunnel, and are controlled or influenced by several factors including the nature of the stress concentration, i.e., compressive versus tensile; the mineralogy and grain size distribution of minerals within the various lithologic units; the *in situ* stress state, particularly the σ_1/σ_3 ratio and the orientation of the principal stresses relative to the tunnel axis; excavation method and sequence; and confinement from within the tunnel.

Numerical modelling carried out during the course of the Mine-by Experiment showed that elastic analyses were adequate for interpreting the monitoring results from the Mine-by test tunnel. However, neither linear nor non-linear continuum analyses adequately predicted the extent of damage around the Mine-by test tunnel, or the shape of the damaged and

failed zones. While the initiation of failure at the boundary of the tunnel can be predicted by continuum models using an appropriate failure criterion, the stages following initiation, which involve dilation, slabbing and spalling, represent discontinuum-type behaviour. It is this transition from continuum to discontinuum behaviour that poses the major difficulty in predicting the shape and extent of the damaged and failed zones around the Mine-by test tunnel and similar underground openings. Despite this limitation, though, elastic models, used in conjunction with the concepts developed in the report regarding progressive failure, are entirely adequate for engineering design purposes.

1. INTRODUCTION

In Canada, as in many countries that employ nuclear power, the concept of deep underground disposal of used nuclear fuel waste is being investigated. The Canadian disposal concept considers the plutonic rock of the Canadian Shield as a potential host medium for a disposal vault located at between 500- and 1000-m depth. As part of the assessment of this concept, Atomic Energy of Canada Limited (AECL) has constructed an Underground Research Laboratory (URL) approximately 120 km northeast of Winnipeg, Manitoba in the Lac du Bonnet granite batholith (Figure 1). The URL constitutes a well-characterized *in situ* environment in a previously undisturbed volume of rock for experiments that address issues of importance in assessing the Canadian disposal concept, and/or that demonstrate elements of the proposed disposal technology.

During development of a disposal facility, knowledge about the response of the rock to excavation will be needed to aid in optimizing many elements of the design, including such things as depth of disposal, layout of tunnels and rooms, excavation method and geometry, spacing of waste containers, and emplacement of seals. The Mine-by Experiment (Read and Martin 1991a), one of the Operating Phase Experiments planned for the URL (Simmons 1990), was designed to monitor rock mass behaviour and damage development around a test tunnel in massive, highly stressed, brittle rock. An essential feature of this type of experiment is that instrumentation is installed and operating prior to excavation of the

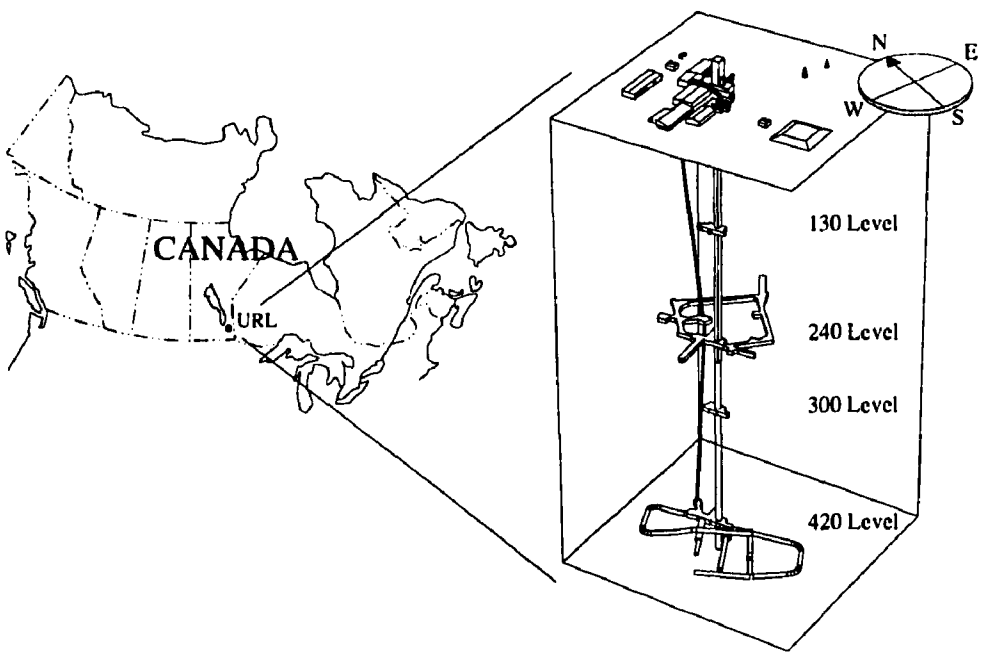

FIGURE 1: Location and arrangement of AECL's Underground Research Laboratory showing the main working levels.

tunnel. In this way, it is possible to monitor the complete excavation-induced response of the rock mass, including effects ahead of the advancing tunnel face.

The experiment location within the URL was selected to be representative of the geology and potentially high stress conditions anticipated at possible candidate disposal sites. The high *in situ* stresses and highly anisotropic stress ratios measured in the experiment area represent an upper bound compared to measurements taken at similar depths elsewhere in the Canadian Shield. Under such conditions, several zones may be defined around the tunnel: 1) a disturbed zone remote from the opening in which the material behaviour is essentially unchanged, but the stress state is perturbed by the opening; 2) a smaller damaged zone, typically within 1 to 1.5 tunnel diameters of the tunnel wall, characterized by changes in both the pre-excavation stress state and in the material behaviour of the rock mass; and 3) a failed zone defined by a region of slabbing or rock fall-out. These zones are shown schematically in Figure 2. The nature and extent of the damaged and failed zones, and the processes responsible for their development, are of particular importance in terms of understanding the likelihood of increased permeability within these regions.

The five specific objectives of the Mine-by Experiment (Read and Martin 1991a) are:

1. to improve our fundamental understanding of *in situ* rock mass behaviour and failure mechanisms;
2. to evaluate the excavation damage created around underground openings, study the causal mechanisms, and establish the factors that control damage;
3. to contribute to studies on the viability of the borehole alternative for emplacing nuclear fuel waste containers;
4. to develop and evaluate underground characterization methods, and characterize the volume of rock in which future sealing experiments are to be conducted; and

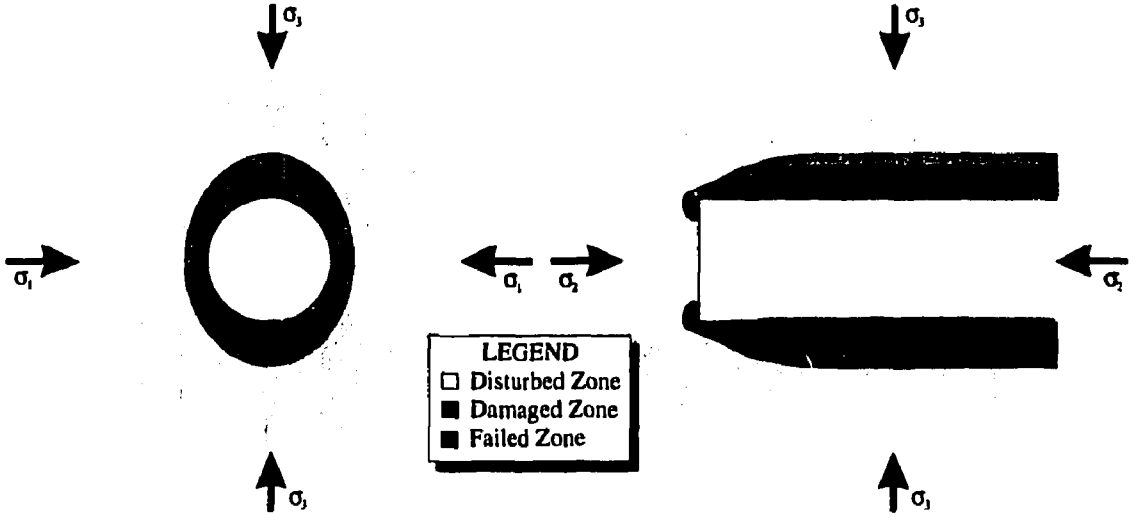

FIGURE 2: Schematic view of the disturbed, damaged and failed zones around a cylindrical tunnel. Compressive stresses are positive, and $\sigma_1 > \sigma_2 > \sigma_3$.

5. to develop and evaluate monitoring instrumentation and data management systems.

This report summarizes the technical findings of the first phase of the Mine-by Experiment (Phase 1: Excavation Response) relative to the experimental objectives. This section defines the objectives and organization of the experiment, and includes a simplified schedule and organizational chart. Section 2 presents results of pre-excavation characterization, details of the underground development and the *as-built* instrumentation arrangement as background for the experiment, and to establish the initial assumptions for analysis. Using these conditions, the mechanical behaviour and progressive failure of granite is investigated in Section 3, comparing results from laboratory testing to observed *in situ* behaviour to explain the mechanisms associated with the development of the failed zone. Section 4 uses back analysis of instrument responses in combination with geophysics studies to characterize the far-field *in situ* stress tensor, the transition between the zones of excavation disturbance and damage, and the material behaviour within the damaged zone. Factors controlling excavation damage development are also discussed in Section 4. Section 5 presents the various approaches taken to model progressive failure, and discusses the application of such models to design. A summary and the main conclusions are presented in Section 6. Three appendices are also included: the first contains a completed experiment schedule, the second presents details of the experiment back analysis, and the third provides a list of related documents and published papers detailing specific analyses. The monitoring results from the Mine-by Experiment test tunnel are summarized separately in a series of nine data summary reports:

Part 1 – Survey Information (COG-93-290, Read et al. 1994),

Part 2 – Triaxial Strain Cell Results (COG-93-353, Read et al. 1994b),

Part 3 – Extensometer Results (COG-93-354, Read et al. 1994a),

Part 4 – Convergence Results (COG-93-177, Read et al. 1993b),

Part 5 – Thermistor Results (COG-93-233, Martino et al. 1993a),

Part 6 – Acoustic Emission/Microseismic Results (COG-93-185, Martino et al. 1993),

Part 7 – Geological Setting and General Geology (COG-93-251, Everitt et al. 1993),

Part 8 – Construction Summary (COG-93-252, Keith and Onagi 1994), and

Part 9 – Observations (COG-93-347, Martino et al. 1994).

Details on the management, archiving and retrieval of experiment data are covered in Martino (1996).

1.1 EXPERIMENT SCHEDULE AND ORGANIZATION

The simplified experiment schedule is shown in Figure 3. The activities are categorized under the general headings 1) Design & Engineering, 2) Construction, 3) Drilling, 4) Characterization & Testing, 5) Equipment & Instrumentation, 6) Test Tunnel Monitoring and 7) Analysis & Reporting. As shown in Figure 3, the main experimental activities were completed close to the planned schedule. The main monitoring phase of the experiment

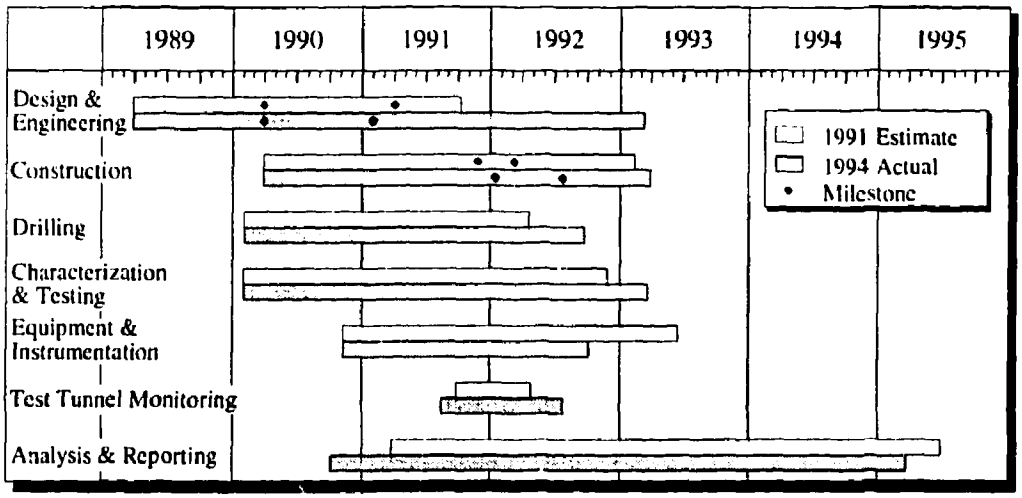

FIGURE 3: Simplified experiment schedule showing planned and completed activities. Milestones in Design and Engineering represent the completion of preliminary and final designs, respectively, and in Construction, the start and completion of the test tunnel.

during the excavation of the test tunnel was delayed approximately 1.5 months as a result of some startup problems with the enthalpy control system. In addition, owing to a lack of previous experience with the selected excavation technique, the test tunnel excavation took about 3 months longer than initially planned, but these changes did not affect the overall completion date for the experiment. The Connected Permeability Experiment, the main associated project for the Mine-by Experiment, was reorganized into a separate phase (Phase 2) of the overall experiment. In addition, a third phase (Heated Failure Tests) was added as an associated project, as detailed in an addendum to the original experiment plan (Read and Martin 1993). Reports summarizing the second and third phases of the Mine-by Experiment will be issued separately. The detailed schedule for the completed experiment is contained in Appendix A.

The organizational structure of the experiment was relatively unchanged from that laid out in the Mine-by Experiment Final Design Report (Read and Martin 1991a), with the exception of additional personnel within the external contracts for various aspects of the experiment. The organizational chart for the main components of the experiment is shown in Figure 4.

2. OVERVIEW OF THE EXPERIMENT

The Mine-by Experiment Final Design Report (Read and Martin 1991a) was used as the design plan for the experiment. Included in that report was a summary of pre-excavation characterization results for the experiment, a detailed experiment schedule, and details of

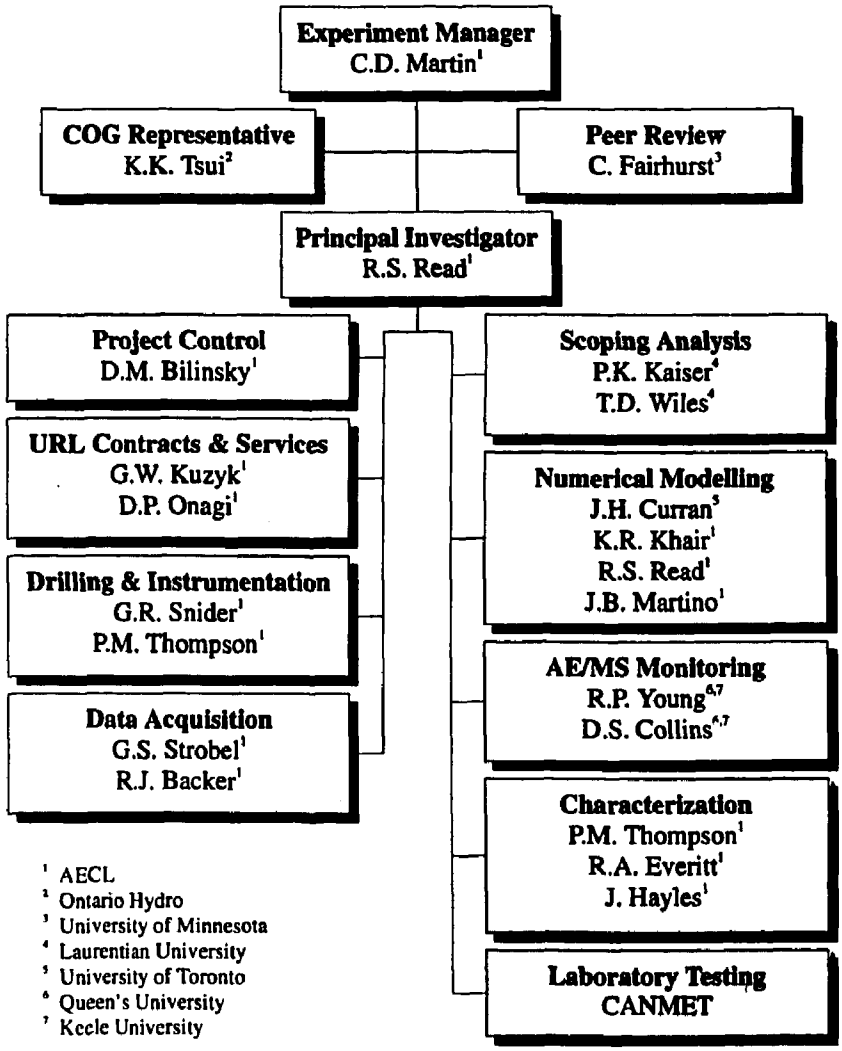

FIGURE 4: Organizational chart showing the main participants in the experiment.

the planned experimental activities. This section provides an overview of the experiment, including a review of the pre-excavation characterization data and *as-built* details.

2.1 PRE-EXCAVATION CHARACTERIZATION

2.1.1 Geology

The URL is located in the Lac du Bonnet batholith, which is considered to be typical of many granitic intrusions of the Precambrian Canadian Shield (Davison et al. 1982). The batholith is an elongated body about 75 by 25 km in plan and about 10 km in depth, trending ENE-WSW. It has been dated as Late Kenoran in age (2680 ± 81 Ma), and lies in the Winnipeg River plutonic complex of the English River gneiss belt of the west-

ern Superior Province. The batholith is a relatively undifferentiated massive porphyritic granite-granodiorite. The massive, medium- to coarse-grained porphyritic granite is relatively uniform in texture and composition over the batholith, although locally it displays subhorizontal gneissic banding (Everitt et al. 1990a).

The geology of the URL has been characterized from detailed logging of drill-core from boreholes, and geological mapping of surface and subsurface exposures. From these investigations, it has been concluded that, near the URL, the batholith is made up of five main rock units: the pink (altered) or grey (unaltered) granite groundmass of the batholith, xenolithic inclusions of various compositions, leucocratic granitic segregations, and subvertical granodiorite and pegmatite dykes. This classification scheme is based primarily on age relationships between the various rock units (Everitt and Brown 1986).

During excavation of the URL shaft, two major thrust faults (Fracture Zones 3 and 2) and their associated splays (Fracture Zones 2.5 and 1.9) were intersected (Figure 5). These faults dip to the southeast at between 20 and 30° and typically contain low-dipping fractures, secondary alteration products such as clay, hematite and chlorite, zones of cataclasite, gouge and rubble, and regions of moderate-to-high groundwater flows.

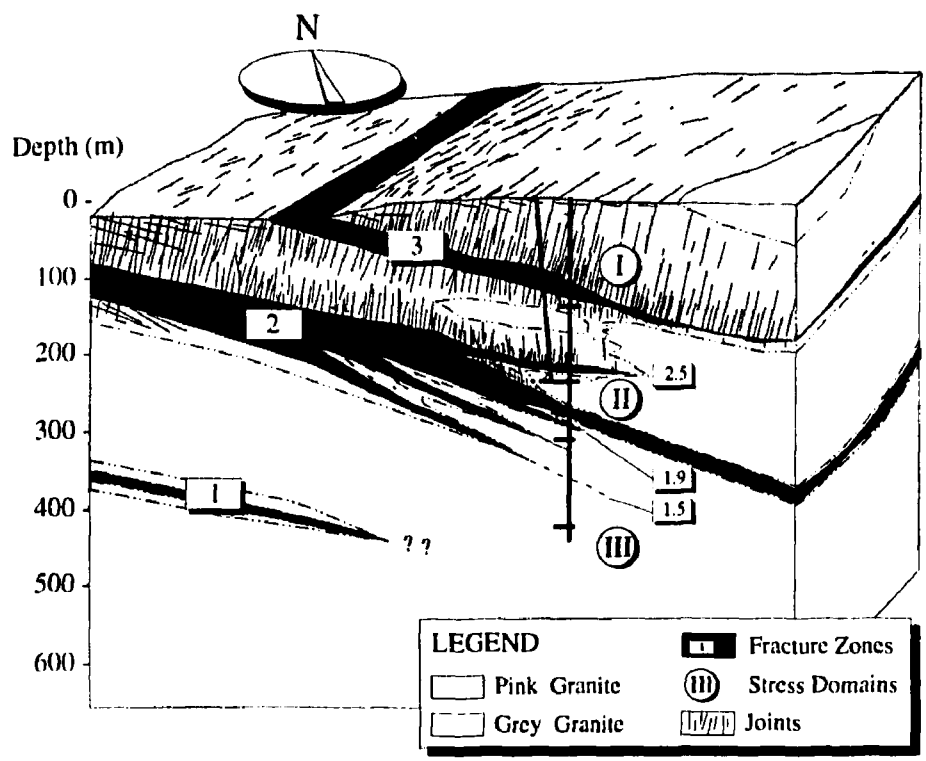

FIGURE 5: General geological setting of the Underground Research Laboratory showing the major Fracture Zones and stress domains (after Everitt et al. 1990a).

Above Fracture Zone 2.5, the rock mass comprises mainly pink granite. In this region, two subvertical joint sets have been identified: a prominent set striking about 020 to 040°, and a less prominent, intermittent set striking about 150 to 180°. Below Fracture Zone 2.5, the rock mass is essentially unfractured, with the exception of Fracture Zone 2 and its associated splays 1.9 and 1.5.

According to Everitt et al. (1990), the rock mass at the 420 Level is composed of three major litho-structural domains: a gneissic grey granite, a leucocratic granite, and a xenolithic-leucocratic granite. A major subvertical granodiorite dyke swarm, approximately 100 m thick and striking NNW, crosscuts these domains and is present throughout the 420 Level. From earlier work by Brown et al. (1989) at the other levels at the URL, the granodiorite is poorer in alkali feldspar and richer in plagioclase than the grey granite, although the transition between the two units is diffuse (Figure 6). Thin pegmatite dykes crosscut all other rock types, but are mostly confined to the larger granodiorite dykes at this level. Detailed petrographic analysis was not conducted on rock types from the 420 Level prior to the Mine-by Experiment because of wide mineralogic variations within each unit. Results from post-excavation petrographic analyses are discussed in Section 4.3.5.

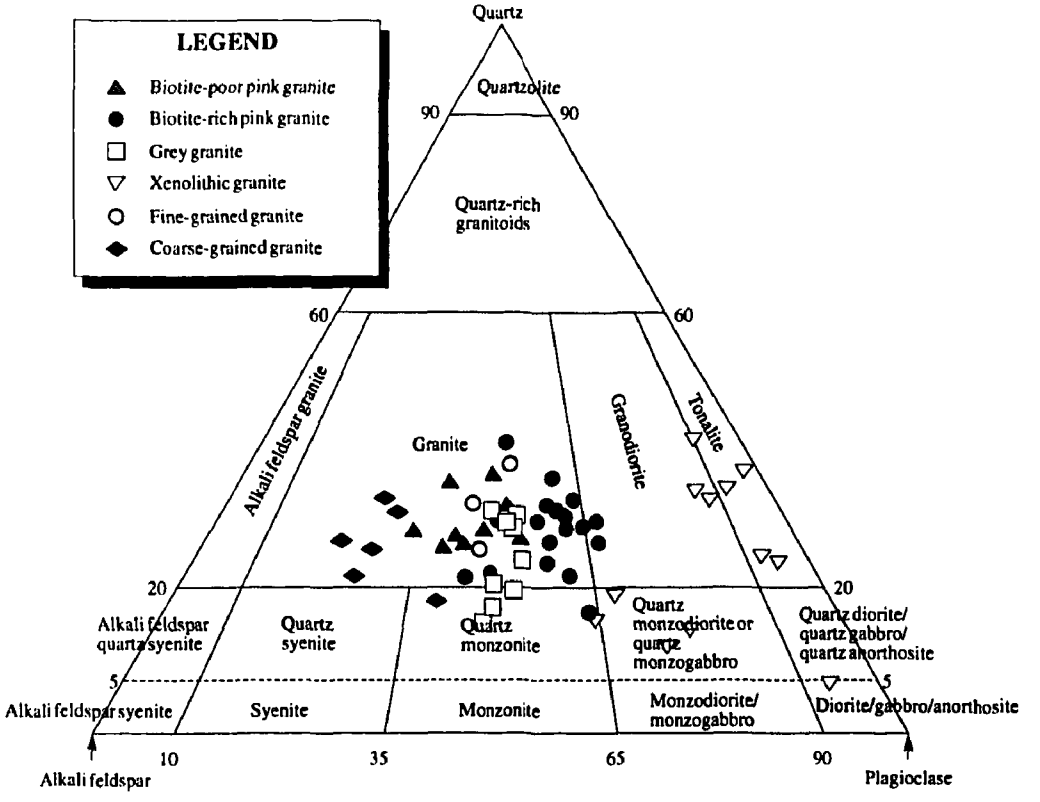

FIGURE 6: Ternary diagram showing the composition of granite and granodiorite for the URL (after Brown et al. 1989). Note that in this classification no distinction was made between the granite and granodiorite, the latter being grouped with biotite-rich granite. The inverted triangles represent xenolith compositions.

A few minor closed fractures, associated with the granodiorite dyke swarm to the west of the station, were identified in drill core from exploratory boreholes for the Mine-by Experiment. However, these fractures were not detected in the tunnel wall following room excavation and hence are of small areal extent (~ 1 m^2). They are essentially isolated from each other and therefore do not affect the overall permeability of the rock mass. This appears to be the only fracture type in the immediate vicinity of the 420 Level. Under such sparsely fractured conditions, the *in situ* hydraulic conductivity of the rock mass is in the order of 10^{-13} m/s.

2.1.2 Geotechnical Properties

The geotechnical properties of core samples of Lac du Bonnet granite have been determined from extensive laboratory testing, e.g., Lajtai (1982), Lajtai (1988), Lajtai and Bielus (1986), Lajtai and Schmidtke (1986), Jackson et al. (1989), Stimpson and Chen (1991) and Martin (1993). However, as discussed later in Section 3, extrapolation of these results to the *in situ* material properties of the rock mass is not straightforward, even in situations where the rock mass has no joints. The difficulty lies in the fact that the rock *in situ* is 'pre-loaded', i.e., subjected to *in situ* stresses which are changed when the rock is disturbed by excavation. A core sample taken from the *in situ* stress environment for laboratory testing is first unloaded during coring and then reloaded in the laboratory. Thus the loading path and stress history of a core sample differ from that of the rock around the excavation. If the stresses relieved during coring are high, the resulting laboratory sample may contain significant damage that is not present in the field. Martin and Stimpson (1994) have shown that sample disturbance attributable to stress relief increases with the depth of sampling at the URL, and that this damage affects the geotechnical properties of the core samples. Samples selected from a low stress regime show a reduction in the amount of sample disturbance, and have properties that are probably more comparable to the *in situ* properties of the virgin rock mass.

The virgin geotechnical properties of rock in the field study area (Table 1) were estimated from laboratory tests performed by the Canada Centre for Mineral and Energy Technology (CANMET) on representative rock samples from the 420 Level, and on samples of granite from the upper 275 m of the batholith. Results from samples taken from the high stress domain at the 420 Level showed a marked decrease in peak strength from those taken at the 240 Level and above, suggesting a substantial amount of sample disturbance caused by induced microcracking. Read and Martin (1992) concluded that results from samples of granite from lower stress domains nearer surface were likely to be the most representative of the virgin *in situ* rock mass properties at the 420 Level. Martin (1993) also showed that samples of Lac du Bonnet granite taken from Cold Spring Quarry, near Seven Sisters, Manitoba, had properties similar to those taken from the upper 275 m of the batholith at the URL.

Mapping of excavation-induced damage during construction of the 300 Level suggested that damage zone development around underground openings was more pronounced in granite than in granodiorite (Everitt et al. 1989). The same was true during development of access tunnels at the 420 Level in the vicinity of discrete granodiorite dykes. However, the difference in excavation-induced damage between the massive granite and the outer

TABLE 1

ESTIMATED VIRGIN GEOTECHNICAL PROPERTIES FOR GRANITE AND GRANODIORITE IN THE EXPERIMENT AREA

Rock Type	Granite	Granodiorite
Density (kg/m^3)	2630 ± 10	2660 ± 20
Uniaxial Compressive Strength (MPa)	213 ± 20	228 ± 20
Tangent Young's Modulus (GPa)	65 ± 5	66 ± 5
Poisson's Ratio	0.25 ± 0.05	0.25 ± 0.05

Values are the mean±3 standard deviations (after Read and Martin 1992).

margin of a large granodiorite dyke was less pronounced in a drill-and-blast excavation (Room 405) driven orthogonal to the σ_1/σ_3 plane. Although laboratory testing suggests that the mechanical properties of the two rock types are similar, the field observations imply that there is a difference in their fracturing characteristics, i.e., the growth and interaction of cracks. As discussed later in Section 4.3.5, owing to its inequigranular structure and the abundance of large feldspar crystals, microcracking is expected to initiate at lower applied stresses in the granite than in the granodiorite. Consequently, regions of granite *in situ* would sustain more initial damage related to stress concentrations ahead of the advancing face, and would develop more pronounced damaged and failed zones behind the advancing face, than regions of granodiorite under identical stress conditions. This difference in fracturing characteristics is noticeable upon stress relief during sampling at the 420 Level.

2.1.3 *In Situ* Stress

A key goal in the design of the Mine-by Experiment was to conduct the investigation in a geological/geotechnical environment similar to that which might be expected between 500- and 1000-m depth in the Canadian Shield. A matter of particular concern was that the *in situ* stress magnitudes in the experiment area be sufficient to damage the rock mass upon tunnel excavation. An extensive characterization program had defined three distinct stress domains at the URL (Martin and Chandler 1993). At the 420 Level, the *in situ* stresses are part of Stress Domain III, which extends from about 300 m to a depth of at least 512 m (Figure 5). Based on the pre-excavation characterization of the 420 Level, it seemed possible to meet the objectives of the experiment by locating the Mine-by Experiment in Stress Domain III, where the stress conditions are similar to those at a depth of about 1000 m in other parts of the Shield.

The highly-stressed condition of this domain posed a problem for stress measurements at the 420 Level. A variety of techniques were tried, with limited success. Overcoring provided questionable results because of exaggerated axial straining (incipient discing). Hydraulic fracturing produced subhorizontal fractures in horizontal and vertical boreholes, from which only the vertical stress could be estimated (Doe 1989). Other studies using convergence measurements (Martino 1989) were limited to estimating only the plane components of the

TABLE 2

INITIAL ESTIMATE OF *IN SITU* STRESSES AT THE 420 LEVEL

Stress Components	σ_1	σ_2	σ_3
Magnitude (MPa)	55 ± 5	48 ± 5	14 ± 1
Trend (°)	135 ± 10	044 ± 10	290 ± 25
Plunge (°)	10 ± 5	05 ± 5	79 ± 5
Stress Ratios	σ_1/σ_2	σ_1/σ_3	σ_2/σ_3
	1.15 ± 0.1	3.93 ± 0.5	3.43 ± 0.5

Values are the mean±3 standard deviations (after Read and Martin 1991a).

stress tensor, and were difficult to interpret. An under-excavation study using CSIRO HI cells around the bored vent raise from the 420 to 240 Level (Kaiser et al. 1991; Wiles and Kaiser 1992) provided an estimate of the complete tensor, but results were affected by uncertainty in the CSIRO HI cell locations and orientations, small induced strains in the axial direction, and non-linear behaviour around the instrument boreholes once the advancing face was within 1 diameter of the instruments. In that study, the estimates of both the magnitude and orientation of the maximum and intermediate stresses were well constrained, but those for the minimum principal stress were not. Results from an acoustic emission/microseismic (AE/MS) array installed in four inclined boreholes around the URL shaft (Talebi and Young 1992) provided estimates of the maximum and minimum horizontal stress directions, which were supported by observations of breakouts in the shaft, but provided no estimates of magnitudes. Doorstopper tests performed in boreholes drilled for the Mine-by Experiment at the 420 Level (Corthésy and Gill 1992) produced an estimate of the stress tensor for the area, but the results for stress magnitudes did not correlate with results from other tests or observed behaviour around excavations at the 420 Level.

A stress tensor for the 420 Level (Table 2) was compiled from the best evidence for principal stress magnitudes and directions from the various testing methods, and from observations of breakouts in the shaft and in tunnels at the 420 Level. The composite nature of the tensor, however, precluded the use of rigorous statistical methods in determining the mean value and confidence intervals of each of the stress components, and their respective orientations. Nevertheless, this composite tensor was sufficient to define the orientation of the experiment test tunnel, which was designed to be approximately parallel to the intermediate principal stress (σ_2) direction.

2.2 UNDERGROUND DEVELOPMENT

2.2.1 *As-built* Experiment Arrangement

The arrangement of the Mine-by Experiment (Figure 7) was the result of an optimization process drawing upon a variety of technical proposals for instrumentation layouts and monitoring methods, evaluation of the practicality and safety of the operations associated with implementation, and evaluation of the most effective use of available resources in conjunc-

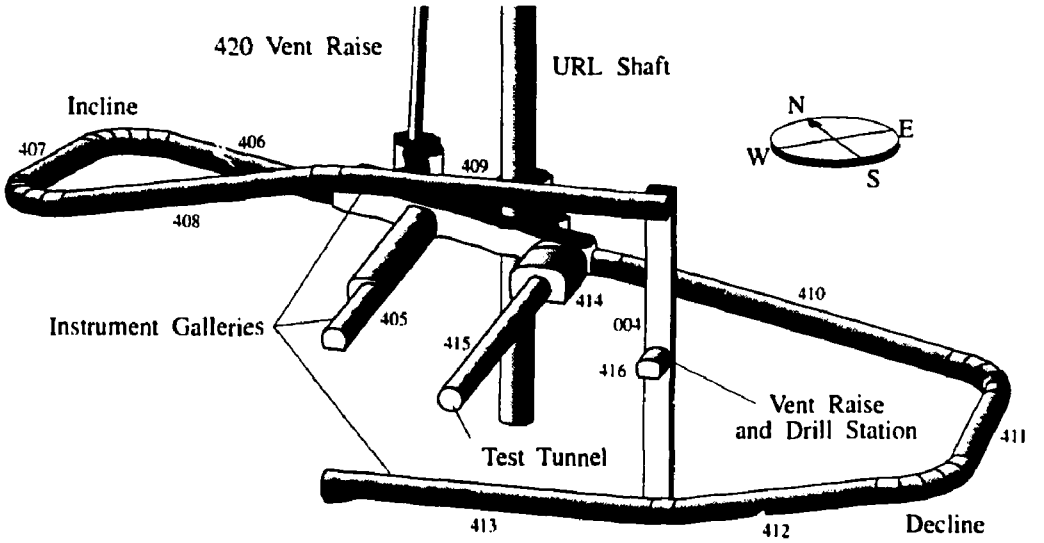

FIGURE 7: Arrangement of the Mine-by Experiment at the 420 Level of the URL.

tion with the overall URL experimental program. The azimuth of the test tunnel (225°) was chosen to maximize the stress ratio in the plane orthogonal to the tunnel axis in order to promote excavation-induced damage development.

Access for installation of instruments was provided by a series of drill-and-blast excavations. An incline and a decline were excavated at 20% grade on tangent, and 10% grade through the curves, to develop an upper and lower instrument gallery, Rooms 409 and 413 respectively, orthogonal to the planned test tunnel. A vertical raise (Room 004) was excavated to connect the upper and lower galleries for ventilation purposes, and a drill station (Room 416) was excavated at mid-height in the raise for instrumentation borehole drilling. A third instrument gallery (Room 405), parallel to the proposed test tunnel, was extended off the existing 420 Level for additional drilling access. All access tunnels were initially 3.4-m wide by 2.9-m high and horseshoe-shaped, but the first 30 m of Room 405 was enlarged to 5.0-m wide by 3.5-m high to accommodate additional testing. The vent raise drill station (Room 416) was excavated as a 3.5-m-wide by 2.7-m-high opening.

Following excavation of the access tunnels and installation of the instrumentation for the experiment, the 3.5-m-diameter circular test tunnel (Room 415) was excavated at 0.5% grade to 46 m in length from an assembly chamber (Room 414). The wall-to-wall spacing between the instrument galleries and the test tunnel was approximately 18.5 m.

2.2.2 Excavation Technique and Equipment

Based on previous experience with the drill-and-blast excavation method in Room 209 and the URL shaft, the damaged zone near the tunnel wall is considered to result from a combination of stress redistribution and blast effects. Similar observations in granite have been

reported by Pusch and Stanfors (1992). Because the intent of the Mine-by Experiment was to study the damage resulting from stress redistribution, the test tunnel was designed as a full-face machine-excavated opening to avoid the undesirable percussive effects of blasting. Initially, a tunnel boring machine (TBM) was considered the best technical option (Read and Martin 1991b), but the costs associated with excavating such a short section of tunnel, including equipment preparation and mobilization, were prohibitive. Consequently, an alternative method was devised.

The excavation method selected (Figure 8) involved line-drilling and reaming a series of 1-m-deep perimeter holes around the design diameter of the tunnel, and then progressively breaking out the interior of the round using hydraulic rock splitters (Figures 9 and 10) in a series of production holes (Keith and Onagi 1994; Onagi et al. 1992). Although the test tunnel was initially designed as a 3.5-m-diameter cylindrical opening with a flat face, the excavation method necessitated a stepped longitudinal profile to accommodate drilling of each round, with a maximum diameter of 3.5 m in each round (Figure 11). Based on previous excavations at the URL, the shape of the face was also expected to deviate somewhat from a perfect plane.

The excavation sequence for the test tunnel incorporated a combination of line-drilling/rock breaking and careful drill-and-blast for the first 10 m of the tunnel, followed by 36 m excavated by line-drilling and rock breaking in 0.5- to 1-m-long rounds. The first 34 m of Room 415 were excavated as full-face rounds, and a pilot-and-slash sequence was used for the final 12 m of the test tunnel. In total, 50 excavation rounds were required to complete the test tunnel. A detailed survey of each excavation round was conducted to accurately determine the face shape and round geometry (Read et al. 1994). Face contour maps were generated from the survey data, and a three-dimensional computer model of the test tunnel was created (Figure 12). A summary of the construction activities related to the Mine-by Experiment, and specific details of the equipment and excavation cycles, is given in Keith and Onagi (1994).

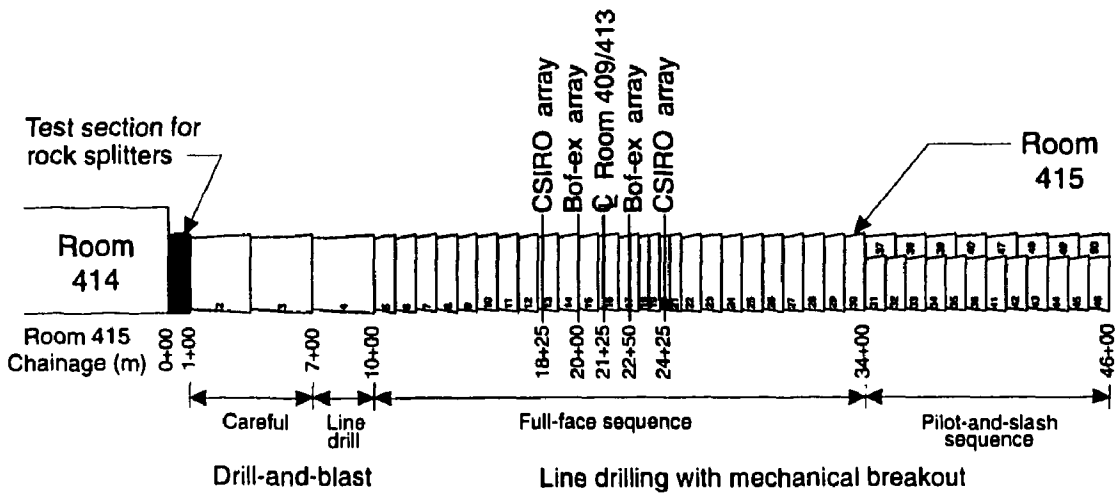

FIGURE 8: Excavation method and sequence used for the Mine-by Experiment.

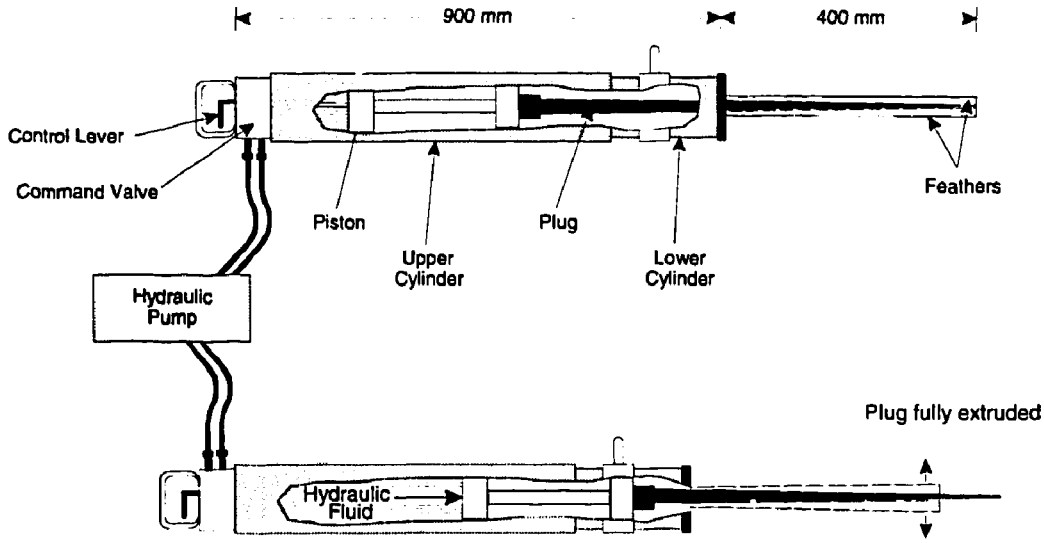

FIGURE 9: Rock splitters for the Mine-by Experiment.

FIGURE 10: Photograph showing the rock splitters in use.

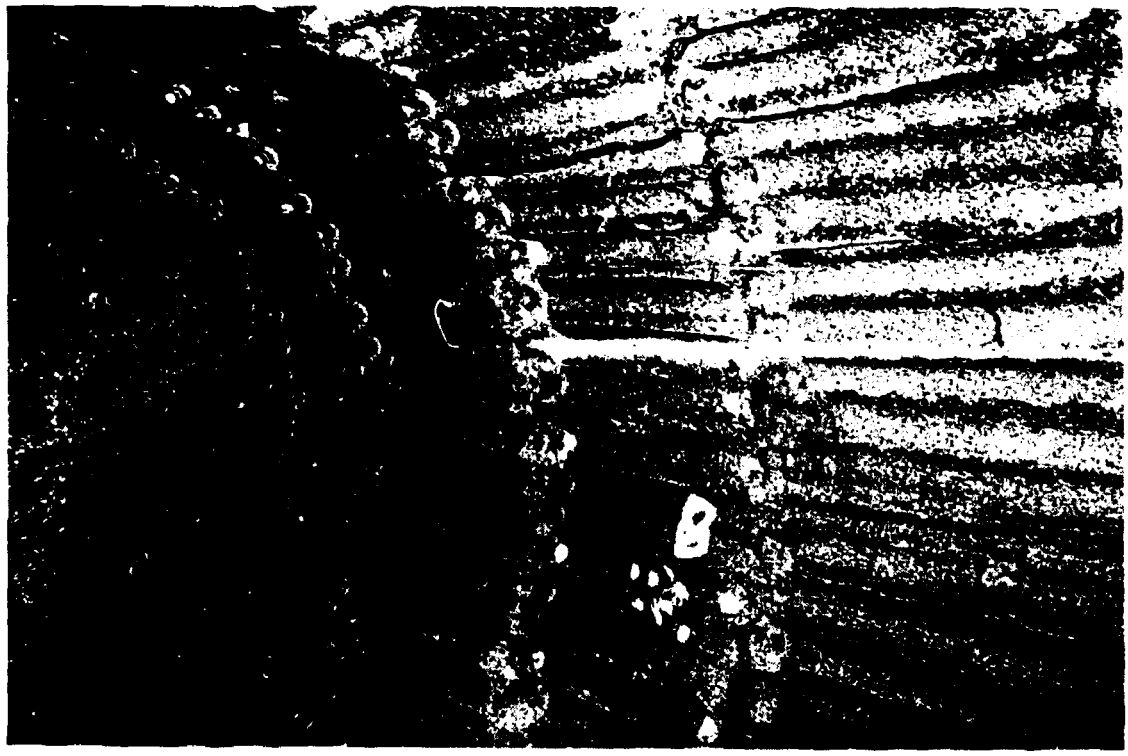

FIGURE 11: Photograph showing the stepped geometry of the tunnel walls.

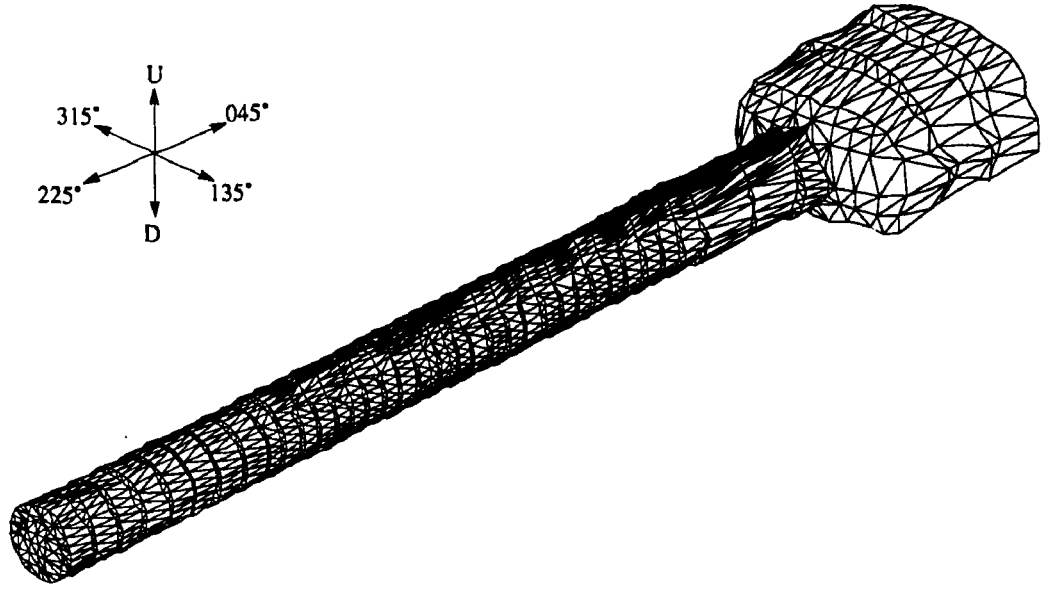

FIGURE 12: Three-dimensional model of the completed Mine-by Experiment test tunnel.

2.2.3 Enthalpy Control

Enthalpy control, i.e., the control of temperature and humidity, was considered important in order to limit the number of variables in the interpretation of the measured responses. A 75 kW capacity system consisting of an air handling unit, a blast cooler, and two compressor/condensor units was installed at the 420 Level to keep the test tunnel as close as possible to the ambient rock conditions, i.e., 10.5°C and > 90% RH, during excavation. Although some short-term spikes in the air temperature were recorded during peak excavation activities, the overall rock temperature was maintained within about 1.5°C of ambient temperature. Relative humidity was consistently above 90%. Details on the performance of the system are given in Keith and Onagi (1994).

2.3 INSTRUMENTATION

The Mine-by Experiment included both geomechanical and geophysical instrumentation. The first was selected on the basis of previous excavation response tests at the URL, and included extensometers and convergence arrays to measure displacements, triaxial strain cells to measure induced strains, and thermistors to measure temperature. The second tier of instrumentation, based on acoustic emission/microseismic (AE/MS) technology, was used to study the development of the damaged zone around the Mine-by Experiment test tunnel (Talebi and Young 1990). Other geophysical surveys were also conducted periodically during the experiment.

2.3.1 Extensometers

Borehole fracture monitor extensometers (Bof-exs) have been used successfully in other major experiments at the URL to monitor very small displacements (Thompson et al. 1989), and formed the majority of the displacement-monitoring system for the Mine-by Experiment. The Bof-ex is an incremental-type extensometer, i.e., it measures relative displacement between anchors. Each extensometer string incorporated ten direct current linear variable differential transformer (DC-LVDT) displacement transducers, eleven mechanical screw-type anchors, Invar or stainless-steel rods, and centralizers (Figure 13). The repeatability of each transducer is $\pm 0.6 \mu$m, and the range is ± 6 mm. Seven thermistors were also included in each extensometer string.

A total of 12 radial Bof-ex strings were installed for the Mine-by Experiment in two instrument arrays at chainages 20+00 and 22+50 in Room 415 (Figure 14). The first array comprised two vertical and two horizontal extensometers, and the second array contained two vertical, two horizontal, and four extensometers inclined at $\pm 45°$ from horizontal. In addition, an axial extensometer was installed in a borehole drilled from Room 414 parallel to the test tunnel axis, approximately 1.3 m from the NW wall of the tunnel at the height of the tunnel centreline.

The 12 radial Bof-ex strings were installed in 75.7-mm-diameter (NQ-3 size) boreholes drilled from the instrument galleries (Rooms 405, 409, 413, and 416) towards the planned location of the test tunnel. These holes penetrated the design section of the test tunnel by

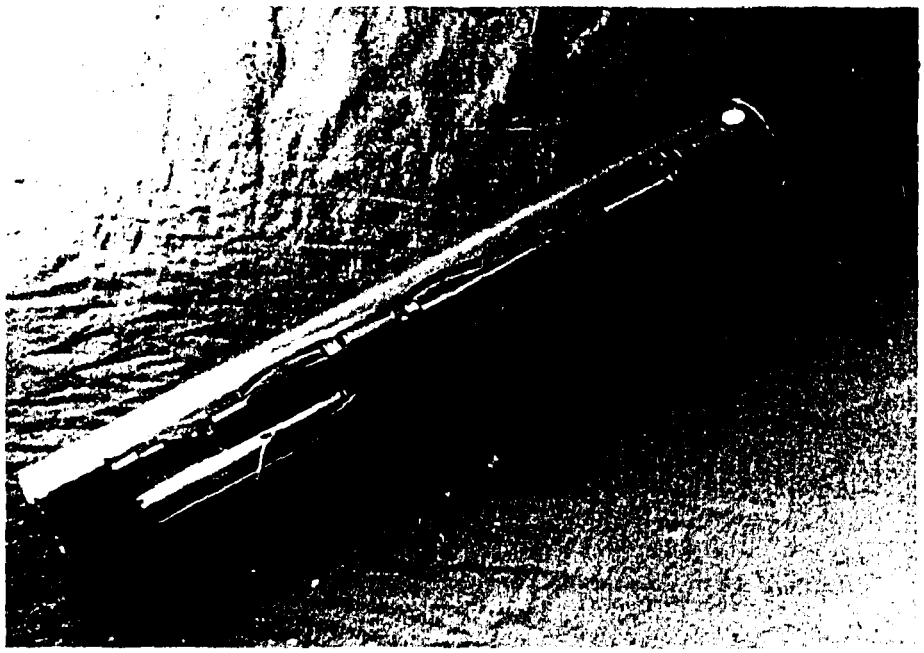

FIGURE 13: Photograph showing one segment of a Bof-ex string. The acrylic tube is 76 mm in diameter.

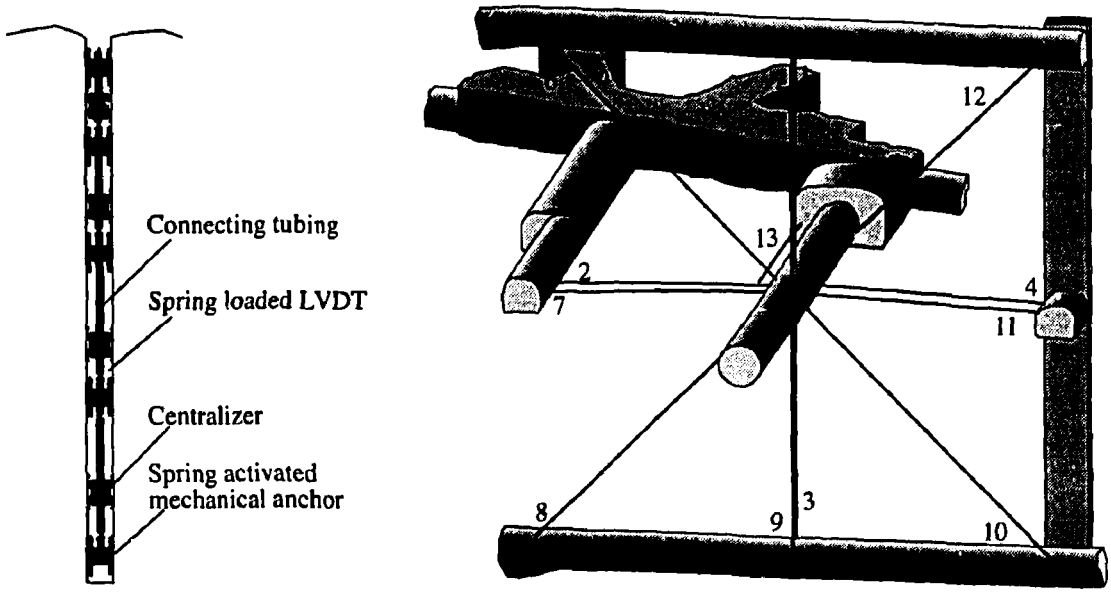

FIGURE 14: Arrangement of Bof-ex boreholes for the Mine-by Experiment and schematic illustration of a typical extensometer installation. There are 12 radial extensometers oriented orthogonal to the tunnel axis, and one axial extensometer parallel to the tunnel axis.

200 mm so that the ends of the boreholes could be located once Room 415 was excavated. Accurate collar surveys and downhole laser surveys in each borehole were conducted to determine the exact collar location and alignment deviation (Read et al. 1994). Alignment deviation was less than 0.5°, so that error in the measured radial displacements was negligible. Borehole anchors were spaced 340 mm apart near the tunnel wall, and less closely away from the tunnel. The innermost anchor was approximately 100 mm outside the design perimeter of the test tunnel in each string. Because they were installed prior to the start of excavation, the response measured by the extensometers represents the total displacement induced by the excavation of Room 415 within the coverage area of the extensometers. These extensometers are typical of *anterior-type* instruments, i.e., instruments installed in the region ahead of the advancing tunnel face.

In addition to the Bof-exs, a series of eight excavation damage extensometers (Ed-exs) were installed at approximately chainage 22+50 (Figure 15). These instruments are a miniaturized version of the Bof-ex, approximately 1 m in length, comprising ten alternating current linear variable differential transformer (AC-LVDT) displacement transducers and eleven anchors. The Ed-exs were installed in 37.7-mm-diameter (EWG size) boreholes drilled radially outward behind the advancing face to provide detailed displacement measurements within 1 m of the tunnel wall. A complete description of the instrument and an example of its application are given in Thompson et al. (1993). Results from the Bof-exs and Ed-exs, and details of their performance, are summarized in Read et al. (1994a).

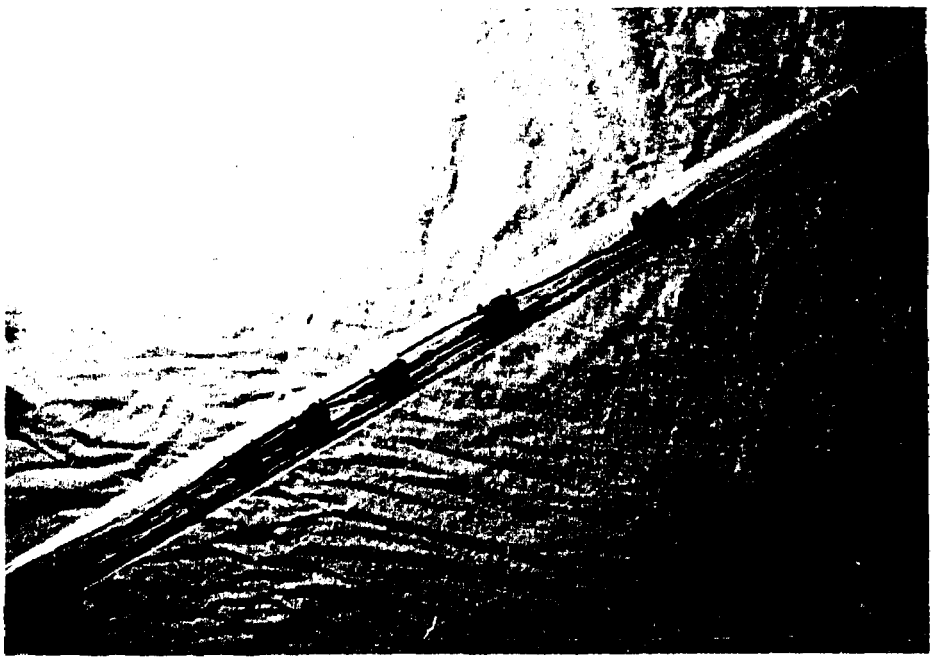

FIGURE 15: Photograph showing an Ed-ex string. The acrylic tube is 38 mm in diameter.

2.3.2 Convergence Arrays

Convergence arrays were installed in Room 415 at eight locations between chainages 10+20 and 31+96 (Table 3). Figure 16 gives details of a typical convergence array installation. Convergence arrays in the experiment comprised 12 pins installed as close to the tunnel face as possible in a measuring plane orthogonal to the tunnel axis. Specially-cut lengths of Invar wire were used in combination with a Kern distometer (Martino 1989) to measure the distance between opposing pins along six diametral measurement lines. Changes in tunnel diameter were recorded following each excavation round, providing a record of tunnel wall convergence versus excavation advance. Additional readings were also taken within each round to determine the tunnel convergence with respect to time. A summary of the convergence data from the Mine-by Experiment is presented in Read et al. (1993b) along with details of instrument performance.

Previous experience with the Kern distometer at the URL has shown a repeatability of ±0.1 mm (Martino 1989). Careful calibration of the instrument and Invar wires was performed underground before and after each use with a standard calibration apparatus. In this way, corrections for temperature were incorporated automatically into each reading. The same operator was also used as much as possible to reduce operator bias in the measurements. A standardized reading procedure, repeating each measurement four times, was followed during the Mine-by Experiment.

The convergence pins consisted of 19-mm-diameter steel reinforcing bar, 200-mm long, with a 100-mm-long stainless steel setting bolt welded to the end to attach the distometer connector. The convergence pins in each array were installed in 32-mm-diameter percussion drill holes, 300-mm deep, an average of 80 mm from the tunnel face. There was, however, some variation in chainage across the face, as shown in face contours for each round (Read et al. 1994a). The floor pins were set in slightly deeper holes, countersunk about 50 mm to protect them from construction equipment. All pins were fixed in place with resin grout. Each array, with the exception of array 415-5, was designed to have convergence pins at 0, 20, 60, 90, 120, 160, 180, 200, 240, 270, 300, and 340° counterclockwise from a NW-trending horizontal line. Array 415-5 had two measurement lines rotated 10° clockwise to avoid interfering with previously installed extensometers.

2.3.3 Triaxial Strain Cells

The CSIRO Hollow Inclusion (HI) triaxial strain cell (Worotnicki and Walton 1976) has been used almost exclusively at the URL to measure incremental strains due to excavation (Figures 17 and 18). Each cell comprises nine 120-Ω strain gauges arranged in three strain gauge rosettes cast into a plastic cylinder. One common lead is attached to a precision (stable) resistor potted in the cell to provide a baseline signal, and two separate leads are connected to a thermistor embedded in the cell. The position and orientation of the strain gauges, and colour coding for the cell, are shown in Read et al. (1994b). Each strain gauge can measure strains up to about 2%. Information gained from these instruments has been used to calculate changes in the *in situ* stress field and to validate results from computer modelling (Wiles and Kaiser 1992; Wiles and Kaiser 1994a; Wiles and Kaiser 1994b).

TABLE 3

LOCATION OF CONVERGENCE ARRAYS IN THE MINE-BY TEST TUNNEL

Array	Chainage (m)	Excavation Round
415-1	10.204	5
415-2	12.531	7
415-3	15.380	10
415-4	18.485	13
415-5	22.565	17
415-6	26.062	22
415-7	28.924	25
415-8	31.964	28

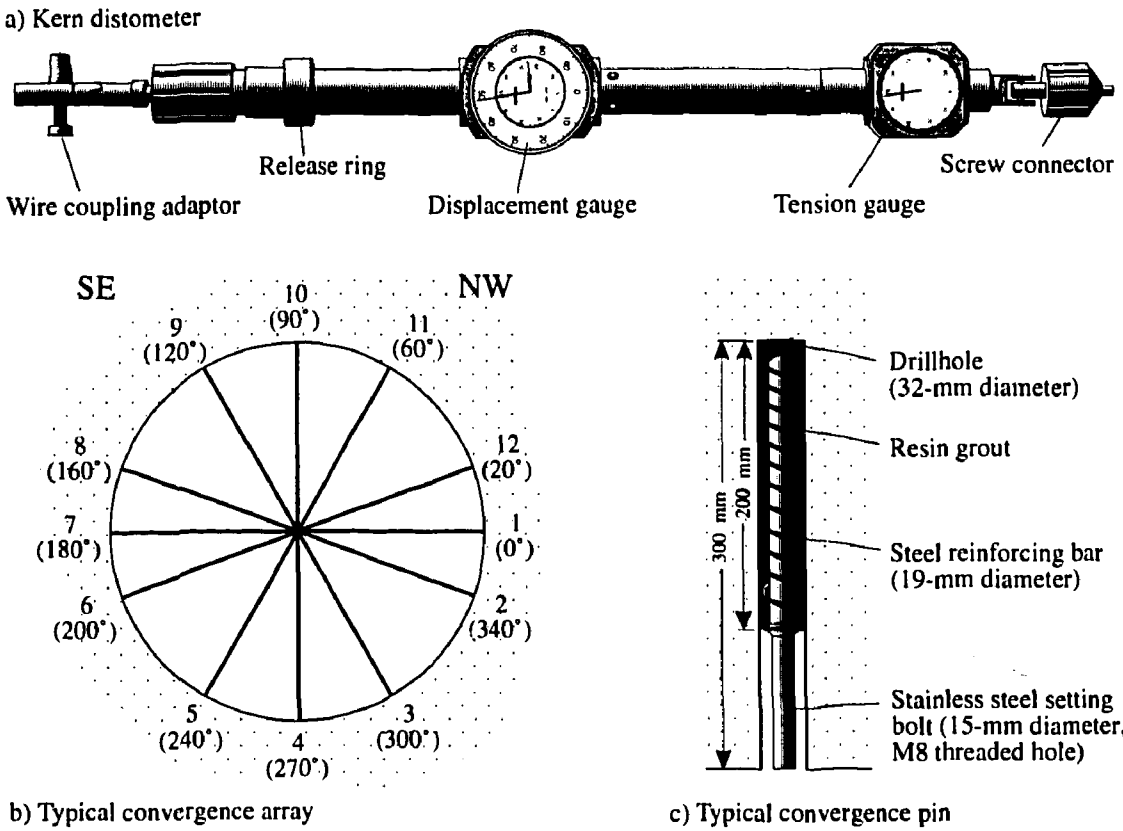

FIGURE 16: Details of the instruments and arrangement of a typical convergence array from the Mine-by Experiment.

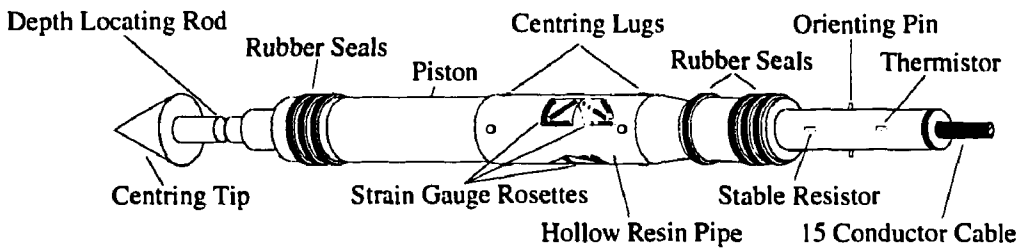

FIGURE 17: Schematic illustration of a CSIRO HI triaxial strain cell.

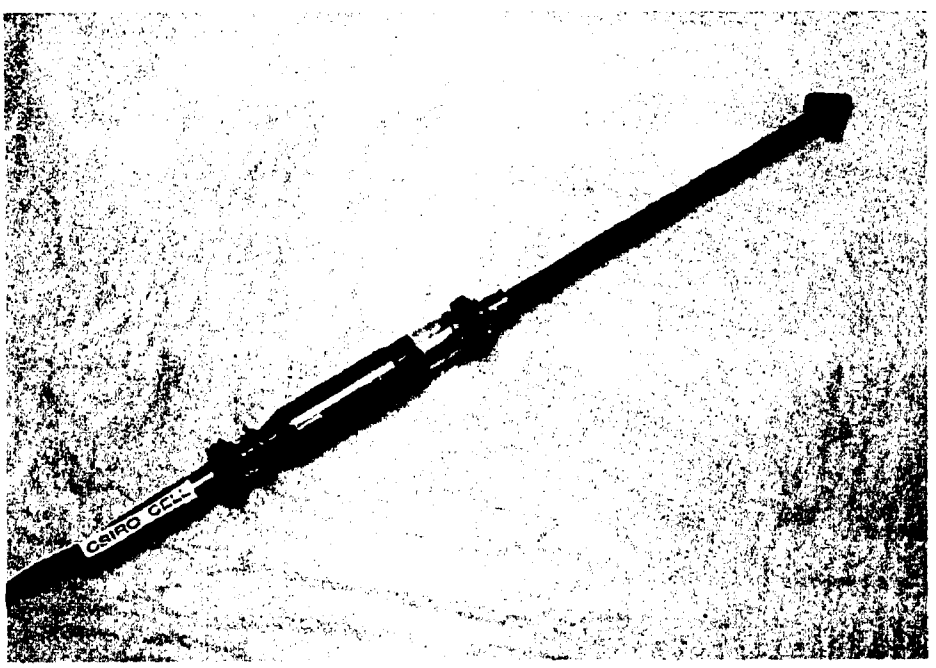

FIGURE 18: Photograph of a CSIRO HI triaxial strain cell. The cell body fits in a 38-mm-diameter (EWG size) borehole.

To install a strain cell, the following procedure was used. A 48.0-mm-diameter (AQ size) borehole was drilled and the end of the hole was flattened with a special drill bit. A 0.5-m-long 37.7-mm-diameter (EWG size) extension hole was then drilled from the flattened end of the AQ-size segment, and the cell was bonded to the wall of the extension hole approximately 0.22 m from its start (Snider et al. 1989). Each of the instrument boreholes was inclined upward to prevent accumulation of water in the hole, and all cells were oriented relative to the top of the borehole during installation to facilitate analysis of the monitoring results.

A total of 12 CSIRO HI cells were installed for the Mine-by Experiment in two arrays (Figure 19). The arrays of boreholes were drilled from Rooms 405, 413 and 416, and were designed to place CSIRO HI cells near the wall of Room 415 at chainages 18+25 and 24+25 in the test tunnel. The first array was designed to have two cells located approximately 2.5 m horizontally either side of the test tunnel centreline, one cell located 2.5 m vertically above the test tunnel centreline, and one cell located at the tunnel centre. The second array contained eight CSIRO HI cells, with design locations 2.5 and 3.25 m from the test tunnel centreline at 0, 90, 180 and 270° clockwise from horizontal. Results from the strain cells, including instrument performance, are summarized in Read et al. (1994b).

As detailed in Read et al. (1994), precise survey control was an important component of the experiment. Accurate collar surveys and downhole laser surveys were conducted for each borehole to determine the spatial position of the collar and alignment deviation. With the exception of the hole containing SM3 (deliberately placed at the tunnel centre), the boreholes did not penetrate the design perimeter of the test tunnel. In order to determine

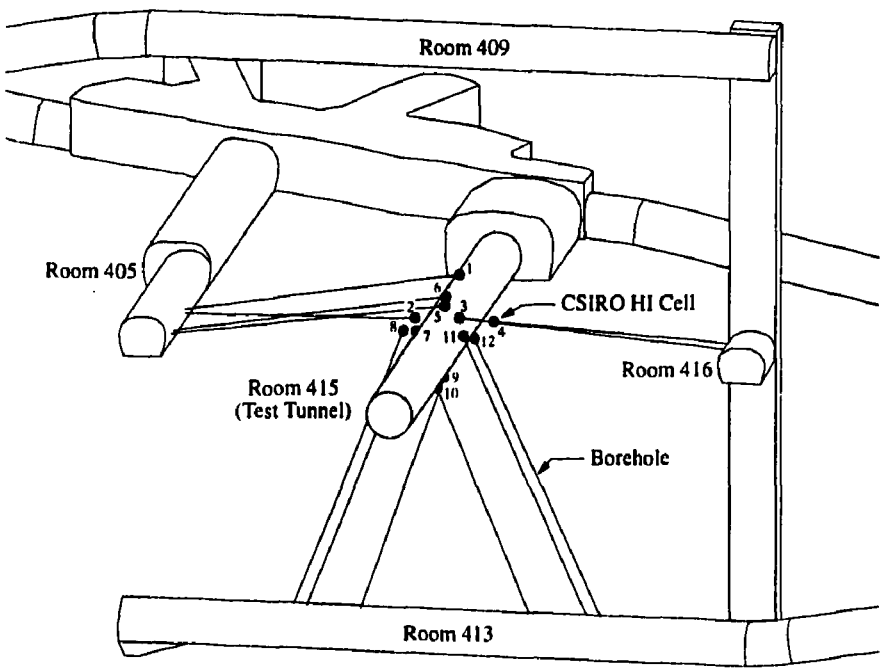

FIGURE 19: Arrangement of 12 CSIRO HI triaxial strain cells in two arrays. Cell 3, located at the centre of the tunnel, was overcored and removed during excavation.

the exact location and orientation of each cell in Universal Transverse Mercator (UTM) coordinates, 150-mm-diameter boreholes were drilled from inside the completed test tunnel to intersect each cell, which was then removed.

2.3.4 Acoustic Emission/Microseismic Monitoring

The results from an AE/MS system, installed to monitor excavation-induced seismicity in the rock mass during extension of the URL shaft, were used to design a more elaborate system for the Mine-by Experiment. The function of this new system was to evaluate the physics of fracturing associated with development of a damaged zone around the test tunnel (Talebi and Young 1990). Two of the objectives of the design were to improve the accuracy of source location determinations and to develop more rigorous source mechanism analysis procedures.

The AE/MS system comprised 16 triaxial accelerometers (Figure 20). The accelerometers, with a frequency range of 50 Hz to 10 kHz (±3 dB), were grouted in place at the end of 96-mm-diameter (HQ size) diamond-drilled boreholes. The accelerometer array (Figure 21) was designed for focal sphere coverage and a source location accuracy of about ±0.25 m near the centre of the tunnel. The sampling frequency was set to 50 kHz, allowing the study of seismic events with moment magnitudes as small as -6. This number of sensors also allowed the use of a moment tensor inversion scheme to perform source mechanism analysis (Feignier and Young 1993). A summary of preliminary AE/MS results for the Mine-by Experiment is given in Martino et al. (1993). Analysis of the AE/MS results is discussed in Section 3.3.1.

Ultrasonic tomography and acoustic emission (AE) data obtained during laboratory hydraulic fracturing tests on two 600-mm-diameter samples of URL granite (Chow et al. 1990) showed that the development of microcracks could be monitored with high-frequency sensors acoustically coupled to the rock surface, and that source locations and mechanisms could be determined for these AE events. This approach was applied to the *in situ* rock mass in the NW sidewall of the test tunnel in conjunction with the Ed-exs to determine the level of activity at various distances from the tunnel wall. From these data, the distribution of acoustic emissions relative to the excavation were determined (Carlson and Young 1993). Findings from this study are summarized in Section 4.3.2.

2.3.5 Geophysical Monitoring

Information on the P and S wave velocities in the rock mass was obtained through several tomographic surveys carried out with AECL's miniCHARTS system between the various excavated openings prior to excavation of the test tunnel (Hayles et al. 1995). This study required two 40- and twenty 1.5-m-long vertical boreholes in the floor of Room 409 and roof of Room 413. Cross-hole tomographic studies were conducted in the Bof-ex instrument boreholes before and after excavation of the test tunnel to detect changes in the rock mass resulting from excavation-induced damage (Hayles et al. 1995). The results from these studies are summarized in Section 4.3.2.

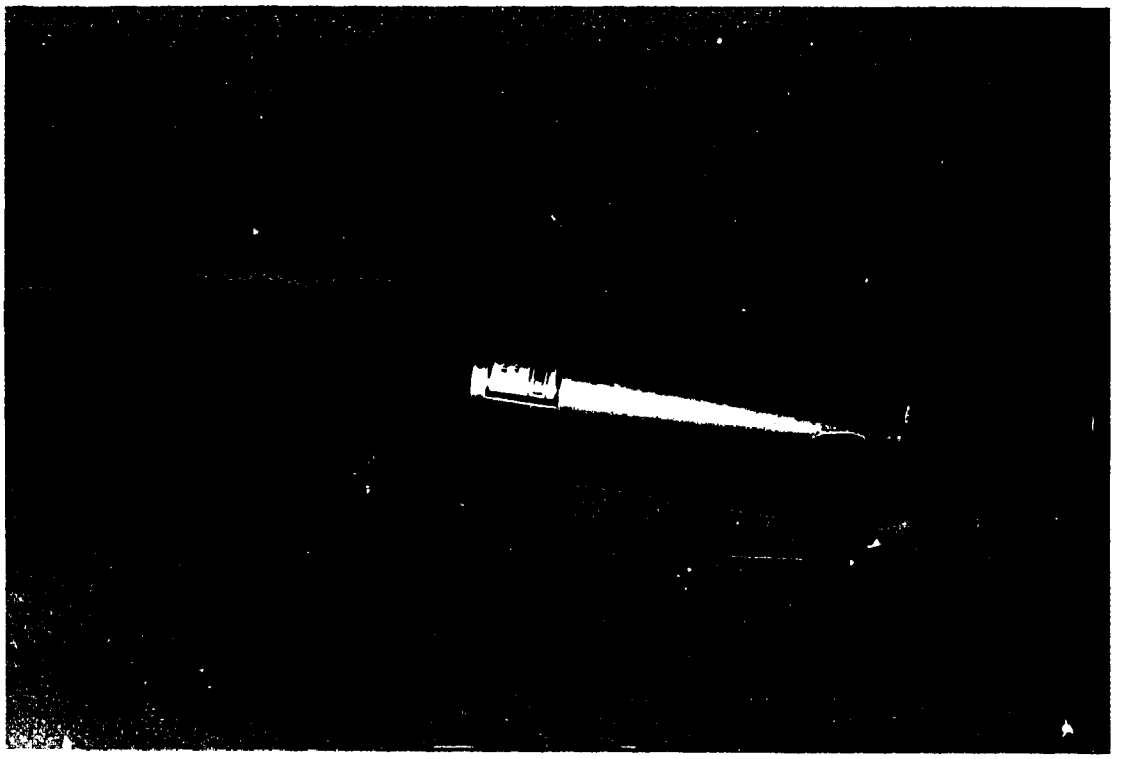

FIGURE 20: Photograph showing a typical triaxial accelerometer sensor. This sensor fits in a 96-mm-diameter (HQ size) borehole.

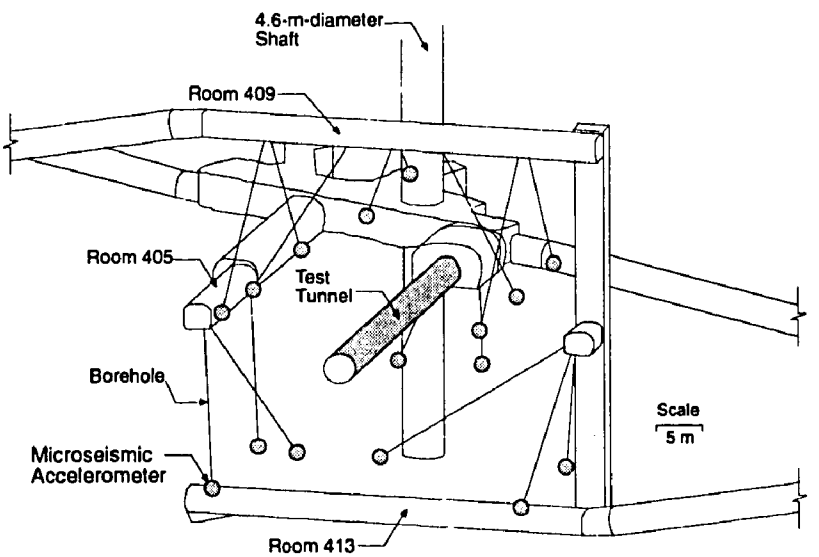

FIGURE 21: Arrangement of the AE/MS triaxial accelerometer sensors around the test tunnel at the 420 Level.

2.3.6 Other Instruments

In addition to the instruments described in the previous sections, three instrumented concrete cylinders were installed in boreholes near the Mine-by test tunnel. This type of strain-monitoring cell is called le cylindre instrumenté de l'Université de Sherbrooke (CIUS). These cells were included in the Mine-by Experiment as a test of their suitability as strain-monitoring devices. The results of the monitoring phase are discussed in Saleh et al. (1992), but no back analysis of stresses from the measured strains was attempted.

2.4 SUMMARY

Pre-excavation characterization of the 420 Level was used to locate a representative site for the experiment, and provided a basis for the final detailed design and development of the Mine-by Experiment. The area chosen for the experiment was found to typify the 420 Level in terms of geology, geotechnical properties and *in situ* stresses.

Underground development was conducted according to the design plan, with slight modifications to the planned excavation sequence for the last 12 m of the tunnel. Instead of using a careful drill-and-blast technique and full-face sequence in this region, line-drilling with mechanical breakout was employed in conjunction with a pilot-and-slash sequence. This change was made to ensure potentially disruptive percussive effects from blasting were eliminated. In addition, Rounds 18 to 21 were excavated as 0.5-m-long rounds instead of the usual 1.0-m length to enhance the number of data points collected near the final two instrumented arrays.

The instrumentation for the Mine-by Experiment was installed in accordance with the design plan. New instruments, such as the Ed-ex, were developed in the course of the experiment and were used to provide additional information on the rock mass behaviour. With the exception of nine of the 210 displacement transducers, the extensometers performed exceptionally well during the main monitoring period of the experiment. Likewise, only one of the 12 CSIRO HI triaxial strain cells appeared to malfunction over the course of the experiment. In total, over 500 data channels were monitored during the main excavation stage of the Mine-by Experiment.

3. ROCK MASS BEHAVIOUR AND FAILURE MECHANISMS

The pre- and post-failure behaviour of Lac du Bonnet granite has been studied extensively in laboratory tests on rock samples. However, interpretation of *in situ* behaviour based on laboratory findings is not straightforward, even for the relatively uniform and unfractured rock mass at the 420 Level of the URL. For example, results from triaxial compression tests have been used to determine a Hoek-Brown failure envelope (Hoek and Brown 1980), given by

$$\sigma_1 = \sigma_3 + \sqrt{m\sigma_c\sigma_3 + s\sigma_c{}^2} \qquad (1)$$

where σ_1 and σ_3 are the maximum and minimum principal stresses, respectively, σ_c is the uniaxial compressive strength of an intact laboratory sample, m is a shape parameter, and s

is a scaling factor to account for the presence of joints or discontinuities *in situ*. Equation 1 is a peak strength criterion, and in the unconfined case reduces to

$$\sigma_1 = \sqrt{s}\sigma_c \tag{2}$$

In cases where there are no *in situ* joints or discontinuities, i.e., $s = 1$, Equation 2 implies that the uniaxial stress required to cause failure *in situ* is equivalent to the uniaxial compressive strength measured in the laboratory.

Several factors can, however, affect the uniaxial compressive strength of laboratory samples, e.g., sample size and loading rate (Martin 1993). In a comparative study of undisturbed Lac du Bonnet granite from Cold Spring Quarry and disturbed Lac du Bonnet granite from the Mine-by Experiment at the 420 Level, Martin and Stimpson (1994) also noted that the laboratory properties, particularly the uniaxial compressive strength, were a function of sample disturbance. Samples taken from a stress environment where the far-field maximum stress was greater than about $0.1\sigma_c$ displayed lower laboratory strengths than samples from areas where the far-field maximum stress was less than $0.1\sigma_c$. This finding implies that the disturbed samples are not representative of the *in situ* undisturbed rock mass. Figure 22 gives the Hoek-Brown failure envelopes for undisturbed and for disturbed Lac du Bonnet granite. Note that the envelope for disturbed granite falls below that for undisturbed granite, and can be described using the undisturbed σ_c value, but decreasing the s and m values to reflect the presence of small microcracks typical of sample disturbance in brittle rocks. Alternatively, if sample disturbance had not been recognized in the 420 Level granite samples, the parameters describing the lower failure envelope would be $\sigma_c = 157.0$ MPa, $m = 35.21$ and $s = 1$.

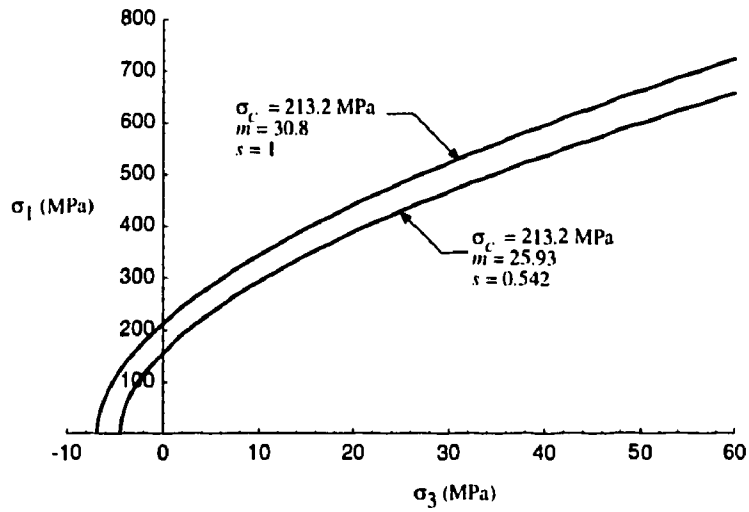

FIGURE 22: Hoek-Brown failure envelope for undisturbed and disturbed Lac du Bonnet granite taken from Cold Spring Quarry and from the 420 Level of the URL, respectively. Envelopes are based on 147 tests for undisturbed granite and 37 tests for disturbed granite (after Martin 1993).

In comparing the back-calculated strength of the rock mass at the perimeter of an underground opening to the uniaxial compressive strength measured in the laboratory, it is common to find the *in situ* strength to be less than half of the laboratory strength (Pelli et al. 1991; Stacey 1981; Myrvang 1991; Herget 1988). This discrepancy in strengths is generally attributed to 'scale-effects', as the laboratory strength is determined on intact samples containing small-scale flaws such as grain boundaries, whereas the rock mass generally contains much larger-scale flaws such as joints/discontinuities. In such cases, s is by definition less than 1.

For the massive granite at the 420 Level of the URL, s is taken as 1 because there are no *in situ* joints or discontinuities to consider. Nevertheless, the back-calculated strength of the rock mass at the perimeter of tunnels at this level is significantly less than that measured in short-term laboratory tests (Martin and Read 1992). Hence, the reduced *in situ* strength cannot be attributed solely to 'scale-effects'.

To determine the factors contributing to the reduced *in situ* strength around tunnels at the 420 Level, an extensive laboratory and *in situ* testing program was undertaken. These studies were intended to characterize the mechanical behaviour of Lac du Bonnet granite, and the processes involved in progressive failure, in both laboratory tests and *in situ*. The studies are summarized in the following sections, and emphasize the potential problems in relying solely on results from laboratory tests to interpret *in situ* behaviour.

3.1 COMPRESSION TESTS ON CYLINDRICAL LABORATORY SAMPLES

Testing procedures for determining the compressive deformational behaviour of rock samples are given by ISRM (Brown 1981). These include recording the axial (ϵ_{axial}) and lateral ($\epsilon_{lateral}$) strains in a sample as it is loaded with or without a fixed confining stress. For a cylindrical sample subjected to axial loading, with or without a confining stress, and under small strains, the volumetric strain (ϵ_v or $\frac{\Delta V}{V}$) is given by:

$$\epsilon_v = \frac{\Delta V}{V} \simeq \epsilon_{axial} + 2\epsilon_{lateral}. \tag{3}$$

Hence by plotting the axial, lateral and the calculated volumetric strains versus the applied axial stress, the loading path of a rock sample to failure can be followed. An example of axial, lateral and volumetric strain versus axial stress curves for Lac du Bonnet granite in uniaxial compression is given in Figure 23.

The stress-strain curves for a brittle material can be divided into five regions (Figure 23). The three most important points on the stress/strain curve are the crack-initiation stress, the crack-damage stress and the peak stress or strength. These points define the transitions between Regions II, III, IV and V.

The onset of stable crack growth, i.e., dilation, marks the beginning of Region III on the stress/strain curve. Brace et al. (1966) found that stable crack growth begins at a stress level of about 0.3 to 0.5 of the peak strength. This stable crack growth is only registered on

the lateral strain gauge, and hence, reflects the growth of axial cracks, i.e., cracks parallel to the direction of the maximum applied load. This stress level is referred to as the crack-initiation stress (σ_{ci}) and can be determined from a plot of crack-volumetric strain versus axial strain. As shown in Figure 23, σ_{ci} is the axial stress at which dilation just begins on the crack-volume plot.

The axial stress level where the total volumetric strain reversal occurs marks the beginning of Region IV and represents the onset of unstable crack growth, as defined by Bieniawski (1967). This axial stress level is typically between 0.7 to 0.85 of the short-term peak strength, and it is at this level that the axial strain departs from linearity (Figure 23). The dominant mechanism resulting in such an increase in axial strain is sliding along inclined surfaces. Lajtai et al. (1991) found that unstable crack growth started at about 0.7 of the short-term peak strength in unconfined samples of Lac du Bonnet granite from Cold Spring Quarry. Martin and Chandler (1994) referred to this stress level as the crack-damage stress (σ_{cd}) because loads above this level result in damage to the material which cannot be tolerated under a permanent load. They found that the crack-damage stress for Lac du Bonnet granite from the URL also occurred at about 0.7 to 0.8 of the short-term peak strength.

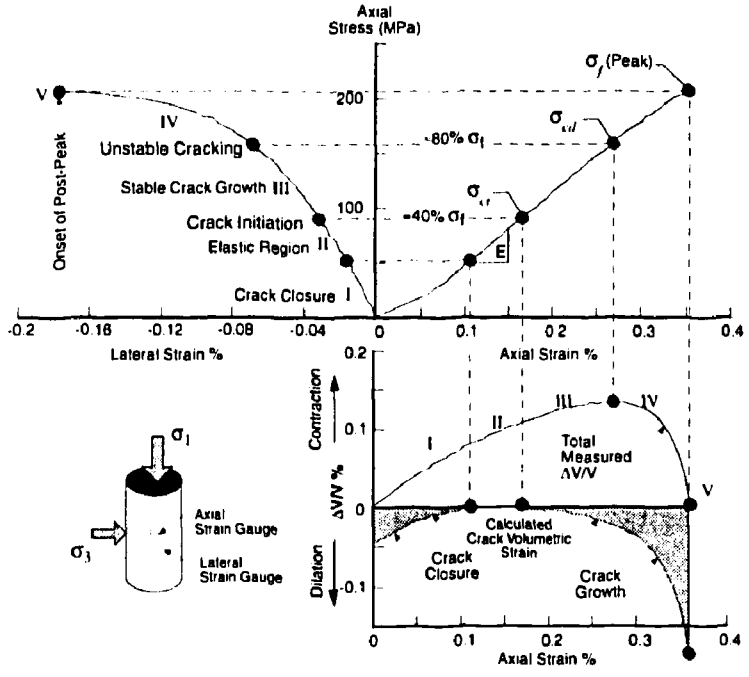

FIGURE 23: Stress-strain diagram obtained from a single uniaxial compression test for Lac du Bonnet granite showing the definition of crack initiation (σ_{ci}), crack damage (σ_{cd}) and peak strength (σ_f). Note that only the axial and lateral strains are measured. The volumetric strain and crack-volumetric strain are calculated.

The peak strength of the material (σ_f) marks the beginning of post-peak behaviour, Region V, and is almost universally used to establish the failure strength envelope. For the unconfined case, the peak strength strength is referred to as σ_c. Martin and Chandler (1994) showed that, of the three characteristic stress levels, only σ_{ci} and σ_{cd} were true material parameters independent of sample volume, and that the peak strength was a function of the particular loading conditions used in the uniaxial test.

3.1.1 Damage-Controlled Tests

Martin and Chandler (1994) presented the results from an extensive set of damage-controlled compression tests that were carried out on samples of Lac du Bonnet granite from the 420 Level to investigate the effect of crack damage on σ_{ci}, σ_{cd} and σ_f. They defined a damage parameter ω as the accumulated permanent volumetric strain

$$\omega = \sum_{i=1}^{n} (\epsilon_v^p)_i \, \%. \tag{4}$$

where ϵ_v^p is the permanent volumetric strain per damage increment i. Plots of σ_f, σ_{cd} and σ_{ci}, versus the damage parameter ω for any one test are referred to as the peak ω locus, the σ_{cd} locus and the σ_{ci} locus (Figure 24).

Based on the test results, the σ_{ci} stress occurs when the load first exceeds about 0.2 to 0.4 of the peak strength (Figure 24). The σ_{cd} stress occurs at about 0.8 of the peak strength. However, unlike the σ_{ci} stress, the σ_{cd} stress reduces significantly in the early stages of the test and reaches a threshold as the damage accumulates in the sample (Figure 24). This phenomenon was seen at all confining stress levels and was quite consistent from test to test. It should, however, be noted that the drop in σ_{cd} is smaller at higher confining stresses (Figure 25). This fact suggests that the growth of cracks and accumulation of damage is more inhibited at higher confining stresses, and hence the strength reduction experienced during the test is less, than at lower confining stress. Martin (1993) pointed out that the threshold value of σ_{cd} corresponds approximately to σ_{ci} when the sample is unconfined, and that as the confining stress is increased, the threshold value of σ_{cd} exceeds σ_{ci}.

Martin and Chandler (1994) showed that the measured σ_{cd} locus could be simulated using the Griffith sliding crack model proposed by Cook (1965). They also showed that the limit for sliding can be expressed as

$$\sigma_1 = 2\sqrt{\frac{2\alpha G}{c\pi(1-\nu)}} \tan\left(45 + \frac{\phi}{2}\right) + \sigma_3 \tan^2\left(45 + \frac{\phi}{2}\right) \tag{5}$$

where ϕ is the friction angle, α is the fracture surface energy, c is the crack half-length, G is the shear modulus and ν is Poisson's ratio.

The shear strength of a frictional material is also often represented by the well-known Mohr-Coulomb criterion

$$\sigma_1 = 2S_o \tan\left(45 + \frac{\phi}{2}\right) + \sigma_3 \tan^2\left(45 + \frac{\phi}{2}\right) \tag{6}$$

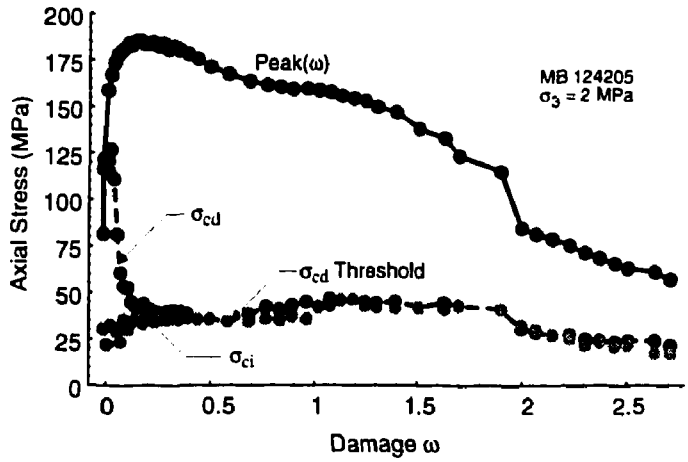

FIGURE 24: Example of the crack-initiation stress and the crack-damage stress as a function of damage. Note that at low confining stresses, the crack-damage stress quickly approaches the crack-initiation stress.

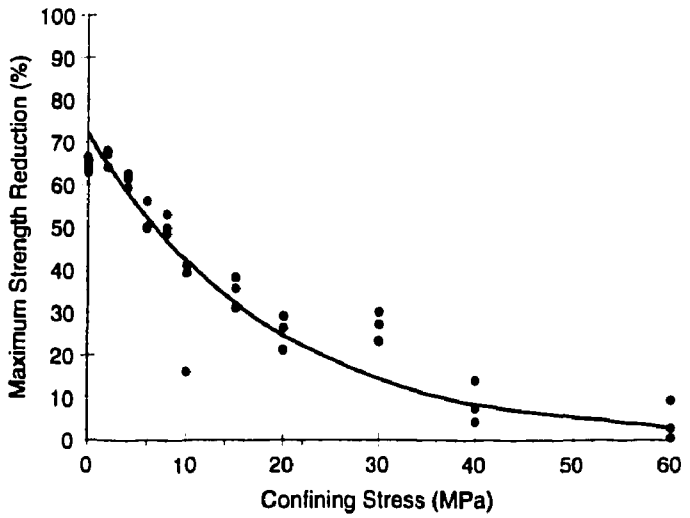

FIGURE 25: Reduction in crack-damage stress from initial to residual value for 37 damage-controlled compression tests. The maximum strength reduction is the difference between the initial and residual values, normalized to the initial value. Note that strength reduction is more pronounced at low confining stress.

where S_o is the empirical cohesion intercept or intrinsic strength. It is interesting to note that the two shear criteria in Equation 5 and Equation 6 are identical. The empirical cohesion of Equation 6 is expressed in terms of fracture surface energy and crack half-length in Equation 5. The Cook criterion provides a fundamental energy balance basis for the Mohr-Coulomb criterion.

Martin and Chandler (1994) used the concepts introduced by Equations 5 and 6 to interpret the stress/strain results from a laboratory compression test in terms of friction and cohesion (Figure 26). In Figure 26, the damage has been normalized with respect to the maximum value of the damage parameter ω at the end of the test and the strength has been normalized to the peak strength. Figure 26 illustrates that the peak friction angle ($\phi_{b+i} = 63°$) is reached only when most of the cohesion is lost. With increasing damage, the friction angle gradually decreases to about 42°. This friction value is similar to the residual friction angle of 42 to 45° for Lac du Bonnet granite reported by others, e.g., Gyenge et al. (1991); Lajtai and Gadi (1989). Thus, for the test presented in Figure 26, it appears that the

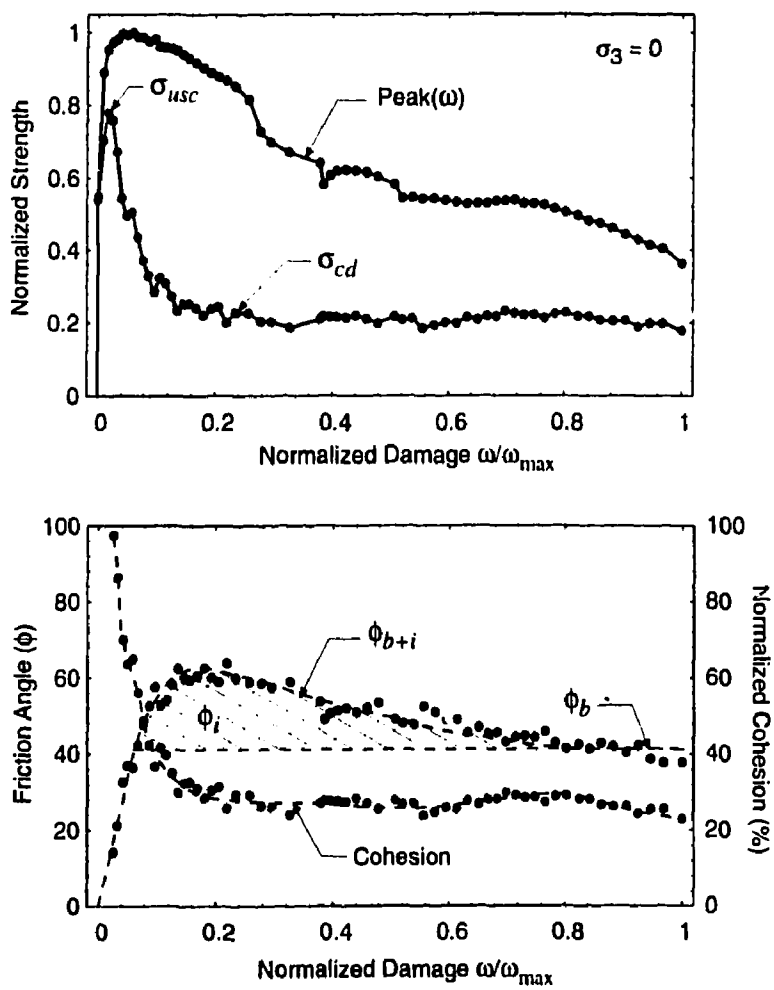

FIGURE 26: Mobilization of friction and cohesion as a function of normalized damage.

residual friction angle is nearly reached. The peak friction angle of 63°, although high, is not unrealistic, e.g., Dusseault and Morgenstern (1979) reported that natural slopes of uncemented locked sands have inclinations greater than 54°. Therefore, 63° does not seem unreasonable for perfectly interlocked mineral grains subjected to small displacements.

Figure 26 also shows that the friction and cohesion components of strength are not mobilized at the same amount of damage. For example, prior to any damage, the rock strength is composed only of cohesion, i.e., friction has not been mobilized and therefore $\phi = 0$ initially. For this condition, Equations 5 and 6 reduce to

$$\sigma_1 - \sigma_3 = \text{ constant } = 2S_o \tag{7}$$

An examination of Equation 5 reveals that the fracture surface energy and crack half-length only apply to the cohesive component of the material and that the frictional strength is not dependent on these parameters. This point is particularly important because it demonstrates that a small increase in crack half-length can have a significant impact on the cohesion or unconfined strength of a material. For example, if a crack half-length of 1 mm is used to represent a material with an average grain size of 2 mm, and the crack half-length is increased to 3 mm, the strength (cohesion) is reduced by approximately 42% (Figure 27).

It is also worth noting that a further 3-fold increase in crack half-length to 9 mm only results in a further decrease in cohesion of about 25% relative to the initial value for a 1 mm crack half-length. Thus initial crack extension of as little as 1 or 2 mm is significant. Laboratory test results (Martin 1993) showed that the cohesion in an unconfined sample

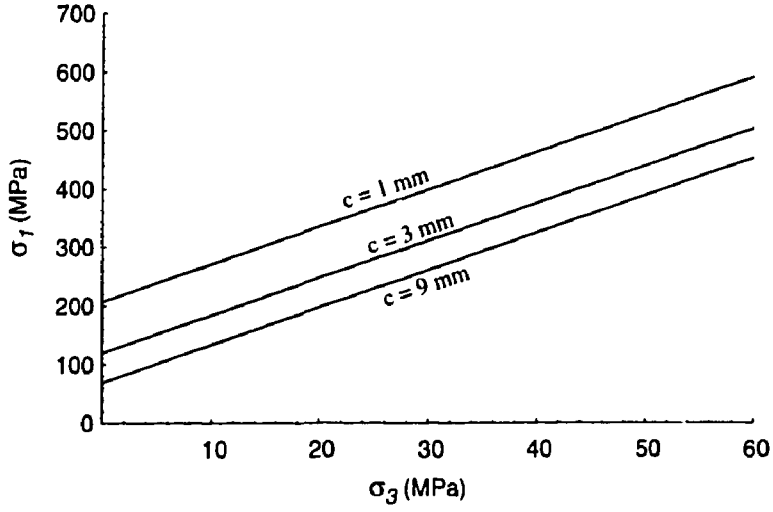

FIGURE 27: Predicted failure envelopes for Lac du Bonnet granite with different crack half-lengths using the sliding crack model given by Equation 5. Note that the increase in crack half-length only affects the cohesion (y-intercept) and not the friction angle (slope).

can be reduced by 70% when the permanent axial strain is as little as 0.03%. Assuming an initial 1 mm crack half-length, this reduction would result from extension of the crack half-length to 11 mm. It is likely that the laboratory-measured permanent strain needed to cause the cohesion loss is greater than that which would be required to cause a similar loss *in situ* because, *in situ*, the rock is more brittle than the disturbed laboratory samples. These results support the idea that the strength reduction of the disturbed samples given in Figure 22 is a consequence of cohesion loss.

In summary, the monotonic loading path in uniaxial and triaxial laboratory tests revealed that the true strength of a brittle rock in compression is defined by the crack-damage stress σ_{cd}, which occurs at about 0.7 to 0.8 of the peak strength (σ_f in Figure 23). At the crack-damage stress level, a macro sliding crack forms and provides a mechanism for ultimate collapse of the sample. Loads above the crack-damage stress value can be maintained for a short duration, i.e., typically less than 1 h, as the frictional resistance of the macro crack is mobilized. However, the mobilization of the frictional resistance results in a dramatic decrease in the initial cohesion of the sample. This decrease in cohesion is a function of the volumetric crack damage in the sample, and hence, is very sensitive to crack half-length.

3.2 LABORATORY AND *IN SITU* STUDIES OF BOREHOLE FAILURE

The laboratory study of cylindrical samples showed that the long-term strength was about 0.7 to 0.8 of the peak strength σ_f. In this section, a comparison is made between the strength around boreholes in the laboratory and *in situ*.

3.2.1 Physical Model Studies

Laboratory studies to investigate the strength around openings typically consist of either hollow-cylinder tests similar to those carried out by Ewy and Cook (1990) or large block tests containing a cylindrical cavity (Figure 28). The latter test is more common as it allows either uniaxial or biaxial loading. The failure in these block tests occurs in the region of

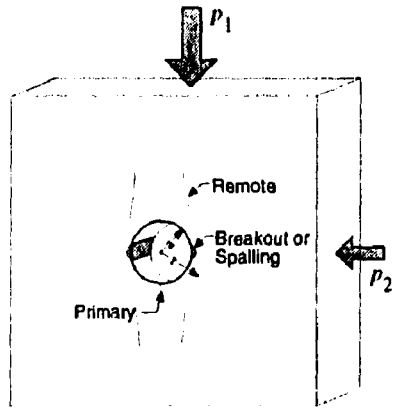

FIGURE 28: Types of fractures found around circular openings in laboratory model tests.

maximum tangential stress around the boundary of the circular opening which is similar to the failure observed *in situ*. The tangential stress around a circular opening, for plane strain conditions, is given by Jaeger and Cook (1979) as

$$\sigma_\theta = \frac{p_1 + p_2}{2}\left(1 + \frac{a^2}{r^2}\right) + \frac{p_1 - p_2}{2}\left(1 + \frac{3a^4}{r^4}\right) \tag{8}$$

where p_1 and p_2 are the applied loads (Figure 28). At the boundary of the opening, $a = r$ and $\sigma_\theta = 3p_1 - p_2$ where $p_1 > p_2$. For the unconfined case, $p_2 = 0$ and the maximum tangential stress at the breakout is $3p_1$.

The effect of size and stress gradients on the failure strength around boreholes has been examined by many researchers using various physical models, e.g., Carter (1992); Ewy and Cook (1990); Haimson and Herrick (1989); Mastin (1984); Hoek (1965). One of the commonly reported outcomes of such tests is that the tangential stress at the boundary of the borehole required to cause breakouts is at least twice the unconfined compressive strength of the material as determined in standard uniaxial tests on solid cylinders.

Martin et al. (1994) reported the results from a series of block tests carried out to investigate the effect of borehole diameter on the sidewall stress required to initiate failure in samples of Lac du Bonnet granite. Thirteen unconfined samples were tested with circular openings ranging in diameter from 5 to 103 mm. Strain gauges were used to monitor the deformations and to determine the onset of breakouts (Martin 1993). The placement of strain gauges on each sample was modified depending on sample size. The results from the thirteen tests are plotted in Figure 29 along with the results from similar tests carried out by Haimson and Herrick (1989), Carter (1992), and Mastin (1984). All results show similar trends and indicate that, with borehole diameters greater than about 75 mm, the sidewall stress required to initiate spalling is about equal to the unconfined compressive strength of the

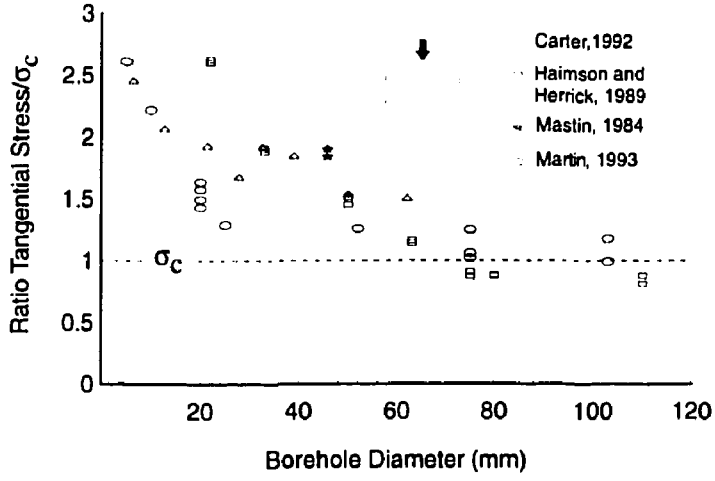

FIGURE 29: Summary of uniaxial testing of blocks containing a circular borehole.

granite. However, the results also show that a significant strength-scale effect is observed for borehole diameters of 20 mm and less.

Carter (1992) and Lajtai (1972) proposed that the strength-scale effect observed in Figure 29 was related to microcracking occurring in the region of high stress gradients, and that the strength-scale effect could be approximated by a stress averaging technique given by

$$\overline{\sigma}_\theta = \frac{p(a+t)}{t}\left\{1 - \frac{a^2}{2(a+t)^2} - \frac{a^4}{2(a+t)^4}\right\} \tag{9}$$

where $\overline{\sigma}_\theta$ is the average maximum tangential stress for a borehole subjected to a uniaxial load p, a is the borehole diameter and t is the distance over which the tangential stress is averaged. Equation 9 was fitted to the Lac du Bonnet granite data and gave a value of t = 13.9 mm (Figure 30). The strength-scale relationship for the uniaxial compressive strength for Lac du Bonnet granite was given by Martin et al. (1994) as

$$\sigma_c/\sigma_{c63} = (63/d)^{0.17} \tag{10}$$

where σ_{c63} is the uniaxial compressive strength of a 63-mm-diameter specimen, and d is the diameter of the specimen in mm. Equation 10 is also shown in Figure 30 for comparison.

What is most obvious in Figures 29 and 30 is the significant increase in the tangential stress required to cause failure for circular openings less than about 75 mm in diameter. Because most laboratory studies are carried out with circular openings of 25-mm diameter or less, a scale effect of at least 2 should be anticipated when comparing the ratio of tangential stress required to cause breakouts to the unconfined compressive stress (Figure 29). However, it would appear that when the circular opening is at least 75 mm in diameter, the strength is close to the unconfined compressive strength and the apparent scale effect is either absent or significantly reduced.

The phenomenon of increased strength around small-diameter boreholes has also been reported for samples tested in biaxial and polyaxial loading. Lee and Haimson (1993) carried

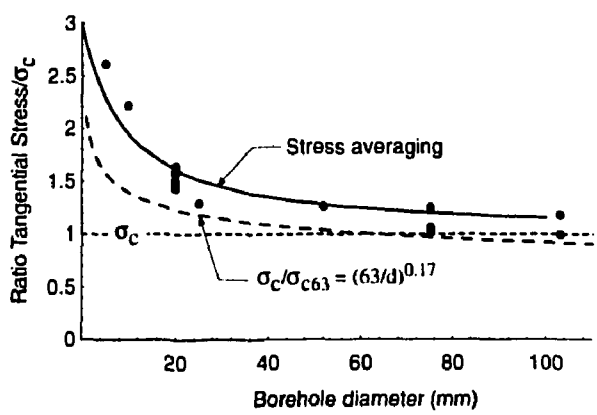

FIGURE 30: Tangential stress required to cause borehole breakouts in Lac du Bonnet granite compared with the strength predicted by Equations 9 and 10.

out polyaxial testing of forty 100-mm cubes of Lac du Bonnet granite containing a 21-mm-diameter borehole. They also found that the tangential stress required to initiate breakouts varied from 1.5 to $2\sigma_c$. Martin (1993) tested one block of Lac du Bonnet granite containing a 60-mm-diameter borehole using a biaxial loading system, and found that the tangential stress required to initiate breakouts was $1.6\sigma_c$. Both the results of Lee and Haimson (1993) and Martin (1993) are in keeping with the scale effect shown in Figure 29. It appears that the strength-scale effect is not related to the type of loading conditions, i.e., one-, two- or three-dimensional, but is a consequence of the stress gradient in the vicinity of the hole or excavation.

3.2.2 *In Situ* Borehole Studies

In order to determine whether or not the strength-scale effects observed in the laboratory were present *in situ*, a series of vertical boreholes with diameters of 75, 150, 300, 600 to 1250 mm were diamond-drilled to a nominal depth of 5 m from the floor of Room 405 at the URL (Figures 31).

Failure, if it occurred, formed immediately during the drilling of the boreholes. The failure in the boreholes extended from the floor of Room 405 to various downhole depths depending on the diameter of the borehole, i.e., the larger the borehole diameter, the longer the breakout, suggesting a scale-effect. The lengths of the breakouts were recorded immediately after drilling and were monitored periodically after completion of the hole. Only minor changes in the lengths of the breakouts were observed over nearly two years of monitoring.

The stress concentrations below the floor of Room 405 decrease with the depth along each borehole. Thus the tangential stress at the point where each breakout ends will also vary.

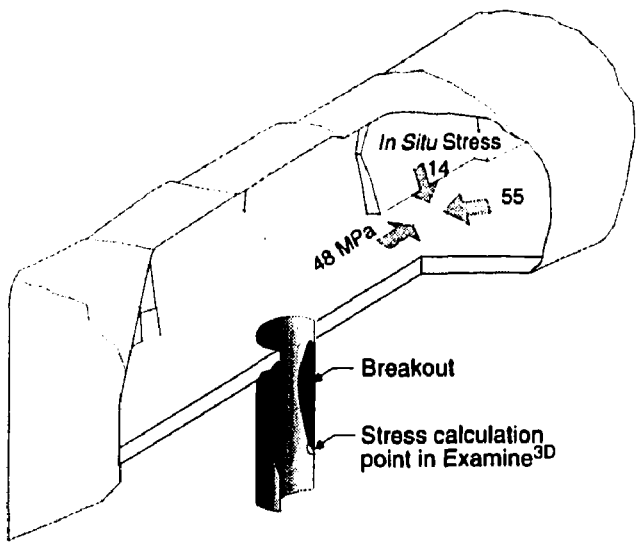

FIGURE 31: Illustration of the three-dimensional geometry used to calculate the stress at the initiation of failure.

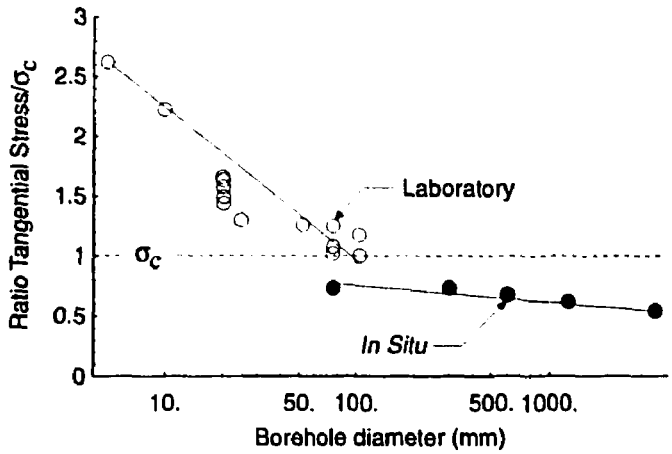

FIGURE 32: Ratio of the calculated tangential stress to σ_c at which breakouts initiate for various borehole diameters.

An elastic three-dimensional stress analysis of Room 405 and each borehole in the floor was carried out using EXAMINE^{3D} (Curran and Corkum 1993) to determine the maximum tangential stress at which the failure terminated (Figure 31). This stress value was considered equivalent to the tangential stress at the initiation of failure in the laboratory studies.

Figure 32 shows the calculated maximum tangential stress required to initiate breakouts normalized to σ_c for the borehole diameters investigated. Also shown, for comparative purposes, is the laboratory data from Figure 30 and the result from the Mine-by test tunnel (discussed in the next section). Figure 32 shows that there is a modest effect of scale for the *in situ* data, and that there is a noticeable change in the effect of scale between the laboratory and *in situ* results. This is also supported by the observation that a 75-mm-diameter borehole drilled near the centre of, and in the same direction as, the test tunnel showed breakouts similar to those observed in the test tunnel.

In summary, laboratory tests involving boreholes with diameters less than about 75 mm tend to show a marked scale/size effect, and require a maximum tangential stress of up to $2\sigma_c$ to initiate breakouts. In contrast, *in situ* boreholes with diameters greater than 75 mm required a maximum tangential stress of as little as $0.5\sigma_c$ to initiate breakouts. In addition, the change in slopes between the *in situ* and laboratory strength versus borehole diameter shown in Figure 32 suggests that there is a fundamental difference between the results from the two sets of experiments. In the laboratory tests, the incremental loading path is monotonic and linear. However, *in situ*, the loading path is complex and non-linear. This issue is discussed in the next section.

3.3 PROGRESSIVE FAILURE AROUND A CYLINDRICAL TUNNEL

The stress distribution around the advancing face of a tunnel is complex. For instance, elastic three-dimensional analyses of the Mine-by test tunnel (Figure 33) showed that, at a few centimetres from the tunnel perimeter, the principal stress magnitudes change rapidly

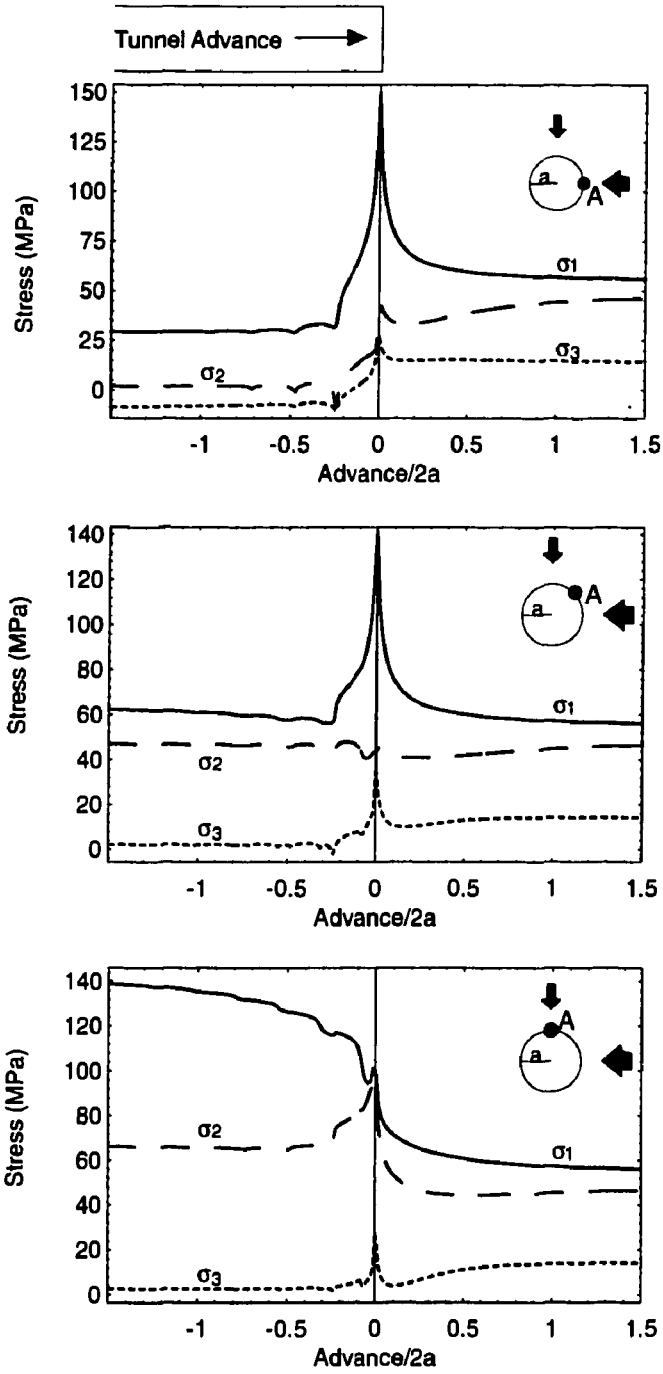

FIGURE 33: Change in principal stress magnitudes around a flat-faced cylindrical tunnel as the tunnel advances. The slight perturbations in the responses are a result of the field points in the model being very close to the tunnel surface.

near the tunnel face. These stress changes are not accounted for in the two-dimensional plane strain analyses that are usually carried out to back calculate the *in situ* strength around a tunnel.

In Section 3.1, it was shown that the first step in the brittle failure process is crack initiation. In the following sections, the role of *in situ* crack initiation in the progressive failure process observed in the Mine-by test tunnel is investigated.

3.3.1 Microseismic Monitoring

It is well known that cracking occurs around an opening excavated in a highly stressed brittle rock mass. For example, earlier work at the URL had established that considerable microseismic activity was associated with the excavation, by drill-and-blast techniques, of a circular shaft from the 240 Level to the 420 Level (Talebi and Young 1992). In order to determine whether or not the microseismic activity was caused by the blasting or simply related to stress redistribution, the test tunnel for the Mine-by Experiment was excavated mechanically, without blasting (see Section 2.2.2).

As described in Section 2.3.4, an array of 16 triaxial accelerometers was installed to monitor the stress-induced microseismicity associated with the excavation of the test tunnel (Figure 34). As shown in Figure 34(a), the accelerometers were grouted in place at the end of diamond-drilled boreholes. The accelerometer array was designed for focal sphere coverage and a source location accuracy of about ±0.25 m near the centre of the tunnel. The sampling rate was set to 50 kHz and the overall system frequency response was 50 Hz to 10 kHz (±3 dB). The dynamic range of the system allowed the study of seismic events with moment magnitudes as small as -6.

The sequencing of the construction schedule for the test tunnel provided about 12 h of quiet time for microseismic monitoring after the initial perimeter drilling and about 12 h of quiet time for microseismic monitoring after mechanical breaking of the rock stub for each round of tunnel advance. Since each round required about 3 days to complete, this provided coverage of approximately 30% of the total excavation cycle per round. This procedure was used for most of the excavation rounds near the start and end of the test tunnel. However, near the instrument arrays, the microseismic monitoring period was extended, e.g., at Round 17 the monitoring period was 193 h. A typical example of the locations of the microseismic events recorded during the 12 h monitoring period after advancing the excavation by 1 m is given in Figure 35.

Preliminary processing of the microseismic data was carried out in the field using automated source location computer software developed at Queen's University (Collins and Young 1992). Over 25 000 events were detected and some 3500 events were source located in this way (Figure 36). Note that the clustering of events in the roof and floor in Figures 35 and 36 confirms that the maximum stress is inclined relative to the horizontal. Additional processing of the 25 000 events was carried out using seismicity software developed in South Africa (ISS 1994). With this automated processing, the main source parameters, related to event magnitude, size and stress drop, were calculated using the assumption of shear failure. Although a previous detailed study of 33 microseismic events from the test tunnel

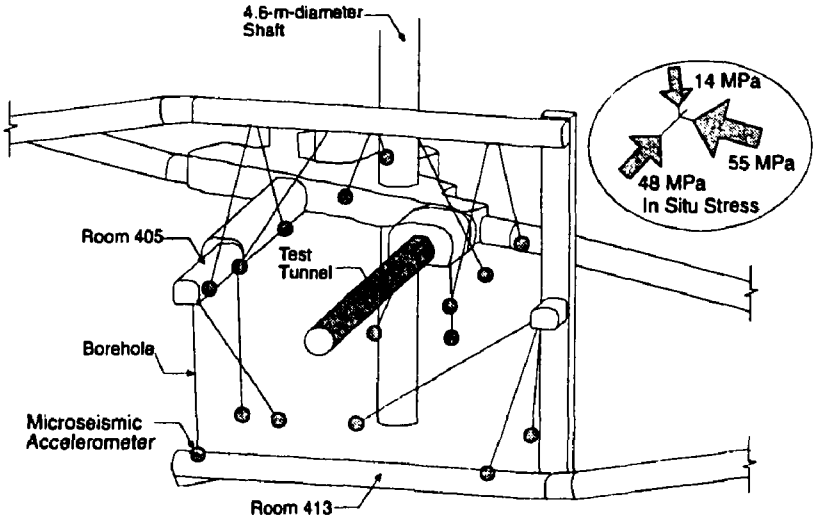

(a) 420 Level Layout

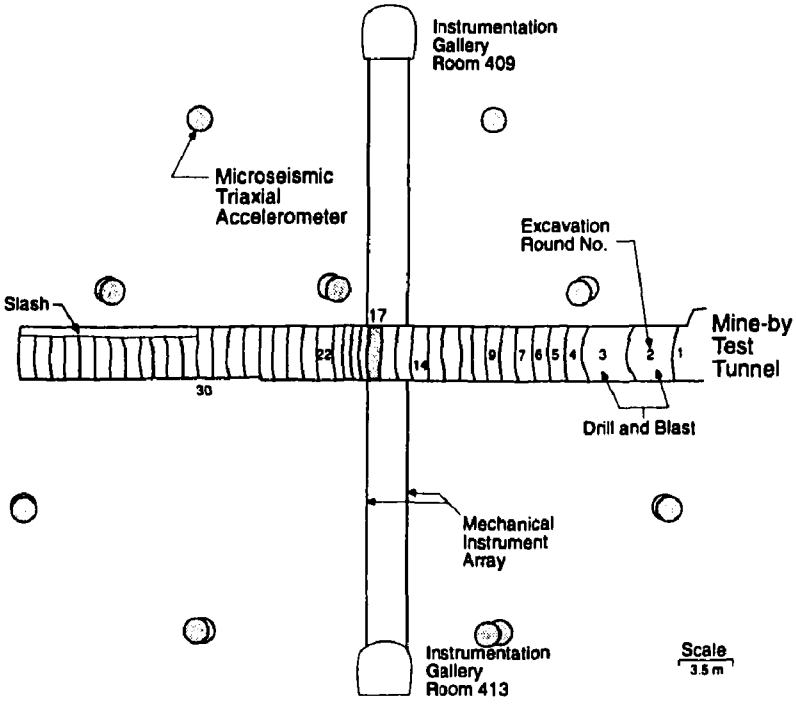

(b) Vertical Section

FIGURE 34: Layout of the 420 Level showing the location of the Mine-by test tunnel, the microseismic triaxial accelerometers and Round 17. The *in situ* principal stress magnitudes used for analysis are $\sigma_1 = 55$, $\sigma_2 = 48$ and $\sigma_3 = 14$ MPa.

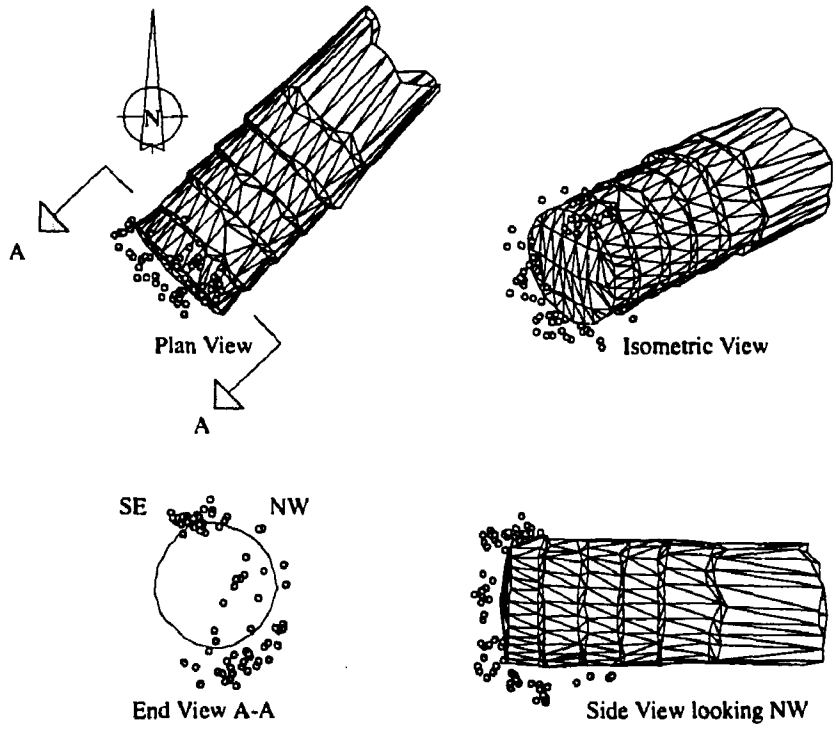

FIGURE 35: Location of the microseismic events recorded during the 12 h monitoring period after excavation of Round 8.

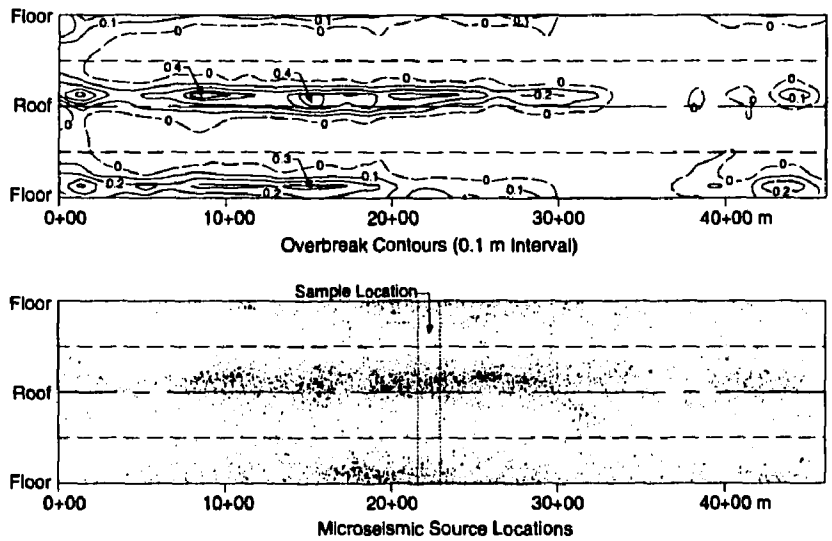

FIGURE 36: Extent of breakouts and location of the computer-picked microseismic events for the test tunnel plotted on unrolled perimeter maps. Also shown is the location of the sample volume chosen for a detailed analysis.

by Feignier and Young (1993) revealed that about 50% of the events had a significant non-shear component, this study was carried out to determine general trends in the data set (Collins et al. 1994). Only the microseismic events between tunnel chainage 10.51 and 34.28 m were analyzed (Rounds 6 to 30 in Figures 34(b) and 36), as the stress conditions, geology and excavation sequence are more complex near the ends of the test tunnel.

3.3.1.1 Source Parameters

Each excavation round between chainage 10.51 and 34.28 m was processed individually, and the location of each microseismic event relative to the tunnel face position X was normalized with respect to the tunnel diameter $2a$. Results are shown in Figure 37. Events ahead of the face are indicated by a positive value of $X/2a$, while those behind the face are negative. Only those microseismic events recorded in the roof of the test tunnel are summarized here because the formation of a breakout notch in the roof was not constrained by construction activities. However, analyses of the complete data set show similar trends for the roof and floor notches (Collins et al. 1994). Figure 37 shows the distribution of microseismic events for Rounds 6 to 30 relative to the tunnel face.

Note that most microseismic activity occurs near the tunnel face and decreases rapidly with distance from the face to about $X/2a = -2$. Considerable microseismic activity also occurs ahead of the tunnel face, starting at about $X/2a = 0.5$, with most of the events within 0.2 diameters of the face. The source parameters for this data set were analyzed using the automated ISS software.

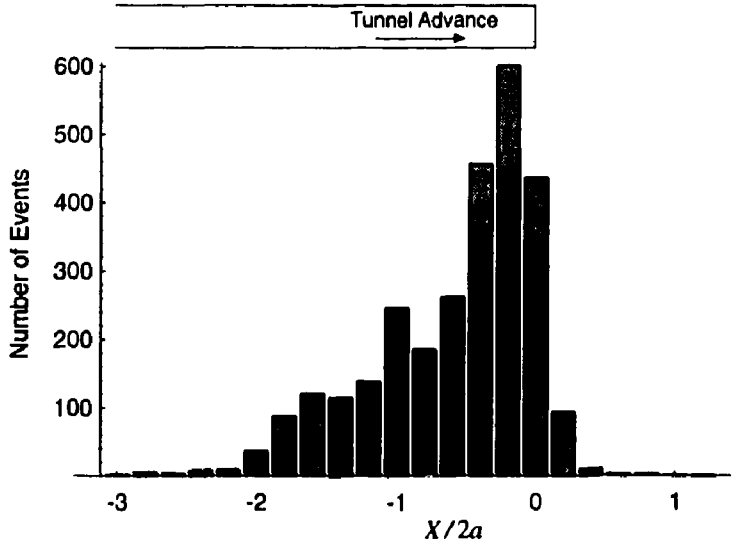

FIGURE 37: Histogram of the microseismic events recorded for Rounds 6 to 30. The location of each event relative to the tunnel face position (X) is normalized with respect to the tunnel diameter ($2a$).

In mining-induced seismicity studies, the seismic event is usually modelled as a simple circular fault (Brune 1970). The shear stress released at the source of such an event can be estimated by the static stress drop ($\Delta\tau$), which is equal to the difference between the initial shear stress acting on the fault and the final shear stress after slip has occurred. As shown by Keilis-Borok (1959), the static stress drop can be calculated from the seismic moment (M_o) and the source radius (r_o) by:

$$\Delta\tau = \frac{7M_o}{16r_o^3} \tag{11}$$

The static stress drop represents the uniform reduction in shear stress acting to produce seismic slip over a circular fault. For most mining-induced tremors, the static stress drop ranges from 0.01 to 10 MPa (McGarr 1994). Figure 38 shows the radiated seismic energy and seismic moment with lines of constant stress drop for the events recorded near the test tunnel (Collins et al. 1994). For the microseismic events recorded, nearly all the events fall between lines for a constant stress drop of 200 Pa and 200 kPa, which is somewhat lower than the values given by McGarr (1994). Interestingly, most of these events are also smaller than seismic events measured in laboratory samples (McGarr 1994). Figure 39 shows the same data set but with the events normalized to the tunnel face position. It appears that the greatest stress drop occurs in the vicinity of the tunnel face. It is also evident that the events that initiate ahead of the tunnel face show a very small stress drop. In the following section, a detailed analysis of Round 17 is carried out to investigate the cracking that occurs near the tunnel face.

3.3.1.2 Source Locations

Excavation Round 17, a central tunnel segment between chainage 21.79 and 22.84 m, was selected for detailed analysis (Figure 36). All of the microseismic events within this nominal 1-m volume were manually source located, resulting in a source location accuracy of ±0.2 m (Collins and Young 1993). Survey profiles of the tunnel perimeter were also taken during the excavation of the test tunnel. These profiles provided quantitative evidence of the formation of the notch, and allowed a comparison of the microseismic events with the notch formation (Figure 36). Surveys of the profile of the notch, combined with the source locations of the microseismic events, provided a unique opportunity to track the development of the notch in the 1-m volume.

The manual source locations gave a total of 113 microseismic events in the 1-m volume for the eight month period between 1992 January and August (Martin et al. 1995). A summary of these events, including a breakdown of those that occurred in the roof and those that occurred in the floor of the tunnel, is given in Figure 40 along with the times that Rounds 17, 18, 22 and 50 were excavated, and the times for the surveyed profiles given in Figure 41.

Inspection of Figure 40 reveals that no microseismic events were recorded in the 1-m volume until the tunnel face was only 1 m from Round 17, and that nearly all of the microseismic events in the roof had occurred by the time Round 22 had been excavated, approximately 3 m past Round 17 (see Figure 34(b) for the location of Round 22). Figure 40 also shows

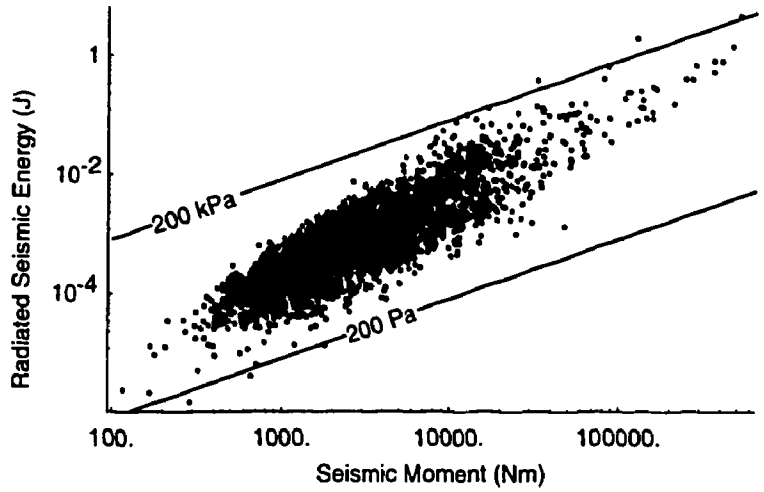

FIGURE 38: Radiated seismic energy versus seismic moment with lines of constant stress drop (after Collins et al. 1994).

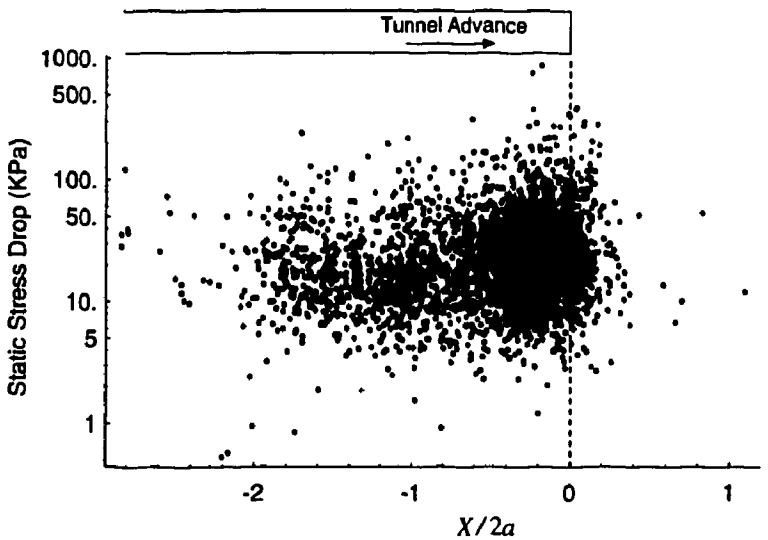

FIGURE 39: Static stress drop for rounds 6 to 30. The location of each event relative to the tunnel face position X is normalized with respect to the tunnel diameter $2a$.

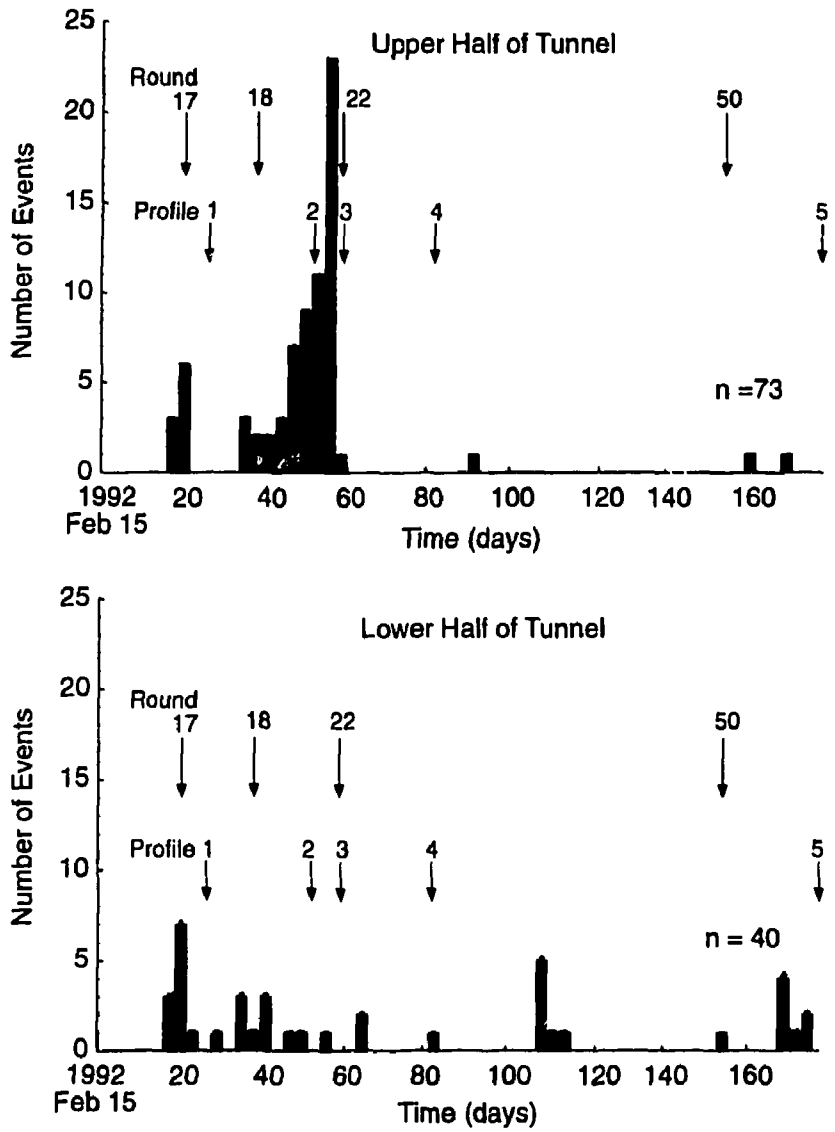

FIGURE 40: Frequency histogram for all the events recorded in the upper half (roof of tunnel) and lower half (floor of tunnel) of the nominal 1-m-long tunnel section (chainage 21.79 to 22.84 m) between 1992 February 15 and August 15. Microseismic activity starting at 170 d is related to removal of 'muck' from the tunnel floor.

that the events in the floor are more evenly distributed. This suggests that the tunnel 'muck' on the floor of the tunnel has an inhibiting effect on the failure process. Once the excavation of the tunnel had been completed, approximately 0.5 m of 'muck' on the floor was removed, starting 1995 August 4. This removal was sufficient to trigger another sequence of microseismic activity, suggesting that the spalling process is extremely sensitive to confining stress.

Figure 40 showed that most of the microseismic activity occurred when the tunnel face was within ±1 tunnel diameter of the 1-m section. Because profiles of the tunnel perimeter were also taken in this same time interval, it is possible to compare the location of the microseismic events and the development of the notch (see Figure 41). Figure 42 shows the progressive development of the notch measured at chainage 22.60 m and the incremental microseismic data that occurred between each profile date. At profile 1, the face of the tunnel is at chainage 22.84 m and at profile 5, the face of the test tunnel is at chainage 46.13 m. At the time of profile 1, the tunnel face has advanced 0.24 m beyond the surveyed section and the tunnel profile is essentially circular, i.e., the notch has not started to develop. At profile 2, the tunnel face has advanced 0.5 m beyond the surveyed section and the tunnel profile shows the initiation of the notch in the roof. Note also, that at profile 2, the microseismic events in the roof cover the area where the notch eventually develops as the tunnel is advanced. This observation suggests that the microseismic activity is a precursor to notch development, and may indicate damage to the rock mass prior to notch formation. Also, note that the notch continues to develop in profiles 4 and 5 without associated microseismic activity. This observation indicates an absence of microseismicity in the periods monitored around the time these profiles were taken, but does not preclude activity in the periods that were not monitored.

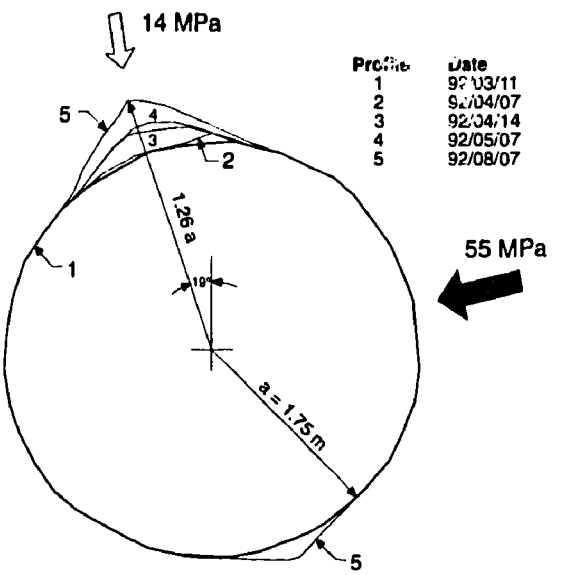

FIGURE 41: Progressive development of the notch geometry in the roof and floor of the Mine-by test tunnel at Round 17 over a five month period.

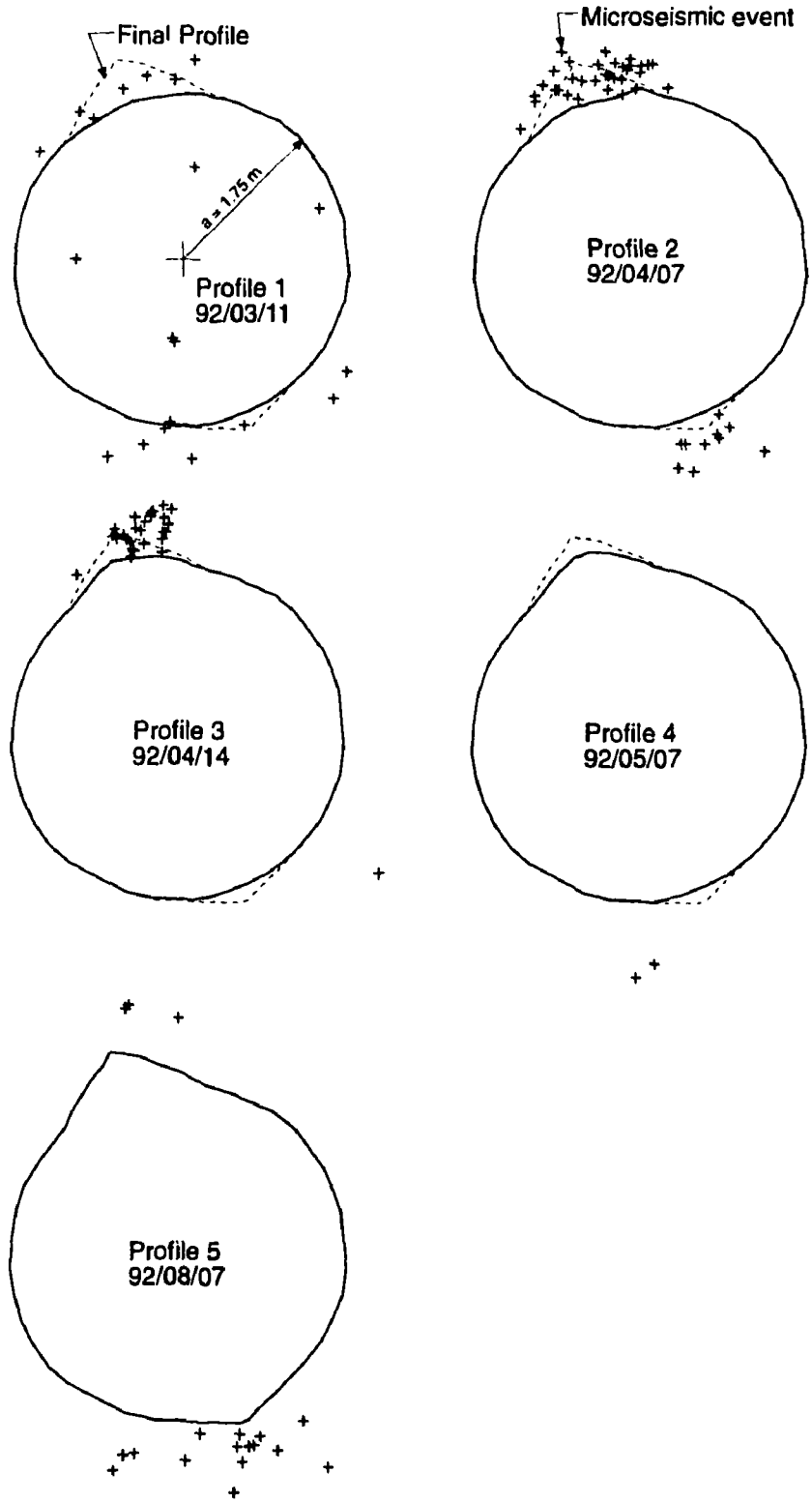

FIGURE 42: Profiles of the test tunnel recorded at different times at Round 17. Also shown are the incremental microseismic events recorded between the dates the profiles were measured.

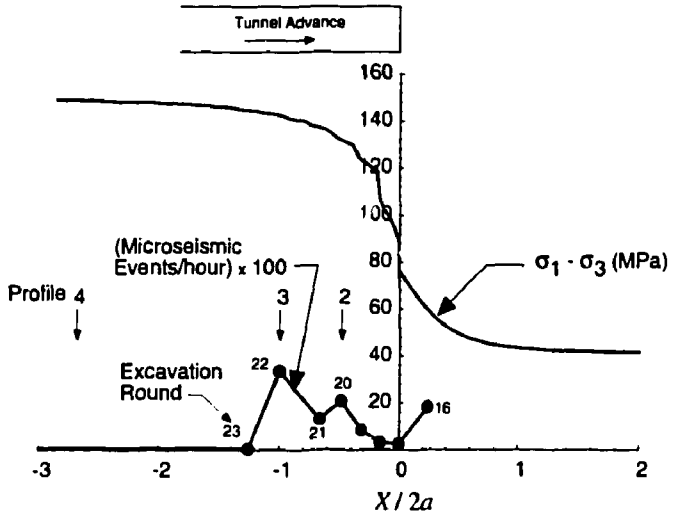

FIGURE 43: Comparison of the maximum deviatoric stress change that occurs in the roof, to the AE/MS rate recorded at Round 17 and the development of the profiles at Round 17. The parameter $X/2a$ refers to the normalized face position of the tunnel.

The previous discussions showed that the microseismic events are concentrated within a narrow zone around the 1-m volume. The microseismic events that were recorded in the 1-m volume and the measured profiles can be related to the position of the test tunnel face. In Figure 43, the face position X is normalized with respect to the tunnel diameter $2a$. This allows direct comparison with the stress changes that occur near the tunnel face. Three-dimensional boundary element analyses were carried out using the program EXAMINE^{3D} (Curran and Corkum 1993) to determine the maximum deviatoric stresses in the roof of the test tunnel. Figure 43 compares the maximum deviatoric stress change that occurs in the roof to the rate of microseismic activity and the development of the notch. Figures 39 and 43 show that nearly all of the microseismic events occur within one tunnel diameter of the face, i.e., where the stress changes are occurring, but that the development of the notch continues for long periods afterward. Also note that the failure process, i.e., crack initiation, begins ahead of the tunnel face.

The microseismic events in Figure 44 cluster strongly in the regions of the maximum compressive stress concentrations in the roof and floor. These regions of microseismic activity are the locations of the breakouts (compare Figure 45 and Figure 44). Note that no microseismic activity was recorded in the regions where remote or tensile fractures are expected to form.

3.3.2 *In Situ* Crack Initiation

The process leading to failure in brittle rocks in unconfined laboratory compression tests initiates with the onset of stable crack growth (Brace et al. 1966) which was referred to in Section 3.1 as the crack-initiation stress σ_{ci}. The crack-initiation stress in laboratory

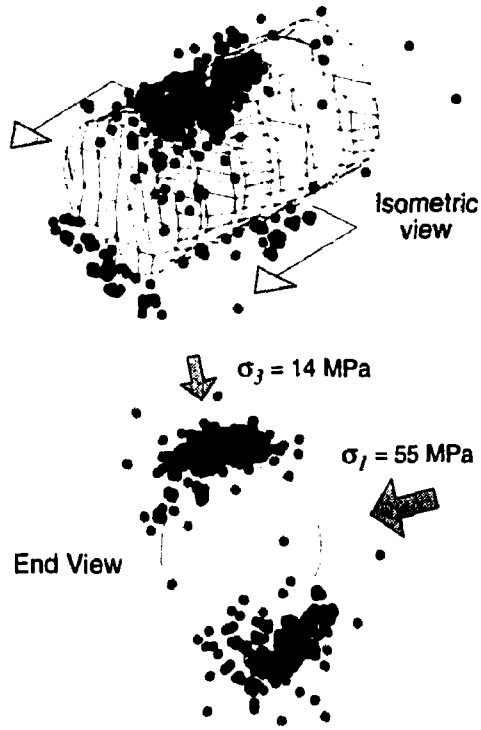

FIGURE 44: Location of microseismic events recorded after the excavation of a 1-m-long round (Round 17) in the test tunnel.

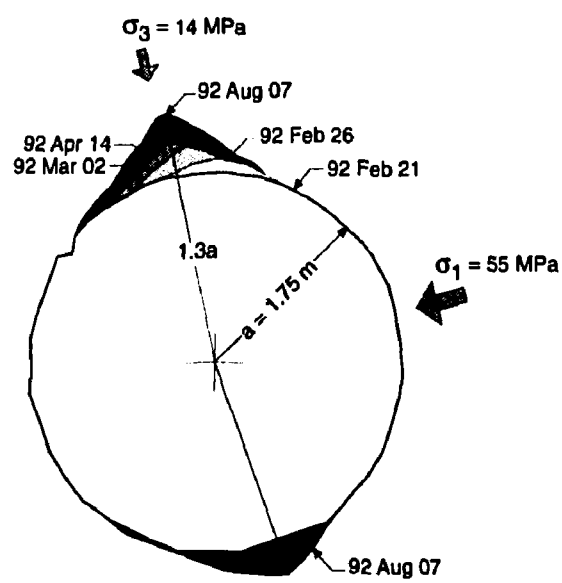

FIGURE 45: Progressive development of a breakout notch *in situ* in Lac du Bonnet granite (chainage 18+50).

samples of Lac du Bonnet granite occurs when the load first exceeds about 0.2 to $0.4\sigma_c$ where σ_c is the unconfined compressive strength (Martin 1993). This value for crack initiation is similar to the crack initiation values of 0.3 to $0.6\sigma_c$ reported by Brace and Byerlee (1968) for various low porosity rocks and concrete.

The microseismic events in Figures 42 and 44 define the regions where cracking initiates *in situ*. As these microseismic events represent the initiation of the failure process, the stress level associated with these events is referred to as the *in situ* crack-initiation stress σ_{ci}. Three-dimensional numerical stress analyses, carried out to determine the crack-initiation stress at each microseismic event location shown in Figure 44, showed that the stress level at which *in situ* cracking initiated could be approximated by

$$\sigma_1 - \sigma_3 \approx 70 \text{ to } 75 \text{ MPa}. \tag{12}$$

Those results are plotted in Figure 46 along with the Hoek-Brown failure envelope for the peak strength determined from laboratory tests. Figure 46 shows that, for low confining stresses, the *in situ* crack-initiation stress occurs at approximately 70 MPa, i.e., about $0.3\sigma_c$, which is only slightly lower than the laboratory findings mentioned earlier. This concept of a constant $(\sigma_1 - \sigma_3)$ threshold is similar to that introduced by Equation 7, which also suggests that the maximum deviatoric stress level required to initiate damage (microcracking) is a constant.

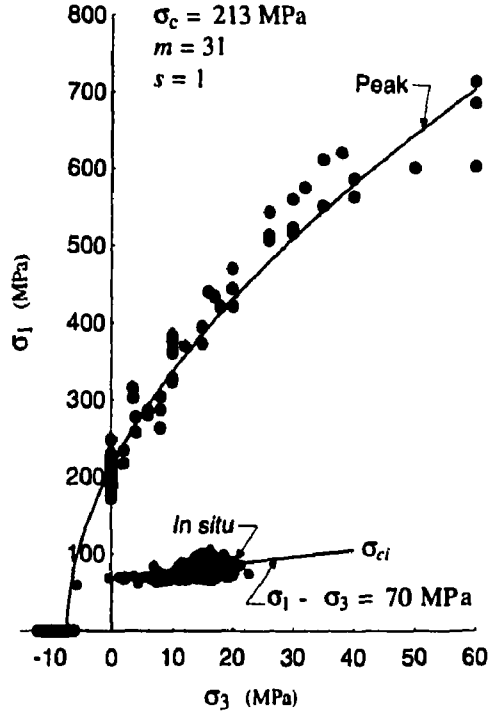

FIGURE 46: Hoek-Brown failure envelope for Lac du Bonnet granite based on laboratory peak strength and *in situ* crack-initiation stress (σ_{ci}) from the microseismic monitoring.

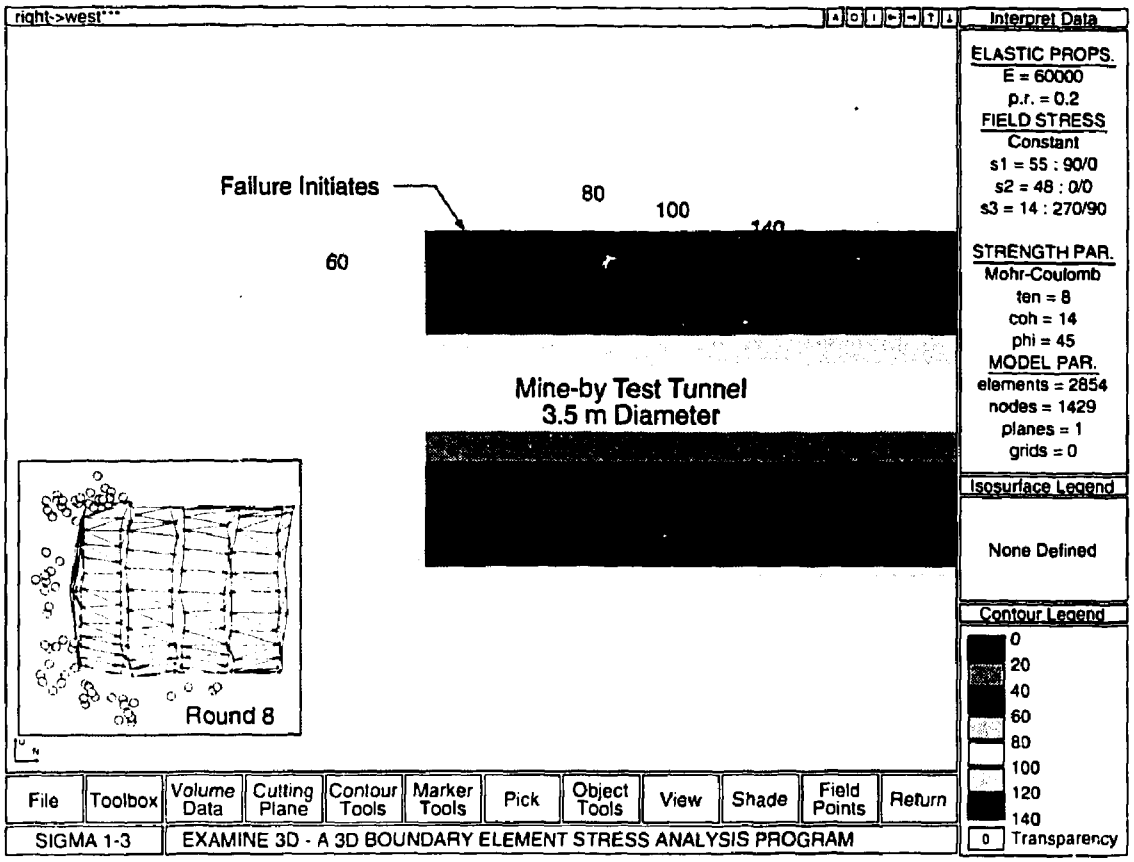

FIGURE 47: Section through the Mine-by test tunnel showing the location of the initiation of failure and the σ_1-σ_3 contours. Note that the microseismic events shown on the insert for Round 8 are concentrated in the areas of maximum deviatoric stress.

Figure 46 demonstrates that the *in situ* crack-initiation can be predicted by the maximum deviatoric stress criterion given in Equation 12. This concept is illustrated in Figure 47 which shows the $\sigma_1 - \sigma_3$ contours in a plane through the maximum compressive stress concentrations around the Mine-by test tunnel. Note the general agreement with the location of the microseismic events near the face of the tunnel and the $\sigma_1 - \sigma_3$ contours. Microseismicity shown in the inset in Figure 47 near the centre of the tunnel ahead of the face is not in the same vertical section shown for the model, but in three-dimensions falls within the $\sigma_1 - \sigma_3 = 70$ MPa isosurface (not shown).

3.3.3 *In Situ* Loading Path

When considering the ultimate strength of a material, it is important to know the loading path that has been followed in reaching the 'strength'. Tests are routinely performed in the laboratory to obtain the tensile strength, the unconfined compressive strength and the 'triaxial' strength. In all of these cases, the loading path increases or decreases monotonically,

and the loading directions do not change (Figure 48). However, *in situ*, the loading path is more complex, involving stress increase, decrease and stress rotation in the regions close to the advancing excavation (Martin 1993).

Using the initial composite estimate of the stress tensor (section 2.1.3), Martin (1993) carried out a series of three-dimensional linear elastic stress analyses to follow the loading path of various reference points ahead of the test tunnel. He investigated the change in stress magnitudes and directions as the tunnel advances towards and passes the reference point. In each analysis, the reference point starts 10 m ahead of the tunnel and is referred to as the 'far-field' (point A in Figure 48) and its stress path is followed until the tunnel has passed the reference point by 10 m (point E in Figure 48). Figures 49 and 50 show two of the analyses carried out by Martin for points near the maximum compressive stress concentration around the tunnel. Figure 49 is the stress path followed by a point in the roof of the tunnel located about 10 mm from the tunnel perimeter; Figure 50 is the stress path followed by a point in the roof of the tunnel located about 500 mm from the tunnel perimeter. These show that, near the tunnel perimeter, the stress path exceeds the crack-initiation stress well ahead of the tunnel face, but that at 500 mm from the tunnel perimeter, the crack-initiation stress is exceeded only as the plane strain condition is reached, i.e., behind the tunnel face. Martin's analyses also showed that, at a distance of 600 to 700 mm radially beyond the tunnel perimeter, the stress remains below the crack-initiation stress. Based on these analyses and results from microseismic monitoring, the compressive regions in which crack initiation occurs *in situ* are localized close to the tunnel perimeter, and extend ahead of the advancing face. Damage generated in compression is therefore limited to these regions of the rock mass.

Having established the regions around the tunnel in which damage could occur, Martin (1993) considered possible mechanisms influencing the development of cracks and crack growth, i.e., damage, within these regions. He suggested that stress rotation is one of the key mechanisms that contributes to *in situ* damage development around tunnels. Martin (1993) showed that the advance of the tunnel face not only causes the stress tensor to change

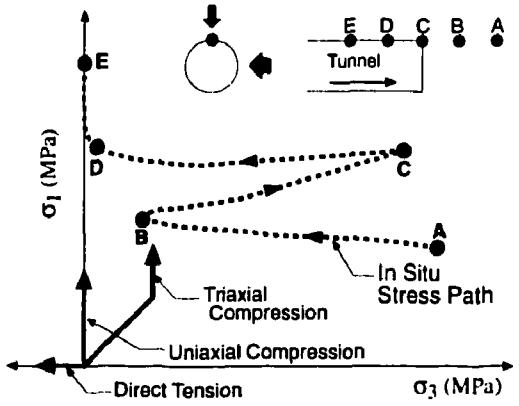

FIGURE 48: Illustration of the loading path in uniaxial and triaxial testing, and the *in situ* loading path around a circular tunnel with anisotropic far-field stresses.

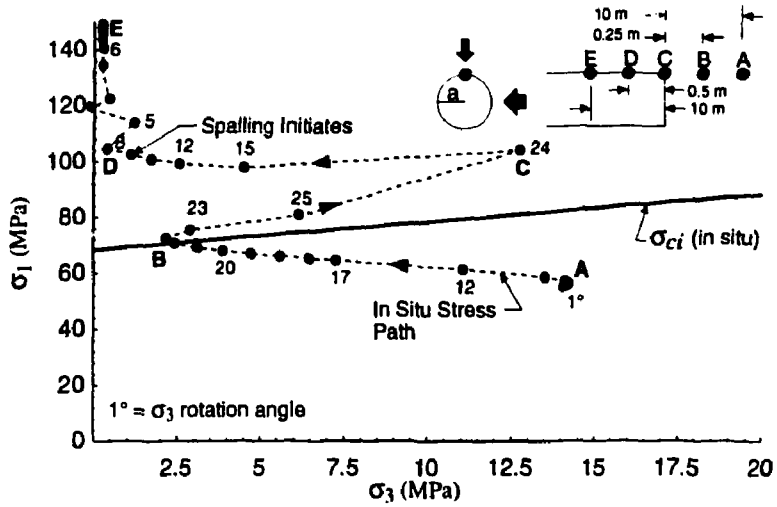

FIGURE 49: Stress path for a point located 10 mm from the tunnel boundary at the maximum compressive stress concentration in the roof. The 'far-field' point in the figure is located 10 m ahead of the face. Note that the first visual signs of failure are observed at point D, about 0.5 m inside the tunnel.

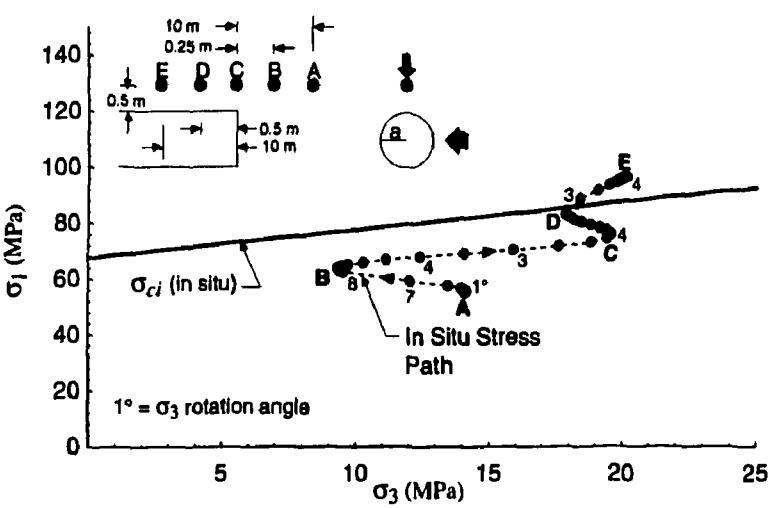

FIGURE 50: Stress path for a point located 500 mm from the tunnel boundary at the maximum compressive stress concentration in the roof. The 'far-field' point in the figure is located 10 m ahead of the face.

in magnitude but to rotate also. If cracks are considered to grow in the plane orthogonal to σ_3, then the rotation of σ_3 represents the rotation of the pole normal to the plane of the crack. From detailed analyses of the region near the face of the test tunnel, Martin (1993) concluded that rotation of σ_3 occurs in all locations around the tunnel face. However, in the roof and floor of the test tunnel, the rotation of σ_3 along the line 10 mm outside the tunnel perimeter is at a maximum of about 20 to 30° between points B and C ahead of the face (Figure 49), decreasing to about 5° in the same region at 500 mm from the tunnel perimeter (Figure 50). In addition, as a result of stress rotation, the magnitude of σ_3 reaches a minimum near point B ahead of the face. This effect is most pronounced along a line close to the tunnel perimeter, where σ_3 approaches zero (Figure 49). Hence, within the regions where crack initiation occurs, there are distinct zones ahead of the face where stress rotation reaches a maximum, and confining stress is low.

Wu and Pollard (1992) conducted tensile tests on a brittle material to investigate the influence of the orientation of existing cracks on crack growth in tension. By rotating the applied tensile stress relative to the orientation of the existing cracks, they demonstrated that the existing cracks influenced the growth of new cracks. They also demonstrated that by simply keeping the stress constant, but rotating its direction, they could generate crack patterns in different directions. At rotation angles from about 0 to 45°, new cracks tended to grow from the tips of existing cracks, i.e., the existing cracks grew longer without an increase in stress.

Martin (1993) suggested that a similar process, induced by stress rotation, occurs near the tunnel face when stresses exceed the crack-initiation stress. As shown in Figure 49, damage initiates *in situ* near point B, where the crack-initiation stress is exceeded and the confining stress is low. As shown in the damage-controlled tests in Section 3.1.1, the amount of damage accumulated in the rock is greatest for conditions of low confinement. The microcracks formed near point B are inclined about 20 to 25° to the tunnel axis, oriented orthogonal to the near-field σ_3 direction. Upon tunnel advance past the volume of rock containing these microcracks, σ_1 and σ_3 rotate to become tangential and radial, respectively, to the tunnel at the perimeter, and σ_2 becomes parallel to the tunnel axis. Near the face, the crack-initiation stress is exceeded in both the axial and tangential directions, which promotes microcracks to form orthogonal to the radial direction, and tends to exploit the existing inclined microcracks. This form of crack growth would result in a loss in the cohesion component of the rock strength because it causes the crack length to increase. The net effect is that the rock mass in this region is weakened and more susceptible to dilation. However, away from the opening, the rock mass strength is unaffected.

In regions of granite lithology, failure in the form of spalling was first observed in the test tunnel roof near point *D* in Figure 49, about 0.3 to 0.5 m behind the tunnel face. Based on the initial stress tensor estimated for the experiment area, σ_3 is zero and σ_1 (the tangential stress) is between 105 and 120 MPa in this area. Although the tangential stress is only 0.5 to $0.6\sigma_c$ for the case described in Figure 49, it is sufficient to exploit the previously formed microcracks in the region of damage exposed at the tunnel perimeter. Consequently, failure occurs at a lower stress level than in laboratory tests. It should be noted that in granodiorite lithology, the point of failure initiation was about 1 m behind the tunnel face.

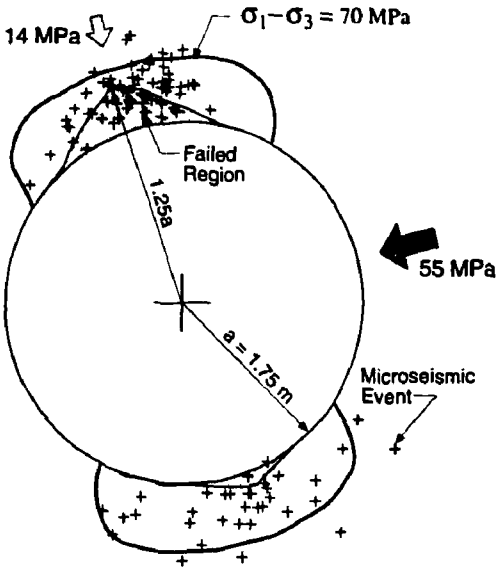

FIGURE 51: Extent of the rock mass around the Mine-by test tunnel where the maximum deviatoric stress ($\sigma_1 - \sigma_3$) has exceeded the crack-initiation stress of about 70 MPa. The principal stress magnitudes used for the analysis are $\sigma_1 = 55$, $\sigma_2 = 48$ and $\sigma_3 = 14$ MPa.

This process of *in situ* strength reduction requires that the stress magnitudes near the tunnel face are sufficient to exceed the *in situ* crack-initiation stress. The microcracks that form once this condition is met reduce the cohesion of the rock mass in localized regions close to the tunnel. By considering the distribution of maximum deviatoric stress around the tunnel under plane strain conditions, the maximum extent of the region over which the crack-initiation stress is exceeded can be approximated. Figure 51 shows the region around the Mine-by test tunnel where the maximum deviatoric stress exceeds the crack-initiation stress. Also plotted in Figure 51 are the microseismic events recorded within a 1-m-thick slice around the test tunnel, as well as the measured shape of the failed zone or notch. It is obvious that the crack-initiation stress does not define the shape of the notch, but it does provide a reasonable estimate of the depth of the notch, shown as $1.25a$ in Figure 51, where a is the radius of the tunnel.

3.3.4 Progressive Failure in Compression

The preceeding sections have shown that the process of failure around the Mine-by test tunnel started when the the maximum deviatoric stress exceeded the stress level required to initiate cracks, or damage, ahead of the advancing tunnel. Following this localized 'pre-conditioning' of the rock mass, the macroscopic failure process commences as the tangential stress at the boundary of the tunnel reaches the strength of the damaged material. In this section, the observations recorded during the process of progressive failure in the regions of maximum tangential stress are described. This process, which was observed in the upper SE

and lower NW quadrants of the test tunnel during its excavation, resulting in well-developed v-shaped notches typical of those found in borehole breakouts (Figure 52).

The processes associated with progressive failure of the Mine-by test tunnel have been described by Martin (1993). Figure 53 illustrates the major processes observed in the progressive development of a notch. In general, the steps involved are: 1) crushing in a very narrow, 5 to 10 cm wide, process zone on the tunnel periphery approximately 0.5 to 1 m back from the tunnel face where the maximum tangential stress exceeds the strength of the damaged rock (Figure 54); 2) dilation and small-scale flaking in this process zone resulting in the formation of thin slabs that are typically as thick as the grain size of the granite (2 to 5 mm) (Figure 55); 3) formation of larger thin slabs on the flanks of the notch as the process zone develops (Figures 56 and 57); 4) stabilization of the process, occurring when the notch geometry provides sufficient confinement at the notch tip. This occurs when the notch geometry takes on a 'tear-drop' like shape (Figure 58). The 'tear-drop' like geometry of the notch re-orients the maximum principal stress trajectory radially outward into the rock mass, which results in high localized values of σ_1 under high confinement conditions at the notch tip (Martin 1993; Zheng et al. 1989). The four processes involved in the development of the notch are described in detail in the photographs that follow.

From the observations during the construction of the Mine-by test tunnel, it is clear that the process zone plays the key role in the initiation, development and stabilization of the v-shaped notch. The failure processes that occur in this zone are complex, and it is difficult to 'look inside' the process zone without disturbing it. Figure 59 shows the process zone at the tip of the notch in Figure 58. Note the large amount of dilation associated with the failure mechanisms in the process zone.

3.3.5 Tensile Failure in the Sidewalls

In the sidewalls of the Mine-by tunnel, the tangential stress at the tunnel wall exceeds the tensile strength of the rock mass, which according to elastic theory, should result in macroscopic tensile cracks. This type of cracking was evident in Room 405, the main level instrument gallery excavated parallel to the Mine-by tunnel using a drill-and-blast technique. Contrary to expectations, there were no macroscopic tensile cracks in the sidewalls of the test tunnel. The development of microscopic damage in the tensile regions was, however, detected by geophysics surveys, and is discussed in Section 4. The differences in the characteristics of damage in the tensile regions in Room 405 and the test tunnel are attributable primarily to the differences in excavation technique.

3.4 SUMMARY

The laboratory testing progam clearly showed that the failure process initiates with small cracks that form in the general direction of the maximum applied load. Stable crack growth starts at the crack-initiation stress which typically occurs at about 0.3 to 0.4 of the peak strength of the sample. This process of stable crack (damage) growth continues until a sufficient density of cracks occurs that allows the development of a macro failure zone in the laboratory sample. The stress level at which this failure zone develops is referred to

FIGURE 52: Final profile of the Mine-by Experiment test tunnel as of 1992 August showing well-developed v-shaped breakout notches in the upper SE and lower NW quadrants.

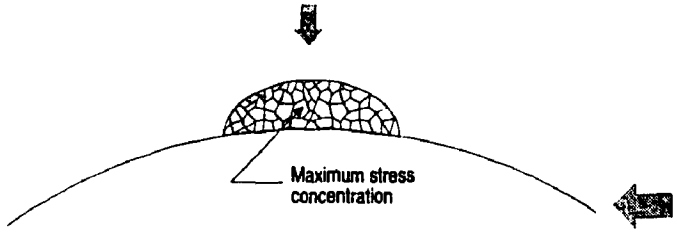

Stage I - Initiation
Critically oriented flaws are exploited in the zone of maximum tangential stress. This process initiates at the boundary of the tunnel.

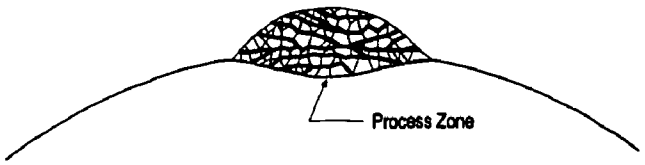

Stage II - Dilation
Shearing and crushing occurs in a very narrow process zone about 5 - 10 cm wide. Extensive dilation, at the grain-size scale, occurs in this process zone.

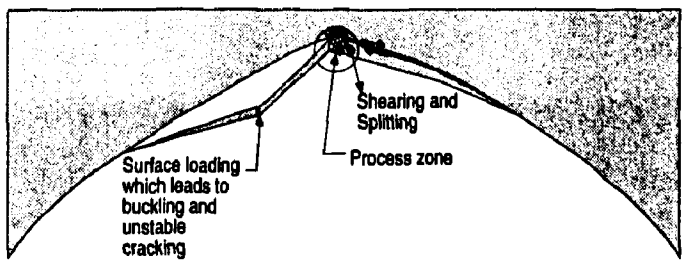

Stage III - Slabbing & Spalling
Development of the process zone leads to formation of thin slab. These thin slabs form by: 1) shearing, 2) splitting, and 3) buckling. The thickness of the slabs varies from 1 to 5 cm. The thickest slabs form as the notch reaches its maximum size. Near the notch tip the slabs are curved.

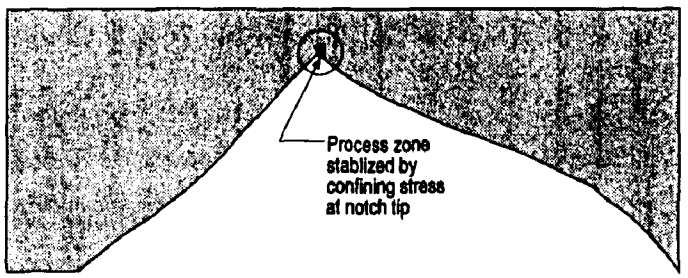

Stage IV - Stabilization
The development of the notch stops when the notch geometry provides sufficient confinement to stabilize the process zone at the notch tip. This usually means there is a slight "tear-drop" like curvature to the notch shape. Alternatively, if the slabs from the side of the notch are held in place by artificial support then the development of the notch will also stop.

FIGURE 53: Illustration of the major processes involved in the initiation, development and stabilization of the v-shaped notch.

FIGURE 54: Stage I: Photo of the initiation of the failure process. Note the faint whitish colour line, caused by crushing, which defines the limits of the process zone. Note also that the tunnel profile at the tunnel face is circular and that the process zone initiates about 0.5 m back from the tunnel face.

FIGURE 55: Stage II-III: Photo of dilation that occurs as the slabs on the flanks of the notch start to form. These slabs are held in place by the safety mesh used during construction.

FIGURE 56: Stage III: Photo of a slab that has buckled on the flank of the notch. This was the only type of large-scale buckling that was observed.

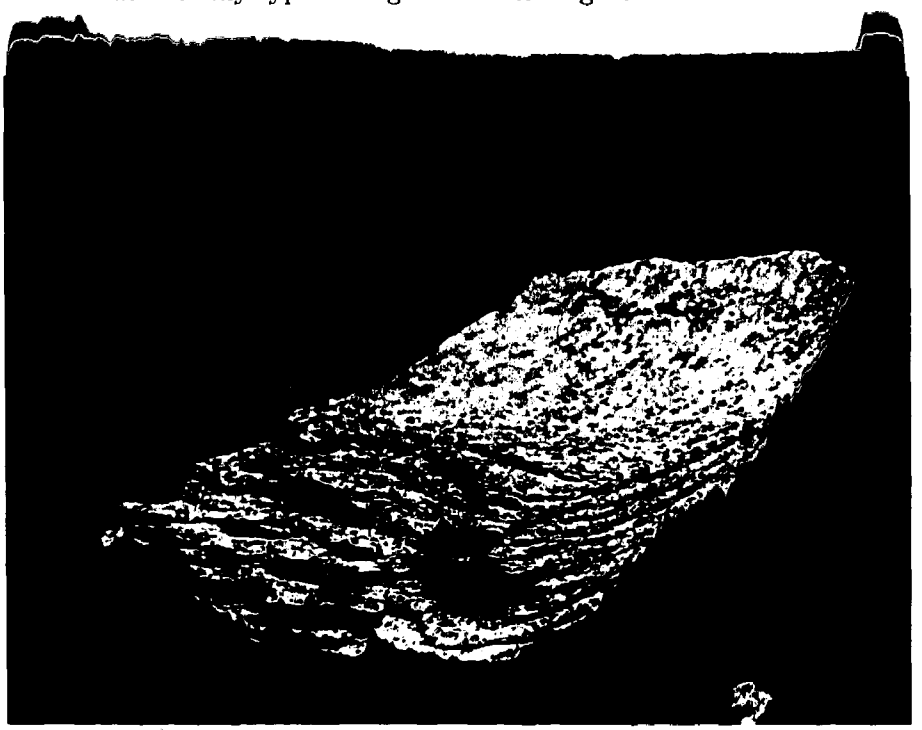

FIGURE 57: Stage III: Photo of a single slab showing the grain-scale fracturing generated at the active notch tip.

FIGURE 58: Stage IV: Photo of the stable v-shaped notch that developed in the floor of the test tunnel. The slot that allowed this photo to be taken was excavated between 1992 October and 1993 January. Note the characteristic 'tear-drop' shape to the geometry of the notch.

FIGURE 59: Photo of the process zone at the tip of the notch in Figure 58. Note the large amount of dilation localized at the notch tip.

as unstable crack growth or crack-damage stress, and typically occurs at about 0.7 to 0.8 of the peak strength. Once a macro failure zone is developed, the sample can no longer sustain the load and failure occurs.

In situ crack initiation was also found to occur at about 0.3 of the undisturbed laboratory strength. However, unlike the laboratory sample, failure, i.e., spalling, initiates when the tangential stress around the tunnel reaches about 100 to 120 MPa, i.e., 0.5 to 0.6 of the undamaged laboratory unconfined strength. As a result of the complex loading path around the advancing face of the tunnel, it is proposed that, *in situ*, the rock accumulates more crack damage for a given stress level than in laboratory tests, and therefore undergoes more pronounced weakening. Consequently, failure *in situ* initiates at lower tangential stress levels than in laboratory tests.

Once failure initiates near the tunnel face, the development of the v-shaped notch accelerates as the face advances, and the tunnel adjusts to the new plane strain conditions. The slabbing process resulting in the development of the v-shaped notch is controlled by the process zone. This zone, although small in size relative to the v-shaped notch, forms at the tip of the v-shaped notch and consists of highly strained, i.e, crushed, rock. Once the development of process zone stablizes, the development of the notch stops. This usually occurs when the geometry of the notch is such that the process zone is confined in a very small region at the notch tip.

The damage process described above occurs near the tunnel face. Points in localized regions ahead of the face experience changes in the principal stress magnitudes and orientations as the tunnel advances, causing micro-scale damage. This damage locally weakens, or 'pre-conditions,' the rock mass near the tunnel. The degree of damage is greatest about one radius from the projected tunnel centreline, and decreases rapidly with increasing radial distance from the tunnel. Upon tunnel advance, these localized regions of damage are exposed at the tunnel perimeter. Hence, the strength of the rock mass around the underground opening varies from point to point, with the strength at any given point depending on the stress history and damage accumulated there as a result of the excavation process. Points located at the tunnel wall in the maximum compressive stress concentration have accumulated the most damage during tunnel advance, and therefore experience the largest strength reduction. Points located further from the opening, or away from the zones of maximum compressive stress concentration, have accumulated less damage and thus have strengths closer to the undamaged laboratory strength.

4. EXCAVATION DISTURBANCE AND DAMAGE

As described in Section 1, the redistribution of stresses around a tunnel results in a zone of excavation disturbance. In general, this zone is characterized by a perturbation to the pre-excavation stress state, but no change in the initial material behaviour of the rock mass. Depending on the far-field stress magnitudes and the strength of the material in which the tunnel is excavated, a zone of excavation-induced damage may develop close to the tunnel within this larger disturbed zone. The damaged zone is characterized by changes in both the pre-excavation stress state and in the material behaviour of the rock mass. Within this

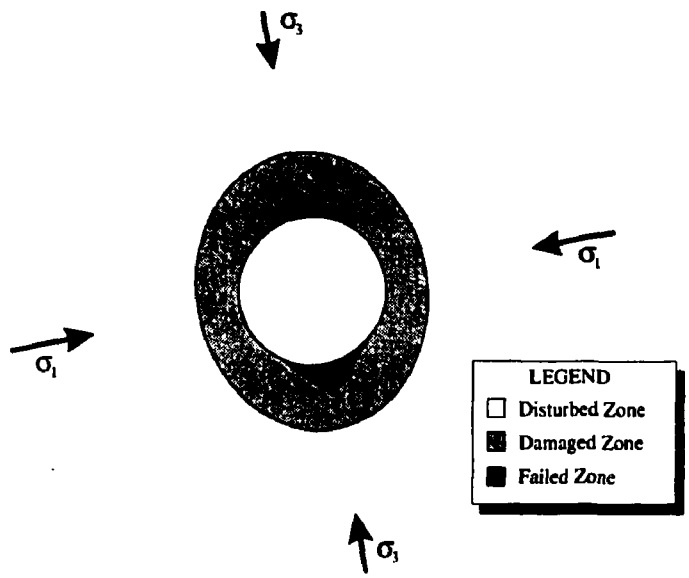

FIGURE 60: Schematic view of the disturbed, damaged and failed zones around the Mine-by Experiment test tunnel.

zone, a smaller failed zone may exist, defined by a region of slabbing or material removal, as described in Section 3. These zones are shown schematically in Figure 60.

Having investigated the zone of progressive failure in compressive regions around the tunnel, the other key objective of the Mine-by Experiment was to define the extent and characteristics of the damaged zone around the test tunnel. Back analysis can establish the stress conditions and material properties in the undisturbed region based on measurements in the disturbed zone. Once these boundary conditions have been defined, it is then possible to assess the extent, material behaviour and characteristics of the damaged zone around the tunnel through field characterization and numerical modelling.

Based on the data contained in the nine data summary reports for the Mine-by Experiment, back analyses of the strain and/or displacement measurements were undertaken (Read 1994; Wiles 1995). These back analyses are described in Sections 4.1 and 4.2, and the principal findings, in terms of characteristics of the disturbed zone, are summarized in Section 4.3. Characterization of the damaged zone and factors controlling excavation damage development are also considered in Section 4.3.

4.1 BACK ANALYSIS OF DISPLACEMENT MEASUREMENTS

Back analysis of *in situ* stresses from radial displacements measured around circular excavations is typically based on the analytical solution for stresses and displacements around a circular hole in an infinite plate under plane strain conditions. This relationship assumes linear elastic material behaviour, and relates the total excavation-induced displacements to the 2D principal stresses acting in the plane of the excavation. To estimate the 3D stress

tensor, multiple orthogonal tunnels are required. In highly-stressed brittle rock masses, excavation-induced damage can result in non-linear/non-elastic material behaviour around a tunnel which can produce a displacement response significantly different from that predicted by elastic theory. In addition, displacement measurements taken from within the excavation (Figure 61) represent only part of the total displacement response, requiring an estimate of the missed proportion occurring ahead of the tunnel face. Under anisotropic far-field stress conditions, this proportion is dependent on a number of factors including axial stress magnitude, face shape, rotation angle and position with respect to the tunnel face (Read 1994).

Using the Mine-by Experiment as a case study, Read (1994) considered the problems associated with analysis and interpretation of displacement measurements taken during excavation of a cylindrical tunnel in a massive, highly-stressed, brittle rock mass. He developed a technique to back analyze the 3D *in situ* stress tensor using radial displacements from the region within ± 1 diameter of the face of a single circular tunnel. The technique is applicable to conditions ranging from low stress regimes, where rock mass behaviour is linear elastic, to highly-stressed regimes where significant damage develops in the tunnel. The stress tensor estimated for the region containing the Mine-by test tunnel was, in turn, used in conjunction with observations from field characterization and numerical modelling to determine the extent and characteristics of excavation damage around the tunnel. This section summarizes the methodology and results of the back analysis conducted by Read (1994) to determine the *in situ* stress tensor and material properties. Details pertaining to nomenclature and mathematical expressions are contained in Appendix B.

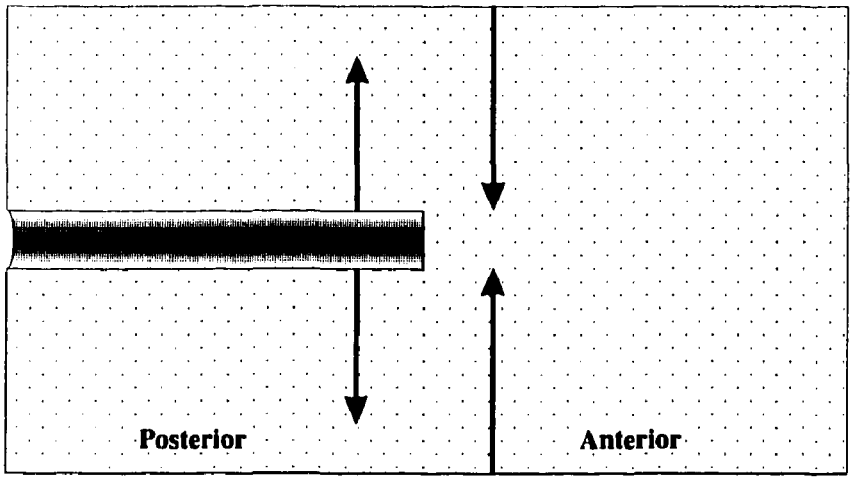

FIGURE 61: Definition of the posterior and anterior domains for an idealized tunnel, and typical direction of instrument installation: for the posterior domain, from the tunnel outwards; and for the anterior domain, from an external opening inwards.

4.1.1 Stress Partitioning Approach

Most previous studies involving displacements around a cylindrical tunnel have considered special stress states involving axial symmetry or zero antiplane shear stresses (Brown et al. 1983; Pelli 1987), i.e., the tunnel axis coincides with a principal stress direction. To assess a general elastic case where the far-field stress components are unequal, and the tunnel axis does not coincide with a principal direction, the principle of superposition can be used to partition a unit stress tensor into a set of three normal stress and three shear stress tensors (Niwa et al. 1979), i.e.,

$$\underbrace{\begin{bmatrix} 1 & 1 & 1 \\ 1 & 1 & 1 \\ 1 & 1 & 1 \end{bmatrix}}_{\sigma} = \underbrace{\begin{bmatrix} 1 & 0 & 0 \\ 0 & 0 & 0 \\ 0 & 0 & 0 \end{bmatrix}}_{\sigma_{11}} + \underbrace{\begin{bmatrix} 0 & 0 & 0 \\ 0 & 1 & 0 \\ 0 & 0 & 0 \end{bmatrix}}_{\sigma_{22}} + \underbrace{\begin{bmatrix} 0 & 0 & 0 \\ 0 & 0 & 0 \\ 0 & 0 & 1 \end{bmatrix}}_{\sigma_{33}} + \underbrace{\begin{bmatrix} 0 & 1 & 0 \\ 1 & 0 & 0 \\ 0 & 0 & 0 \end{bmatrix}}_{\sigma_{12}} + \underbrace{\begin{bmatrix} 0 & 0 & 0 \\ 0 & 0 & 1 \\ 0 & 1 & 0 \end{bmatrix}}_{\sigma_{23}} + \underbrace{\begin{bmatrix} 0 & 0 & 1 \\ 0 & 0 & 0 \\ 1 & 0 & 0 \end{bmatrix}}_{\sigma_{13}} \tag{13}$$

By applying scalar multipliers to the six partitioned tensors, any general stress tensor can be described. Hence, by describing the displacement responses for the six base cases, the response for any combination of the six tensors can be found by adding the individual displacement responses. Of the six partitioned tensors, σ_{11}, σ_{33} and σ_{13} represent plane components of stress, i.e., oriented in the cross-sectional plane orthogonal to the tunnel axis, while σ_{22}, σ_{12} and σ_{23} are antiplane components (Filon 1937). The components of the partitioned stress tensor are illustrated in Figure 62.

A numerical modeling study was undertaken to characterize the radial displacement responses associated with each component of the partitioned tensor. EXAMINE^{3D} (Curran and Corkum 1993), a 3D boundary element code, was used to model the displacement response of a cylindrical tunnel in a linear elastic medium. Values of $a = 1.75$ m, $\nu = 0.25$ and $G = 26$ GPa were used for the study. The level of discretization (72 elements around the perimeter) was selected by comparing results with those from an axisymmetric finite difference model, and a non-axisymmetric finite element model (Grabinsky and Curran 1993). Radial displacements far from the tunnel face were compared to the analytical plane strain solution, e.g., (Goodman 1989). In terms of the coordinate system used for the model, σ_{11} is coincident with the y-axis, σ_{22} with the x-axis, and σ_{33} with the z-axis.

The study showed that the radial displacement response at the tunnel wall can be considered the result of superposition of six *characteristic radial displacement surfaces*. In these 3D plots, the x, y and z axes correspond to normalized face position X/D, rotation angle θ and normalized radial displacement $U_r/U_{r_{max}}$, respectively. Of the six responses, there are only three unique surfaces (Figure 63), the others being, or comprising, surfaces of the same shape, but with different phase constants. Aside from the obvious differences in shape, the

most notable difference between these three surfaces is that the periodicity for the plane component surface is 180°, while the antiplane normal component surface is axisymmetric and the antiplane shear component surface has a periodicity of 360°.

Mathematical expressions were developed to describe the *characteristic radial displacement surfaces* at $r/a = 1$. These surfaces can be represented in 2D by considering the radial displacement response versus either face position for a fixed rotation angle, or rotation angle for a fixed face position. The *spliced logistic function* was developed as a general approximating function for the radial displacement response versus face position. Parametric functions describing the radial displacement response versus rotation angle were also derived, and the *spliced logistic function* was used to describe the variation in the equation parameters α and β with face position.

Using the same developmental approach, a general approximating function comprising an inverse polynomial series was developed to describe the radial displacement response versus radial distance. This approximating function was, in turn, used with the general parametric equations for the radial displacement response versus rotation angle to represent *characteristic radial displacement surfaces* in the $r-\theta$ plane at five axial positions in the tunnel. The approximating and parametric functions for each of these types of surface are presented in Appendix B.

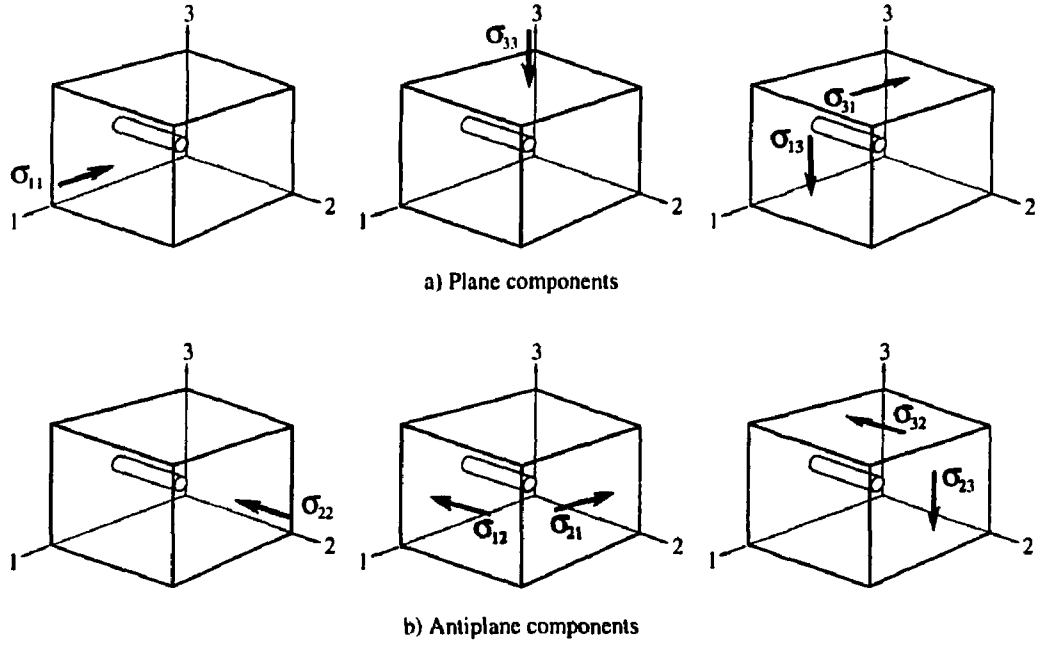

FIGURE 62: Components of the partitioned stress tensor: a) plane components, and b) antiplane components.

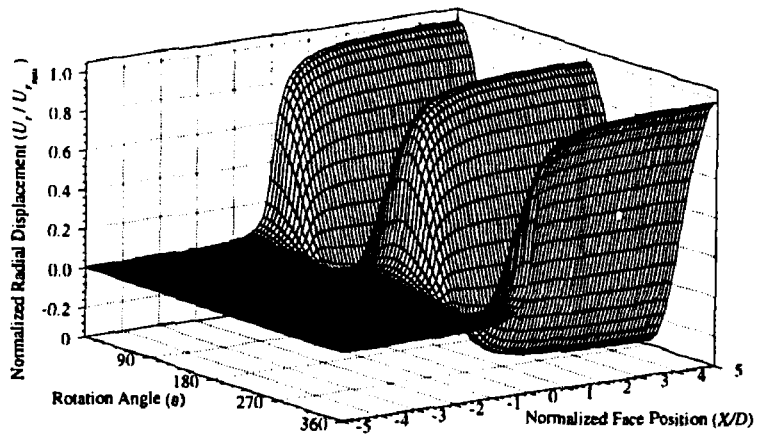

(a) σ_{11} tensor.

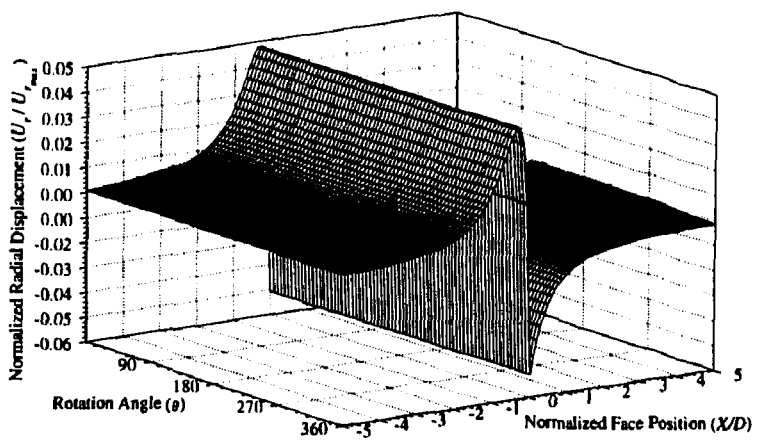

(b) σ_{22} tensor.

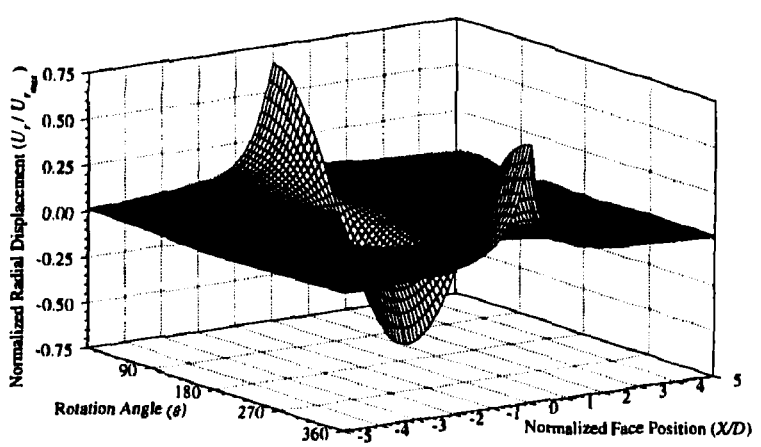

(c) σ_{12} tensor.

FIGURE 63: *Characteristic radial displacement surfaces* at $r/a = 1$.

4.1.2 Least-Squares Technique

Using a least-squares approach (Livesley 1989) and the equations developed to describe the *characteristic radial displacement surfaces*, all six components of the *in situ* stress tensor can be estimated from radial displacements measured within ±1 diameter of the tunnel face. The combined parametric functions associated with the radial displacement surface for a general stress case represent a linear combination of six unknowns of the form

$$\frac{U_r}{U_{r_{max}}} = c_1 f_1(r,\theta,x) + c_2 f_2(r,\theta,x) + c_3 f_3(r,\theta,x) + c_4 f_4(r,x) + c_5 f_5(r,\theta,x) + c_6 f_6(r,\theta,x). \quad (14)$$

In Equation 14, functions f_{1-6} are described by the *characteristic radial displacement surfaces* for the partitioned stress tensor components. The coefficients c_1, c_2, c_3, c_4, c_5 and c_6 are equal to the stress magnitude (in MPa) of σ_{11}, σ_{33}, σ_{13}, σ_{22}, σ_{12}, and σ_{23}, respectively, if the shear modulus of the rock mass and diameter of the tunnel under consideration are the same as those used in the model study. For cases where the actual tunnel parameters differ from those in the model, the matrix of coefficients is related to the matrix of stress magnitudes by

$$\{C\} = C_f\{\sigma\}, \quad C_f = \frac{a_{\text{model}} G_{\text{field}}}{a_{\text{field}} G_{\text{model}}}. \quad (15)$$

In matrix notation, given m equations with known values of F and U, and n unknowns C, i.e.,

$$\underbrace{[F]}_{m\times n}\underbrace{\{C\}}_{n\times 1} = \underbrace{\{U\}}_{m\times 1} \quad (16)$$

and substituting for $\{C\}$ using Equation 15, the solution for 6 unknowns σ can be written

$$\underbrace{\{\sigma\}}_{6\times 1} = \frac{1}{C_f}\underbrace{\left[\underbrace{[F]^{\mathrm{T}}}_{6\times m}\underbrace{[F]}_{m\times 6}\right]^{-1}}_{6\times 6}\underbrace{[F]^{\mathrm{T}}}_{6\times m}\underbrace{\{U\}}_{m\times 1}. \quad (17)$$

In this case, the matrix F corresponds to the parametric functions $f_1 - f_6$, U corresponds to the measured radial displacements normalized to $U_{r_{max}}$, and σ is the matrix of unknown stress magnitudes.

Because the maxima and minima of the radial displacement responses for the antiplane components occur near the tunnel face, back analysis of the antiplane stress components is only possible if measurements from the region $-1 \leq X/D \leq 1$ account for a large proportion of the data set. Measurements outside this region in the posterior domain will help establish the plane components if the material behaviour is linear elastic, but will not constrain the estimates of antiplane components. Supplemental equations relating the various stress components can also be added to the analysis to provide additional constraint on the estimated tensor. Weighting of a particular measurement or constraint can be accomplished by repeating the equation associated with the measurement within the system of equations.

The radial displacement response measured by posterior extensometers can be considered a partial *characteristic radial displacement surface*. The functions given in Equation 14 can be modified to reflect this fact. In the α and β expressions in the parametric functions, described by *spliced logistic functions* for each component of the partitioned stress tensor, the y-intercept parameter D_l is set to zero. This change results in new functions $f_{1_e-6_e}$.

For convergence measurements, the functions $f_{1_e-6_e}$ require a further modification to account for the relative nature of the measurement, i.e., the relative displacement between pins on opposite sides of the tunnel is measured rather than the absolute displacement of individual convergence pins. To this end, the functions $f_{1_e-6_e}$ for posterior extensometers on opposite sides of the tunnel are added to define new functions $f_{1_c-6_c}$. A direct consequence of this modification is that the new functions $f_{5_c-6_c}$ associated with the antiplane shear components of the stress tensor are zero because of the antisymmetric nature of the radial displacement responses produced by them. In other words, convergence measurements are unaffected by antiplane shear stresses, and therefore cannot be used to back calculate these components of the tensor.

4.1.3 Verification of the Method using EXAMINE^{3D}

The parametric functions, their coefficients and the least-squares technique were tested using displacement results from EXAMINE^{3D} for a general stress case. The applied stresses in the model were $\sigma_1 = 55$, $\sigma_2 = 48$ and $\sigma_3 = 14$ MPa, with σ_1 orthogonal to the tunnel axis and inclined 14.5° from horizontal. Subsets of radial displacement data were assessed to determine the sensitivity of stress predictions to measurement type and location relative to the tunnel. Three measurement types were simulated: 1) radial displacements at the tunnel wall from extensometers, 2) wall convergence from convergence arrays, and 3) radial displacements remote from the tunnel wall from extensometers. Results of the study (Figure 64) are shown as predicted stress components based on Wall (Types 1 and 2), Radial (Type 3), and Combined (Types 1, 2 and 3) measurements from the anterior, posterior and combined domains within ±1 diameter of the tunnel face. To illustrate the effect of incorporating additional information into the predictions, 10 equations constraining the σ_{11}/σ_{22} ratio were added to each data set. The resulting predictions are shown as Constrained in Figure 64.

The model simulation showed that the various subsets of three different measurement types all produced good estimates of the stress components. In each case, the predicted axial stress component showed more uncertainty than the other components owing to the relatively small radial displacement response associated with the σ_{22} tensor. Radial displacement measurements remote from the tunnel wall, on their own and in combination with measurements at the tunnel wall, produced less uncertainty in the predicted stresses than tunnel wall displacement measurements alone. The inclusion of additional constraint equations illustrated that information from other stress determinations can be used to improve stress predictions, provided the constraints have less uncertainty associated with them than individual displacement measurements. Based on the results of this study, combinations of different measurement types from different domains were recommended to optimize

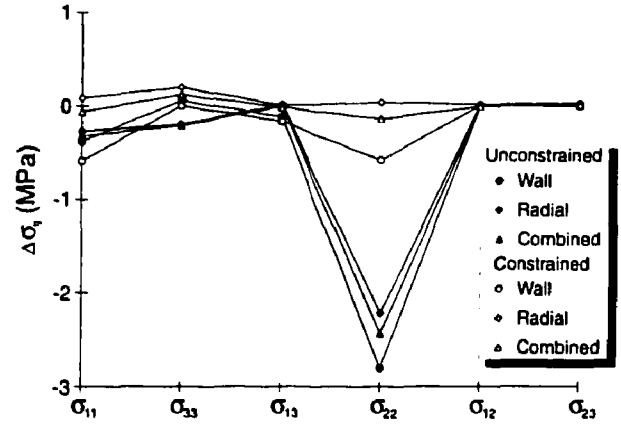

(a) Data from anterior domain $-1 \leq X/D \leq 0$.

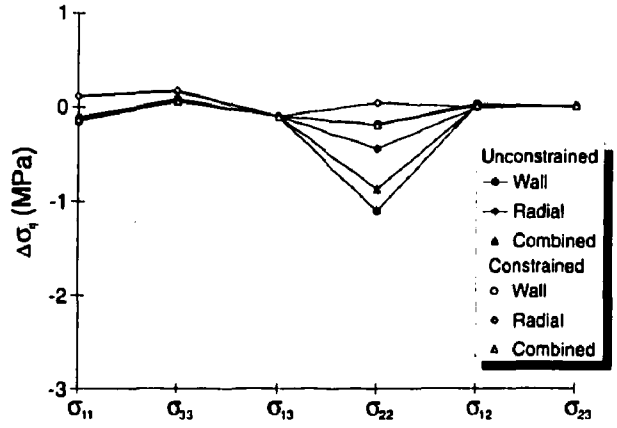

(b) Data from posterior domain $0 \leq X/D \leq 1$.

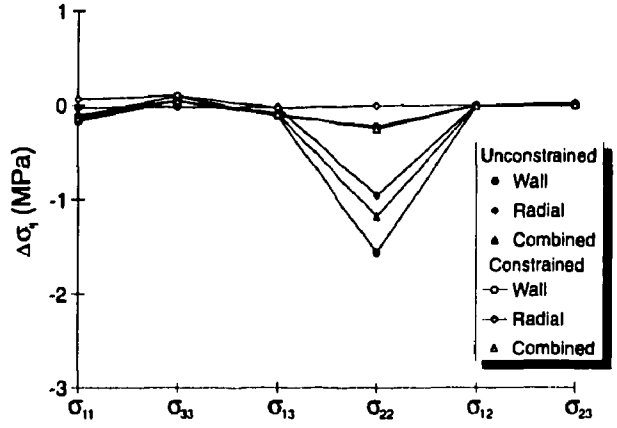

(c) Data from both domains $-1 \leq X/D \leq 1$.

FIGURE 64: Difference between predicted stress components and those used in the numerical model for various subsets of data.

the data set used in this back analysis technique. However, departure from linear elastic behaviour in the posterior domain might preclude some, or all, of the data from that region.

4.1.4 Application to the Mine-by Experiment

4.1.4.1 Methodology

Following development of the back analysis technique, a methodology was established to standardize field measurements of radial displacement in an enhanced data set, where the values of displacement at specific axial positions were interpolated, and the amount of displacement missed by each instrument was estimated (Read 1994). It was found that displacements occurring beyond the outermost extensometer anchors could be a significant proportion compared to the measured response. Displacements missed ahead of the tunnel face, in contrast, were found to be negligible if the first measurement was taken approximately three tunnel diameters ahead of the face.

As part of the analysis of measurements from the field study, Read (1994) compared results from extensometers directly to those from convergence arrays (Figure 65). He found

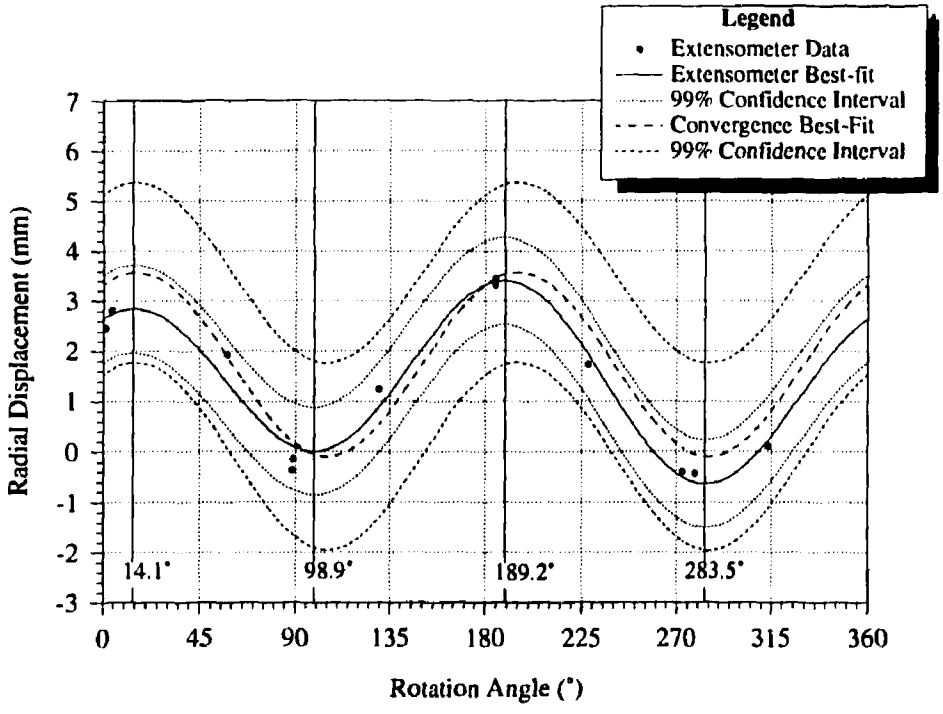

FIGURE 65: Comparison of posterior radial displacement results from extensometers and convergence arrays. The radial displacement for the convergence arrays is taken as one-half the total measured convergence. Results from all eight convergence arrays were considered. Note the asymmetry in the magnitude and rotation angle of the maxima and minima for the extensometer data.

TABLE 4

PROPORTION OF RADIAL DISPLACEMENT RESPONSE IN THE ANTERIOR DOMAIN UNDER AXISYMMETRIC STRESS CONDITIONS

Face Shape	Proportion of Total Radial Displacement in Anterior Domain (%)						
	K=1,0,1	1,$\frac{1}{4}$,1	1,$\frac{1}{2}$,1	1,1,1	1,2,1	1,3,1	1,4,1
Flat	29	26	24	20	13	6	-1
Filleted	38	36	33	30	23	16	9
Curved (0.071)	37	34	31	25	16	5	-6
Curved (0.143)	43	39	37	31	19	7	-4
Hemispherical	51	49	47	44	37	30	23

Value in parentheses for the curved faces is the difference in chainage of face edge and centre normalized to tunnel diameter.

that the two measurement types produced consistent results, but that convergence measurements were, by their nature, unaffected by antiplane shear components of the stress tensor. Consequently, plots of convergence versus rotation angle have symmetric maxima and minima for $0 \leq \theta \leq 360°$. Extensometer results, on the other hand, were shown to be sensitive to antiplane shear stresses near the tunnel face, which result in asymmetry in the magnitude and angular positions of the maxima and minima of the radial displacement response versus rotation angle for $0 \leq \theta \leq 360°$.

In comparison with the 27% reported in previous studies, Read (1994) found the amount of radial displacement occurring ahead of the advancing tunnel face to be about 30% in the case of a flat face under conditions of zero antiplane stress components. Results from an axisymmetric finite difference model study for the proportion of the total displacement response occurring in the anterior domain for various face shapes and axial stress ratios are shown in Table 4. The face shapes used in the study are given in Figure 66. For the general case, the proportion of displacement occurring in the anterior domain varies with the shape of the tunnel face, and the magnitude of the axial stress component (Figure 67). Stepped

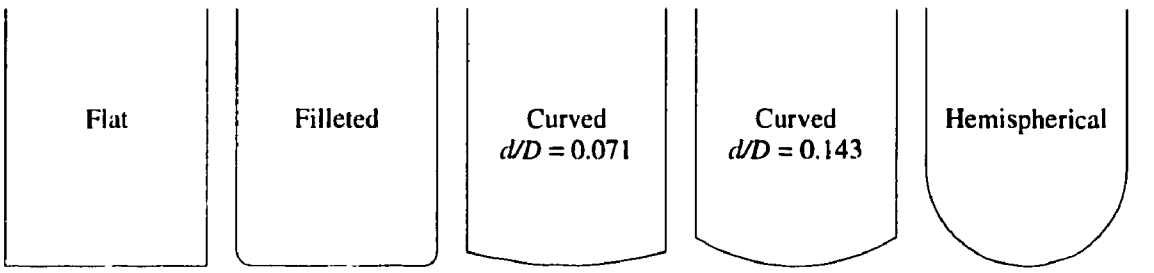

FIGURE 66: Five face shapes considered in the numerical modelling study. The ratio d/D is the difference in axial positions of the edge and centre of the tunnel face normalized to the tunnel diameter.

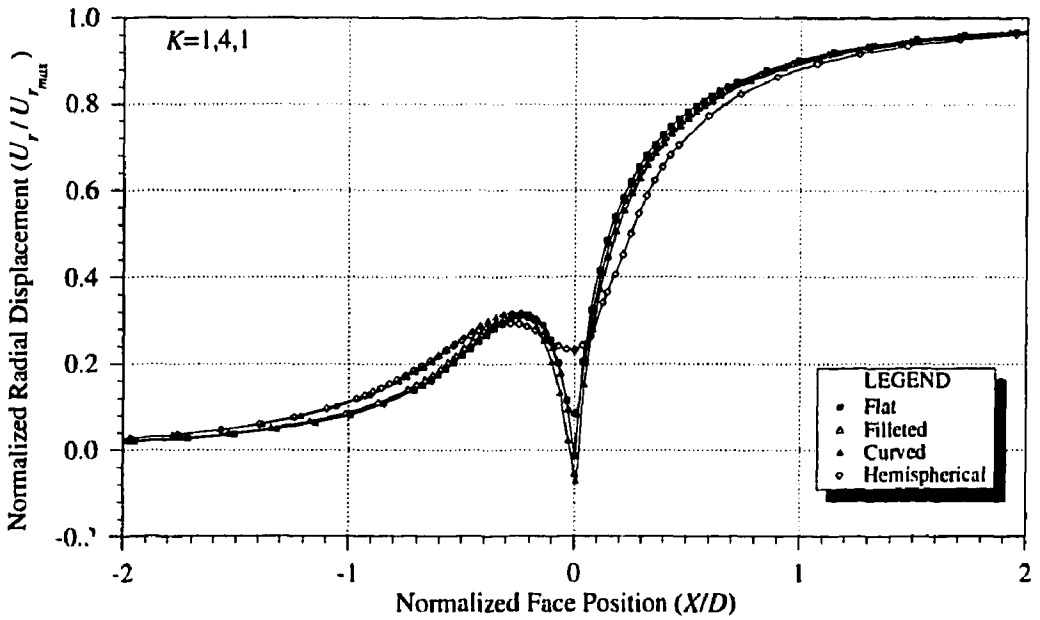

(a) Effect of face shape.

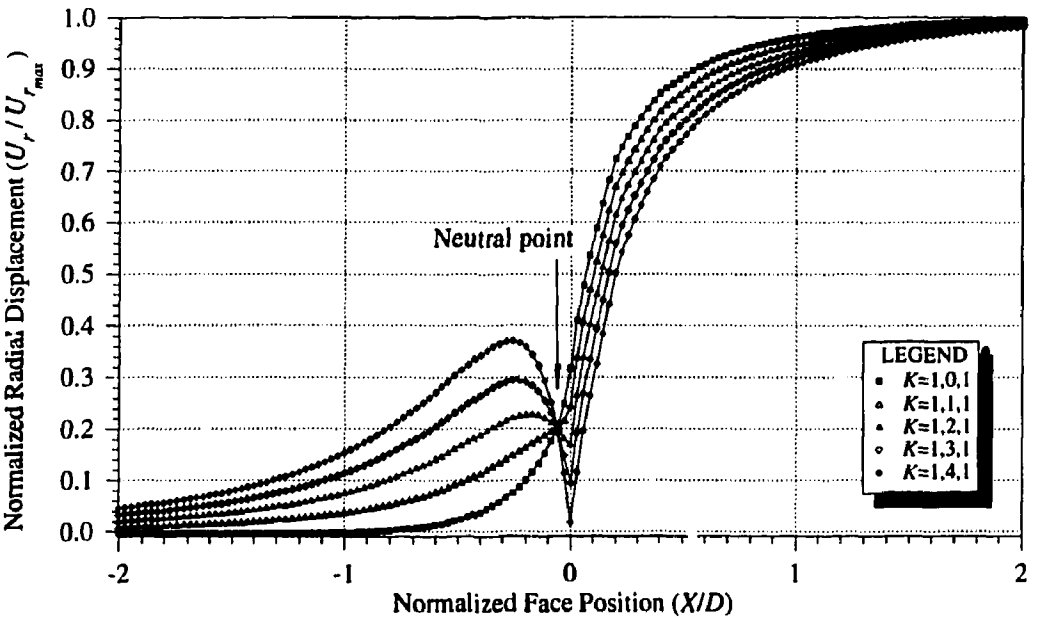

(b) Effect of axial stress component.

FIGURE 67: Effect of face shape and axial stress component on the radial displacement response versus face position at $r/a = 1$.

longitudinal tunnel geometry was also found to affect the radial displacement response in the posterior domain, but had a negligible effect on the response in the anterior domain (Read 1994).

4.1.4.2 Results from the Mine-by Experiment

Once the field data from the Mine-by Experiment were standardized, back analysis of the *in situ* stress tensor was conducted. Because of the large number of measurements (1107 extensometer and 138 convergence measurements), data were grouped systematically into subsets by measurement type. The measurement types were defined as:

- radial displacement for $r/a > 1$
  - i) including all extensometer measurements, and
  - ii) excluding all vertical extensometer measurements for $X/D > -0.4$;
- radial displacement for $r/a = 1$
  - i) including all extensometer measurements, and
  - ii) excluding all vertical extensometer measurements; and
- convergence measurements at the tunnel wall
  - i) including all measurements, and
  - ii) excluding vertical measurements.

Incremental predictions of the *in situ* stress tensor were made for each subset, and plots of stress invariants were used to assess the reliability of the individual estimates. The most reliable data for the different measurement types were then combined to produce eleven refined stress predictions.

The mean and standard deviation tensors were calculated from the eleven predicted tensors, weighting each prediction by the number of measurements upon which it was based. The calculated mean and standard deviation tensors, expressed in terms of the tunnel coordinate system with values in MPa, are

$$\overline{\sigma} = \begin{bmatrix} 57.18 & -3.60 & 10.81 \\ -3.60 & 45.50 & 3.00 \\ 10.81 & 3.00 & 11.08 \end{bmatrix}$$

$$S_{\overline{\sigma}} = \begin{bmatrix} 0.13 & 0.32 & 0.70 \\ 0.32 & 1.74 & 0.21 \\ 0.70 & 0.21 & 0.42 \end{bmatrix}$$

A Monte Carlo simulation was also conducted using the same eleven predicted tensors to determine the mean and expected range of values for the principal stresses. The expected range was taken as three standard deviations either side of the mean value. From this simulation, the estimated principal stress magnitudes were 60 ± 2, 45 ± 4 and 8 ± 3 for σ_1, σ_2 and σ_3, respectively. The principal stress magnitudes and directions associated with the estimates from the eleven combined data sets used to calculate the mean and

TABLE 5

ESTIMATED PRINCIPAL STRESSES FROM BACK ANALYSIS OF DISPLACEMENT MEASUREMENTS

Data	σ_1			σ_2			σ_3		
Set	MPa	Trend	Plunge	MPa	Trend	Plunge	MPa	Trend	Plunge
r_{1-3}	61.70	147.00	12.77	48.12	54.98	8.87	6.50	291.07	74.37
CR_1	60.19	148.08	11.25	42.90	56.31	8.86	8.32	288.89	75.61
cR_1	60.63	150.19	10.36	43.51	58.53	9.00	9.63	288.33	76.21
CW_1	59.40	144.93	11.68	46.28	53.60	6.43	7.79	295.30	76.62
cW_1	59.53	145.09	11.13	46.31	53.81	6.51	8.94	294.01	77.07
cw_1	59.52	144.03	11.04	46.31	52.65	7.09	9.82	290.53	76.83
R_1CW_1	59.76	146.46	11.53	45.01	54.99	7.21	7.68	293.58	76.35
R_1Cw_1	59.74	145.65	11.63	44.77	54.07	7.60	8.09	291.58	76.04
R_1cW_1	59.89	146.37	11.12	44.80	54.93	7.26	8.59	292.40	76.67
R_1cw_1	59.93	145.41	11.08	44.29	53.89	7.70	9.43	289.76	76.45
$r_{1-3}cw_1$	60.14	145.85	11.59	45.36	54.06	8.68	8.44	288.06	75.45
Mean Estimate									
	60.16	146.48	11.51	45.30	54.84	7.99	8.30	290.80	75.92
Best Combined Estimate									
R_1cw_1	59.93	145.41	11.08	44.29	53.89	7.70	9.43	289.76	76.45

standard deviation tensors are shown in Table 5. The magnitudes of the principal stress components are very consistent between the eleven estimates, with the most variability noted in the estimate of σ_2. As noted by Read (1994), the estimates of σ_2 and σ_3 appear to be interdependent, with estimates showing a high value of σ_2 having an associated low value for σ_3.

Although the mean tensor $\overline{\sigma}$ and the mean principal stresses are good approximations to the *in situ* stress tensor, it was difficult to define appropriate weights for the eleven estimates used in their determination given that the estimates were not completely independent, i.e., individual subsets of data were used in more than one estimate. An alternative to using the mean tensor as the final estimate of the *in situ* stress tensor was to use the most reliable of the eleven refined estimates. The 'best' estimate was based on a data set which comprised 223 measurements, incorporated all three measurement types, and excluded those values potentially affected by excavation damage or inaccurate extrapolation. On this basis, the 'best' estimate of the principal stresses is

	MPa	Trend	Plunge
σ_1	59.9	145.4	11.1
σ_2	44.3	53.9	7.7
σ_3	9.4	289.8	76.5

Figure 68 shows the 'best' estimate of the principal stresses, both in terms of magnitude and orientation, along with the expected range of magnitudes and 90% confidence intervals

on orientation. What is particularly striking about the eleven estimates shown in Figure 68 is the consistency in the orientations of the principal stress components. The estimates that do not include radial displacement measurements at $r/a = 1$ tend to deviate most from the cluster around the mean orientations.

4.1.4.3 Comparison with Previous Results

As discussed in Section 2.1.3, the initial estimate of the *in situ* stress tensor at the 420 Level of the URL was based on results from a variety of stress measurement techniques. Of the techniques tried, only the overcoring and under-excavation studies produced estimates of the complete *in situ* stress tensor. However, as detailed in Section 2.1.3, each of these estimates was affected by testing difficulties related, in part, to the high *in situ* stresses at this level. Consequently, a composite tensor was estimated from the various techniques. The composite nature of the tensor posed some difficulties, however, in constraining the relative magnitudes of the various components.

In comparing the 'best' estimate from the back analysis to the initial composite estimate (Figure 68), the two tensors are remarkably similar, especially when the uncertainty in the composite tensor is taken into consideration. One of the most notable differences is that σ_2 in the new estimate is not parallel to the test tunnel axis. In fact, the tunnel axis deviates 8.9° in trend, and 7.7° in plunge from σ_2. This condition implies that antiplane

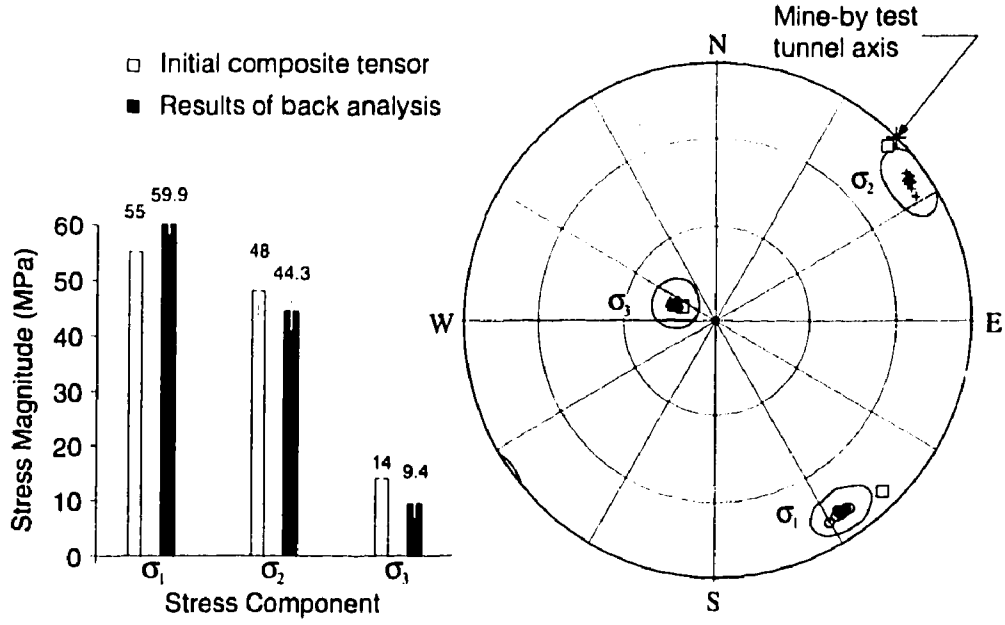

FIGURE 68: Magnitude and orientation of principal stresses estimated from back analysis of displacement measurements. Note the consistency in orientation for the eleven individual estimates shown on the lower hemisphere stereoplot. The estimates of stress magnitudes and orientations from the initial composite tensor are shown for comparison.

shear stresses near the tunnel face in the anterior domain are distributed in an asymmetric manner with respect to the tunnel axis, and precludes back analysis techniques based on the assumption of parallelism between the tunnel axis and a principal stress direction. The implications of this difference are examined in Section 4.3.

The other main difference between the estimates is the magnitude of σ_3. In the composite tensor, σ_3 was based primarily on results of hydraulic fracturing tests conducted in horizontal boreholes at the 420 Level of the URL. Doe (1989) interpreted the shut-in pressure in tests producing subhorizontal fractures in horizontal boreholes as σ_3, based on the assumption that the fractures formed orthogonal to the minimum principal stress direction. However, Haimson et al. (1993) showed that, in a vertical borehole in the same region of the rock mass near the 420 Level, nine hydraulically-produced fractures had dips ranging from 15 to 39° and dip directions ranging from 068 to 245°, illustrating that the induced fractures do not necessarily form orthogonal to σ_3. They further showed that, by assuming the vertical stress to be equal to the calculated lithostatic stress, the best estimate of the maximum horizontal stress near the 420 Level of the URL was approximately 54 MPa. In retrospect, the uncertainty associated with σ_3 in the initial composite tensor was underestimated, and should have been in the same range as that for the other stress components, i.e., ±5 MPa.

The calculated lithostatic stress at the 420 Level of the URL is approximately 11 MPa. The magnitudes of the vertical stress σ_{33} in both the best combined estimate and the mean estimate of the *in situ* stress tensor based on results from the field study compare favourably with this value. The fact that no additional constraint equations were required to achieve this value provides a degree of confidence in the estimated tensor and the elastic constants used in the back analysis (E = 65 GPa and ν = 0.25). The values of the elastic constants are in keeping with those shown in Section 2.1.2 from previous laboratory testing, and are believed representative of the portion of the rock mass from which the measurements used in the back analysis were taken, i.e., primarily from the anterior domain and remote from the excavation. The estimated stress components are directly proportional to Young's modulus.

In addition to predicting a vertical stress component close to lithostatic, the orientation of σ_1 is almost parallel to the average orientation of the fracture zones identified at the URL. The fact that σ_1 is not horizontal can be attributed to a reduction in shear stress parallel to the dip direction of the fracture zones. Observed large-scale shear displacement in the upper portion of the Lac du Bonnet batholith, such as reverse thrusting of up to 7.3 m along Fracture Zone 2 (Everitt et al. 1990a), is evidence for this type of stress relief. Using two simple numerical models, Chandler and Martin (1994) showed that stress redistribution associated with shearing along the major fracture zones also accounts for perturbations in the stresses in the upper part of the batholith. This process generates high stresses in the dip direction of the fracture zones, which results in rotation of the azimuth of the maximum principal stress. Further confirmation of the estimated stress tensor using patterns of excavation damage is undertaken in Section 4.3.

4.2 BACK ANALYSIS USING DBEM3D

In addition to the study described in the previous section, back analysis of the Mine-by Experiment was also conducted using the direct back analysis method developed for the under-excavation technique (Wiles and Kaiser 1994a; Wiles and Kaiser 1994b). This additional analysis was meant to provide confidence in the estimated stress tensor, and to directly assess the effects of face shape and external openings, i.e., other excavations near the experiment area. DBEM3D (Wiles 1992), a PC-based computer program, was used for two studies: one to assess various combinations of instrument results (Wiles 1995), and a complementary study to assess a specific data set selected on the basis of instrument and rock mass behaviour during the Mine-by Experiment. Because the results of the second study have not yet been published, they are included in this report in some detail.

DBEM3D is based on linear elasticity and uses constant intensity triangular and quadrilateral boundary elements solved by the indirect boundary element technique to back calculate initial *in situ* stresses from measured excavation-induced strains and displacements. It is coupled with a statistical package, STAT3D, which allows the user to evaluate the quality of the input data and the confidence of the stress prediction. There are two main control parameters in STAT3D: α controls the number of rounds and therefore the number of individual measurements to include in a particular analysis, while δ controls the number of rounds over which to calculate the incremental responses and hence the magnitude of each measurement used in the analysis.

4.2.1 Sensitivity Analysis

As part of these studies, the sensitivity of the method to various parameters used in the numerical approximation, and to the quality of input data, was assessed using a simple test case. The geometry for this test case was a uniformly discretized rectangular excavation with seven extensometers. The excavation started as a cube with a side-length of 2 m, and was extended 1 m in a single excavation step (Figure 69). Using uniform discretization, it was found that the accuracy in predicted stresses was related primarily to the discretization of the underground openings. As illustrated in Figure 70, the predicted displacement at a single extensometer point approaches an asymptote with increasing number of boundary elements. Likewise, the predicted stresses also approach an asymptote as the number of boundary elements increases. Wiles (1995) further found that the error in predicted stresses was similar to the error in input, e.g., a 5% uncertainty in displacement values produced about a 5% uncertainty in predicted stress magnitudes. Similar results were found using a simple cylindrical model, and using non-uniform discretization.

4.2.2 Application to the Mine-by Experiment

Excavation of the Mine-by test tunnel was simulated using boundary element models constructed to match the surveyed location of each instrument and excavation face position. The complete set of data for the back analysis consisted of displacement measurements from 13 Bof-ex extensometers (11 anchors each) and strains from 12 CSIRO HI triaxial strain cells (9 strain gauges each). The test tunnel advanced past the two CSIRO arrays in Rounds 13

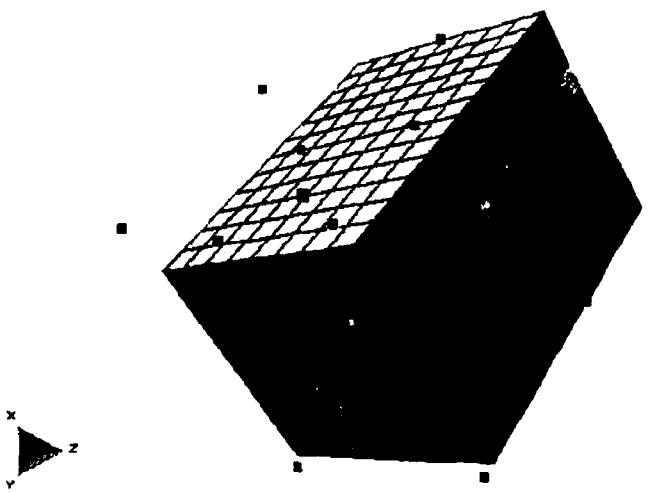

FIGURE 69: Block model used in the sensitivity analysis. The block is initially 2-m long with a 1 m by 1 m square cross-section, and represents the boundary of an opening. Instrument locations are shown as small squares around the block.

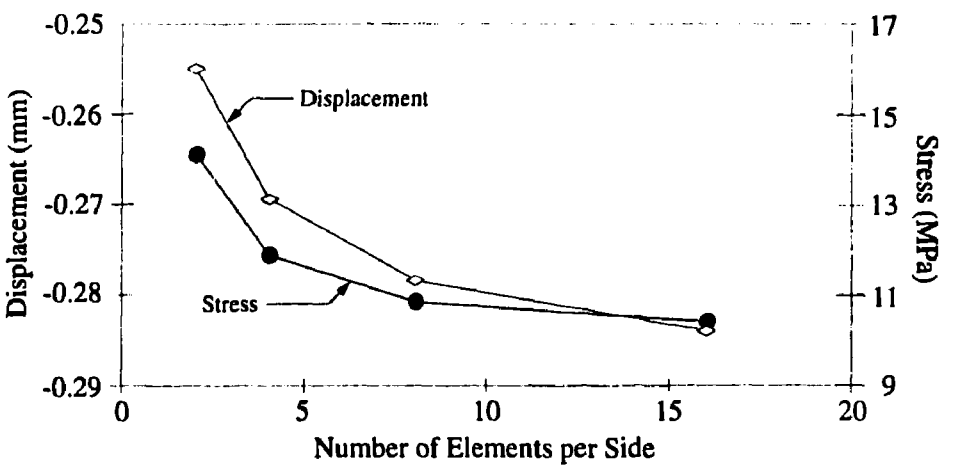

FIGURE 70: Illustration of the effect of discretization on the displacements and stresses predicted for a simple block model. The number of elements refers to the discretization of each side of the square cross-section.

and 20, and past the two extensometer arrays in Rounds 15 and 17, respectively. To obtain well-constrained stress estimates, it was desirable to maximize the number of instrument readings used in each estimate, while eliminating or minimizing the effects of: 1) readings from faulty instruments, 2) readings from regions affected by non-linear/non-elastic material behaviour, and 3) readings from rounds far from the instruments where the measured response was of the order of the instrument error. A series of simulations were conducted using various subsets of instruments to identify the best combination of instruments and excavation rounds to use for the stress estimates. Wiles (1995) considered different combinations of instrument readings, and different combinations of excavation rounds, from those described here.

From previous results with the under-excavation method using CSIRO HI cells (Wiles and Kaiser 1992), it was shown that strain measurements included a large non-linear/non-elastic component once the tunnel face had approached and passed the instrument array, resulting in erratic stress estimates. In the Mine-by Experiment, this type of behaviour was noted in the first CSIRO array starting from Round 12, and in the second CSIRO array from Round 19. Given the position of the first CSIRO array relative to the other instrument arrays, results from the first CSIRO array past Round 12 could not be used in combination with those from the other arrays, and, consequently, cells SM1 to 4 were excluded from the analyses. Likewise, because measurements for Rounds 19 and greater included a large non-linear/non-elastic component, they were not included in the analyses. Of the instruments used for the experiment, only one gauge on one CSIRO cell (cell SM5, gauge 9) was found to be faulty for measurements taken up to Round 18. This gauge was not included in any of the analyses.

In order to maximize the number of instruments included in each stress estimate, it was desirable to take advantage of the overlap in responses measured at the two extensometer arrays, and in the second CSIRO array. However, extensometer results from the Mine-by Experiment showed evidence of non-linear/non-elastic behaviour close to the tunnel wall once the tunnel face had passed the instruments (Read 1994). To reduce the influence of this non-linear/non-elastic behaviour on results of the back analysis, the inner two measurement intervals in the first extensometer array, and the inner measurement interval in the second array, were excluded from the analysis. This approach also minimized the effect of differences between the model geometry and the actual *in situ* tunnel geometry, such as the stepped longitudinal profile of the test tunnel, and the effect of discretization of the tunnel boundary in the model. The outer measurement interval in each extensometer was also dropped because of the proximity of the outer anchor to the external instrument galleries. In the axial extensometer (EXT13), the two intervals closest to Room 414 were also excluded.

The incremental instrument responses, i.e., the change in response between successive excavation rounds, from 100 displacement transducers in the extensometers and 71 strain gauges in the second CSIRO array were used to estimate the *in situ* stress tensor. Independent estimates, based on the incremental responses from each individual excavation step, were obtained by setting the parameters α and δ in STAT3D to 1. These estimates were evaluated to determine the range of excavation rounds that produced consistent results. In evaluating predicted stress orientations and magnitudes, individual estimates from Rounds 1 to 14

showed erratic orientations and/or negative values of σ_3, and were therefore not considered reliable. Likewise, individual estimates from Round 19 and greater were erratic, and were excluded from the analysis. Individual estimates from Rounds 15 to 18 showed consistent stress orientations and magnitudes.

Improved stress estimates were obtained by increasing the number of measurements in the data set upon which each estimate was based. By setting $\alpha > 1$ in STAT3D, the incremental instrument responses from between 2 and 7 consecutive rounds were combined into individual data sets. STAT3D uses a least-squares method to minimize the residuals between measured and predicted strains or displacements, weighting individual responses according to their magnitude. Consequently, estimates obtained from multiple rounds are based on more measurements than those for individual rounds, and are therefore better constrained. Between Rounds 15 and 18, estimates based on the combined incremental responses from as far away as Round 11 were consistent in orientation and magnitude. Based on the number of measurements included in the analysis, the 'best' estimate of the *in situ* stress tensor is that for Round 18 with $\alpha = 7$, which considers the incremental instrument responses for Rounds 11 to 18 in one data set.

In order to assess the variability in stress predictions, a data set of 22 estimates was compiled by considering measurements from Rounds 15 to 18, varying α from 1 to 7 for Round 18, from 1 to 6 for Round 17, and so on. These estimates were, however, not completely independent because individual measurements were used in more than one estimate. From the 22 estimates, the mean and standard deviation tensors of stresses in the tunnel coordinate system, along with the mean and 90% confidence limits of the principal stress tensor, were determined using the method described by Walker et al. (1990). This scheme implicitly weighted measurements from Rounds 15 and 16 most heavily, i.e., 9.5% for Round 18, 16.2% for Round 17, 20.3% for Round 16, 21.6% for Round 15, 16.2% for Round 14, 10.8% for Round 13 and 5.4% for Round 12. As a result of this implicit weighting, there were some differences between the mean estimate and the 'best' estimate given by Round 18 with $\alpha = 7$. Nevertheless, the estimated mean and variability from this group of instruments and excavation rounds was used as a basis for comparison in the different model simulations.

Three types of models were used to simulate the Mine-by Experiment: one incorporating a flat-faced cylindrical tunnel with no external openings, the others using a cylindrical tunnel but accounting for a non-planar tunnel face shape and external openings. Several subcases were run with each model to assess effects of discretization and 'leaks' in the tunnel geometry. Except where noted, Young's modulus was 65 GPa and Poisson's ratio was 0.2 in each case. Discretization was controlled by two parameters, DOL and AL. DOL relates the boundary element side-length L to the distance D from a boundary element to the closest field point, and AL is the minimum element size. The use of constant values of DOL and AL results in fine discretization close to instrument locations, and coarser discretization remote from the instruments. According to Wiles (1995), the error in predictions decreases with increasing values of DOL and decreasing values of AL.

4.2.3 Cylindrical Tunnel with a Flat Face

The first analysis was conducted using a flat-faced, 3.5-m-diameter cylindrical tunnel with no external openings (Figure 71). Three sub-cases, using different values of DOL and AL, were run: a coarse discretization with AL=1 and DOL=2, an intermediate discretization with AL=0.5 and DOL=1.5, and a fine discretization with AL=0.5 and DOL=2. Using the 22 estimates described in the previous section, the mean and standard deviation tensors (in MPa) for the fine discretization sub-case are, respectively,

$$\bar{\sigma} = \begin{bmatrix} 55.87 & -2.94 & 13.21 \\ -2.94 & 44.40 & 1.65 \\ 13.21 & 1.65 & 13.82 \end{bmatrix}$$

$$S_{\bar{\sigma}} = \begin{bmatrix} 1.44 & 0.94 & 2.14 \\ 0.94 & 0.90 & 0.67 \\ 2.14 & 0.67 & 1.53 \end{bmatrix}$$

The standard deviation tensor for the intermediate sub-case was found to be similar to that for the fine sub-case. By comparison, the coarse discretization increased the standard deviation of σ_{11} by about 1 MPa, and of the σ_{22} and σ_{33} components by about 0.5 MPa. The same trend was apparent in comparing the range of values for the principal stress magnitudes and orientations: the fine and intermediate sub-cases compared closely, while the coarse sub-case showed markedly increased variability in both magnitudes and orientations.

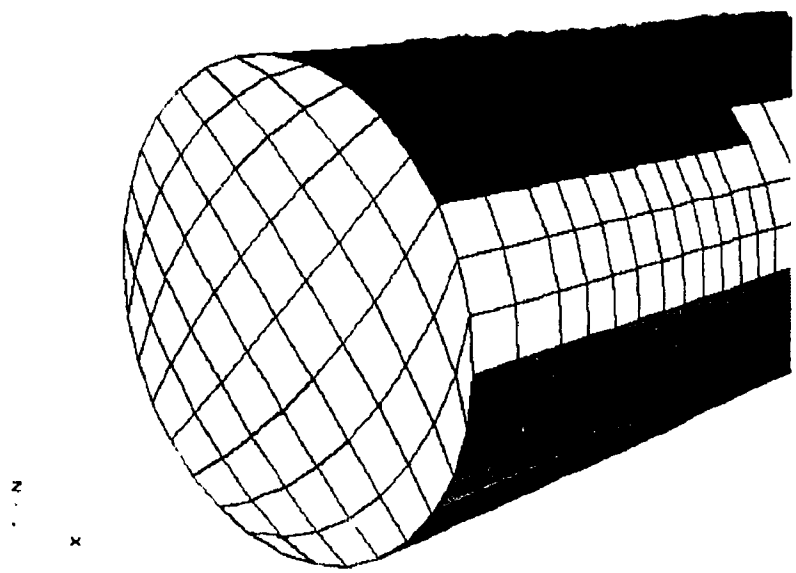

FIGURE 71: Flat-faced cylinder model of the Mine-by Experiment test tunnel used for back calculations. Control parameters are DOL=2 and AL=0.5 in this case.

The results from a Monte Carlo simulation to determine the mean and 90% confidence limits on the principal stress magnitudes and orientations for the fine discretization sub-case are shown in Figure 72. Given the small amount of variability in principal stress magnitudes and orientations shown by the 90% confidence limits for the flat-faced cylindrical tunnel model, it appears that the model adequately represents the *in situ* tunnel geometry. Using a Poisson's ratio of 0.2, the 'best' estimate of the principal stress tensor, given by Round 18 with $\alpha = 7$, is

	MPa	Trend	Plunge
σ_1	59.6	145.1	14.5
σ_2	44.1	53.5	6.3
σ_3	11.1	300.8	74.1

The effect of changing Poisson's ratio from 0.2 to 0.25 was assessed in a simulation using the flat-faced cylinder with intermediate discretization described above. The net result was a decrease of 0.2 MPa in the mean σ_1 value, a 0.5 MPa increase in the mean σ_2 value and a 0.6 MPa decrease in the mean σ_3 value. Changes of less than 0.7° were noted in the mean orientation angles, except for the trend of σ_3 which increased by 1.9°. These changes in magnitude and orientation are generally of the same order as the variability related to the change from fine to intermediate discretization. The 'best' estimate of the *in situ*

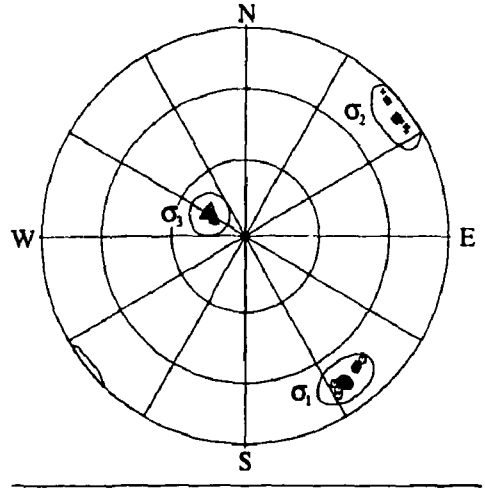

Cylinder with Flat Face

	● σ_1	♦ σ_2	▲ σ_3
Magnitude (MPa)			
-90% CL	57.1	42.5	6.1
Mean	60.0	44.2	9.9
+90% CL	63.4	45.7	13.6
Mean Orientation (°)			
Trend	144.1	052.3	300.1
Plunge	15.4	6.5	73.2

FIGURE 72: Mean and 90% confidence intervals on principal stress magnitudes and orientations for a cylindrical tunnel with a flat face (AL=0.5, DOL=2).

stress tensor (as described previously) using a Poisson's ratio of 0.25 and an intermediate discretization is

	MPa	Trend	Plunge
σ_1	59.8	145.0	14.6
σ_2	45.2	53.5	5.8
σ_3	11.0	302.6	74.2

The results for a flat-faced cylinder compare favourably with those presented in Section 4.1 (duplicated below) using a Poisson's ratio of 0.25.

	MPa	Trend	Plunge
σ_1	59.9	145.4	11.1
σ_2	44.3	53.9	7.7
σ_3	9.4	289.8	76.5

The most notable difference between the estimates is the plunge of σ_1 and the resulting rotation of σ_3. The magnitude of σ_3 is also slightly larger in the DBEM3D back analysis. However, these differences are well within the 90% confidence limits shown in Figure 72. The fact that the two estimates compare so closely is significant in that the approaches, while both based on a cylindrical tunnel model, use different data sets, different types of instruments, and different back analysis methodologies.

4.2.4 Cylindrical Tunnel with a Curved Face

The second analysis was conducted using a 3.5-m-diameter cylindrical tunnel with a curved face to account for deviations from planarity measured during excavation of the test tunnel. To simulate the face curvature, a small central element was required ahead of the tunnel to represent the deepest point on the face. This central element was arbitrarily chosen as a square with a diagonal length of 1 m.

As a result of including the central element ahead of the face, the discretization of the face was altered from that for a flat-faced cylinder (see Figure 71), resulting in some gaps or 'leaks' in the discretized face surface (Figure 73). The effect of these gaps on the stress estimates, without the added effect of face curvature, was investigated using a flat-faced cylinder with a pre-defined central face element. Using values of DOL=1.5 and AL=0.5, and comparing to the flat-faced cylinder with identical control parameter values, it was found that the altered face discretization produced a decrease of about 0.6 MPa in the mean σ_1 and σ_3 values, and a 0.8 MPa increase in the mean σ_2 value. Changes in the mean orientations were less than 0.6° for both trend and plunge angles. Results from the flat-faced cylinder with a central face element were used as the basis for comparison in subsequent simulations with different face curvature.

Face curvature was simulated by positioning the central face element ahead of the plane defined by the mean edge position of the face, then joining the tunnel edge and central face element in one of two ways. In the first case, the tunnel edge and central element were joined using a simple circular arc, similar to the curved faces shown in Section 4.1.4. This shape resulted in a change in the intersection angle between the tunnel wall and face at

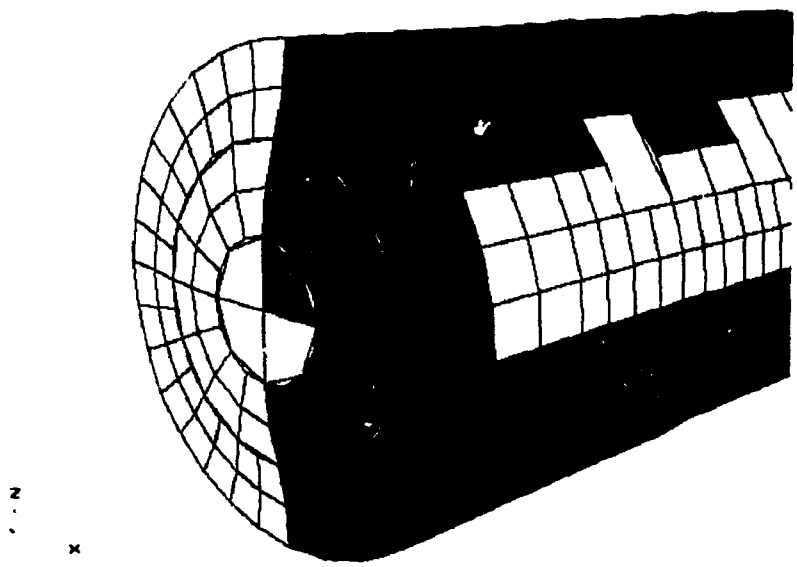

FIGURE 73: Typical face discretization, using a pre-defined central element, for a single-inflection curved face. Note the gaps or 'leaks' in the discretized surface.

the tunnel perimeter. In the second case, the tunnel edge and central element were joined using a single-inflection curve. This shape maintained the right-angle between the tunnel wall and face at the perimeter, more in keeping with field observations. Both approaches assumed axial symmetry in the face shape for each round, and used control parameters of DOL=1.5 and AL=0.5. A typical single-inflection curved face is shown in Figure 73.

Estimates of the *in situ* stress tensor were obtained using both types of face curvature in separate simulations to match surveyed edge and centre positions for each excavation round. In both simulations, the variability in the principal stress magnitudes and orientations was much larger than for the flat-faced cylinder, mainly as a result of a large change in magnitudes and orientations estimated for Round 17. This particular excavation round has a large influence on the mean and variability of the stress estimates because the magnitudes of the displacement and strain responses associated with it are large. The results from a Monte Carlo simulation using the single-inflection shape are shown in Figure 74. The variability in principal stresses represented by the 90% confidence limits is large compared to the flat-faced cylinder case. This increased variability is reflected in the standard deviation tensor for the stresses in the tunnel coordinate system. The mean and standard deviation tensors for this case are given respectively by

$$\overline{\sigma} = \begin{bmatrix} 51.54 & -2.77 & 12.52 \\ -2.77 & 43.46 & 2.11 \\ 12.52 & 2.11 & 12.11 \end{bmatrix}$$

$$S_{\overline{\sigma}} = \begin{bmatrix} 4.98 & 1.25 & 1.06 \\ 1.25 & 2.10 & 0.38 \\ 1.06 & 0.38 & 1.29 \end{bmatrix}$$

As expected, results for the simple circular arc shape showed more variability than those for the single-inflection shape, suggesting that the single-inflection shape is more representative of the *in situ* tunnel geometry than is the circular arc shape.

The *in situ* stress tensor was also estimated using constant values of 50 and 100 mm, in separate simulations, for the difference between the edge and centre positions for each excavation face. Compared to the flat-faced case, results from these simulations showed a decrease in mean principal stress magnitudes, and an increase in variability in both magnitudes and orientations, with increasing amounts of face curvature. However, the maximum change in mean principal stress magnitudes relative to the flat-faced case was only 0.6 and 1.4 MPa in the two simulations, respectively. Based on the variability in stress estimates, these findings suggest that models with constant face curvature are more representative of the *in situ* tunnel geometry than those based on surveyed centre positions within each round. On the same basis, the flat-faced cylinder appears to be the best representation of the Mine-by test tunnel geometry.

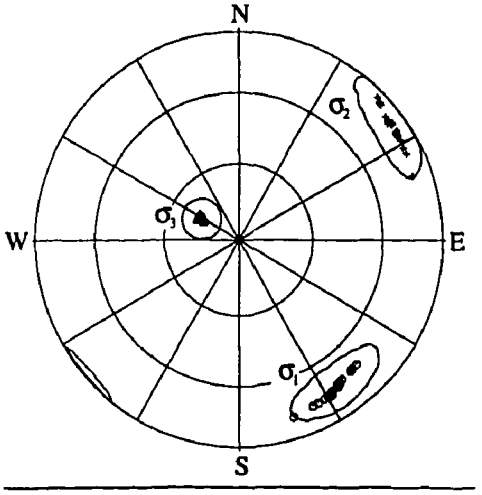

Cylinder with Single-Inflection Curved Face

	▫ σ_1	+ σ_2	▵ σ_3
Magnitude (MPa)			
-90% CL	47.7	39.7	6.2
Mean	55.5	43.3	8.3
+90% CL	63.9	46.5	10.3
Mean Orientation (°)			
Trend	145.3	53.3	298.4
Plunge	15.3	7.4	72.9

FIGURE 74: Mean and 90% confidence intervals on principal stress magnitudes and orientations for a cylindrical tunnel with a single-inflection curved face (AL=0.5, DOL=1.5).

4.2.5 Cylindrical Tunnel with External Openings

A final analysis was conducted using a 3.5-m-diameter cylindrical tunnel with a curved face shape and included the shaft station and instrumentation galleries of the Mine-by Experiment. The discretization parameters used for this simulation were AL=0.5 and DOL=1.5. Results from a Monte Carlo simulation based on the 22 stress predictions associated with this model showed only a very slight change in mean values and variability in principal stress magnitudes and orientations compared to the same case with no external openings. In terms of mean stress magnitudes, inclusion of the external openings resulted in an increase of about 0.2 MPa in σ_1, a decrease of about 0.2 MPa in σ_2 and a decrease of about 0.5 MPa in σ_3. Changes in principal stress orientations were limited to less than 0.5° in both trend and plunge. Consequently, the effect of the external openings on the back analysis results is very minor.

4.2.6 Summary of the DBEM3D Back Analysis

The DBEM3D back analysis provided an independent estimate of the *in situ* stress tensor at the 420 Level of the URL, and illustrated the level of detail required in modelling the Mine-by Experiment to achieve consistent stress estimates. All the simulations showed that the stress estimates were affected by model discretization, although there were only small differences between results using a fine and an intermediate discretization. Estimates using a flat tunnel face with a central element were also more variable than those using a uniform face discretization with identical control parameters.

The face shape used in the model was found to affect the variability in stress estimates. Of all the face shapes considered, the flat-faced cylinder produced the least amount of variability in stress estimates. Assuming the *in situ* stress tensor is relatively constant from round to round, the small variability associated with the flat face suggests that this face shape is most representative of the *in situ* tunnel geometry. In attempting to account for face curvature, the use of a single-inflection curved face produced less variable results than the simple circular arc shape. However, it was shown that simulations with constant face curvature for each round produced less variable results than those based on surveyed positions of the face centre in each round. This finding suggests that the *in situ* tunnel face geometry is not well-represented by assuming a smooth transition from the edge to the centre of the face.

The effect of external openings, i.e., other excavations around the experiment area, on stress estimates was found to be very minor, and could be eliminated in simpler models by dropping the outermost extensometer anchors close to these openings. Stress estimates were also found to be relatively insensitive to an increase in Poisson's ratio from 0.2 to 0.25. Based on the variability in stress estimates, the 'best' estimate of the *in situ* stress tensor at the 420 Level was achieved using a finely-discretized, flat-faced cylinder model with no external openings. Results from the back analysis associated with this model compared favourably with those given in Section 4.1.

In terms of instrumentation, the back analysis showed that the measurements from the 12 radial extensometers and 8 strain cells from the second CSIRO array were consistent with linear elastic behaviour over Rounds 15 to 18. The back analysis further showed that the CSIRO HI cells in the Mine-by Experiment were extremely sensitive, and displayed non-linear/non-elastic behaviour once the tunnel face was within about 1 m of the CSIRO array. Results from the axial extensometer were also consistent with those from the other instruments, but did not significantly affect the stress estimates because of the small displacements measured by the instrument. Overall, the combination of the two extensometer arrays and the second CSIRO array produced well-constrained stress estimates.

4.3 CHARACTERIZING THE DAMAGED ZONE

From the results in Section 3., it was demonstrated that the process of progressive failure starts with crack initiation ahead of the tunnel face in compressive regions where the maximum deviatoric stress is concentrated. For Lac du Bonnet granite around the Mine-by test tunnel, the damaged zone can be considered bounded by the $\sigma_1 - \sigma_3 \approx 70$ MPa contour both for two- and three-dimensions. Within this boundary, the crack-initiation threshold has been exceeded, and the cohesion component of the rock strength has been reduced, i.e., the rock has been weakened. Nevertheless, because of the very small amount of damage, i.e., inelastic straining, required to reduce the cohesion, the elastic properties of the rock mass ahead of the tunnel face are essentially unchanged. Once exposed at the tunnel perimeter as the tunnel is advanced, these localized zones of reduced strength are subjected to the tangential stresses generated around the tunnel by stress redistribution, producing a failed zone typified by breakout notches. However, the failure process results in fall-out or removal of only a portion of the damaged material, so that localized zones of excavation damage remain around the final test tunnel periphery.

The characteristics of the damaged zone, including its extent and material behaviour, were investigated in a series of geophysics studies, a post-excavation characterization program, and a numerical modelling study. As background for interpreting results from these studies, the stress redistribution around the Mine-by test tunnel associated with the back-analyzed stress tensor was investigated (Section 4.3.1). The geophysics studies are summarized in Section 4.3.2. Results of characterization and numerical modelling to determine the damaged zone characteristics are covered in Section 4.3.4.

4.3.1 Stresses around the Mine-by Test Tunnel

The *in situ* stresses and material properties in the elastic region represent boundary conditions around the test tunnel. Based on the back analysis of displacement measurements (Read 1994), the estimated principal stresses in the elastic region are

	MPa	Trend	Plunge
σ_1	59.9	145.4	11.1
σ_2	44.3	53.9	7.7
σ_3	9.4	289.8	76.5

These values are based on a Poisson's ratio of 0.25 and a Young's modulus of 65 GPa. As pointed out by Read (1994), the estimated stress magnitudes are directly proportional to Young's modulus chosen for the back analysis. This estimate of the *in situ* stress tensor indicates a slightly larger ratio of σ_1 to σ_3 than the estimate from the DBEM3D back analysis, which results in more extreme stress concentrations around the opening.

Under these boundary conditions, the introduction of a circular tunnel in an elastic medium alters the stress distribution significantly. Figure 75 shows contour plots of the principal stress magnitudes and of the angle between each principal stress trajectory and the plane orthogonal to the tunnel axis, i.e., the antiplane angle. The most significant features in the plots of stress magnitude are the highly compressive region in the roof and floor of the tunnel in the σ_1 plot, the slight tensile region in the sidewalls in the σ_2 plot, and the highly tensile region in the sidewalls in the σ_3 plot. The plots of antiplane angle are particularly useful in illustrating the crossover in σ_1 and σ_2 in the sidewalls of the tunnel, σ_1 corresponding to the axial stress in these regions. They also illustrate that σ_3 in the sidewalls is oriented approximately 7° out of plane, thus comprising both a tangential and an axial component. The slight rotation of σ_3 would tend to cause en echelon tensile cracking as opposed to contiguous tensile cracking in the highly tensile sidewall region.

The stress state around the tunnel can also be represented in terms of mean and distortional stresses (Figure 76). For brittle rock, the intermediate stress component is not usually considered an important contributor to failure and consequently failure criteria are written in terms of σ_1 and σ_3 only, e.g., Hoek-Brown and Mohr-Coulomb criteria. In this case, the mean stress is $\frac{1}{2}(\sigma_1 + \sigma_3)$ and the maximum shear stress is $\frac{1}{2}(\sigma_1 - \sigma_3)$. These two-dimensional criteria have also been extended to three-dimensions and are typically expressed in terms of the stress invariants. In principal stress space, the position along the space diagonal (i.e., the line given by $\sigma_1 = \sigma_2 = \sigma_3$) is expressed as $I_1/\sqrt{3}$ and the orthogonal distance from the space diagonal to the point in stress space is given as $\sqrt{2J_2}$, where I_1 and J_2 are the first stress invariant and the second deviator stress invariant, respectively.

Figure 77 shows a Hoek-Brown failure criterion based on results of laboratory tests on samples from the test tunnel, with $\sigma_c = 157$ MPa, $m = 35.2$ and $s = 1.0$. Although most points fall below the failure envelope, there are some points around the tunnel that fall outside the failure envelope, and therefore represent failure states. In a plot of factor of safety, where values greater than unity represent points within the failure envelope, and values less than unity represent failure states, the stress conditions around the circular tunnel produce zones of compressional failure in the roof and floor, and zones of tensile failure in the sidewalls. While this is an idealized illustration of the conditions around the test tunnel, it captures the general trend of the stress changes around the tunnel. As discussed in Section 3., the progressive development of a v-shaped notch in the roof and floor of the test tunnel tends to exaggerate the stress concentrations in these regions, focusing the highly compressive concentration in a small region at the notch tip. An example of the stress distribution around the notched tunnel geometry is shown in Figure 78.

The analysis of progressive failure conducted in Section 3. was based on the initial estimate of stresses at the 420 Level of the URL (see Table 2). For that stress state, the compressive and tensile stress concentrations around the test tunnel are less severe in magnitude, and

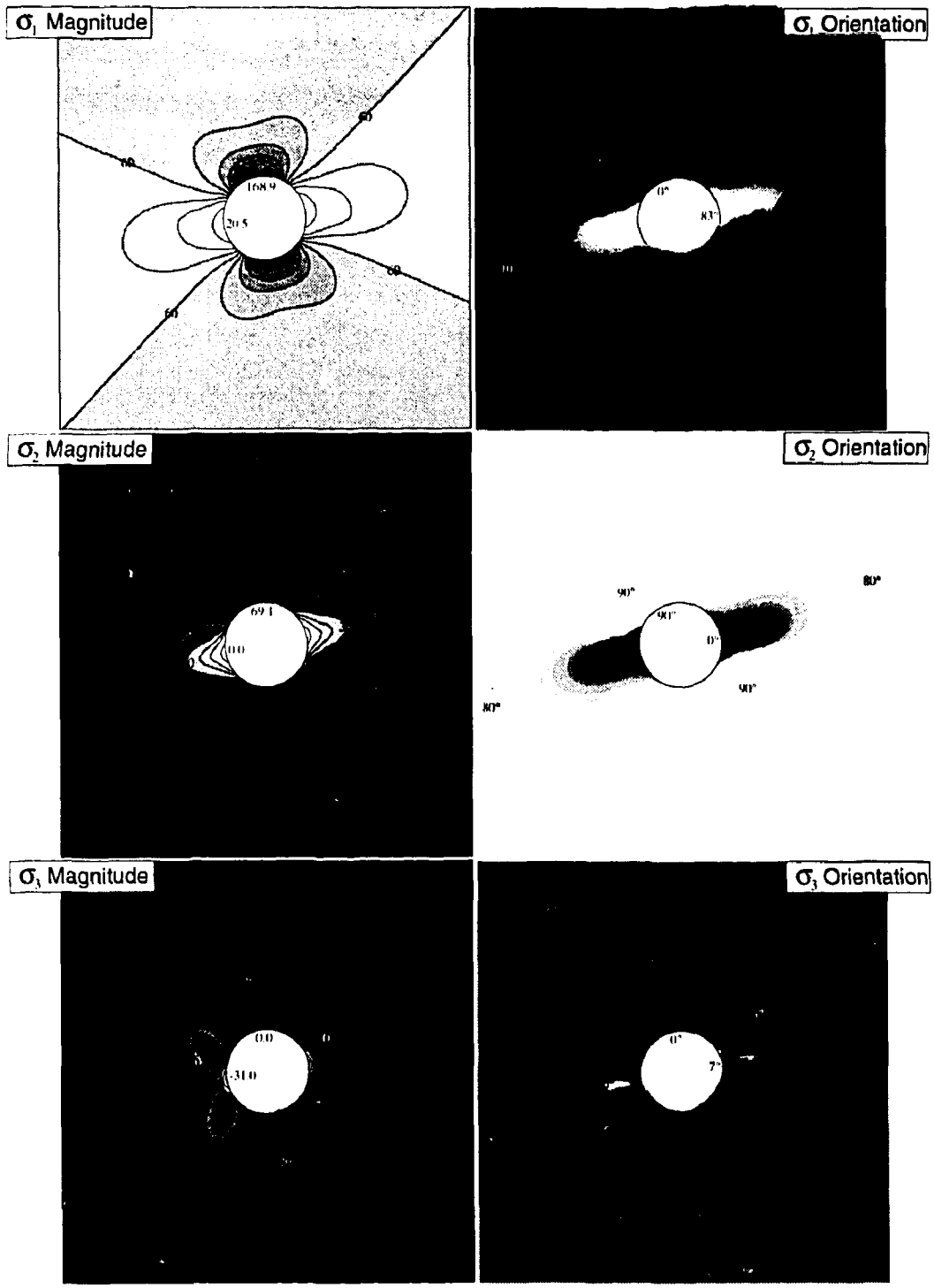

FIGURE 75: Principal stresses around the test tunnel. The figures in the left column are the magnitudes of σ_1 (top), σ_2 (middle) and σ_3 (bottom) in 10 MPa contours. The figures in the right column show the angle between each principal stress trajectory and the plane of the paper in 5° contours. Shades range from black for trajectories within the plane, to white for trajectories out of the plane. Boundary values are shown in each plot.

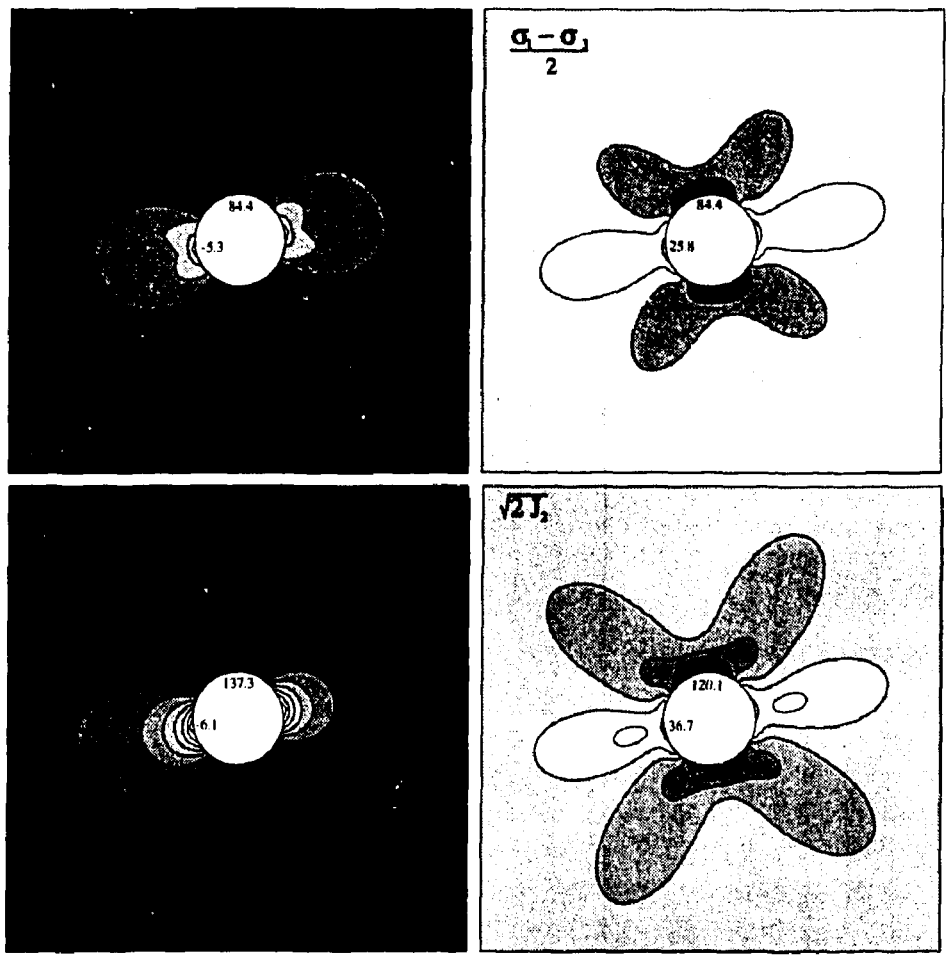

FIGURE 76: Various representations of mean and distortional stresses around a tunnel.

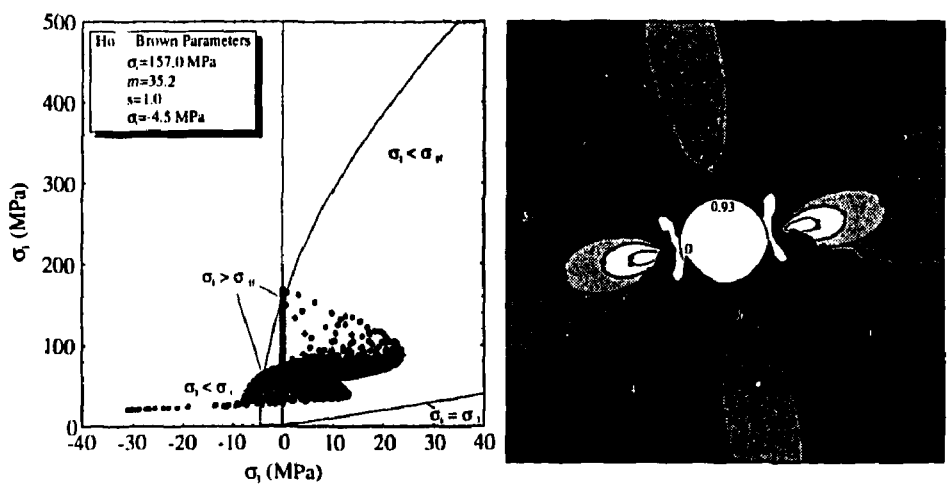

FIGURE 77: Example of a typical Hoek-Brown failure envelope and a factor of safety plot.

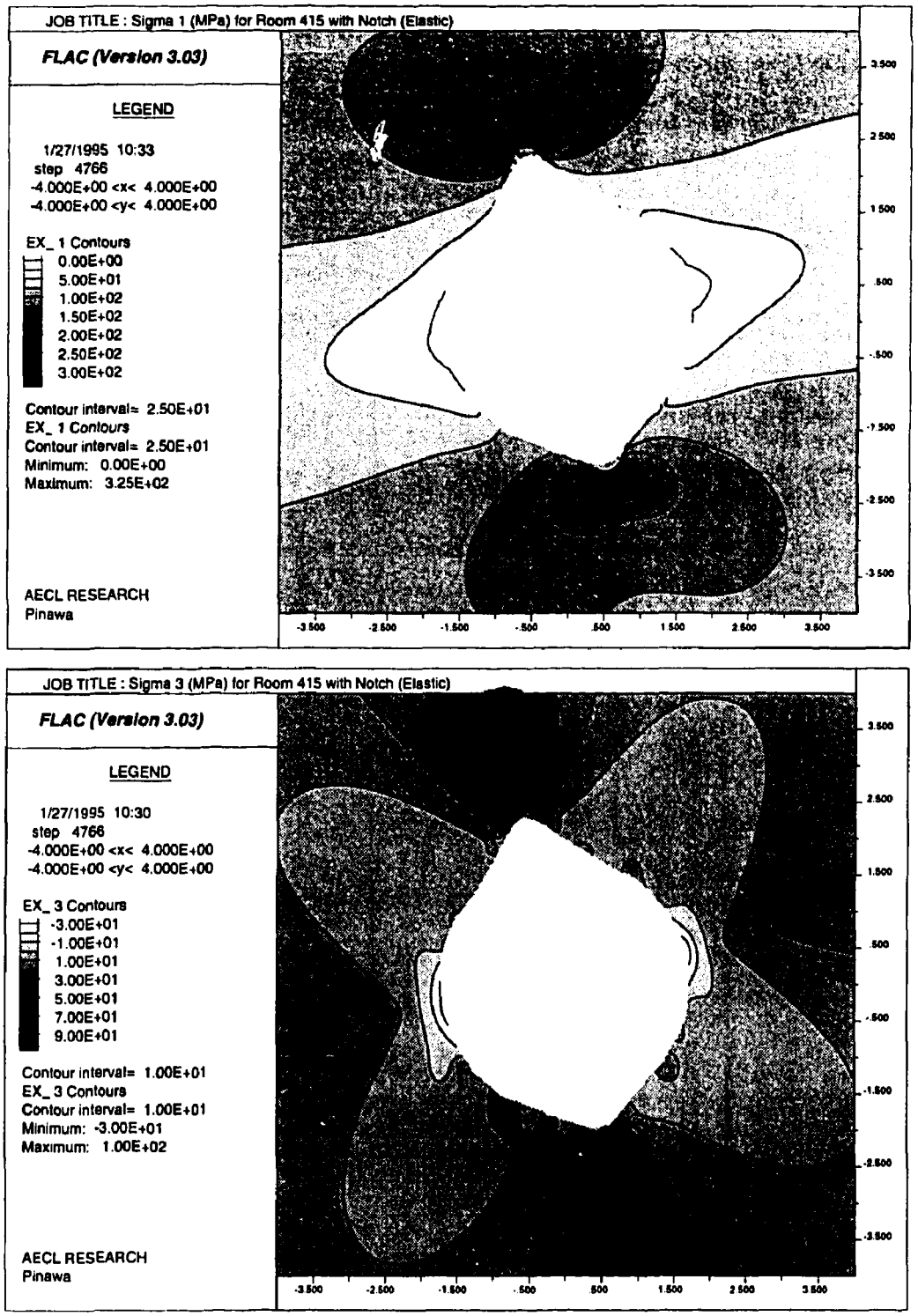

FIGURE 78: Principal stresses around the test tunnel showing the effects of a notched tunnel geometry. Results are based on the back-analyzed stress tensor.

the minimum principal stress shows no antiplane rotation in the two-dimensional plane strain analysis. Nevertheless, the overall pattern of stress concentrations is not significantly different than that presented in this section, and consequently the interpretations associated with the process of progressive failure are unaffected. One slight adjustment is that, using the back-analyzed stress tensor, the lower bound of the crack-initiation threshold is closer to 73 MPa for grey granite as compared to the 70 MPa shown in Section 3. However, this adjustment is relatively insignificant in comparison to the effects of *in situ* variability on the crack-initiation threshold, as discussed later in Section 4.3.5.

4.3.2 Geophysics Studies of Excavation Damage

The geophysics studies conducted for the Mine-by Experiment included a series of crosshole seismic tomography surveys, an acoustic emission (AE) study in the sidewall region of the tunnel, and velocity imaging based on a study of wave propagation effects of an underground opening.

4.3.2.1 Crosshole Seismic Tomography Surveys

Four crosshole seismic surveys were conducted in a vertical plane orthogonal to the axis of the Mine-by test tunnel to observe excavation-induced changes in seismic velocity and mechanical properties of the granite (Hayles et al. 1995). Two of these surveys were done prior to the excavation, one to observe far-field, and the other to observe near-field, velocity conditions. These two surveys were then repeated after excavation of the Mine-by test tunnel to observe changes in the P- and S-wave velocity distribution resulting from tunnel excavation.

The velocity surveys were done in two arrays of 76-mm-diameter (NQ size) diamond-drilled boreholes, referred to as the far-field (or main) panel and the near-field panel. The main panel configuration consisted of 22 cored boreholes, all in a single vertical 33 m by 40 m plane orthogonal to the tunnel axis. The tunnel intersected the centre of the main panel at approximately chainage 21+25 in Room 415. The near-field panel consisted of 8 extensometer boreholes, all drilled in approximately the same plane as the main panel, and intersecting the Mine-by test tunnel in a radial pattern.

All measurements were made with mini-CHARTS Hayles et al. (1992), a miniature crosshole seismic system developed by AECL for geological mapping and engineering assessment of granite. The instrument is a small-scale version of the larger and more powerful CHARTS (Cross-Hole Audio-frequency Rock Testing System) initially developed for AECL at the University of Toronto (Wong et al. 1987). The transducers for the surveys operated from 5 to 80 kHz. The receiver and transmitter transducers are designed for use in either dry or wet boreholes to generate good quality P- and S-waves to distances of > 60 m. The instrument is similar to that described by Gladwin and Stacey (1974) and by Paulsson and King (1980) and Paulsson (1983).

The relationship between microcracks (i.e., damage), stress and seismic velocity is fairly well understood for rock samples and cores. Preferentially-oriented open microcrack populations

in the rock matrix will tend to close upon compressive loading resulting in increased seismic velocity, and will tend to open upon tensile loading causing a velocity reduction. As shown by Martin (1993), the extraction process induces microcracks in samples of granite from depth at the URL. Stesky (1980) and (1985) has shown that, for such samples of Lac du Bonnet granite, most microcracks are fully closed for stresses above about 200 MPa. Beyond this point the relation between stress and elastic wave velocity is more subtle.

According to Everitt and McGregor (1996), there are two low-dipping, NE-striking sets of pre-existing microcracks in the rock mass at the 420 Level of the URL, comprising healed fluid inclusions within quartz grains. *In situ*, these features do not constitute open crack porosity, and, consequently, would not be expected to affect P- or S-wave velocities upon increased compressive loading. However, in conjunction with the development of new microcracks under tensile loading, i.e., extensional damage, it is possible that these healed microcrack sets are preferentially exploited and reopened upon stress relief. The development of excavation-induced damage in tensile regions around the Mine-by test tunnel is the dominant cause of velocity variations *in situ*, resulting in directionally-dependent decreases in seismic velocities near the tunnel wall.

Velocity statistics for 13 horizontal rays and 10 vertical rays extracted from the 1991 pre-excavation surveys of the main panel show means of 5878±18 and 5911±23 m/s, respectively. These values represent a velocity anisotropy of about 0.5% within the main panel. A region of slightly higher P-wave velocity, corresponding to an area of granodiorite, was noticeable in the upper NW corner of the main panel in both the pre- and post-excavation survey. The main panel velocity tomograms showed velocity changes of ±20-40 m/s for the region away from the tunnel excavation. The repeat survey results showed the tunnel outline as a low velocity zone in the geometric centre of the panel. In this region, P- and S-wave velocities were reduced by 180 to 250 m/s owing to the presence of the tunnel. After excavation, the dynamic Poisson's ratio decreased slightly, while the static Young's modulus (determined through an empirical relation from Eissa and Kazi 1988) was virtually unchanged except for the region immediately around the tunnel.

In contrast to the main panel survey, anisotropy in the post-excavation near-field survey was very strong and heterogeneous, i.e., variable around the opening. Table 6 shows the average P- and S-wave velocities for all rays in the near-field panels for the pre- and post-excavation surveys. The sidewall panels show a reduction in the average velocities of about 4%, with a preferential decrease in vertical ray paths, consistent with excavation-induced damage in these regions. These findings are consistent with the development of subhorizontal microcracks in the highly tensile region resulting from excavation-induced stress redistribution. Where the compressive stress increased in the crown and floor, there was no definite indication of increased seismic velocity, although the survey uncertainty was perhaps too large to observe a change. The lack of an increase in seismic velocity upon increased compressive loading suggests that the volume of open microcracks, i.e., porosity, under the initial *in situ* stress conditions prior to tunnel excavation is very small compared to the excavation-induced damage in the tensile regions.

Results from the near-field velocity surveys show lower P-wave velocities, and a more extensive zone of damage, in the granite on the SE side of the tunnel than in the granodiorite

TABLE 6

AVERAGE NEAR-FIELD VELOCITIES PRE- AND POST-EXCAVATION

	Pre-excavation			Post-excavation		
Panel	No.	P-Wave	S-Wave	No.	P-Wave	S-Wave
EXT7-6	418	5843 ± 100	3399 ± 75	160	5715 ± 158	3405 ± 46
EXT12-6	351	5853 ± 250	3428 ± 200	160	5855 ± 82	3453 ± 44
EXT11-12	403	5782 ± 100	3397 ± 60	355	5575 ± 158	3386 ± 61

After Hayles et al. (1995).

on the NW side. A P-wave velocity reduction of more than 300 m/s was detected to about 1.1 m from the SE sidewall of the tunnel, whereas a similar reduction in the NW sidewall was limited to within about 0.6 m of the opening. These patterns were also apparent in the velocity difference and mechanical property tomograms. Read (1994) has shown that, in laboratory tests, grey granite is more susceptible to damage than granodiorite in both compression and tension as a result of its inequigranular grain distribution. Consequently, under identical stress conditions, samples of granite tend to sustain more damage, and hence contain more extensive microcracks, than granodiorite. Results from the near-field velocity surveys confirm the same trend *in situ*.

In summary, the crosshole seismic tomography surveys were successful in identifying zones of reduced velocity, corresponding to excavation-induced damage, in the tensile sidewall regions of the tunnel. Although the surveys did not define the boundaries of the damaged zone precisely, the extent and intensity of this damage was shown to depend on the rock type, granite showing more signs of damage than granodiorite. In the compressive regions around the test tunnel, there were no indications of velocity increases, suggesting there are no significant pre-existing open microcracks *in situ* in the experiment area.

4.3.2.2 AE Study in the Tunnel Sidewall

Small-scale acoustic emission (AE) monitoring and ultrasonic velocity measurements were conducted by Carlson and Young (1993) on a portion of the Mine-by Experiment test tunnel sidewall. An AE array was installed along the NW wall after the test tunnel had been excavated approximately 22 m (Round 17). Four 76-mm-diameter (NQ size) boreholes arranged in a diamond pattern were drilled parallel to the far-field σ_1 direction, inclined about 11° to the SE. The array enclosed a rectangular prism of rock approximately 0.7 x 0.7 m in cross-section and 1.1 m deep. Five 1 MHz compressional transducers installed in each borehole, and three additional transducers attached to the tunnel wall, were used to carry out AE monitoring and velocity surveys.

AE monitoring began 1992 March 13, seven days after Round 17 was completed, and continued for 3.5 weeks, during which time two half-metre rounds (Rounds 18 and 19) were completed and a third (Round 20) begun. Source location uncertainty was estimated at 44 mm near the centre of the array, while event locations further than 0.75 m from the

TABLE 7

ANISOTROPY IN AVERAGE P-WAVE VELOCITIES IN THE SIDEWALL OF THE MINE-BY EXPERIMENT TEST TUNNEL

Round	Compressional Velocity (m/s)						Anisotropy (%)		
	Max.(a)	Int.(b)	Min.(c)	Avg.(a,b)	Avg.(a,c)	Avg.(b,c)	(a,b)	(a,c)	(b,c)
17	5815	5590	5075	5703	5445	5333	3.9	13.6	9.7
18	5650	5440	5080	5545	5365	5260	3.8	10.6	6.8
19	5660	5490	5070	5575	5365	5280	3.0	11.0	8.0
20	5660	5500	5040	5580	5350	5270	2.9	11.6	8.7

After Carlson and Young (1993).

array centre were approximate at best. Focal mechanisms were also calculated for events that located within 0.75 m of the array centre and that had at least eight polarity picks. These were classified as tensile, shear, compressive or indeterminate. Velocity surveys were made immediately before and after each AE monitoring period, with errors in velocity determinations due to uncertainties in transducer location estimated at ±40 m/s (Carlson and Young 1993).

A velocity survey conducted at the 420 Level prior to excavation of the Mine-by Experiment test tunnel confirmed that the rock is quite homogeneous and isotropic. The measured compressional velocity was 5880 ± 60 m/s with a weak anisotropy of approximately 0.5%, vertical rays travelling slightly faster than horizontal rays (Hayles et al. 1995). In contrast, compressional velocities from the initial velocity survey conducted in the AE study were much more anisotropic within the surveyed portion of the tunnel wall. For Rounds 17 to 20, the maximum velocity was approximately parallel to the tunnel axis (axial direction a), the intermediate velocity was subvertical (tangential direction θ) and the slow velocity was approximately orthogonal to the tunnel axis (radial direction r). These directions correspond approximately with the *far-field* σ_2, σ_3 and σ_1 directions, respectively. The magnitudes of the maximum, intermediate and minimum compressional velocities, and the calculated anisotropy in the various principal velocity planes, are given in Table 7. These values are based on an ellipsoidal model which averages velocities of similarly-oriented rays, independent of distance from the tunnel wall.

From the results in Table 7, average compressional velocities are strongly anisotropic (8-14%) in the r-θ and the r-a planes, and moderately anisotropic (3-4%) in the a-θ plane. Compared to the pre-excavation value of 5880 m/s, the maximum, intermediate and minimum velocities measured for Round 17 represent a decrease of 1.1, 4.9 and 13.7%, respectively. The maximum and intermediate velocities further decreased between Rounds 17 and 18 by about 3%, but were essentially unchanged for later rounds. The maximum and intermediate velocities for Round 18 represent a reduction of 3.9 and 7.5%, respectively, from the pre-excavation velocity. The minimum velocity remained fairly constant for all four rounds.

Compressional and shear velocity variations with distance from the tunnel wall were also considered for selected raypaths in the a-θ plane (Figure 79). Compressional velocities were measured horizontally and vertically, while shear velocities were measured at $\pm 45°$ from vertical. Both sets of measurements indicate a decrease in velocities near the tunnel wall. At 0.15 m from the tunnel wall, compressional velocities for horizontal raypaths tangential to the tunnel wall decreased just over 5% from the pre-excavation velocity of 5880 m/s, while those 0.75 m or deeper into the tunnel wall were virtually unchanged. Likewise, for subvertical raypaths tangential to the tunnel wall, compressional velocities at 0.15 m into the rock mass decreased by over 10% of the pre-excavation velocity, but were within about 2% past 0.75 m. Similar trends were apparent in the shear velocities (Carlson and Young 1993). The rapid rise in both shear and compressional velocities with distance from the tunnel wall indicates that open microcracks in the tunnel sidewall are concentrated near the free surface, and do not extend beyond about 0.75 m from the wall. In addition, the shear velocity trend rules out desaturation as the sole cause of the compressional velocity variation.

Locations for 1307 AE events were determined manually from compressional wave arrivals. Of these event locations, only 199 (12%) were within 0.75 m of the array centre, and therefore considered accurate. These 199 events were concentrated near the sidewall surface

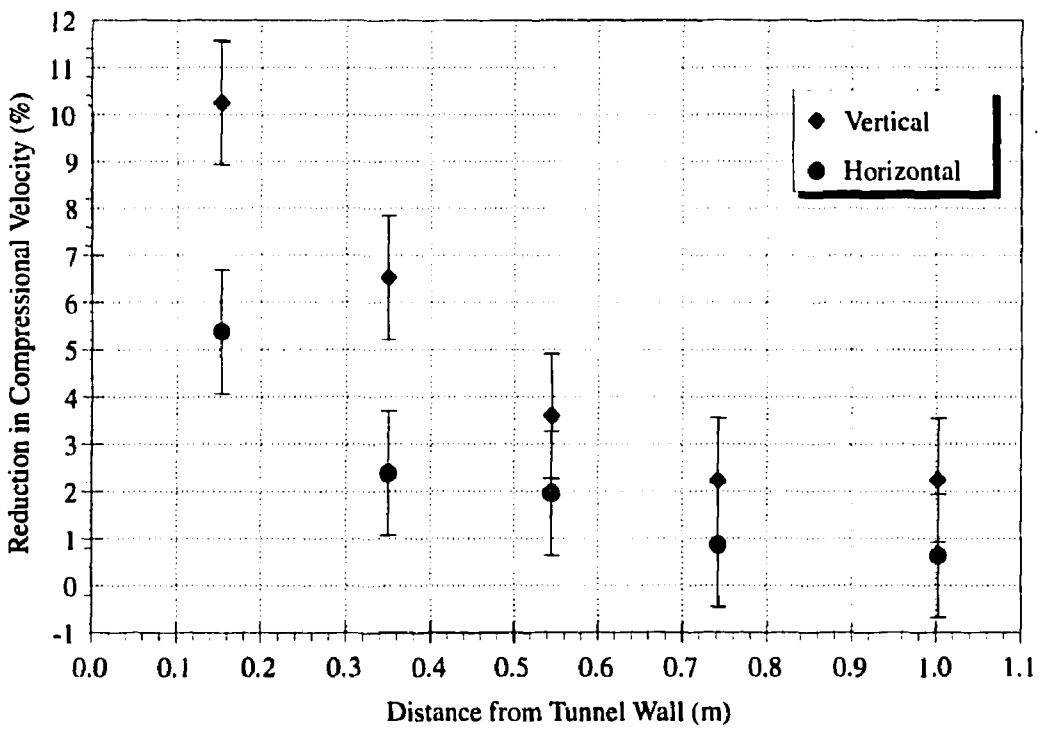

FIGURE 79: Results from ultrasonic velocity survey in sidewall of the test tunnel. Reduction in compressional velocity near the tunnel wall is more pronounced in vertical than in horizontal rays. Results indicate open crack porosity within about 0.5 m of the tunnel wall.

and towards the working face of the tunnel, with the most prominent cluster of activity just above the top borehole. Most of the events occurred within 0.8 m of the tunnel wall, with over two-thirds within the first 0.4 m (Figure 80). The mean 'event-to-free-surface' distance was 0.35 m. The strong concentration of events in the first 0.4 m of the tunnel wall is further evidence that open microcracks are concentrated near the tunnel wall.

Focal mechanism solutions were possible for 107 of the 199 events. Of the 107 solutions, 27 were tensile, 76 were shear and only 4 were compressive mechanisms. The recorded sequence of AE events (Carlson and Young 1993) suggests that the tensile events are a result of tunnel advance, which increases tensile stresses in the sidewall region. The other events tend to occur during periods where the face position is constant, and are related to stress redistribution resulting, in part, from the tensile microcracking. This sequence of tensile events followed by shear events is most notable in Round 18, but also occurs in Rounds 19 and 20. Round 17 shows primarily shear events because the AE array was installed after the initial advance of the round, and the tensile events related to the face advance were therefore not recorded. In addition, the tangential stress in the centre of Round 17 is close to the transition from compression to tension.

The spatial distribution of events (Figure 81) shows that the tensile events align with the *far-field* σ_1 direction, and cluster in the region where macroscopic tensile cracking is expected, given that the ratio of principal stresses in the cross-sectional plane is significantly greater than 3:1. In this region, σ_3 is tensile and approximately tangential to the tunnel wall, σ_2 is radial and tensile over a small distance from the tunnel wall, and σ_1 is axial and compressive. The shear events tend to occur on the flanks of the tensile region near the

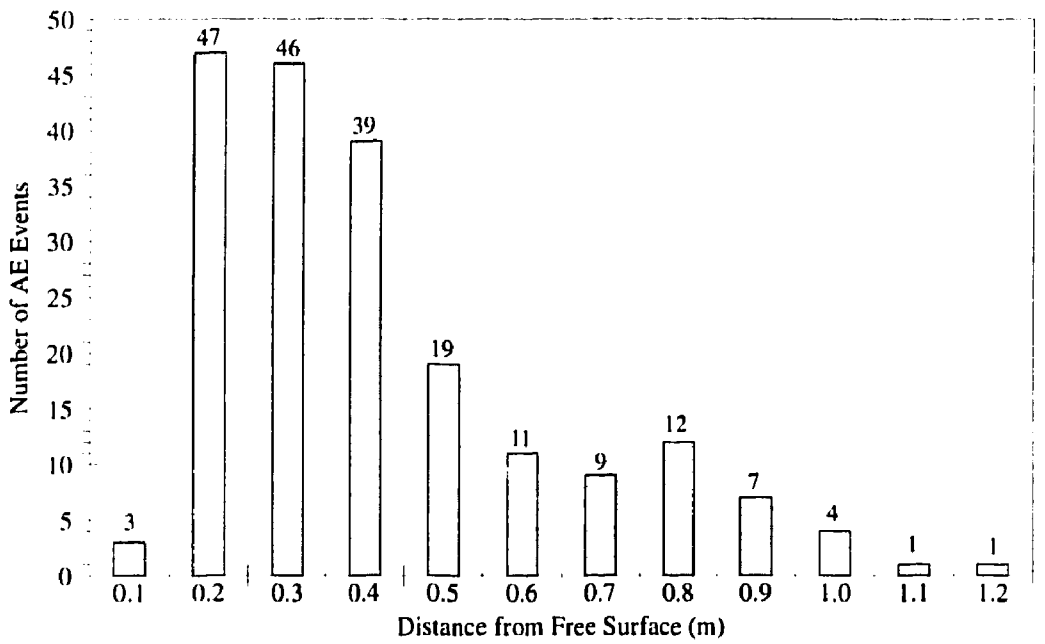

FIGURE 80: Number of AE events with distance from the sidewall surface. The total number of events is 199.

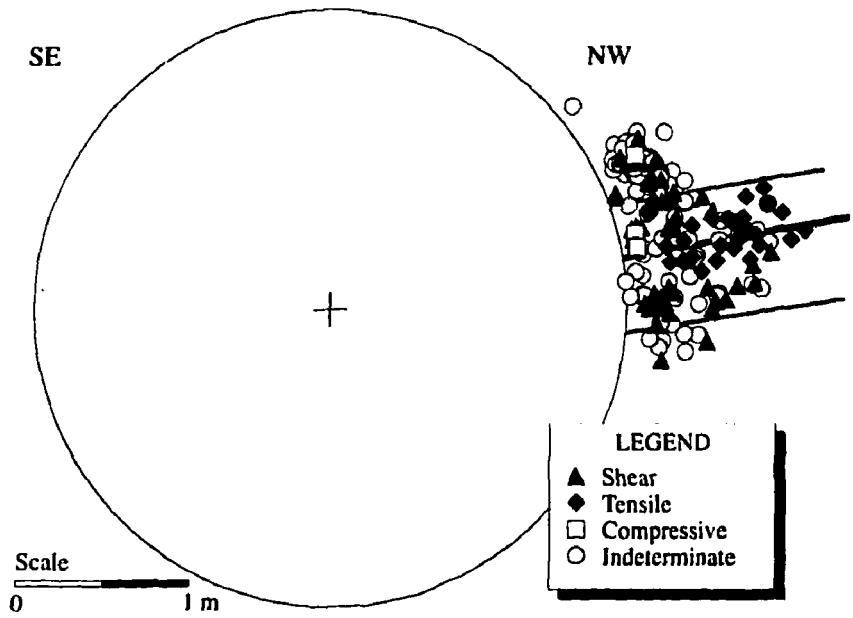

FIGURE 81: All AE locations within 0.75 m of the array centre. Note how the tensile events align with the *far-field* σ_1 direction.

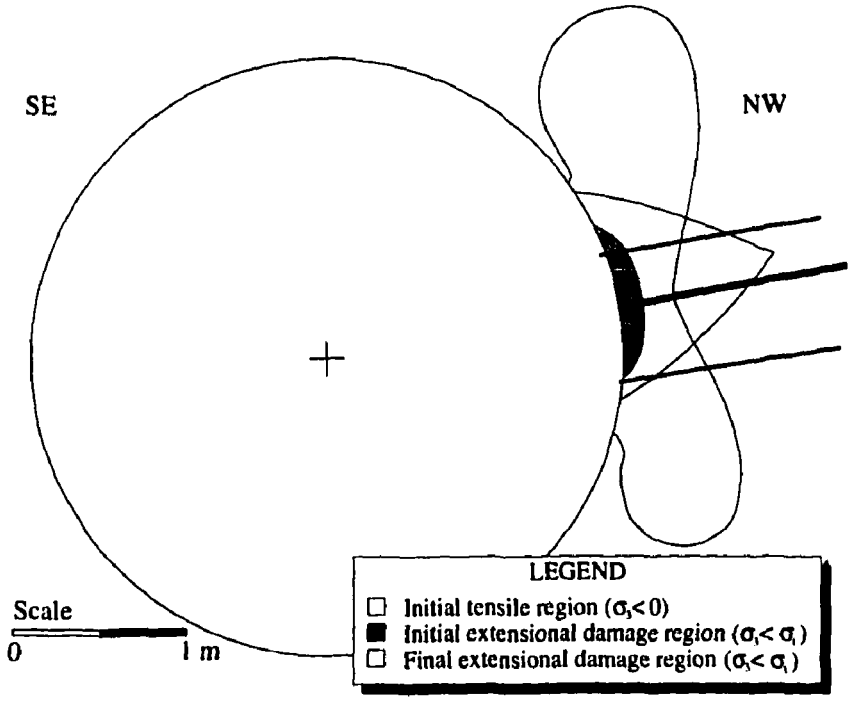

FIGURE 82: Extent of initial and final region where extensional cracking is expected for the Mine-by test tunnel. The initial region is based on the stress distribution around the tunnel related to Round 18.

opening. The compressive events are also located close to the tunnel wall. As described in Section 4.3.4, Read (1994) tracked the development of extensional damage in the sidewall region using an iterative finite difference analysis, substituting oriented ubiquitous joint elements for elastic elements that had failed in tension. The analysis showed that the initial region where $\sigma_3 < \sigma_t$ for the Mine-by test tunnel is confined to within 0.14 m of the tunnel wall, but grows to 0.94 m from the wall as a result of stress redistribution caused by progressive extensional cracking (Figure 82). Although the analysis was limited in its scope, the shape and extent of the eventual zone of extensional damage is similar to that recorded by the AE system. These results suggest that the tensile region in the sidewall has sustained excavation-induced damage to about 1.0 m from the wall, with the most significant damage within about 0.5 m of the tunnel wall, and only very minor damage past 0.75 m.

4.3.2.3 Three-Dimensional Seismic Velocity Imaging

Standard seismic velocity surveys measure the travel time of a seismic ray between known source and receiver positions, from which an average or apparent velocity is calculated assuming a straight raypath. However, when conducted close to an underground opening, these types of surveys do not account for ray diffraction around the opening, or variations in velocity along a given raypath. Consequently, the calculated apparent velocities may not reflect the actual velocity structure of the rock mass close to the opening. These effects can be compensated for by using three-dimensional seismic velocity imaging (Maxwell and Young 1994).

A near-field seismic P-wave velocity calibration study (Maxwell and Young 1994) was performed by detonating small explosions in short holes down the length of the Mine-by test tunnel, and recording the travel times to the AE/MS monitoring sensors. Considering only rays that were not subject to diffraction, i.e., straight raypaths that did not intersect the tunnel, a composite stereoplot of velocities measured from different sources around the tunnel was compiled (Figure 83). The stereoplot shows two main clusters of low velocity (black areas), one subvertical and the other subhorizontal, approximately orthogonal to the test tunnel azimuth (225°). The subvertical cluster comprises two subsets of low velocity. From the results of the AE study in the sidewall of the test tunnel (Carlson and Young 1993) and *in situ* characterization, the low velocity clusters are associated with those raypaths that intersect the localized excavation-induced damage in the tunnel sidewalls. The apparent velocity and anisotropy patterns represented by Figure 83 are therefore not expected to be pervasive around the actual tunnel but, nonetheless, can be used as an initial starting model for the inversion.

From Figure 83, the composite seismic velocities in the horizontal plane are noticeably anisotropic (5900 to 5500 m/s), with the fast direction (base velocity) parallel to the test tunnel axis. Comparison of results from the near-field survey to those from a far-field survey in intact rock away from openings (Figure 84) illustrates a common base velocity oriented at azimuth 045° for horizontal rays in the two surveys. The figure also illustrates that the magnitude of the anisotropy for the intact rock (5900 to 5800 m/s) is less than the apparent anisotropy in the near-field survey. Therefore, excavation damage around the Mine-by test

tunnel significantly reduces apparent velocities on some raypaths between the tunnel and the microseismic array.

To address the issues of diffraction and velocity variation, three-dimensional seismic velocity imaging was carried out using results from the near-field seismic P-wave velocity calibration study (Maxwell and Young 1994). P-wave arrivals were significantly delayed due to diffraction of raypaths around the opening, which was accounted for using a finite difference technique. This technique followed the wavefront propagation from a specific source location and allowed the actual raypath lengths from source to receiver, including the effects of diffraction, to be computed. Using the improved raypaths, three-dimensional seismic velocity imaging was conducted to determine the near-field velocity variations around the test tunnel (Maxwell and Young 1994). A least-squares estimate of the anisotropy observed for all the raypaths, based on the velocity distribution shown in Figure 83, was used as the initial starting model for velocities and anisotropy throughout the rock mass. While this assumption did not account for the variable and position-dependent nature of velocities around the test tunnel, i.e., localized induced damage, the model provided a starting point against which to compare the computed velocity variations.

A damped least-squares inversion technique was employed to determine the velocity variations around the tunnel. A grid of points with a 1 m spacing was set up around the tunnel,

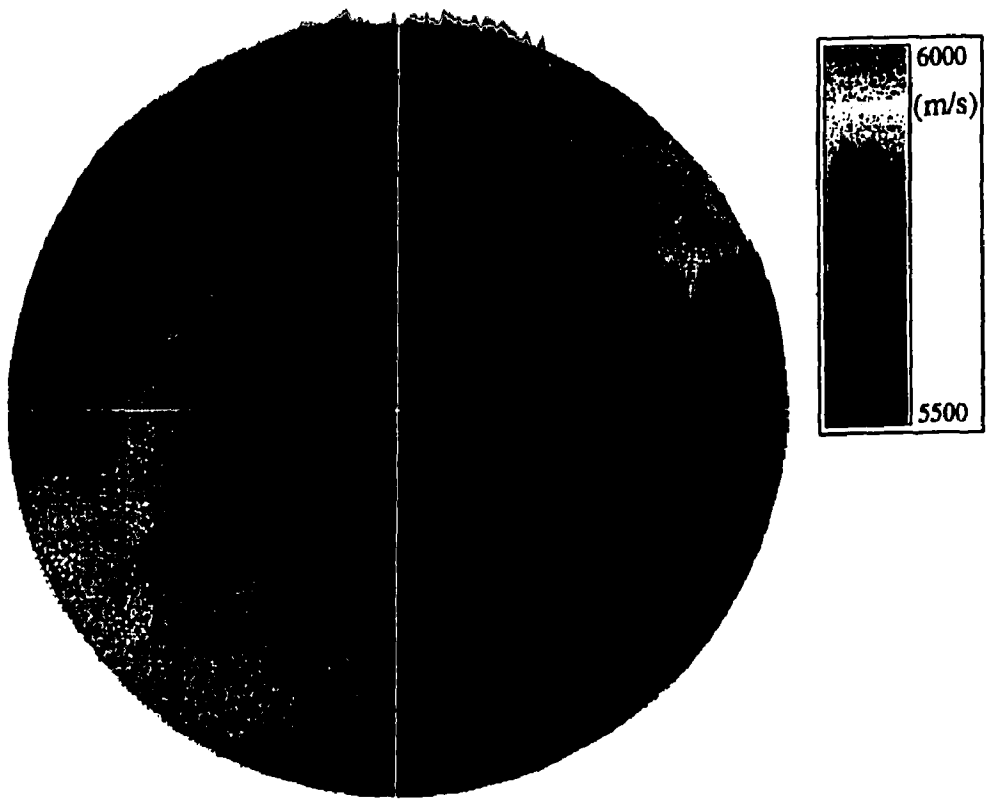

FIGURE 83: Contoured equal-area lower-hemisphere stereographic plot of apparent velocities (without diffraction effects) measured along raypaths originating at various points around the test tunnel perimeter.

and station corrections were used to account for heterogeneities outside of the image grid. The inversion included a parameter for the base velocity as well as anisotropy parameters to account for velocities along the unique anisotropy directions. However, because of numerical limitations related to the raypath coverage, it was not possible to resolve images of the velocity variations in the unique directions of the anisotropy. Instead, equivalent isotropic variations in velocity were computed. Consequently, there was no way to determine whether or not increases in velocity were related to an increase in the base velocity, or to a decrease in anisotropy relative to the initial starting model.

Results of the inversion showed a 250 m/s velocity increase in roof and floor regions of the tunnel, and a 150 m/s decrease in the sidewalls of the tunnel (Figure 85), relative to the velocities assumed in the starting model. Because there is evidence from other studies (e.g., Hayles et al. 1995; Everitt and McGregor 1995) to suggest that the base velocity does not increase above the background value of about 5900 m/s anywhere around the test tunnel, the regions of increased velocity in the roof and floor in Figure 85 most likely represent a reduction in the anisotropy assumed in the initial model (400 m/s) to about 150 m/s in these regions. This reduced anisotropy is similar to that measured in the far-field velocity survey for rock undisturbed by openings. This finding suggests that, in the roof and floor,

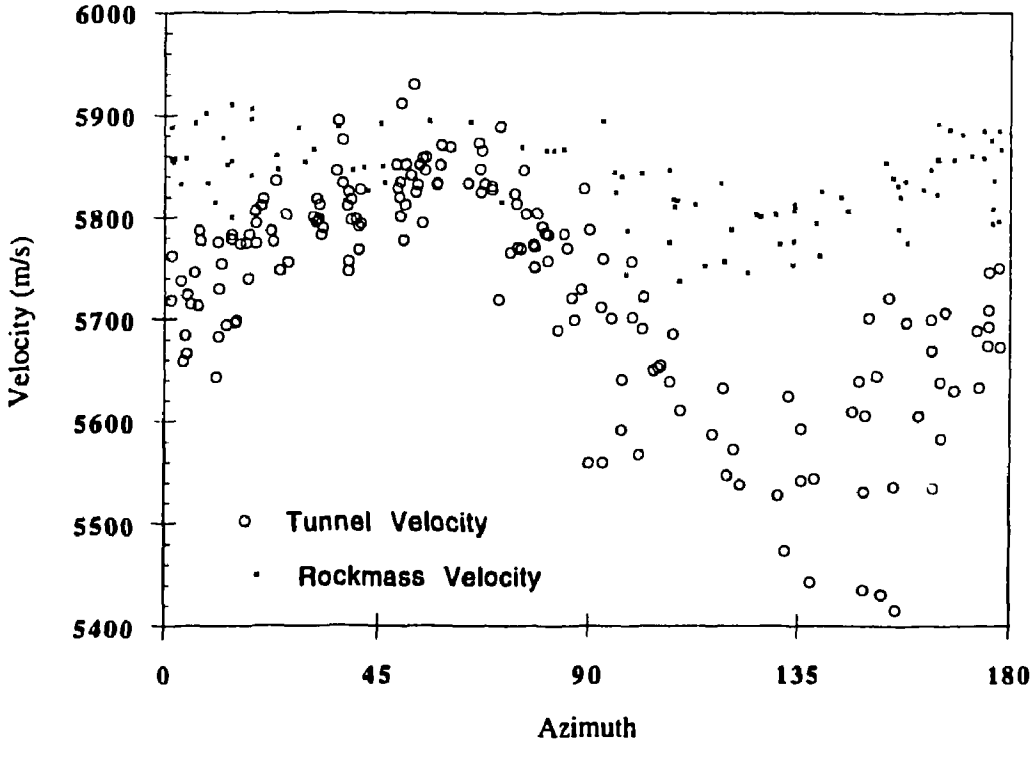

FIGURE 84: Apparent velocity versus azimuth for raypaths within 20° of horizontal for the tunnel survey and undisturbed rock survey. Results for the rock mass are pervasive, while those for the tunnel are dependent on position around the tunnel, i.e., roof versus sidewall.

there is little or no change in velocities or anisotropy compared to results from the far-field survey, i.e., the rock mass characteristics are relatively unaffected by tunnel excavation in these regions. In the sidewalls, the reduction in velocity of 150 m/s indicates that the equivalent isotropic velocity *in situ* close to the tunnel wall is lower than that assumed in the initial model. This finding is consistent with extensional damage localized in the tensile regions around the test tunnel.

Velocity images were also produced from the microseismic data using a simultaneous velocity-hypocentre inversion technique. A subset of microseismic events was selected from the centre of the tunnel, recorded over a 2 day interval. A 0.25 m spaced image grid was constructed in the region of the notch in the crown of the tunnel, and damped least-squares velocity perturbations were computed relative to the initial starting model described above. Figure 86 shows a wedge of decreased velocity (140 m/s) next to the tunnel, increasing in extent into the rock away from the tunnel face, above which there is a region of increased velocity (140 m/s). Compared to the far-field survey results, these findings suggest a net decrease in the equivalent isotropic velocity variations near the area of progressive failure in the roof. Another microseismic data subset was selected containing a significant number of events ahead of the tunnel face. Inversion results indicated a region of reduced velocity (200 m/s) generally corresponding to a tensile region.

These findings suggest that velocity imaging techniques, using both velocity calibration survey results and microseismic data, offer the possibility of analyzing the velocity variations in a specific region of interest at a particular instant in time. These techniques are particularly applicable in assessing excavation-induced damage around underground openings. However, in both velocity imaging techniques described above, the calculated velocity variations are changes relative to an initial starting model. In order to directly interpret these variations as *in situ* changes caused by tunnel excavation, the initial model must be representative of the undisturbed condition of the rock mass prior to tunnel excavation, and the back analysis technique must be sensitive to the initial starting model. Otherwise, only an indirect interpretation of *in situ* changes is possible.

4.3.3 Time-dependent Behaviour

Time-dependent behaviour, or creep, is characterized by a change in measured response over time under constant boundary conditions, e.g., static fatigue tests where the loading and environmental conditions are held constant. Responses measured during excavation of the Mine-by test tunnel typically reflected the advance of the tunnel in combination with changes in the tunnel geometry and in material behaviour caused by progressive failure. Effects caused by temperature variations, while minimized by the enthalpy control system, also contributed to the measured response. Consequently, in most circumstances, changes in the measured response with time were related primarily to changes in boundary conditions.

It was possible to separate out the effects of tunnel advance by observing changes in the measured response within a given excavation round during periods where there was no excavation activity. However, it was not as easy to isolate the effects of non-elastic material behaviour, i.e., creep, from those of tunnel geometry changes and temperature variations.

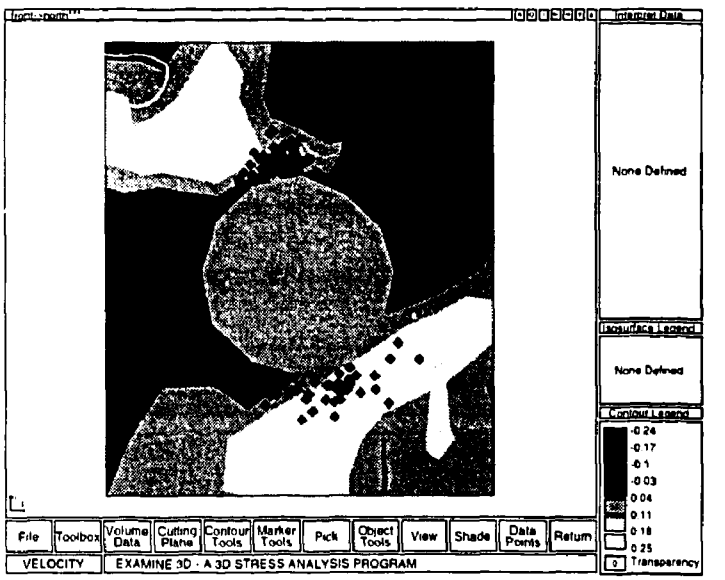

FIGURE 85: View normal to the tunnel axis of P-wave velocity variations, relative to the initial starting model, computed from controlled source data. Microseismic event locations and the tunnel outline are superimposed on the image.

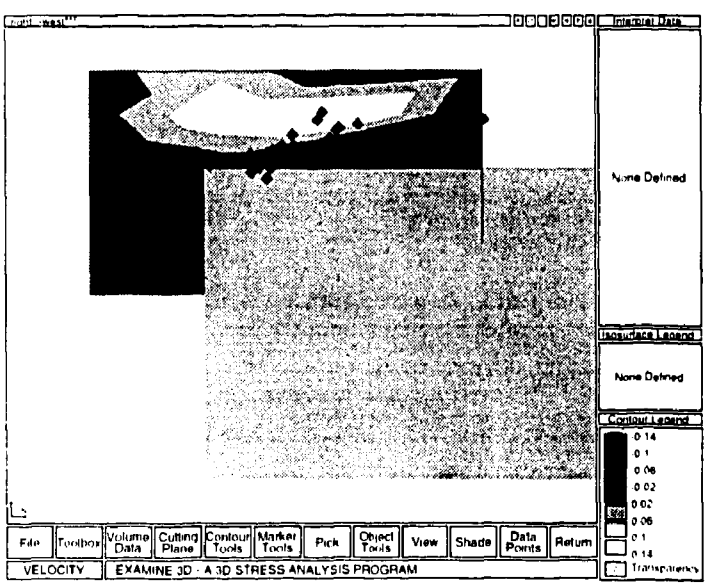

FIGURE 86: Vertical axial view of the tunnel with P-wave velocity variations relative to the initial starting model in the upper notch region computed from simultaneous velocity and hypocenter inversion of the microseismic data. Microseismic event locations and the tunnel outline are superimposed on the image.

During a 13-day period following the excavation of Round 17, changes were noted in the radial displacement responses around the Mine-by test tunnel. While there was no excavation activity in this period, there were ongoing construction and experimental activities involving drilling and instrument installation. Nevertheless, the position of the tunnel face did not change over this time interval. Tunnel profiles taken at the extensometer array near chainage 22+50, immediately behind the tunnel face, indicated that the geometry of the tunnel at this location changed only slightly due to minor spalling over the 13-day period. Therefore, the changes in radial displacement measured in this time interval were attributed mainly to changes in temperature and time-dependent behaviour.

The shapes of the individual radial displacement responses measured by the Bof-exs over this period were similar to the displacement responses measured during advancement of the test tunnel, showing an increase in divergence in the vertical extensometers, and an increase in convergence in the other extensometers. The radial displacement response measured by a horizontal extensometer (EXT11) and the associated downhole temperatures measured at six of the extensometer anchors are shown in Figure 87, along with the periods of activity in the test tunnel. Measurements at anchor 1, closest to the tunnel wall, reflect the air temperature in the test tunnel, while those at the other anchors reflect rock temperature.

As shown in Figure 87, temperature variations were held to less than 1.5°C at anchor 1, and to less than 0.3°C at anchor 3 and beyond. Changes in temperature were noticeable as far out as anchor 9, approximately 6.7 m from the tunnel wall. Martino (1995a) reported that rock-temperature variations of about 1°C around the URL shaft produced radial displacements of about 0.02 mm between Bof-ex anchors spaced 0.4 m apart. This spacing is similar to that between the first 4 anchors in EXT11. From March 12 to 19, a variation in temperature of 0.19°C was noted in EXT11 at anchor 3, and a change of 3.7 μm was recorded between anchors 2 and 3. Based on the results from the shaft, a thermally-induced change of 3.8 μm would be expected over this measurement interval. Consequently, the recorded changes in displacement after March 12 appear consistent with those expected from the small observed temperature variations. Therefore, there is no significant creep component in the measured response over this time interval.

For the period between March 7 and 9, there were only very minor temperature variations in EXT11. Nevertheless, the radial displacement response in Figure 87 shows relatively large changes, levelling off at anchors 2 to 10 by about noon on March 10. The change in displacements between March 7 and 9 is unrelated to temperature or underground activities, and therefore appears to be an indication of true time-dependent behaviour. However, this behaviour is fairly short-lived, spanning only 3.5 days following excavation of Round 17. This time frame is consistent with the period of microseismic activity typically observed within 1 m of the tunnel face after excavation of each round. For example, Figure 40 shows that the microseismicity associated with excavating Round 17 occurs within three days of completing excavation. Hence, the non-elastic displacement that occurs in this period is related to time-dependent damage development, and represents about 0.6% of the total displacement measured in EXT11. Similar non-elastic displacement was observed in the vertical extensometers, representing about 1.4% of the total measured displacement in this direction.

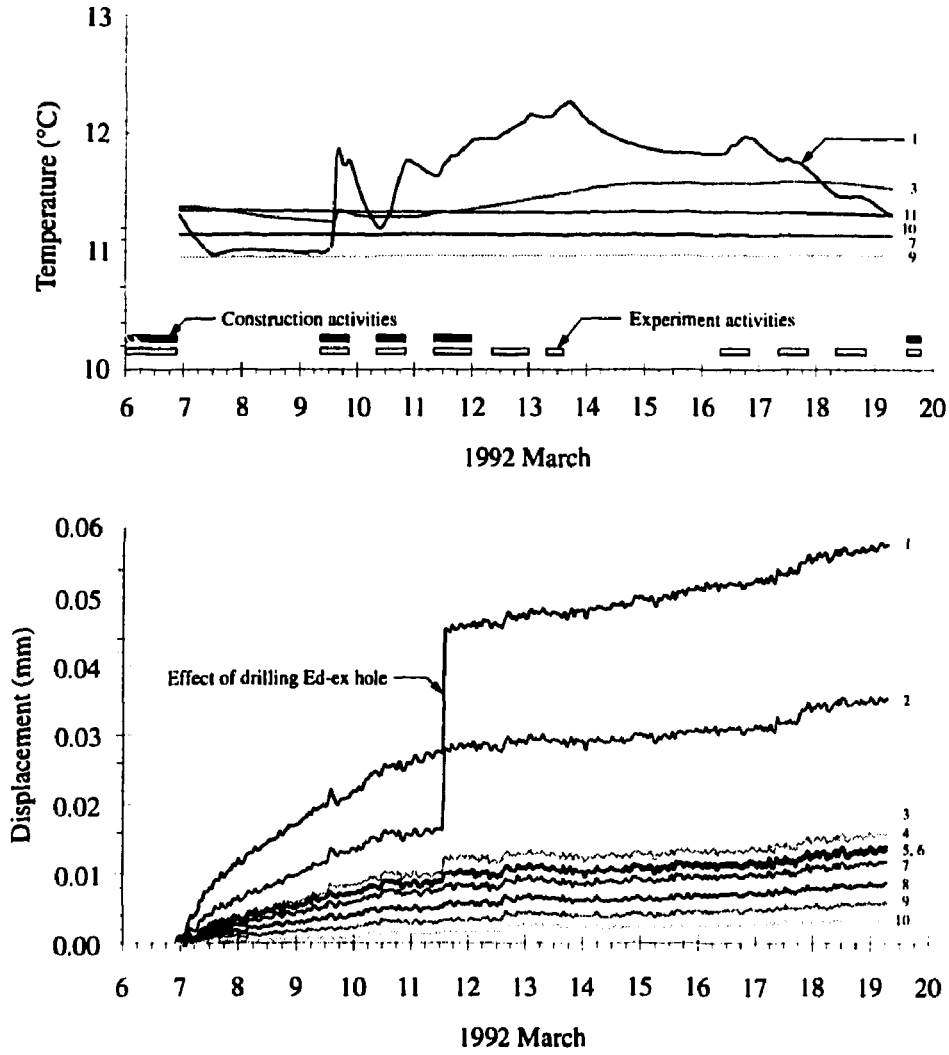

FIGURE 87: Changes in temperature (top) and radial displacement (bottom) in EXT11 for a constant tunnel face position over a 13-day period. Small numbers on the right indicate anchor numbers, anchor 1 being closest to the tunnel wall. The displacements shown are cumulative, i.e., referenced to the deepest anchor. Note that the large jump in displacement on March 11 is a result of drilling an Ed-ex hole adjacent to the Bof-ex borehole containing EXT11.

From Figure 87, it is apparent that the rock mass around the tunnel is very sensitive to small changes in boundary conditions. For instance, drilling of a 1-m-deep Ed-ex borehole near EXT11 caused a sharp increase in permanent deformation within about 1 m of the tunnel wall. Likewise, temperature variations in the tunnel, although cyclical, caused a monotonic increase in permanent deformation at anchor 1. Similar observations were made in Room 405, where very slight changes in temperature caused a small, but measurable, increase in breakout length in a 1.24-m-diameter vertical borehole. These observations suggest that even small changes in boundary conditions tend to promote the development of damage close to the tunnel wall, causing permanent non-elastic deformation. The displacements measured in EXT11 are consistent with the development of damage within about 1 m of the SE sidwall of the tunnel.

In summary, changes in measured responses over time can generally be attributed to changes in boundary conditions. However, there is evidence that true time-dependent behaviour occurs over a short period of about 3.5 days, in which microseismic activity is also observed, immediately behind the tunnel face following excavation advance. The permanent non-elastic deformation associated with this behaviour, however, is in the order of only about 1% of the total measured deformation, and is localized close to the tunnel wall.

4.3.4 Characteristics of the Damaged Zone

The extent and material behaviour of the damaged zone were determined by conducting a detailed *in situ* characterization of the test tunnel (Read 1994). This investigation used a series of slots and boreholes cut across the main notch area of the tunnel to identify any observable damage in these regions. Incorporating these observations into a two-dimensional finite difference model, the material behaviour around the tunnel in the damaged zone was then investigated, using the measured radial displacements from the experiment as a means of assessing model results (Read 1994).

4.3.4.1 Field Observations

From the post-excavation characterization program (Read 1994), it was determined that the only visible signs of damage to the rock mass occurred in the region of the notch tip in the roof and floor of the test tunnel. In the roof, the damage extends about 180 mm into the rock mass, and occurs up to about 500 mm either side of the notch tip in the flanks of the notch. In the floor, the damage extends to about 240 mm depth, dying out within 500 mm on the NW flank, and within 800 mm on the SE flank (Figure 88). The damaged zone comprises a series of closely spaced fractures that are parallel to the free surface. Consequently, the rock in the damaged zones has a much lower elastic modulus than the intact rock, and is therefore destressed. This view is supported by the fact that, in boreholes or slots drilled through these regions from within the tunnel, breakouts occur only in the sections beyond the observed damaged. Figure 89 shows the observable extent of excavation damage on a typical tunnel profile taken at chainage 20+40.

In the tensile sidewall regions of the test tunnel, there is no visible damage to the rock mass, i.e., no discrete tension cracks. However, as shown by the geophysics results, there

FIGURE 88: Damage in the floor slot drilled across the notch tip. Note that the fractures extend 200 mm into the rock mass, and show significant dilation. Fracturing diminishes on the flanks of the notch away from the apex.

is evidence for small-scale cracking in these regions as far as about 1 m from the opening, although the main region of damage is concentrated within about 0.35 m of the wall.

4.3.4.2 Back Analysis of Damaged Material Behaviour

A series of two-dimensional finite difference model simulations were conducted to investigate the material behaviour in the damaged zone around the tunnel. A staged approach was used in the numerical modelling exercise, starting with a simple elastic model, then progressively adding details consistent with observations from the *in situ* characterization of the test tunnel. Table 8 summarizes the various cases that were considered in the study. The main modifications made to the elastic model included: 1) a low modulus zone beyond the notch tips to account for observed *in situ* cracking in these regions; 2) a uniaxial tensile failure criterion using ubiquitous joints to simulate a unidirectional reduction in tensile strength in

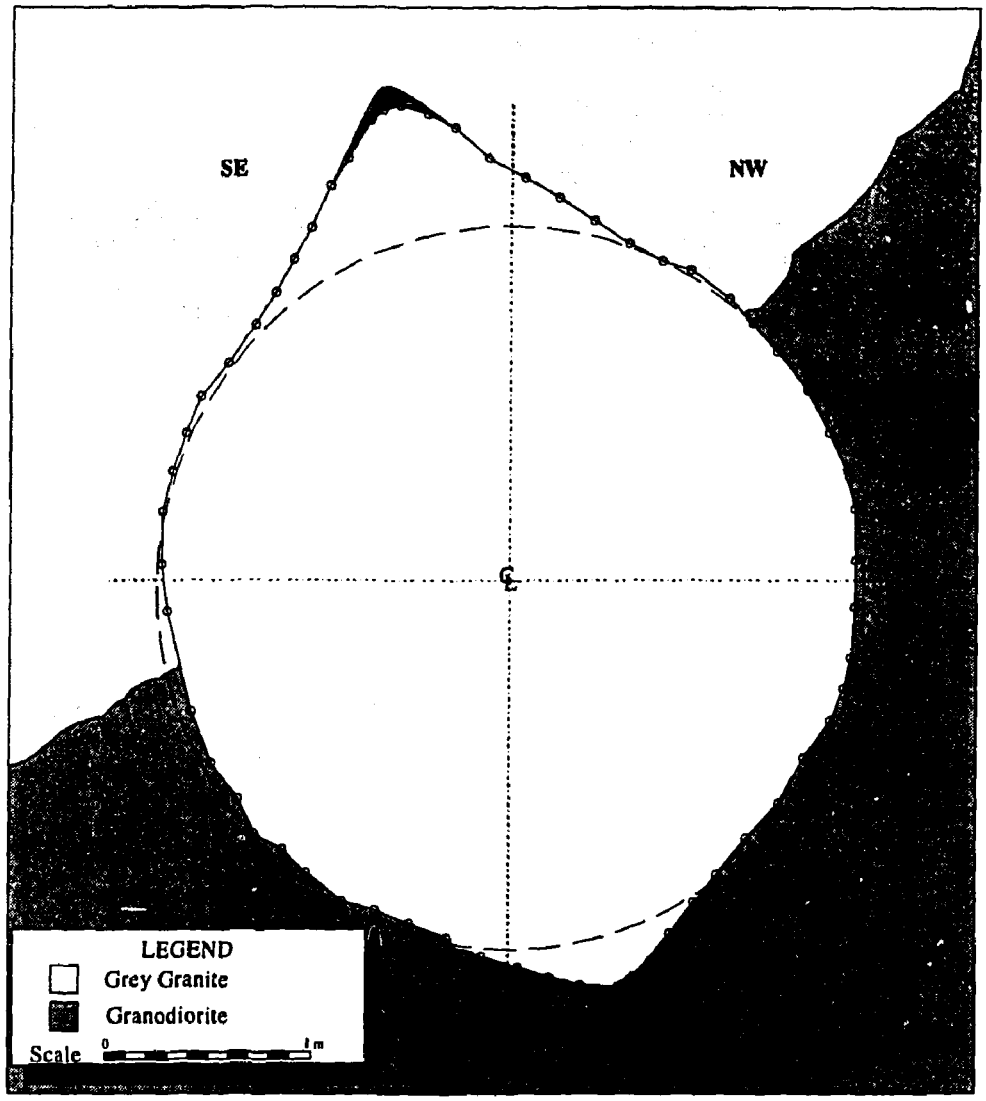

FIGURE 89: Typical tunnel profile at chainage 20+40 showing the extent of excavation-induced damage observable around Room 415. The damaged zone in the roof is about 180 mm thick, while that in the floor is 240 mm thick.

regions where $\sigma_3 < \sigma_t$; 3) a softening criterion to account for reduction of the shear modulus for regions where $\sigma_3 < \sigma_t$; and 4) two different material types, each with unique properties and failure characteristics, to account for the variations in geology near the extensometer arrays.

As a base case, the radial displacement responses versus normalized radial distance for a purely elastic model were generated for eight rotation angles (Figure 90). To assess the effect of the damage beyond the notch tip shown in Figure 89, zones of reduced elastic modulus were added to the model in these regions. The damaged modulus in these zones was arbitrarily taken as 10% and 1% of the intact modulus in separate simulations. The resulting radial displacement responses using a damaged modulus equal to 10% of the intact modulus are compared to the base elastic case in Figure 90. It is readily apparent from these plots that the damage observed *in situ* in the roof and floor of the tunnel has no significant effect on the radial displacement responses, producing only a marginal increase in displacement in the sidewalls. The same was true of the results using a damaged modulus equal to 1% of the intact modulus. The major role of the damage beyond the notch tip is to drive the point of maximum tangential stress into the rock mass away from the tunnel boundary, thus allowing sufficient confining stress to develop at that point to prevent further failure, i.e., the stresses at the point of maximum tangential stress would fall inside the failure envelope in principal stress space.

The measured radial displacement responses for the two extensometer arrays used in the Mine-by Experiment are shown in Figure 91. The responses represent the measured displacements at the end of Round 36, when the tunnel face was almost five tunnel diameters past the second instrument array. In comparison to the results in Figure 90, the measured displacement responses deviate from the elastic responses starting about one tunnel radius from the wall. The most notable differences are for instruments oriented at $\theta = 0$, 135, 180 and 315°. For the horizontal instruments, the gradient of the measured radial displacement responses is much steeper within one radius of the tunnel wall than for the elastic case. In the regions containing these instruments, the tangential stress near the tunnel is highly tensile, exceeding the tensile strength of the rock for distances within about 200 mm of the wall.

Martin (1993) showed that accumulated damage in the rock results in an increase in Poisson's ratio and a decrease in the Young's modulus, effectively reducing the shear modulus G of the damaged material. Comparing the results from the elastic model and the measured results, the difference in the horizontal responses is consistent with a reduction in the shear modulus in the zone within about one radius of the sidewalls. Likewise, the large increase in radial displacement in EXT12 in the upper SE quadrant of the tunnel indicates a similar change in the material properties in this region.

The studies by Hayles et al. (1995) and Carlson and Young (1993) support the idea of damage development in the tensile regions around the test tunnel, resulting in induced anisotropy, i.e., directional cracking, and reduced shear modulus. Several relatively simple models were used to simulate this process, and the resulting radial displacement responses. An elastic model, (case 4 in Table 8), using a softening criterion to reduce the shear modulus in zones where $\sigma_3 < \sigma_t$, produced only marginal changes in the radial displacement response,

TABLE 8

SUMMARY OF MODELS USED TO SIMULATE RADIAL DISPLACEMENT PATTERNS OBSERVED IN THE POSTERIOR DOMAIN OF THE TEST TUNNEL

Model	Material Model	Yield Criterion	Post-Yield Behaviour	Comments
1	Elastic	None	Elastic	Base case with notch geometry
2	Elastic	None	Elastic	Reduced E at notch tips
3	Elastic/ Ubiq/Mohr	Hoek-Brown	Non-associated plastic flow	Reduced E at notch tips
4	Elastic	Tension Cutoff	Elastic	Reduced E at notch tips, reduced G for $\sigma_3 < \sigma_t$
5	Elastic/ Ubiq	Tension Cutoff	Elastic	Reduced E at notch tips, reduced G for $\sigma_3 < \sigma_t$, uniaxial reduction in tensile strength
6	Elastic/ Ubiq	Tension Cutoff	Elastic	Reduced E at notch tips, reduced G for $\sigma_3 < \sigma_t$, uniaxial reduction in tensile strength, two material types

Note:
UBIQ - Ubiquitous Joint
MOHR - Mohr-Coulomb

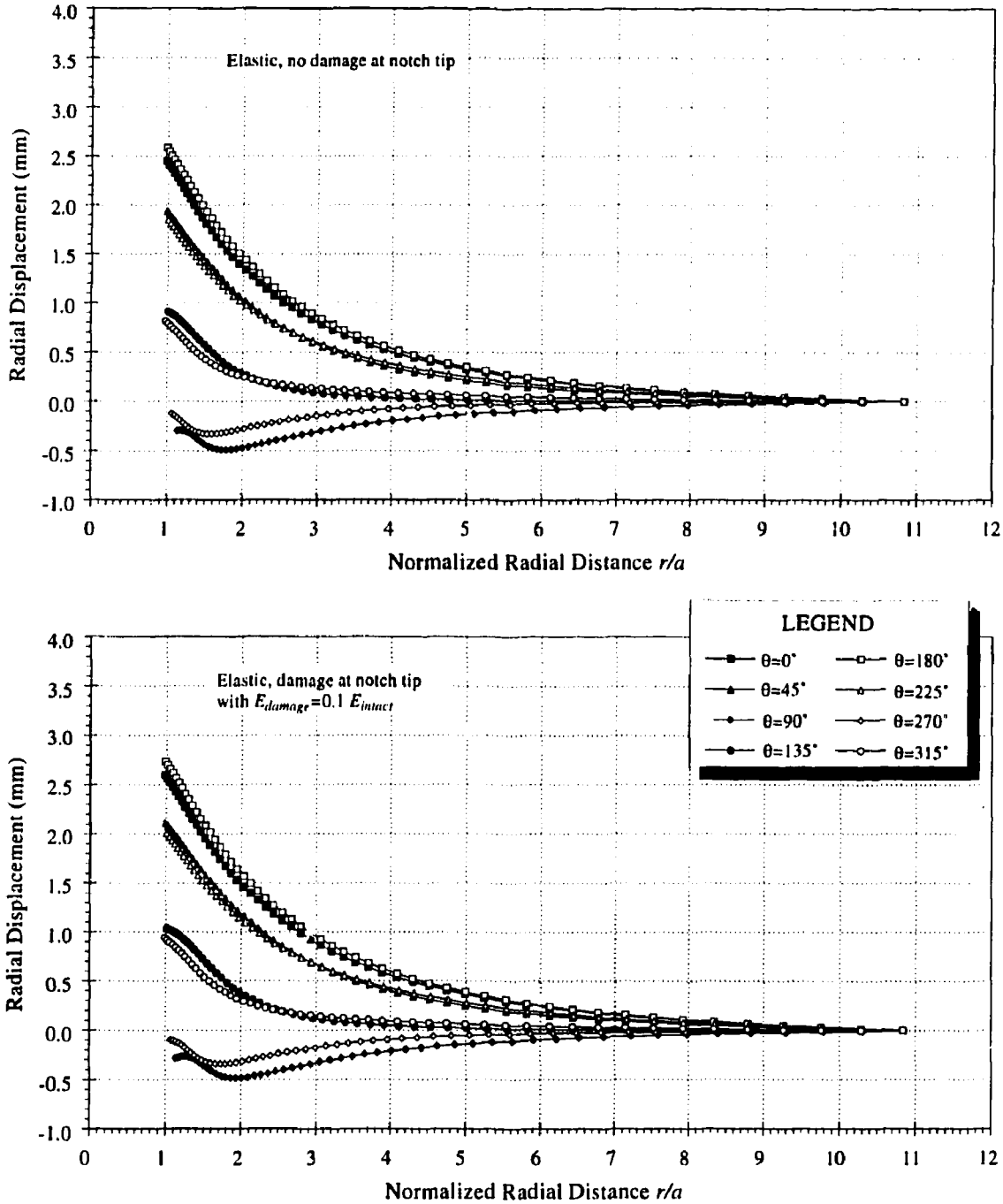

FIGURE 90: Radial displacement responses for elastic models excluding and including damage beyond the notch tip. Note that there is only a marginal difference in the responses resulting from the inclusion of additional damage at the notch tips.

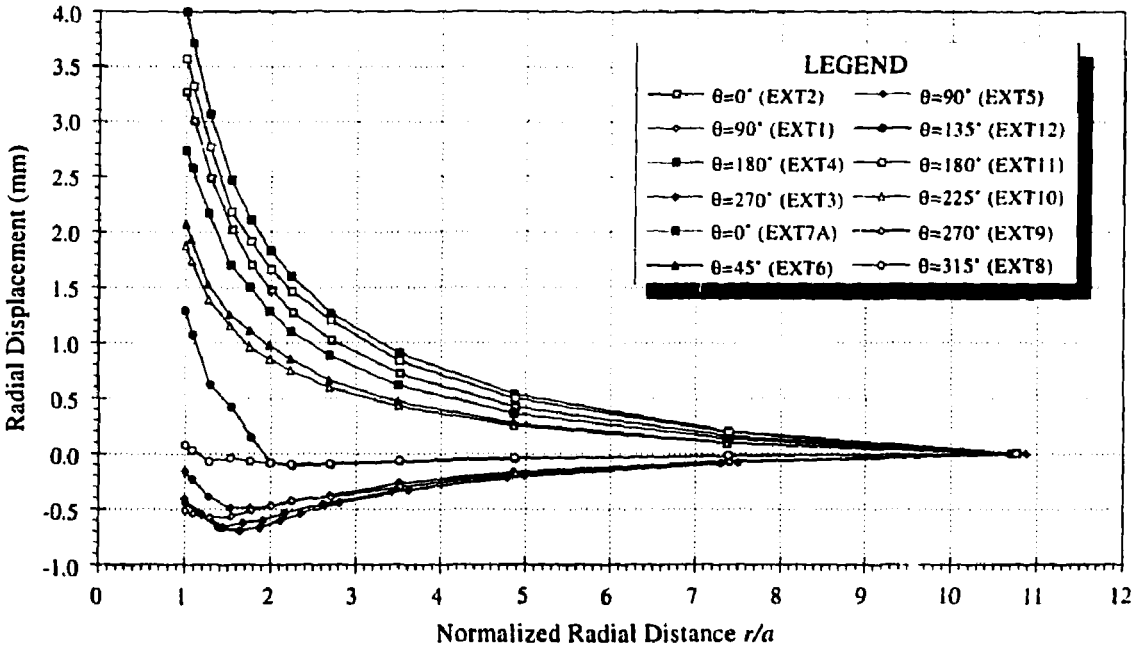

FIGURE 91: Radial displacement responses for the two extensometer arrays in the field study. Results from Array 1 are shaded in grey. Note the differences in these responses within one radius of the tunnel wall compared to the elastic case.

even when the shear modulus was reduced by an order of magnitude. To account for the reduction in tensile load-bearing capacity orthogonal to the induced cracking in the damaged material, ubiquitous joint elements were introduced into the zones where $\sigma_3 < \sigma_t$ (case 5). Stress redistribution associated with the reduction in tensile stresses near the tunnel wall was captured by iteratively checking for new zones where $\sigma_3 < \sigma_t$, substituting ubiquitous joint elements for those elastic elements that violated the tensile cutoff criterion, then allowing the model to equilibrate. In this way, the zone of damaged material propagated away from the tunnel wall until equilibrium was reached. Depending on the value selected for σ_t, the final extent of the zone of extensional damage could be significantly larger than the region that initially exceeded the tension cutoff. The tensile strength defined by the Hoek-Brown criterion is

$$\sigma_t = \frac{\sigma_c}{2}\left[m - \left(m^2 + 4s\right)^{\frac{1}{2}}\right] \tag{18}$$

The redistribution of stresses increased the radial displacement near the tunnel wall measured by the horizontal instruments. By incorporating a reduced shear modulus in the ubiquitous joint elements, the resulting displacement response from the model was very similar to the measured response.

Using this approach, it was found that differences in radial displacements between the two sides of the tunnel were more pronounced in the measured results than in the model results. As determined from *in situ* characterization of the test tunnel near extensometer array 2 (Everitt et al. 1993), the upper SE quadrant and part of the upper NW quadrant are primarily grey granite, while the other quadrants are granodiorite (Figure 89). The granite

typically shows more visible signs of cracking along grain boundaries than the granodiorite upon stress-relief, both *in situ* and in laboratory samples. The significance of lithology on excavation damage development is considered in Section 4.3.5. Lajtai et al. (1990) noted that, in tension, stresses at fracture nucleation and failure are assumed to be identical. The crack-damage stress for granite in tension was measured as 7.4 MPa from Brazilian tests, and as low as 1.5 MPa from direct tension tests on damaged samples from the 420 Level of the URL (Martin 1993). Recent Brazilian tests by Alexander (pers. comm.) have given tensile strengths of 6.5 ± 1.2 MPa for granite, and 10.0 ± 1.3 MPa for granodiorite from the 420 Level.

The elastic/ubiquitous joint model was modified to account for the two material types in the vicinity of the second extensometer array. A sensitivity study was then conducted, considering different tensile cutoff stresses and reduced shear moduli for the two rock types. As shown in Figure 92, reasonable agreement with the measured radial displacement response was obtained when tensile cutoff stresses of 6 and 11 MPa, and reduced shear moduli of 5 and 10 GPa, were used respectively for granite and granodiorite. The values of shear moduli represent reductions of 81 and 62% for granite and granodiorite, respectively. The extent of the zone of extensional damage is shown in Figure 93.

While this modelling approach appears to capture some of the mechanistic features observed *in situ*, it has several limitations. The most significant of these is that a tension cutoff in FLAC implies that, once a stress component falls below the tensile limit, it is cut to zero and cannot be tensile from that point on. In reality, the reduction in tensile strength related to the development of induced anisotropy as directional cracking along grain boundaries is directly related to the amount of damage sustained by the material (Martin 1993). Because the cracking is at the grain scale (Carlson and Young 1993), and the cracks are not necessarily connected, damaged material would still be able to sustain tensile loading, albeit at a reduced level. The tensile limit of the material would therefore increase towards the boundary of the tensile region, and, consequently, the stress redistribution *in situ* would be less extensive than suggested by the model. Nevertheless, the model illustrates that stress redistribution and a reduction in shear modulus resulting from induced cracking in the tensile region can account for the difference between the measured and modelled radial displacement responses.

4.3.5 Factors Controlling Excavation Damage Development

4.3.5.1 Effect of Geology

Extensive underground mapping (Everitt et al. 1993) and laboratory analyses of drill core samples from representative areas of the test tunnel were conducted as part of the post-excavation characterization. During the excavation of Room 415, six closed fractures were encountered, each with an areal extent on the order of 1 m^2. These types of fractures are interpreted as cooling fractures associated with the margins of a granodiorite dyke, and are tight with minor infillings of chlorite, serecite, hematite and carbonate (Everitt et al. 1993). They do not constitute paths of increased hydraulic conductivity because they are not connected, and are of very limited size.

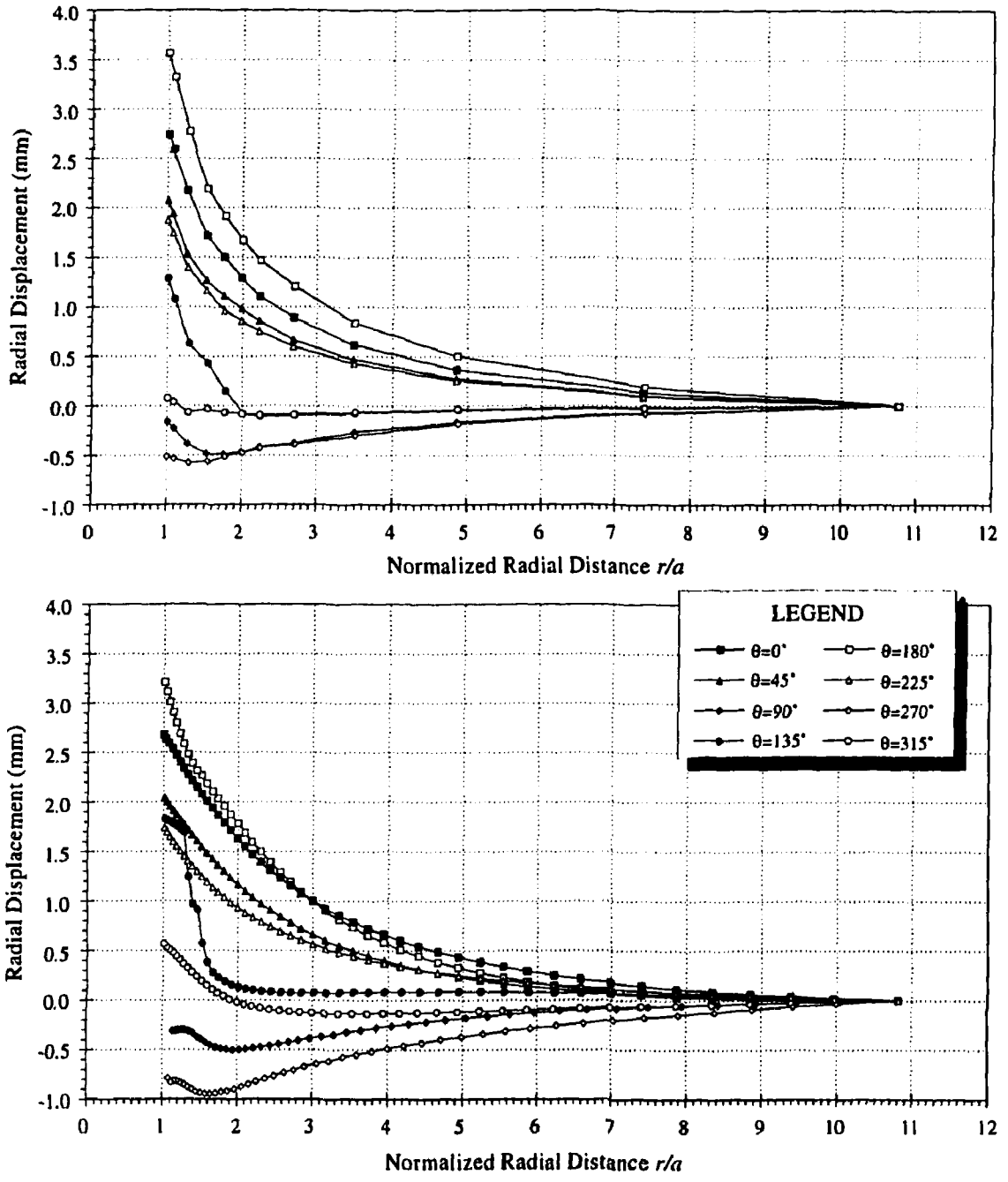

FIGURE 92: Radial displacement responses from the tension cutoff model (bottom) compared to measured results from extensometer array 2 (top).

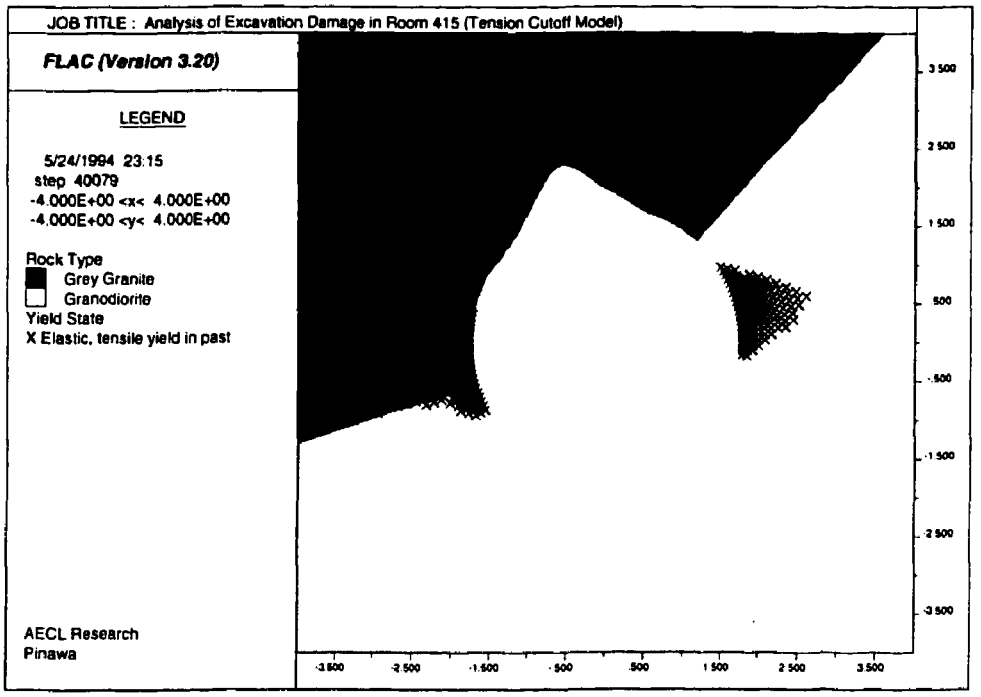

FIGURE 93: Extent of the zone of extensional damage in the tension cutoff model. Because of limitations in the model, the extent of the damaged region is overestimated.

As originally expected from exploratory drilling and excavation of the access tunnels for the Mine-by Experiment, the test tunnel was excavated in an area of mixed granite-granodiorite lithology. The distribution of grey granite and granodiorite is depicted on an unfolded perimeter map of the tunnel in Figure 94. Note that, with increasing chainage, the proportion of granodiorite increases to a maximum of 100% near chainage 30+00, then decreases again towards the end of the tunnel. In comparing the geology perimeter map to similar maps of overbreak contours and of microseismic activity occurring outside the design perimeter of the tunnel, it is clear that there is a correlation between geology, microseismic activity, and breakout development. Regions where granite was predominant showed more microseismic activity during excavation, and developed more pronounced breakouts as the tunnel advanced, than regions of granodiorite. This correlation is also apparent in tunnel profiles taken at various points in the test tunnel (Figure 95).

Petrographic analysis of nine samples carried out at Laurentian University (Kelly et al. 1993) showed that, although the rock types had previously been identified as granite and granodiorite, all rock types within the test tunnel volume fall within the International Union of Geological Sciences (IUGS) granite classification. However, to avoid confusion, the terms granite and granodiorite have been retained. The results of the petrographic analysis are summarized in Kelly et al. (1993).

Mineralogically, the samples are similar, with minor variations in mineral proportions. According to Kelly et al. (1993), the samples originally described as granodiorite contain

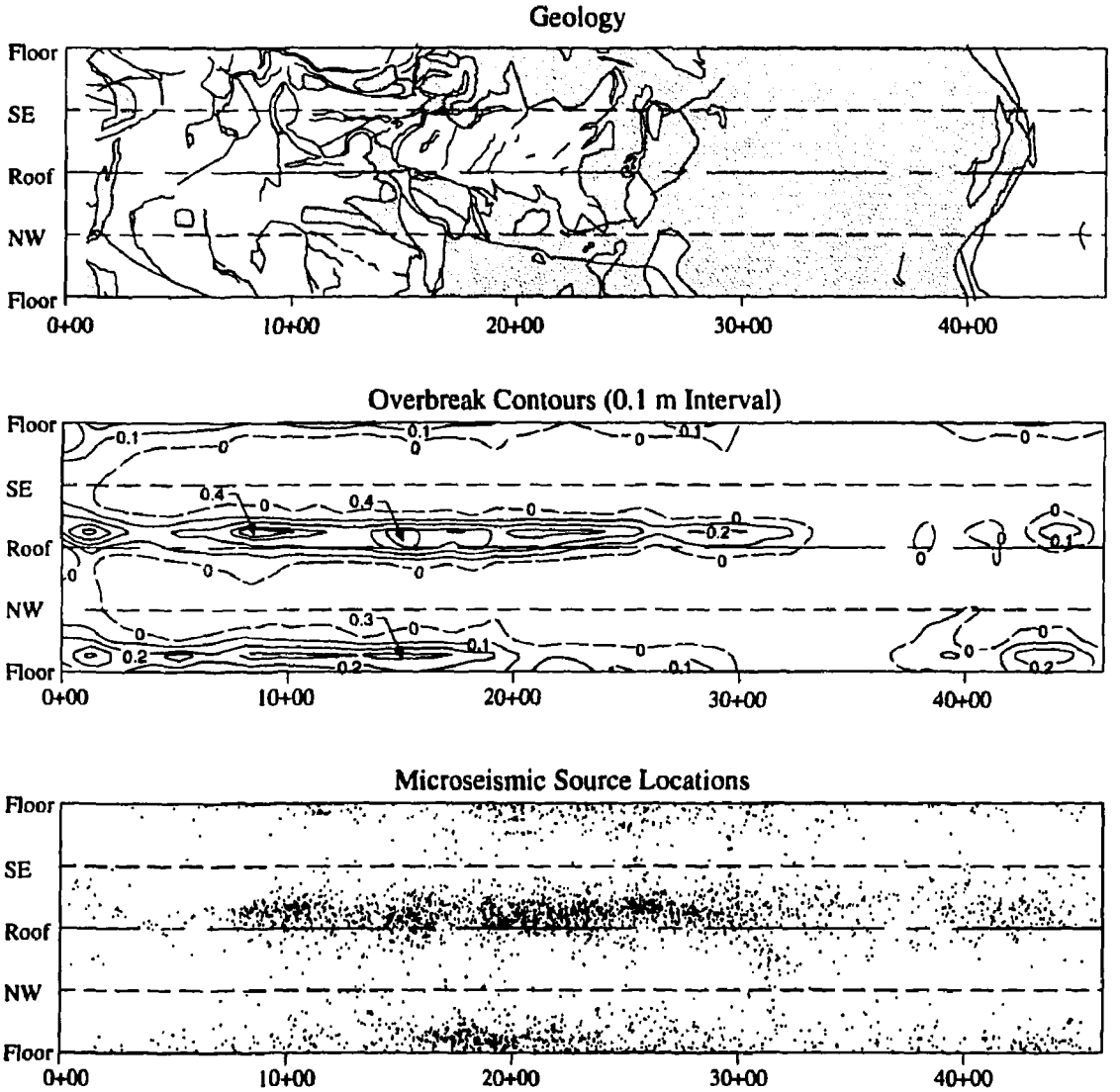

FIGURE 94: Perimeter maps of geology, overbreak and microseismic activity. Granite is shown as the light regions and granodiorite as the dark regions on the geology map. Note the correlation between areas of grey granite, overbreak and concentrated microseismic activity. Distance is shown as chainage (m) from the start of Room 415.

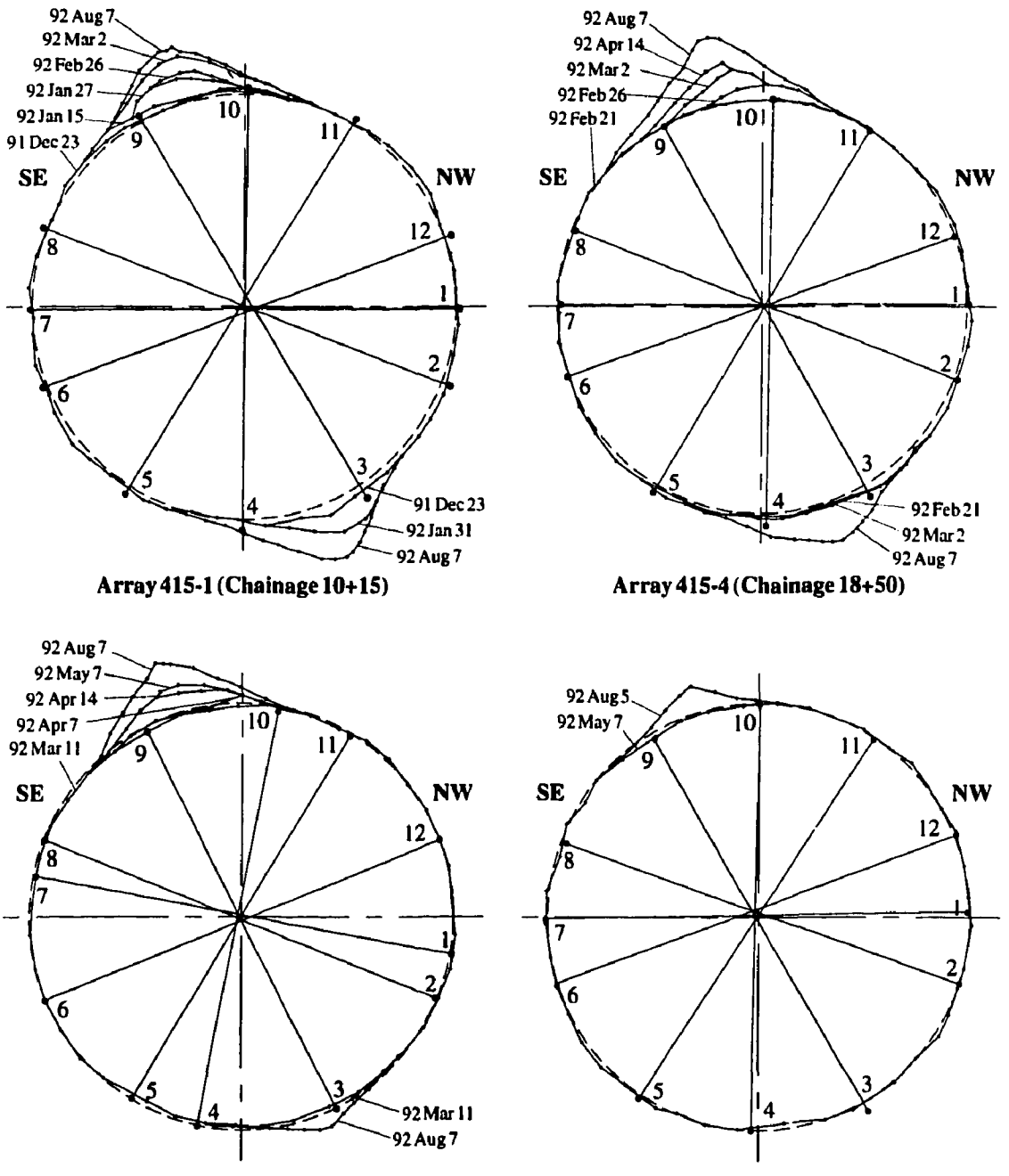

FIGURE 95: Comparison of tunnel profiles at convergence Arrays 415-1, 4, 5 and 8. These profiles represent a progression from a predominantly granite to a predominantly granodiorite region. Note that the extent of large-scale notch development is much less pronounced for Array 415-8 located completely in granodiorite.

TABLE 9

GRAIN SIZES OF THE MAIN MINERALS IN NINE SAMPLES FROM THE EXPERIMENT AREA

Mineral	Grain Size (mm)								
	AE1	AE2	AE3	AE4	AE5	AE6	AE7	AE8	AE9
Alkali Feldspar									
Min.	1.0	0.5	1.0	0.25	1.0	0.5	0.5	0.5	1.0
Max.	8.0	3.5	7.0	2.0	7.0	2.5	3.0	2.5	6.0
Mean	4.0	3.0	4.0	1.0	4.5	1.0	1.0	1.0	3.0
Plagioclase									
Min.	0.5	0.5	1.0	0.5	0.5	0.5	0.5	<0.5	2.0
Max.	6.0	6.0	5.0	2.0	4.0	2.0	2.5	1.5	5.0
Mean	4.0	3.5	3.0	1.5	2.0	1.0	1.0	1.0	3.0
Quartz									
Min.	0.5	0.25	0.25	<0.25	<0.25	<0.25	<0.25	<0.5	<0.25
Max.	4.0	3.0	4.0	1.0	4.0	1.5	1.5	1.5	3.0
Mean	2.0	1.5	2.5	0.75	2.0	0.5	0.75	0.75	0.75
Biotite									
Min.	0.25	<0.25	<0.25	<0.25	<0.25	<0.25	<0.25	<0.25	<0.25
Max.	2.0	2.0	2.0	1.0	2.5	0.5	1.5	2.0	2.0
Mean	1.0	0.75	1.0	0.25	1.0	0.5	0.5	1.0	0.75

Samples AE1, 2, 3, 5 and 9 are granite, the others granodiorite.
After Kelly et al. (1993).

between 7.6 and 13.2% biotite, while samples initially classified as grey granite contain between 1.8 and 7.8% biotite. This difference in biotite content accounts for the darker appearance of the granodiorite. Mineralogical alteration was found to be minor, and consistent throughout the sample set. Biotite was faintly to slightly altered to chlorite, and the feldspars were faintly sericitized. Minor abundances of epidote and carbonate were noted in the granodiorite samples.

As shown in the petrofabric analysis conducted by Kelly et al. (1993), the main difference between the two lithologic units is related to grain size and texture. The grey granite samples are generally coarsely crystalline, and inequigranular, containing large metamorphosed crystals of both alkali feldspar and plagioclase. The granodiorite is finely crystalline and equigranular by comparison. Table 9 presents the range and average grain sizes for the main minerals in each sample. The large feldspars characteristic of the grey granite were noted to be often significantly more fractured than finer-grained crystals, indicative of more brittle behaviour. It was concluded that differences in the rock mass characteristics of the two rock types are probably related to their grain size and textural characteristics rather than compositional differences (Kelly et al. 1993). Figure 96 shows core samples of granite (left) and granodiorite (right), illustrating the obvious differences in their grain structure.

The granite shows more visible signs of damage related to cracking of the larger feldspar crystals caused by stress relief during sampling.

As discussed in Section 3, Martin (1993) showed that the crack half-length is an important parameter in determining rock strength. Longer cracks imply more damage, and result in a greater reduction in the cohesion component of rock strength. He suggested that the crack half-length was related, in part, to the grain size of the rock. Work by Cundall (pers. comm.) using a particle flow code (PFC^{2D}) also suggests that inequigranular materials are more susceptible to cracking than equigranular materials. Owing to its inequigranular structure and the abundance of large feldspar crystals, the grey granite is expected to have a lower crack-initiation stress σ_{ci} and a lower crack-damage stress σ_{cd} than granodiorite. Based on the back-analyzed stress tensor, the *in situ* crack-initiation threshold for granite was found to be 73 MPa, similar to laboratory results from uniaxial compression tests conducted by Lajtai (1988). Results from laboratory tests on granodiorite samples suggest that the average crack-initiation threshold for granodiorite is about 100 MPa. Consequently, regions

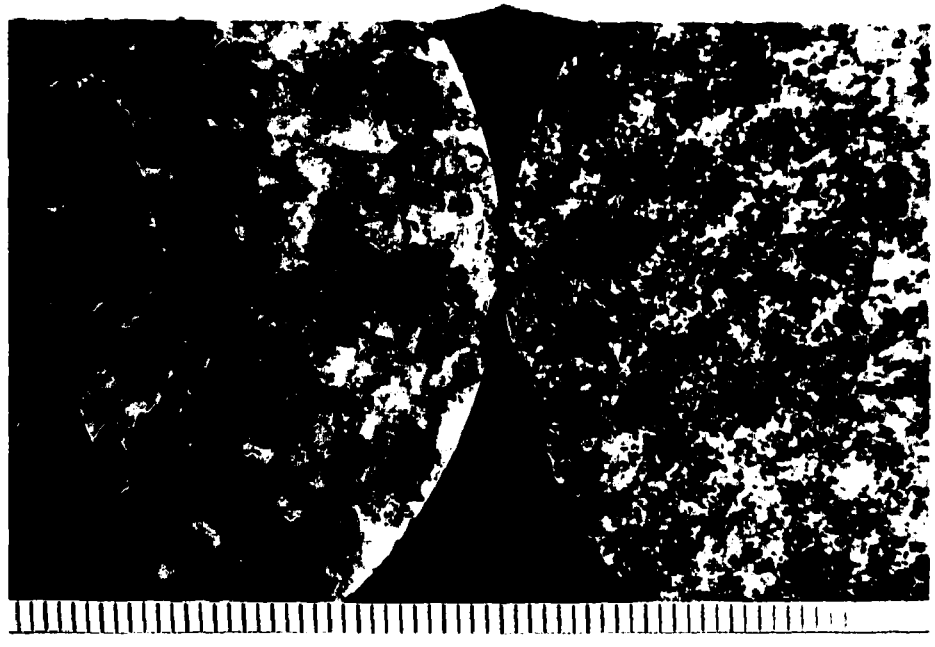

FIGURE 96: Core samples of grey granite (left) and granodiorite (right), illustrating the difference in petrofabric. Note the much larger crystals and inequigranular structure in the granite sample compared to the equigranular granodiorite sample. The small divisions at the bottom of the photograph are millimetres.

of granodiorite *in situ* would sustain less initial damage related to stress concentrations ahead of the advancing face, and would develop less pronounced breakouts behind the advancing face, than regions of granite under identical stress conditions. The same is true for the development of extensional damage in tensile regions, as discussed in Section 4.3.4.2.

4.3.5.2 Effect of Tunnel Orientation

In conjunction with the Mine-by Experiment, borehole breakouts have been studied extensively *in situ* at the URL (Martin et al. 1994; Read 1994; Read et al. 1995). In a series of boreholes with diameters ranging from 150 to 1240 mm, observed borehole breakouts did not form diametrically opposite one another in the plane orthogonal to the borehole axis. None of the boreholes were drilled parallel to a principal stress direction. The same observation was true of breakouts in the 3.5-m-diameter test tunnel for the Mine-by Experiment. This phenomenon is contrary to the idea that borehole breakouts initiate at the points of maximum tangential stress concentration around the borehole because, in an elastic medium subjected to an anisotropic stress field, these points are diametrically opposite one another on the borehole wall.

Read et al. (1995) showed that the distribution of maximum deviatoric stress ahead of the face is significantly affected by the orientation of the borehole relative to the principal directions (Figure 97). In conditions where the borehole is oriented parallel to a principal direction, the maximum deviatoric stress ahead of the face is distributed symmetrically with respect to the borehole axis. However, for situations where the borehole axis is not parallel to a principal direction, such as the Mine-by Experiment test tunnel, the distribution of the maximum deviatoric stress ahead of the face becomes asymmetric. Transforming the principal stress tensor to the cylindrical coordinate system of the borehole, this second situation has non-zero antiplane shear stress components, i.e., shear components in a plane containing the tunnel axis. Read (1994) has shown that these antiplane shear stresses are responsible for the asymmetric pattern of stresses ahead of the face of a cylindrical opening.

As described in Section 3, the combination of high deviatoric stresses and rotation of principal stresses ahead of the Mine-by test tunnel face generates local weakened zones that are eventually exposed at the tunnel perimeter as the tunnel advances. These zones are distributed asymmetrically with respect to the tunnel axis because the tunnel is not aligned with a principal direction. Consequently, even though the points of maximum tangential stress at the tunnel wall resulting from tunnel advance are distributed symmetrically with respect to the tunnel axis, breakouts develop asymmetrically, initiating in the regions of reduced strength.

Similar effects are also apparent in vertical boreholes at the URL. For example, a 1.24-m-diameter borehole was drilled to a depth of 5 m in the concrete-lined floor of Room 405. This horizontal room is horse-shoe-shaped, oriented towards azimuth 225°, and was excavated using a drill-and-blast technique. Excavation damage related to the development of the room, characterized by multiple subhorizontal fractures, was present to a depth of 0.76 m below the top of the concrete floor. Below this zone of damage, breakouts developed in the borehole during drilling, following the advancing face as the hole was deepened.

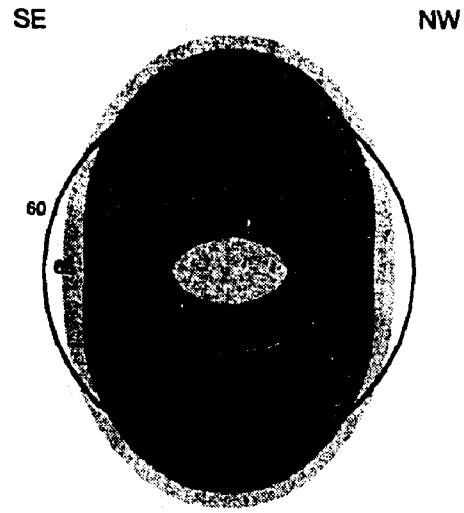

(a) Tunnel parallel to σ_2. Stress orientations (given as trend/plunge): σ_1 = 135°/0°, σ_2 = 225°/0° and σ_3 vertical.

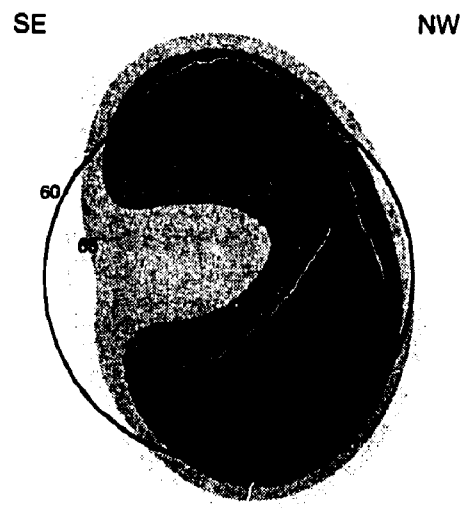

(b) Tunnel not aligned with a principal stress direction. Stress orientations: σ_1 = 145.4°/11.1°, σ_2 = 053.9°/07.7° and σ_3 = 289.8°/76.4°.

FIGURE 97: Pattern of maximum deviatoric stress from EXAMINE^{3D} in a plane 0.6 m ahead of a 3.5-m-diameter tunnel. The horizontal tunnel is oriented towards azimuth 225°. Principal stresses are 59.9, 44.3 and 9.4 MPa for σ_1, σ_2 and σ_3, respectively. Case (b) is typical of the Mine-by Experiment test tunnel.

As shown in Figure 98, the breakout pattern was asymmetrical in terms of the azimuths of the breakouts, and their depths of termination in the borehole. The azimuth of the SW breakout varied with depth away from Room 405, but near 2.0-m depth averaged 251°. The azimuth of the NE breakout, about 048°, was consistent with depth. At 2.0-m depth, the angular asymmetry, or offset from diametrically opposite positions, was 23°. In addition, the asymmetry in breakout lengths was 0.54 m, with the NE and SW breakouts extending to depths of 3.50 and 2.96 m, respectively. The hole was cylindrical and diamond-drilled vertically in homogeneous granite, thus ruling out the effects of gravity and excavation method that might contribute to asymmetry in the development of borehole breakouts.

A three-dimensional boundary element model of Room 405 and the 1.24-m-diameter borehole was constructed using EXAMINE^{3D} (Curran and Corkum 1993). Three borehole depths (2.3, 3.4 and 5.0 m) were chosen to assess the conditions ahead of the face during drilling at: 1) a point where the breakouts formed on both sides of the borehole, 2) a point

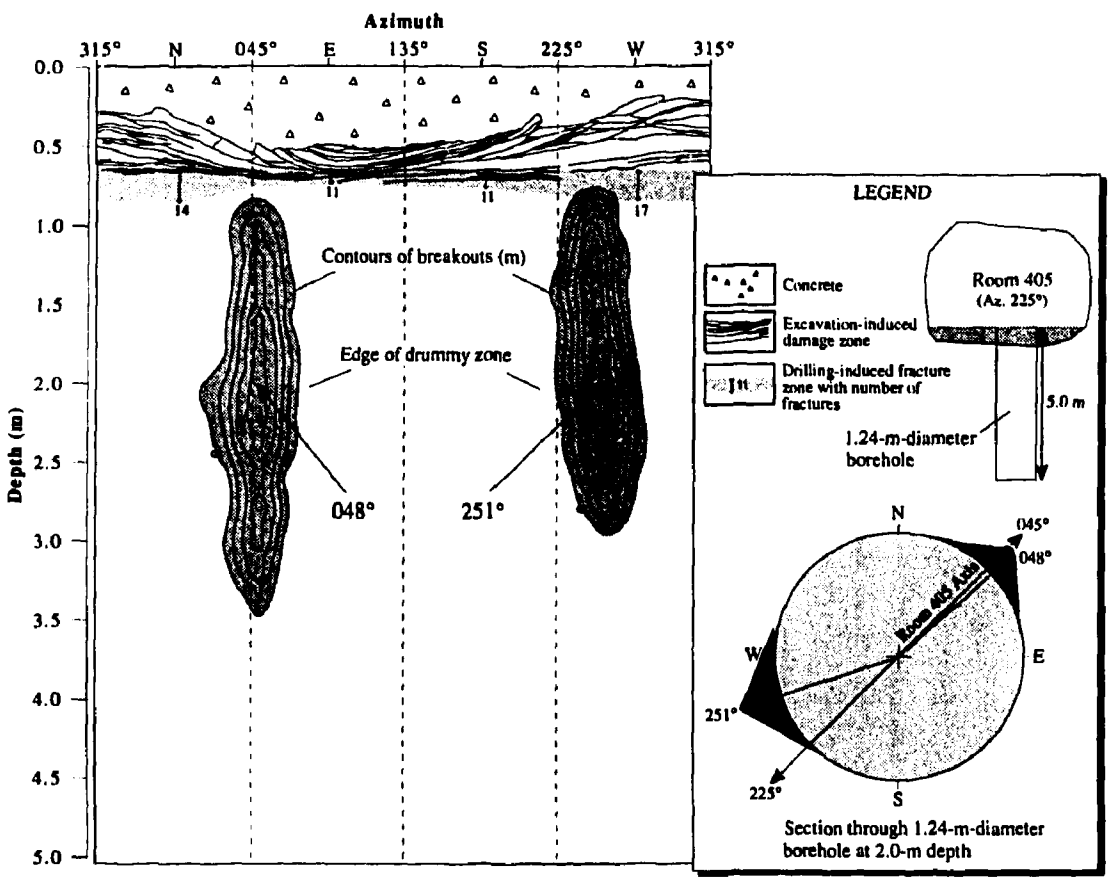

FIGURE 98: Perimeter map showing borehole breakouts in 1.24-m-diameter borehole in Room 405. Note the asymmetry in the azimuth and depth of breakouts on opposite sides of the borehole. The borehole location relative to Room 405 is shown in the inset.

where the borehole breakout occurred on one side only, and 3) a point where no breakouts were evident. Owing to the absence of breakouts in the excavation-induced damaged zone, it was inferred that the stresses within this zone had been shed to the adjacent intact rock. To account for this stress-relieved region, the floor of the room in the model was adjusted to coincide with the bottom of the damaged zone.

Stresses were determined at 0.1 diameters ahead of the face at the design perimeter. The maximum deviatoric stress was plotted versus azimuth to determine if the position of the peaks in the response correlated with the apex of each breakout (Figure 99). In addition, the magnitudes of the maximum deviatoric stress concentrations were compared with the crack-initiation threshold to determine if they were high enough to initiate damage ahead of the face, and if there was any asymmetry in their values.

As shown in Figure 99, the model produced a pattern of maximum deviatoric stress ahead of the face consistent with the observed pattern of breakouts, i.e., the azimuth of each breakout and the difference in their extent. At 2.3-m depth, where breakouts are present on both sides of the borehole, both peaks in the maximum deviatoric stress response ahead of the face exceed the threshold. At 3.4-m depth, where breakout occurs only on the NE side of the hole, the NE peak in the maximum deviatoric stress response exceeds the threshold, but the SW peak does not. At 5.0-m depth, there were no breakouts near the face. The peaks in the maximum deviatoric stress response ahead of the face confirm that, at this depth, the crack-initiation threshold is not exceeded at the design perimeter. In terms of azimuth, the positions of the peaks in the maximum deviatoric stress response at 0.1 borehole diameters ahead of the face correlate closely with those of the borehole breakouts.

Using a 600-mm-diameter borehole drilled parallel to the σ_3 direction, the asymmetry in the borehole breakouts was reduced from that in a vertical 1.24-m-diameter borehole, both in terms of the difference in breakout azimuths, and in breakout depths. The final breakouts extended to a depth of 2.29 m on the NE and 2.47 m on the SW side of the borehole. The

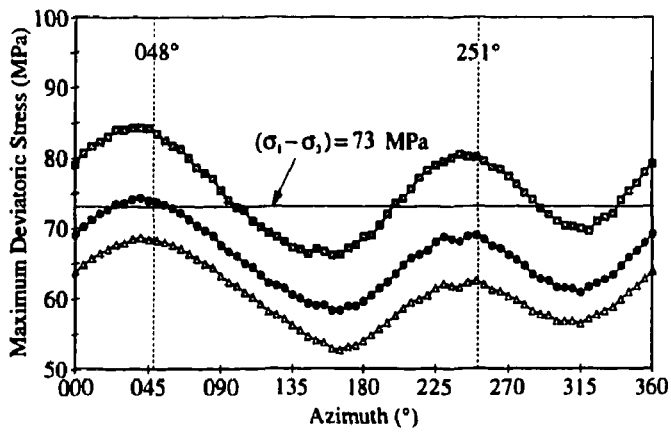

FIGURE 99: Maximum deviatoric stress pattern 0.1 diameters ahead of the 1.24-m-diameter borehole face at hole depths of 2.3 (upper), 3.4 (middle) and 5.0 m (bottom). Note the asymmetry of the peaks, both in magnitude and azimuth.

azimuths of the breakouts were 035° and 242° near the top of the hole, but approached 045° and 232° as the depth away from the room increased. Consequently, the amount of angular asymmetry near 2.0-m depth was reduced from 23° in the vertical 1.24-m-diameter borehole to 7° in the inclined 600-mm-diameter borehole. Likewise, the asymmetry in breakout length was reduced from 0.54 m to 0.18 m in the two holes, respectively. The orientations and magnitudes of the maximum deviatoric stress concentrations ahead of the borehole face are therefore consistent with field observations of breakouts in both the inclined and vertical borehole.

This study supports the notion that the complex loading path at the borehole face is responsible for initiating the damage which ultimately leads to the development of a breakout. It also confirms that the stress tensor predicted in Section 4.1.4 is consistent with observations of *in situ* breakouts. Read (1994) has shown that tunnel orientation relative to the principal stress directions is an important consideration in the interpretation of measured displacement responses.

4.3.5.3 Effect of Excavation Sequence

To determine whether or not excavation sequence was a contributing factor to the progressive failure process, the final 12 m section of the tunnel was excavated using a pilot-and-slash sequence. The rationale for this excavation approach was that, by first excavating a small full-face tunnel, the excavation damage associated with the three-dimensional face effects would be localized close to the pilot tunnel. By then slashing the small tunnel to a larger size, the excavation damage related to the pilot tunnel would be removed. In addition, because the slash would not involve a full-face excavation approach, the damage induced by the slash would be less than that associated with the pilot tunnel.

To assess the difference between the extent of breakouts associated with the pilot and the slash, the 2.5-m-diameter pilot tunnel was excavated with its floor at the same level as the main tunnel. The roof of the pilot tunnel was then slashed to increase its diameter to 3.5 m. In this way, breakout development in the floor would reflect the damage associated with the full-face pilot tunnel, and breakout development in the roof would reflect damage caused by the slash. Overall, the extent of excavation-induced damage was expected to be reduced from that caused by the full-face 3.5-m-diameter test tunnel owing to the initial smaller dimension of the pilot tunnel and the two-step approach to excavation.

Following excavation, the tunnel profile was surveyed to define the extent of breakouts. Although notch development in the roof of the tunnel initially appeared to be suppressed relative to development in the floor, the difference was less noticeable over time. In addition, it was difficult to draw any definite conclusions about the effect of excavation sequence owing to the presence of granodiorite in the test section, and the proximity of the test section to the end of the tunnel.

4.3.5.4 Effect of Artificial Support and Confinement

During excavation of the Mine-by test tunnel, it was necessary to install safety mesh to prevent loose material in the roof of the tunnel from falling (Keith and Onagi 1994). The mesh was held in place using 0.6-m-long mechanical rock bolts. However, the bolts were not tensioned, and were installed with rectangular wooden spacers, leaving approximately 100 mm between the rock and the bolt head. This arrangement provided protection in the event of large-scale spalling, but was specifically designed to avoid producing confining pressure in the region of the breakout notch.

In order to survey the tunnel profile, the rock bolts and mesh near the profile were periodically taken down, and any loose material was removed. During these periods, the extensometers close to the measured profile showed increased displacements, and there was evidence of increased AE/MS activity and subtle geometry changes in the roof notch. Similar observations were made in the floor of the tunnel when tunnel 'muck' used as rail ballast was removed. The differences between the patterns of microseismicity in the roof and in the floor are evident in Figure 40, which shows microseismic activity at 170 d related to removal of 'muck' from the tunnel floor. The temporary confinement provided by the spalled rock in the roof mesh, and by the tunnel 'muck' in the floor of the tunnel, therefore helped limit the progressive failure process, and reduced the development of excavation damage. These observations confirm that the progressive failure process and the development of excavation damage are very sensitive to small changes in confining pressure.

4.4 SUMMARY

Back analysis of displacement and strain measurements from the Mine-by Experiment provided confirmation that the *in situ* stress tensor used in the initial analysis of the experimental data was sufficient for the purposes of understanding the process of progressive failure and the development of excavation-induced damage. In addition, the back analysis improved the estimate of the stress orientations and the relative magnitudes of the various components within the tensor. Using the new tensor, it was shown that the orientation of the principal stresses relative to the tunnel axis can affect the pattern of excavation damage observed *in situ*, i.e., the development of asymmetric borehole breakouts. Variations in the relative magnitudes of the stress components were also shown to affect the absolute magnitudes of the stress concentrations around the tunnel, but did not change the overall pattern of stress concentrations or the interpretation of the experiment results.

Based on results from underground characterization, geophysics studies and numerical modelling, the excavation-induced damage around the Mine-by Experiment tunnel is concentrated in the regions of compressive stress concentrations in the roof and floor, and in the regions of tensile stress concentration in the sidewalls. The extent and characteristics of these damaged zones is shown schematically in Figure 100.

The damaged zone in the roof and floor comprises three distinct regions with different characteristics. The outer limit of damage is defined by the $\sigma_1 - \sigma_3 \approx 70$ MPa contour which extends approximately 0.7 m beyond the original tunnel perimeter. Within this

region, the rock mass has been damaged (weakened) as a result of high deviatoric stresses and stress rotation associated with the advancing tunnel face. The failed zone within this damaged region is v-shaped and extends to about 0.6 m beyond the original perimeter in the roof, and about 0.4 m in the floor. At the tip of each v-shaped notch is a localized process zone where the rock is crushed. Although the material in these zones is no longer part of the elastic continuum around the tunnel, it can be treated as a material that has been weakened and whose elastic modulus has been reduced (softened). The extent of the various regions in the compressive damaged zone varies depending on geology. AE/MS events recorded in these zones were typically in the 50 Hz to 10 kHz range.

In contrast, the damaged zone in the tensile sidewall regions of the tunnel is much more subtle than that in the roof and floor. The AE activity in this zone was typically in the 1 MHz range, indicating much smaller-scale cracking than in the compressive regions. Back analysis using extensometer results showed that the material behaviour in this zone can be characterized by softening of the shear modulus and anisotropic weakening (extensional cracking). In the NW sidewall (granodiorite), the AE activity indicates that most damage occurs within 0.35 m of the tunnel wall, and extends to about 1 m from the tunnel, dying out with distance from the sidewall. In granite, this zone of damage is more extensive, tending to expand into the tensile stress concentration lobes defined approximately by the

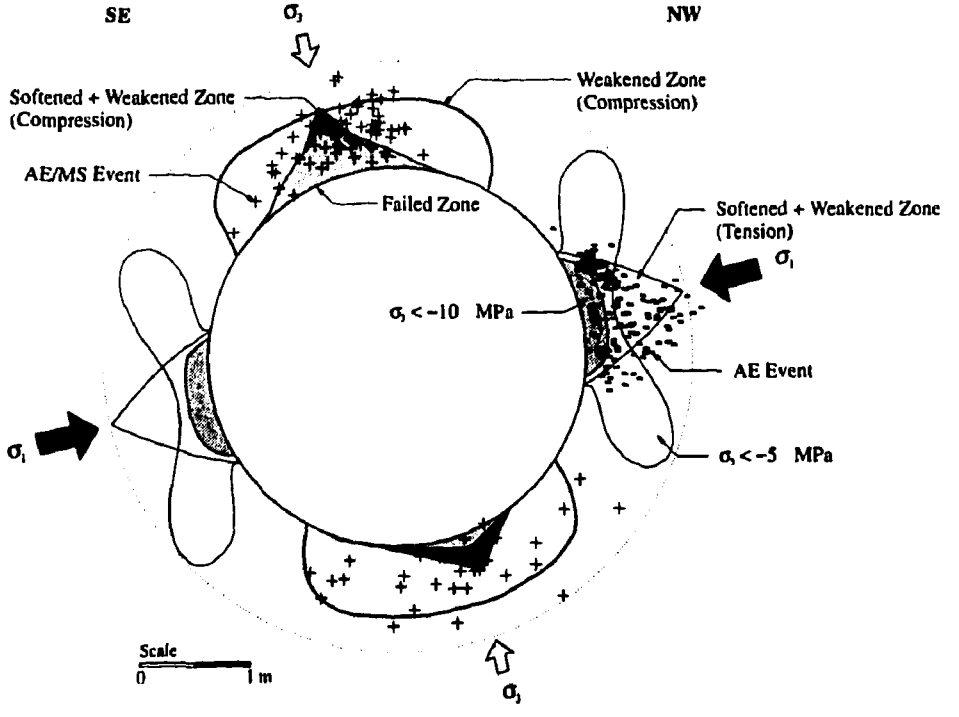

FIGURE 100: Schematic view of the extent and characteristics of excavation-induced damage around the Mine-by Experiment test tunnel. In the compressive regions, the damaged (weakened) zone is defined by $\sigma_1 - \sigma_3 \approx 70$ MPa and captures most of the AE/MS activity monitored in these regions. In the sidewalls, the damage initiates where $\sigma_3 < \sigma_t$, and migrates in a progressive fashion.

$\sigma_3 \approx -5$ MPa contour shown in Figure 100. The radial extent of the zone in granite, however, is similar to that in granodiorite. As with the compressive zones of damage, the extent of the damage zone in the tensile region is, in part, a function of geology.

In summary, the excavation-induced damage associated with the Mine-by Experiment test tunnel is limited to within about 1 m from the original tunnel perimeter. However, the characteristics of this damaged zone are variable around the tunnel, and are controlled or influenced by several factors. These factors include the nature of the stress concentration, i.e., compressive versus tensile; the mineralogy and grain size distribution of minerals within the various lithologic units; the *in situ* stress state, particularly the σ_1/σ_3 ratio; orientation of the principal stresses relative to the tunnel axis; excavation method and sequence; and confining pressure.

5. MODELLING PROGRESSIVE FAILURE

The philosophy adopted for numerical modelling of the Mine-by Experiment was that a staged approach was necessary to assess the state-of-the-art in numerical models and the ability of available models to predict the *in situ* rock mass behaviour. However, it was recognized early on in the Mine-by Experiment that none of the available numerical models was capable of simulating the complex processes involved in the progressive failure of brittle rock. Consequently, instead of comparing forward predictions with measured results, the emphasis of the numerical modelling component of the experiment was to improve our fundamental understanding of rock mass failure. It was hoped that, by advancing our understanding of the processes involved in progressive failure, numerical models could be developed which could later be used as predictive tools. Nonetheless, numerical modelling was an important element of the Mine-by Experiment, as it was an essential tool for scoping calculations and for back analyses of the measured results, e.g., see Sections 3 and 4.

Numerical modelling for the Mine-by Experiment was carried out using a variety of methods, as detailed in Table 10. The constitutive models used with the various numerical codes varied from linear elastic through to an extensive elastic-brittle-ductile (EBD) damage model developed by Ofoegbu and Curran (1991). The parameter values used in the EBD model were obtained from laboratory testing on representative samples of granite from the URL. However, none of the constitutive models used in the continuum models simulated the transition from a continuum to a discontinuum, an essential characteristic of progressive failure. Likewise, models using finite discrete fractures, and those based on a discontinuum, were also unable to adequately simulate the transition. Therefore, it is fair to say that the numerical modelling carried out during the course of the experiment was not successful in predicting *á priori* the extent and shape of failed region around the Mine-by test tunnel. In the following sections a brief overview is presented of the major findings from the modelling exercises conducted for the experiment.

TABLE 10

SUMMARY OF NUMERICAL MODELS USED IN THE MINE-BY EXPERIMENT

Model	Type	Use
Kirsch Solution	Analytical (2D)	Circular opening in an elastic continuum under plane strain conditions
EXAMINE^{2D}	Boundary element (2D)	Arbitrary 2D openings in an elastic continuum, explicit failure criteria
EXAMINE^{3D}	Boundary element (3D)	Arbitrary 3D openings in an elastic continuum, explicit failure criteria
MAP3D	Boundary element (3D)	Arbitrary 3D openings in an elastic continuum, multiple material types, displacement discontinuities, explicit failure criteria
FLAC	Finite difference (2D)	Arbitrary 2D openings in a continuum, multiple material types and constitutive models, explicit failure criteria
PHASES	Hybrid boundary element/finite element (2D)	Arbitrary 2D openings in an elastic continuum, multiple material types, explicit failure criteria
ABAQUS	Finite element (2D/3D)	Arbitrary 2 and 3D openings in a continuum, multiple material types, standard and custom constitutive models, explicit failure criteria
UDEC	Distinct element (2D)	Arbitrary 2D openings in an elastic discontinuum, multiple material types and constitutive models, explicit failure criteria
INSIGHT2D	Finite element (2D)	Arbitrary 2D openings in an elastic continuum, specialized meshing algorithm for finite discrete cracks, explicit failure criteria
EXAMINE^{FRAC}	Boundary element (2D)	Arbitrary 2D openings in an elastic continuum with discrete fractures, LEFM fracture propagation criterion

5.1 ELASTIC ANALYSES

Throughout the course of the experiment, it was demonstrated that relatively simple linear elastic models were illustrative of many aspects of the behaviour observed around the Mine-by test tunnel (Read 1991; Martin 1993). Elastic analyses were entirely adequate to predict the stresses and displacements around the test tunnel in regions that were not affected by the development of excavation-induced damage. Read (1994) successfully used elastic analyses to aid in back calculating the stress tensor at the 420 Level and to explain the occurrence of asymmetry in borehole breakouts, and Martin (1993) used elastic analyses to back-calculate the strength of Lac du Bonnet granite around the 420 Level tunnels. Elastic analyses were also routinely used to calculate the stress magnitude at which failure initiated, and to estimate the extent of the failed region based on the *in situ* crack-initiation stress (see Section 3).

In another study, Martin and Read (1992) showed that the slabbing process could be approximated using elastic analysis in conjunction with an elastic-brittle constitutive model. They simulated the failure process by performing iterative elastic analyses, removing slabs of rock next to the tunnel perimeter where the strength to stress ratio was 1 or less in each iteration. Their simulation started with the design profile and progressed through five steps (Figure 101). The analysis showed that the final excavated profile was stable except for a small region near the tip of the v-shaped notch (Figure 101). The numerical simulation used by Martin and Read (1992) is phenomenological, i.e., there is no attempt to follow the actual failure process. In addition, calibration of the unconfined compressive strength σ_c used in the model was required to match the observed behaviour. In this case, the unconfined strength used in the Hoek-Brown failure criterion was reduced from 157 to 100 MPa to obtain a reasonable match. This reduction in σ_c shifts the failure envelope downwards, and implies that the rock strength everywhere is reduced. From the microseismic data, it is clear that the rock strength is only locally damaged, and therefore the assumption that the rock strength everywhere is damaged is incorrect. This inherent assumption is one of the major drawbacks with analysis of this type, and can lead to pessimistic conclusions with regards to the rock strength *in situ*.

5.2 CONSTITUTIVE MODELS

In attempting to simulate the failure process in brittle rock, some form of strain-softening is generally used. In a strain-softening model, the elastic modulus and/or the strength of the rock is reduced as the load exceeds a critical value. By this process, load is redistributed from the region of failed material to other regions around the opening below the critical load.

Strain-softening behaviour around the Mine-by test tunnel was simulated by Khair and Chan (1994) using a two-dimensional finite element model. In their approach, iterative elastic analyses were performed, checking for material yield at each step. The yield criterion used was a Hoek-Brown envelope with $\sigma_c = 81.4$, $m = 16.4$ and $s = 1$. At each step, the Young's modulus of elements exceeding the yield limit was reduced by 20%. This reduction resulted in stress redistribution in successive steps, and was repeated until all elements were

below their yield limit. The equilibrium state at the end of the analysis showed only a very limited region of reduced modulus, i.e., yield, within the first row of elements next to the tunnel boundary. The modulus values in this region were reduced a maximum of 36%. The excavation-damaged zone predicted by the model was much smaller, and had a different shape, than that observed *in situ*. Read (1991) found similar results using FLAC.

In an attempt to simulate the slabbing process observed *in situ*, Read (1991) developed a routine within **FLAC** to conduct an iterative elastic analysis with explicit checks for tensile, compressive (shear) and slabbing failure based on a Hoek-Brown failure criterion with $\sigma_c = 100$, $m = 12$ and $s = 1$. A unidirectional tensile cutoff criterion was used in the case of tensile failure, which resulted in minor stress redistribution in the sidewalls of the tunnel. As in the previous analysis, compressive failure was noted close to the tunnel boundary in the roof and floor regions of the tunnel. Using a confining stress criterion in combination with a buckling criterion as a basis for removing elements at the free boundary, i.e., where the confinement was zero, Read (1991) found that the zone of removed material grew progressively, and was similar in shape to that observed *in situ*. He concluded that this type of modelling predicted responses for the instrumentation that were significantly different from those predicted by closed-form solutions for a circular hole in an infinite elastic medium. He also found that the shape of the predicted v-shaped notch was very dependent on the element removal scheme. Without the buckling constraint on the element removal scheme, Read (1991) found that the depth of the v-shaped notch approached $2a$ where a is the radius of the tunnel. However, with the buckling constraint, the depth of the v-shaped notch was reduced to $1.5a$ (Figure 102).

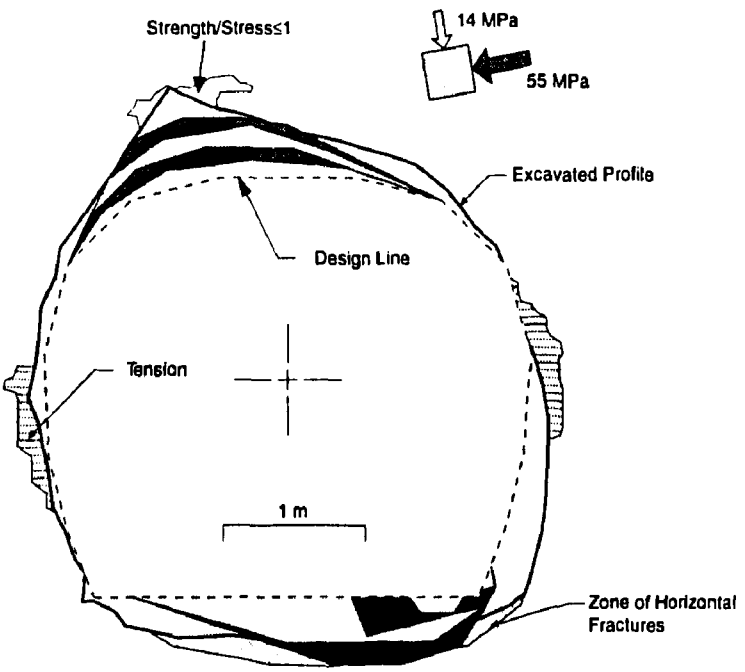

FIGURE 101: Numerical simulation of the slabbing process using elastic analyses and an elastic-brittle constitutive model.

The EBD model developed by Ofoegbu and Curran (1991) was implemented in the three-dimensional finite element program ABAQUS, and was used by Curran et al. (1992) to predict the stresses, displacements and damage around the Mine-by test tunnel. By comparing the results from linear elastic analyses and the EBD analyses, the zone of fracturing around the tunnel was predicted to extend to a depth of about 0.75 m, or about $1.4a$. These predictions were based on continuum analyses without accounting for progressive slabbing at the tunnel wall and changes in the excavation geometry. Thus, if the formation of the v-shaped notch had been accounted for in the analyses, the zone of fracturing would exceed 0.75 m. An example of the displacements predicted using the EBD model and the elastic model is presented in Figure 103. Note that both models predict very similar displacements. These results are similar to those of Read (1991) who also found that the inclusion of softened zones to represent failure did not significantly affect the predicted displacement response.

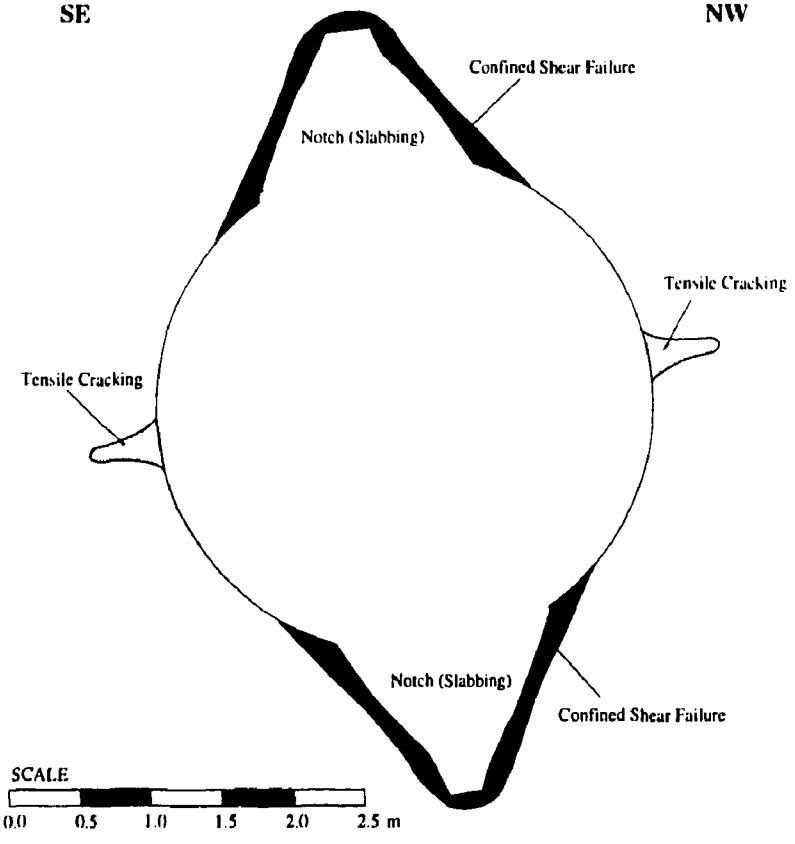

FIGURE 102: Predicted excavation damage around the Mine-by test tunnel, after Read (1991).

5.3 SUMMARY OF NUMERICAL MODELLING LIMITATIONS

The numerical modelling carried out during the course of the Mine-by Experiment showed that elastic analyses were adequate for interpreting the montoring results from the Mine-by test tunnel. However, both linear and nonlinear continuum analyses did not adequately predict the extent of damage around the Mine-by test tunnel, or the shape of the damaged zone. As discussed in Section 3, the process of progressive failure has several stages, starting with initiation at the boundary of the tunnel. This stage of the process can be predicted by continuum models, using an appropriate failure criterion. However, the stages following initiation, which involve dilation, slabbing and spalling, represent discontinuum-type behaviour. It is this behaviour that poses the major difficulty in using continuum models to predict the extent and shape of excavation damage. Until this limitation of the continuum models is overcome, current numerical models are of limited use in predicting the shape and extent of the failed region around the Mine-by test tunnel and similar underground openings. Despite this limitation, though, elastic modelling used in conjunction with the concepts developed in Section 3, are entirely adequate for engineering design purposes.

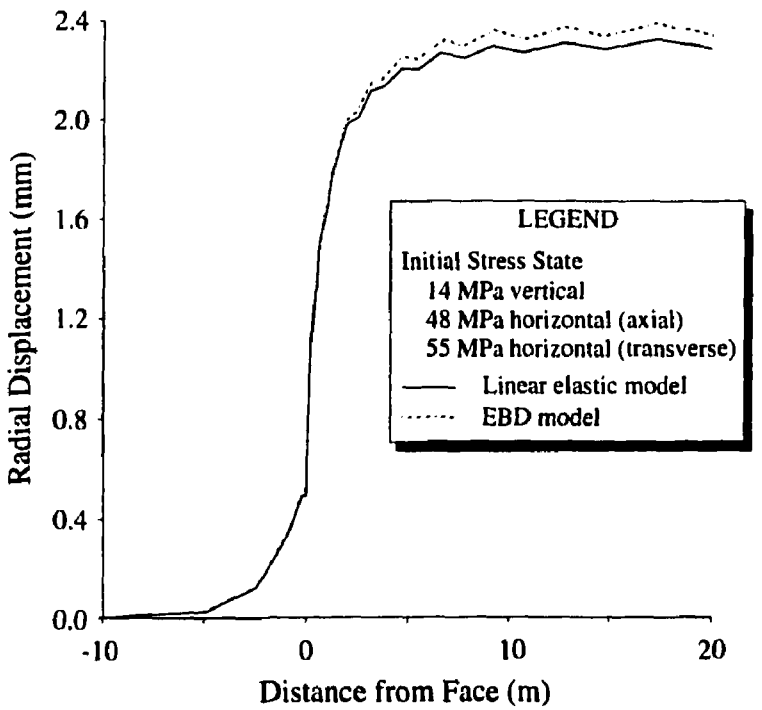

FIGURE 103: Predicted wall convergence around the Mine-by test tunnel at the sidewall ($\theta = 0°$), after Curran et al. (1992).

6. SUMMARY AND CONCLUSIONS

Phase 1 of the Mine-by Experiment was conducted at the 420 Level of the URL to investigate the response induced in the rock mass by excavating a 3.5-m-diameter circular test tunnel using a non-explosive technique. The main objectives of the experiment were to improve our fundamental understanding of *in situ* rock mass behaviour and failure mechanisms, and to evaluate the excavation damage created around underground openings. These two objectives were addressed in the investigations described in Sections 3 and 4, respectively. The findings from these investigations, and specifically the various studies using large-diameter boreholes in the floor of the underground openings, also contributed to the studies on the viability of the borehole alternative for emplacing nuclear fuel waste containers. The other two objectives, related to the development and evaluation of characterization methods and monitoring instrumentation, were addressed during the design and monitoring stages of the experiment. For example, characterization techniques and results of the characterization of the experiment area are detailed in Part 7 of the data summary reports for the experiment.

6.1 *IN SITU* ROCK MASS BEHAVIOUR AND FAILURE MECHANISMS

Back-analyses of tunnels excavated at the 420 Level of the URL showed that the *in situ* strength of Lac du Bonnet granite was less than that measured in short-term laboratory tests. However, because the tunnels were excavated in massive granite with no macroscopic discontinuities, the strength reduction could not be attributed to 'scale-effects'. Consequently, research into the role of the stress path on brittle rock strength was undertaken, comparing results from standard laboratory tests to those from *in situ* monitoring. In cylindrical laboratory samples, the sequence of events leading to failure is as follows:

- The failure process initiates with small cracks that form in the general direction of the maximum applied load. Stable crack growth starts at the crack-initiation stress, approximately 0.3 to 0.4 of the short-term peak strength of the sample.
- Stable crack growth continues until the density of cracks is sufficient to develop a macro failure zone. The stress level at which this occurs is about 0.7 to 0.8 of the short-term peak strength, and is referred to as unstable crack growth or crack-damage stress σ_{cd}.
- Once a macro failure zone is developed, the sample can no longer sustain the load and failure occurs.

In laboratory tests involving blocks with central boreholes, holes with diameters less than about 75 mm tend to show a marked scale/size effect, and require a maximum tangential stress of up to $2\sigma_c$ to initiate breakouts. For holes 75 mm or greater, this scale effect disappears, with tangential stress values approximately equal to σ_c at failure.

The sequence of events leading to failure around *in situ* openings is similar to that in the laboratory, but the stress level at failure is different. Based on results from the acoustic emission/microseismic (AE/MS) monitoring system used for the experiment:

- *In situ* crack initiation occurs at about 0.3 of the undisturbed laboratory strength.

- Spalling initiates when the tangential stress around the tunnel reaches about 100 to 120 MPa, i.e., 0.5 to 0.6 of the undamaged laboratory unconfined strength σ_c.
- Once failure initiates near the tunnel face, progressive development of a v-shaped notch occurs as the face advances. The failure process is controlled by a small process zone, consisting of highly strained/crushed rock at the tip of the notch. The failure process is multi-staged, involving crushing at the notch tip, dilation, then subsequent development of slabs, buckling and spalling. Development of the notch stops when the process zone is confined in a very small region at the notch tip, and the geometry of the notch is 'tear-drop' shaped.

Martin and Chandler (1994) showed that the measured σ_{cd} locus could be simulated using the Griffith sliding crack model proposed by Cook (1965). Using this model, they showed that stress/strain results from a laboratory compression test can be interpreted in terms of an interaction between friction and cohesion, in which the two components of strength are not mobilized at the same amount of damage. Initially, prior to any damage, the rock strength is composed of cohesion only, and can be described by

$$\sigma_1 - \sigma_3 = \text{ constant.} \tag{19}$$

The development of damage in a sample results in a rapid reduction in cohesion, and an associated increase in friction. Strength reduction of disturbed samples is thus related to cohesion loss.

The difference between the laboratory and *in situ* stress levels at which failure occurs is a result of the complex loading path around the advancing face of the tunnel *in situ*. As the tunnel advances, the principal stresses near the tunnel face change significantly in both magnitude and direction. Stress concentrations around the opening in excess of the crack-initiation stress, occurring at any period in the rock's loading history, result in a localized increase of damage to the rock and a corresponding loss of cohesion, i.e., weakening (see Section 3). The degree of damage is highest at the surface of the opening where confinement is zero and stress concentrations are greatest, and decreases with increasing distance into the rock.

Results from the AE/MS system showed that most microseismic activity is located within about 1 tunnel diameter of the face. Ahead of the tunnel face, the regions of microseismic activity correlate with the regions of compressive stress concentrations, which eventually result in breakout notches. This AE/MS activity is an indication of *in situ* damage development resulting from the complex loading path around the advancing face of the tunnel. Because of this loading path influence, the rock accumulates more crack damage for a given stress level than in laboratory tests, and undergoes more pronounced weakening. Consequently, failure *in situ* begins at lower compressive stress levels than in laboratory tests.

6.2 EXCAVATION DISTURBANCE AND DAMAGE

Numerical modelling and *in situ* characterization studies were conducted to establish the extent and characteristics of the damaged zone around the test tunnel. Back analyses of measured displacements and strains allowed the *in situ* stresses and material properties to

be deduced, leading to an improved estimate of the principal stress tensor at the 420 Level of the URL. This indicated that:

- The orientation of the principal stresses relative to the tunnel axis can affect the pattern of excavation damage observed *in situ*, in that borehole breakouts develop asymmetrically. The patterns of breakouts observed *in situ* were consistent with the new estimate of the stress tensor.
- Although the new estimate of the stress tensor changed the relative magnitudes of the stress components and the absolute magnitudes of the stress concentrations around the tunnel, it did not change the overall pattern of stress concentrations or the interpretation of the experiment results obtained using the previous estimate of the stress tensor.
- The complete *in situ* stress tensor can be determined u ing radial displacement measurements taken within 1-tunnel diameter of the face, using extensometers installed ahead of the face.
- Back analysis using a flat-faced cylinder model of the tunnel produced the lowest variability in the estimated tensor. External openings and small changes in Poisson's ratio had no significant effect on the results of the back analysis.

Results from underground characterization, geophysics studies and numerical modelling showed that the excavation-induced damage around the Mine-by Experiment tunnel is concentrated in the regions of compressive stress concentrations in the roof and floor, and in the regions of tensile stress concentration in the sidewalls. The damaged zone in the roof and floor comprises the following three distinct regions with different characteristics:

1. The outer limit of damage is defined by the $\sigma_1 - \sigma_3 \approx 70$ MPa contour which extends approximately 0.7 m beyond the original tunnel perimeter. Within this region, the rock mass has been damaged (weakened) as a result of high deviatoric stresses and stress rotation associated with the advancing tunnel face.
2. The failed zone within this damaged region is v-shaped and extends to about 0.6 m beyond the original tunnel perimeter in the roof, and about 0.4 m in the floor.
3. At the tip of each v-shaped notch is a localized process zone where the rock is crushed. Although the material in these zones is no longer part of the elastic continuum around the tunnel, it can be treated as a material that has been weakened, with a correspondingly reduced elastic modulus.

AE/MS events recorded in these three zones were in the 50 Hz to 10 kHz range.

The damaged zone in the tensile sidewall regions of the tunnel is much more subtle than that in the roof and floor. Thus,

- The AE events in this zone were typically in the 1 MHz range, indicating much smaller-scale cracking than in the compressive regions.
- Back analysis using extensometer results showed that the material behaviour in this zone can be characterized by softening of the shear modulus and anisotropic weakening (extensional cracking).

- In the NW sidewall, consisting primarily of granodiorite, the AE activity indicates that most damage occurs within 0.35 m of the tunnel wall. This activity extends to about 1 m from the tunnel, decreasing with distance from the sidewall. In granite, this zone of damage is more extensive.

Results of *in situ* characterization and numerical modelling showed that the excavation-induced damage associated with the Mine-by Experiment test tunnel occurs within about 1 m from the original tunnel perimeter. Within this region, however, the damage characteristics are highly variable around the tunnel, and are controlled or influenced by

- the nature of the stress concentration, i.e., compressive versus tensile;
- the geology of the rock mass, specifically the grain size distribution of minerals within the various lithologic units;
- the *in situ* stress state, particularly the σ_1/σ_3 ratio and the orientation of the principal stresses relative to the tunnel axis;
- excavation method and sequence, although the full influence of this factor was not quantified; and
- confining pressure.

Time-dependent behaviour was observed to occur immediately behind the tunnel face, typically over a period of about 3.5 days. However, the amount of non-elastic deformation was small, representing about 1% of the total deformation, and was localized close to the tunnel wall in the damaged zone.

6.3 NUMERICAL MODELLING

As described in Section 5, a thorough review of available numerical models showed that none was capable of simulating the transition from continuum to discontinuum behaviour, an essential feature in the progressive failure process. Consequently, the numerical modelling conducted for the Mine-by Experiment focused on improving our understanding of rock mass failure rather than conducting forward predictions and comparison with measured responses. Numerical models were used extensively in back analyses, as detailed in Section 4.

6.4 CONCLUDING REMARKS

In conclusion, the technical findings from the first phase of the Mine-by Experiment have improved our understanding of the processes involved in progressive failure and damage development. The most significant finding, from a practical viewpoint, is that the rock strength immediately around the test tunnel is only about 50% of the unconfined strength obtained in laboratory tests. This strength reduction occurs at very small levels of damage, and is related to cohesion loss. In addition, the development of damage *in situ* around the test tunnel was found to follow a complex path caused by effects of stress changes at the tunnel face. The rock underground undergoes stress changes from an initially loaded condition, whereas laboratory tests usually follow much different paths, starting from an

initially unloaded condition. Interpretation of laboratory test results assumes plane strain conditions in two-dimensions.

The findings from the Mine-by Experiment demonstrate the value in performing large-scale *in situ* experiments in combination with laboratory and numerical modelling studies in order to develop an understanding of the fundamental processes involved in the rock mass response to excavation.

ACKNOWLEDGEMENTS

The Mine-by Experiment is an activity within the Canadian Nuclear Fuel Waste Management Program, which is jointly funded by AECL and Ontario Hydro under the auspices of the CANDU Owners Group. The authors wish to thank Prof. Charles Fairhurst, Prof. Peter Kaiser, Prof. R. Paul Young, Prof. John Curran and Dr. Kam Tsui for their involvement in the Mine-by Experiment, and their technical review of this report.

REFERENCES

Barlow, J. P. (1986). Interpretation of tunnel convergence measurements. Master's thesis, Department of Civil Engineering, University of Alberta, Edmonton, AB.

Bieniawski, Z. T. (1967). Mechanism of brittle fracture of rock, Parts I, II and III. *Int. J. Rock Mech. Min. Sci. & Geomech. Abstr. 4*(4), 395–430.

Brace, W. F. and J. D. Byerlee (1968). Recent experimental studies of brittle fracture of rocks. In C. Fairhurst (Ed.), *Proc. 8th U.S. Symp. on Rock Mechanics, Minneapolis*, pp. 58–81. American Institute of Mining Engineers.

Brace, W. F., B. Paulding, and C. Scholz (1966). Dilatancy in the fracture of crystalline rocks. *J. Geophys. Res. 71*, 3939–3953.

Brown, A., N. M. Soonawala, R. A. Everitt, and D. C. Kamineni (1989). Geology and geophysics of the Underground Research Laboratory site, Lac du Bonnet Batholith, Manitoba. *Can. J. Earth Sci. 26*, 404–425.

Brown, E. T. (Ed.) (1981). *Rock characterization testing and monitoring, ISRM suggested methods*, pp. 107–127. Pergamon Press, Oxford.

Brown, E. T., J. W. Bray, B. Ladanyi, and E. Hoek (1983). Ground response curves for rock tunnels. *J. Geotech. Engng. Div. ASCE 109*(1), 15–39.

Brune, J. N. (1970). Tectonic stress and the spectra of seismic shear waves from earthquakes. *J. Geophys. Res. 75*, 4997–5009.

Carlson, S. R. and R. P. Young (1993). Acoustic emission and ultrasonic velocity study of excavation-induced microcrack damage at the Underground Research Laboratory. *Int. J. Rock Mech. Min. Sci. & Geomech. Abstr. 30*(7), 901–907.

Carter, B. J. (1992). Size and stress gradients effects on fracture around cavities. *Rock Mech. and Rock Engin. 25*(3), 167–186.

Chandler, N. A. and C. D. Martin (1994). The influence of near surface faults on in situ stresses in the Canadian Shield. In *Proc. 1st North American Rock Mech. Symp., Austin*, pp.369–376. Balkema, Rotterdam.

Chandler, N. A. (1993). Bored raise overcoring for in situ stress determination at the Underground Research Laboratory. *Int. J. Rock Mech. Min. Sci. & Geomech. Abstr. 30*(7), 989–992.

Chow, T., S. D. Falls, S. R. Carlson, and R. P. Young (1990). Ultrasonic imaging and acoustic emission monitoring of laboratory hydraulic fracturing experiments in Lac du Bonnet grey granite from AECL's Underground Research Laboratory. Contractor's Report to AECL Research, Contract No. WS-29J-54491, RP008AECL, Queen's University.

Collins, D. S., C. Baker, and R. P. Young (1994). Source parameters of excavation-induced seismicity from the Mine-by tunnel. Report to Atomic Energy of Canada Ltd. RP028AECL, Applied Seismology and Rock Physics Laboratory, Keele University, Staffordshire, U.K.

Collins, D. S. and R. P. Young (1992). Monitoring and source location of microseismicity induced by excavation of the Mine-by Test Tunnel: Preliminary analysis. Report to Atomic Energy of Canada Ltd. RP013AECL, Engineering Seismology Laboratory, Queen's University, Kingston, Canada.

Collins, D. S. and R. P. Young (1993). The spatial and temporal distribution of microseismicity recorded in Round 17 of the Mine-by tunnel. Report to Atomic Energy of Canada Ltd. RP023AECL, Applied Seismology and Rock Physics Laboratory, Keele University, Staffordshire, U.K.

Cook, N. G. W. (1965). The failure of rock. *Int. J. Rock Mech. Min. Sci. & Geomech. Abstr. 2*, 389–403.

Corthésy, R. and D. Gill (1992). Doorstopper stress measurements at the 420 Level of the URL. Final Report to AECL Research, le Centre de Développement Technologique de l'École Polytechnique de Montréal.

Curran, J. H. and B. T. Corkum (1993). *EXAMINE^{3D} - Three-Dimensional Excavation Analysis for Mines, Version 2.0.* Data Visualization Laboratory, Department of Civil Engineering, University of Toronto.

Curran, J. H., G. I. Ofoegbu, and M. W. Grabinsky (1992). Three dimensional finite element analyses of the URL Mine-by test tunnel. Contractor's Report to AECL Research, Contract No. WS-29J-54421 92-01, Data Visualization Laboratory, University of Toronto.

Davison, C. C., A. Brown, and N. M. Soonawala (1982). Preconstruction site evaluation program at the Canadian Underground Research Laboratory. In *Proc. 14th Information Meeting Nuclear Fuel Waste Management Program (1982 General Meeting).* Also Atomic Energy of Canada Limited Technical Record, TR-207, pages 162-187.

Doe, T. (1989). Hydraulic-fracturing stress measurements in horizontal holes at the 240- and 420-m Levels of the Underground Research Laboratory. Consulting Report to AECL Research 893-1002, Golder Associates.

Dusseault, M. B. and N. R. Morgenstern (1979). Locked sands. *Quarterly J. Engineering Geology 12*, 117–131.

Eissa, E. A. and A. Kazi (1988). Technical note - Relation between static and dynamic Young's moduli of rocks. *Int. J. Rock Mech. Min. Sci. & Geomech. Abstr. 25*(6), 479–482.

Everitt, R. A. and A. Brown (1986). Subsurface geology of the Underground Research Laboratory: An overview of recent developments. In *Proc. 20th Information Meeting Can. Nuclear Fuel Waste Management Program (1985 General Meeting), Vol. 1*, pp. 146–181. Also Atomic Energy of Canada Limited Technical Record, TR-375.

Everitt, R. A., A. Brown, C. C. Davison, M. Gascoyne, and C. D. Martin (1990a). Regional and local setting of the Underground Research Laboratory. In R. Sinha (Ed.), *Proc. Int. Symp. on Unique Underground Structures, Vol. 2, Denver, Colorado*, pp. 64:1–23. CSM Press, Denver.

Everitt, R. A., P. Chernis, D. Good, and A. Grogan (1989). Mapping of the excavation damage zone around the circular access shaft at Atomic Energy of Canada Limited's Underground Research Laboratory. In *Excavation Response in Geological Repositories for Radioactive Waste, Proc. NEA Workshop, Winnipeg, MB, 1988 April*, pp. 271 -282.

Everitt, R. A., P. Gann, and D. M. Boychuk (1993). Mine-by Experiment data summary: Part 7 - Geological setting and general geology. Report RC-1080, COG-93-251, Atomic Energy of Canada Limited.

Everitt, R. A. and C. McGregor (1996). Natural microcrack orientations as indicators of macro-scale fracture orientations and in situ stress orientations at AECL's Underground Research Laboratory. Submitted to *Can. J. Earth Sci.*

Everitt, R. A., D. Woodcock, P. Gann, and D. Robinson (1990). Geology of the 420 Level of the Underground Research Laboratory. Technical Record TR-529, Atomic Energy of Canada Limited.

Ewy, R. T. and N. G. W. Cook (1990). Deformation and fracture around cylindrical openings in rock, Parts I and II. *Int. J. Rock Mech. Min. Sci. & Geomech. Abstr. 27*, 387–427.

Feignier, B. and R. P. Young (1993). Moment tensor inversion of induced microseismic events: evidence of non-shear failures in the $-4 < M < -2$ moment magnitude range. *Geophys. Res. Lett. 19*(14), 1503–1506.

Filon, L. N. G. (1937). On antiplane stress in an elastic solid. *Proc. R. Soc. London A160*, 137–154.

Gladwin, M. T. and F. D. Stacey (1974). Ultrasonic pulse velocity as a rock stress sensor. *Tectonophysics 21*, 39–45.

Goodman, R. E. (1989). *Introduction to rock mechanics.* John Wiley and Sons, NY.

Grabinsky, M. W. and J. H. Curran (1993). Harmonic finite element analysis of a cylindrical excavation in an infinite medium. Contractor's Report to AECL Research, Contract No. W108113 Publication 93-02, Rock Engineering Group, Department of Civil Engineering, University of Toronto.

Gyenge, M., R. Jackson, and B. Gorski (1991). Residual strength envelopes using the confined shear test method. In J.-C. Roegiers (Ed.), *Proc. 32th U.S.Symposium on Rock Mechanics, Norman*, pp. 629-635. A.A. Balkema, Rotterdam.

Haimson, B., M. Lee, N. Chandler, and C. D. Martin (1993). Estimating the state of stress from subhorizontal hydraulic fractures at the Underground Research Laboratory, Manitoba. *Int. J. Rock Mech. Min. Sci. & Geomech. Abstr. 30*(7), 959-964.

Haimson, B. C. and C. G. Herrick (1989). Borehole breakouts and *in situ* stress. In *Proc. 12th Annual Energy-Sources Technology Cof. & Exhibition, Drilling Symp.*, pp. 17-22. American Society Mechanical Engineers, New York.

Hayles, J. G., M. H. Serzu, and G. S. Lodha (1995). Cross-hole seismic tomography surveys for the Mine-by Experiment. Technical Record TR-678, COG-95-021, Atomic Energy of Canada Limited.

Hayles, J. G., K. M. Stevens, M. H. Serzu, and G. S. Lodha (1992). Developments in the mini-CHARTS system and field trial results for excavation damage assessment in granite. In *Proc. Fourth Int. Symp. on Borehole Geophysics for Minerals, Geotechnical and Groundwater Applications, Toronto, Canada, August 18-23, 1991.*

Herget, G. (1988). *Stresses in rock*. A. A. Balkema, Rotterdam.

Hiramatsu, Y. and Y. Oka (1968). Determination of the stresses in rock unaffected by boreholes or drifts, from measured strains or deformations. *Int. J. Rock Mech. Min. Sci. 5*(4), 337-353.

Hock, E. (1965). Rock fracture under static stress conditions. CSIR Report MEG 383, National Mechanical Engineering Research Institute, Council for Scientific and Industrial Research, Pretoria, South Africa.

Hock, E. and E. T. Brown (1980). *Underground excavations in rock*. Inst. Min. Metall., London.

Hoskins, E. R. (1968). Strain rosette relief measurements in hemispherically ended boreholes. *Int. J. Rock Mech. Min. Sci. 5*(6), 551-559.

ISS (1994). *Guide to seismic monitoring in mines*. Welkom, South Africa: ISS International Limited.

Jackson, R., J. S. O. Lau, and A. Annor (1989). Mechanical, thermo-mechanical and joint properties of rock samples from the site of AECL's Underground Research Laboratory, Lac du Bonnet, Manitoba. In *Proc. 42nd Canadian Geotechnical Conference, Winnipeg, MB*, pp. 41-49.

Jaeger, J. C. and N. G. W. Cook (1979). *Fundamentals of rock mechanics* (Third ed.). Chapman and Hall, London.

Kaiser, P. K., T. D. Wiles, and D. Zou (1991). Two- and three-dimensional stress back-analysis. Report to Atomic Energy of Canada Limited under contract WS-29J-54460, Laurentian University.

Keilis-Borok, V. I. (1959). The study of earthquake mechanism. In J. H. Hodgson (Ed.), *The mechanics of faulting with special reference to the fault-plane work*, pp. 279. Dominion Observatory, Ottawa.

Keith, S. G. and D. P. Onagi (1994). Mine-by Experiment data summary: Part 8 - Construction summary. Report COG-93-252, Atomic Energy of Canada Limited.

Kelly, D., D. C. Peck, and R. S. James (1993). Petrography of granitic rock samples from the 420 m Level of the Underground Research Laboratory, Pinawa, Manitoba. Contractor's report to AECL Research, Laurentian University.

Khair, K. R. and T. Chan (1994). Finite element modelling of the geomechanical responses of the Mine-by Experiment. Technical Record TR-610, COG-93-242, Atomic Energy of Canada Limited.

Kobayashi, S., N. Nishimura, and K. Matsumoto (1988). Displacements and strains around a non-flat-end borehole. In *Proc. 2nd Int. Symp. on Field Measurements in Geomechanics*, pp. 1079–1084.

Lajtai, E. Z. (1972). Effect of tensile stress gradient on brittle fracture initiation. *Int. J. Rock Mech. Min. Sci. & Geomech. Abstr. 9*, 569–578.

Lajtai, E. Z. (1982). The fracture of Lac du Bonnet granite. Office of Industrial Research report TR-M-00007, University of Manitoba, Geological Engineering Department.

Lajtai, E. Z. (1988). The deformation, fracture and strength of Lac du Bonnet granite. Research report 19, University of Manitoba, Geological Engineering Department.

Lajtai, E. Z. and L. P. Bielus (1986). Stress corrosion cracking of Lac du Bonnet granite in tension and compression. *Rock Mech. Rock Engng. 19*, 71–87.

Lajtai, E. Z., B. J. Carter, and M. L. Ayari (1990). Criteria for brittle fracture in compression. *Eng. Frac. Mech. 37*(1), 59–74.

Lajtai, E. Z., B. J. Carter, and E. J. S. Duncan (1991). Mapping the state of fracture around cavities. *Engineering Geology 31*, 277–289.

Lajtai, E. Z. and A. M. Gadi (1989). Friction on a granite to granite interface. *Rock Mech. and Rock Engin. 22*, 25–49.

Lajtai, E. Z. and R. H. Schmidtke (1986). Delayed failure in rock loaded in uniaxial compression. *Rock Mech. Rock Engng. 19*, 11–25.

Lee, M. Y. and B. C. Haimson (1993). Laboratory study of borehole breakouts in Lac du Bonnet granite: A case of extensile failure mechanism. *Int. J. Rock Mech. Min. Sci. & Geomech. Abstr. 30*(7), 1039–1045.

Livesley, R. K. (1989). *Mathematical methods for engineers*. Ellis Horwood Limited, Chichester, 1st edition.

Martin, C. D. (1993). *The strength of massive Lac du Bonnet granite around underground openings*. Ph. D. thesis, Department of Civil and Geological Engineering, University of Manitoba, Winnipeg, MB.

Martin, C. D. and N. A. Chandler (1993). Stress heterogeneity and geological structures. *Int. J. Rock Mech. Min. Sci. & Geomech. Abstr. 30*(7), 993–999.

Martin, C. D. and N. A. Chandler (1994). The progressive fracture of Lac du Bonnet granite. *Int. J. Rock Mech. Min. Sci. & Geomech. Abstr. 31*(6), 643–659.

Martin, C. D., N. A. Chandler, and R. S. Read (1994). The role of convergence measurements in characterizing a rock mass. In *47th Canadian Geotechnical Conference, Halifax, NS.*

Martin, C. D., J. B. Martino, and E. J. Dzik (1994). Comparison of borehole breakouts from laboratory and field tests. In *Proc. EUROCK'94, SPE/ISRM Rock Mechanics in Petroleum Engineering Delft*, pp. 183–190. A.A. Balkema, Rotterdam.

Martin, C. D. and R. S. Read (1992). The *in situ* strength of massive granite around excavations. In *Proc. 16th Can. Rock Mech. Conf., Sudbury*, pp. 1–10.

Martin, C. D. and B. Stimpson (1994). The effect of sample disturbance on laboratory properties of Lac du Bonnet granite. *Can. Geotech. J. 31*(5), 692–702.

Martin, C. D., R. P. Young, and D. S. Collins (1995). Monitoring progressive failure around a tunnel in massive granite. In *Proc. 8th ISRM Congress on Rock Mechanics, Tokyo.* A.A. Balkema, Rotterdam.

Martino, J. B. (1989). Distometer convergence readings in the shaft extension of Atomic Energy of Canada Limited's Underground Research Laboratory. Technical Record TR-482, Atomic Energy of Canada Limited.

Martino, J. B. (1996). A guide to information archiving and retrieving for the Mine-by Experiment Excavation Response Phase. Technical Record in preparation, Atomic Energy of Canada Limited.

Martino, J. B. (1995a). Long-term shaft excavation response recorded by Bof-ex extensometers from 1988 to 1993 at the 324 and 384 instrumentation arrays. Technical Record TR-680, Atomic Energy of Canada Limited.

Martino, J. B., R. S. Read, and D. Collins (1993). Mine-by Experiment data summary report: Part 6 - Acoustic emission/ microseismic results. Technical Record TR-597, COG-93-185, Atomic Energy of Canada Limited.

Martino, J. B., R. S. Read, and S. G. Keith (1994). Mine-by Experiment data summary report: Part 9 - Observations. Report COG-93-347, Atomic Energy of Canada Limited.

Martino, J. B., R. S. Read, and J. H. Mitchell (1993a). Mine-by Experiment data summary report: Part 5 - Thermistor results. Technical Report RC-1079, COG-93-233, Atomic Energy of Canada Limited.

Mastin, L. (1984). The development of borehole breakouts in sandstone. Master's thesis, Stanford University, Berkley, Calfornia.

Maxwell, S. C. and R. P. Young (1994). Wave propagation effects of an underground opening. Contractor's Report to Atomic Energy of Canada Limited RP025AECL, Keele University.

McGarr, A. (1994). Some comparisons between mining-induced and laboratory earthquakes. *PAGEOPH 142*(3/4), 467–489.

Myrvang, A. M. (1991). Estimation of *in situ* compressive strength of rocks from *in situ* stress measurements in highly stressed rock structures. In W. Wittke (Ed.), *Proc. 7th ISRM Congress on Rock mechanics, Aachen*, pp. 573–575. A.A. Balkema, Rotterdam.

Niwa, Y., S. Kobayashi, and T. Fukui (1979). Stresses and displacements around an advancing face of a tunnel. In *Proc. 4th Int. Congr. Rock Mech., Vol. 1, Montreux*, pp. 703–710.

Ofoegbu, G. I. and J. H. Curran (1991). Development and numerical implementation of an elastic-brittle-ductile constitutive model. Contractor's Report to Atomic Energy of Canada Limited, Department of Civil Engineering, University of Toronto.

Onagi, D. P., S. G. Keith, and G. W. Kuzyk (1992). Non-explosive excavation technique developed for the excavation of AECL's Mine-by Experiment test tunnel at the Underground Research Laboratory. In *Proc. 10th Annual Tunnelling Assoc. of Canada Conf., Banff, AB.*

Panet, M. and A. Guenot (1982). Analysis of convergence behind the face of a tunnel. In *Proc. 3rd Int. Symp. on Tunnelling, Brighton, England*, pp. 197–204.

Paulsson, B. N. P. (1983). *Seismic velocities and attenuation in a heated underground granitic repository.* Ph. D. thesis, University of California, Berkeley, CA.

Paulsson, B. N. P. and M. S. King (1980). Between-hole acoustic surveying and monitoring of a granite rock mass. *Int. J. Rock Mech. Min. Sci. & Geomech. Abstr. 17*, 317–367.

Pelli, F. (1987). *The influence of near face behaviour on monitoring of deep tunnels.* Ph.D. thesis, Department of Civil Engineering, University of Alberta, Edmonton, AB.

Pelli, F., P. K. Kaiser, and N. R. Morgenstern (1991). An interpretation of ground movements recorded during construction of the Donkin-Morien tunnel. *Can. Geotech. J. 28*(2), 239–254.

Pusch, R. and R. Stanfors (1992). The zone of disturbance around blasted tunnels at depth. *Int. J. Rock Mech. Min. Sci. & Geomech. Abstr. 29*(5), 447–456.

Read, R. S. (1991). Mine-by Experiment - prediction of excavation-induced rock mass response. Technical Memorandum URL-EXP-022-M048, Atomic Energy of Canada Limited.

Read, R. S. (1994). *Interpreting excavation-induced displacements around a tunnel in highly stressed granite.* Ph. D. thesis, Department of Civil and Geological Engineering, University of Manitoba, Winnipeg, MB.

Read, R. S. and C. D. Martin (1991a). Mine-by Experiment final design report. Report AECL-10430, Atomic Energy of Canada Limited.

Read, R. S. and C. D. Martin (1991b). The Underground Research Laboratory Mine-by Experiment - a research perspective on tunnel design. *Canadian Tunnelling 7*, 75–88.

Read, R. S. and C. D. Martin (1992). Monitoring the excavation-induced response of granite. In *Proc. 33rd U.S. Symp. on Rock Mech., Santa Fe*, pp. 201–210. Balkema:Rotterdam.

Read, R. S. and C. D. Martin (1993). Mine-by Experiment plan, Underground Research Laboratory - Addendum 1: Mine-by Experiment heated failure tests. Quality Assurance Document DE010.086, Atomic Energy of Canada Limited.

Read, R. S., C. D. Martin, and E. J. Dzik (1995). Asymmetric borehole breakouts at the URL. In *Proc. 35th US Rock Mech. Symp., Lake Tahoe*, pp. 879-884. Balkema:Rotterdam.

Read, R. S., J. B. Martino, G. R. Karklin, E. Jacobs, and G. Hiltz (1994). Mine-by Experiment data summary: Part 1 - Survey results. Report COG-93-290, Atomic Energy of Canada Limited.

Read, R. S., J. B. Martino, and J. H. Mitchell (1993b). Mine-by Experiment data summary: Part 4 - Convergence results. Technical Record TR-595, COG-93-177, Atomic Energy of Canada Limited.

Read, R. S., J. B. Martino, and J. H. Mitchell (1994b). Mine-by Experiment data summary: Part 2 - Triaxial strain cell results. Report COG-93-353, Atomic Energy of Canada Limited.

Read, R. S., J. B. Martino, J. H. Mitchell, and M. H. Spinney (1994a). Mine-by Experiment data summary: Part 3 - Extensometer results. Report COG-93-354, Atomic Energy of Canada Limited.

Saleh, K., A.-P. Bois, and G. Ballivy (1992). Instrumentation des parios rocheuses à l'aide des Cylindres Instrumentés de l'Université de Sherbrooke. 2nd Progress Report GR-92-09-1, Laboratoire de mécanique des roches et de géologie appliquée, Département de génie civil, Faculté des sciences appliquées, Université de Sherbrooke, Québec, Canada.

Simmons, G. R. (1990). Operating phase experiments planned for Atomic Energy of Canada Limited's Underground Research Laboratory. In R. S. Sinha (Ed.), *Proc. Int. Symp. on Unique Underground Structures, Denver*, Volume 2, pp. 67:1-19. CSM Press, Denver.

Snider, G. R., P. A. Lang, and P. M. Thompson (1989). Procedures used for installing and monitoring geomechanical instrumentation during sinking of the URL shaft. Technical Record TR-486, Atomic Energy of Canada Limited.

Stacey, T. R. (1981). A simple extension strain criterion for fracture of brittle rock. *Int. J. Rock Mech. Min. Sci. & Geomech. Abstr. 18*(6), 469-474.

Stesky, R. M. (1980). Elastic properties and strain measurements of rock cores from Atomic Energy of Canada Ltd. Chalk River, Ontario and Whiteshell, Manitoba test areas. Contractor's Report DSS File No. 17ST.23233-8-1344, Atomic Energy of Canada Limited. Available from the AECL Records Management Office, Whiteshell Laboratories, Pinawa, Manitoba.

Stesky, R. M. (1985). Characterization of microcrack properties of deep granite samples through analysis of elastic properties. Contractor's Report DSS File No. 20SU.23233-2-1480, Atomic Energy of Canada Limited. Available from the AECL Records Management Office, Whiteshell Laboratories, Pinawa, Manitoba.

Stimpson, B. and R. Chen (1991). A new technique for measuring the bimodularity of rock. In *Proc. Canadian Conf. on Appl. Mechanics, Winnipeg, MB.*

Sugawara, K. and Y. Obara (1986). Measurement of in-situ rock stress by hemispherical-ended borehole technique. *Min. Sci. Technol. 3*, 287-300.

Talebi, S. and R. P. Young (1990). Design of a microseismic system for the URL Mine-by Experiment. Contractor's Report to AECL Research, Contract No. WS-30J-54474 RP006AECL, Queen's University.

Talebi, S. and R. P. Young (1992). Microseismic monitoring in highly stressed granite: relation between shaft-wall cracking and *in situ* stress. *Int. J. Rock Mech. Min. Sci. & Geomech. Abstr. 29*(1), 25–34.

Thompson, P. M., E. T. Kozak, and C. D. Martin (1989). Rock displacement instrumentation and coupled hydraulic pressure/rock displacement instrumentation for use in stiff crystalline rock. In *Excavation Response in Geological Repositories for Radioactive Waste, Proceedings of a NEA Workshop, Winnipeg, MB, 1988 April*, pp. 257–270.

Thompson, P. M., J. B. Martino, and M. H. Spinney (1993). Detailed measurements of deformation in the excavation disturbed zone. In *Proc. 34th U.S. Symposium on Rock Mechanics, 1993 June 27-30, Madison, Vol. 2*, pp. 757–760.

van Heerden, W. L. (1969). Potential fracture zones around boreholes with flat and spherical ends. *Int. J. Rock Mech. Min. Sci. 6*(5), 453–463.

Walker, J. R., C. D. Martin, and E. J. Dzik (1990). Technical note - Confidence intervals for in situ stress measurements. *Int. J. Rock Mech. Min. Sci. & Geomech. Abstr. 27*(2), 139–141.

Wiles, T. (1992). *Direct Boundary Element Method in 3-Dimensions.* Laurentian University, Sudbury, Canada: Geomechanics Research Centre.

Wiles, T. D. (1995). Back analysis of the Mine-by Experiment using the direct boundary element method. Contractor's report to Atomic Energy of Canada Limited, Mine Modelling Ltd.

Wiles, T. D. and P. K. Kaiser (1992). Under excavation method incremental analysis of 420 Level vent raise and Room 209 data. Contractor's report to Atomic Energy of Canada Limited, Laurentian University.

Wiles, T. D. and P. K. Kaiser (1994a). In situ stress determination using the under-excavation technique – Part 1: Theory. *Int. J. Rock Mech. Min. Sci. & Geomech. Abstr. 31*(5), 439–446.

Wiles, T. D. and P. K. Kaiser (1994b). In situ stress determination using the under-excavation technique – Part 2: Application. *Int. J. Rock Mech. Min. Sci. & Geomech. Abstr. 31*(5), 447–456.

Wong, J., N. Bregman, G. F. West, and P. Hurley (1987). Cross-hole seismic scanning and tomography. *Geophysics - The Leading Edge*, 36–41.

Woodcock, D. R. (1994). Geological data summary for the CSIRO-series boreholes drilled for the Mine-by Experiment at the Underground Research Laboratory. Technical Report COG-94-282, Atomic Energy of Canada Limited. Protected.

Worotnicki, G. and R. J. Walton (1976). Triaxial "hollow inclusion" gauges for the determination of rock stresses in situ. In *Proc. Symp. on Investigation of Stresses in Rock and Advances in Stress Measurement, supplement*, pp. 108.

Wu, H. and D. D. Pollard (1992). Possible secondary fracture patterns due to a change in the direction of loading. In *Preprints Conf. on Fractured and Jointed Rock Masses, Lake Tahoe*, Volume 2, pp. 505–512. US Dept of Energy.

Zheng, Z., J. Kemeny, and N. Cook (1989). Analysis of borehole breakouts. *J. Geophys. Res. 94*(B6), 7171–7182.

APPENDIX A

COMPLETED EXPERIMENT SCHEDULE

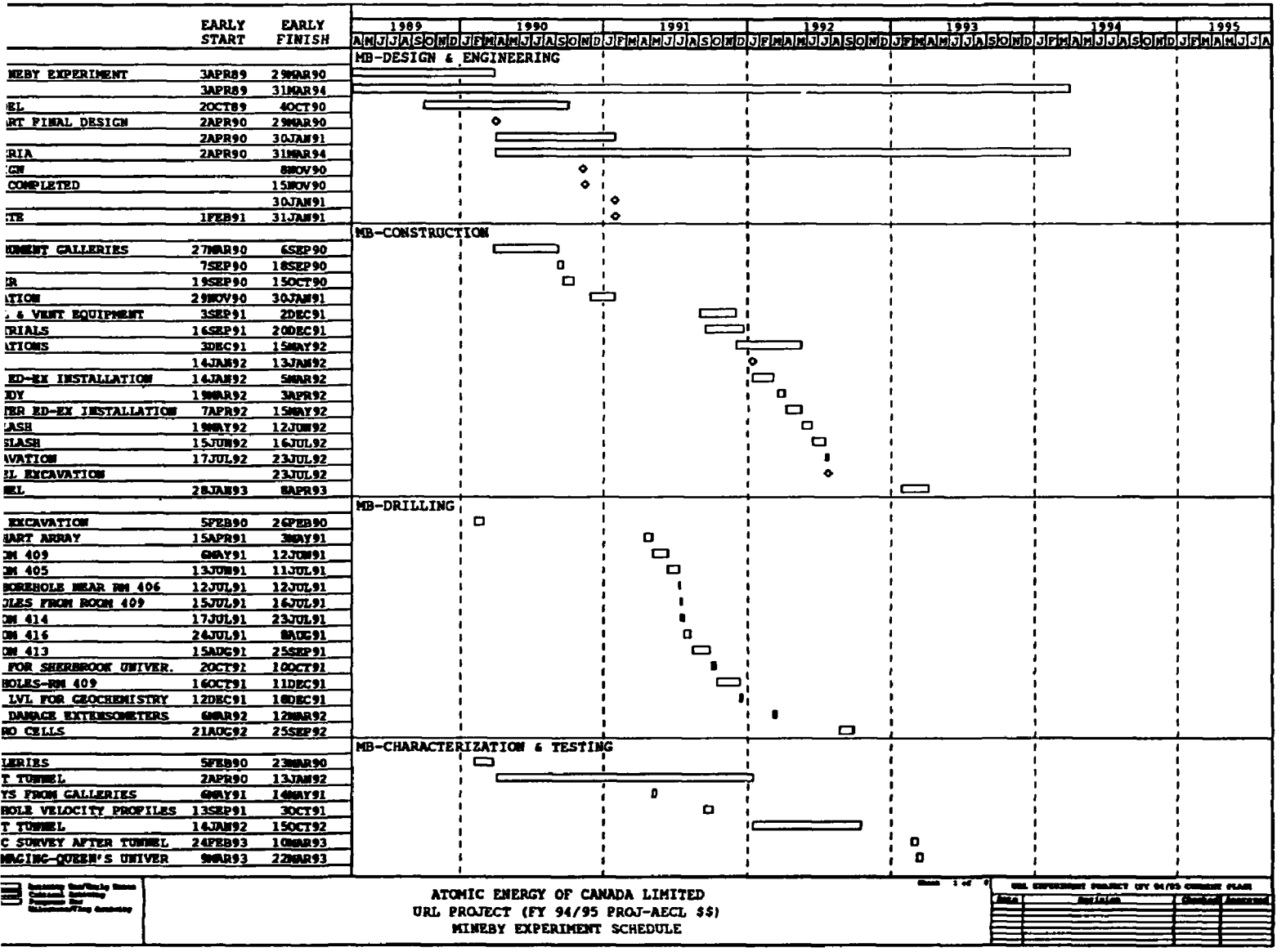

ATOMIC ENERGY OF CANADA LIMITED
URL PROJECT (FY 94/95 PROJ-AECL $$)
MINEBY EXPERIMENT SCHEDULE

ACTIVITY DESCRIPTION	EARLY START	EARLY FINISH
MB-PROCURE AE/MS INSTRUMENTS	9NOV90	5APR91
MB-PROCURE EXCAVATION RESPONSE INSTRUMENTS	1FEB91	24JUL91
MB-PROCURE VENT/ENTHALPY EQUIPMENT	1FEB91	30AUG91
MB-INSTALL AE/MS	17JUL91	15AUG91
MB-AE/MS SYSTEM INSTALLATION COMPLETE	16AUG91	15AUG91
MB-INSTALL EXCAVATION RESPONSE INSTRUMENTS	4OCT91	1NOV91
MB-INSTALL CONCRETE CYLINDERS UNIV OF SHERBROOKE	13JAN92	17JAN92
MB-INSTALL & MONITOR CONVERGENCE ARRAYS	14JAN92	23JUL92
MB-AE ARRAY INSTALLATION	13MAR92	17MAR92
MB-INSTALL EXCAVATION DAMAGE EXTENSOMETERS	13MAR92	18MAR92
MB-RETRIEVE INSTRUMENTS AFTER TEST TUNNEL	3SEP92	2OCT92
MB-START MINEBY EXPERIMENT	3APR89	
MB-MONITOR AE/MS SYSTEM	16AUG91	23JUL92
MB-MONITOR INSTRUMENTS B4 TEST TUNNEL	4NOV91	13JAN92
MB-MONITOR INSTRUMENTS DURING TEST TUNNEL	13JAN92	23JUL92
MB-MONITOR AE ARRAY DURING STUDY	18MAR92	6APR92
MB-FINISH MINE-BY EXPERIMENT		2NOV95
MB-MODELLING PREDICTIONS	5OCT90	4OCT91
MB-ANALYSIS & REPORTING OF AE/MS RESULTS	16AUG91	31MAR94
MB-REFINE MODELLING PREDICTIONS	7OCT91	30SEP92
MB-PRELIMINARY ANALYSIS	4NOV91	19AUG92
MB-MINEBY CONSTRUCTION COMPLETION REPORT	24JUL92	30SEP92
MB-DATA SUMMARY REPORTS	24JUL92	31MAR94
MB-EXCAVATION RESPONSE ANALYSIS	28SEP92	31OCT94
MB-FRACTURE CODE MODEL DEVELOPMENT	1APR93	30SEP93
MB-PUBLISH DATA REPORTS		31MAR94
MB-SUMMARY REPORT FOR PHASE 1	1APR94	30NOV94
MB-BACK ANALYSIS OF STRAINS	3OCT94	30MAR95
MB-COMMITTEE SUMMARY REPORT	1DEC94	30MAR95

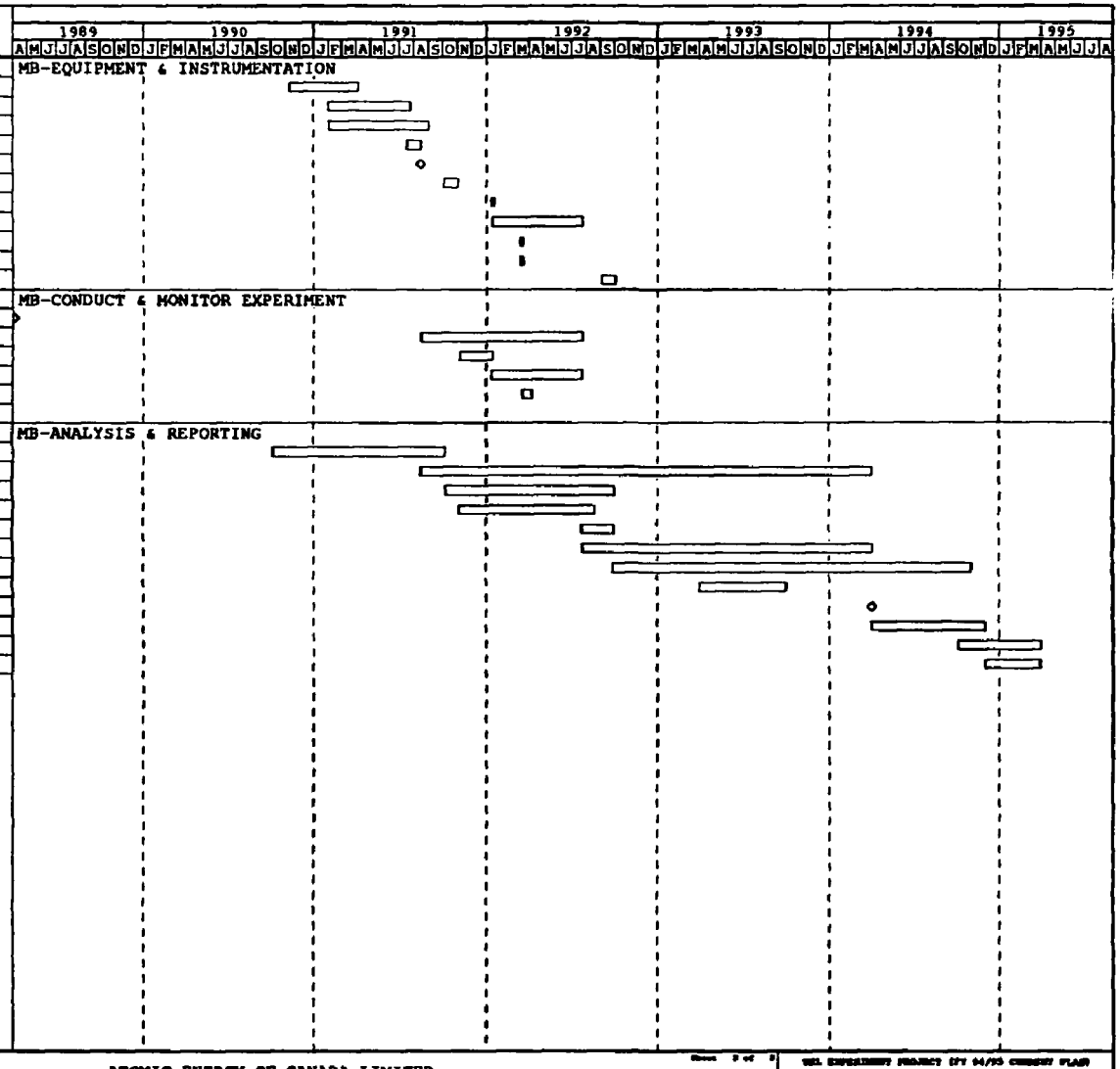

ATOMIC ENERGY OF CANADA LIMITED
URL PROJECT (FY 94/95 PROJ-AECL $$)
MINEBY EXPERIMENT SCHEDULE

APPENDIX B

DETAILS OF DISPLACEMENT BACK ANALYSIS METHOD

B.1 NOMENCLATURE

a = tunnel radius
D = tunnel diameter
r = radial distance from the tunnel centre
σ_{ij} = Components of partitioned stress tensor
σ_1 = Maximum principal stress
σ_2 = Intermediate principal stress
σ_3 = Minimum principal stress
G = shear modulus
E = Young's modulus
ν = Poisson's ratio
θ = rotation angle measured CCW from point on right sidewall at height of centreline
x, y, z = rectangular cartesion coordinates with tunnel axis parallel to x
r, θ, x = cylindrical coordinates with tunnel axis parallel to x
x_f = axial position of tunnel face
x_i = axial position of instrument
X = face position $x_f - x_i$
R = normalized radial position r/a
U_r = radial displacement
U_{r_o} = radial displacement at the tunnel face
$U_{r_{max}}$ = normalizing factor $a(1-\nu)/G$
K_{max} = stress ratio σ_{11}/σ_{33}
K_{axial} = stress ratio σ_{22}/σ_{33}
K_{min} = stress ratio σ_{22}/σ_{33}
$K_{a,b,c}$ = stress ratios relative to σ_{33}
D_l = radial displacement at $X = 0$ in the *spliced logistic function*
λ = scaling factor in the *spliced logistic function*
E_l = radial displacement at $X = +\infty$ in the *spliced logistic function*
for the posterior domain, and at $X = -\infty$ in the anterior domain
F = $(E_l - D_l)$ in the posterior domain and $(D_l - E_l)$ in the anterior domain
A = abscissa of pivot point controlling the shape of the *spliced logistic function*
B = slope parameter in the *spliced logistic function*
α = mean displacement response
β = amplitude about the mean of the harmonic component of the displacement response

ψ = phase constant

A_i = shape parameter in the inverse polynomial series approximating function

$$sign\,(x) = \begin{cases} 1 & x > 0 \\ 0 & x = 0 \\ -1 & x < 0 \end{cases}$$

B.2 APPROXIMATING AND PARAMETRIC FUNCTIONS

B.2.1 Approximating Functions

Spliced Logistic Function

Function to describe surface U_r vs. θ,X/D at $R = 1$

$$U_r\,(x) = y + \lambda \frac{d^2y}{dx^2}$$

where

$$y = D_l + sign\,(x)\,F\left[1 + \left|\frac{x}{A}\right|^B\right]^{\frac{1}{B}}$$

$$\frac{d^2y}{dx^2} = sign\,(x)\,\frac{F\,(B-1)}{|A|^B}\left\{\left[1 + \left|\frac{x}{A}\right|^B\right]^{\left(\frac{1}{B}-1\right)} |x|^{(B-2)}\right\} -$$

$$sign\,(x)\,\frac{F\,(B-1)}{|A|^{2B}}\left\{\left[1 + \left|\frac{x}{A}\right|^B\right]^{\left(\frac{1}{B}-2\right)} |x|^{2(B-1)}\right\}$$

When used to describe α and β parameters in the parametric functions, $\lambda = 0$.

Inverse Polynomial Series

Function to describe surface U_r vs. θ,R at $-0.4 \leq X/D \leq 0.4$

$$\frac{U_r}{U_{r_{max}}} = \sum_{i=1}^{3} \frac{A_i}{R^i} \text{ where } 1 \leq R \leq +\infty$$

Outside this region up to 5 diameters from the face, two additional terms are required for approximating purposes.

B.2.2 Parametric Functions

Examples of parametric functions describing the surface U_r vs. θ,X/D at $R = 1$, showing an application of the *spliced logistic function*. For characteristic surfaces U_r vs. θ,r/a, the parameters α and β are of the form given by the inverse polynomial series approximating function.

Plane normal components

$$\frac{U_r}{U_{r_{max}}} = \alpha_{11} + \beta_{11} \cos\left[2\,(\theta - \psi)\right]$$

where

$$\alpha_{11} = D_\alpha + sign\,(x)\,F_\alpha \left[1 + \left|\frac{x}{A_\alpha}\right|^{B_\alpha}\right]^{\frac{1}{n_\alpha}}$$

$$\beta_{11} = D_\beta + sign\,(x)\,F_\beta \left[1 + \left|\frac{x}{A_\beta}\right|^{B_\beta}\right]^{\frac{1}{n_\beta}}$$

and

$\psi = 0°$ for σ_{11}, $90°$ for σ_{33}

Plane shear component

$$\frac{U_r}{U_{r_{max}}} = 2\beta_{11} \sin(2\theta)$$

Antiplane normal component

$$\frac{U_r}{U_{r_{max}}} = \alpha_1 + \alpha_2 + \alpha_3$$

where

$$\alpha_1 = D_{\alpha_1} + sign\,(x)\,F_{\alpha_1} \left[1 + \left|\frac{x}{A_{\alpha_1}}\right|^{B_{\alpha_1}}\right]^{\frac{1}{n_{\alpha_1}}}$$

$$\alpha_2 = D_{\alpha_2} + sign\,(x)\,F_{\alpha_2} \left[1 + \left|\frac{x}{A_{\alpha_2}}\right|^{B_{\alpha_2}}\right]^{\frac{1}{n_{\alpha_2}}}$$

$$\alpha_3 = D_{\alpha_3} + sign\,(x)\,F_{\alpha_3} \left[1 + \left|\frac{x}{A_{\alpha_3}}\right|^{B_{\alpha_3}}\right]^{\frac{1}{n_{\alpha_3}}}$$

Antiplane shear components

$$\frac{U_r}{U_{r_{max}}} = \beta_{12} \cos(\theta - \psi)$$

where

$$\beta_{12} = D_\beta + sign\,(x)\,F_\beta \left[1 + \left|\frac{x}{A_\beta}\right|^{B_\beta}\right]^{\frac{1}{n_\beta}}$$

and

$\psi = 0°$ for σ_{12}, $90°$ for σ_{23}

B.2.3 Tables of Coefficients

TABLE 11

COEFFICIENTS FOR PARAMETRIC EQUATION DESCRIBING THE σ_{11} *CHARACTERISTIC RADIAL DISPLACEMENT SURFACE*

Mean Radial Displacement Component α			Harmonic Radial Displacement Component β		
Parameter	Anterior Domain	Posterior Domain	Parameter	Anterior Domain	Posterior Domain
A_α	0.1615	0.2182	A_β	0.2494	0.3241
B_α	-1.5602	-1.3371	B_β	-1.4120	-1.3072
D_α	0.1037	0.1037	D_β	0.2063	0.2063
E_α	0.0	0.3333	E_β	0.0	0.6667
F_α	0.1037	0.2296	F_β	0.2063	0.4603

Note that, for the σ_{11} tensor, the phase shift $\psi = 0$.
The coefficient of determination $r^2 = 0.9999$.

TABLE 12

COEFFICIENTS FOR PARAMETRIC EQUATION DESCRIBING THE σ_{22} *CHARACTERISTIC RADIAL DISPLACEMENT SURFACE*

Parameter	Radial Displacement Component		
	α_1 $X/D > 0$	α_2 $X/D < 0$	α_3 $X/D < 0$
A_α	0.7032	0.9592	0.1622
B_α	-1.5660	-1.9329	-1.2281
D_α	-0.0507	0.1417	-0.1924
E_α	0.0	0.0	0.0
F_α	0.0507	0.1417	-0.1924

The coefficient of determination $r^2 = 0.9993$.

TABLE 13

COEFFICIENTS FOR PARAMETRIC EQUATION DESCRIBING THE σ_{12} *CHARACTERISTIC RADIAL DISPLACEMENT SURFACE*

	Harmonic Radial Displacement Component β	
Parameter	Anterior Domain	Posterior Domain
A_β	0.6855	0.2846
B_β	-1.7715	-1.1961
D_β	0.6542	0.6542
E_β	0.0	0.0
F_β	0.6542	-0.6542

Note that, for the σ_{12} tensor, the phase shift $\psi = 0$.
The coefficient of determination $r^2 = 0.9996$.

TABLE 14

COEFFICIENTS FOR RADIAL DISPLACEMENT VERSUS RADIAL DISTANCE RELATIONSHIP AT FIVE FACE POSITIONS

X/D	Stress Component	Coefficient					
		A_{1_α}	A_{2_α}	A_{3_α}	A_{1_β}	A_{2_β}	A_{3_β}
-0.4	σ_{11}	0.16398	-0.31322	0.16253	0.47221	- 0.78082	0.36698
	σ_{22}	-0.03828	0.20895	-0.12166	-	-	-
	σ_{12}	-	-	-	0.62975	-0.13572	-0.17374
-0.1	σ_{11}	0.16940	-0.13616	0.01981	0.48948	- 0.40147	0.04170
	σ_{22}	-0.00979	-0.02801	0.05548	-	-	-
	σ_{12}	-	-	-	0.51860	0.38300	-0.32683
0.0	σ_{11}	0.16343	-0.05508	-0.00394	0.47141	- 0.18398	-0.08200
	σ_{22}	-0.02103	0.01009	-0.03731	-	-	-
	σ_{12}	-	-	-	0.57078	0.12493	-0.04398
0.1	σ_{11}	0.17067	-0.04119	0.05548	0.47115	- 0.06017	-0.08213
	σ_{22}	0.00722	-0.14289	0.08844	-	-	-
	σ_{12}	-	-	-	0.50707	0.43688	-0.47057
0.4	σ_{11}	0.15446	0.22335	-0.09864	0.43503	0.55103	-0.48399
	σ_{22}	-0.02745	-0.09091	0.09422	-	-	-
	σ_{12}	-	-	-	0.67066	-0.42177	-0.02677

APPENDIX C

LIST OF RELATED REPORTS AND PUBLICATIONS

C.1 DESIGN & ENGINEERING

- Mine-by Preliminary Design Report (URL-EXP-022-M044, Read and Martin 1990)†
- Mine-by Preliminary Scoping Calculations (URL-EXP-022-M045, Read 1990)†
- 3D Scoping Interaction of Adjacent Openings in Terms of Stress (Wiles 1990a)†
- AECL Mine-by Experiment Instrument Sensitivity Evaluation (Wiles 1990b)†
- Mine-by Experiment Plan - Underground Research Laboratory (DE010-011, Martin 1991)†
- Mine-by Experiment Final Design Report (AECL-10430, Read and Martin 1991)
- Mechanical Excavation of URL-Excavation Response Experiment Conceptual Engineering (Dynatec Engineering 1989)†
- Conceptual Design Report for: 1). Enthalpy Control System, 2). 420 Level Development 3). Electrical & Mechanical Services (Kuzyk 1990)†
- Conceptual Design Report for Enthalpy Control System Mine-by (MB) Experiment, Underground Research Laboratory, Depth 420 m (McCormac et al. 1990)†
- Underground Research Laboratory 420 Level Development and Mine-by Experiment Mechanical and Electrical Furnishings (Wardrop Engineering 1990)†

C.2 CHARACTERIZATION & EXPERIMENT MONITORING

Progress Reports

- Report 1 (URL-EXP-022-M050, Read et al. 1991)†
- Report 2 (URL-EXP-022-M051, Read et al. 1992)†
- Report 3 (URL-EXP-022-M052, Read et al. 1992)†
- Report 4 (URL-EXP-022-M053, Read et al. 1992)†
- Report 5 (URL-EXP-022-M054, Read et al. 1992)†
- Report 6 (URL-EXP-022-M055, Read et al. 1992)†
- Report 7 (URL-EXP-022-M056, Read et al. 1992)†

Data Summary Reports

- Part 1 - Survey Information (COG-93-290, Read et al. 1994)‡
- Part 2 - Triaxial Strain Cell Results (COG-93-353, Read et al. 1994b)‡
- Part 3 - Extensometer Results (COG-93-354, Read et al. 1994a)‡
- Part 4 - Convergence Results (TR-595, COG-93-177, Read et al. 1993b)
- Part 5 - Thermistor Results (RC-1079, COG-93-233, Martino et al. 1993a)
- Part 6 - Acoustic Emission/Microseismic Results (TR-597, COG-93-185, Martino et al. 1993)
- Part 7 - Geological Setting and General Geology (RC-1080, COG-93-251, Everitt et al. 1993)‡
- Part 8 - Construction Summary (COG-93-252, Keith and Onagi 1994)‡
- Part 9 - Observations (COG-93-347, Martino et al. 1994)‡

Corelogging Reports

- Geological Data Summary for the MB-Series Boreholes Drilled for the Mine-by Experiment at the Underground Research Laboratory (TR-577-9, COG-92-433, Woodcock 1993)
- Geological Data Summary for the GP-Series and MBW-Series Boreholes Drilled for the Mine-by Experiment at the Underground Research Laboratory (TR-577-10, COG-93-91, Woodcock 1993)
- Geological Data Summary for the AE/MS Series Boreholes Drilled for the Mine-by Experiment at the Underground Research Laboratory (RC-1080-11, COG-93-92, Woodcock 1993)‡
- Geological Data Summary for the Bof-Ex Extensometer-Series Boreholes Drilled for the Mine-by Experiment at the Underground Research Laboratory (RC-1080-12, COG-93-93, Woodcock, In review)‡
- Geological Data Summary for the CSIRO-Series Boreholes Drilled for the Mine-by Experiment at the Underground Research Laboratory (RC-1080-13, COG-94-282, Woodcock 1994)‡
- Geological Data Summary for the Microseismic Calibration-Series Boreholes Drilled for the Mine-by Experiment at the Underground Research Laboratory (RC-1080-14, COG-94-283, Woodcock, In review)‡
- Geological Data Summary for the Excavation Damage Assessment Series and the Acoustic Emission Series Boreholes Drilled for the Mine-by Experiment at the Underground Research Laboratory (RC-1080-15, COG-94-284, Woodcock, In review)‡
- Geological Data Summary for the Scale Effects Boreholes Drilled for the Mine-by Experiment at the Underground Research Laboratory (RC-1080-16, COG-94-285, Woodcock, In prep.)‡

General Characterization Reports

- Doorstoppers Stress Measurements at the 420 Level of the URL (Corthésy et al. 1993)†
- Instrumentation des parios rocheuses a l'aide des Cylindres Instrumentes de l'Universitè de Sherbrooke (Saleh et al. 1992)†
- Assessment of Rock Burst Risk in the URL Pinawa Manitoba Canada (Steffan et al. 1992)†
- Petrography of Granitic Rock Samples from the 420 Level of the Underground Research Laboratory, Pinawa, Manitoba (Kelly et al. 1993)†
- Orientation and Distribution of Inclusion Bearing Microcracks in Core from the 420 Level of the Underground Research Laboratory, Pinawa, Manitoba (Rousell 1993)†
- Petrofabric analysis of natural microfractures in quartz of the Lac du Bonnet Batholith (McArthur 1994)†
- Geology of the Mine-by Experiment Connected Permeability Phase Floor Slot (RC-1080-2, URL-EXP-022-R29, Gann and Everitt 1994)‡
- Geology of the Mine-by Experiment Test Tunnel Expansion (RC-1080-3, COG-94-227, URL-EXP-022-R30, Gann and Everitt 1994)‡
- Geology of the Observation Slot at the 420 Level of the Underground Research Laboratory, (RC-1080-4, COG-93-319, URL-EXP-022-R31, Gann and Everitt 1994)‡
- Block Sample Testing to Study the Effect of Stress Rotation on Rock Strength (Lau et al. 1994)†
- Cross-hole seismic tomography surveys for the Mine-by Experiment (TR-678, COG-95-021, Hayles et al. 1995)

AE/MS and Geophysics Reports (Queen's University and Keele University)

- Microseismic Monitoring and Excavation Damage Assessment at Atomic Energy of Canada Limited's Underground Research Laboratory (RP001AECL, Young and Talebi 1988)†
- Manual source locations of microseismic events induced by shaft extension at the Underground Research Laboratory (RP002AECL, Young and Talebi 1989)†
- Final Report on Source Location of Microseismic Events Induced by Shaft Excavation at the Underground Research Laboratory (RP003AECL, Talebi and Young 1989)†
- In Situ Measurements of P & S Wave Velocities at the Underground Research Laboratory (RP004AECL, Talebi and Young 1989)†
- Borehole Breakouts: A review of the Theory and a Discussion of their Investigation using Seismic Methods (RP005AECL, Rawlence 1990)†

- Design of a Microseismic System for the URL Mine-by Experiment (RP006AECL, Talebi and Young 1990)†
- Seismic and Radar Characterization at the 240-m Level of the Underground Research Laboratory (RP007AECL, Talebi and Young 1990)†
- Ultrasonic Imaging and Acoustic Emission Monitoring of Laboratory Hydraulic Fracturing Experiments in Lac du Bonnet Grey Granite from AECL'S Underground Research Laboratory (RP008AECL, Chow et al. 1990)†
- Analysis of the Microseismicity Induced by the 420 Level Development at the Underground Research Laboratory (RP009AECL, Talebi et al. 1991)†
- Calibration of the Queen's microseismic system at the Underground Research Laboratory (RP010AECL, Feustel and Young 1992)†
- In Situ Velocity Measurements for the Mine-by Experiment. (RP011AECL, Talebi and Young 1992)†
- Preliminary AE/MS results from the Mine-by Experiment (RP012AECL, Talebi and Young 1992)†
- Monitoring and Source Location of Microseismicity Induced by Excavation of the Mine-by Experiment Tunnel: Preliminary Analysis (RP013AECL, Collins and Young, 1992)†
- Uniaxial compression testing of large samples of Lac du Bonnet granite at low strain rates, Part 1: Studies of Acoustic emission rate (RP014AECL, Falls and Young 1992)†
- Acoustic Emission and Ultrasonic Velocity Study of Excavation-Induced Microcrack Damage in the Mine-by Tunnel at the Underground Research Laboratory (RP015AECL, Carlson and Young 1992)†
- AE/MS Source Location Calibration and Velocity Results: Two Surveys Performed After the Mine-by Tunnel Excavation (RP016AECL, Collins and Young 1993)†
- The Spatial and Temporal Distribution of AE/MS Source Locations Following the Mine-by Tunnel Excavation of Round 17 (RP017AECL, Young and Collins 1993)†
- Ultrasonic Imaging of Damage Induced by Cyclic Loading of Lac du Bonnet Granite (RP018AECL, Chow et al. 1993)†
- AE Monitoring During Loading of Lac du Bonnet Granite Blocks Containing Central Holes (RP019AECL, Meglis et al. 1993)†
- Thermally Induced Fracturing of Lac du Bonnet Granite (RP020AECL, Carlson et al. 1993)†
- Source Mechanism Studies at the Underground Research Laboratory (RP021AECL, Feignier and Young 1993)†

- Attenuation Analysis at the AECL Underground Research Laboratory Using the Spectral Ratio Method; Preliminary Results (RP022AECL, Feustal and Young 1993)†
- The spatial and temporal distribution of microseismicity recorded in Round 17 of the Mine-by Tunnel (RP023AECL, Collins and Young 1993)†
- Initial Progress Report on Acoustic Emission Monitoring of Stage 1 of the Mine-by Heated-Failure Tests (RP024AECL, Falls and Young 1994)†
- Wave Propagation Effects of an Underground Opening (RP025AECL, Maxwell and Young 1994)†
- Comparison of the excavation-induced microseismicity from the granite and granodiorite sections of the Mine-by Tunnel (RP026AECL, Collins and Young 1994)†
- Acoustic Emission and Ultrasonic Velocity Studies of the Mine-by Heated Failure Test - Phase 1 (RP027AECL, Falls and Young 1994)†
- Source Parameters of Excavation Induced Seismicity from the Mine-by Tunnel (RP028AECL, Collins et al. 1994)†

C.3 NUMERICAL MODELLING AND ANALYSIS

- Finite-Element Modelling of the Geomechanical Responses of the Mine-by Experiment (TR-610, COG-93-242, Khair and Chan 1991)
- Mine-By Experiment - Prediction of Excavation Induced Rock Mass Response Using UDEC (URL-EXP-009-M003, Martino 1991)†
- Mine-by Experiment - Prediction of Excavation Induced Rock Mass Response (URL-EXP-022-M048, Read 1991)†
- Rock Fracture Around Underground Openings for Nuclear Waste Disposal (WS-31J-98299, Ayari and DeClaire 1993)†
- Development and Numerical Implementation of an Elastic-Brittle-Ductile Constitutive Model (WS-29J-54421, Ofoegbu and Curran 1991)†
- URL Mine-by Experiment Rock Mass Response Predictions (WS-29J-54421, Curran et al. 1991)†
- Three Dimensional Finite Element Analyses of the URL Mine-by Test Tunnel (WS-29J-54421, Curran et al. 1992)†
- Harmonic Finite Element Analysis of a Cylindrical Excavation in an Infinite Medium (Grabinsky and Curran, 1993)†
- Two-dimensional Fracture Propagation Modelling of the URL Mine-by Test Tunnel (Curran et al. 1994)†
- Numerical Analysis of the AECL Mine-by Experiment (Post-construction Phase) Part 2a - Triaxial Strain Cell Results for a Circular Excavation (Curran et al. 1994)†

- Numerical Analysis of the AECL Mine-by Experiment (Post-construction Phase) Part 3a - Extensometer Results for a Circular Excavation (Curran et al. 1994)†
- Numerical Analysis of the AECL Mine-by Experiment (Post-construction Phase) Part 4a - Convergence Results for a Circular Excavation (Curran et al. 1994)†

C.4 PUBLISHED PAPERS RELATED TO THE MINE-BY EXPERIMENT

- AECL's Mine-by Experiment - From Concept to Construction (Onagi et al.1991)
- Design and Construction of Two Major Experiments at the URL (Thompson et al. 1992)
- Developments in the Mini-CHARTS System and Field Trial Results in Measuring Excavation Damage in Granite (Hayles et al. 1992)
- Preliminary analysis of shear-wave splitting in granite at the Underground Research Laboratory, Manitoba (Holmes et al. 1992)
- Acoustic emission and ultrasonic velocity study of excavation-induced microcrack damage at the Underground Research Laboratory (Carlson and Young 1993)
- An analysis of laboratory and long-term rock strength using a sliding crack model (Chandler and Martin 1995)
- The influence of near surface faults on *in situ* stresses (Chandler and Martin 1994)
- Numerical modelling of discrete fracture in granite (Dzik et al. 1994)
- Ultrasonic imaging and acoustic emission monitoring of thermally induced microcracks in Lac du Bonnet granite (Jansen et al. 1993)
- Near-face cracking and strength around underground openings (Martin et al. 1995)
- Brittle failure: Laboratory and *in situ* (Martin 1995)
- Monitoring progressive failure around a tunnel in massive granite (Martin et al. 1995)
- The progressive fracture of Lac du Bonnet granite (Martin and Chandler 1994)
- The effect of sample disturbance on laboratory properties of Lac du Bonnet granite (Martin and Stimpson 1994)
- Comparison of borehole breakouts from laboratory and field tests (Martin et al. 1994)
- Quantifying drilling-induced damage in samples of Lac du Bonnet granite (Martin 1994)
- The role of convergence measurements in characterizing a rock mass (Martin et al. 1994)
- The Underground Research Laboratory: an opportunity for basic rock mechanics (Martin and Simmons 1993)
- The effect of excavation-induced seismicity on the strength of Lac du Bonnet granite (Martin and Young 1993)

- Crack damage in the post-peak region (Martin and Lajtai, In prep.)
- The *in situ* strength of massive granite around excavations (Martin and Read 1992)
- Asymmetric borehole breakouts at the URL (Read et al. 1995)
- Monitoring the excavation-induced response of granite (Read and Martin 1992)
- The Underground Research Laboratory Mine-by Experiment - a research perspective on tunnel design (Read and Martin 1990)
- Potential role of acoustic emission/microseismicity investigations in the site characterization and performance monitoring of nuclear waste repositories (Young and Martin 1993)

C.5 REFERENCES

Ayari, M. L. and M. DeClaire (1993). Rock fracture around underground openings for nuclear waste disposals. Department of Mechanical and Industrial Engineering, University of Manitoba, Winnipeg, MB.†

Carlson, S. R. and R. P. Young (1992). Acoustic emission and ultrasonic velocity study of excavation-induced microcrack damage in the Mine-by Tunnel at the Underground Research Laboratory. Report to Atomic Energy of Canada Limited RP015AECL, Queen's University, Kingston, ON.†

Carlson, S. R. and R. P. Young (1993). Acoustic emission and ultrasonic velocity study of excavation-induced microcrack damage at the Underground Research Laboratory. *Int. J. Rock Mech. Min. Sci. & Geomech. Abstr.*, 30(7):901–907.

Carlson, S. R., D. P. Jansen and R. P. Young (1993). Thermally induced fracturing of Lac du Bonnet Granite. Report to Atomic Energy of Canada Limited RP020AECL, Queen's University, Kingston, ON.†

Chandler, N. A. and C. D. Martin (1995). An analysis of laboratory and long-term rock strength using a sliding crack model. In J. Daemen and R. Schultz, editors, *Proc. 35th U.S. Rock Mechanics Symposium, Lake Tahoe.* A.A. Balkema, Rotterdam.

Chandler, N. A. and C. D. Martin (1994). The influence of near surface faults on *in situ* stresses. In P. P. Nelson and S. E. Laubach, editors, *Proc. 1st North American Rock Mechanics Symposium, Austin*, pages 369–376. A.A. Balkema, Rotterdam.

Chow, T., S. D. Falls, S. R. Carlson and R. P. Young (1990). Ultrasonic imaging and acoustic emission monitoring of laboratory hydraulic fracturing experiments in Lac du Bonnet grey granite from AECL's Underground Research Laboratory. Report to Atomic Energy of Canada Limited RP008AECL, Queen's University, Kingston, ON.†

Chow, T., I. Meglis and R. P. Young (1993). Ultrasonic imaging of damage induced by cyclic loading of Lac du Bonnet granite. Report to Atomic Energy of Canada Limited RP018AECL, Queen's University, Kingston, ON.†

Collins, D. S. and R. P. Young (1992). Monitoring and source location of microseismicity induced by excavation of the Mine-by Experiment tunnel: preliminary analysis. Report to Atomic Energy of Canada Limited RP013AECL, Queen's University, Kingston, ON.†

Collins, D. S. and R. P. Young (1993). AE/MS source location calibration and velocity results: two surveys performed after the Mine-by Tunnel excavation. Report to Atomic Energy of Canada Limited RP016AECL, Queen's University, Kingston, ON.†

Collins, D. S. and R. P. Young (1994). The spatial and temporal distribution of microseismicity recorded in Round 17 of the Mine-by Tunnel. Report to Atomic Energy of Canada Limited RP023AECL, University of Keele.†

Collins, D. S. and R. P. Young (1994). Comparison of the excavation-induced microseismicity from the granite and granodiorite sections of the Mine-by Tunnel. Report to Atomic Energy of Canada Limited RP026AECL, University of Keele.†

Collins, D. S., C. Baker and R. P. Young (1994). Source parameters of excavation induced seismicity from the Mine-by Tunnel. Report to Atomic Energy of Canada Limited RP028AECL, University of Keele.†

Corthésy, R., D. E. Gill and M. H. Leite (1993). Doorstopper stress measurements at the 420 Level of the URL. C.D.T. Project P1596, l'Ecole Polytechnique de Montréal.†

Curran, J. H., G. I. Ofoegbu and M. W. Grabinsky (1991). URL Mine-by Experiment rock mass response predictions. Department of Civil Engineering, University of Toronto.†

Curran, J. H., G. I. Ofoegbu and M. W. Grabinsky (1992). Three dimensional finite element analyses of the URL Mine-by Test Tunnel. Department of Civil Engineering, University of Toronto.†

Curran, J. H., M. W. Grabinsky and B. T. Corkum (1994). Two-dimensional fracture propagation modelling of the URL Mine-by test tunnel. Department of Civil Engineering, University of Toronto.†

Curran, J. H., M. W. Grabinsky and B. T. Corkum (1994). Numerical analysis of the AECL Mine-by Experiment (Post-construction Phase) Part 2a - triaxial strain cell results for a circular excavation. Department of Civil Engineering, University of Toronto.†

Curran, J. H., M. W. Grabinsky and B. T. Corkum (1994). Numerical analysis of the AECL Mine-by Experiment (Post-construction Phase) Part 3a - extensometer results for a circular excavation. Department of Civil Engineering, University of Toronto.†

Curran, J. H., M. W. Grabinsky and B. T. Corkum (1994). Numerical analysis of the AECL Mine-by Experiment (Post-construction Phase) Part 4a - Convergence results for a circular excavation. Department of Civil Engineering, University of Toronto.†

Dynatec Engineering Inc. (1989). Mechanical excavation of URL-Excavation Response Experiment conceptual engineering. Project E238.R. Richmond Hill, ON.†

Dzik, E. J., E. Z. Lajtai and C. D. Martin (1994). Numerical modelling of discrete fracture in granite. In H.J. Siriwardane, editor, *Proc. 8th Int. Conf. on Computer Methods and Advances in Geomechanics (IACMAG94), Morgantown, West Virginia*, Volume 3. A.A. Balkema, Rotterdam.

Everitt, R. A., P. Gann and D. M. Boychuk (1993). Mine-by Experiment data summary: Part 7 - General Geology and Geological Setting. Atomic Energy of Canada Limited Report, RC-1080, COG-93-251.‡

Falls, S. D. and R. P. Young (1994). Uniaxial compression testing of large samples of Lac du Bonnet granite at low strain rates, Part 1: Studies of Acoustic emission rate. Report to Atomic Energy of Canada Limited RP014AECL, University of Keele.†

Falls, S. D. and R. P. Young (1994). Initial progress report on acoustic emission monitoring of Stage 1 of the Mine-by Heated-Failure Tests. Report to Atomic Energy of Canada Limited RP024AECL, University of Keele.†

Falls, S. D. and R. P. Young (1994). Acoustic emission and ultrasonic velocity studies of the Mine-by Heated Failure Test - Phase 1. Report to Atomic Energy of Canada Limited RP027AECL, University of Keele.†

Feigner, B. and R. P. Young (1993). Source mechanism studies at the Underground Research Laboratory. Report to Atomic Energy of Canada Limited RP021AECL, Queen's University, Kingston, ON.†

Feustel, A. J. and R. P. Young (1993). Attenuation analysis at the AECL Underground Research Laboratory using the spectral ratio method; preliminary results. Report to Atomic Energy of Canada Limited RP022AECL, Queen's University, Kingston, ON.†

Gann, P. and R. A. Everitt (1994). Geology of the Mine-by Experiment Connected Permeability Phase floor slot. Atomic Energy of Canada Limited Report RC-1080-2, URL-EXP-022-R29.‡

Gann, P. and R. A. Everitt (1994). Geology of the Mine-by Experiment Test Tunnel Expansion. Atomic Energy of Canada Limited Report RC-1080-3, COG-94-227, URL-EXP-022-R30.‡

Gann, P. and R. A. Everitt (1994). Geology of the observation slot at the 420 Level of the Underground Research Laboratory. Atomic Energy of Canada Limited Report RC-1080-4, COG-93-319, URL-EXP-022-R31.‡

Grabinsky, M. W. and J. H. Curran (1993). Harmonic finite element analysis of a cylindrical excavation in an infinite medium. Department of Civil Engineering, University of Toronto, 93-2.†

Hayles, J. G., M. H. Serzu, and G. S. Lodha (1995). Cross-hole seismic tomography surveys for the Mine-by Experiment. Atomic Energy of Canada Limited Technical Record TR-678. COG-95-021.

Hayles, J. G., K. M. Stevens, M. H. Serzu and G. S. Lodha (1992). Developments in the mini-CHARTS system and field trial results in measuring excavation damage in granite. In *Proc. 4th International MGLS/EGS Symposium on Borehole Geophysics for Minerals, Geotechnical and Groundwater Applications; Toronto*, 18-22 August 1991.

Holmes, G. M., S. Crampin and R. P. Young (1992). Preliminary analysis of shear-wave splitting in granite at the Underground Research Laboratory, Manitoba. In *Proc. Fifth International Workshop on Seismic Anisotropy, Banff*, 17-22 May.

Jansen, D. P., S. R. Carlson, R. P. Young, and D. A. Hutchins (1993). Ultrasonic imaging and acoustic emission monitoring of thermally induced microcracks in Lac du Bonnet Granite. *J. Geophysical Research*, 98(B12):22231-22243.

Keith, S. G. and D. P. Onagi (1994). Mine-by Experiment data summary: Part 8 - Construction summary. Atomic Energy of Canada Limited Report COG-93-252.‡

Kelly, D., D. C. Peck and R. S. James (1993). Petrography of granitic rock samples from the 420 Level of the Underground Research Laboratory, Pinawa, Manitoba. Laurentian University, Sudbury, Ontario.†

Khair, K. R. and T. Chan (1994). Finite-element modelling of the geomechanical responses of the Mine-by Experiment. Atomic Energy of Canada Limited Technical Record TR-610, COG-93-242.

Kuzyk, G. W. (1990). Conceptual design report for: 1. Enthalpy Control System 2. 420 Level Development 3. Electrical & Mechanical Services. Atomic Energy of Canada Design Report†

Lau, J. S. O., B. Gorski, B. Conlon, L. Butler and J. Folta (1994). Block sample testing to study the effect of stress rotation on rock strength. Canada Centre for Mineral and Energy Technology, MRL 94-004(CL).†

Martin, C. D., R. S. Read, and E. J. Dzik (1995). Near-face cracking and strength around underground openings. In H. P. Rossmanith, editor, *Proc. 2nd, Int. Conf. on Mechanics of Jointed and Faulted Rock*, pages 747–752. A.A. Balkema, Rotterdam.

Martin, C. D. (1995). Brittle failure: Laboratory and *in situ*. In *Proc. 8th, ISRM Congress on Rock Mechanics, Tokyo*. A.A. Balkema, Rotterdam.

Martin, C. D., R. P. Young, and D. S. Collins (1995). Monitoring progressive failure around a tunnel in massive granite. In *Proc. 8th ISRM Congress on Rock Mechanics, Tokyo*. A.A. Balkema, Rotterdam.

Martin, C. D. and N. A. Chandler (1994). The progressive fracture of Lac du Bonnet granite. *Int. J. Rock Mech. Min. Sci. & Geomech. Abstr.*, 31(6):643–659.

Martin, C. D. and B. Stimpson (1994). The effect of sample disturbance on laboratory properties of Lac du Bonnet granite. *Can. Geotech. J.*, 31(5):692–702.

Martin, C. D., J. B. Martino, and E. J. Dzik (1994). Comparison of borehole breakouts from laboratory and field tests. In *Proc. EUROCK'94, SPE/ISRM Rock Mechanics in Petroleum Engineering Delft*, pages 183–190. A.A. Balkema, Rotterdam.

Martin, C. D. (1994). Quantifying drilling-induced damage in samples of Lac du Bonnet granite. In P. P. Nelson and S. E. Laubach, editors, *Proc. 1st North American Rock Mechanics Symposium, Austin*, pages 419–426. A.A. Balkema, Rotterdam.

Martin, C. D., N. A. Chandler, and R. S. Read (1994). The role of convergence measurements in characterizing a rock mass. In *Proc. 47th Canadian Geotechnical Conference, Halifax.*

Martin, C. D. and G. R. Simmons (1992). The Underground Research Laboratory: an opportunity for basic rock mechanics. *ISRM News Journal*, 1(1):2–8.

Martin, C. D. and R. P Young (1993). The effect of excavation-induced seismicity on the strength of Lac du Bonnet granite. In R. P. Young, editor, *Proc. 3rd Int. Symp. on Rockbursts and Seismicity in Mines, Kingston*, pages 367–371. A.A. Balkema, Rotterdam.

Martin, C. D. and E. Z. Lajtai (In prep.). Crack damage in the post-peak region. *Int. J. Rock Mech. Min. Sci. & Geomech. Abstr.*.

Martin, C. D. and R. S. Read (1992). The *in situ* strength of massive granite around excavations. In P.K. Kaiser and D. McCreath, editors, *Proc. 16th Canadian Rock Mechanics Conference, Sudbury*, pages 1–10.

Martin, C.D. (1991). Mine-by experiment plan -Underground Research Laboratory. DE010-011. Atomic Energy of Canada Limited Disposal Technology Division Quality Assurance Document.†

Martino, J. B., R. S. Read, and J. H. Mitchell (1993a). Mine-by Experiment data summary: Part 5 – Thermistor results. Atomic Energy of Canada Limited Report RC-1079, COG-93-233.‡

Martino, J. B., R. S. Read, and D. Collins (1993). Mine-by Experiment data summary: Part 6 – Acoustic Emission/Microseismic results. Atomic Energy of Canada Limited Technical Record, TR-597, COG-93-185.‡

Martino J. B., R. S. Read and S. G. Keith (1994). Mine-by Experiment data summary: Part 9 – Observations. Atomic Energy of Canada Limited Report, COG-93-347.‡

Maxwell, S. C. and R. P. Young (1994). Wave propagation effects of an underground opening. Report to Atomic Energy of Canada Limited RP025AECL, University of Keele.†

McArthur, J. R. (1994). Petrofabric analysis of natural microfractures in quartz of the Lac du Bonnet Batholith. Report to Atomic Energy of Canada Limited.†

McCormac, D. D., E. L. Schatzlein, and D. T. K. Au (1990). Conceptual design report for Enthalpy Control System Mine-by (MB) Experiment Underground Research Laboratory depth 420 m. Atomic Energy of Canada Limited Design Report.†

Meglis, I. L., T. Chow and R. P. Young (1993). AE monitoring during loading of Lac du Bonnet granite blocks containing central holes. Report to Atomic Energy of Canada Limited RP019AECL, Queen's University, Kingston, ON.†

Ofoegbu, G. I. and J. H. Curran (1991). Development and numerical implementation of an elastic-brittle-ductile constitutive model. Department of Civil Engineering, University of Toronto.†

Onagi, D. P., R. S. Read and G. W. Kuzyk (1991). AECL's Mine-by Experiment - From concept to construction. In *Proc. Society for Mining, Metallurgy and Exploration Inc. Annual Meeting, Denver, CO*, 1991 February 25-28.

Rawlence, L. (1990). Borehole breakouts: a review of the theory and a discussion of their investigation using seismic methods. Report to Atomic Energy of Canada Limited RP005AECL, Queen's University, Kingston, ON.†

Read, R. S. (1990). Mine-by experiment preliminary scoping calculations. Atomic Energy of Canada Limited Technical Memorandum URL-EXP-022-M045.†

Read, R. S. and C. D. Martin (1990). Mine-by Experiment preliminary design report. Atomic Energy of Canada Limited Technical Memorandum URL-EXP-022-M044.†

Read, R. S. and C. D. Martin (1991). Mine-by Experiment final design report. Atomic Energy of Canada Limited Report AECL-10430.

Read, R. S., J. B. Martino, G. R. Karklin, E. Jacobs and G. Hiltz (1994). Mine-by Experiment data summary: Part 1 - Survey information. Atomic Energy of Canada Limited Report RC-1076, COG-93-290.‡

Read, R. S., J. B. Martino, and J. H. Mitchell (1994b). Mine-by Experiment data summary: Part 2 Triaxial strain cell results. Atomic Energy of Canada Limited Report RC-1077, COG-93-353.‡

Read, R. S., J. B. Martino, J. H. Mitchell and M.H. Spinney (1994). Mine-by Experiment data summary: Part 3 - Extensometer results. Atomic Energy of Canada Limited Report RC-1078, COG-93-354.‡

Read, R. S., J. B. Martino, J. H. Mitchell (1993b). Mine-by Experiment data summary: Part 4 - Convergence results. Atomic Energy of Canada Limited Technical Record TR-595, COG-93-177.‡

Read, R. S., C. D. Martin, and E. J. Dzik (1995). Asymmetric borehole breakouts at the URL. In J. Daemen and R. Schultz, editors, *Proc. 35th U.S. Rock Mechanics Symposium, Lake Tahoe*, pages 879-884. A.A. Balkema, Rotterdam.

Read, R. S. and C. D. Martin (1992). Monitoring the excavation-induced response of granite. In J.A. Tillerson and W.R. Wawersik, editors, *Proc. 33rd U.S. Symp. on Rock Mechanics, Santa Fe*, pages 201-210. A.A. Balkema, Rotterdam.

Read, R. S. and C. D. Martin (1990). The Underground Research Laboratory Mine-by Experiment - a research perspective on tunnel design. In *Proc. 8th Canadian Tunnelling Conference, Vancouver*, pages 213-226. BiTech Publishers Ltd, Vancouver. Also In *Canadian Tunnelling* (1991), pp. 75-88.

Rousell, D. H. (1993). Orientation and distribution of inclusion bearing microcracks in core from the 420 Level of the Underground Research Laboratory, Pinawa, Manitoba. Report to Atomic Energy of Canada Limited, Laurentian University, Sudbury, Ontario.†

Saleh, K., A-P. Bois, G. Ballivy (1992). Instrumentation des parios rocheuses à l'aide des Cylindres Instrumentés de l'Université de Sherbrooke. Laboratoire de méchanique des roches et de géologie appliquée, Département de génie civil, Faculté des sciences appliquées, Université de Sherbrooke, Québec, Canada.†

Talebi, S. and R. P. Young (1989). Final report on source location of microseismic events induced by shaft excavation at the Underground Research Laboratory. Report to Atomic Energy of Canada Limited RP003AECL, Queen's University, Kingston, ON.†

Talebi, S. and R. P. Young (1989). In situ measurements of P & S wave velocities at the Underground Research Laboratory. Report to Atomic Energy of Canada Limited RP004AECL. Queen's University, Kingston, ON.†

Talebi, S. and R. P. Young (1990). Design of a microseismic system for the URL Mine-by Experiment. Report to Atomic Energy of Canada Limited RP006AECL, Queen's University, Kingston, ON.†

Talebi, S. and R. P. Young (1990). Seismic and radar characterization at the 240 m level of the Underground Research Laboratory. Report to Atomic Energy of Canada Limited RP007AECL, Queen's University, Kingston, ON.†

Talebi, S., B. Feigner and R. P. Young (1991). Analysis of the microseismicity induced by the 420 Level development at the Underground Research Laboratory. Report to Atomic Energy of Canada Limited RP009AECL, Queen's University, Kingston, ON.†

Talebi, S. and R. P. Young (1992). In situ velocity measurements for the Mine-by Experiment. Report to Atomic Energy of Canada Limited RP011AECL, Queen's University, Kingston, ON.†

Talebi, S. and R. P. Young (1992). Preliminary AE/MS results from the Mine-by experiment. Report to Atomic Energy of Canada Limited RP012AECL, Queen's University, Kingston, ON.†

Thompson, P. M., B. H. Kjartanson and R. S. Read (1992). Design and construction of two major experiments at the URL. In *Proc. 1992 International High-Level Radioactive Waste Management Conference, Las Vegas, NV, Vol. 1*, pages 1082-1089, 1992.

Wardrop Engineering Inc. (1990). Underground Research Laboratory 420 Level development and Mine-by Experiment mechanical and electrical furnishings. Project No. 890025-02-00. Winnipeg, MB.†

Wiles, T. D. (1990a). 3D scoping interaction of adjacent openings in terms of stress. Final Technical Report Phase 1. Geomechanics Research Centre, Laurentian University, Sudbury, ON.†

Wiles, T. D. (1990b). AECL Mine-by Experient instrument sensitivity evaluation. Final Technical Report Phase 2. Mine Modelling Limited, Copper Cliff, ON.†

Woodcock, D. R. (1993). Geological data summary for the MB-series boreholes drilled for the Mine-by Experiment at the Underground Research Laboratory. Atomic Energy of Canada Limited Technical Record TR-577-9, COG-92-433.

Woodcock, D. R. (1993). Geological data summary for the GP-series and MBW-series boreholes drilled for the Mine-by Experiment at the Underground Research Laboratory. Atomic Energy of Canada Limited Technical Record TR-577-10, COG-93-91.

Woodcock, D. R. (1993). Geological data summary for the AE/MS series boreholes drilled for the Mine-by Experiment at the Underground Research Laboratory. Atomic Energy of Canada Limited Report RC-1080-11, COG-93-92.‡

Woodcock, D. R. (In review). Geological data summary for the Bof-ex extensometer-series boreholes drilled for the Mine-by Experiment at the Underground Research Laboratory. Atomic Energy of Canada Limited Report RC-1080-12, COG-93-93.‡

Woodcock, D. R. (1994). Geological data summary for the CSIRO-series boreholes drilled for the Mine-by Experiment at the Underground Research Laboratory. Atomic Energy of Canada Limited Report RC-1080-13, COG-94-282.‡

Woodcock, D. R. (In review). Geological data summary for the microseismic calibration-series boreholes drilled for the Mine-by Experiment at the Underground Research Laboratory. Atomic Energy of Canada Limited Report RC-1080-14, COG-94-283.‡

Woodcock, D. R. (In review). Geological data summary for the excavation damage assessment series and the acoustic emission series boreholes drilled for the Mine-by Experiment at the Underground Research Laboratory. Atomic Energy of Canada Limited Report RC-1080-15, COG-94-284.‡

Woodcock, D. R. (In prep.). Geological data summary for the scale effects boreholes drilled for the Mine-by Experiment at the Underground Research Laboratory. Atomic Energy of Canada Limited Report RC-1080-16, COG-94-285.‡

Young, R. P. and D. S. Collins (1993). The spatial and temporal distribution of AE/MS source locations following the Mine-by Tunnel excavation of Round 17. Report to Atomic Energy of Canada Limited RP017AECL, Queen's University, Kingston, ON.†

Young, R. P. and C. D. Martin (1993). Potential role of acoustic emission/microseismicity investigations in the site characterization and performance monitoring of nuclear waste repositories. *Int. J. Rock Mech. Min. Sci. & Geomech. Abstr.*, 30(7):797-803.

Young, R. P. and S. Talebi (1988). Microseismic monitoring and excavation damage assessment at Atomic Energy of Canada Limited's Underground Research Laboratory. Report to Atomic Energy of Canada Limited RP001AECL, Queen's University, Kingston, ON. †

Young, R. P. and S. Talebi (1989). Manual source locations of microseismic events induced by shaft extension at the Underground Research Laboratory. Report to Atomic Energy of Canada Limited RP002AECL, Queen's University, Kingston, ON.†

---

† Unpublished
‡ Protected

Cat. No. / N° de cat.: CC2-11311E
ISBN 0-660-16394-2
ISSN 0067-0367

To identify individual documents in the series, we have assigned an AECL- number to each. Please refer to the AECL- number when requesting additional copies of this document from

Scientific Document Distribution Office (SDDO)
AECL
Chalk River, Ontario
Canada K0J 1J0

Fax: (613) 584-1745 Tel.: (613) 584-3311
ext. 4623

Price: D

Pour identifier les rapports individuels faisant partie de cette série, nous avons affecté un numéro AECL- à chacun d'eux. Veuillez indiquer le numéro AECL- lorsque vous demandez d'autres exemplaires de ce rapport au

Service de Distribution des documents officiels (SDDO)
EACL
Chalk River (Ontario)
Canada K0J 1J0

Fax: (613) 584-1745 Tél.: (613) 584-3311
poste 4623

Prix: D

AECL EACL

AECL-11311, COG-95-171

Technical Summary of AECL's Mine-by Experiment Phase 1: Excavation Response

Résumé du rapport technique d'EACL sur l'essai au voisinage de l'excavation Phase 1: Reaction à l'excavation

R.S. Read, C.D. Martin

February 1996 février

AECL

TECHNICAL SUMMARY OF AECL'S MINE-BY EXPERIMENT PHASE 1: EXCAVATION RESPONSE

by

R.S. Read and C.D. Martin

Whiteshell Laboratories
Pinawa, Manitoba R0E 1L0
1996

AECL-11311
COG-95-171

TECHNICAL SUMMARY OF AECL'S MINE-BY EXPERIMENT PHASE 1: EXCAVATION RESPONSE

by

R.S. Read and C.D. Martin

ABSTRACT

The first phase of the Mine-by Experiment was conducted at the 420 Level of the Underground Research Laboratory (URL) to investigate the response induced in the rock mass by excavating a 3.5-m-diameter circular tunnel using a non-explosive technique. The main objective of the experiment was to study the processes involved in progressive failure and the development of excavation-induced damage around underground openings. To this end, state-of-the-art geomechanical and geophysical instrumentation was used to monitor the excavation of the 46-m-long Mine-by Experiment test tunnel. The results from the experiment show that progressive failure in compressive regions around the tunnel initiates at stresses about 50% of the rock strength measured in uniaxial compression tests in the laboratory. The difference between the laboratory and *in situ* behaviour is attributed to complex stress changes that occur during excavation of the tunnel, especially in the vicinity of the advancing face. These effects are not simulated in standard laboratory tests. Numerical modelling and *in situ* characterization studies were conducted to establish the extent and characteristics of the damaged zone around the test tunnel. As part of this study, *in situ* stresses and material properties were established through back analysis of measured displacements and strains. Using these boundary conditions, it was shown that the damaged zone was limited to within 1 m of the original tunnel perimeter. The characteristics of the damaged zone, however, were found to be highly variable around the tunnel, and were dependent on the nature of the stress concentrations, geology, stress magnitudes and orientations and, to a lesser extent, the excavation method and sequence.

AECL
Whiteshell Laboratories
Pinawa, Manitoba R0E 1L0
1996

AECL-11311
COG-95-171

RÉSUMÉ DU RAPPORT TECHNIQUE D'EACL SUR L'ESSAI AU VOISINAGE DE L'EXCAVATION PHASE 1 : RÉACTION À L'EXCAVATION

par

R.S. Read et C.D. Martin

RÉSUMÉ

La première phase de l'Essai au voisinage de l'excavation a été menée au niveau 420 du Laboratoire de recherches souterrain (LRS) en vue d'étudier la réaction induite dans la masse rocheuse en creusant une galerie circulaire de 3,5 m de diamètre au moyen d'un procédé technique sans utilisation d'explosifs. Le but principal de cet essai était d'analyser les processus de rupture progressive mis en jeu et l'évolution des dommages causés par les travaux d'excavation à la périphérie des accès souterrains. On a eu recours, à cette fin, à des instruments de géophysique et de géomécanique d'avant-garde pour surveiller les travaux de forage de la galerie de 46 m de longueur de l'Essai au voisinage de l'excavation. Les résultats de cet essai indiquent que la rupture progressive dans les régions qui subissent des sollicitations en compression autour de la galerie s'amorce à des contraintes d'environ 50 % de la résistance de la roche mesurée par des essais de compression uniaxiale réalisés au laboratoire. La différence de comportement notée entre les résultats obtenus au laboratoire et ceux obtenus *in situ* est attribuée à des modifications de contraintes complexes qui se manifestent au cours du forage de la galerie, en particulier au voisinage du front d'attaque. Dans les essais de laboratoire normaux, ces effets ne sont pas simulés. On a réalisé des études de modélisation numérique et de caractérisation *in situ* en vue d'établir l'étendue et les caractéristiques de la zone endommagée autour de la galerie d'essai. Dans le cadre de cette étude, les contraintes *in situ* et les propriétés des matériaux ont été établies par rétroanalyse des déplacements et des déformations qui ont été mesurés. Il a été démontré, en se fondant sur ces conditions aux limites, que la zone endommagée était limitée à une distance de moins de 1 m du périmètre initial de la galerie. On s'est toutefois rendu compte que les caractéristiques de la zone endommagée étaient très variables à la périphérie de la galerie et qu'elles étaient fonction des concentrations de contraintes, de la géologie, de l'ampleur et de l'orientation des contraintes ainsi que, dans une moindre mesure, de la méthode et de la séquence de réalisation des travaux.

EACL
Laboratoires de Whiteshell
Pinawa (Manitoba) R0E 1L0
1996

AECL-11311
COG-95-171

CONTENTS

continued ...

CONTENTS (continued)

continued ...

CONTENTS (concluded)

EXECUTIVE SUMMARY

Atomic Energy of Canada Limited (AECL) has constructed an Underground Research Laboratory (URL) approximately 120 km northeast of Winnipeg, Manitoba. The URL has been excavated to a depth of 443 m in the Lac du Bonnet granite batholith, with horizontal developments at 240-m depth (240 Level) and 420-m depth (420 Level). These developments provide access to conduct *in situ* multi-disciplinary experiments, such as the Mine-by Experiment, in rock mass conditions that are representative of many granitic plutons within the Canadian Shield.

In 1989, an external Peer Review Panel was selected by AECL to review the experiments planned for the URL. The report from this review stated:

> *The Mine-by Experiment must be conducted on the 420 Level. Failure to experiment at this level could ultimately result in the need to exclude environments at candidate repository sites where similar high horizontal stresses were found, since it would not be possible to argue that the concept had been tested under appropriate conditions deep within plutons. Horizontal stresses might thus limit the depth at which a repository could be developed.*

In light of this recommendation, the rock mass at the 420 Level was characterized to locate a representative site for the Mine-by Experiment. The area chosen for the experiment typifies the 420 Level in terms of geology, geotechnical properties and *in situ* stresses. The high *in situ* stresses and highly anisotropic stress ratios measured in the experiment area represent an upper bound compared to measurements taken at similar depths elsewhere in the Canadian Shield. Under such conditions, three zones are expected around an underground opening: 1) a disturbed zone remote from the opening in which the material behaviour is essentially unchanged, but the stress state is perturbed by the opening; 2) a smaller damaged zone near the tunnel wall characterized by changes in both the pre-excavation stress state and in the material behaviour of the rock mass; and 3) a failed zone defined by a region of slabbing or rock fall-out. The nature and extent of the damaged and failed zones, and the processes responsible for their development, are important in terms of understanding the probability of increased permeability within these regions.

Rock mass behaviour and damage development were monitored around a 3.5-m-diameter test tunnel, excavated using a non-explosive technique involving line-drilling and hydraulic rock splitting. An essential feature of the Mine-by Experiment is that instrumentation was installed and operating prior to excavation of the test tunnel. In this way, it was possible to monitor the complete excavation-induced response of the rock mass, including effects ahead of the advancing tunnel face. Geomechanical and geophysical instruments, including extensometers, convergence arrays, triaxial strain cells and an acoustic emission/microseismic (AE/MS) monitoring system, were installed for the experiment. New instruments, such as the excavation damage extensometer (Ed-ex), were also developed to provide detailed measurements close to the tunnel wall. In total, over 500 data channels were monitored during the main excavation stage of the experiment.

During excavation of the test tunnel, a multi-stage process of progressive brittle failure resulted in the development of 'v-shaped' notches, typical of borehole breakouts, in the areas of compressive stress concentration in the roof and floor. The sequence of events leading to failure was similar to that observed in laboratory tests on block samples containing a central hole. However, the compressive stress at the point of failure on the tunnel wall was only about 50% of the rock strength determined from uniaxial compression tests in the laboratory. The difference between the laboratory and *in situ* strengths is attributed to stress changes that occur slightly ahead of the advancing tunnel face. As the tunnel advances, the magnitudes and orientations of the principal stresses in parts of this region change significantly, causing micro-scale damage which locally weakens, or 'pre-conditions', the rock mass. Upon tunnel advance, the degree of damage is highest at the surface of the opening where confinement is zero and compressive stress concentrations are greatest. Hence, the rock strength is lowest at the tunnel wall and increases away from the opening up to a value comparable to that measured in the laboratory. These effects are not simulated in standard laboratory tests.

Two separate back analyses, using strain and/or displacement measurements from the Mine-by Experiment, were conducted to verify the stress boundary conditions upon which the initial interpretation of the *in situ* failure process was based. The two analyses produced consistent results, constituting an improved estimate of the principal stress orientations and magnitudes at the 420 Level. While this estimate differed somewhat from the stress tensor used in the initial analysis of progressive failure, the results confirmed that the original estimate was sufficient for the purpose of understanding the failure process. The back analyses highlighted the potential difficulties in determining *in situ* stresses in highly-stressed conditions using traditional stress measurement techniques.

The refined estimate of the stress tensor was used to identify regions of non-linear/non-elastic behaviour by comparing the measured rock mass response to the expected elastic response. The comparison showed that the region ahead of the advancing face exhibits essentially linear elastic behaviour, but that the region behind the face is affected by the development of excavation-induced damage. Results from underground characterization, geophysics surveys and numerical modelling indicate that damage is most evident in areas of compressive stress concentration in the roof and floor of the test tunnel, and, to a lesser extent, in areas of tensile stress concentration in the sidewalls. These results also show that the damaged zone associated with the Mine-by Experiment test tunnel is limited to within about 1 m from the original tunnel perimeter. However, the characteristics of the damaged zone are highly variable around the tunnel, and are controlled or influenced by several factors including the nature of the stress concentration, i.e., compressive versus tensile; the mineralogy and grain size distribution of minerals within the various lithologic units; the *in situ* stress state, particularly the σ_1/σ_3 ratio and the orientation of the principal stresses relative to the tunnel axis; excavation method and sequence; and confinement from within the tunnel.

Numerical modelling carried out during the course of the Mine-by Experiment showed that elastic analyses were adequate for interpreting the monitoring results from the Mine-by test tunnel. However, neither linear nor non-linear continuum analyses adequately predicted the extent of damage around the Mine-by test tunnel, or the shape of the damaged and

failed zones. While the initiation of failure at the boundary of the tunnel can be predicted by continuum models using an appropriate failure criterion, the stages following initiation, which involve dilation, slabbing and spalling, represent discontinuum-type behaviour. It is this transition from continuum to discontinuum behaviour that poses the major difficulty in predicting the shape and extent of the damaged and failed zones around the Mine-by test tunnel and similar underground openings. Despite this limitation, though, elastic models, used in conjunction with the concepts developed in the report regarding progressive failure, are entirely adequate for engineering design purposes.

1. INTRODUCTION

In Canada, as in many countries that employ nuclear power, the concept of deep underground disposal of used nuclear fuel waste is being investigated. The Canadian disposal concept considers the plutonic rock of the Canadian Shield as a potential host medium for a disposal vault located at between 500- and 1000-m depth. As part of the assessment of this concept, Atomic Energy of Canada Limited (AECL) has constructed an Underground Research Laboratory (URL) approximately 120 km northeast of Winnipeg, Manitoba in the Lac du Bonnet granite batholith (Figure 1). The URL constitutes a well-characterized *in situ* environment in a previously undisturbed volume of rock for experiments that address issues of importance in assessing the Canadian disposal concept, and/or that demonstrate elements of the proposed disposal technology.

During development of a disposal facility, knowledge about the response of the rock to excavation will be needed to aid in optimizing many elements of the design, including such things as depth of disposal, layout of tunnels and rooms, excavation method and geometry, spacing of waste containers, and emplacement of seals. The Mine-by Experiment (Read and Martin 1991a), one of the Operating Phase Experiments planned for the URL (Simmons 1990), was designed to monitor rock mass behaviour and damage development around a test tunnel in massive, highly stressed, brittle rock. An essential feature of this type of experiment is that instrumentation is installed and operating prior to excavation of the

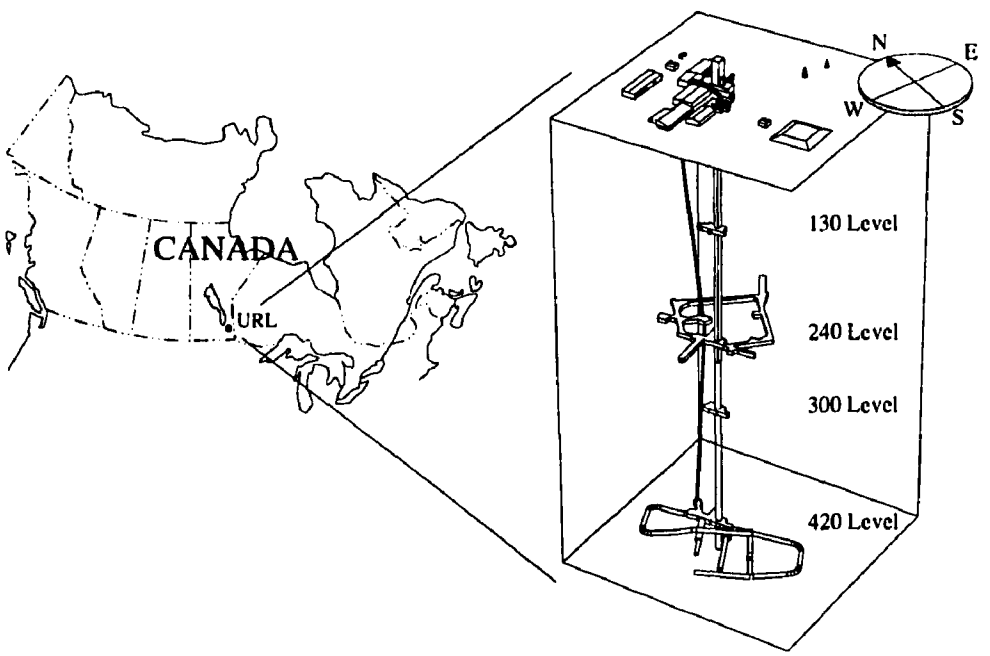

FIGURE 1: Location and arrangement of AECL's Underground Research Laboratory showing the main working levels.

tunnel. In this way, it is possible to monitor the complete excavation-induced response of the rock mass, including effects ahead of the advancing tunnel face.

The experiment location within the URL was selected to be representative of the geology and potentially high stress conditions anticipated at possible candidate disposal sites. The high *in situ* stresses and highly anisotropic stress ratios measured in the experiment area represent an upper bound compared to measurements taken at similar depths elsewhere in the Canadian Shield. Under such conditions, several zones may be defined around the tunnel: 1) a disturbed zone remote from the opening in which the material behaviour is essentially unchanged, but the stress state is perturbed by the opening; 2) a smaller damaged zone, typically within 1 to 1.5 tunnel diameters of the tunnel wall, characterized by changes in both the pre-excavation stress state and in the material behaviour of the rock mass; and 3) a failed zone defined by a region of slabbing or rock fall-out. These zones are shown schematically in Figure 2. The nature and extent of the damaged and failed zones, and the processes responsible for their development, are of particular importance in terms of understanding the likelihood of increased permeability within these regions.

The five specific objectives of the Mine-by Experiment (Read and Martin 1991a) are:

1. to improve our fundamental understanding of *in situ* rock mass behaviour and failure mechanisms;
2. to evaluate the excavation damage created around underground openings, study the causal mechanisms, and establish the factors that control damage;
3. to contribute to studies on the viability of the borehole alternative for emplacing nuclear fuel waste containers;
4. to develop and evaluate underground characterization methods, and characterize the volume of rock in which future sealing experiments are to be conducted; and

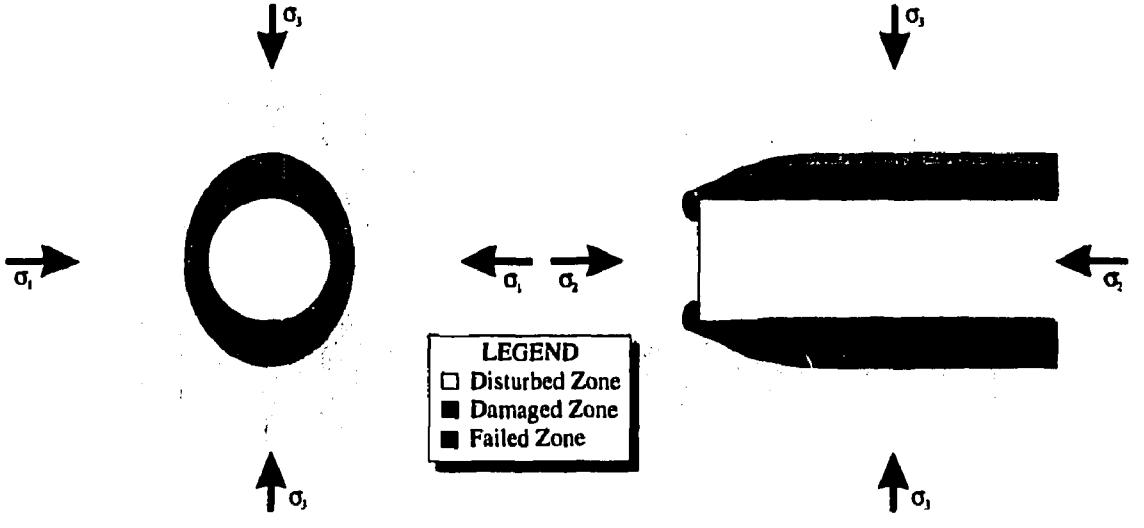

FIGURE 2: Schematic view of the disturbed, damaged and failed zones around a cylindrical tunnel. Compressive stresses are positive, and $\sigma_1 > \sigma_2 > \sigma_3$.

5. to develop and evaluate monitoring instrumentation and data management systems.

This report summarizes the technical findings of the first phase of the Mine-by Experiment (Phase 1: Excavation Response) relative to the experimental objectives. This section defines the objectives and organization of the experiment, and includes a simplified schedule and organizational chart. Section 2 presents results of pre-excavation characterization, details of the underground development and the *as-built* instrumentation arrangement as background for the experiment, and to establish the initial assumptions for analysis. Using these conditions, the mechanical behaviour and progressive failure of granite is investigated in Section 3, comparing results from laboratory testing to observed *in situ* behaviour to explain the mechanisms associated with the development of the failed zone. Section 4 uses back analysis of instrument responses in combination with geophysics studies to characterize the far-field *in situ* stress tensor, the transition between the zones of excavation disturbance and damage, and the material behaviour within the damaged zone. Factors controlling excavation damage development are also discussed in Section 4. Section 5 presents the various approaches taken to model progressive failure, and discusses the application of such models to design. A summary and the main conclusions are presented in Section 6. Three appendices are also included: the first contains a completed experiment schedule, the second presents details of the experiment back analysis, and the third provides a list of related documents and published papers detailing specific analyses. The monitoring results from the Mine-by Experiment test tunnel are summarized separately in a series of nine data summary reports:

Part 1 – Survey Information (COG-93-290, Read et al. 1994),

Part 2 – Triaxial Strain Cell Results (COG-93-353, Read et al. 1994b),

Part 3 – Extensometer Results (COG-93-354, Read et al. 1994a),

Part 4 – Convergence Results (COG-93-177, Read et al. 1993b),

Part 5 – Thermistor Results (COG-93-233, Martino et al. 1993a),

Part 6 – Acoustic Emission/Microseismic Results (COG-93-185, Martino et al. 1993),

Part 7 – Geological Setting and General Geology (COG-93-251, Everitt et al. 1993),

Part 8 – Construction Summary (COG-93-252, Keith and Onagi 1994), and

Part 9 – Observations (COG-93-347, Martino et al. 1994).

Details on the management, archiving and retrieval of experiment data are covered in Martino (1996).

1.1 EXPERIMENT SCHEDULE AND ORGANIZATION

The simplified experiment schedule is shown in Figure 3. The activities are categorized under the general headings 1) Design & Engineering, 2) Construction, 3) Drilling, 4) Characterization & Testing, 5) Equipment & Instrumentation, 6) Test Tunnel Monitoring and 7) Analysis & Reporting. As shown in Figure 3, the main experimental activities were completed close to the planned schedule. The main monitoring phase of the experiment

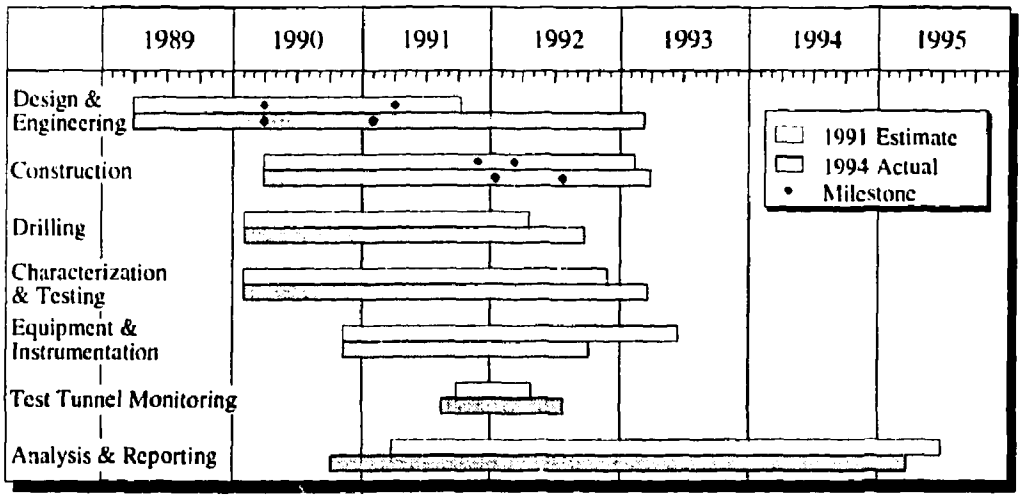

FIGURE 3: Simplified experiment schedule showing planned and completed activities. Milestones in Design and Engineering represent the completion of preliminary and final designs, respectively, and in Construction, the start and completion of the test tunnel.

during the excavation of the test tunnel was delayed approximately 1.5 months as a result of some startup problems with the enthalpy control system. In addition, owing to a lack of previous experience with the selected excavation technique, the test tunnel excavation took about 3 months longer than initially planned, but these changes did not affect the overall completion date for the experiment. The Connected Permeability Experiment, the main associated project for the Mine-by Experiment, was reorganized into a separate phase (Phase 2) of the overall experiment. In addition, a third phase (Heated Failure Tests) was added as an associated project, as detailed in an addendum to the original experiment plan (Read and Martin 1993). Reports summarizing the second and third phases of the Mine-by Experiment will be issued separately. The detailed schedule for the completed experiment is contained in Appendix A.

The organizational structure of the experiment was relatively unchanged from that laid out in the Mine-by Experiment Final Design Report (Read and Martin 1991a), with the exception of additional personnel within the external contracts for various aspects of the experiment. The organizational chart for the main components of the experiment is shown in Figure 4.

2. OVERVIEW OF THE EXPERIMENT

The Mine-by Experiment Final Design Report (Read and Martin 1991a) was used as the design plan for the experiment. Included in that report was a summary of pre-excavation characterization results for the experiment, a detailed experiment schedule, and details of

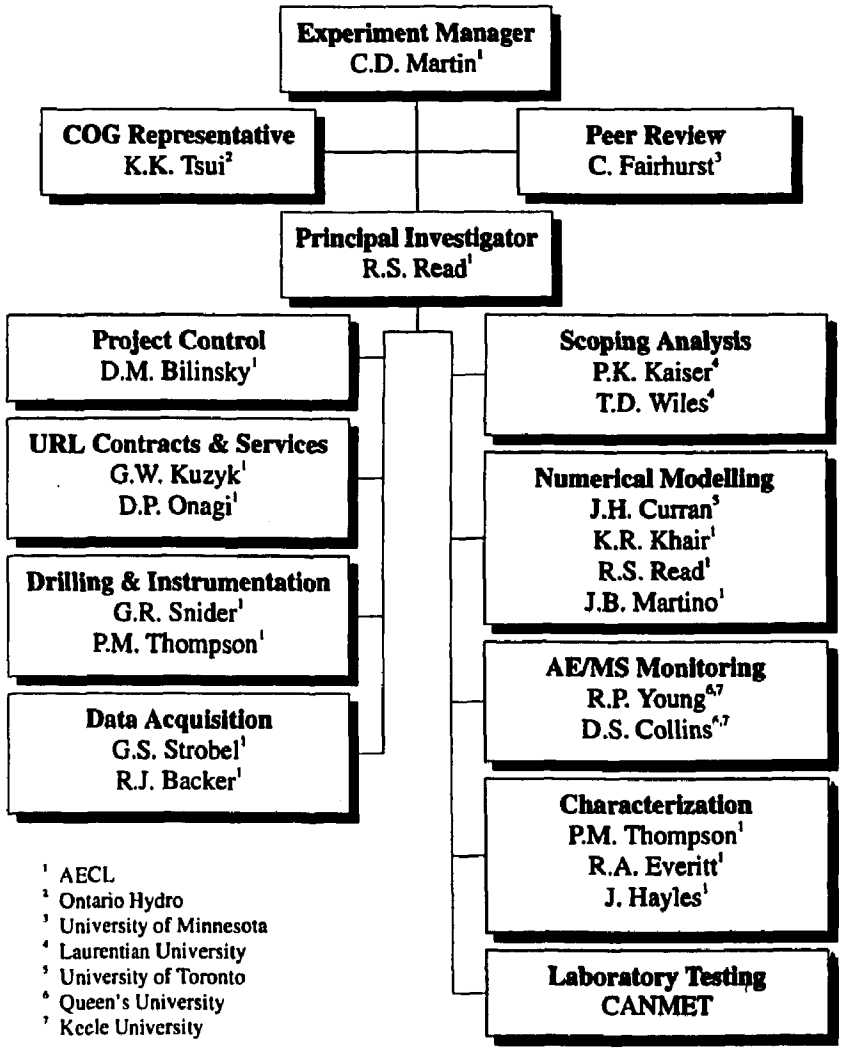

FIGURE 4: Organizational chart showing the main participants in the experiment.

the planned experimental activities. This section provides an overview of the experiment, including a review of the pre-excavation characterization data and *as-built* details.

2.1 PRE-EXCAVATION CHARACTERIZATION

2.1.1 Geology

The URL is located in the Lac du Bonnet batholith, which is considered to be typical of many granitic intrusions of the Precambrian Canadian Shield (Davison et al. 1982). The batholith is an elongated body about 75 by 25 km in plan and about 10 km in depth, trending ENE-WSW. It has been dated as Late Kenoran in age (2680 ± 81 Ma), and lies in the Winnipeg River plutonic complex of the English River gneiss belt of the west-

ern Superior Province. The batholith is a relatively undifferentiated massive porphyritic granite-granodiorite. The massive, medium- to coarse-grained porphyritic granite is relatively uniform in texture and composition over the batholith, although locally it displays subhorizontal gneissic banding (Everitt et al. 1990a).

The geology of the URL has been characterized from detailed logging of drill-core from boreholes, and geological mapping of surface and subsurface exposures. From these investigations, it has been concluded that, near the URL, the batholith is made up of five main rock units: the pink (altered) or grey (unaltered) granite groundmass of the batholith, xenolithic inclusions of various compositions, leucocratic granitic segregations, and subvertical granodiorite and pegmatite dykes. This classification scheme is based primarily on age relationships between the various rock units (Everitt and Brown 1986).

During excavation of the URL shaft, two major thrust faults (Fracture Zones 3 and 2) and their associated splays (Fracture Zones 2.5 and 1.9) were intersected (Figure 5). These faults dip to the southeast at between 20 and 30° and typically contain low-dipping fractures, secondary alteration products such as clay, hematite and chlorite, zones of cataclasite, gouge and rubble, and regions of moderate-to-high groundwater flows.

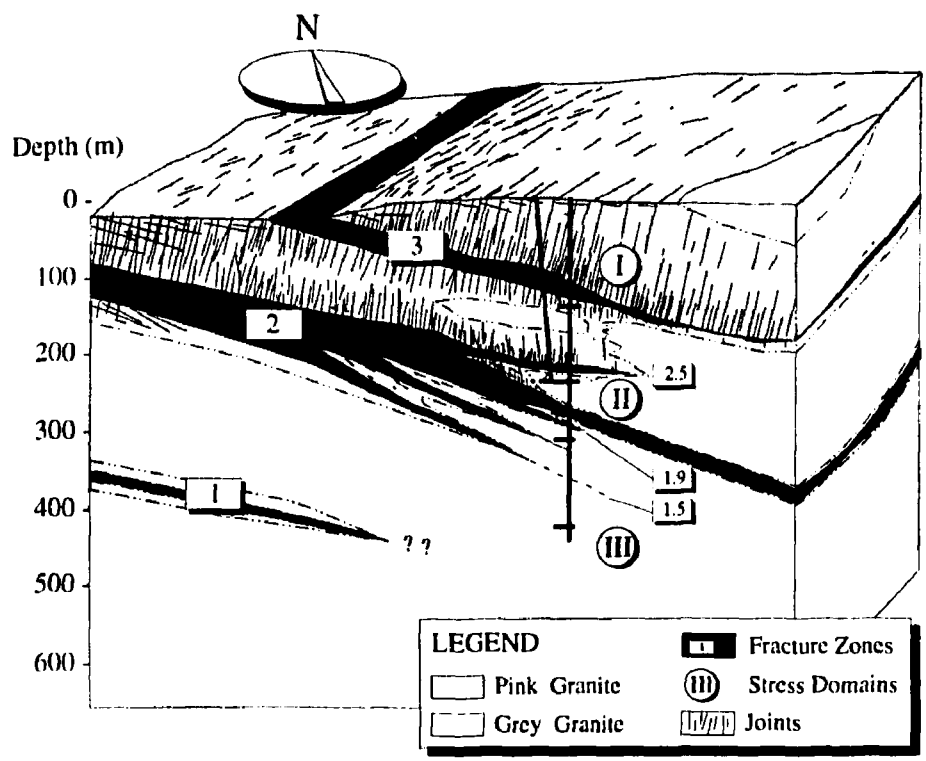

FIGURE 5: General geological setting of the Underground Research Laboratory showing the major Fracture Zones and stress domains (after Everitt et al. 1990a).

Above Fracture Zone 2.5, the rock mass comprises mainly pink granite. In this region, two subvertical joint sets have been identified: a prominent set striking about 020 to 040°, and a less prominent, intermittent set striking about 150 to 180°. Below Fracture Zone 2.5, the rock mass is essentially unfractured, with the exception of Fracture Zone 2 and its associated splays 1.9 and 1.5.

According to Everitt et al. (1990), the rock mass at the 420 Level is composed of three major litho-structural domains: a gneissic grey granite, a leucocratic granite, and a xenolithic-leucocratic granite. A major subvertical granodiorite dyke swarm, approximately 100 m thick and striking NNW, crosscuts these domains and is present throughout the 420 Level. From earlier work by Brown et al. (1989) at the other levels at the URL, the granodiorite is poorer in alkali feldspar and richer in plagioclase than the grey granite, although the transition between the two units is diffuse (Figure 6). Thin pegmatite dykes crosscut all other rock types, but are mostly confined to the larger granodiorite dykes at this level. Detailed petrographic analysis was not conducted on rock types from the 420 Level prior to the Mine-by Experiment because of wide mineralogic variations within each unit. Results from post-excavation petrographic analyses are discussed in Section 4.3.5.

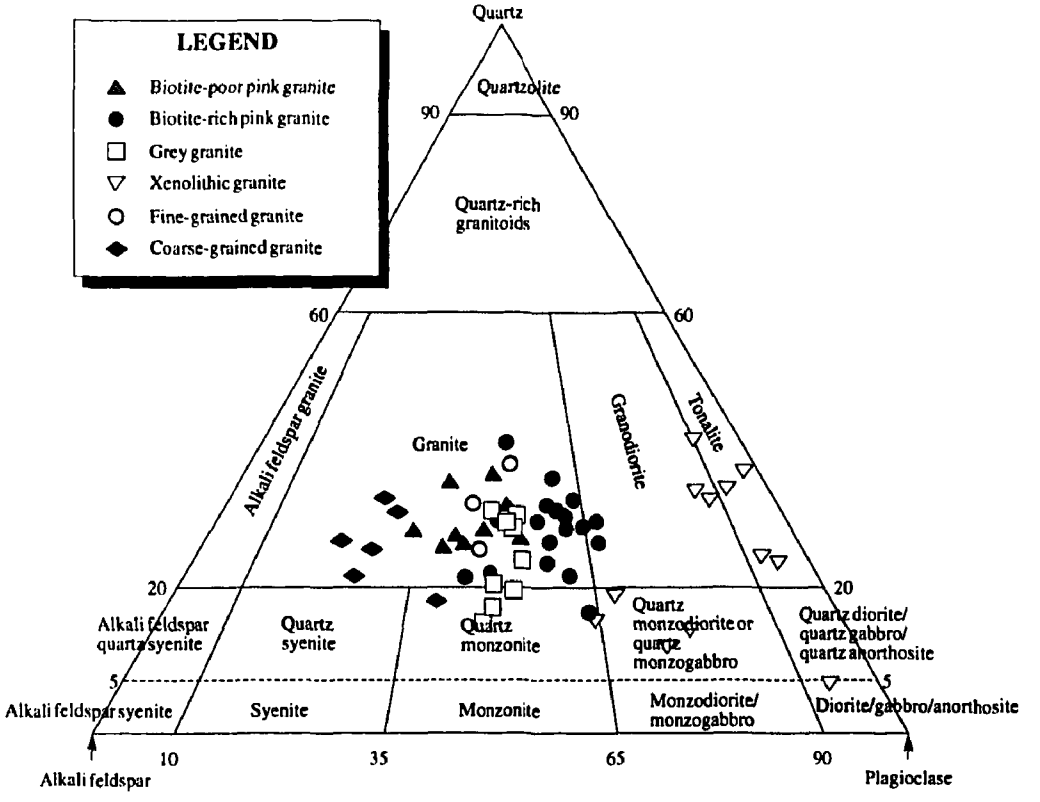

FIGURE 6: Ternary diagram showing the composition of granite and granodiorite for the URL (after Brown et al. 1989). Note that in this classification no distinction was made between the granite and granodiorite, the latter being grouped with biotite-rich granite. The inverted triangles represent xenolith compositions.

A few minor closed fractures, associated with the granodiorite dyke swarm to the west of the station, were identified in drill core from exploratory boreholes for the Mine-by Experiment. However, these fractures were not detected in the tunnel wall following room excavation and hence are of small areal extent (~ 1 m^2). They are essentially isolated from each other and therefore do not affect the overall permeability of the rock mass. This appears to be the only fracture type in the immediate vicinity of the 420 Level. Under such sparsely fractured conditions, the *in situ* hydraulic conductivity of the rock mass is in the order of 10^{-13} m/s.

2.1.2 Geotechnical Properties

The geotechnical properties of core samples of Lac du Bonnet granite have been determined from extensive laboratory testing, e.g., Lajtai (1982), Lajtai (1988), Lajtai and Bielus (1986), Lajtai and Schmidtke (1986), Jackson et al. (1989), Stimpson and Chen (1991) and Martin (1993). However, as discussed later in Section 3, extrapolation of these results to the *in situ* material properties of the rock mass is not straightforward, even in situations where the rock mass has no joints. The difficulty lies in the fact that the rock *in situ* is 'pre-loaded', i.e., subjected to *in situ* stresses which are changed when the rock is disturbed by excavation. A core sample taken from the *in situ* stress environment for laboratory testing is first unloaded during coring and then reloaded in the laboratory. Thus the loading path and stress history of a core sample differ from that of the rock around the excavation. If the stresses relieved during coring are high, the resulting laboratory sample may contain significant damage that is not present in the field. Martin and Stimpson (1994) have shown that sample disturbance attributable to stress relief increases with the depth of sampling at the URL, and that this damage affects the geotechnical properties of the core samples. Samples selected from a low stress regime show a reduction in the amount of sample disturbance, and have properties that are probably more comparable to the *in situ* properties of the virgin rock mass.

The virgin geotechnical properties of rock in the field study area (Table 1) were estimated from laboratory tests performed by the Canada Centre for Mineral and Energy Technology (CANMET) on representative rock samples from the 420 Level, and on samples of granite from the upper 275 m of the batholith. Results from samples taken from the high stress domain at the 420 Level showed a marked decrease in peak strength from those taken at the 240 Level and above, suggesting a substantial amount of sample disturbance caused by induced microcracking. Read and Martin (1992) concluded that results from samples of granite from lower stress domains nearer surface were likely to be the most representative of the virgin *in situ* rock mass properties at the 420 Level. Martin (1993) also showed that samples of Lac du Bonnet granite taken from Cold Spring Quarry, near Seven Sisters, Manitoba, had properties similar to those taken from the upper 275 m of the batholith at the URL.

Mapping of excavation-induced damage during construction of the 300 Level suggested that damage zone development around underground openings was more pronounced in granite than in granodiorite (Everitt et al. 1989). The same was true during development of access tunnels at the 420 Level in the vicinity of discrete granodiorite dykes. However, the difference in excavation-induced damage between the massive granite and the outer

TABLE 1

ESTIMATED VIRGIN GEOTECHNICAL PROPERTIES FOR GRANITE AND GRANODIORITE IN THE EXPERIMENT AREA

Rock Type	Granite	Granodiorite
Density (kg/m^3)	2630 ± 10	2660 ± 20
Uniaxial Compressive Strength (MPa)	213 ± 20	228 ± 20
Tangent Young's Modulus (GPa)	65 ± 5	66 ± 5
Poisson's Ratio	0.25 ± 0.05	0.25 ± 0.05

Values are the mean±3 standard deviations (after Read and Martin 1992).

margin of a large granodiorite dyke was less pronounced in a drill-and-blast excavation (Room 405) driven orthogonal to the σ_1/σ_3 plane. Although laboratory testing suggests that the mechanical properties of the two rock types are similar, the field observations imply that there is a difference in their fracturing characteristics, i.e., the growth and interaction of cracks. As discussed later in Section 4.3.5, owing to its inequigranular structure and the abundance of large feldspar crystals, microcracking is expected to initiate at lower applied stresses in the granite than in the granodiorite. Consequently, regions of granite *in situ* would sustain more initial damage related to stress concentrations ahead of the advancing face, and would develop more pronounced damaged and failed zones behind the advancing face, than regions of granodiorite under identical stress conditions. This difference in fracturing characteristics is noticeable upon stress relief during sampling at the 420 Level.

2.1.3 *In Situ* Stress

A key goal in the design of the Mine-by Experiment was to conduct the investigation in a geological/geotechnical environment similar to that which might be expected between 500- and 1000-m depth in the Canadian Shield. A matter of particular concern was that the *in situ* stress magnitudes in the experiment area be sufficient to damage the rock mass upon tunnel excavation. An extensive characterization program had defined three distinct stress domains at the URL (Martin and Chandler 1993). At the 420 Level, the *in situ* stresses are part of Stress Domain III, which extends from about 300 m to a depth of at least 512 m (Figure 5). Based on the pre-excavation characterization of the 420 Level, it seemed possible to meet the objectives of the experiment by locating the Mine-by Experiment in Stress Domain III, where the stress conditions are similar to those at a depth of about 1000 m in other parts of the Shield.

The highly-stressed condition of this domain posed a problem for stress measurements at the 420 Level. A variety of techniques were tried, with limited success. Overcoring provided questionable results because of exaggerated axial straining (incipient discing). Hydraulic fracturing produced subhorizontal fractures in horizontal and vertical boreholes, from which only the vertical stress could be estimated (Doe 1989). Other studies using convergence measurements (Martino 1989) were limited to estimating only the plane components of the

TABLE 2

INITIAL ESTIMATE OF *IN SITU* STRESSES AT THE 420 LEVEL

Stress Components	σ_1	σ_2	σ_3
Magnitude (MPa)	55 ± 5	48 ± 5	14 ± 1
Trend (°)	135 ± 10	044 ± 10	290 ± 25
Plunge (°)	10 ± 5	05 ± 5	79 ± 5
Stress Ratios	σ_1/σ_2	σ_1/σ_3	σ_2/σ_3
	1.15 ± 0.1	3.93 ± 0.5	3.43 ± 0.5

Values are the mean±3 standard deviations (after Read and Martin 1991a).

stress tensor, and were difficult to interpret. An under-excavation study using CSIRO HI cells around the bored vent raise from the 420 to 240 Level (Kaiser et al. 1991; Wiles and Kaiser 1992) provided an estimate of the complete tensor, but results were affected by uncertainty in the CSIRO HI cell locations and orientations, small induced strains in the axial direction, and non-linear behaviour around the instrument boreholes once the advancing face was within 1 diameter of the instruments. In that study, the estimates of both the magnitude and orientation of the maximum and intermediate stresses were well constrained, but those for the minimum principal stress were not. Results from an acoustic emission/microseismic (AE/MS) array installed in four inclined boreholes around the URL shaft (Talebi and Young 1992) provided estimates of the maximum and minimum horizontal stress directions, which were supported by observations of breakouts in the shaft, but provided no estimates of magnitudes. Doorstopper tests performed in boreholes drilled for the Mine-by Experiment at the 420 Level (Corthésy and Gill 1992) produced an estimate of the stress tensor for the area, but the results for stress magnitudes did not correlate with results from other tests or observed behaviour around excavations at the 420 Level.

A stress tensor for the 420 Level (Table 2) was compiled from the best evidence for principal stress magnitudes and directions from the various testing methods, and from observations of breakouts in the shaft and in tunnels at the 420 Level. The composite nature of the tensor, however, precluded the use of rigorous statistical methods in determining the mean value and confidence intervals of each of the stress components, and their respective orientations. Nevertheless, this composite tensor was sufficient to define the orientation of the experiment test tunnel, which was designed to be approximately parallel to the intermediate principal stress (σ_2) direction.

2.2 UNDERGROUND DEVELOPMENT

2.2.1 *As-built* Experiment Arrangement

The arrangement of the Mine-by Experiment (Figure 7) was the result of an optimization process drawing upon a variety of technical proposals for instrumentation layouts and monitoring methods, evaluation of the practicality and safety of the operations associated with implementation, and evaluation of the most effective use of available resources in conjunc-

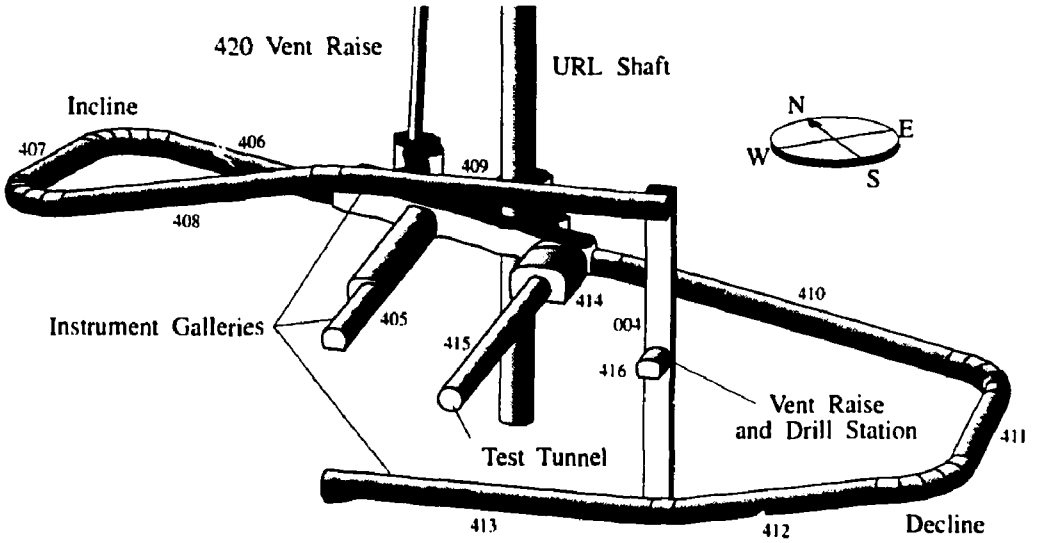

FIGURE 7: Arrangement of the Mine-by Experiment at the 420 Level of the URL.

tion with the overall URL experimental program. The azimuth of the test tunnel (225°) was chosen to maximize the stress ratio in the plane orthogonal to the tunnel axis in order to promote excavation-induced damage development.

Access for installation of instruments was provided by a series of drill-and-blast excavations. An incline and a decline were excavated at 20% grade on tangent, and 10% grade through the curves, to develop an upper and lower instrument gallery, Rooms 409 and 413 respectively, orthogonal to the planned test tunnel. A vertical raise (Room 004) was excavated to connect the upper and lower galleries for ventilation purposes, and a drill station (Room 416) was excavated at mid-height in the raise for instrumentation borehole drilling. A third instrument gallery (Room 405), parallel to the proposed test tunnel, was extended off the existing 420 Level for additional drilling access. All access tunnels were initially 3.4-m wide by 2.9-m high and horseshoe-shaped, but the first 30 m of Room 405 was enlarged to 5.0-m wide by 3.5-m high to accommodate additional testing. The vent raise drill station (Room 416) was excavated as a 3.5-m-wide by 2.7-m-high opening.

Following excavation of the access tunnels and installation of the instrumentation for the experiment, the 3.5-m-diameter circular test tunnel (Room 415) was excavated at 0.5% grade to 46 m in length from an assembly chamber (Room 414). The wall-to-wall spacing between the instrument galleries and the test tunnel was approximately 18.5 m.

2.2.2 Excavation Technique and Equipment

Based on previous experience with the drill-and-blast excavation method in Room 209 and the URL shaft, the damaged zone near the tunnel wall is considered to result from a combination of stress redistribution and blast effects. Similar observations in granite have been

reported by Pusch and Stanfors (1992). Because the intent of the Mine-by Experiment was to study the damage resulting from stress redistribution, the test tunnel was designed as a full-face machine-excavated opening to avoid the undesirable percussive effects of blasting. Initially, a tunnel boring machine (TBM) was considered the best technical option (Read and Martin 1991b), but the costs associated with excavating such a short section of tunnel, including equipment preparation and mobilization, were prohibitive. Consequently, an alternative method was devised.

The excavation method selected (Figure 8) involved line-drilling and reaming a series of 1-m-deep perimeter holes around the design diameter of the tunnel, and then progressively breaking out the interior of the round using hydraulic rock splitters (Figures 9 and 10) in a series of production holes (Keith and Onagi 1994; Onagi et al. 1992). Although the test tunnel was initially designed as a 3.5-m-diameter cylindrical opening with a flat face, the excavation method necessitated a stepped longitudinal profile to accommodate drilling of each round, with a maximum diameter of 3.5 m in each round (Figure 11). Based on previous excavations at the URL, the shape of the face was also expected to deviate somewhat from a perfect plane.

The excavation sequence for the test tunnel incorporated a combination of line-drilling/rock breaking and careful drill-and-blast for the first 10 m of the tunnel, followed by 36 m excavated by line-drilling and rock breaking in 0.5- to 1-m-long rounds. The first 34 m of Room 415 were excavated as full-face rounds, and a pilot-and-slash sequence was used for the final 12 m of the test tunnel. In total, 50 excavation rounds were required to complete the test tunnel. A detailed survey of each excavation round was conducted to accurately determine the face shape and round geometry (Read et al. 1994). Face contour maps were generated from the survey data, and a three-dimensional computer model of the test tunnel was created (Figure 12). A summary of the construction activities related to the Mine-by Experiment, and specific details of the equipment and excavation cycles, is given in Keith and Onagi (1994).

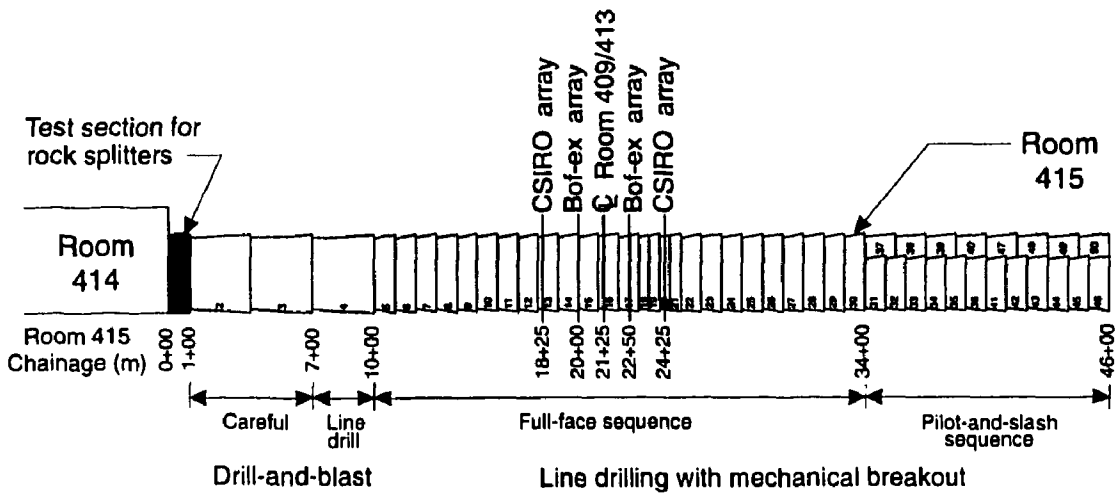

FIGURE 8: Excavation method and sequence used for the Mine-by Experiment.

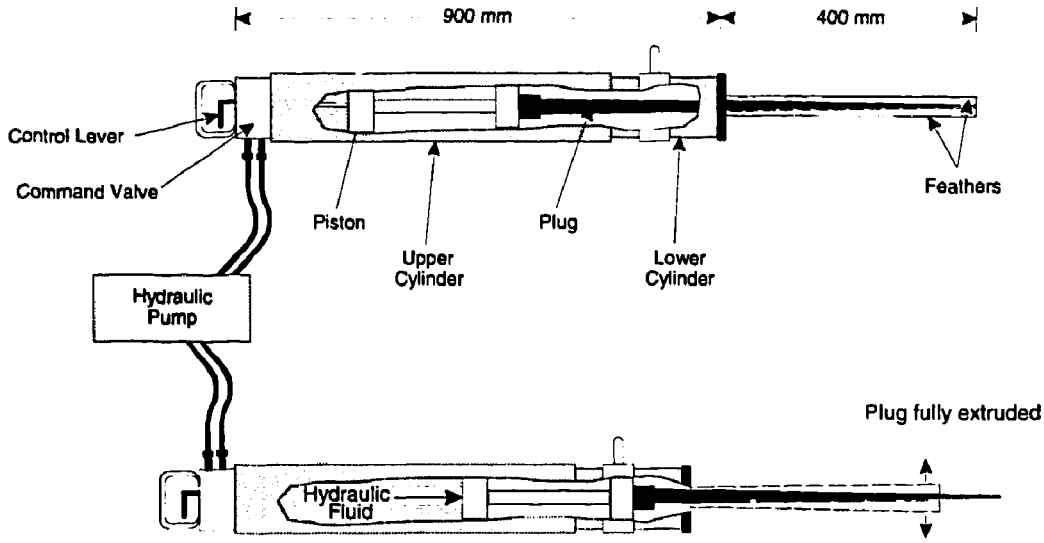

FIGURE 9: Rock splitters for the Mine-by Experiment.

FIGURE 10: Photograph showing the rock splitters in use.

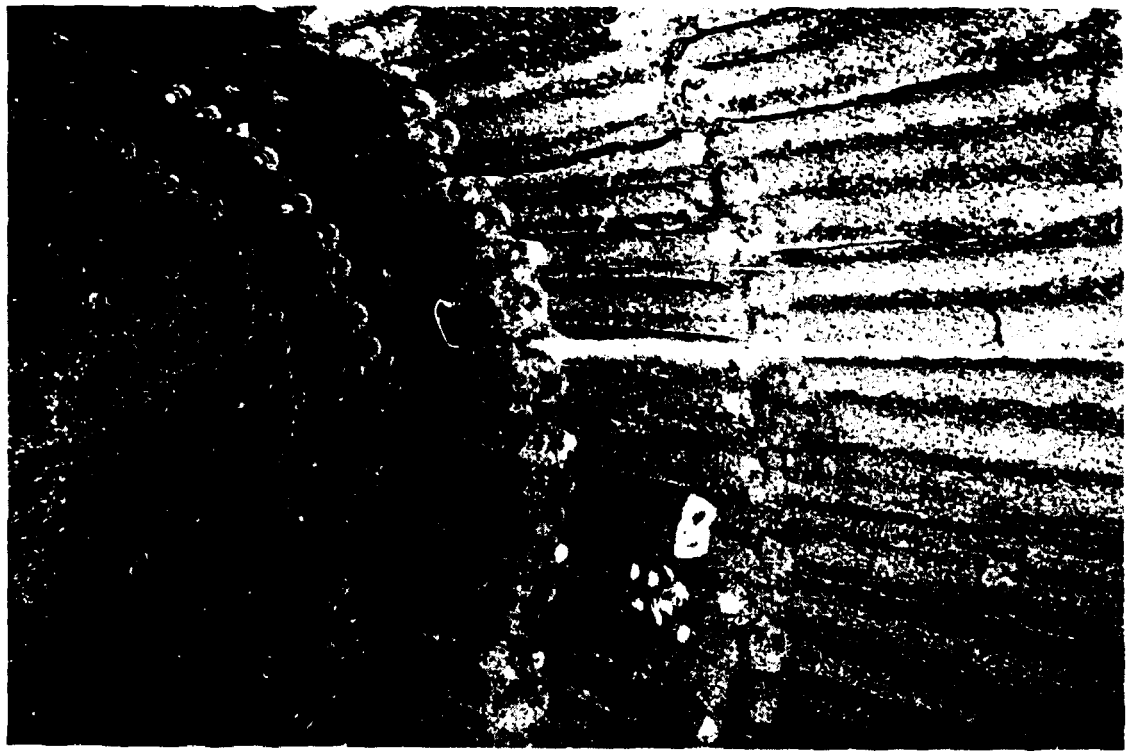

FIGURE 11: Photograph showing the stepped geometry of the tunnel walls.

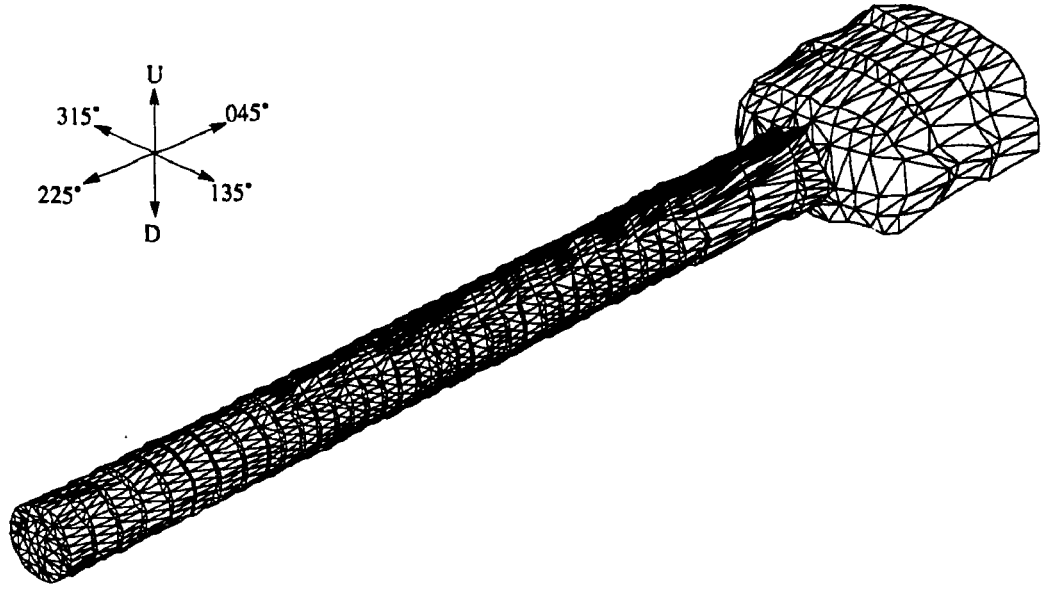

FIGURE 12: Three-dimensional model of the completed Mine-by Experiment test tunnel.

2.2.3 Enthalpy Control

Enthalpy control, i.e., the control of temperature and humidity, was considered important in order to limit the number of variables in the interpretation of the measured responses. A 75 kW capacity system consisting of an air handling unit, a blast cooler, and two compressor/condensor units was installed at the 420 Level to keep the test tunnel as close as possible to the ambient rock conditions, i.e., 10.5°C and > 90% RH, during excavation. Although some short-term spikes in the air temperature were recorded during peak excavation activities, the overall rock temperature was maintained within about 1.5°C of ambient temperature. Relative humidity was consistently above 90%. Details on the performance of the system are given in Keith and Onagi (1994).

2.3 INSTRUMENTATION

The Mine-by Experiment included both geomechanical and geophysical instrumentation. The first was selected on the basis of previous excavation response tests at the URL, and included extensometers and convergence arrays to measure displacements, triaxial strain cells to measure induced strains, and thermistors to measure temperature. The second tier of instrumentation, based on acoustic emission/microseismic (AE/MS) technology, was used to study the development of the damaged zone around the Mine-by Experiment test tunnel (Talebi and Young 1990). Other geophysical surveys were also conducted periodically during the experiment.

2.3.1 Extensometers

Borehole fracture monitor extensometers (Bof-exs) have been used successfully in other major experiments at the URL to monitor very small displacements (Thompson et al. 1989), and formed the majority of the displacement-monitoring system for the Mine-by Experiment. The Bof-ex is an incremental-type extensometer, i.e., it measures relative displacement between anchors. Each extensometer string incorporated ten direct current linear variable differential transformer (DC-LVDT) displacement transducers, eleven mechanical screw-type anchors, Invar or stainless-steel rods, and centralizers (Figure 13). The repeatability of each transducer is $\pm 0.6 \mu$m, and the range is ± 6 mm. Seven thermistors were also included in each extensometer string.

A total of 12 radial Bof-ex strings were installed for the Mine-by Experiment in two instrument arrays at chainages 20+00 and 22+50 in Room 415 (Figure 14). The first array comprised two vertical and two horizontal extensometers, and the second array contained two vertical, two horizontal, and four extensometers inclined at $\pm 45°$ from horizontal. In addition, an axial extensometer was installed in a borehole drilled from Room 414 parallel to the test tunnel axis, approximately 1.3 m from the NW wall of the tunnel at the height of the tunnel centreline.

The 12 radial Bof-ex strings were installed in 75.7-mm-diameter (NQ-3 size) boreholes drilled from the instrument galleries (Rooms 405, 409, 413, and 416) towards the planned location of the test tunnel. These holes penetrated the design section of the test tunnel by

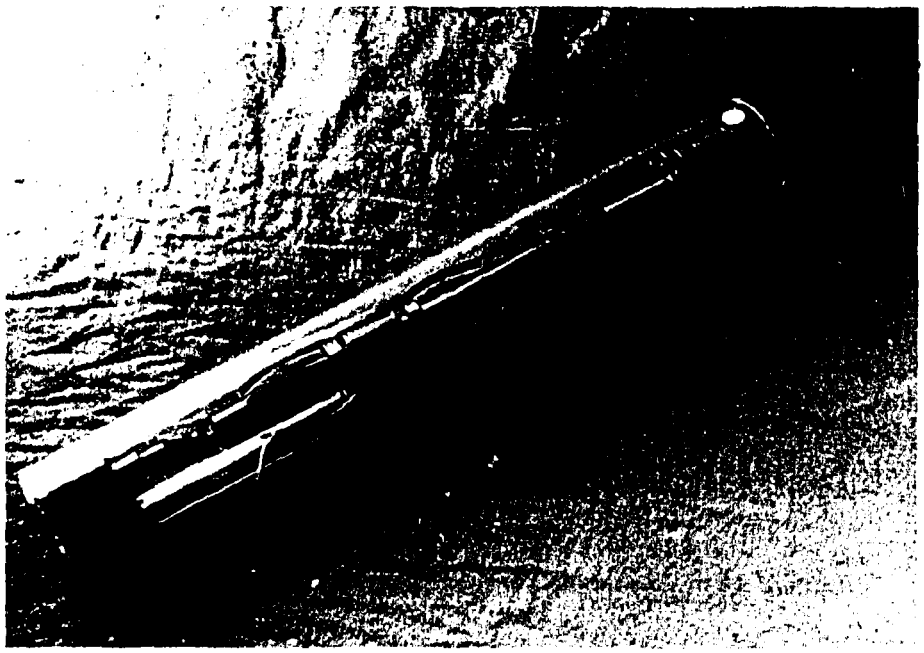

FIGURE 13: Photograph showing one segment of a Bof-ex string. The acrylic tube is 76 mm in diameter.

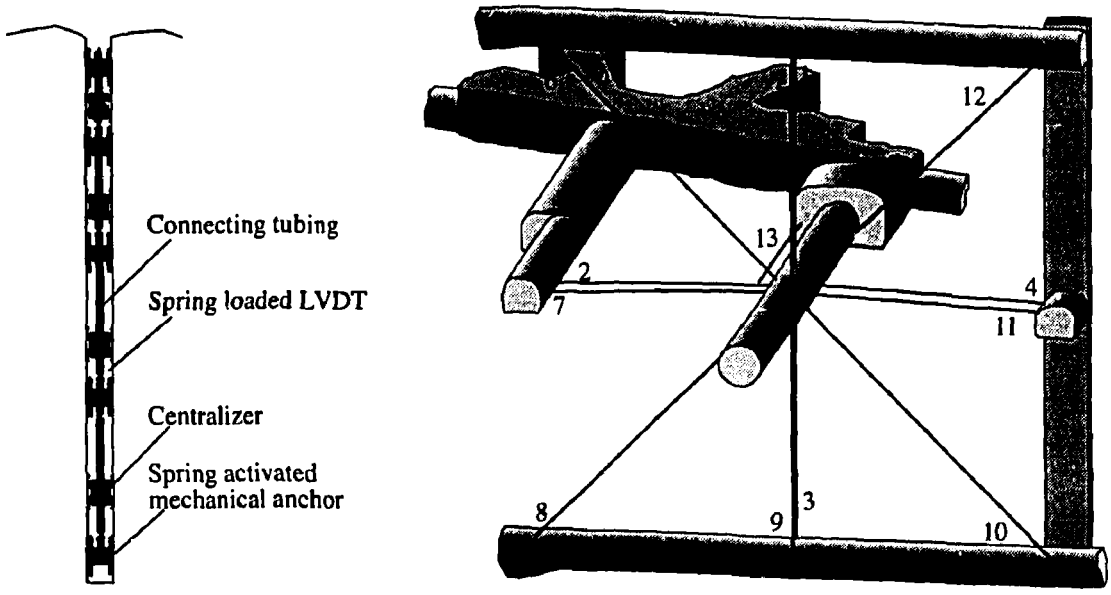

FIGURE 14: Arrangement of Bof-ex boreholes for the Mine-by Experiment and schematic illustration of a typical extensometer installation. There are 12 radial extensometers oriented orthogonal to the tunnel axis, and one axial extensometer parallel to the tunnel axis.

200 mm so that the ends of the boreholes could be located once Room 415 was excavated. Accurate collar surveys and downhole laser surveys in each borehole were conducted to determine the exact collar location and alignment deviation (Read et al. 1994). Alignment deviation was less than 0.5°, so that error in the measured radial displacements was negligible. Borehole anchors were spaced 340 mm apart near the tunnel wall, and less closely away from the tunnel. The innermost anchor was approximately 100 mm outside the design perimeter of the test tunnel in each string. Because they were installed prior to the start of excavation, the response measured by the extensometers represents the total displacement induced by the excavation of Room 415 within the coverage area of the extensometers. These extensometers are typical of *anterior-type* instruments, i.e., instruments installed in the region ahead of the advancing tunnel face.

In addition to the Bof-exs, a series of eight excavation damage extensometers (Ed-exs) were installed at approximately chainage 22+50 (Figure 15). These instruments are a miniaturized version of the Bof-ex, approximately 1 m in length, comprising ten alternating current linear variable differential transformer (AC-LVDT) displacement transducers and eleven anchors. The Ed-exs were installed in 37.7-mm-diameter (EWG size) boreholes drilled radially outward behind the advancing face to provide detailed displacement measurements within 1 m of the tunnel wall. A complete description of the instrument and an example of its application are given in Thompson et al. (1993). Results from the Bof-exs and Ed-exs, and details of their performance, are summarized in Read et al. (1994a).

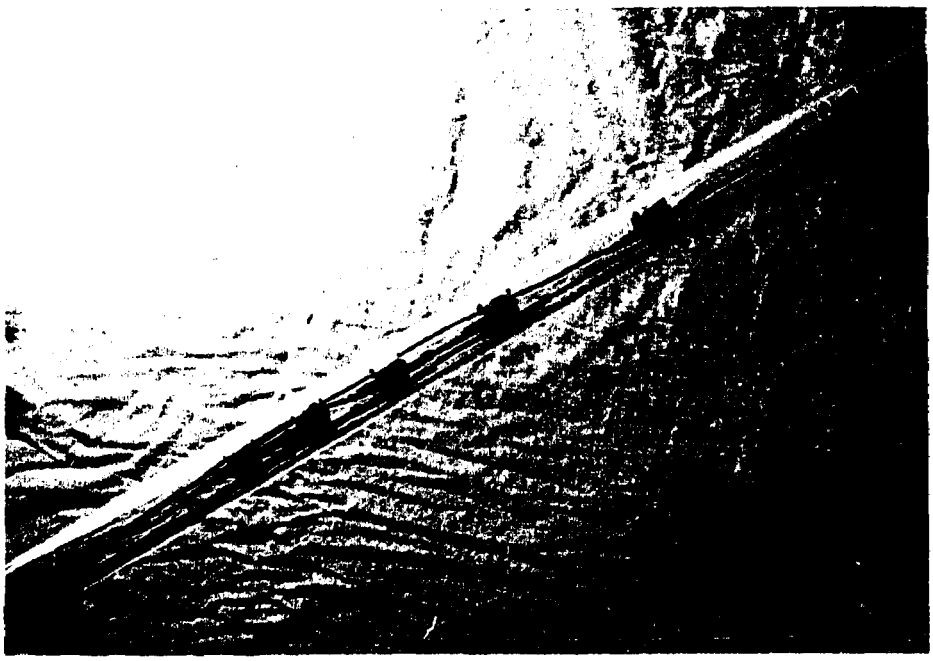

FIGURE 15: Photograph showing an Ed-ex string. The acrylic tube is 38 mm in diameter.

2.3.2 Convergence Arrays

Convergence arrays were installed in Room 415 at eight locations between chainages 10+20 and 31+96 (Table 3). Figure 16 gives details of a typical convergence array installation. Convergence arrays in the experiment comprised 12 pins installed as close to the tunnel face as possible in a measuring plane orthogonal to the tunnel axis. Specially-cut lengths of Invar wire were used in combination with a Kern distometer (Martino 1989) to measure the distance between opposing pins along six diametral measurement lines. Changes in tunnel diameter were recorded following each excavation round, providing a record of tunnel wall convergence versus excavation advance. Additional readings were also taken within each round to determine the tunnel convergence with respect to time. A summary of the convergence data from the Mine-by Experiment is presented in Read et al. (1993b) along with details of instrument performance.

Previous experience with the Kern distometer at the URL has shown a repeatability of ±0.1 mm (Martino 1989). Careful calibration of the instrument and Invar wires was performed underground before and after each use with a standard calibration apparatus. In this way, corrections for temperature were incorporated automatically into each reading. The same operator was also used as much as possible to reduce operator bias in the measurements. A standardized reading procedure, repeating each measurement four times, was followed during the Mine-by Experiment.

The convergence pins consisted of 19-mm-diameter steel reinforcing bar, 200-mm long, with a 100-mm-long stainless steel setting bolt welded to the end to attach the distometer connector. The convergence pins in each array were installed in 32-mm-diameter percussion drill holes, 300-mm deep, an average of 80 mm from the tunnel face. There was, however, some variation in chainage across the face, as shown in face contours for each round (Read et al. 1994a). The floor pins were set in slightly deeper holes, countersunk about 50 mm to protect them from construction equipment. All pins were fixed in place with resin grout. Each array, with the exception of array 415-5, was designed to have convergence pins at 0, 20, 60, 90, 120, 160, 180, 200, 240, 270, 300, and 340° counterclockwise from a NW-trending horizontal line. Array 415-5 had two measurement lines rotated 10° clockwise to avoid interfering with previously installed extensometers.

2.3.3 Triaxial Strain Cells

The CSIRO Hollow Inclusion (HI) triaxial strain cell (Worotnicki and Walton 1976) has been used almost exclusively at the URL to measure incremental strains due to excavation (Figures 17 and 18). Each cell comprises nine 120-Ω strain gauges arranged in three strain gauge rosettes cast into a plastic cylinder. One common lead is attached to a precision (stable) resistor potted in the cell to provide a baseline signal, and two separate leads are connected to a thermistor embedded in the cell. The position and orientation of the strain gauges, and colour coding for the cell, are shown in Read et al. (1994b). Each strain gauge can measure strains up to about 2%. Information gained from these instruments has been used to calculate changes in the *in situ* stress field and to validate results from computer modelling (Wiles and Kaiser 1992; Wiles and Kaiser 1994a; Wiles and Kaiser 1994b).

TABLE 3

LOCATION OF CONVERGENCE ARRAYS IN THE MINE-BY TEST TUNNEL

Array	Chainage (m)	Excavation Round
415-1	10.204	5
415-2	12.531	7
415-3	15.380	10
415-4	18.485	13
415-5	22.565	17
415-6	26.062	22
415-7	28.924	25
415-8	31.964	28

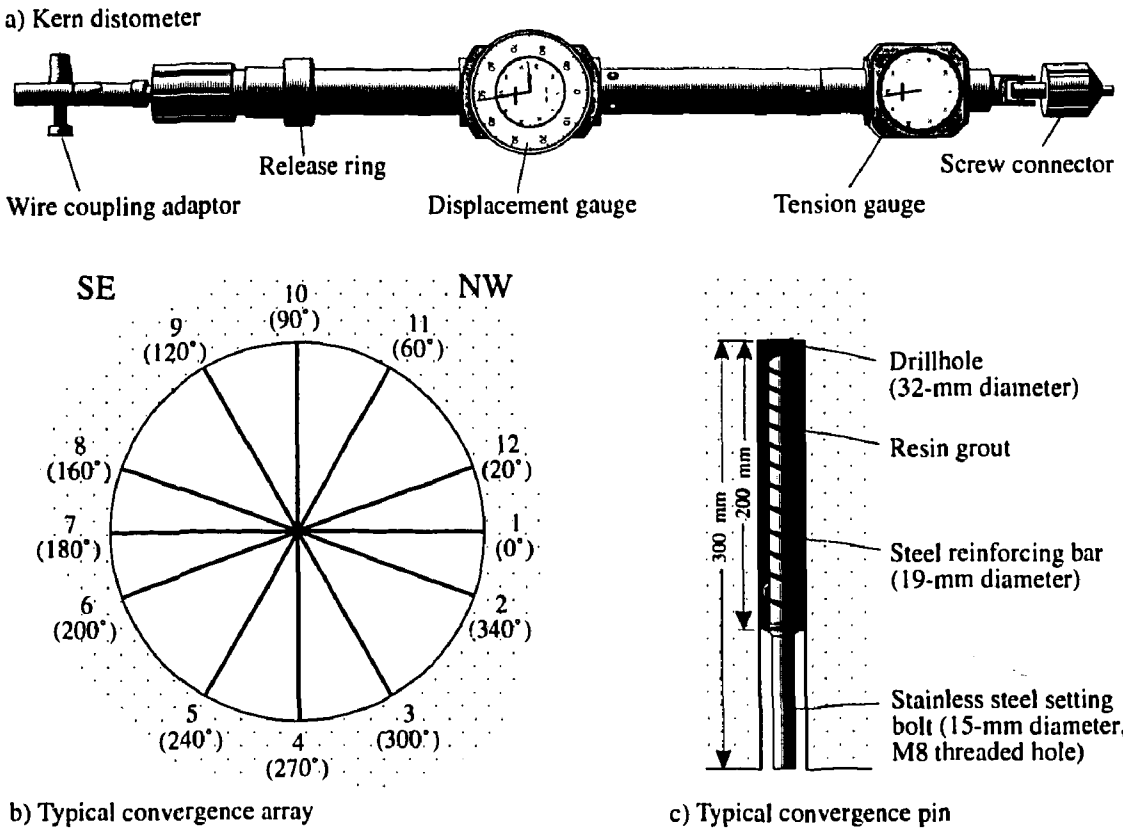

FIGURE 16: Details of the instruments and arrangement of a typical convergence array from the Mine-by Experiment.

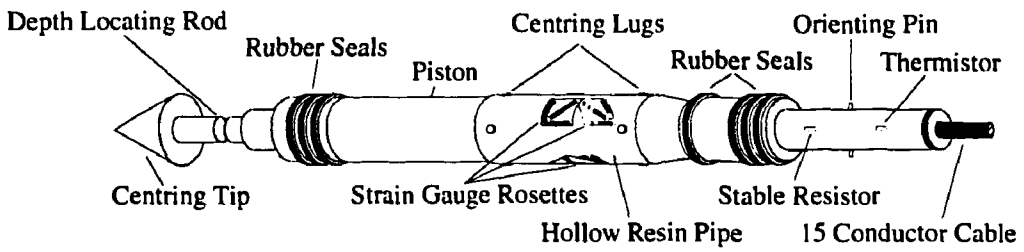

FIGURE 17: Schematic illustration of a CSIRO HI triaxial strain cell.

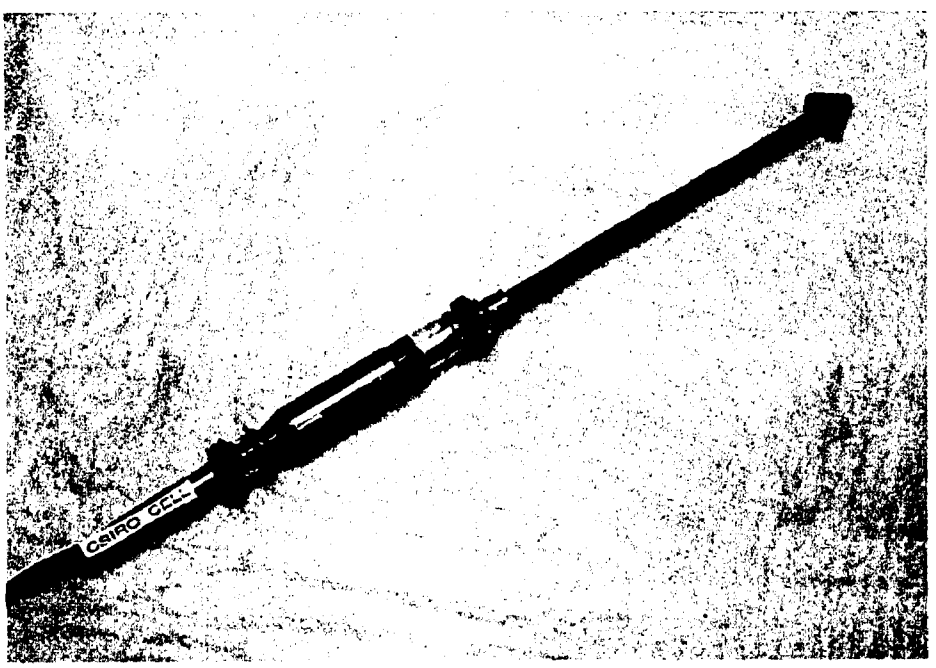

FIGURE 18: Photograph of a CSIRO HI triaxial strain cell. The cell body fits in a 38-mm-diameter (EWG size) borehole.

To install a strain cell, the following procedure was used. A 48.0-mm-diameter (AQ size) borehole was drilled and the end of the hole was flattened with a special drill bit. A 0.5-m-long 37.7-mm-diameter (EWG size) extension hole was then drilled from the flattened end of the AQ-size segment, and the cell was bonded to the wall of the extension hole approximately 0.22 m from its start (Snider et al. 1989). Each of the instrument boreholes was inclined upward to prevent accumulation of water in the hole, and all cells were oriented relative to the top of the borehole during installation to facilitate analysis of the monitoring results.

A total of 12 CSIRO HI cells were installed for the Mine-by Experiment in two arrays (Figure 19). The arrays of boreholes were drilled from Rooms 405, 413 and 416, and were designed to place CSIRO HI cells near the wall of Room 415 at chainages 18+25 and 24+25 in the test tunnel. The first array was designed to have two cells located approximately 2.5 m horizontally either side of the test tunnel centreline, one cell located 2.5 m vertically above the test tunnel centreline, and one cell located at the tunnel centre. The second array contained eight CSIRO HI cells, with design locations 2.5 and 3.25 m from the test tunnel centreline at 0, 90, 180 and 270° clockwise from horizontal. Results from the strain cells, including instrument performance, are summarized in Read et al. (1994b).

As detailed in Read et al. (1994), precise survey control was an important component of the experiment. Accurate collar surveys and downhole laser surveys were conducted for each borehole to determine the spatial position of the collar and alignment deviation. With the exception of the hole containing SM3 (deliberately placed at the tunnel centre), the boreholes did not penetrate the design perimeter of the test tunnel. In order to determine

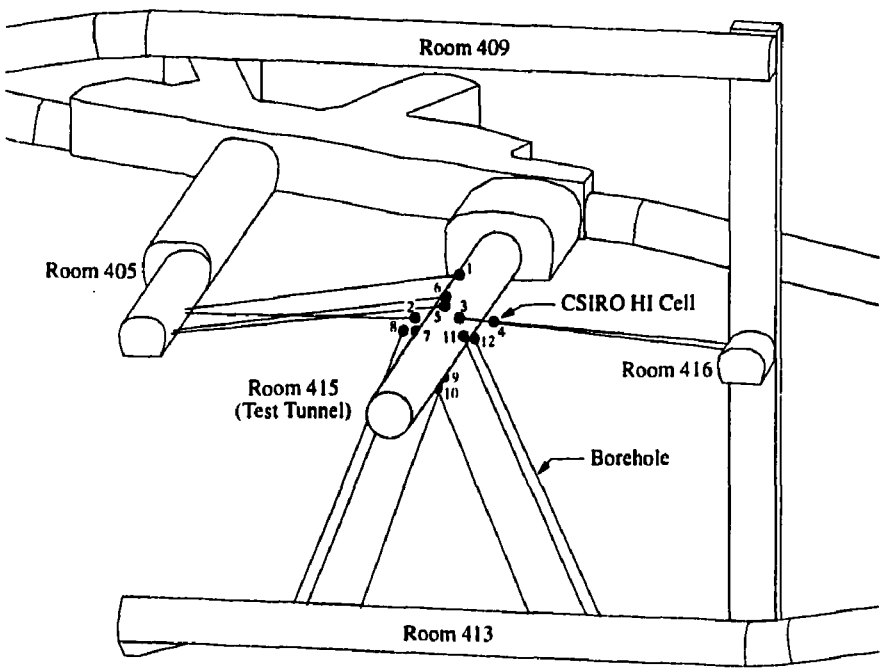

FIGURE 19: Arrangement of 12 CSIRO HI triaxial strain cells in two arrays. Cell 3, located at the centre of the tunnel, was overcored and removed during excavation.

the exact location and orientation of each cell in Universal Transverse Mercator (UTM) coordinates, 150-mm-diameter boreholes were drilled from inside the completed test tunnel to intersect each cell, which was then removed.

2.3.4 Acoustic Emission/Microseismic Monitoring

The results from an AE/MS system, installed to monitor excavation-induced seismicity in the rock mass during extension of the URL shaft, were used to design a more elaborate system for the Mine-by Experiment. The function of this new system was to evaluate the physics of fracturing associated with development of a damaged zone around the test tunnel (Talebi and Young 1990). Two of the objectives of the design were to improve the accuracy of source location determinations and to develop more rigorous source mechanism analysis procedures.

The AE/MS system comprised 16 triaxial accelerometers (Figure 20). The accelerometers, with a frequency range of 50 Hz to 10 kHz (±3 dB), were grouted in place at the end of 96-mm-diameter (HQ size) diamond-drilled boreholes. The accelerometer array (Figure 21) was designed for focal sphere coverage and a source location accuracy of about ±0.25 m near the centre of the tunnel. The sampling frequency was set to 50 kHz, allowing the study of seismic events with moment magnitudes as small as -6. This number of sensors also allowed the use of a moment tensor inversion scheme to perform source mechanism analysis (Feignier and Young 1993). A summary of preliminary AE/MS results for the Mine-by Experiment is given in Martino et al. (1993). Analysis of the AE/MS results is discussed in Section 3.3.1.

Ultrasonic tomography and acoustic emission (AE) data obtained during laboratory hydraulic fracturing tests on two 600-mm-diameter samples of URL granite (Chow et al. 1990) showed that the development of microcracks could be monitored with high-frequency sensors acoustically coupled to the rock surface, and that source locations and mechanisms could be determined for these AE events. This approach was applied to the *in situ* rock mass in the NW sidewall of the test tunnel in conjunction with the Ed-exs to determine the level of activity at various distances from the tunnel wall. From these data, the distribution of acoustic emissions relative to the excavation were determined (Carlson and Young 1993). Findings from this study are summarized in Section 4.3.2.

2.3.5 Geophysical Monitoring

Information on the P and S wave velocities in the rock mass was obtained through several tomographic surveys carried out with AECL's miniCHARTS system between the various excavated openings prior to excavation of the test tunnel (Hayles et al. 1995). This study required two 40- and twenty 1.5-m-long vertical boreholes in the floor of Room 409 and roof of Room 413. Cross-hole tomographic studies were conducted in the Bof-ex instrument boreholes before and after excavation of the test tunnel to detect changes in the rock mass resulting from excavation-induced damage (Hayles et al. 1995). The results from these studies are summarized in Section 4.3.2.

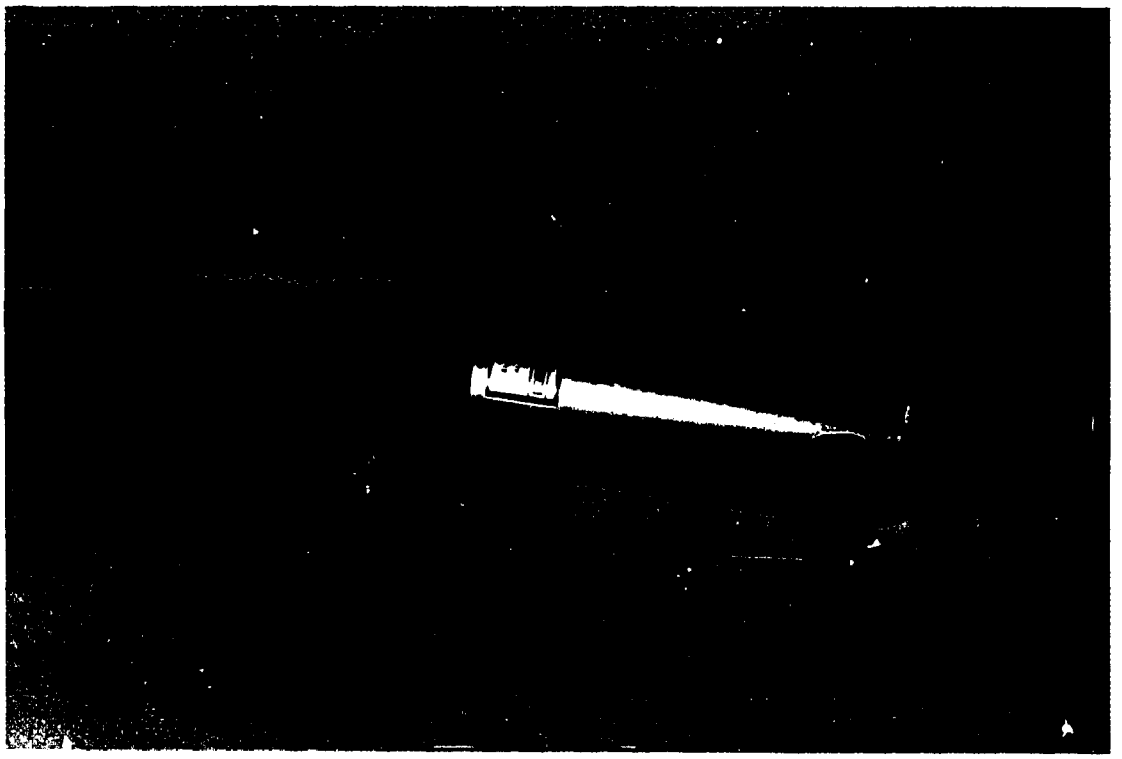

FIGURE 20: Photograph showing a typical triaxial accelerometer sensor. This sensor fits in a 96-mm-diameter (HQ size) borehole.

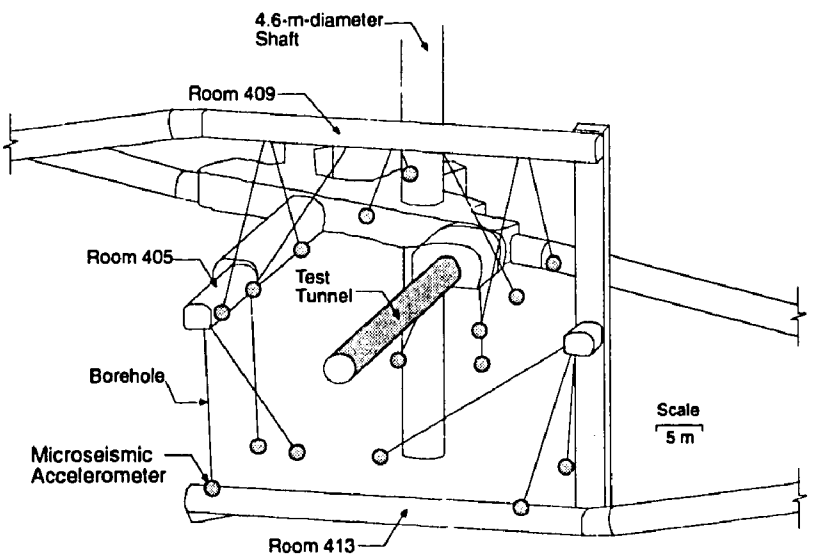

FIGURE 21: Arrangement of the AE/MS triaxial accelerometer sensors around the test tunnel at the 420 Level.

2.3.6 Other Instruments

In addition to the instruments described in the previous sections, three instrumented concrete cylinders were installed in boreholes near the Mine-by test tunnel. This type of strain-monitoring cell is called le cylindre instrumenté de l'Université de Sherbrooke (CIUS). These cells were included in the Mine-by Experiment as a test of their suitability as strain-monitoring devices. The results of the monitoring phase are discussed in Saleh et al. (1992), but no back analysis of stresses from the measured strains was attempted.

2.4 SUMMARY

Pre-excavation characterization of the 420 Level was used to locate a representative site for the experiment, and provided a basis for the final detailed design and development of the Mine-by Experiment. The area chosen for the experiment was found to typify the 420 Level in terms of geology, geotechnical properties and *in situ* stresses.

Underground development was conducted according to the design plan, with slight modifications to the planned excavation sequence for the last 12 m of the tunnel. Instead of using a careful drill-and-blast technique and full-face sequence in this region, line-drilling with mechanical breakout was employed in conjunction with a pilot-and-slash sequence. This change was made to ensure potentially disruptive percussive effects from blasting were eliminated. In addition, Rounds 18 to 21 were excavated as 0.5-m-long rounds instead of the usual 1.0-m length to enhance the number of data points collected near the final two instrumented arrays.

The instrumentation for the Mine-by Experiment was installed in accordance with the design plan. New instruments, such as the Ed-ex, were developed in the course of the experiment and were used to provide additional information on the rock mass behaviour. With the exception of nine of the 210 displacement transducers, the extensometers performed exceptionally well during the main monitoring period of the experiment. Likewise, only one of the 12 CSIRO HI triaxial strain cells appeared to malfunction over the course of the experiment. In total, over 500 data channels were monitored during the main excavation stage of the Mine-by Experiment.

3. ROCK MASS BEHAVIOUR AND FAILURE MECHANISMS

The pre- and post-failure behaviour of Lac du Bonnet granite has been studied extensively in laboratory tests on rock samples. However, interpretation of *in situ* behaviour based on laboratory findings is not straightforward, even for the relatively uniform and unfractured rock mass at the 420 Level of the URL. For example, results from triaxial compression tests have been used to determine a Hoek-Brown failure envelope (Hoek and Brown 1980), given by

$$\sigma_1 = \sigma_3 + \sqrt{m\sigma_c\sigma_3 + s\sigma_c{}^2} \qquad (1)$$

where σ_1 and σ_3 are the maximum and minimum principal stresses, respectively, σ_c is the uniaxial compressive strength of an intact laboratory sample, m is a shape parameter, and s

is a scaling factor to account for the presence of joints or discontinuities *in situ*. Equation 1 is a peak strength criterion, and in the unconfined case reduces to

$$\sigma_1 = \sqrt{s}\sigma_c \tag{2}$$

In cases where there are no *in situ* joints or discontinuities, i.e., $s = 1$, Equation 2 implies that the uniaxial stress required to cause failure *in situ* is equivalent to the uniaxial compressive strength measured in the laboratory.

Several factors can, however, affect the uniaxial compressive strength of laboratory samples, e.g., sample size and loading rate (Martin 1993). In a comparative study of undisturbed Lac du Bonnet granite from Cold Spring Quarry and disturbed Lac du Bonnet granite from the Mine-by Experiment at the 420 Level, Martin and Stimpson (1994) also noted that the laboratory properties, particularly the uniaxial compressive strength, were a function of sample disturbance. Samples taken from a stress environment where the far-field maximum stress was greater than about $0.1\sigma_c$ displayed lower laboratory strengths than samples from areas where the far-field maximum stress was less than $0.1\sigma_c$. This finding implies that the disturbed samples are not representative of the *in situ* undisturbed rock mass. Figure 22 gives the Hoek-Brown failure envelopes for undisturbed and for disturbed Lac du Bonnet granite. Note that the envelope for disturbed granite falls below that for undisturbed granite, and can be described using the undisturbed σ_c value, but decreasing the s and m values to reflect the presence of small microcracks typical of sample disturbance in brittle rocks. Alternatively, if sample disturbance had not been recognized in the 420 Level granite samples, the parameters describing the lower failure envelope would be $\sigma_c = 157.0$ MPa, $m = 35.21$ and $s = 1$.

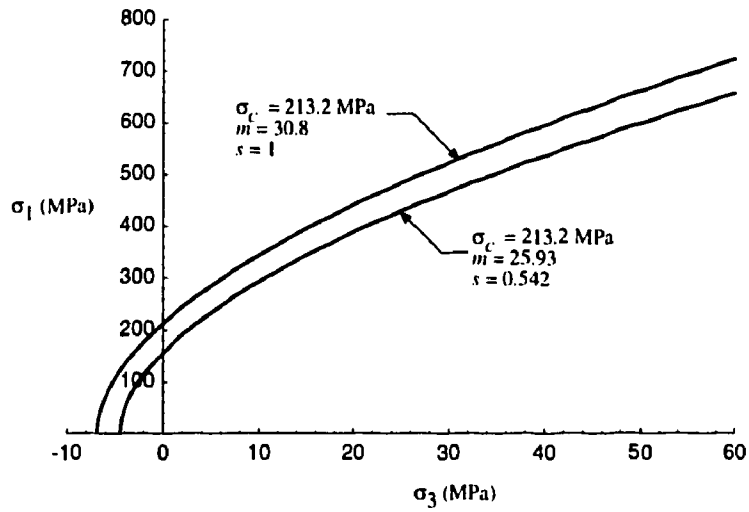

FIGURE 22: Hoek-Brown failure envelope for undisturbed and disturbed Lac du Bonnet granite taken from Cold Spring Quarry and from the 420 Level of the URL, respectively. Envelopes are based on 147 tests for undisturbed granite and 37 tests for disturbed granite (after Martin 1993).

In comparing the back-calculated strength of the rock mass at the perimeter of an underground opening to the uniaxial compressive strength measured in the laboratory, it is common to find the *in situ* strength to be less than half of the laboratory strength (Pelli et al. 1991; Stacey 1981; Myrvang 1991; Herget 1988). This discrepancy in strengths is generally attributed to 'scale-effects', as the laboratory strength is determined on intact samples containing small-scale flaws such as grain boundaries, whereas the rock mass generally contains much larger-scale flaws such as joints/discontinuities. In such cases, s is by definition less than 1.

For the massive granite at the 420 Level of the URL, s is taken as 1 because there are no *in situ* joints or discontinuities to consider. Nevertheless, the back-calculated strength of the rock mass at the perimeter of tunnels at this level is significantly less than that measured in short-term laboratory tests (Martin and Read 1992). Hence, the reduced *in situ* strength cannot be attributed solely to 'scale-effects'.

To determine the factors contributing to the reduced *in situ* strength around tunnels at the 420 Level, an extensive laboratory and *in situ* testing program was undertaken. These studies were intended to characterize the mechanical behaviour of Lac du Bonnet granite, and the processes involved in progressive failure, in both laboratory tests and *in situ*. The studies are summarized in the following sections, and emphasize the potential problems in relying solely on results from laboratory tests to interpret *in situ* behaviour.

3.1 COMPRESSION TESTS ON CYLINDRICAL LABORATORY SAMPLES

Testing procedures for determining the compressive deformational behaviour of rock samples are given by ISRM (Brown 1981). These include recording the axial (ϵ_{axial}) and lateral ($\epsilon_{lateral}$) strains in a sample as it is loaded with or without a fixed confining stress. For a cylindrical sample subjected to axial loading, with or without a confining stress, and under small strains, the volumetric strain (ϵ_v or $\frac{\Delta V}{V}$) is given by:

$$\epsilon_v = \frac{\Delta V}{V} \simeq \epsilon_{axial} + 2\epsilon_{lateral}. \tag{3}$$

Hence by plotting the axial, lateral and the calculated volumetric strains versus the applied axial stress, the loading path of a rock sample to failure can be followed. An example of axial, lateral and volumetric strain versus axial stress curves for Lac du Bonnet granite in uniaxial compression is given in Figure 23.

The stress-strain curves for a brittle material can be divided into five regions (Figure 23). The three most important points on the stress/strain curve are the crack-initiation stress, the crack-damage stress and the peak stress or strength. These points define the transitions between Regions II, III, IV and V.

The onset of stable crack growth, i.e., dilation, marks the beginning of Region III on the stress/strain curve. Brace et al. (1966) found that stable crack growth begins at a stress level of about 0.3 to 0.5 of the peak strength. This stable crack growth is only registered on

the lateral strain gauge, and hence, reflects the growth of axial cracks, i.e., cracks parallel to the direction of the maximum applied load. This stress level is referred to as the crack-initiation stress (σ_{ci}) and can be determined from a plot of crack-volumetric strain versus axial strain. As shown in Figure 23, σ_{ci} is the axial stress at which dilation just begins on the crack-volume plot.

The axial stress level where the total volumetric strain reversal occurs marks the beginning of Region IV and represents the onset of unstable crack growth, as defined by Bieniawski (1967). This axial stress level is typically between 0.7 to 0.85 of the short-term peak strength, and it is at this level that the axial strain departs from linearity (Figure 23). The dominant mechanism resulting in such an increase in axial strain is sliding along inclined surfaces. Lajtai et al. (1991) found that unstable crack growth started at about 0.7 of the short-term peak strength in unconfined samples of Lac du Bonnet granite from Cold Spring Quarry. Martin and Chandler (1994) referred to this stress level as the crack-damage stress (σ_{cd}) because loads above this level result in damage to the material which cannot be tolerated under a permanent load. They found that the crack-damage stress for Lac du Bonnet granite from the URL also occurred at about 0.7 to 0.8 of the short-term peak strength.

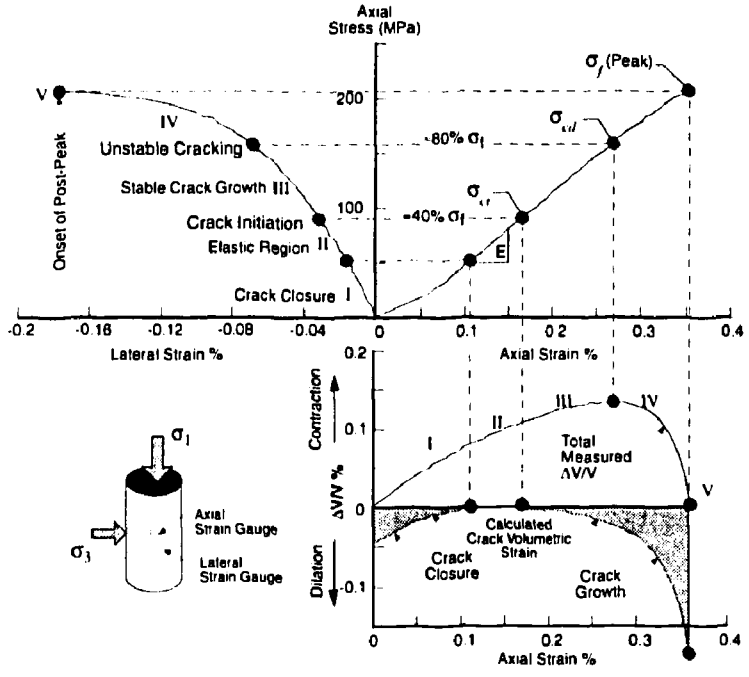

FIGURE 23: Stress-strain diagram obtained from a single uniaxial compression test for Lac du Bonnet granite showing the definition of crack initiation (σ_{ci}), crack damage (σ_{cd}) and peak strength (σ_f). Note that only the axial and lateral strains are measured. The volumetric strain and crack-volumetric strain are calculated.

The peak strength of the material (σ_f) marks the beginning of post-peak behaviour, Region V, and is almost universally used to establish the failure strength envelope. For the unconfined case, the peak strength strength is referred to as σ_c. Martin and Chandler (1994) showed that, of the three characteristic stress levels, only σ_{ci} and σ_{cd} were true material parameters independent of sample volume, and that the peak strength was a function of the particular loading conditions used in the uniaxial test.

3.1.1 Damage-Controlled Tests

Martin and Chandler (1994) presented the results from an extensive set of damage-controlled compression tests that were carried out on samples of Lac du Bonnet granite from the 420 Level to investigate the effect of crack damage on σ_{ci}, σ_{cd} and σ_f. They defined a damage parameter ω as the accumulated permanent volumetric strain

$$\omega = \sum_{i=1}^{n} (\epsilon_v^p)_i \, \%. \tag{4}$$

where ϵ_v^p is the permanent volumetric strain per damage increment i. Plots of σ_f, σ_{cd} and σ_{ci}, versus the damage parameter ω for any one test are referred to as the peak ω locus, the σ_{cd} locus and the σ_{ci} locus (Figure 24).

Based on the test results, the σ_{ci} stress occurs when the load first exceeds about 0.2 to 0.4 of the peak strength (Figure 24). The σ_{cd} stress occurs at about 0.8 of the peak strength. However, unlike the σ_{ci} stress, the σ_{cd} stress reduces significantly in the early stages of the test and reaches a threshold as the damage accumulates in the sample (Figure 24). This phenomenon was seen at all confining stress levels and was quite consistent from test to test. It should, however, be noted that the drop in σ_{cd} is smaller at higher confining stresses (Figure 25). This fact suggests that the growth of cracks and accumulation of damage is more inhibited at higher confining stresses, and hence the strength reduction experienced during the test is less, than at lower confining stress. Martin (1993) pointed out that the threshold value of σ_{cd} corresponds approximately to σ_{ci} when the sample is unconfined, and that as the confining stress is increased, the threshold value of σ_{cd} exceeds σ_{ci}.

Martin and Chandler (1994) showed that the measured σ_{cd} locus could be simulated using the Griffith sliding crack model proposed by Cook (1965). They also showed that the limit for sliding can be expressed as

$$\sigma_1 = 2\sqrt{\frac{2\alpha G}{c\pi(1-\nu)}} \tan\left(45 + \frac{\phi}{2}\right) + \sigma_3 \tan^2\left(45 + \frac{\phi}{2}\right) \tag{5}$$

where ϕ is the friction angle, α is the fracture surface energy, c is the crack half-length, G is the shear modulus and ν is Poisson's ratio.

The shear strength of a frictional material is also often represented by the well-known Mohr-Coulomb criterion

$$\sigma_1 = 2S_o \tan\left(45 + \frac{\phi}{2}\right) + \sigma_3 \tan^2\left(45 + \frac{\phi}{2}\right) \tag{6}$$

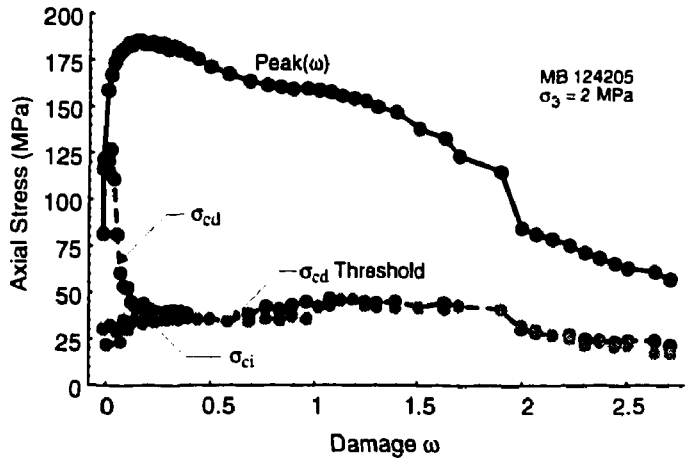

FIGURE 24: Example of the crack-initiation stress and the crack-damage stress as a function of damage. Note that at low confining stresses, the crack-damage stress quickly approaches the crack-initiation stress.

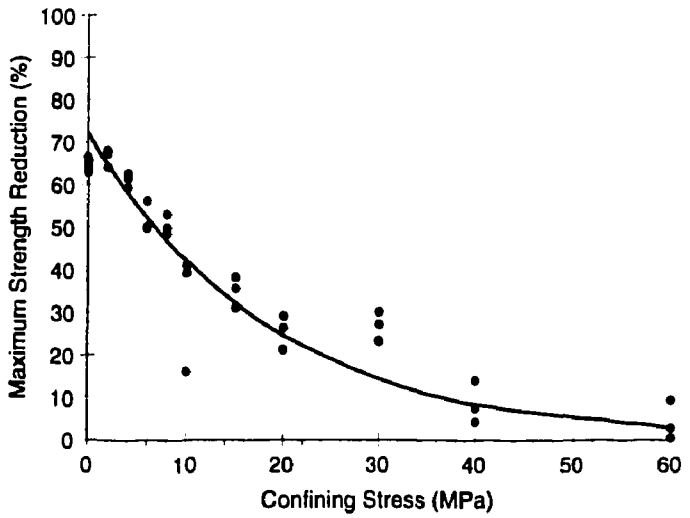

FIGURE 25: Reduction in crack-damage stress from initial to residual value for 37 damage-controlled compression tests. The maximum strength reduction is the difference between the initial and residual values, normalized to the initial value. Note that strength reduction is more pronounced at low confining stress.

where S_o is the empirical cohesion intercept or intrinsic strength. It is interesting to note that the two shear criteria in Equation 5 and Equation 6 are identical. The empirical cohesion of Equation 6 is expressed in terms of fracture surface energy and crack half-length in Equation 5. The Cook criterion provides a fundamental energy balance basis for the Mohr-Coulomb criterion.

Martin and Chandler (1994) used the concepts introduced by Equations 5 and 6 to interpret the stress/strain results from a laboratory compression test in terms of friction and cohesion (Figure 26). In Figure 26, the damage has been normalized with respect to the maximum value of the damage parameter ω at the end of the test and the strength has been normalized to the peak strength. Figure 26 illustrates that the peak friction angle ($\phi_{b+i} = 63°$) is reached only when most of the cohesion is lost. With increasing damage, the friction angle gradually decreases to about 42°. This friction value is similar to the residual friction angle of 42 to 45° for Lac du Bonnet granite reported by others, e.g., Gyenge et al. (1991); Lajtai and Gadi (1989). Thus, for the test presented in Figure 26, it appears that the

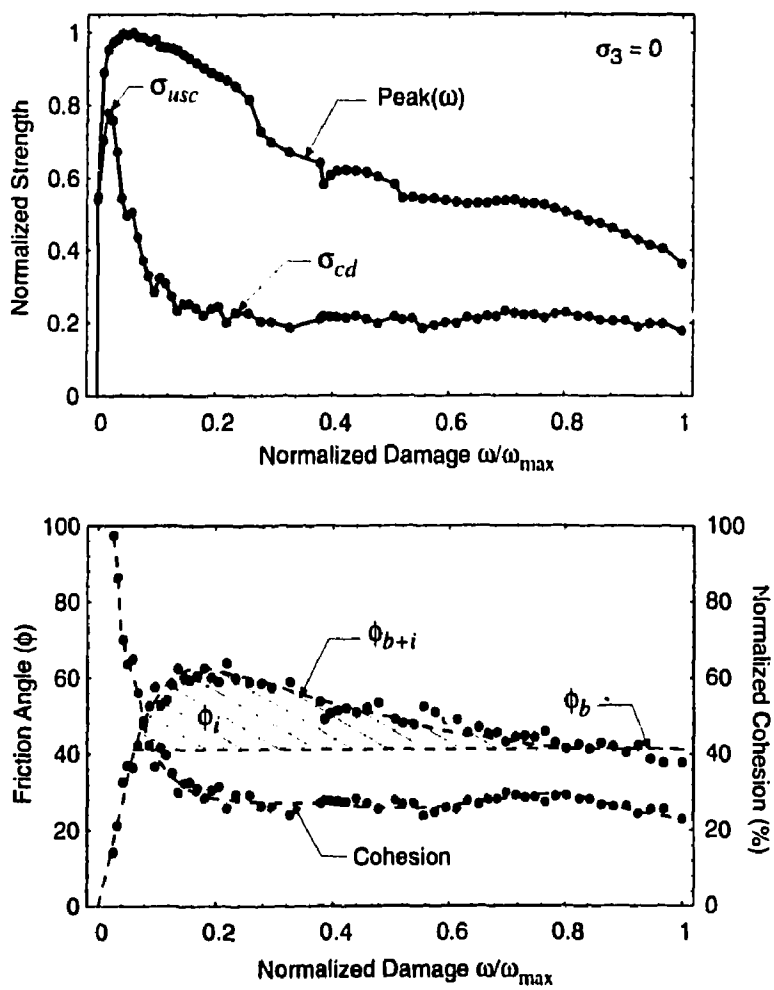

FIGURE 26: Mobilization of friction and cohesion as a function of normalized damage.

residual friction angle is nearly reached. The peak friction angle of 63°, although high, is not unrealistic, e.g., Dusseault and Morgenstern (1979) reported that natural slopes of uncemented locked sands have inclinations greater than 54°. Therefore, 63° does not seem unreasonable for perfectly interlocked mineral grains subjected to small displacements.

Figure 26 also shows that the friction and cohesion components of strength are not mobilized at the same amount of damage. For example, prior to any damage, the rock strength is composed only of cohesion, i.e., friction has not been mobilized and therefore $\phi = 0$ initially. For this condition, Equations 5 and 6 reduce to

$$\sigma_1 - \sigma_3 = \text{ constant } = 2S_o \tag{7}$$

An examination of Equation 5 reveals that the fracture surface energy and crack half-length only apply to the cohesive component of the material and that the frictional strength is not dependent on these parameters. This point is particularly important because it demonstrates that a small increase in crack half-length can have a significant impact on the cohesion or unconfined strength of a material. For example, if a crack half-length of 1 mm is used to represent a material with an average grain size of 2 mm, and the crack half-length is increased to 3 mm, the strength (cohesion) is reduced by approximately 42% (Figure 27).

It is also worth noting that a further 3-fold increase in crack half-length to 9 mm only results in a further decrease in cohesion of about 25% relative to the initial value for a 1 mm crack half-length. Thus initial crack extension of as little as 1 or 2 mm is significant. Laboratory test results (Martin 1993) showed that the cohesion in an unconfined sample

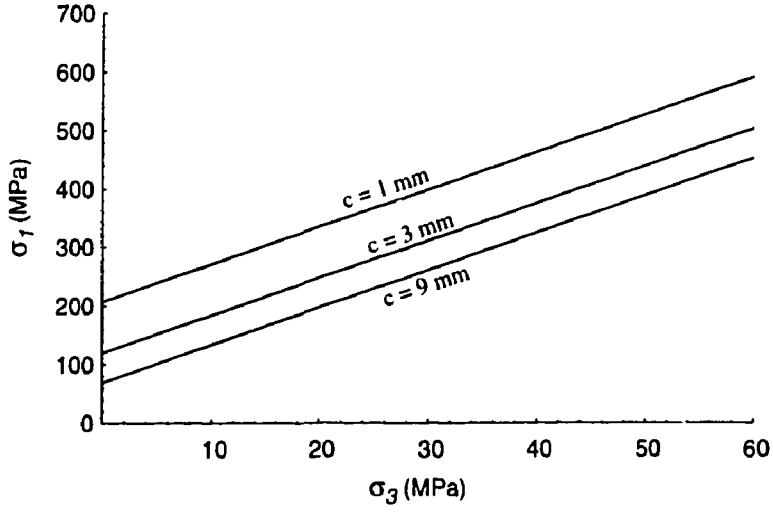

FIGURE 27: Predicted failure envelopes for Lac du Bonnet granite with different crack half-lengths using the sliding crack model given by Equation 5. Note that the increase in crack half-length only affects the cohesion (y-intercept) and not the friction angle (slope).

can be reduced by 70% when the permanent axial strain is as little as 0.03%. Assuming an initial 1 mm crack half-length, this reduction would result from extension of the crack half-length to 11 mm. It is likely that the laboratory-measured permanent strain needed to cause the cohesion loss is greater than that which would be required to cause a similar loss *in situ* because, *in situ*, the rock is more brittle than the disturbed laboratory samples. These results support the idea that the strength reduction of the disturbed samples given in Figure 22 is a consequence of cohesion loss.

In summary, the monotonic loading path in uniaxial and triaxial laboratory tests revealed that the true strength of a brittle rock in compression is defined by the crack-damage stress σ_{cd}, which occurs at about 0.7 to 0.8 of the peak strength (σ_f in Figure 23). At the crack-damage stress level, a macro sliding crack forms and provides a mechanism for ultimate collapse of the sample. Loads above the crack-damage stress value can be maintained for a short duration, i.e., typically less than 1 h, as the frictional resistance of the macro crack is mobilized. However, the mobilization of the frictional resistance results in a dramatic decrease in the initial cohesion of the sample. This decrease in cohesion is a function of the volumetric crack damage in the sample, and hence, is very sensitive to crack half-length.

3.2 LABORATORY AND *IN SITU* STUDIES OF BOREHOLE FAILURE

The laboratory study of cylindrical samples showed that the long-term strength was about 0.7 to 0.8 of the peak strength σ_f. In this section, a comparison is made between the strength around boreholes in the laboratory and *in situ*.

3.2.1 Physical Model Studies

Laboratory studies to investigate the strength around openings typically consist of either hollow-cylinder tests similar to those carried out by Ewy and Cook (1990) or large block tests containing a cylindrical cavity (Figure 28). The latter test is more common as it allows either uniaxial or biaxial loading. The failure in these block tests occurs in the region of

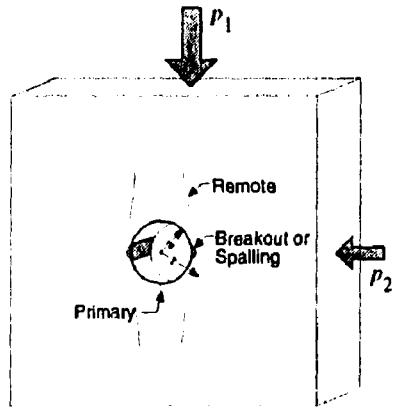

FIGURE 28: Types of fractures found around circular openings in laboratory model tests.

maximum tangential stress around the boundary of the circular opening which is similar to the failure observed *in situ*. The tangential stress around a circular opening, for plane strain conditions, is given by Jaeger and Cook (1979) as

$$\sigma_\theta = \frac{p_1 + p_2}{2}\left(1 + \frac{a^2}{r^2}\right) + \frac{p_1 - p_2}{2}\left(1 + \frac{3a^4}{r^4}\right) \tag{8}$$

where p_1 and p_2 are the applied loads (Figure 28). At the boundary of the opening, $a = r$ and $\sigma_\theta = 3p_1 - p_2$ where $p_1 > p_2$. For the unconfined case, $p_2 = 0$ and the maximum tangential stress at the breakout is $3p_1$.

The effect of size and stress gradients on the failure strength around boreholes has been examined by many researchers using various physical models, e.g., Carter (1992); Ewy and Cook (1990); Haimson and Herrick (1989); Mastin (1984); Hoek (1965). One of the commonly reported outcomes of such tests is that the tangential stress at the boundary of the borehole required to cause breakouts is at least twice the unconfined compressive strength of the material as determined in standard uniaxial tests on solid cylinders.

Martin et al. (1994) reported the results from a series of block tests carried out to investigate the effect of borehole diameter on the sidewall stress required to initiate failure in samples of Lac du Bonnet granite. Thirteen unconfined samples were tested with circular openings ranging in diameter from 5 to 103 mm. Strain gauges were used to monitor the deformations and to determine the onset of breakouts (Martin 1993). The placement of strain gauges on each sample was modified depending on sample size. The results from the thirteen tests are plotted in Figure 29 along with the results from similar tests carried out by Haimson and Herrick (1989), Carter (1992), and Mastin (1984). All results show similar trends and indicate that, with borehole diameters greater than about 75 mm, the sidewall stress required to initiate spalling is about equal to the unconfined compressive strength of the

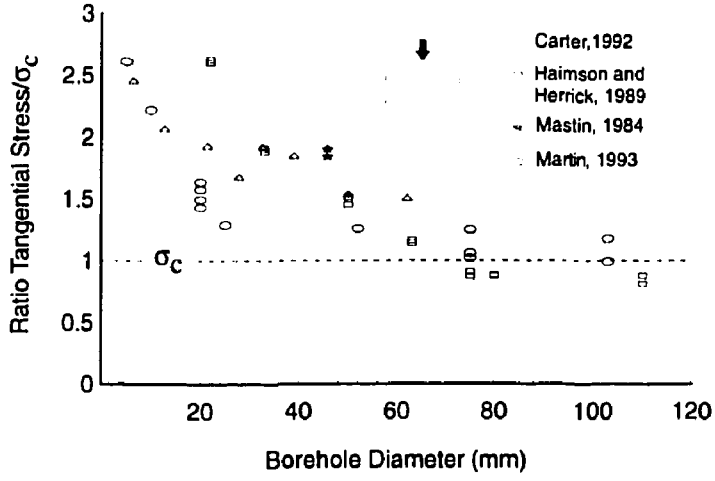

FIGURE 29: Summary of uniaxial testing of blocks containing a circular borehole.

granite. However, the results also show that a significant strength-scale effect is observed for borehole diameters of 20 mm and less.

Carter (1992) and Lajtai (1972) proposed that the strength-scale effect observed in Figure 29 was related to microcracking occurring in the region of high stress gradients, and that the strength-scale effect could be approximated by a stress averaging technique given by

$$\overline{\sigma}_\theta = \frac{p(a+t)}{t}\left\{1 - \frac{a^2}{2(a+t)^2} - \frac{a^4}{2(a+t)^4}\right\} \tag{9}$$

where $\overline{\sigma}_\theta$ is the average maximum tangential stress for a borehole subjected to a uniaxial load p, a is the borehole diameter and t is the distance over which the tangential stress is averaged. Equation 9 was fitted to the Lac du Bonnet granite data and gave a value of t = 13.9 mm (Figure 30). The strength-scale relationship for the uniaxial compressive strength for Lac du Bonnet granite was given by Martin et al. (1994) as

$$\sigma_c/\sigma_{c63} = (63/d)^{0.17} \tag{10}$$

where σ_{c63} is the uniaxial compressive strength of a 63-mm-diameter specimen, and d is the diameter of the specimen in mm. Equation 10 is also shown in Figure 30 for comparison.

What is most obvious in Figures 29 and 30 is the significant increase in the tangential stress required to cause failure for circular openings less than about 75 mm in diameter. Because most laboratory studies are carried out with circular openings of 25-mm diameter or less, a scale effect of at least 2 should be anticipated when comparing the ratio of tangential stress required to cause breakouts to the unconfined compressive stress (Figure 29). However, it would appear that when the circular opening is at least 75 mm in diameter, the strength is close to the unconfined compressive strength and the apparent scale effect is either absent or significantly reduced.

The phenomenon of increased strength around small-diameter boreholes has also been reported for samples tested in biaxial and polyaxial loading. Lee and Haimson (1993) carried

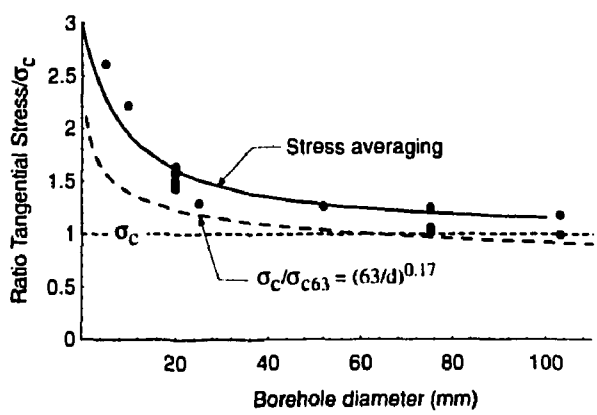

FIGURE 30: Tangential stress required to cause borehole breakouts in Lac du Bonnet granite compared with the strength predicted by Equations 9 and 10.

out polyaxial testing of forty 100-mm cubes of Lac du Bonnet granite containing a 21-mm-diameter borehole. They also found that the tangential stress required to initiate breakouts varied from 1.5 to $2\sigma_c$. Martin (1993) tested one block of Lac du Bonnet granite containing a 60-mm-diameter borehole using a biaxial loading system, and found that the tangential stress required to initiate breakouts was $1.6\sigma_c$. Both the results of Lee and Haimson (1993) and Martin (1993) are in keeping with the scale effect shown in Figure 29. It appears that the strength-scale effect is not related to the type of loading conditions, i.e., one-, two- or three-dimensional, but is a consequence of the stress gradient in the vicinity of the hole or excavation.

3.2.2 *In Situ* Borehole Studies

In order to determine whether or not the strength-scale effects observed in the laboratory were present *in situ*, a series of vertical boreholes with diameters of 75, 150, 300, 600 to 1250 mm were diamond-drilled to a nominal depth of 5 m from the floor of Room 405 at the URL (Figures 31).

Failure, if it occurred, formed immediately during the drilling of the boreholes. The failure in the boreholes extended from the floor of Room 405 to various downhole depths depending on the diameter of the borehole, i.e., the larger the borehole diameter, the longer the breakout, suggesting a scale-effect. The lengths of the breakouts were recorded immediately after drilling and were monitored periodically after completion of the hole. Only minor changes in the lengths of the breakouts were observed over nearly two years of monitoring.

The stress concentrations below the floor of Room 405 decrease with the depth along each borehole. Thus the tangential stress at the point where each breakout ends will also vary.

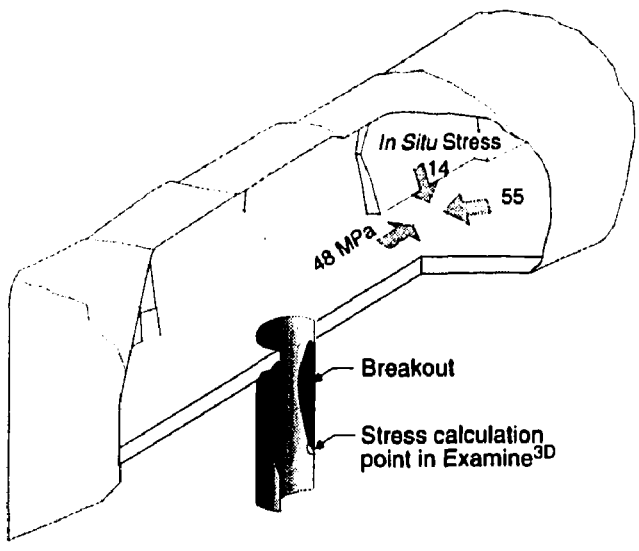

FIGURE 31: Illustration of the three-dimensional geometry used to calculate the stress at the initiation of failure.

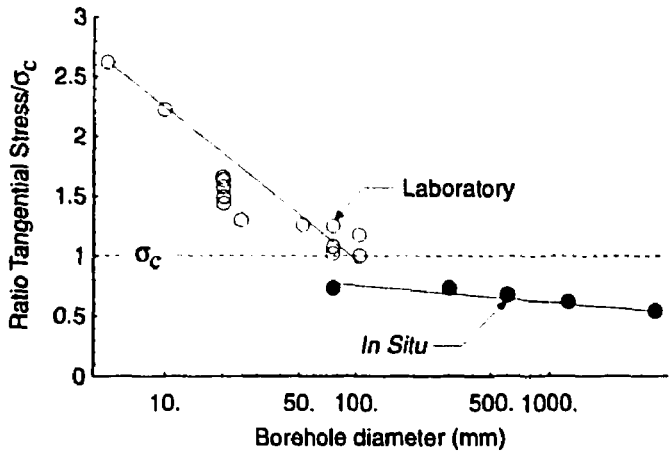

FIGURE 32: Ratio of the calculated tangential stress to σ_c at which breakouts initiate for various borehole diameters.

An elastic three-dimensional stress analysis of Room 405 and each borehole in the floor was carried out using EXAMINE^{3D} (Curran and Corkum 1993) to determine the maximum tangential stress at which the failure terminated (Figure 31). This stress value was considered equivalent to the tangential stress at the initiation of failure in the laboratory studies.

Figure 32 shows the calculated maximum tangential stress required to initiate breakouts normalized to σ_c for the borehole diameters investigated. Also shown, for comparative purposes, is the laboratory data from Figure 30 and the result from the Mine-by test tunnel (discussed in the next section). Figure 32 shows that there is a modest effect of scale for the *in situ* data, and that there is a noticeable change in the effect of scale between the laboratory and *in situ* results. This is also supported by the observation that a 75-mm-diameter borehole drilled near the centre of, and in the same direction as, the test tunnel showed breakouts similar to those observed in the test tunnel.

In summary, laboratory tests involving boreholes with diameters less than about 75 mm tend to show a marked scale/size effect, and require a maximum tangential stress of up to $2\sigma_c$ to initiate breakouts. In contrast, *in situ* boreholes with diameters greater than 75 mm required a maximum tangential stress of as little as $0.5\sigma_c$ to initiate breakouts. In addition, the change in slopes between the *in situ* and laboratory strength versus borehole diameter shown in Figure 32 suggests that there is a fundamental difference between the results from the two sets of experiments. In the laboratory tests, the incremental loading path is monotonic and linear. However, *in situ*, the loading path is complex and non-linear. This issue is discussed in the next section.

3.3 PROGRESSIVE FAILURE AROUND A CYLINDRICAL TUNNEL

The stress distribution around the advancing face of a tunnel is complex. For instance, elastic three-dimensional analyses of the Mine-by test tunnel (Figure 33) showed that, at a few centimetres from the tunnel perimeter, the principal stress magnitudes change rapidly

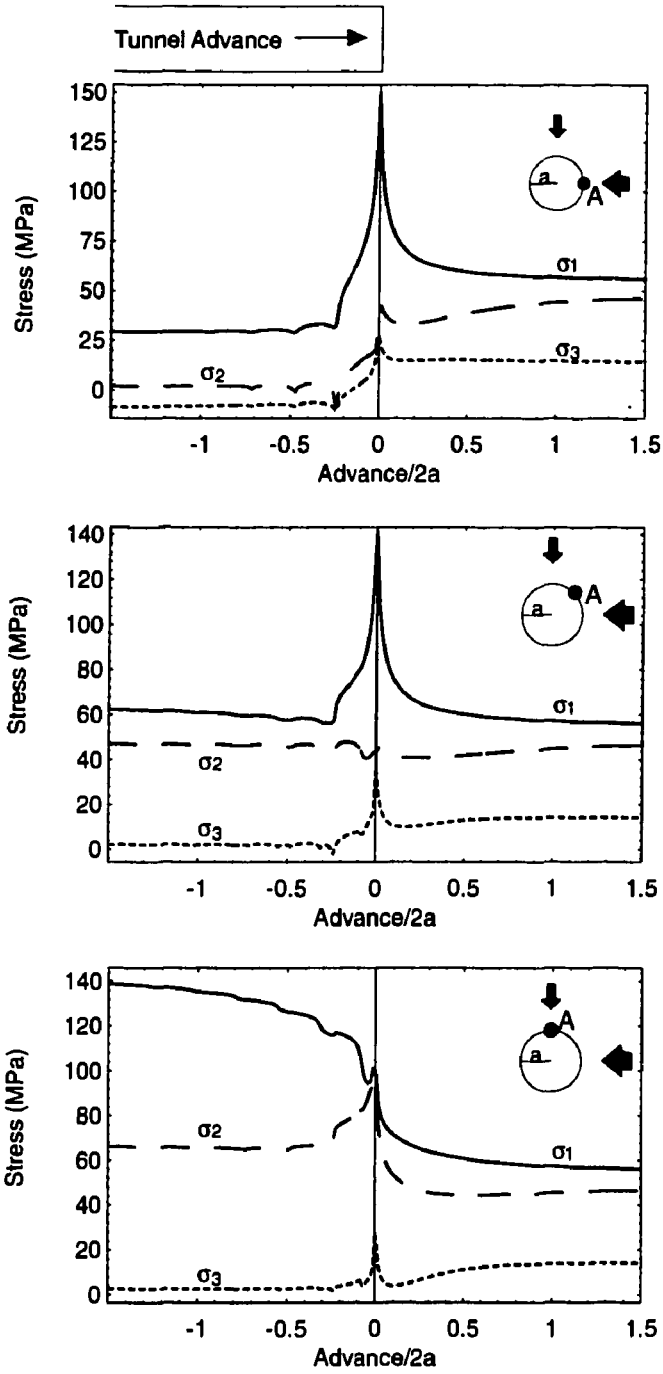

FIGURE 33: Change in principal stress magnitudes around a flat-faced cylindrical tunnel as the tunnel advances. The slight perturbations in the responses are a result of the field points in the model being very close to the tunnel surface.

near the tunnel face. These stress changes are not accounted for in the two-dimensional plane strain analyses that are usually carried out to back calculate the *in situ* strength around a tunnel.

In Section 3.1, it was shown that the first step in the brittle failure process is crack initiation. In the following sections, the role of *in situ* crack initiation in the progressive failure process observed in the Mine-by test tunnel is investigated.

3.3.1 Microseismic Monitoring

It is well known that cracking occurs around an opening excavated in a highly stressed brittle rock mass. For example, earlier work at the URL had established that considerable microseismic activity was associated with the excavation, by drill-and-blast techniques, of a circular shaft from the 240 Level to the 420 Level (Talebi and Young 1992). In order to determine whether or not the microseismic activity was caused by the blasting or simply related to stress redistribution, the test tunnel for the Mine-by Experiment was excavated mechanically, without blasting (see Section 2.2.2).

As described in Section 2.3.4, an array of 16 triaxial accelerometers was installed to monitor the stress-induced microseismicity associated with the excavation of the test tunnel (Figure 34). As shown in Figure 34(a), the accelerometers were grouted in place at the end of diamond-drilled boreholes. The accelerometer array was designed for focal sphere coverage and a source location accuracy of about ±0.25 m near the centre of the tunnel. The sampling rate was set to 50 kHz and the overall system frequency response was 50 Hz to 10 kHz (±3 dB). The dynamic range of the system allowed the study of seismic events with moment magnitudes as small as -6.

The sequencing of the construction schedule for the test tunnel provided about 12 h of quiet time for microseismic monitoring after the initial perimeter drilling and about 12 h of quiet time for microseismic monitoring after mechanical breaking of the rock stub for each round of tunnel advance. Since each round required about 3 days to complete, this provided coverage of approximately 30% of the total excavation cycle per round. This procedure was used for most of the excavation rounds near the start and end of the test tunnel. However, near the instrument arrays, the microseismic monitoring period was extended, e.g., at Round 17 the monitoring period was 193 h. A typical example of the locations of the microseismic events recorded during the 12 h monitoring period after advancing the excavation by 1 m is given in Figure 35.

Preliminary processing of the microseismic data was carried out in the field using automated source location computer software developed at Queen's University (Collins and Young 1992). Over 25 000 events were detected and some 3500 events were source located in this way (Figure 36). Note that the clustering of events in the roof and floor in Figures 35 and 36 confirms that the maximum stress is inclined relative to the horizontal. Additional processing of the 25 000 events was carried out using seismicity software developed in South Africa (ISS 1994). With this automated processing, the main source parameters, related to event magnitude, size and stress drop, were calculated using the assumption of shear failure. Although a previous detailed study of 33 microseismic events from the test tunnel

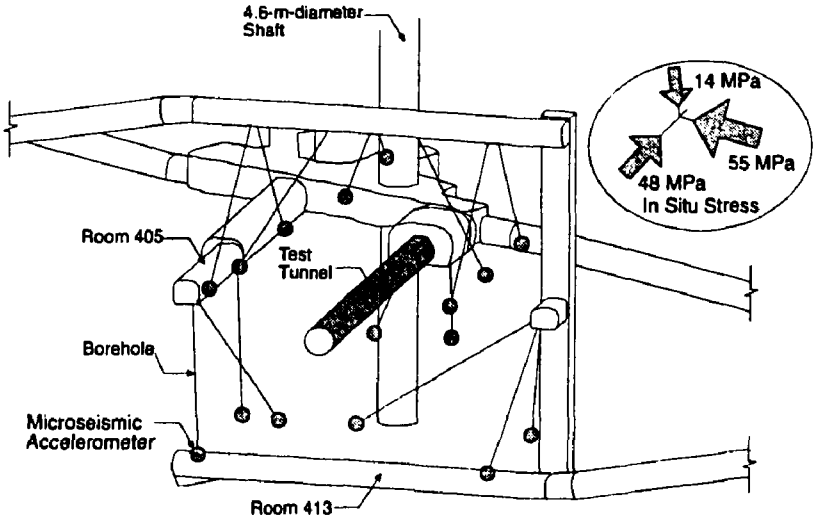

(a) 420 Level Layout

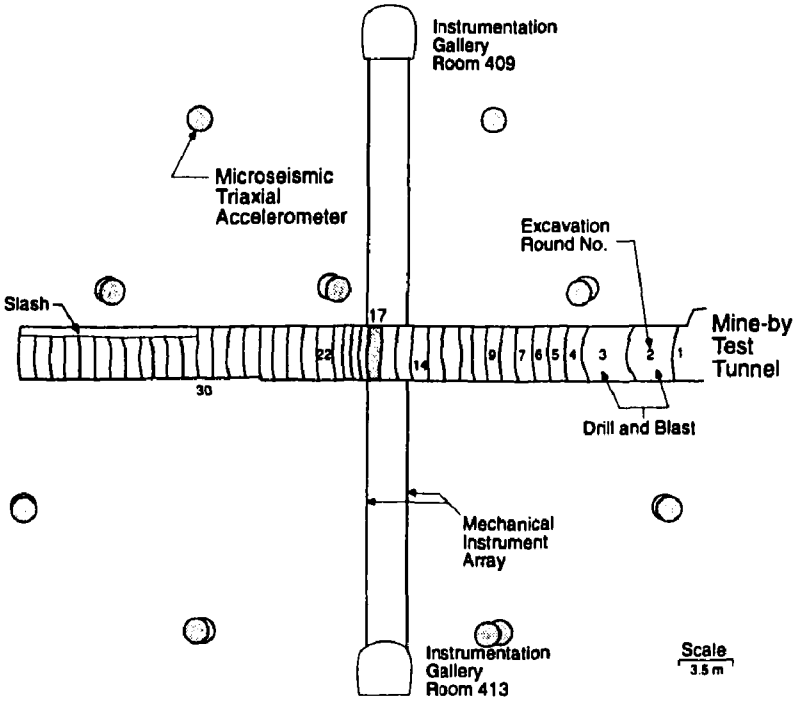

(b) Vertical Section

FIGURE 34: Layout of the 420 Level showing the location of the Mine-by test tunnel, the microseismic triaxial accelerometers and Round 17. The *in situ* principal stress magnitudes used for analysis are $\sigma_1 = 55$, $\sigma_2 = 48$ and $\sigma_3 = 14$ MPa.

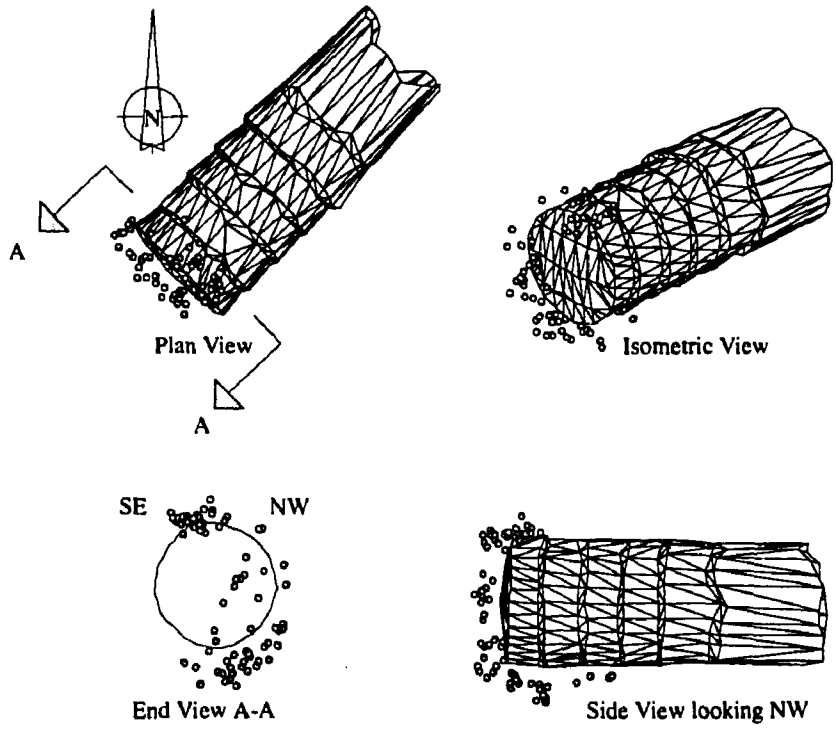

FIGURE 35: Location of the microseismic events recorded during the 12 h monitoring period after excavation of Round 8.

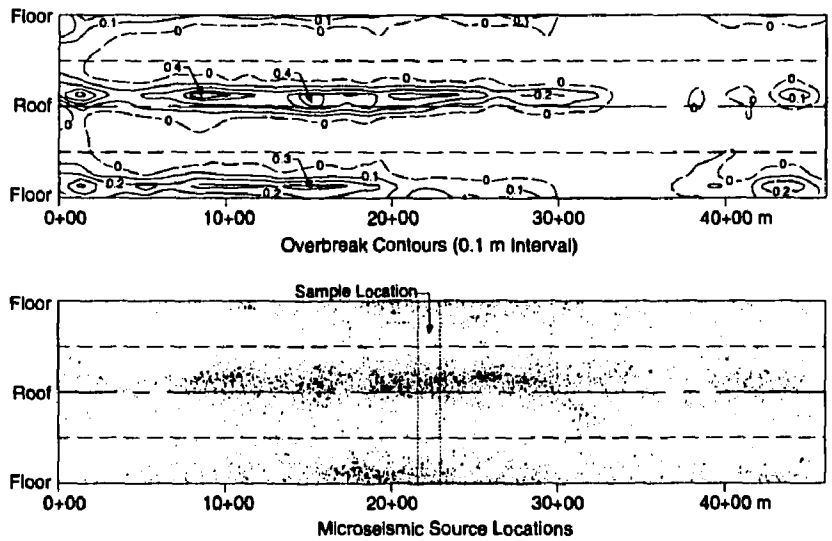

FIGURE 36: Extent of breakouts and location of the computer-picked microseismic events for the test tunnel plotted on unrolled perimeter maps. Also shown is the location of the sample volume chosen for a detailed analysis.

by Feignier and Young (1993) revealed that about 50% of the events had a significant non-shear component, this study was carried out to determine general trends in the data set (Collins et al. 1994). Only the microseismic events between tunnel chainage 10.51 and 34.28 m were analyzed (Rounds 6 to 30 in Figures 34(b) and 36), as the stress conditions, geology and excavation sequence are more complex near the ends of the test tunnel.

3.3.1.1 Source Parameters

Each excavation round between chainage 10.51 and 34.28 m was processed individually, and the location of each microseismic event relative to the tunnel face position X was normalized with respect to the tunnel diameter $2a$. Results are shown in Figure 37. Events ahead of the face are indicated by a positive value of $X/2a$, while those behind the face are negative. Only those microseismic events recorded in the roof of the test tunnel are summarized here because the formation of a breakout notch in the roof was not constrained by construction activities. However, analyses of the complete data set show similar trends for the roof and floor notches (Collins et al. 1994). Figure 37 shows the distribution of microseismic events for Rounds 6 to 30 relative to the tunnel face.

Note that most microseismic activity occurs near the tunnel face and decreases rapidly with distance from the face to about $X/2a = -2$. Considerable microseismic activity also occurs ahead of the tunnel face, starting at about $X/2a = 0.5$, with most of the events within 0.2 diameters of the face. The source parameters for this data set were analyzed using the automated ISS software.

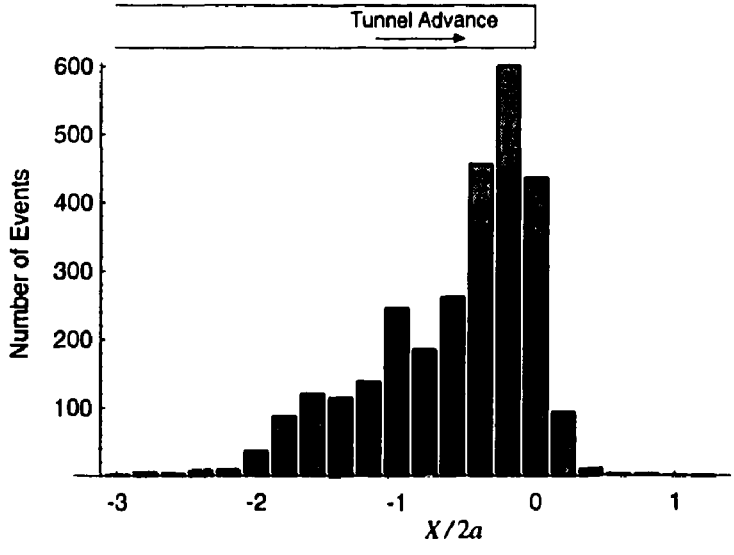

FIGURE 37: Histogram of the microseismic events recorded for Rounds 6 to 30. The location of each event relative to the tunnel face position (X) is normalized with respect to the tunnel diameter ($2a$).

In mining-induced seismicity studies, the seismic event is usually modelled as a simple circular fault (Brune 1970). The shear stress released at the source of such an event can be estimated by the static stress drop ($\Delta\tau$), which is equal to the difference between the initial shear stress acting on the fault and the final shear stress after slip has occurred. As shown by Keilis-Borok (1959), the static stress drop can be calculated from the seismic moment (M_o) and the source radius (r_o) by:

$$\Delta\tau = \frac{7M_o}{16r_o^3} \tag{11}$$

The static stress drop represents the uniform reduction in shear stress acting to produce seismic slip over a circular fault. For most mining-induced tremors, the static stress drop ranges from 0.01 to 10 MPa (McGarr 1994). Figure 38 shows the radiated seismic energy and seismic moment with lines of constant stress drop for the events recorded near the test tunnel (Collins et al. 1994). For the microseismic events recorded, nearly all the events fall between lines for a constant stress drop of 200 Pa and 200 kPa, which is somewhat lower than the values given by McGarr (1994). Interestingly, most of these events are also smaller than seismic events measured in laboratory samples (McGarr 1994). Figure 39 shows the same data set but with the events normalized to the tunnel face position. It appears that the greatest stress drop occurs in the vicinity of the tunnel face. It is also evident that the events that initiate ahead of the tunnel face show a very small stress drop. In the following section, a detailed analysis of Round 17 is carried out to investigate the cracking that occurs near the tunnel face.

3.3.1.2 Source Locations

Excavation Round 17, a central tunnel segment between chainage 21.79 and 22.84 m, was selected for detailed analysis (Figure 36). All of the microseismic events within this nominal 1-m volume were manually source located, resulting in a source location accuracy of ±0.2 m (Collins and Young 1993). Survey profiles of the tunnel perimeter were also taken during the excavation of the test tunnel. These profiles provided quantitative evidence of the formation of the notch, and allowed a comparison of the microseismic events with the notch formation (Figure 36). Surveys of the profile of the notch, combined with the source locations of the microseismic events, provided a unique opportunity to track the development of the notch in the 1-m volume.

The manual source locations gave a total of 113 microseismic events in the 1-m volume for the eight month period between 1992 January and August (Martin et al. 1995). A summary of these events, including a breakdown of those that occurred in the roof and those that occurred in the floor of the tunnel, is given in Figure 40 along with the times that Rounds 17, 18, 22 and 50 were excavated, and the times for the surveyed profiles given in Figure 41.

Inspection of Figure 40 reveals that no microseismic events were recorded in the 1-m volume until the tunnel face was only 1 m from Round 17, and that nearly all of the microseismic events in the roof had occurred by the time Round 22 had been excavated, approximately 3 m past Round 17 (see Figure 34(b) for the location of Round 22). Figure 40 also shows

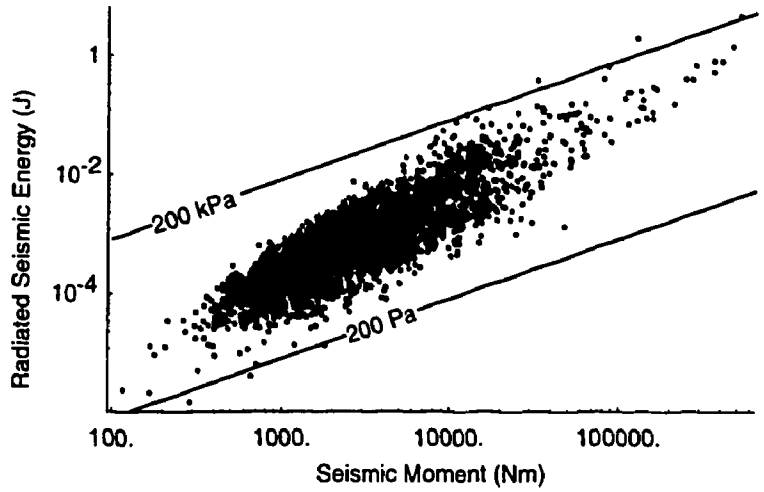

FIGURE 38: Radiated seismic energy versus seismic moment with lines of constant stress drop (after Collins et al. 1994).

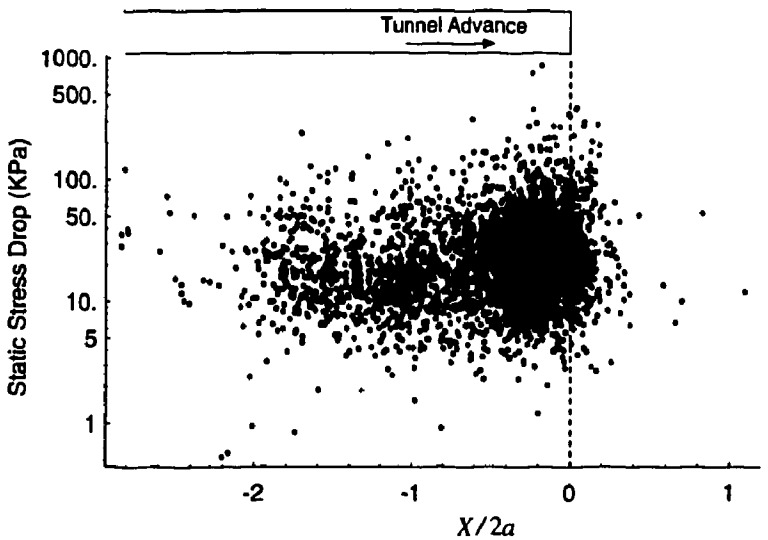

FIGURE 39: Static stress drop for rounds 6 to 30. The location of each event relative to the tunnel face position X is normalized with respect to the tunnel diameter $2a$.

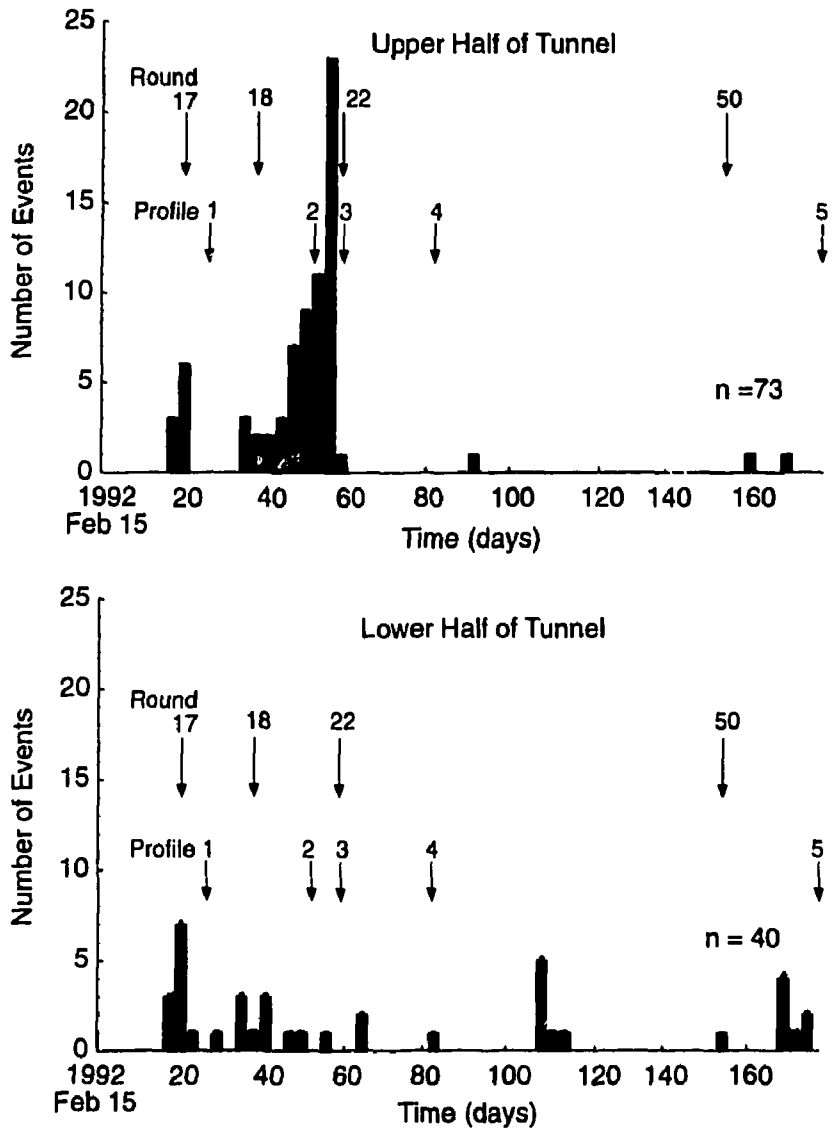

FIGURE 40: Frequency histogram for all the events recorded in the upper half (roof of tunnel) and lower half (floor of tunnel) of the nominal 1-m-long tunnel section (chainage 21.79 to 22.84 m) between 1992 February 15 and August 15. Microseismic activity starting at 170 d is related to removal of 'muck' from the tunnel floor.

that the events in the floor are more evenly distributed. This suggests that the tunnel 'muck' on the floor of the tunnel has an inhibiting effect on the failure process. Once the excavation of the tunnel had been completed, approximately 0.5 m of 'muck' on the floor was removed, starting 1995 August 4. This removal was sufficient to trigger another sequence of microseismic activity, suggesting that the spalling process is extremely sensitive to confining stress.

Figure 40 showed that most of the microseismic activity occurred when the tunnel face was within ±1 tunnel diameter of the 1-m section. Because profiles of the tunnel perimeter were also taken in this same time interval, it is possible to compare the location of the microseismic events and the development of the notch (see Figure 41). Figure 42 shows the progressive development of the notch measured at chainage 22.60 m and the incremental microseismic data that occurred between each profile date. At profile 1, the face of the tunnel is at chainage 22.84 m and at profile 5, the face of the test tunnel is at chainage 46.13 m. At the time of profile 1, the tunnel face has advanced 0.24 m beyond the surveyed section and the tunnel profile is essentially circular, i.e., the notch has not started to develop. At profile 2, the tunnel face has advanced 0.5 m beyond the surveyed section and the tunnel profile shows the initiation of the notch in the roof. Note also, that at profile 2, the microseismic events in the roof cover the area where the notch eventually develops as the tunnel is advanced. This observation suggests that the microseismic activity is a precursor to notch development, and may indicate damage to the rock mass prior to notch formation. Also, note that the notch continues to develop in profiles 4 and 5 without associated microseismic activity. This observation indicates an absence of microseismicity in the periods monitored around the time these profiles were taken, but does not preclude activity in the periods that were not monitored.

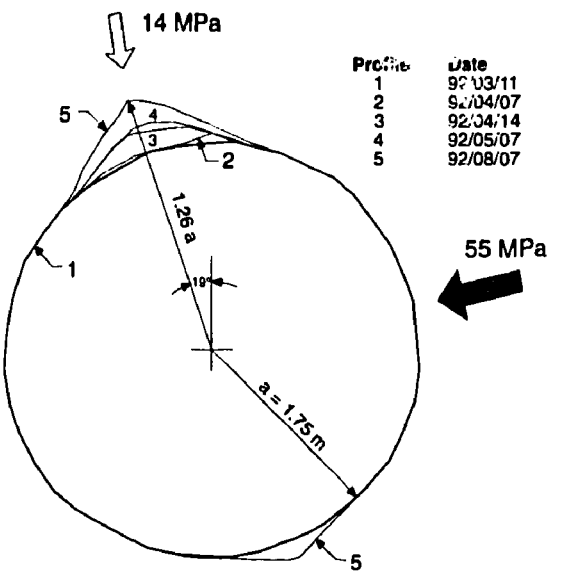

FIGURE 41: Progressive development of the notch geometry in the roof and floor of the Mine-by test tunnel at Round 17 over a five month period.

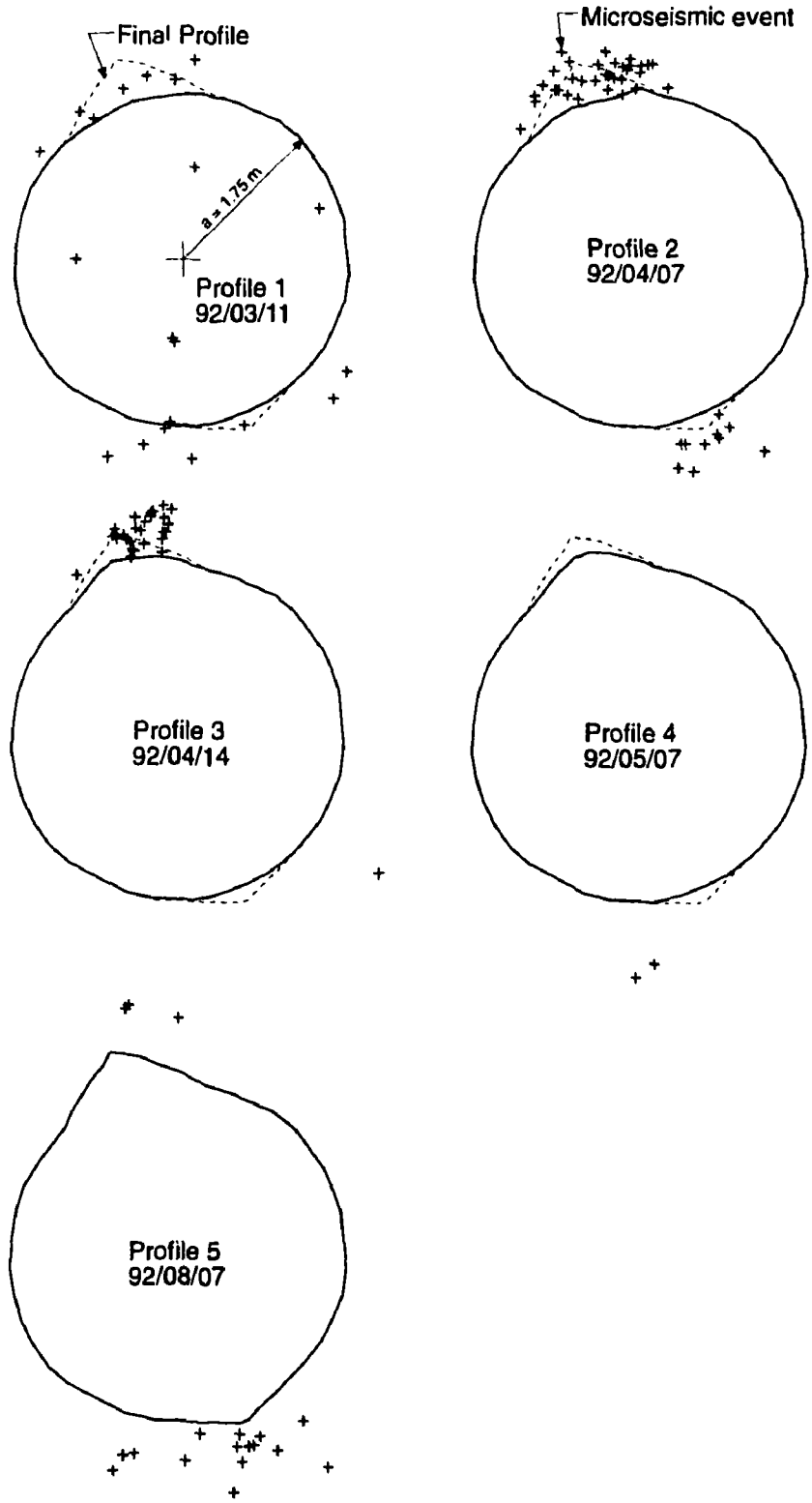

FIGURE 42: Profiles of the test tunnel recorded at different times at Round 17. Also shown are the incremental microseismic events recorded between the dates the profiles were measured.

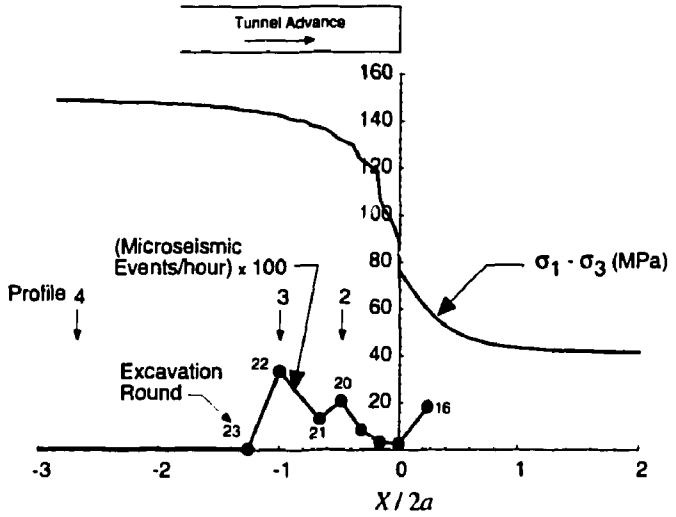

FIGURE 43: Comparison of the maximum deviatoric stress change that occurs in the roof, to the AE/MS rate recorded at Round 17 and the development of the profiles at Round 17. The parameter $X/2a$ refers to the normalized face position of the tunnel.

The previous discussions showed that the microseismic events are concentrated within a narrow zone around the 1-m volume. The microseismic events that were recorded in the 1-m volume and the measured profiles can be related to the position of the test tunnel face. In Figure 43, the face position X is normalized with respect to the tunnel diameter $2a$. This allows direct comparison with the stress changes that occur near the tunnel face. Three-dimensional boundary element analyses were carried out using the program EXAMINE^{3D} (Curran and Corkum 1993) to determine the maximum deviatoric stresses in the roof of the test tunnel. Figure 43 compares the maximum deviatoric stress change that occurs in the roof to the rate of microseismic activity and the development of the notch. Figures 39 and 43 show that nearly all of the microseismic events occur within one tunnel diameter of the face, i.e., where the stress changes are occurring, but that the development of the notch continues for long periods afterward. Also note that the failure process, i.e., crack initiation, begins ahead of the tunnel face.

The microseismic events in Figure 44 cluster strongly in the regions of the maximum compressive stress concentrations in the roof and floor. These regions of microseismic activity are the locations of the breakouts (compare Figure 45 and Figure 44). Note that no microseismic activity was recorded in the regions where remote or tensile fractures are expected to form.

3.3.2 *In Situ* Crack Initiation

The process leading to failure in brittle rocks in unconfined laboratory compression tests initiates with the onset of stable crack growth (Brace et al. 1966) which was referred to in Section 3.1 as the crack-initiation stress σ_{ci}. The crack-initiation stress in laboratory

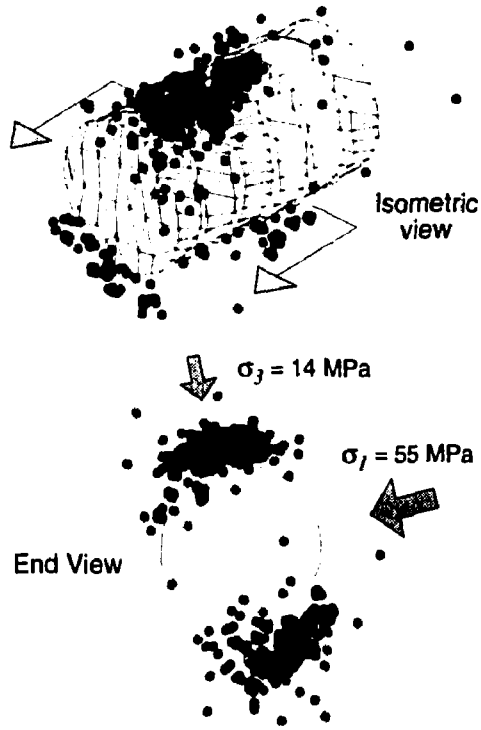

FIGURE 44: Location of microseismic events recorded after the excavation of a 1-m-long round (Round 17) in the test tunnel.

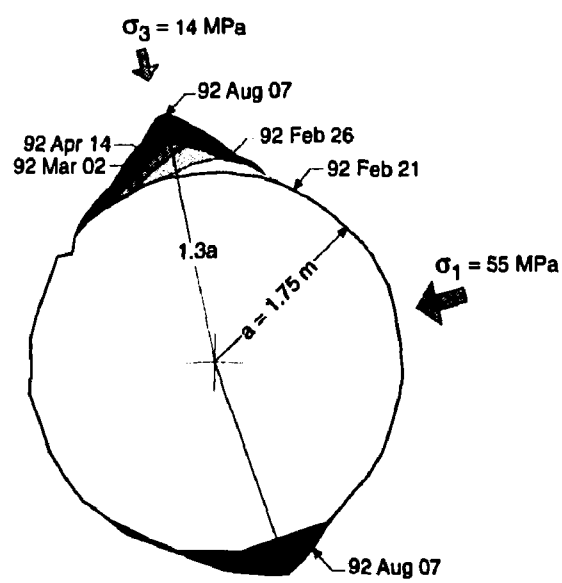

FIGURE 45: Progressive development of a breakout notch *in situ* in Lac du Bonnet granite (chainage 18+50).

samples of Lac du Bonnet granite occurs when the load first exceeds about 0.2 to $0.4\sigma_c$ where σ_c is the unconfined compressive strength (Martin 1993). This value for crack initiation is similar to the crack initiation values of 0.3 to $0.6\sigma_c$ reported by Brace and Byerlee (1968) for various low porosity rocks and concrete.

The microseismic events in Figures 42 and 44 define the regions where cracking initiates *in situ*. As these microseismic events represent the initiation of the failure process, the stress level associated with these events is referred to as the *in situ* crack-initiation stress σ_{ci}. Three-dimensional numerical stress analyses, carried out to determine the crack-initiation stress at each microseismic event location shown in Figure 44, showed that the stress level at which *in situ* cracking initiated could be approximated by

$$\sigma_1 - \sigma_3 \approx 70 \text{ to } 75 \text{ MPa}. \tag{12}$$

Those results are plotted in Figure 46 along with the Hoek-Brown failure envelope for the peak strength determined from laboratory tests. Figure 46 shows that, for low confining stresses, the *in situ* crack-initiation stress occurs at approximately 70 MPa, i.e., about $0.3\sigma_c$, which is only slightly lower than the laboratory findings mentioned earlier. This concept of a constant $(\sigma_1 - \sigma_3)$ threshold is similar to that introduced by Equation 7, which also suggests that the maximum deviatoric stress level required to initiate damage (microcracking) is a constant.

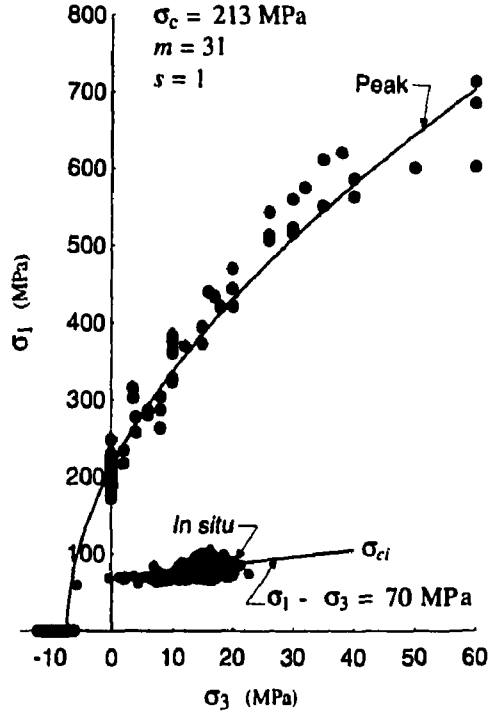

FIGURE 46: Hoek-Brown failure envelope for Lac du Bonnet granite based on laboratory peak strength and *in situ* crack-initiation stress (σ_{ci}) from the microseismic monitoring.

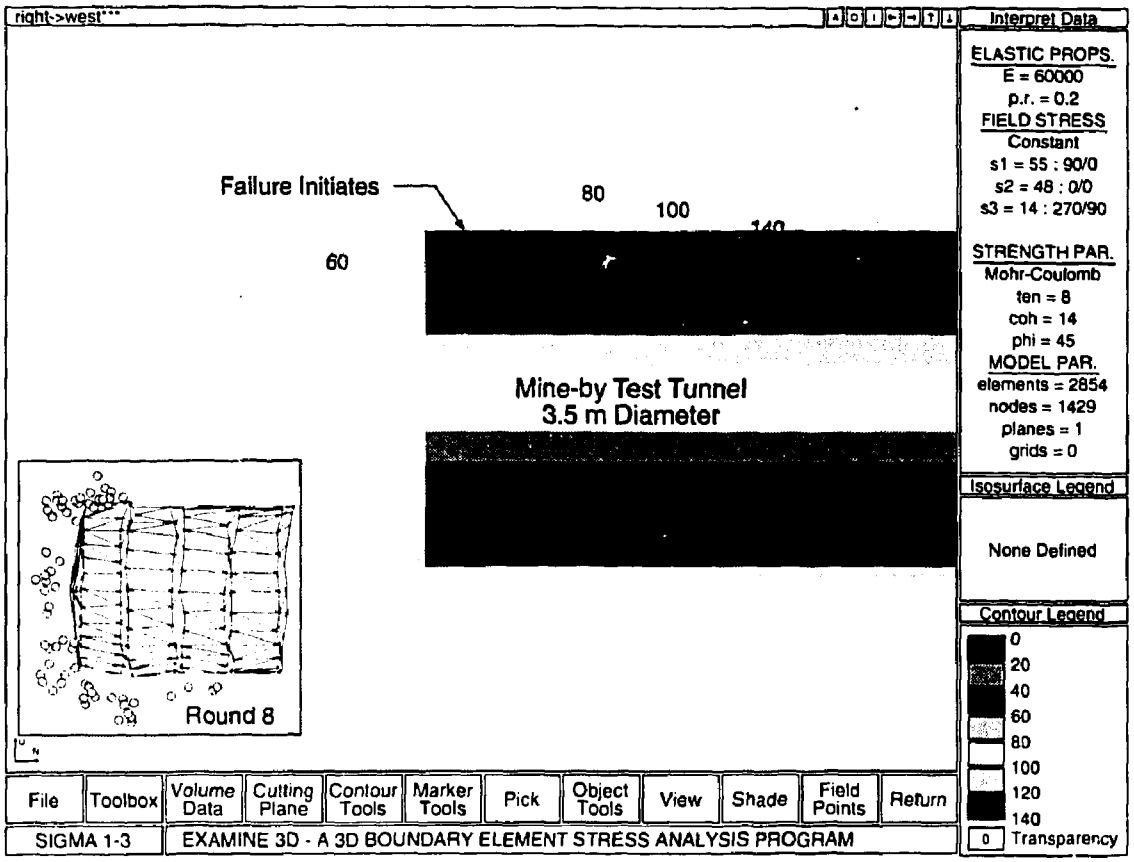

FIGURE 47: Section through the Mine-by test tunnel showing the location of the initiation of failure and the σ_1-σ_3 contours. Note that the microseismic events shown on the insert for Round 8 are concentrated in the areas of maximum deviatoric stress.

Figure 46 demonstrates that the *in situ* crack-initiation can be predicted by the maximum deviatoric stress criterion given in Equation 12. This concept is illustrated in Figure 47 which shows the $\sigma_1 - \sigma_3$ contours in a plane through the maximum compressive stress concentrations around the Mine-by test tunnel. Note the general agreement with the location of the microseismic events near the face of the tunnel and the $\sigma_1 - \sigma_3$ contours. Microseismicity shown in the inset in Figure 47 near the centre of the tunnel ahead of the face is not in the same vertical section shown for the model, but in three-dimensions falls within the $\sigma_1 - \sigma_3 = 70$ MPa isosurface (not shown).

3.3.3 *In Situ* Loading Path

When considering the ultimate strength of a material, it is important to know the loading path that has been followed in reaching the 'strength'. Tests are routinely performed in the laboratory to obtain the tensile strength, the unconfined compressive strength and the 'triaxial' strength. In all of these cases, the loading path increases or decreases monotonically,

and the loading directions do not change (Figure 48). However, *in situ*, the loading path is more complex, involving stress increase, decrease and stress rotation in the regions close to the advancing excavation (Martin 1993).

Using the initial composite estimate of the stress tensor (section 2.1.3), Martin (1993) carried out a series of three-dimensional linear elastic stress analyses to follow the loading path of various reference points ahead of the test tunnel. He investigated the change in stress magnitudes and directions as the tunnel advances towards and passes the reference point. In each analysis, the reference point starts 10 m ahead of the tunnel and is referred to as the 'far-field' (point A in Figure 48) and its stress path is followed until the tunnel has passed the reference point by 10 m (point E in Figure 48). Figures 49 and 50 show two of the analyses carried out by Martin for points near the maximum compressive stress concentration around the tunnel. Figure 49 is the stress path followed by a point in the roof of the tunnel located about 10 mm from the tunnel perimeter; Figure 50 is the stress path followed by a point in the roof of the tunnel located about 500 mm from the tunnel perimeter. These show that, near the tunnel perimeter, the stress path exceeds the crack-initiation stress well ahead of the tunnel face, but that at 500 mm from the tunnel perimeter, the crack-initiation stress is exceeded only as the plane strain condition is reached, i.e., behind the tunnel face. Martin's analyses also showed that, at a distance of 600 to 700 mm radially beyond the tunnel perimeter, the stress remains below the crack-initiation stress. Based on these analyses and results from microseismic monitoring, the compressive regions in which crack initiation occurs *in situ* are localized close to the tunnel perimeter, and extend ahead of the advancing face. Damage generated in compression is therefore limited to these regions of the rock mass.

Having established the regions around the tunnel in which damage could occur, Martin (1993) considered possible mechanisms influencing the development of cracks and crack growth, i.e., damage, within these regions. He suggested that stress rotation is one of the key mechanisms that contributes to *in situ* damage development around tunnels. Martin (1993) showed that the advance of the tunnel face not only causes the stress tensor to change

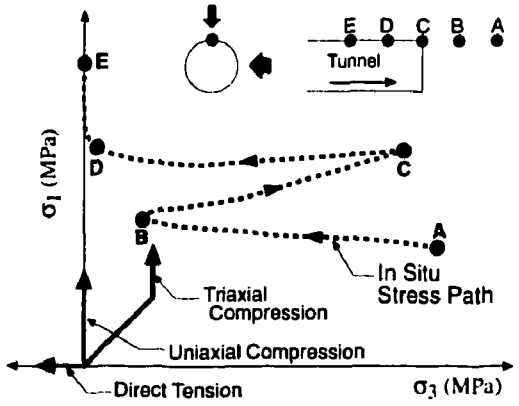

FIGURE 48: Illustration of the loading path in uniaxial and triaxial testing, and the *in situ* loading path around a circular tunnel with anisotropic far-field stresses.

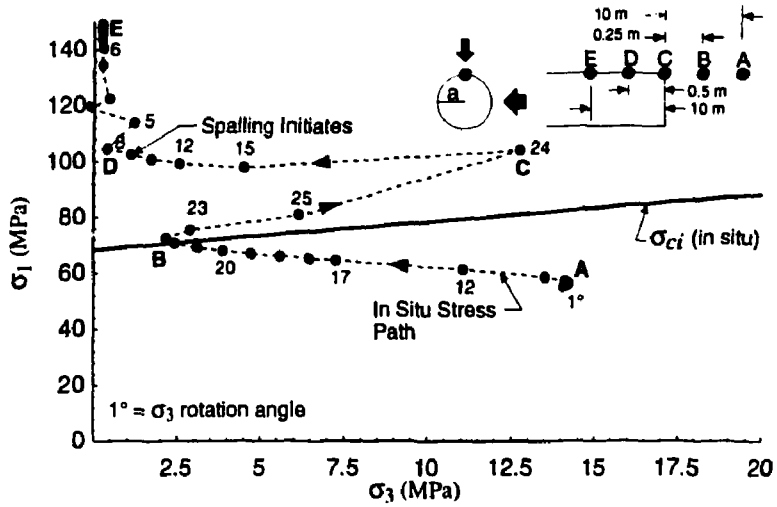

FIGURE 49: Stress path for a point located 10 mm from the tunnel boundary at the maximum compressive stress concentration in the roof. The 'far-field' point in the figure is located 10 m ahead of the face. Note that the first visual signs of failure are observed at point D, about 0.5 m inside the tunnel.

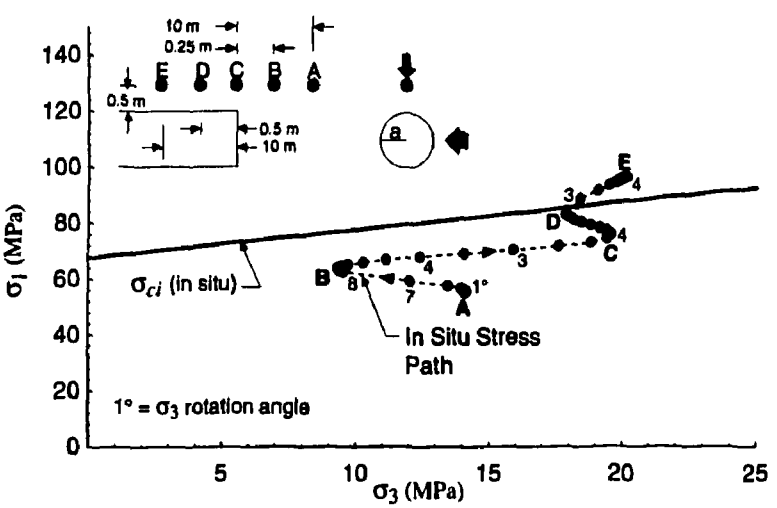

FIGURE 50: Stress path for a point located 500 mm from the tunnel boundary at the maximum compressive stress concentration in the roof. The 'far-field' point in the figure is located 10 m ahead of the face.

in magnitude but to rotate also. If cracks are considered to grow in the plane orthogonal to σ_3, then the rotation of σ_3 represents the rotation of the pole normal to the plane of the crack. From detailed analyses of the region near the face of the test tunnel, Martin (1993) concluded that rotation of σ_3 occurs in all locations around the tunnel face. However, in the roof and floor of the test tunnel, the rotation of σ_3 along the line 10 mm outside the tunnel perimeter is at a maximum of about 20 to 30° between points B and C ahead of the face (Figure 49), decreasing to about 5° in the same region at 500 mm from the tunnel perimeter (Figure 50). In addition, as a result of stress rotation, the magnitude of σ_3 reaches a minimum near point B ahead of the face. This effect is most pronounced along a line close to the tunnel perimeter, where σ_3 approaches zero (Figure 49). Hence, within the regions where crack initiation occurs, there are distinct zones ahead of the face where stress rotation reaches a maximum, and confining stress is low.

Wu and Pollard (1992) conducted tensile tests on a brittle material to investigate the influence of the orientation of existing cracks on crack growth in tension. By rotating the applied tensile stress relative to the orientation of the existing cracks, they demonstrated that the existing cracks influenced the growth of new cracks. They also demonstrated that by simply keeping the stress constant, but rotating its direction, they could generate crack patterns in different directions. At rotation angles from about 0 to 45°, new cracks tended to grow from the tips of existing cracks, i.e., the existing cracks grew longer without an increase in stress.

Martin (1993) suggested that a similar process, induced by stress rotation, occurs near the tunnel face when stresses exceed the crack-initiation stress. As shown in Figure 49, damage initiates *in situ* near point B, where the crack-initiation stress is exceeded and the confining stress is low. As shown in the damage-controlled tests in Section 3.1.1, the amount of damage accumulated in the rock is greatest for conditions of low confinement. The microcracks formed near point B are inclined about 20 to 25° to the tunnel axis, oriented orthogonal to the near-field σ_3 direction. Upon tunnel advance past the volume of rock containing these microcracks, σ_1 and σ_3 rotate to become tangential and radial, respectively, to the tunnel at the perimeter, and σ_2 becomes parallel to the tunnel axis. Near the face, the crack-initiation stress is exceeded in both the axial and tangential directions, which promotes microcracks to form orthogonal to the radial direction, and tends to exploit the existing inclined microcracks. This form of crack growth would result in a loss in the cohesion component of the rock strength because it causes the crack length to increase. The net effect is that the rock mass in this region is weakened and more susceptible to dilation. However, away from the opening, the rock mass strength is unaffected.

In regions of granite lithology, failure in the form of spalling was first observed in the test tunnel roof near point *D* in Figure 49, about 0.3 to 0.5 m behind the tunnel face. Based on the initial stress tensor estimated for the experiment area, σ_3 is zero and σ_1 (the tangential stress) is between 105 and 120 MPa in this area. Although the tangential stress is only 0.5 to $0.6\sigma_c$ for the case described in Figure 49, it is sufficient to exploit the previously formed microcracks in the region of damage exposed at the tunnel perimeter. Consequently, failure occurs at a lower stress level than in laboratory tests. It should be noted that in granodiorite lithology, the point of failure initiation was about 1 m behind the tunnel face.

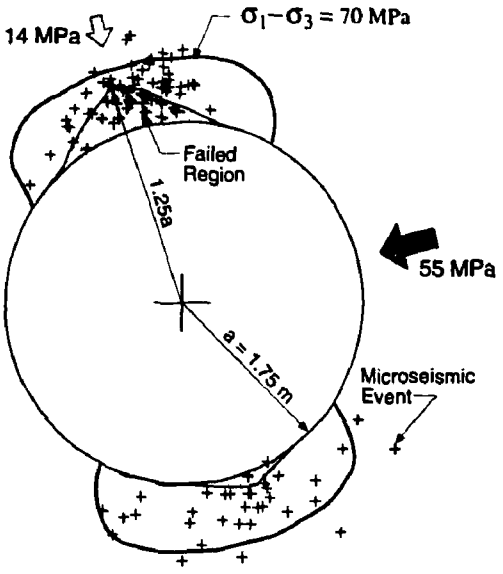

FIGURE 51: Extent of the rock mass around the Mine-by test tunnel where the maximum deviatoric stress ($\sigma_1 - \sigma_3$) has exceeded the crack-initiation stress of about 70 MPa. The principal stress magnitudes used for the analysis are $\sigma_1 = 55$, $\sigma_2 = 48$ and $\sigma_3 = 14$ MPa.

This process of *in situ* strength reduction requires that the stress magnitudes near the tunnel face are sufficient to exceed the *in situ* crack-initiation stress. The microcracks that form once this condition is met reduce the cohesion of the rock mass in localized regions close to the tunnel. By considering the distribution of maximum deviatoric stress around the tunnel under plane strain conditions, the maximum extent of the region over which the crack-initiation stress is exceeded can be approximated. Figure 51 shows the region around the Mine-by test tunnel where the maximum deviatoric stress exceeds the crack-initiation stress. Also plotted in Figure 51 are the microseismic events recorded within a 1-m-thick slice around the test tunnel, as well as the measured shape of the failed zone or notch. It is obvious that the crack-initiation stress does not define the shape of the notch, but it does provide a reasonable estimate of the depth of the notch, shown as $1.25a$ in Figure 51, where a is the radius of the tunnel.

3.3.4 Progressive Failure in Compression

The preceeding sections have shown that the process of failure around the Mine-by test tunnel started when the the maximum deviatoric stress exceeded the stress level required to initiate cracks, or damage, ahead of the advancing tunnel. Following this localized 'pre-conditioning' of the rock mass, the macroscopic failure process commences as the tangential stress at the boundary of the tunnel reaches the strength of the damaged material. In this section, the observations recorded during the process of progressive failure in the regions of maximum tangential stress are described. This process, which was observed in the upper SE

and lower NW quadrants of the test tunnel during its excavation, resulting in well-developed v-shaped notches typical of those found in borehole breakouts (Figure 52).

The processes associated with progressive failure of the Mine-by test tunnel have been described by Martin (1993). Figure 53 illustrates the major processes observed in the progressive development of a notch. In general, the steps involved are: 1) crushing in a very narrow, 5 to 10 cm wide, process zone on the tunnel periphery approximately 0.5 to 1 m back from the tunnel face where the maximum tangential stress exceeds the strength of the damaged rock (Figure 54); 2) dilation and small-scale flaking in this process zone resulting in the formation of thin slabs that are typically as thick as the grain size of the granite (2 to 5 mm) (Figure 55); 3) formation of larger thin slabs on the flanks of the notch as the process zone develops (Figures 56 and 57); 4) stabilization of the process, occurring when the notch geometry provides sufficient confinement at the notch tip. This occurs when the notch geometry takes on a 'tear-drop' like shape (Figure 58). The 'tear-drop' like geometry of the notch re-orients the maximum principal stress trajectory radially outward into the rock mass, which results in high localized values of σ_1 under high confinement conditions at the notch tip (Martin 1993; Zheng et al. 1989). The four processes involved in the development of the notch are described in detail in the photographs that follow.

From the observations during the construction of the Mine-by test tunnel, it is clear that the process zone plays the key role in the initiation, development and stabilization of the v-shaped notch. The failure processes that occur in this zone are complex, and it is difficult to 'look inside' the process zone without disturbing it. Figure 59 shows the process zone at the tip of the notch in Figure 58. Note the large amount of dilation associated with the failure mechanisms in the process zone.

3.3.5 Tensile Failure in the Sidewalls

In the sidewalls of the Mine-by tunnel, the tangential stress at the tunnel wall exceeds the tensile strength of the rock mass, which according to elastic theory, should result in macroscopic tensile cracks. This type of cracking was evident in Room 405, the main level instrument gallery excavated parallel to the Mine-by tunnel using a drill-and-blast technique. Contrary to expectations, there were no macroscopic tensile cracks in the sidewalls of the test tunnel. The development of microscopic damage in the tensile regions was, however, detected by geophysics surveys, and is discussed in Section 4. The differences in the characteristics of damage in the tensile regions in Room 405 and the test tunnel are attributable primarily to the differences in excavation technique.

3.4 SUMMARY

The laboratory testing progam clearly showed that the failure process initiates with small cracks that form in the general direction of the maximum applied load. Stable crack growth starts at the crack-initiation stress which typically occurs at about 0.3 to 0.4 of the peak strength of the sample. This process of stable crack (damage) growth continues until a sufficient density of cracks occurs that allows the development of a macro failure zone in the laboratory sample. The stress level at which this failure zone develops is referred to

FIGURE 52: Final profile of the Mine-by Experiment test tunnel as of 1992 August showing well-developed v-shaped breakout notches in the upper SE and lower NW quadrants.

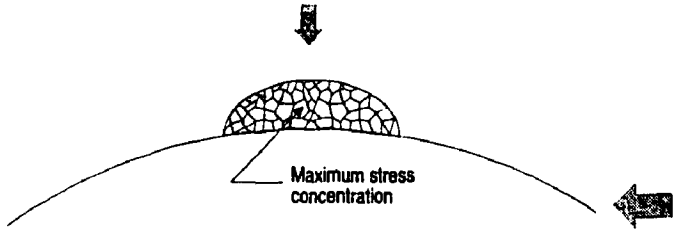

Stage I - Initiation
Critically oriented flaws are exploited in the zone of maximum tangential stress. This process initiates at the boundary of the tunnel.

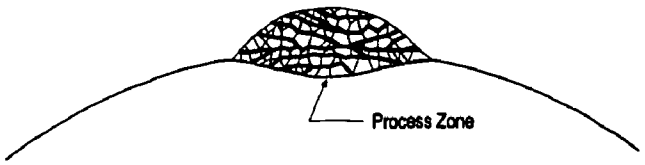

Stage II - Dilation
Shearing and crushing occurs in a very narrow process zone about 5 - 10 cm wide. Extensive dilation, at the grain-size scale, occurs in this process zone.

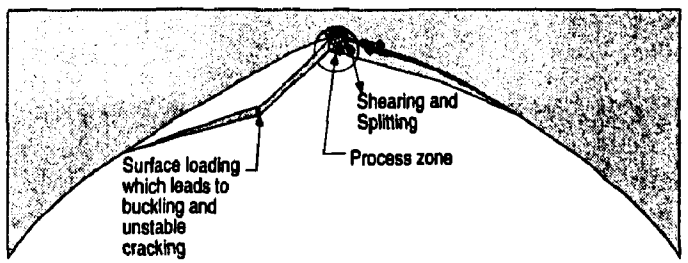

Stage III - Slabbing & Spalling
Development of the process zone leads to formation of thin slab. These thin slabs form by: 1) shearing, 2) splitting, and 3) buckling. The thickness of the slabs varies from 1 to 5 cm. The thickest slabs form as the notch reaches its maximum size. Near the notch tip the slabs are curved.

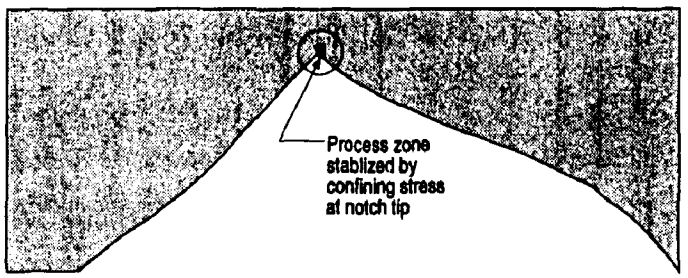

Stage IV - Stabilization
The development of the notch stops when the notch geometry provides sufficient confinement to stabilize the process zone at the notch tip. This usually means there is a slight "tear-drop" like curvature to the notch shape. Alternatively, if the slabs from the side of the notch are held in place by artificial support then the development of the notch will also stop.

FIGURE 53: Illustration of the major processes involved in the initiation, development and stabilization of the v-shaped notch.

FIGURE 54: Stage I: Photo of the initiation of the failure process. Note the faint whitish colour line, caused by crushing, which defines the limits of the process zone. Note also that the tunnel profile at the tunnel face is circular and that the process zone initiates about 0.5 m back from the tunnel face.

FIGURE 55: Stage II-III: Photo of dilation that occurs as the slabs on the flanks of the notch start to form. These slabs are held in place by the safety mesh used during construction.

FIGURE 56: Stage III: Photo of a slab that has buckled on the flank of the notch. This was the only type of large-scale buckling that was observed.

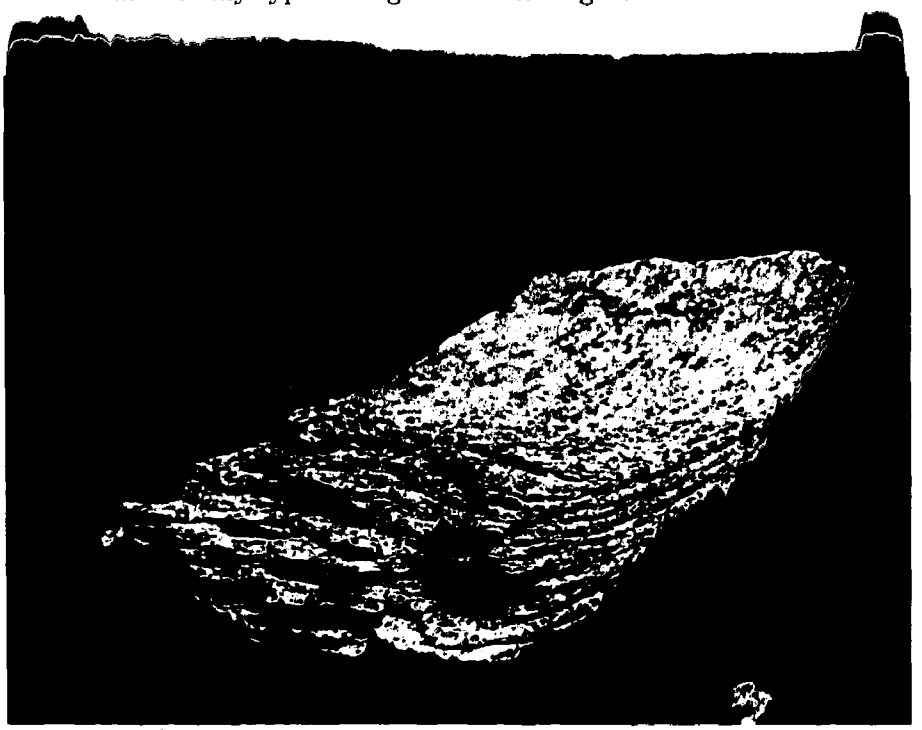

FIGURE 57: Stage III: Photo of a single slab showing the grain-scale fracturing generated at the active notch tip.

FIGURE 58: Stage IV: Photo of the stable v-shaped notch that developed in the floor of the test tunnel. The slot that allowed this photo to be taken was excavated between 1992 October and 1993 January. Note the characteristic 'tear-drop' shape to the geometry of the notch.

FIGURE 59: Photo of the process zone at the tip of the notch in Figure 58. Note the large amount of dilation localized at the notch tip.

as unstable crack growth or crack-damage stress, and typically occurs at about 0.7 to 0.8 of the peak strength. Once a macro failure zone is developed, the sample can no longer sustain the load and failure occurs.

In situ crack initiation was also found to occur at about 0.3 of the undisturbed laboratory strength. However, unlike the laboratory sample, failure, i.e., spalling, initiates when the tangential stress around the tunnel reaches about 100 to 120 MPa, i.e., 0.5 to 0.6 of the undamaged laboratory unconfined strength. As a result of the complex loading path around the advancing face of the tunnel, it is proposed that, *in situ*, the rock accumulates more crack damage for a given stress level than in laboratory tests, and therefore undergoes more pronounced weakening. Consequently, failure *in situ* initiates at lower tangential stress levels than in laboratory tests.

Once failure initiates near the tunnel face, the development of the v-shaped notch accelerates as the face advances, and the tunnel adjusts to the new plane strain conditions. The slabbing process resulting in the development of the v-shaped notch is controlled by the process zone. This zone, although small in size relative to the v-shaped notch, forms at the tip of the v-shaped notch and consists of highly strained, i.e, crushed, rock. Once the development of process zone stablizes, the development of the notch stops. This usually occurs when the geometry of the notch is such that the process zone is confined in a very small region at the notch tip.

The damage process described above occurs near the tunnel face. Points in localized regions ahead of the face experience changes in the principal stress magnitudes and orientations as the tunnel advances, causing micro-scale damage. This damage locally weakens, or 'pre-conditions,' the rock mass near the tunnel. The degree of damage is greatest about one radius from the projected tunnel centreline, and decreases rapidly with increasing radial distance from the tunnel. Upon tunnel advance, these localized regions of damage are exposed at the tunnel perimeter. Hence, the strength of the rock mass around the underground opening varies from point to point, with the strength at any given point depending on the stress history and damage accumulated there as a result of the excavation process. Points located at the tunnel wall in the maximum compressive stress concentration have accumulated the most damage during tunnel advance, and therefore experience the largest strength reduction. Points located further from the opening, or away from the zones of maximum compressive stress concentration, have accumulated less damage and thus have strengths closer to the undamaged laboratory strength.

4. EXCAVATION DISTURBANCE AND DAMAGE

As described in Section 1, the redistribution of stresses around a tunnel results in a zone of excavation disturbance. In general, this zone is characterized by a perturbation to the pre-excavation stress state, but no change in the initial material behaviour of the rock mass. Depending on the far-field stress magnitudes and the strength of the material in which the tunnel is excavated, a zone of excavation-induced damage may develop close to the tunnel within this larger disturbed zone. The damaged zone is characterized by changes in both the pre-excavation stress state and in the material behaviour of the rock mass. Within this

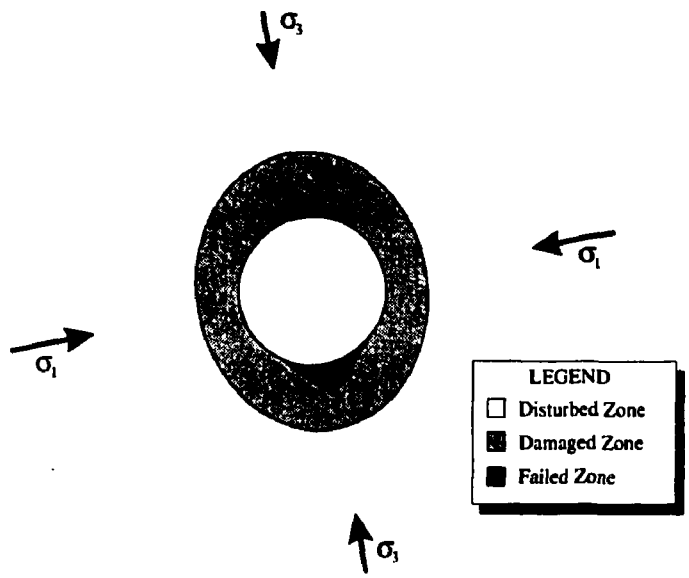

FIGURE 60: Schematic view of the disturbed, damaged and failed zones around the Mine-by Experiment test tunnel.

zone, a smaller failed zone may exist, defined by a region of slabbing or material removal, as described in Section 3. These zones are shown schematically in Figure 60.

Having investigated the zone of progressive failure in compressive regions around the tunnel, the other key objective of the Mine-by Experiment was to define the extent and characteristics of the damaged zone around the test tunnel. Back analysis can establish the stress conditions and material properties in the undisturbed region based on measurements in the disturbed zone. Once these boundary conditions have been defined, it is then possible to assess the extent, material behaviour and characteristics of the damaged zone around the tunnel through field characterization and numerical modelling.

Based on the data contained in the nine data summary reports for the Mine-by Experiment, back analyses of the strain and/or displacement measurements were undertaken (Read 1994; Wiles 1995). These back analyses are described in Sections 4.1 and 4.2, and the principal findings, in terms of characteristics of the disturbed zone, are summarized in Section 4.3. Characterization of the damaged zone and factors controlling excavation damage development are also considered in Section 4.3.

4.1 BACK ANALYSIS OF DISPLACEMENT MEASUREMENTS

Back analysis of *in situ* stresses from radial displacements measured around circular excavations is typically based on the analytical solution for stresses and displacements around a circular hole in an infinite plate under plane strain conditions. This relationship assumes linear elastic material behaviour, and relates the total excavation-induced displacements to the 2D principal stresses acting in the plane of the excavation. To estimate the 3D stress

tensor, multiple orthogonal tunnels are required. In highly-stressed brittle rock masses, excavation-induced damage can result in non-linear/non-elastic material behaviour around a tunnel which can produce a displacement response significantly different from that predicted by elastic theory. In addition, displacement measurements taken from within the excavation (Figure 61) represent only part of the total displacement response, requiring an estimate of the missed proportion occurring ahead of the tunnel face. Under anisotropic far-field stress conditions, this proportion is dependent on a number of factors including axial stress magnitude, face shape, rotation angle and position with respect to the tunnel face (Read 1994).

Using the Mine-by Experiment as a case study, Read (1994) considered the problems associated with analysis and interpretation of displacement measurements taken during excavation of a cylindrical tunnel in a massive, highly-stressed, brittle rock mass. He developed a technique to back analyze the 3D *in situ* stress tensor using radial displacements from the region within ± 1 diameter of the face of a single circular tunnel. The technique is applicable to conditions ranging from low stress regimes, where rock mass behaviour is linear elastic, to highly-stressed regimes where significant damage develops in the tunnel. The stress tensor estimated for the region containing the Mine-by test tunnel was, in turn, used in conjunction with observations from field characterization and numerical modelling to determine the extent and characteristics of excavation damage around the tunnel. This section summarizes the methodology and results of the back analysis conducted by Read (1994) to determine the *in situ* stress tensor and material properties. Details pertaining to nomenclature and mathematical expressions are contained in Appendix B.

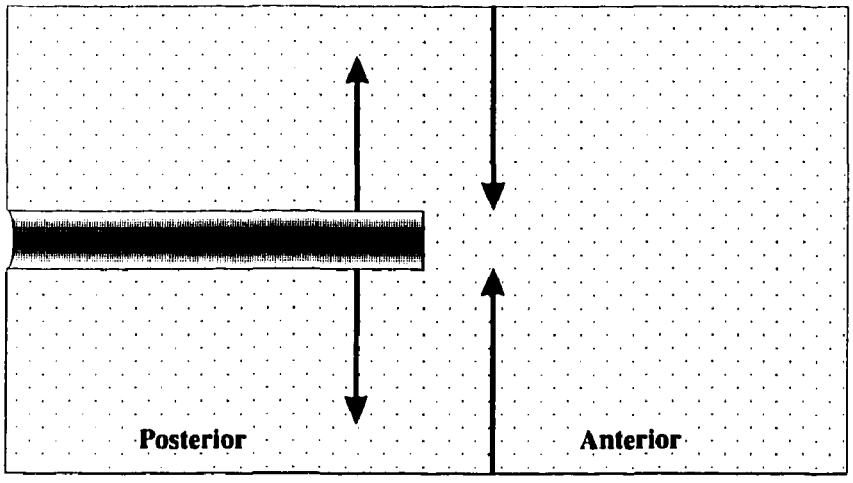

FIGURE 61: Definition of the posterior and anterior domains for an idealized tunnel, and typical direction of instrument installation: for the posterior domain, from the tunnel outwards; and for the anterior domain, from an external opening inwards.

4.1.1 Stress Partitioning Approach

Most previous studies involving displacements around a cylindrical tunnel have considered special stress states involving axial symmetry or zero antiplane shear stresses (Brown et al. 1983; Pelli 1987), i.e., the tunnel axis coincides with a principal stress direction. To assess a general elastic case where the far-field stress components are unequal, and the tunnel axis does not coincide with a principal direction, the principle of superposition can be used to partition a unit stress tensor into a set of three normal stress and three shear stress tensors (Niwa et al. 1979), i.e.,

$$\underbrace{\begin{bmatrix} 1 & 1 & 1 \\ 1 & 1 & 1 \\ 1 & 1 & 1 \end{bmatrix}}_{\sigma} = \underbrace{\begin{bmatrix} 1 & 0 & 0 \\ 0 & 0 & 0 \\ 0 & 0 & 0 \end{bmatrix}}_{\sigma_{11}} + \underbrace{\begin{bmatrix} 0 & 0 & 0 \\ 0 & 1 & 0 \\ 0 & 0 & 0 \end{bmatrix}}_{\sigma_{22}} + \underbrace{\begin{bmatrix} 0 & 0 & 0 \\ 0 & 0 & 0 \\ 0 & 0 & 1 \end{bmatrix}}_{\sigma_{33}} + \underbrace{\begin{bmatrix} 0 & 1 & 0 \\ 1 & 0 & 0 \\ 0 & 0 & 0 \end{bmatrix}}_{\sigma_{12}} + \underbrace{\begin{bmatrix} 0 & 0 & 0 \\ 0 & 0 & 1 \\ 0 & 1 & 0 \end{bmatrix}}_{\sigma_{23}} + \underbrace{\begin{bmatrix} 0 & 0 & 1 \\ 0 & 0 & 0 \\ 1 & 0 & 0 \end{bmatrix}}_{\sigma_{13}} \tag{13}$$

By applying scalar multipliers to the six partitioned tensors, any general stress tensor can be described. Hence, by describing the displacement responses for the six base cases, the response for any combination of the six tensors can be found by adding the individual displacement responses. Of the six partitioned tensors, σ_{11}, σ_{33} and σ_{13} represent plane components of stress, i.e., oriented in the cross-sectional plane orthogonal to the tunnel axis, while σ_{22}, σ_{12} and σ_{23} are antiplane components (Filon 1937). The components of the partitioned stress tensor are illustrated in Figure 62.

A numerical modeling study was undertaken to characterize the radial displacement responses associated with each component of the partitioned tensor. EXAMINE^{3D} (Curran and Corkum 1993), a 3D boundary element code, was used to model the displacement response of a cylindrical tunnel in a linear elastic medium. Values of $a = 1.75$ m, $\nu = 0.25$ and $G = 26$ GPa were used for the study. The level of discretization (72 elements around the perimeter) was selected by comparing results with those from an axisymmetric finite difference model, and a non-axisymmetric finite element model (Grabinsky and Curran 1993). Radial displacements far from the tunnel face were compared to the analytical plane strain solution, e.g., (Goodman 1989). In terms of the coordinate system used for the model, σ_{11} is coincident with the y-axis, σ_{22} with the x-axis, and σ_{33} with the z-axis.

The study showed that the radial displacement response at the tunnel wall can be considered the result of superposition of six *characteristic radial displacement surfaces*. In these 3D plots, the x, y and z axes correspond to normalized face position X/D, rotation angle θ and normalized radial displacement $U_r/U_{r_{max}}$, respectively. Of the six responses, there are only three unique surfaces (Figure 63), the others being, or comprising, surfaces of the same shape, but with different phase constants. Aside from the obvious differences in shape, the

most notable difference between these three surfaces is that the periodicity for the plane component surface is 180°, while the antiplane normal component surface is axisymmetric and the antiplane shear component surface has a periodicity of 360°.

Mathematical expressions were developed to describe the *characteristic radial displacement surfaces* at $r/a = 1$. These surfaces can be represented in 2D by considering the radial displacement response versus either face position for a fixed rotation angle, or rotation angle for a fixed face position. The *spliced logistic function* was developed as a general approximating function for the radial displacement response versus face position. Parametric functions describing the radial displacement response versus rotation angle were also derived, and the *spliced logistic function* was used to describe the variation in the equation parameters α and β with face position.

Using the same developmental approach, a general approximating function comprising an inverse polynomial series was developed to describe the radial displacement response versus radial distance. This approximating function was, in turn, used with the general parametric equations for the radial displacement response versus rotation angle to represent *characteristic radial displacement surfaces* in the $r-\theta$ plane at five axial positions in the tunnel. The approximating and parametric functions for each of these types of surface are presented in Appendix B.

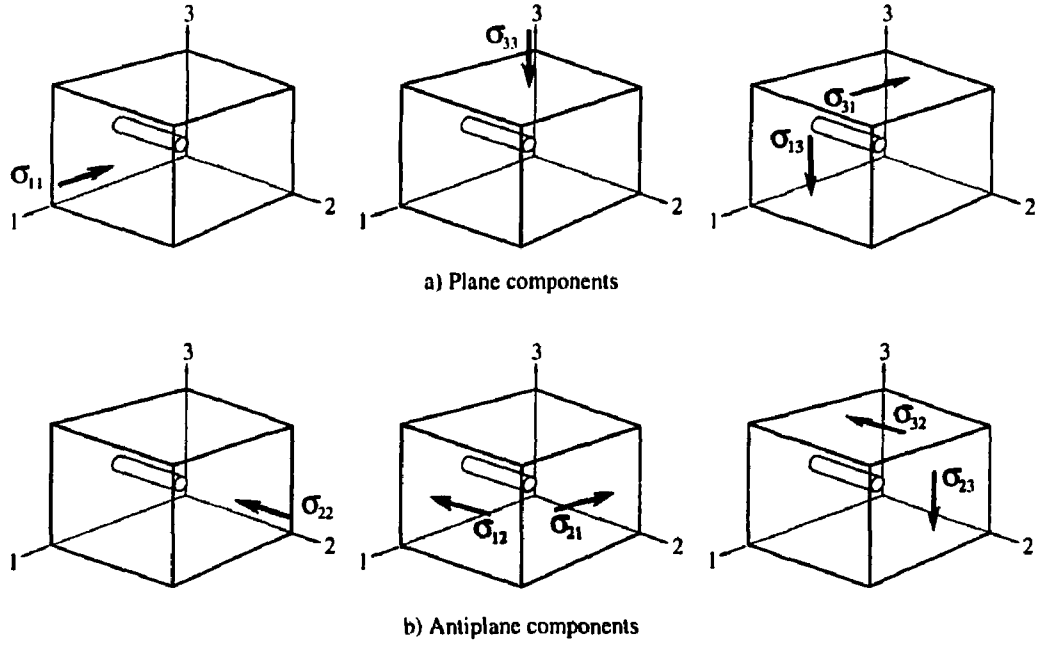

FIGURE 62: Components of the partitioned stress tensor: a) plane components, and b) antiplane components.

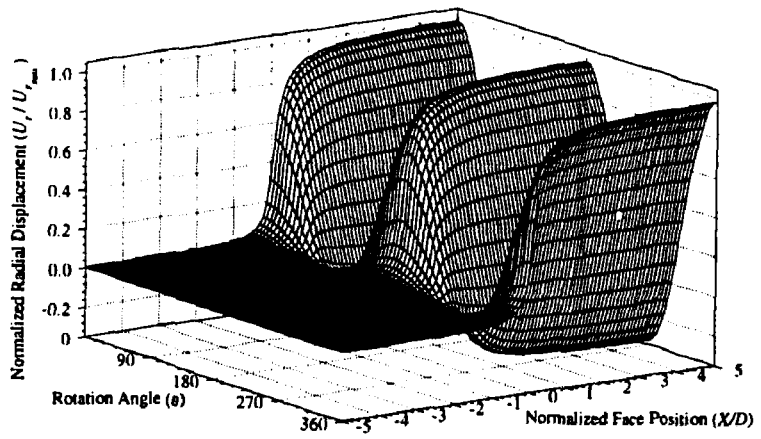

(a) σ_{11} tensor.

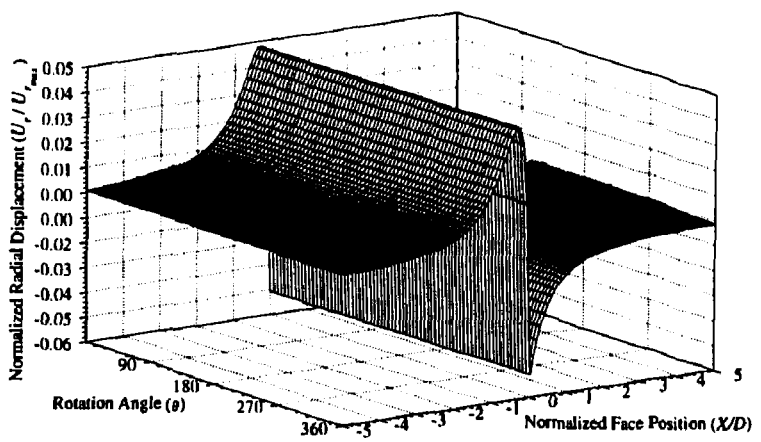

(b) σ_{22} tensor.

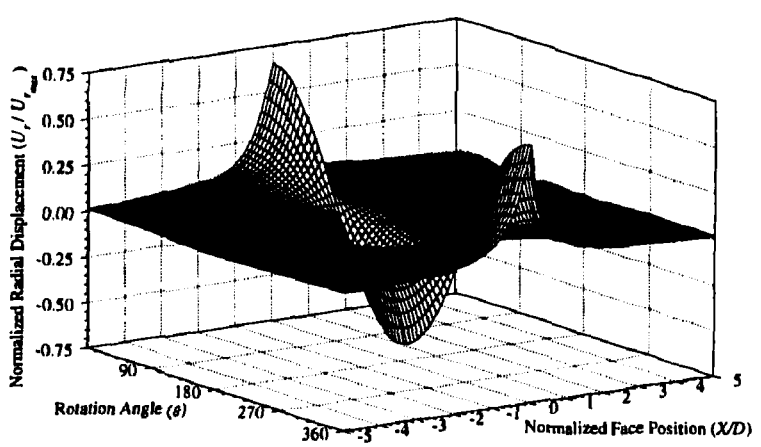

(c) σ_{12} tensor.

FIGURE 63: *Characteristic radial displacement surfaces* at $r/a = 1$.

4.1.2 Least-Squares Technique

Using a least-squares approach (Livesley 1989) and the equations developed to describe the *characteristic radial displacement surfaces*, all six components of the *in situ* stress tensor can be estimated from radial displacements measured within ±1 diameter of the tunnel face. The combined parametric functions associated with the radial displacement surface for a general stress case represent a linear combination of six unknowns of the form

$$\frac{U_r}{U_{r_{max}}} = c_1 f_1(r,\theta,x) + c_2 f_2(r,\theta,x) + c_3 f_3(r,\theta,x) + c_4 f_4(r,x) + c_5 f_5(r,\theta,x) + c_6 f_6(r,\theta,x). \quad (14)$$

In Equation 14, functions f_{1-6} are described by the *characteristic radial displacement surfaces* for the partitioned stress tensor components. The coefficients c_1, c_2, c_3, c_4, c_5 and c_6 are equal to the stress magnitude (in MPa) of σ_{11}, σ_{33}, σ_{13}, σ_{22}, σ_{12}, and σ_{23}, respectively, if the shear modulus of the rock mass and diameter of the tunnel under consideration are the same as those used in the model study. For cases where the actual tunnel parameters differ from those in the model, the matrix of coefficients is related to the matrix of stress magnitudes by

$$\{C\} = C_f\{\sigma\}, \quad C_f = \frac{a_{\text{model}} G_{\text{field}}}{a_{\text{field}} G_{\text{model}}}. \quad (15)$$

In matrix notation, given m equations with known values of F and U, and n unknowns C, i.e.,

$$\underbrace{[F]}_{m\times n}\underbrace{\{C\}}_{n\times 1} = \underbrace{\{U\}}_{m\times 1} \quad (16)$$

and substituting for $\{C\}$ using Equation 15, the solution for 6 unknowns σ can be written

$$\underbrace{\{\sigma\}}_{6\times 1} = \frac{1}{C_f}\underbrace{\left[\underbrace{[F]^{\mathrm{T}}}_{6\times m}\underbrace{[F]}_{m\times 6}\right]^{-1}}_{6\times 6}\underbrace{[F]^{\mathrm{T}}}_{6\times m}\underbrace{\{U\}}_{m\times 1}. \quad (17)$$

In this case, the matrix F corresponds to the parametric functions $f_1 - f_6$, U corresponds to the measured radial displacements normalized to $U_{r_{max}}$, and σ is the matrix of unknown stress magnitudes.

Because the maxima and minima of the radial displacement responses for the antiplane components occur near the tunnel face, back analysis of the antiplane stress components is only possible if measurements from the region $-1 \leq X/D \leq 1$ account for a large proportion of the data set. Measurements outside this region in the posterior domain will help establish the plane components if the material behaviour is linear elastic, but will not constrain the estimates of antiplane components. Supplemental equations relating the various stress components can also be added to the analysis to provide additional constraint on the estimated tensor. Weighting of a particular measurement or constraint can be accomplished by repeating the equation associated with the measurement within the system of equations.

The radial displacement response measured by posterior extensometers can be considered a partial *characteristic radial displacement surface*. The functions given in Equation 14 can be modified to reflect this fact. In the α and β expressions in the parametric functions, described by *spliced logistic functions* for each component of the partitioned stress tensor, the y-intercept parameter D_l is set to zero. This change results in new functions $f_{1_e-6_e}$.

For convergence measurements, the functions $f_{1_e-6_e}$ require a further modification to account for the relative nature of the measurement, i.e., the relative displacement between pins on opposite sides of the tunnel is measured rather than the absolute displacement of individual convergence pins. To this end, the functions $f_{1_e-6_e}$ for posterior extensometers on opposite sides of the tunnel are added to define new functions $f_{1_c-6_c}$. A direct consequence of this modification is that the new functions $f_{5_c-6_c}$ associated with the antiplane shear components of the stress tensor are zero because of the antisymmetric nature of the radial displacement responses produced by them. In other words, convergence measurements are unaffected by antiplane shear stresses, and therefore cannot be used to back calculate these components of the tensor.

4.1.3 Verification of the Method using EXAMINE^{3D}

The parametric functions, their coefficients and the least-squares technique were tested using displacement results from EXAMINE^{3D} for a general stress case. The applied stresses in the model were $\sigma_1 = 55$, $\sigma_2 = 48$ and $\sigma_3 = 14$ MPa, with σ_1 orthogonal to the tunnel axis and inclined 14.5° from horizontal. Subsets of radial displacement data were assessed to determine the sensitivity of stress predictions to measurement type and location relative to the tunnel. Three measurement types were simulated: 1) radial displacements at the tunnel wall from extensometers, 2) wall convergence from convergence arrays, and 3) radial displacements remote from the tunnel wall from extensometers. Results of the study (Figure 64) are shown as predicted stress components based on Wall (Types 1 and 2), Radial (Type 3), and Combined (Types 1, 2 and 3) measurements from the anterior, posterior and combined domains within ±1 diameter of the tunnel face. To illustrate the effect of incorporating additional information into the predictions, 10 equations constraining the σ_{11}/σ_{22} ratio were added to each data set. The resulting predictions are shown as Constrained in Figure 64.

The model simulation showed that the various subsets of three different measurement types all produced good estimates of the stress components. In each case, the predicted axial stress component showed more uncertainty than the other components owing to the relatively small radial displacement response associated with the σ_{22} tensor. Radial displacement measurements remote from the tunnel wall, on their own and in combination with measurements at the tunnel wall, produced less uncertainty in the predicted stresses than tunnel wall displacement measurements alone. The inclusion of additional constraint equations illustrated that information from other stress determinations can be used to improve stress predictions, provided the constraints have less uncertainty associated with them than individual displacement measurements. Based on the results of this study, combinations of different measurement types from different domains were recommended to optimize

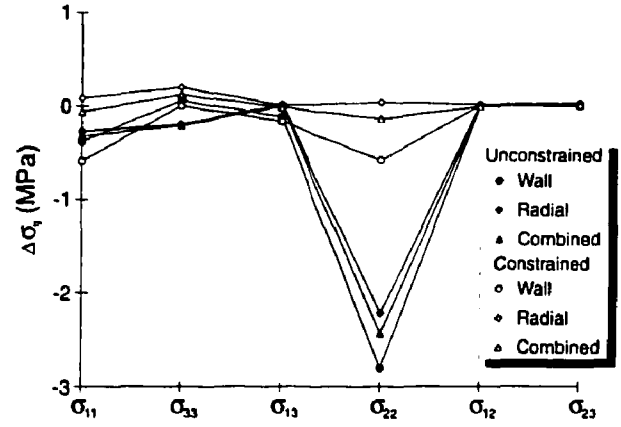

(a) Data from anterior domain $-1 \leq X/D \leq 0$.

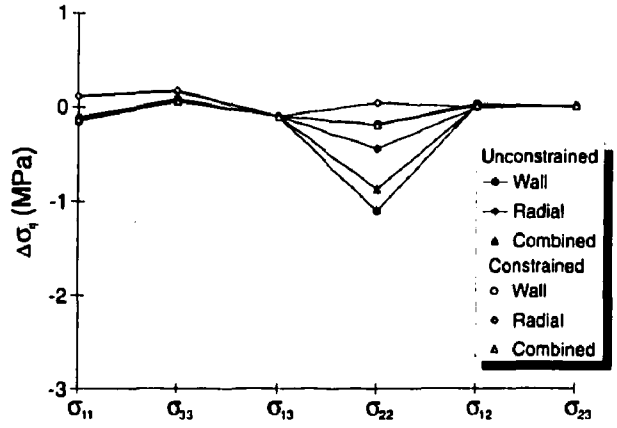

(b) Data from posterior domain $0 \leq X/D \leq 1$.

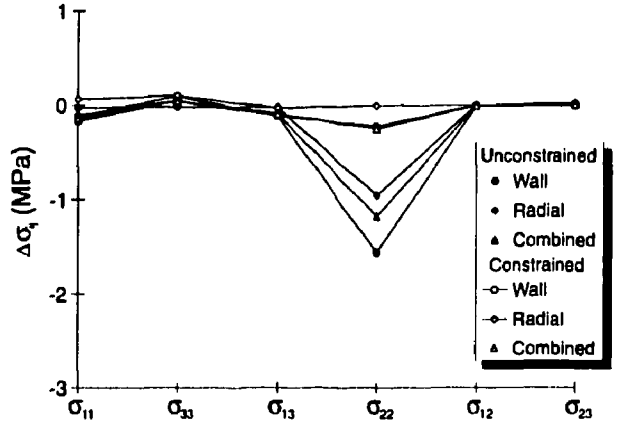

(c) Data from both domains $-1 \leq X/D \leq 1$.

FIGURE 64: Difference between predicted stress components and those used in the numerical model for various subsets of data.

the data set used in this back analysis technique. However, departure from linear elastic behaviour in the posterior domain might preclude some, or all, of the data from that region.

4.1.4 Application to the Mine-by Experiment

4.1.4.1 Methodology

Following development of the back analysis technique, a methodology was established to standardize field measurements of radial displacement in an enhanced data set, where the values of displacement at specific axial positions were interpolated, and the amount of displacement missed by each instrument was estimated (Read 1994). It was found that displacements occurring beyond the outermost extensometer anchors could be a significant proportion compared to the measured response. Displacements missed ahead of the tunnel face, in contrast, were found to be negligible if the first measurement was taken approximately three tunnel diameters ahead of the face.

As part of the analysis of measurements from the field study, Read (1994) compared results from extensometers directly to those from convergence arrays (Figure 65). He found

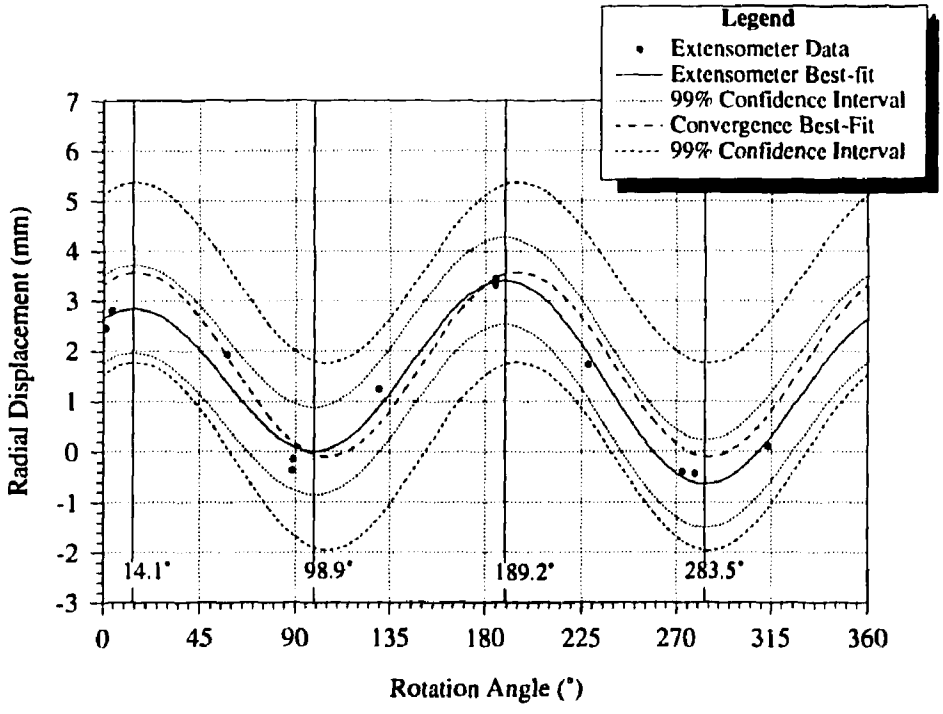

FIGURE 65: Comparison of posterior radial displacement results from extensometers and convergence arrays. The radial displacement for the convergence arrays is taken as one-half the total measured convergence. Results from all eight convergence arrays were considered. Note the asymmetry in the magnitude and rotation angle of the maxima and minima for the extensometer data.

TABLE 4

PROPORTION OF RADIAL DISPLACEMENT RESPONSE IN THE ANTERIOR DOMAIN UNDER AXISYMMETRIC STRESS CONDITIONS

Face Shape	Proportion of Total Radial Displacement in Anterior Domain (%)						
	K=1,0,1	1,$\frac{1}{4}$,1	1,$\frac{1}{2}$,1	1,1,1	1,2,1	1,3,1	1,4,1
Flat	29	26	24	20	13	6	-1
Filleted	38	36	33	30	23	16	9
Curved (0.071)	37	34	31	25	16	5	-6
Curved (0.143)	43	39	37	31	19	7	-4
Hemispherical	51	49	47	44	37	30	23

Value in parentheses for the curved faces is the difference in chainage of face edge and centre normalized to tunnel diameter.

that the two measurement types produced consistent results, but that convergence measurements were, by their nature, unaffected by antiplane shear components of the stress tensor. Consequently, plots of convergence versus rotation angle have symmetric maxima and minima for $0 \leq \theta \leq 360°$. Extensometer results, on the other hand, were shown to be sensitive to antiplane shear stresses near the tunnel face, which result in asymmetry in the magnitude and angular positions of the maxima and minima of the radial displacement response versus rotation angle for $0 \leq \theta \leq 360°$.

In comparison with the 27% reported in previous studies, Read (1994) found the amount of radial displacement occurring ahead of the advancing tunnel face to be about 30% in the case of a flat face under conditions of zero antiplane stress components. Results from an axisymmetric finite difference model study for the proportion of the total displacement response occurring in the anterior domain for various face shapes and axial stress ratios are shown in Table 4. The face shapes used in the study are given in Figure 66. For the general case, the proportion of displacement occurring in the anterior domain varies with the shape of the tunnel face, and the magnitude of the axial stress component (Figure 67). Stepped

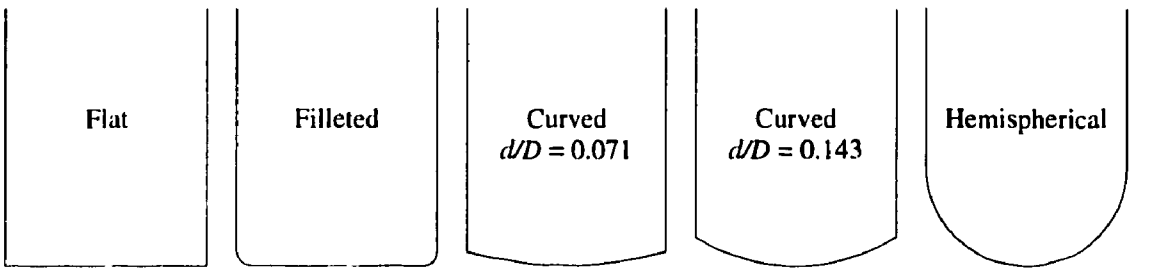

FIGURE 66: Five face shapes considered in the numerical modelling study. The ratio d/D is the difference in axial positions of the edge and centre of the tunnel face normalized to the tunnel diameter.

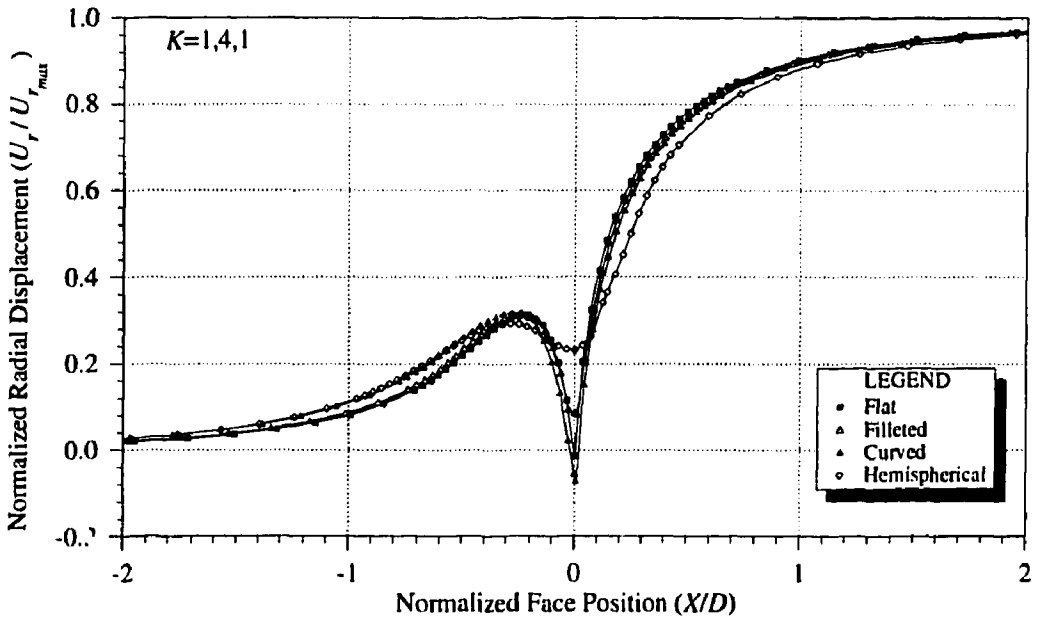

(a) Effect of face shape.

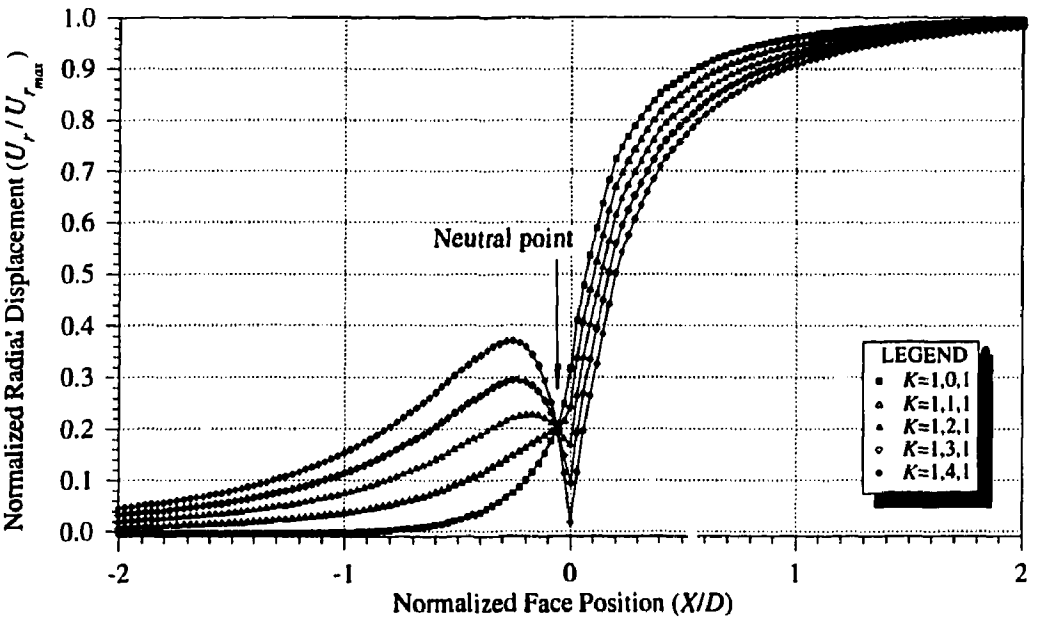

(b) Effect of axial stress component.

FIGURE 67: Effect of face shape and axial stress component on the radial displacement response versus face position at $r/a = 1$.

longitudinal tunnel geometry was also found to affect the radial displacement response in the posterior domain, but had a negligible effect on the response in the anterior domain (Read 1994).

4.1.4.2 Results from the Mine-by Experiment

Once the field data from the Mine-by Experiment were standardized, back analysis of the *in situ* stress tensor was conducted. Because of the large number of measurements (1107 extensometer and 138 convergence measurements), data were grouped systematically into subsets by measurement type. The measurement types were defined as:

- radial displacement for $r/a > 1$
  - i) including all extensometer measurements, and
  - ii) excluding all vertical extensometer measurements for $X/D > -0.4$;
- radial displacement for $r/a = 1$
  - i) including all extensometer measurements, and
  - ii) excluding all vertical extensometer measurements; and
- convergence measurements at the tunnel wall
  - i) including all measurements, and
  - ii) excluding vertical measurements.

Incremental predictions of the *in situ* stress tensor were made for each subset, and plots of stress invariants were used to assess the reliability of the individual estimates. The most reliable data for the different measurement types were then combined to produce eleven refined stress predictions.

The mean and standard deviation tensors were calculated from the eleven predicted tensors, weighting each prediction by the number of measurements upon which it was based. The calculated mean and standard deviation tensors, expressed in terms of the tunnel coordinate system with values in MPa, are

$$\overline{\sigma} = \begin{bmatrix} 57.18 & -3.60 & 10.81 \\ -3.60 & 45.50 & 3.00 \\ 10.81 & 3.00 & 11.08 \end{bmatrix}$$

$$S_{\overline{\sigma}} = \begin{bmatrix} 0.13 & 0.32 & 0.70 \\ 0.32 & 1.74 & 0.21 \\ 0.70 & 0.21 & 0.42 \end{bmatrix}$$

A Monte Carlo simulation was also conducted using the same eleven predicted tensors to determine the mean and expected range of values for the principal stresses. The expected range was taken as three standard deviations either side of the mean value. From this simulation, the estimated principal stress magnitudes were 60 ± 2, 45 ± 4 and 8 ± 3 for σ_1, σ_2 and σ_3, respectively. The principal stress magnitudes and directions associated with the estimates from the eleven combined data sets used to calculate the mean and

TABLE 5

ESTIMATED PRINCIPAL STRESSES FROM BACK ANALYSIS OF DISPLACEMENT MEASUREMENTS

Data	σ_1			σ_2			σ_3		
Set	MPa	Trend	Plunge	MPa	Trend	Plunge	MPa	Trend	Plunge
r_{1-3}	61.70	147.00	12.77	48.12	54.98	8.87	6.50	291.07	74.37
CR_1	60.19	148.08	11.25	42.90	56.31	8.86	8.32	288.89	75.61
cR_1	60.63	150.19	10.36	43.51	58.53	9.00	9.63	288.33	76.21
CW_1	59.40	144.93	11.68	46.28	53.60	6.43	7.79	295.30	76.62
cW_1	59.53	145.09	11.13	46.31	53.81	6.51	8.94	294.01	77.07
cw_1	59.52	144.03	11.04	46.31	52.65	7.09	9.82	290.53	76.83
R_1CW_1	59.76	146.46	11.53	45.01	54.99	7.21	7.68	293.58	76.35
R_1Cw_1	59.74	145.65	11.63	44.77	54.07	7.60	8.09	291.58	76.04
R_1cW_1	59.89	146.37	11.12	44.80	54.93	7.26	8.59	292.40	76.67
R_1cw_1	59.93	145.41	11.08	44.29	53.89	7.70	9.43	289.76	76.45
$r_{1-3}cw_1$	60.14	145.85	11.59	45.36	54.06	8.68	8.44	288.06	75.45
Mean Estimate									
	60.16	146.48	11.51	45.30	54.84	7.99	8.30	290.80	75.92
Best Combined Estimate									
R_1cw_1	59.93	145.41	11.08	44.29	53.89	7.70	9.43	289.76	76.45

standard deviation tensors are shown in Table 5. The magnitudes of the principal stress components are very consistent between the eleven estimates, with the most variability noted in the estimate of σ_2. As noted by Read (1994), the estimates of σ_2 and σ_3 appear to be interdependent, with estimates showing a high value of σ_2 having an associated low value for σ_3.

Although the mean tensor $\overline{\sigma}$ and the mean principal stresses are good approximations to the *in situ* stress tensor, it was difficult to define appropriate weights for the eleven estimates used in their determination given that the estimates were not completely independent, i.e., individual subsets of data were used in more than one estimate. An alternative to using the mean tensor as the final estimate of the *in situ* stress tensor was to use the most reliable of the eleven refined estimates. The 'best' estimate was based on a data set which comprised 223 measurements, incorporated all three measurement types, and excluded those values potentially affected by excavation damage or inaccurate extrapolation. On this basis, the 'best' estimate of the principal stresses is

	MPa	Trend	Plunge
σ_1	59.9	145.4	11.1
σ_2	44.3	53.9	7.7
σ_3	9.4	289.8	76.5

Figure 68 shows the 'best' estimate of the principal stresses, both in terms of magnitude and orientation, along with the expected range of magnitudes and 90% confidence intervals

on orientation. What is particularly striking about the eleven estimates shown in Figure 68 is the consistency in the orientations of the principal stress components. The estimates that do not include radial displacement measurements at $r/a = 1$ tend to deviate most from the cluster around the mean orientations.

4.1.4.3 Comparison with Previous Results

As discussed in Section 2.1.3, the initial estimate of the *in situ* stress tensor at the 420 Level of the URL was based on results from a variety of stress measurement techniques. Of the techniques tried, only the overcoring and under-excavation studies produced estimates of the complete *in situ* stress tensor. However, as detailed in Section 2.1.3, each of these estimates was affected by testing difficulties related, in part, to the high *in situ* stresses at this level. Consequently, a composite tensor was estimated from the various techniques. The composite nature of the tensor posed some difficulties, however, in constraining the relative magnitudes of the various components.

In comparing the 'best' estimate from the back analysis to the initial composite estimate (Figure 68), the two tensors are remarkably similar, especially when the uncertainty in the composite tensor is taken into consideration. One of the most notable differences is that σ_2 in the new estimate is not parallel to the test tunnel axis. In fact, the tunnel axis deviates 8.9° in trend, and 7.7° in plunge from σ_2. This condition implies that antiplane

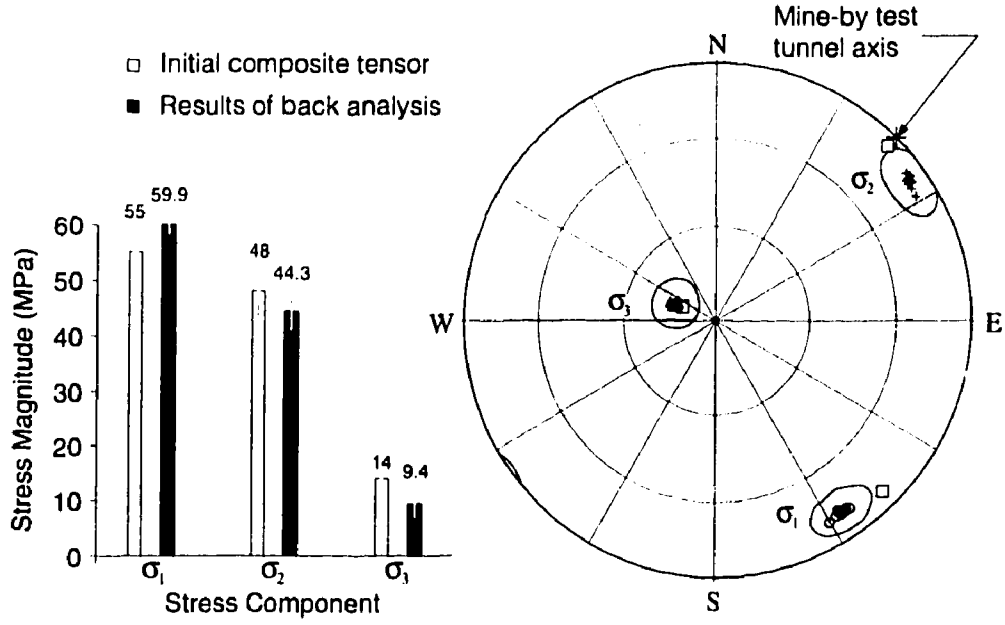

FIGURE 68: Magnitude and orientation of principal stresses estimated from back analysis of displacement measurements. Note the consistency in orientation for the eleven individual estimates shown on the lower hemisphere stereoplot. The estimates of stress magnitudes and orientations from the initial composite tensor are shown for comparison.

shear stresses near the tunnel face in the anterior domain are distributed in an asymmetric manner with respect to the tunnel axis, and precludes back analysis techniques based on the assumption of parallelism between the tunnel axis and a principal stress direction. The implications of this difference are examined in Section 4.3.

The other main difference between the estimates is the magnitude of σ_3. In the composite tensor, σ_3 was based primarily on results of hydraulic fracturing tests conducted in horizontal boreholes at the 420 Level of the URL. Doe (1989) interpreted the shut-in pressure in tests producing subhorizontal fractures in horizontal boreholes as σ_3, based on the assumption that the fractures formed orthogonal to the minimum principal stress direction. However, Haimson et al. (1993) showed that, in a vertical borehole in the same region of the rock mass near the 420 Level, nine hydraulically-produced fractures had dips ranging from 15 to 39° and dip directions ranging from 068 to 245°, illustrating that the induced fractures do not necessarily form orthogonal to σ_3. They further showed that, by assuming the vertical stress to be equal to the calculated lithostatic stress, the best estimate of the maximum horizontal stress near the 420 Level of the URL was approximately 54 MPa. In retrospect, the uncertainty associated with σ_3 in the initial composite tensor was underestimated, and should have been in the same range as that for the other stress components, i.e., ±5 MPa.

The calculated lithostatic stress at the 420 Level of the URL is approximately 11 MPa. The magnitudes of the vertical stress σ_{33} in both the best combined estimate and the mean estimate of the *in situ* stress tensor based on results from the field study compare favourably with this value. The fact that no additional constraint equations were required to achieve this value provides a degree of confidence in the estimated tensor and the elastic constants used in the back analysis (E = 65 GPa and ν = 0.25). The values of the elastic constants are in keeping with those shown in Section 2.1.2 from previous laboratory testing, and are believed representative of the portion of the rock mass from which the measurements used in the back analysis were taken, i.e., primarily from the anterior domain and remote from the excavation. The estimated stress components are directly proportional to Young's modulus.

In addition to predicting a vertical stress component close to lithostatic, the orientation of σ_1 is almost parallel to the average orientation of the fracture zones identified at the URL. The fact that σ_1 is not horizontal can be attributed to a reduction in shear stress parallel to the dip direction of the fracture zones. Observed large-scale shear displacement in the upper portion of the Lac du Bonnet batholith, such as reverse thrusting of up to 7.3 m along Fracture Zone 2 (Everitt et al. 1990a), is evidence for this type of stress relief. Using two simple numerical models, Chandler and Martin (1994) showed that stress redistribution associated with shearing along the major fracture zones also accounts for perturbations in the stresses in the upper part of the batholith. This process generates high stresses in the dip direction of the fracture zones, which results in rotation of the azimuth of the maximum principal stress. Further confirmation of the estimated stress tensor using patterns of excavation damage is undertaken in Section 4.3.

4.2 BACK ANALYSIS USING DBEM3D

In addition to the study described in the previous section, back analysis of the Mine-by Experiment was also conducted using the direct back analysis method developed for the under-excavation technique (Wiles and Kaiser 1994a; Wiles and Kaiser 1994b). This additional analysis was meant to provide confidence in the estimated stress tensor, and to directly assess the effects of face shape and external openings, i.e., other excavations near the experiment area. DBEM3D (Wiles 1992), a PC-based computer program, was used for two studies: one to assess various combinations of instrument results (Wiles 1995), and a complementary study to assess a specific data set selected on the basis of instrument and rock mass behaviour during the Mine-by Experiment. Because the results of the second study have not yet been published, they are included in this report in some detail.

DBEM3D is based on linear elasticity and uses constant intensity triangular and quadrilateral boundary elements solved by the indirect boundary element technique to back calculate initial *in situ* stresses from measured excavation-induced strains and displacements. It is coupled with a statistical package, STAT3D, which allows the user to evaluate the quality of the input data and the confidence of the stress prediction. There are two main control parameters in STAT3D: α controls the number of rounds and therefore the number of individual measurements to include in a particular analysis, while δ controls the number of rounds over which to calculate the incremental responses and hence the magnitude of each measurement used in the analysis.

4.2.1 Sensitivity Analysis

As part of these studies, the sensitivity of the method to various parameters used in the numerical approximation, and to the quality of input data, was assessed using a simple test case. The geometry for this test case was a uniformly discretized rectangular excavation with seven extensometers. The excavation started as a cube with a side-length of 2 m, and was extended 1 m in a single excavation step (Figure 69). Using uniform discretization, it was found that the accuracy in predicted stresses was related primarily to the discretization of the underground openings. As illustrated in Figure 70, the predicted displacement at a single extensometer point approaches an asymptote with increasing number of boundary elements. Likewise, the predicted stresses also approach an asymptote as the number of boundary elements increases. Wiles (1995) further found that the error in predicted stresses was similar to the error in input, e.g., a 5% uncertainty in displacement values produced about a 5% uncertainty in predicted stress magnitudes. Similar results were found using a simple cylindrical model, and using non-uniform discretization.

4.2.2 Application to the Mine-by Experiment

Excavation of the Mine-by test tunnel was simulated using boundary element models constructed to match the surveyed location of each instrument and excavation face position. The complete set of data for the back analysis consisted of displacement measurements from 13 Bof-ex extensometers (11 anchors each) and strains from 12 CSIRO HI triaxial strain cells (9 strain gauges each). The test tunnel advanced past the two CSIRO arrays in Rounds 13

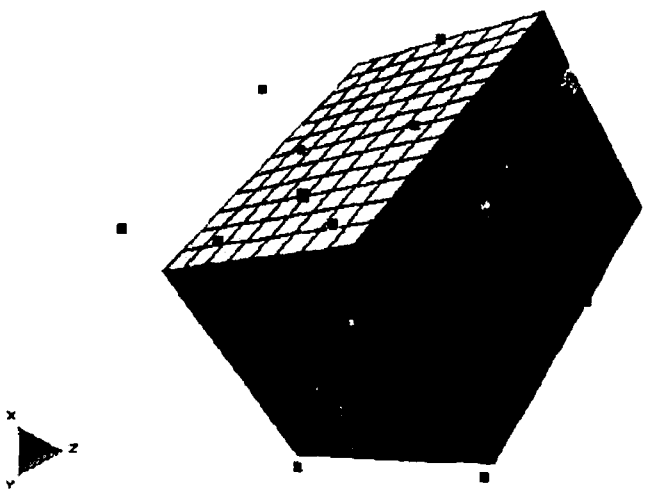

FIGURE 69: Block model used in the sensitivity analysis. The block is initially 2-m long with a 1 m by 1 m square cross-section, and represents the boundary of an opening. Instrument locations are shown as small squares around the block.

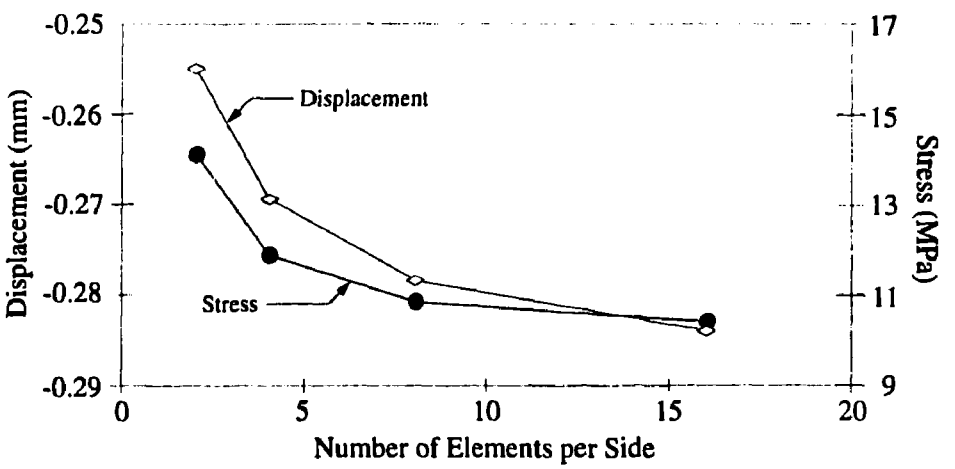

FIGURE 70: Illustration of the effect of discretization on the displacements and stresses predicted for a simple block model. The number of elements refers to the discretization of each side of the square cross-section.

and 20, and past the two extensometer arrays in Rounds 15 and 17, respectively. To obtain well-constrained stress estimates, it was desirable to maximize the number of instrument readings used in each estimate, while eliminating or minimizing the effects of: 1) readings from faulty instruments, 2) readings from regions affected by non-linear/non-elastic material behaviour, and 3) readings from rounds far from the instruments where the measured response was of the order of the instrument error. A series of simulations were conducted using various subsets of instruments to identify the best combination of instruments and excavation rounds to use for the stress estimates. Wiles (1995) considered different combinations of instrument readings, and different combinations of excavation rounds, from those described here.

From previous results with the under-excavation method using CSIRO HI cells (Wiles and Kaiser 1992), it was shown that strain measurements included a large non-linear/non-elastic component once the tunnel face had approached and passed the instrument array, resulting in erratic stress estimates. In the Mine-by Experiment, this type of behaviour was noted in the first CSIRO array starting from Round 12, and in the second CSIRO array from Round 19. Given the position of the first CSIRO array relative to the other instrument arrays, results from the first CSIRO array past Round 12 could not be used in combination with those from the other arrays, and, consequently, cells SM1 to 4 were excluded from the analyses. Likewise, because measurements for Rounds 19 and greater included a large non-linear/non-elastic component, they were not included in the analyses. Of the instruments used for the experiment, only one gauge on one CSIRO cell (cell SM5, gauge 9) was found to be faulty for measurements taken up to Round 18. This gauge was not included in any of the analyses.

In order to maximize the number of instruments included in each stress estimate, it was desirable to take advantage of the overlap in responses measured at the two extensometer arrays, and in the second CSIRO array. However, extensometer results from the Mine-by Experiment showed evidence of non-linear/non-elastic behaviour close to the tunnel wall once the tunnel face had passed the instruments (Read 1994). To reduce the influence of this non-linear/non-elastic behaviour on results of the back analysis, the inner two measurement intervals in the first extensometer array, and the inner measurement interval in the second array, were excluded from the analysis. This approach also minimized the effect of differences between the model geometry and the actual *in situ* tunnel geometry, such as the stepped longitudinal profile of the test tunnel, and the effect of discretization of the tunnel boundary in the model. The outer measurement interval in each extensometer was also dropped because of the proximity of the outer anchor to the external instrument galleries. In the axial extensometer (EXT13), the two intervals closest to Room 414 were also excluded.

The incremental instrument responses, i.e., the change in response between successive excavation rounds, from 100 displacement transducers in the extensometers and 71 strain gauges in the second CSIRO array were used to estimate the *in situ* stress tensor. Independent estimates, based on the incremental responses from each individual excavation step, were obtained by setting the parameters α and δ in STAT3D to 1. These estimates were evaluated to determine the range of excavation rounds that produced consistent results. In evaluating predicted stress orientations and magnitudes, individual estimates from Rounds 1 to 14

showed erratic orientations and/or negative values of σ_3, and were therefore not considered reliable. Likewise, individual estimates from Round 19 and greater were erratic, and were excluded from the analysis. Individual estimates from Rounds 15 to 18 showed consistent stress orientations and magnitudes.

Improved stress estimates were obtained by increasing the number of measurements in the data set upon which each estimate was based. By setting $\alpha > 1$ in STAT3D, the incremental instrument responses from between 2 and 7 consecutive rounds were combined into individual data sets. STAT3D uses a least-squares method to minimize the residuals between measured and predicted strains or displacements, weighting individual responses according to their magnitude. Consequently, estimates obtained from multiple rounds are based on more measurements than those for individual rounds, and are therefore better constrained. Between Rounds 15 and 18, estimates based on the combined incremental responses from as far away as Round 11 were consistent in orientation and magnitude. Based on the number of measurements included in the analysis, the 'best' estimate of the *in situ* stress tensor is that for Round 18 with $\alpha = 7$, which considers the incremental instrument responses for Rounds 11 to 18 in one data set.

In order to assess the variability in stress predictions, a data set of 22 estimates was compiled by considering measurements from Rounds 15 to 18, varying α from 1 to 7 for Round 18, from 1 to 6 for Round 17, and so on. These estimates were, however, not completely independent because individual measurements were used in more than one estimate. From the 22 estimates, the mean and standard deviation tensors of stresses in the tunnel coordinate system, along with the mean and 90% confidence limits of the principal stress tensor, were determined using the method described by Walker et al. (1990). This scheme implicitly weighted measurements from Rounds 15 and 16 most heavily, i.e., 9.5% for Round 18, 16.2% for Round 17, 20.3% for Round 16, 21.6% for Round 15, 16.2% for Round 14, 10.8% for Round 13 and 5.4% for Round 12. As a result of this implicit weighting, there were some differences between the mean estimate and the 'best' estimate given by Round 18 with $\alpha = 7$. Nevertheless, the estimated mean and variability from this group of instruments and excavation rounds was used as a basis for comparison in the different model simulations.

Three types of models were used to simulate the Mine-by Experiment: one incorporating a flat-faced cylindrical tunnel with no external openings, the others using a cylindrical tunnel but accounting for a non-planar tunnel face shape and external openings. Several subcases were run with each model to assess effects of discretization and 'leaks' in the tunnel geometry. Except where noted, Young's modulus was 65 GPa and Poisson's ratio was 0.2 in each case. Discretization was controlled by two parameters, DOL and AL. DOL relates the boundary element side-length L to the distance D from a boundary element to the closest field point, and AL is the minimum element size. The use of constant values of DOL and AL results in fine discretization close to instrument locations, and coarser discretization remote from the instruments. According to Wiles (1995), the error in predictions decreases with increasing values of DOL and decreasing values of AL.

4.2.3 Cylindrical Tunnel with a Flat Face

The first analysis was conducted using a flat-faced, 3.5-m-diameter cylindrical tunnel with no external openings (Figure 71). Three sub-cases, using different values of DOL and AL, were run: a coarse discretization with AL=1 and DOL=2, an intermediate discretization with AL=0.5 and DOL=1.5, and a fine discretization with AL=0.5 and DOL=2. Using the 22 estimates described in the previous section, the mean and standard deviation tensors (in MPa) for the fine discretization sub-case are, respectively,

$$\bar{\sigma} = \begin{bmatrix} 55.87 & -2.94 & 13.21 \\ -2.94 & 44.40 & 1.65 \\ 13.21 & 1.65 & 13.82 \end{bmatrix}$$

$$S_{\bar{\sigma}} = \begin{bmatrix} 1.44 & 0.94 & 2.14 \\ 0.94 & 0.90 & 0.67 \\ 2.14 & 0.67 & 1.53 \end{bmatrix}$$

The standard deviation tensor for the intermediate sub-case was found to be similar to that for the fine sub-case. By comparison, the coarse discretization increased the standard deviation of σ_{11} by about 1 MPa, and of the σ_{22} and σ_{33} components by about 0.5 MPa. The same trend was apparent in comparing the range of values for the principal stress magnitudes and orientations: the fine and intermediate sub-cases compared closely, while the coarse sub-case showed markedly increased variability in both magnitudes and orientations.

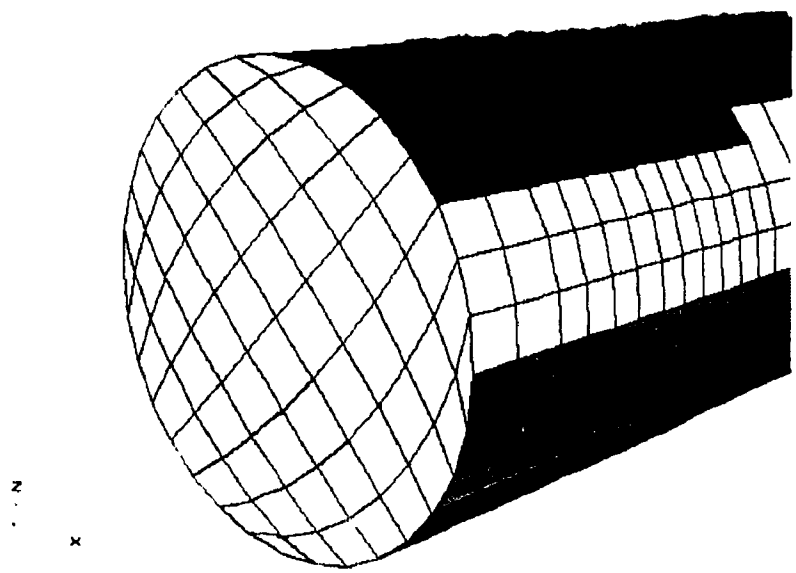

FIGURE 71: Flat-faced cylinder model of the Mine-by Experiment test tunnel used for back calculations. Control parameters are DOL=2 and AL=0.5 in this case.

The results from a Monte Carlo simulation to determine the mean and 90% confidence limits on the principal stress magnitudes and orientations for the fine discretization sub-case are shown in Figure 72. Given the small amount of variability in principal stress magnitudes and orientations shown by the 90% confidence limits for the flat-faced cylindrical tunnel model, it appears that the model adequately represents the *in situ* tunnel geometry. Using a Poisson's ratio of 0.2, the 'best' estimate of the principal stress tensor, given by Round 18 with $\alpha = 7$, is

	MPa	Trend	Plunge
σ_1	59.6	145.1	14.5
σ_2	44.1	53.5	6.3
σ_3	11.1	300.8	74.1

The effect of changing Poisson's ratio from 0.2 to 0.25 was assessed in a simulation using the flat-faced cylinder with intermediate discretization described above. The net result was a decrease of 0.2 MPa in the mean σ_1 value, a 0.5 MPa increase in the mean σ_2 value and a 0.6 MPa decrease in the mean σ_3 value. Changes of less than 0.7° were noted in the mean orientation angles, except for the trend of σ_3 which increased by 1.9°. These changes in magnitude and orientation are generally of the same order as the variability related to the change from fine to intermediate discretization. The 'best' estimate of the *in situ*

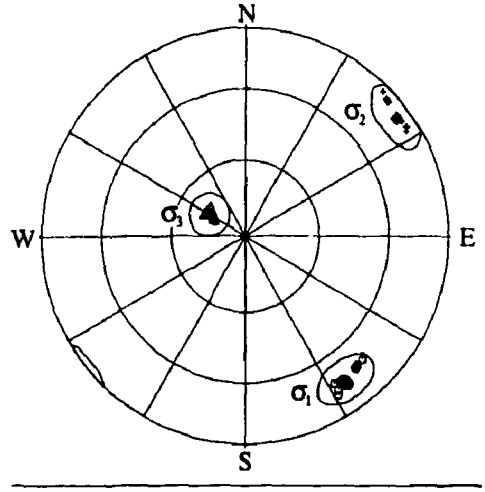

Cylinder with Flat Face

	● σ_1	♦ σ_2	▲ σ_3
Magnitude (MPa)			
-90% CL	57.1	42.5	6.1
Mean	60.0	44.2	9.9
+90% CL	63.4	45.7	13.6
Mean Orientation (°)			
Trend	144.1	052.3	300.1
Plunge	15.4	6.5	73.2

FIGURE 72: Mean and 90% confidence intervals on principal stress magnitudes and orientations for a cylindrical tunnel with a flat face (AL=0.5, DOL=2).

stress tensor (as described previously) using a Poisson's ratio of 0.25 and an intermediate discretization is

	MPa	Trend	Plunge
σ_1	59.8	145.0	14.6
σ_2	45.2	53.5	5.8
σ_3	11.0	302.6	74.2

The results for a flat-faced cylinder compare favourably with those presented in Section 4.1 (duplicated below) using a Poisson's ratio of 0.25.

	MPa	Trend	Plunge
σ_1	59.9	145.4	11.1
σ_2	44.3	53.9	7.7
σ_3	9.4	289.8	76.5

The most notable difference between the estimates is the plunge of σ_1 and the resulting rotation of σ_3. The magnitude of σ_3 is also slightly larger in the DBEM3D back analysis. However, these differences are well within the 90% confidence limits shown in Figure 72. The fact that the two estimates compare so closely is significant in that the approaches, while both based on a cylindrical tunnel model, use different data sets, different types of instruments, and different back analysis methodologies.

4.2.4 Cylindrical Tunnel with a Curved Face

The second analysis was conducted using a 3.5-m-diameter cylindrical tunnel with a curved face to account for deviations from planarity measured during excavation of the test tunnel. To simulate the face curvature, a small central element was required ahead of the tunnel to represent the deepest point on the face. This central element was arbitrarily chosen as a square with a diagonal length of 1 m.

As a result of including the central element ahead of the face, the discretization of the face was altered from that for a flat-faced cylinder (see Figure 71), resulting in some gaps or 'leaks' in the discretized face surface (Figure 73). The effect of these gaps on the stress estimates, without the added effect of face curvature, was investigated using a flat-faced cylinder with a pre-defined central face element. Using values of DOL=1.5 and AL=0.5, and comparing to the flat-faced cylinder with identical control parameter values, it was found that the altered face discretization produced a decrease of about 0.6 MPa in the mean σ_1 and σ_3 values, and a 0.8 MPa increase in the mean σ_2 value. Changes in the mean orientations were less than 0.6° for both trend and plunge angles. Results from the flat-faced cylinder with a central face element were used as the basis for comparison in subsequent simulations with different face curvature.

Face curvature was simulated by positioning the central face element ahead of the plane defined by the mean edge position of the face, then joining the tunnel edge and central face element in one of two ways. In the first case, the tunnel edge and central element were joined using a simple circular arc, similar to the curved faces shown in Section 4.1.4. This shape resulted in a change in the intersection angle between the tunnel wall and face at

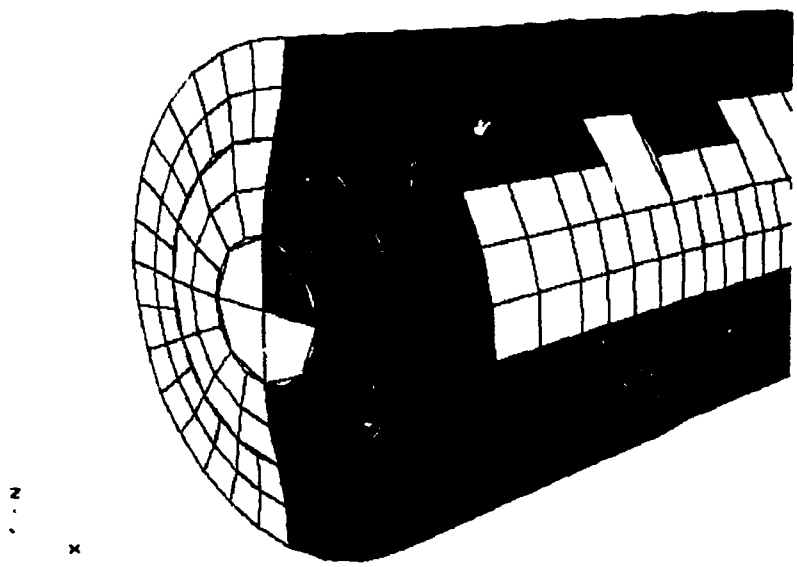

FIGURE 73: Typical face discretization, using a pre-defined central element, for a single-inflection curved face. Note the gaps or 'leaks' in the discretized surface.

the tunnel perimeter. In the second case, the tunnel edge and central element were joined using a single-inflection curve. This shape maintained the right-angle between the tunnel wall and face at the perimeter, more in keeping with field observations. Both approaches assumed axial symmetry in the face shape for each round, and used control parameters of DOL=1.5 and AL=0.5. A typical single-inflection curved face is shown in Figure 73.

Estimates of the *in situ* stress tensor were obtained using both types of face curvature in separate simulations to match surveyed edge and centre positions for each excavation round. In both simulations, the variability in the principal stress magnitudes and orientations was much larger than for the flat-faced cylinder, mainly as a result of a large change in magnitudes and orientations estimated for Round 17. This particular excavation round has a large influence on the mean and variability of the stress estimates because the magnitudes of the displacement and strain responses associated with it are large. The results from a Monte Carlo simulation using the single-inflection shape are shown in Figure 74. The variability in principal stresses represented by the 90% confidence limits is large compared to the flat-faced cylinder case. This increased variability is reflected in the standard deviation tensor for the stresses in the tunnel coordinate system. The mean and standard deviation tensors for this case are given respectively by

$$\overline{\sigma} = \begin{bmatrix} 51.54 & -2.77 & 12.52 \\ -2.77 & 43.46 & 2.11 \\ 12.52 & 2.11 & 12.11 \end{bmatrix}$$

$$S_{\overline{\sigma}} = \begin{bmatrix} 4.98 & 1.25 & 1.06 \\ 1.25 & 2.10 & 0.38 \\ 1.06 & 0.38 & 1.29 \end{bmatrix}$$

As expected, results for the simple circular arc shape showed more variability than those for the single-inflection shape, suggesting that the single-inflection shape is more representative of the *in situ* tunnel geometry than is the circular arc shape.

The *in situ* stress tensor was also estimated using constant values of 50 and 100 mm, in separate simulations, for the difference between the edge and centre positions for each excavation face. Compared to the flat-faced case, results from these simulations showed a decrease in mean principal stress magnitudes, and an increase in variability in both magnitudes and orientations, with increasing amounts of face curvature. However, the maximum change in mean principal stress magnitudes relative to the flat-faced case was only 0.6 and 1.4 MPa in the two simulations, respectively. Based on the variability in stress estimates, these findings suggest that models with constant face curvature are more representative of the *in situ* tunnel geometry than those based on surveyed centre positions within each round. On the same basis, the flat-faced cylinder appears to be the best representation of the Mine-by test tunnel geometry.

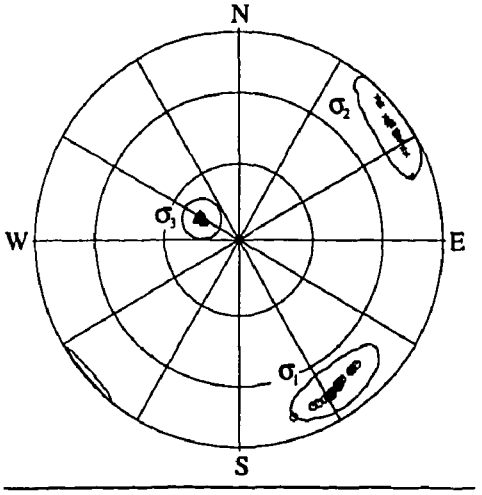

Cylinder with Single-Inflection Curved Face

	▫ σ_1	+ σ_2	▵ σ_3
Magnitude (MPa)			
-90% CL	47.7	39.7	6.2
Mean	55.5	43.3	8.3
+90% CL	63.9	46.5	10.3
Mean Orientation (°)			
Trend	145.3	53.3	298.4
Plunge	15.3	7.4	72.9

FIGURE 74: Mean and 90% confidence intervals on principal stress magnitudes and orientations for a cylindrical tunnel with a single-inflection curved face (AL=0.5, DOL=1.5).

4.2.5 Cylindrical Tunnel with External Openings

A final analysis was conducted using a 3.5-m-diameter cylindrical tunnel with a curved face shape and included the shaft station and instrumentation galleries of the Mine-by Experiment. The discretization parameters used for this simulation were AL=0.5 and DOL=1.5. Results from a Monte Carlo simulation based on the 22 stress predictions associated with this model showed only a very slight change in mean values and variability in principal stress magnitudes and orientations compared to the same case with no external openings. In terms of mean stress magnitudes, inclusion of the external openings resulted in an increase of about 0.2 MPa in σ_1, a decrease of about 0.2 MPa in σ_2 and a decrease of about 0.5 MPa in σ_3. Changes in principal stress orientations were limited to less than 0.5° in both trend and plunge. Consequently, the effect of the external openings on the back analysis results is very minor.

4.2.6 Summary of the DBEM3D Back Analysis

The DBEM3D back analysis provided an independent estimate of the *in situ* stress tensor at the 420 Level of the URL, and illustrated the level of detail required in modelling the Mine-by Experiment to achieve consistent stress estimates. All the simulations showed that the stress estimates were affected by model discretization, although there were only small differences between results using a fine and an intermediate discretization. Estimates using a flat tunnel face with a central element were also more variable than those using a uniform face discretization with identical control parameters.

The face shape used in the model was found to affect the variability in stress estimates. Of all the face shapes considered, the flat-faced cylinder produced the least amount of variability in stress estimates. Assuming the *in situ* stress tensor is relatively constant from round to round, the small variability associated with the flat face suggests that this face shape is most representative of the *in situ* tunnel geometry. In attempting to account for face curvature, the use of a single-inflection curved face produced less variable results than the simple circular arc shape. However, it was shown that simulations with constant face curvature for each round produced less variable results than those based on surveyed positions of the face centre in each round. This finding suggests that the *in situ* tunnel face geometry is not well-represented by assuming a smooth transition from the edge to the centre of the face.

The effect of external openings, i.e., other excavations around the experiment area, on stress estimates was found to be very minor, and could be eliminated in simpler models by dropping the outermost extensometer anchors close to these openings. Stress estimates were also found to be relatively insensitive to an increase in Poisson's ratio from 0.2 to 0.25. Based on the variability in stress estimates, the 'best' estimate of the *in situ* stress tensor at the 420 Level was achieved using a finely-discretized, flat-faced cylinder model with no external openings. Results from the back analysis associated with this model compared favourably with those given in Section 4.1.

In terms of instrumentation, the back analysis showed that the measurements from the 12 radial extensometers and 8 strain cells from the second CSIRO array were consistent with linear elastic behaviour over Rounds 15 to 18. The back analysis further showed that the CSIRO HI cells in the Mine-by Experiment were extremely sensitive, and displayed non-linear/non-elastic behaviour once the tunnel face was within about 1 m of the CSIRO array. Results from the axial extensometer were also consistent with those from the other instruments, but did not significantly affect the stress estimates because of the small displacements measured by the instrument. Overall, the combination of the two extensometer arrays and the second CSIRO array produced well-constrained stress estimates.

4.3 CHARACTERIZING THE DAMAGED ZONE

From the results in Section 3., it was demonstrated that the process of progressive failure starts with crack initiation ahead of the tunnel face in compressive regions where the maximum deviatoric stress is concentrated. For Lac du Bonnet granite around the Mine-by test tunnel, the damaged zone can be considered bounded by the $\sigma_1 - \sigma_3 \approx 70$ MPa contour both for two- and three-dimensions. Within this boundary, the crack-initiation threshold has been exceeded, and the cohesion component of the rock strength has been reduced, i.e., the rock has been weakened. Nevertheless, because of the very small amount of damage, i.e., inelastic straining, required to reduce the cohesion, the elastic properties of the rock mass ahead of the tunnel face are essentially unchanged. Once exposed at the tunnel perimeter as the tunnel is advanced, these localized zones of reduced strength are subjected to the tangential stresses generated around the tunnel by stress redistribution, producing a failed zone typified by breakout notches. However, the failure process results in fall-out or removal of only a portion of the damaged material, so that localized zones of excavation damage remain around the final test tunnel periphery.

The characteristics of the damaged zone, including its extent and material behaviour, were investigated in a series of geophysics studies, a post-excavation characterization program, and a numerical modelling study. As background for interpreting results from these studies, the stress redistribution around the Mine-by test tunnel associated with the back-analyzed stress tensor was investigated (Section 4.3.1). The geophysics studies are summarized in Section 4.3.2. Results of characterization and numerical modelling to determine the damaged zone characteristics are covered in Section 4.3.4.

4.3.1 Stresses around the Mine-by Test Tunnel

The *in situ* stresses and material properties in the elastic region represent boundary conditions around the test tunnel. Based on the back analysis of displacement measurements (Read 1994), the estimated principal stresses in the elastic region are

	MPa	Trend	Plunge
σ_1	59.9	145.4	11.1
σ_2	44.3	53.9	7.7
σ_3	9.4	289.8	76.5

These values are based on a Poisson's ratio of 0.25 and a Young's modulus of 65 GPa. As pointed out by Read (1994), the estimated stress magnitudes are directly proportional to Young's modulus chosen for the back analysis. This estimate of the *in situ* stress tensor indicates a slightly larger ratio of σ_1 to σ_3 than the estimate from the DBEM3D back analysis, which results in more extreme stress concentrations around the opening.

Under these boundary conditions, the introduction of a circular tunnel in an elastic medium alters the stress distribution significantly. Figure 75 shows contour plots of the principal stress magnitudes and of the angle between each principal stress trajectory and the plane orthogonal to the tunnel axis, i.e., the antiplane angle. The most significant features in the plots of stress magnitude are the highly compressive region in the roof and floor of the tunnel in the σ_1 plot, the slight tensile region in the sidewalls in the σ_2 plot, and the highly tensile region in the sidewalls in the σ_3 plot. The plots of antiplane angle are particularly useful in illustrating the crossover in σ_1 and σ_2 in the sidewalls of the tunnel, σ_1 corresponding to the axial stress in these regions. They also illustrate that σ_3 in the sidewalls is oriented approximately 7° out of plane, thus comprising both a tangential and an axial component. The slight rotation of σ_3 would tend to cause en echelon tensile cracking as opposed to contiguous tensile cracking in the highly tensile sidewall region.

The stress state around the tunnel can also be represented in terms of mean and distortional stresses (Figure 76). For brittle rock, the intermediate stress component is not usually considered an important contributor to failure and consequently failure criteria are written in terms of σ_1 and σ_3 only, e.g., Hoek-Brown and Mohr-Coulomb criteria. In this case, the mean stress is $\frac{1}{2}(\sigma_1 + \sigma_3)$ and the maximum shear stress is $\frac{1}{2}(\sigma_1 - \sigma_3)$. These two-dimensional criteria have also been extended to three-dimensions and are typically expressed in terms of the stress invariants. In principal stress space, the position along the space diagonal (i.e., the line given by $\sigma_1 = \sigma_2 = \sigma_3$) is expressed as $I_1/\sqrt{3}$ and the orthogonal distance from the space diagonal to the point in stress space is given as $\sqrt{2J_2}$, where I_1 and J_2 are the first stress invariant and the second deviator stress invariant, respectively.

Figure 77 shows a Hoek-Brown failure criterion based on results of laboratory tests on samples from the test tunnel, with $\sigma_c = 157$ MPa, $m = 35.2$ and $s = 1.0$. Although most points fall below the failure envelope, there are some points around the tunnel that fall outside the failure envelope, and therefore represent failure states. In a plot of factor of safety, where values greater than unity represent points within the failure envelope, and values less than unity represent failure states, the stress conditions around the circular tunnel produce zones of compressional failure in the roof and floor, and zones of tensile failure in the sidewalls. While this is an idealized illustration of the conditions around the test tunnel, it captures the general trend of the stress changes around the tunnel. As discussed in Section 3., the progressive development of a v-shaped notch in the roof and floor of the test tunnel tends to exaggerate the stress concentrations in these regions, focusing the highly compressive concentration in a small region at the notch tip. An example of the stress distribution around the notched tunnel geometry is shown in Figure 78.

The analysis of progressive failure conducted in Section 3. was based on the initial estimate of stresses at the 420 Level of the URL (see Table 2). For that stress state, the compressive and tensile stress concentrations around the test tunnel are less severe in magnitude, and

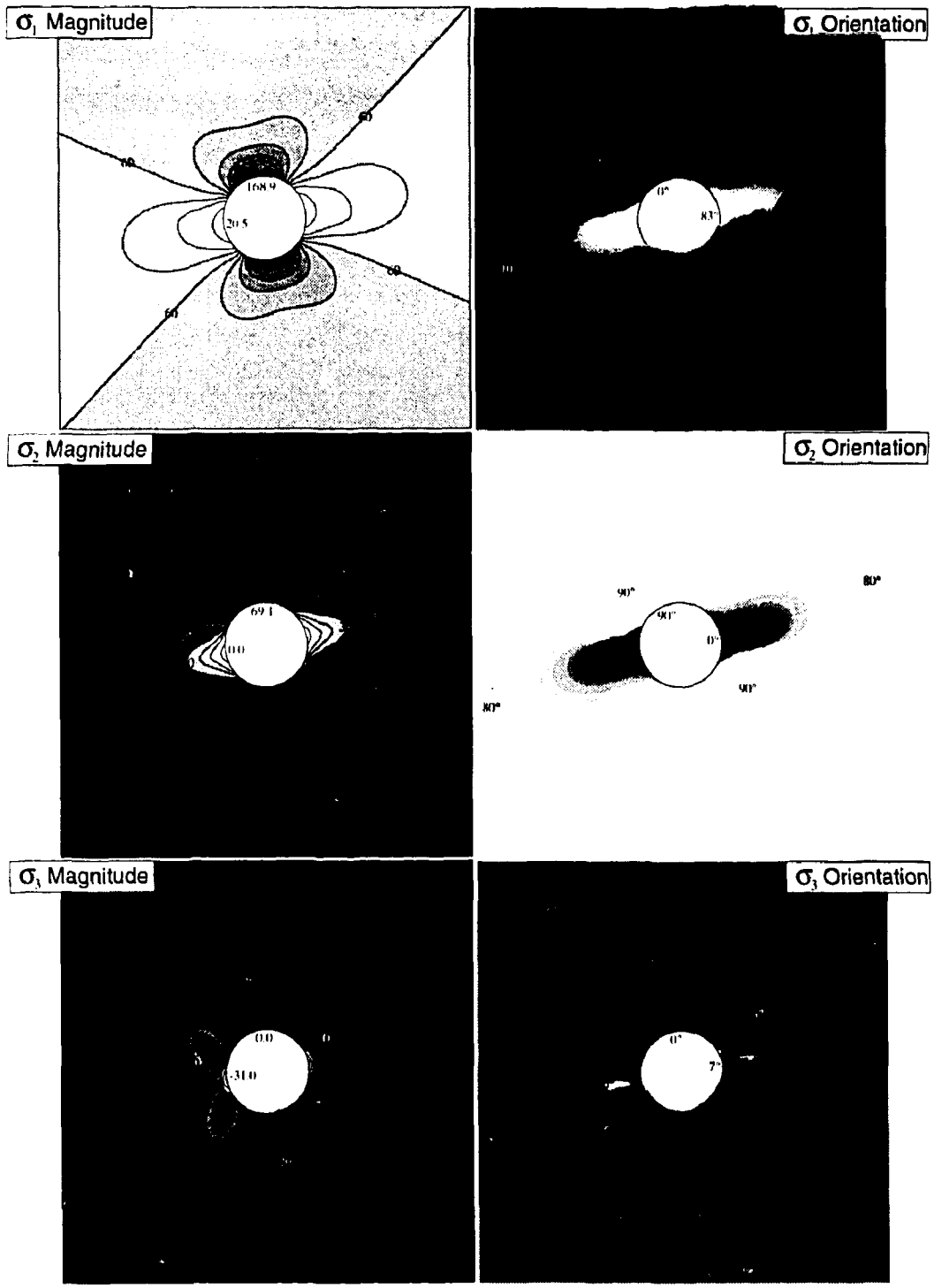

FIGURE 75: Principal stresses around the test tunnel. The figures in the left column are the magnitudes of σ_1 (top), σ_2 (middle) and σ_3 (bottom) in 10 MPa contours. The figures in the right column show the angle between each principal stress trajectory and the plane of the paper in 5° contours. Shades range from black for trajectories within the plane, to white for trajectories out of the plane. Boundary values are shown in each plot.

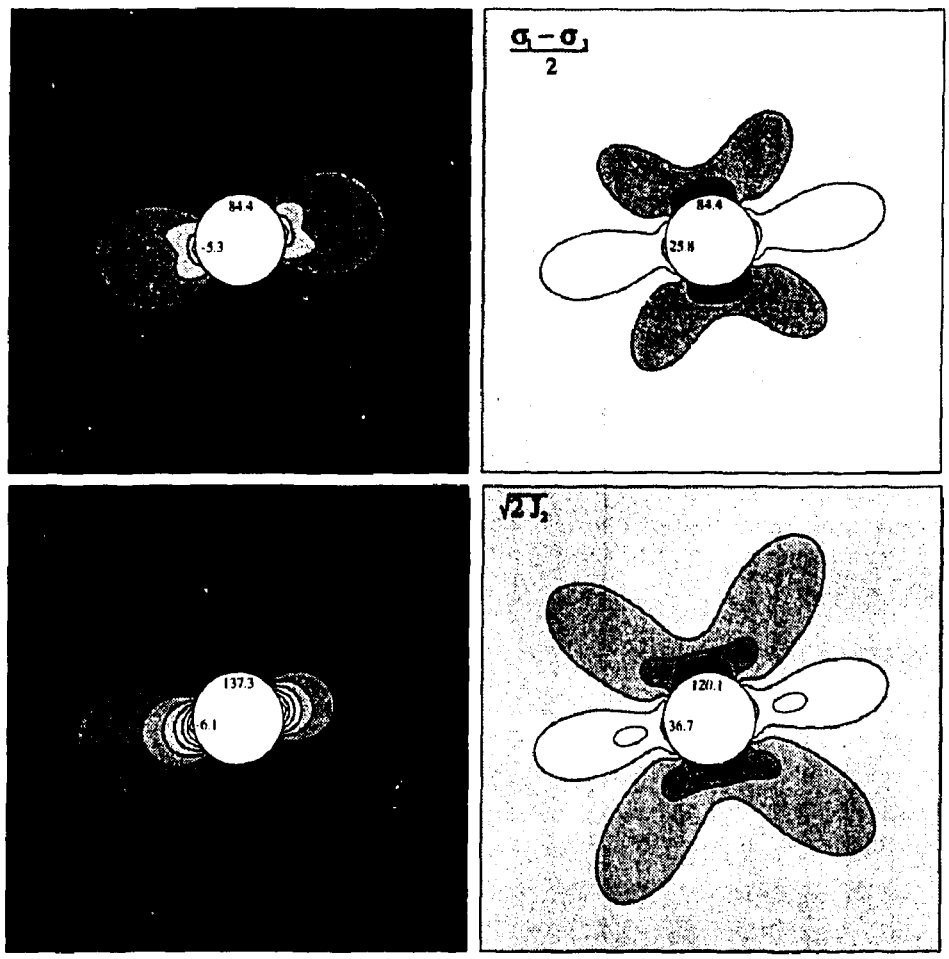

FIGURE 76: Various representations of mean and distortional stresses around a tunnel.

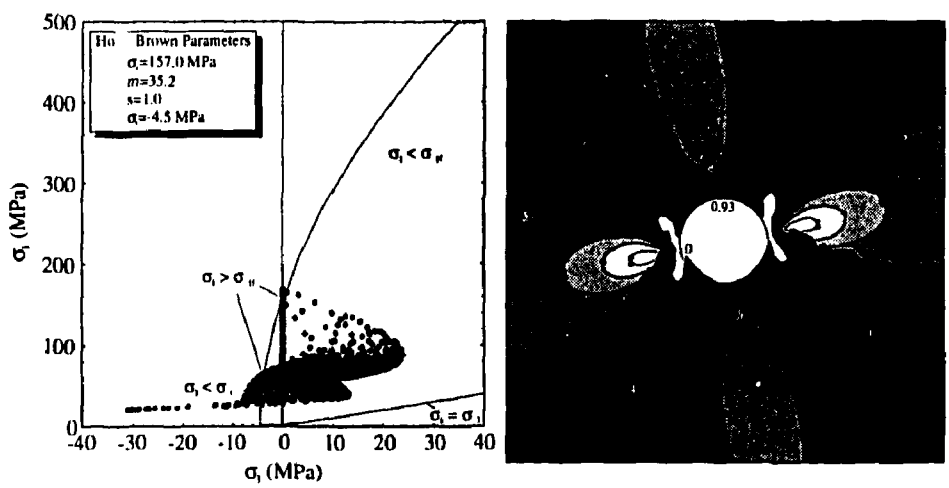

FIGURE 77: Example of a typical Hoek-Brown failure envelope and a factor of safety plot.

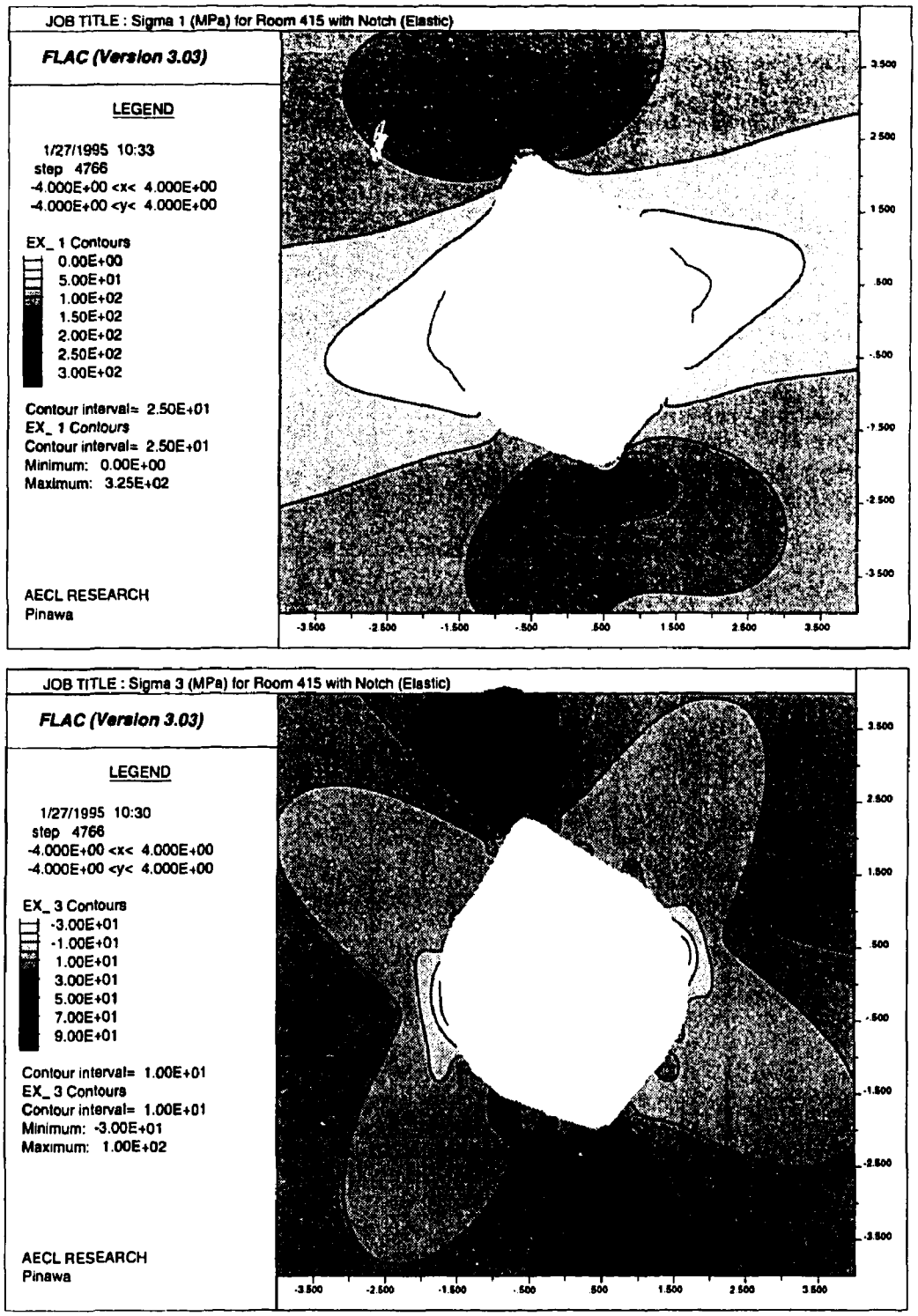

FIGURE 78: Principal stresses around the test tunnel showing the effects of a notched tunnel geometry. Results are based on the back-analyzed stress tensor.

the minimum principal stress shows no antiplane rotation in the two-dimensional plane strain analysis. Nevertheless, the overall pattern of stress concentrations is not significantly different than that presented in this section, and consequently the interpretations associated with the process of progressive failure are unaffected. One slight adjustment is that, using the back-analyzed stress tensor, the lower bound of the crack-initiation threshold is closer to 73 MPa for grey granite as compared to the 70 MPa shown in Section 3. However, this adjustment is relatively insignificant in comparison to the effects of *in situ* variability on the crack-initiation threshold, as discussed later in Section 4.3.5.

4.3.2 Geophysics Studies of Excavation Damage

The geophysics studies conducted for the Mine-by Experiment included a series of crosshole seismic tomography surveys, an acoustic emission (AE) study in the sidewall region of the tunnel, and velocity imaging based on a study of wave propagation effects of an underground opening.

4.3.2.1 Crosshole Seismic Tomography Surveys

Four crosshole seismic surveys were conducted in a vertical plane orthogonal to the axis of the Mine-by test tunnel to observe excavation-induced changes in seismic velocity and mechanical properties of the granite (Hayles et al. 1995). Two of these surveys were done prior to the excavation, one to observe far-field, and the other to observe near-field, velocity conditions. These two surveys were then repeated after excavation of the Mine-by test tunnel to observe changes in the P- and S-wave velocity distribution resulting from tunnel excavation.

The velocity surveys were done in two arrays of 76-mm-diameter (NQ size) diamond-drilled boreholes, referred to as the far-field (or main) panel and the near-field panel. The main panel configuration consisted of 22 cored boreholes, all in a single vertical 33 m by 40 m plane orthogonal to the tunnel axis. The tunnel intersected the centre of the main panel at approximately chainage 21+25 in Room 415. The near-field panel consisted of 8 extensometer boreholes, all drilled in approximately the same plane as the main panel, and intersecting the Mine-by test tunnel in a radial pattern.

All measurements were made with mini-CHARTS Hayles et al. (1992), a miniature crosshole seismic system developed by AECL for geological mapping and engineering assessment of granite. The instrument is a small-scale version of the larger and more powerful CHARTS (Cross-Hole Audio-frequency Rock Testing System) initially developed for AECL at the University of Toronto (Wong et al. 1987). The transducers for the surveys operated from 5 to 80 kHz. The receiver and transmitter transducers are designed for use in either dry or wet boreholes to generate good quality P- and S-waves to distances of > 60 m. The instrument is similar to that described by Gladwin and Stacey (1974) and by Paulsson and King (1980) and Paulsson (1983).

The relationship between microcracks (i.e., damage), stress and seismic velocity is fairly well understood for rock samples and cores. Preferentially-oriented open microcrack populations

in the rock matrix will tend to close upon compressive loading resulting in increased seismic velocity, and will tend to open upon tensile loading causing a velocity reduction. As shown by Martin (1993), the extraction process induces microcracks in samples of granite from depth at the URL. Stesky (1980) and (1985) has shown that, for such samples of Lac du Bonnet granite, most microcracks are fully closed for stresses above about 200 MPa. Beyond this point the relation between stress and elastic wave velocity is more subtle.

According to Everitt and McGregor (1996), there are two low-dipping, NE-striking sets of pre-existing microcracks in the rock mass at the 420 Level of the URL, comprising healed fluid inclusions within quartz grains. *In situ*, these features do not constitute open crack porosity, and, consequently, would not be expected to affect P- or S-wave velocities upon increased compressive loading. However, in conjunction with the development of new microcracks under tensile loading, i.e., extensional damage, it is possible that these healed microcrack sets are preferentially exploited and reopened upon stress relief. The development of excavation-induced damage in tensile regions around the Mine-by test tunnel is the dominant cause of velocity variations *in situ*, resulting in directionally-dependent decreases in seismic velocities near the tunnel wall.

Velocity statistics for 13 horizontal rays and 10 vertical rays extracted from the 1991 pre-excavation surveys of the main panel show means of 5878±18 and 5911±23 m/s, respectively. These values represent a velocity anisotropy of about 0.5% within the main panel. A region of slightly higher P-wave velocity, corresponding to an area of granodiorite, was noticeable in the upper NW corner of the main panel in both the pre- and post-excavation survey. The main panel velocity tomograms showed velocity changes of ±20-40 m/s for the region away from the tunnel excavation. The repeat survey results showed the tunnel outline as a low velocity zone in the geometric centre of the panel. In this region, P- and S-wave velocities were reduced by 180 to 250 m/s owing to the presence of the tunnel. After excavation, the dynamic Poisson's ratio decreased slightly, while the static Young's modulus (determined through an empirical relation from Eissa and Kazi 1988) was virtually unchanged except for the region immediately around the tunnel.

In contrast to the main panel survey, anisotropy in the post-excavation near-field survey was very strong and heterogeneous, i.e., variable around the opening. Table 6 shows the average P- and S-wave velocities for all rays in the near-field panels for the pre- and post-excavation surveys. The sidewall panels show a reduction in the average velocities of about 4%, with a preferential decrease in vertical ray paths, consistent with excavation-induced damage in these regions. These findings are consistent with the development of subhorizontal microcracks in the highly tensile region resulting from excavation-induced stress redistribution. Where the compressive stress increased in the crown and floor, there was no definite indication of increased seismic velocity, although the survey uncertainty was perhaps too large to observe a change. The lack of an increase in seismic velocity upon increased compressive loading suggests that the volume of open microcracks, i.e., porosity, under the initial *in situ* stress conditions prior to tunnel excavation is very small compared to the excavation-induced damage in the tensile regions.

Results from the near-field velocity surveys show lower P-wave velocities, and a more extensive zone of damage, in the granite on the SE side of the tunnel than in the granodiorite

TABLE 6

AVERAGE NEAR-FIELD VELOCITIES PRE- AND POST-EXCAVATION

	Pre-excavation			Post-excavation		
Panel	No.	P-Wave	S-Wave	No.	P-Wave	S-Wave
EXT7-6	418	5843 ± 100	3399 ± 75	160	5715 ± 158	3405 ± 46
EXT12-6	351	5853 ± 250	3428 ± 200	160	5855 ± 82	3453 ± 44
EXT11-12	403	5782 ± 100	3397 ± 60	355	5575 ± 158	3386 ± 61

After Hayles et al. (1995).

on the NW side. A P-wave velocity reduction of more than 300 m/s was detected to about 1.1 m from the SE sidewall of the tunnel, whereas a similar reduction in the NW sidewall was limited to within about 0.6 m of the opening. These patterns were also apparent in the velocity difference and mechanical property tomograms. Read (1994) has shown that, in laboratory tests, grey granite is more susceptible to damage than granodiorite in both compression and tension as a result of its inequigranular grain distribution. Consequently, under identical stress conditions, samples of granite tend to sustain more damage, and hence contain more extensive microcracks, than granodiorite. Results from the near-field velocity surveys confirm the same trend *in situ*.

In summary, the crosshole seismic tomography surveys were successful in identifying zones of reduced velocity, corresponding to excavation-induced damage, in the tensile sidewall regions of the tunnel. Although the surveys did not define the boundaries of the damaged zone precisely, the extent and intensity of this damage was shown to depend on the rock type, granite showing more signs of damage than granodiorite. In the compressive regions around the test tunnel, there were no indications of velocity increases, suggesting there are no significant pre-existing open microcracks *in situ* in the experiment area.

4.3.2.2 AE Study in the Tunnel Sidewall

Small-scale acoustic emission (AE) monitoring and ultrasonic velocity measurements were conducted by Carlson and Young (1993) on a portion of the Mine-by Experiment test tunnel sidewall. An AE array was installed along the NW wall after the test tunnel had been excavated approximately 22 m (Round 17). Four 76-mm-diameter (NQ size) boreholes arranged in a diamond pattern were drilled parallel to the far-field σ_1 direction, inclined about 11° to the SE. The array enclosed a rectangular prism of rock approximately 0.7 x 0.7 m in cross-section and 1.1 m deep. Five 1 MHz compressional transducers installed in each borehole, and three additional transducers attached to the tunnel wall, were used to carry out AE monitoring and velocity surveys.

AE monitoring began 1992 March 13, seven days after Round 17 was completed, and continued for 3.5 weeks, during which time two half-metre rounds (Rounds 18 and 19) were completed and a third (Round 20) begun. Source location uncertainty was estimated at 44 mm near the centre of the array, while event locations further than 0.75 m from the

TABLE 7

ANISOTROPY IN AVERAGE P-WAVE VELOCITIES IN THE SIDEWALL OF THE MINE-BY EXPERIMENT TEST TUNNEL

Round	Compressional Velocity (m/s)						Anisotropy (%)		
	Max.(a)	Int.(b)	Min.(c)	Avg.(a,b)	Avg.(a,c)	Avg.(b,c)	(a,b)	(a,c)	(b,c)
17	5815	5590	5075	5703	5445	5333	3.9	13.6	9.7
18	5650	5440	5080	5545	5365	5260	3.8	10.6	6.8
19	5660	5490	5070	5575	5365	5280	3.0	11.0	8.0
20	5660	5500	5040	5580	5350	5270	2.9	11.6	8.7

After Carlson and Young (1993).

array centre were approximate at best. Focal mechanisms were also calculated for events that located within 0.75 m of the array centre and that had at least eight polarity picks. These were classified as tensile, shear, compressive or indeterminate. Velocity surveys were made immediately before and after each AE monitoring period, with errors in velocity determinations due to uncertainties in transducer location estimated at ±40 m/s (Carlson and Young 1993).

A velocity survey conducted at the 420 Level prior to excavation of the Mine-by Experiment test tunnel confirmed that the rock is quite homogeneous and isotropic. The measured compressional velocity was 5880 ± 60 m/s with a weak anisotropy of approximately 0.5%, vertical rays travelling slightly faster than horizontal rays (Hayles et al. 1995). In contrast, compressional velocities from the initial velocity survey conducted in the AE study were much more anisotropic within the surveyed portion of the tunnel wall. For Rounds 17 to 20, the maximum velocity was approximately parallel to the tunnel axis (axial direction a), the intermediate velocity was subvertical (tangential direction θ) and the slow velocity was approximately orthogonal to the tunnel axis (radial direction r). These directions correspond approximately with the *far-field* σ_2, σ_3 and σ_1 directions, respectively. The magnitudes of the maximum, intermediate and minimum compressional velocities, and the calculated anisotropy in the various principal velocity planes, are given in Table 7. These values are based on an ellipsoidal model which averages velocities of similarly-oriented rays, independent of distance from the tunnel wall.

From the results in Table 7, average compressional velocities are strongly anisotropic (8-14%) in the r-θ and the r-a planes, and moderately anisotropic (3-4%) in the a-θ plane. Compared to the pre-excavation value of 5880 m/s, the maximum, intermediate and minimum velocities measured for Round 17 represent a decrease of 1.1, 4.9 and 13.7%, respectively. The maximum and intermediate velocities further decreased between Rounds 17 and 18 by about 3%, but were essentially unchanged for later rounds. The maximum and intermediate velocities for Round 18 represent a reduction of 3.9 and 7.5%, respectively, from the pre-excavation velocity. The minimum velocity remained fairly constant for all four rounds.

Compressional and shear velocity variations with distance from the tunnel wall were also considered for selected raypaths in the a-θ plane (Figure 79). Compressional velocities were measured horizontally and vertically, while shear velocities were measured at $\pm 45°$ from vertical. Both sets of measurements indicate a decrease in velocities near the tunnel wall. At 0.15 m from the tunnel wall, compressional velocities for horizontal raypaths tangential to the tunnel wall decreased just over 5% from the pre-excavation velocity of 5880 m/s, while those 0.75 m or deeper into the tunnel wall were virtually unchanged. Likewise, for subvertical raypaths tangential to the tunnel wall, compressional velocities at 0.15 m into the rock mass decreased by over 10% of the pre-excavation velocity, but were within about 2% past 0.75 m. Similar trends were apparent in the shear velocities (Carlson and Young 1993). The rapid rise in both shear and compressional velocities with distance from the tunnel wall indicates that open microcracks in the tunnel sidewall are concentrated near the free surface, and do not extend beyond about 0.75 m from the wall. In addition, the shear velocity trend rules out desaturation as the sole cause of the compressional velocity variation.

Locations for 1307 AE events were determined manually from compressional wave arrivals. Of these event locations, only 199 (12%) were within 0.75 m of the array centre, and therefore considered accurate. These 199 events were concentrated near the sidewall surface

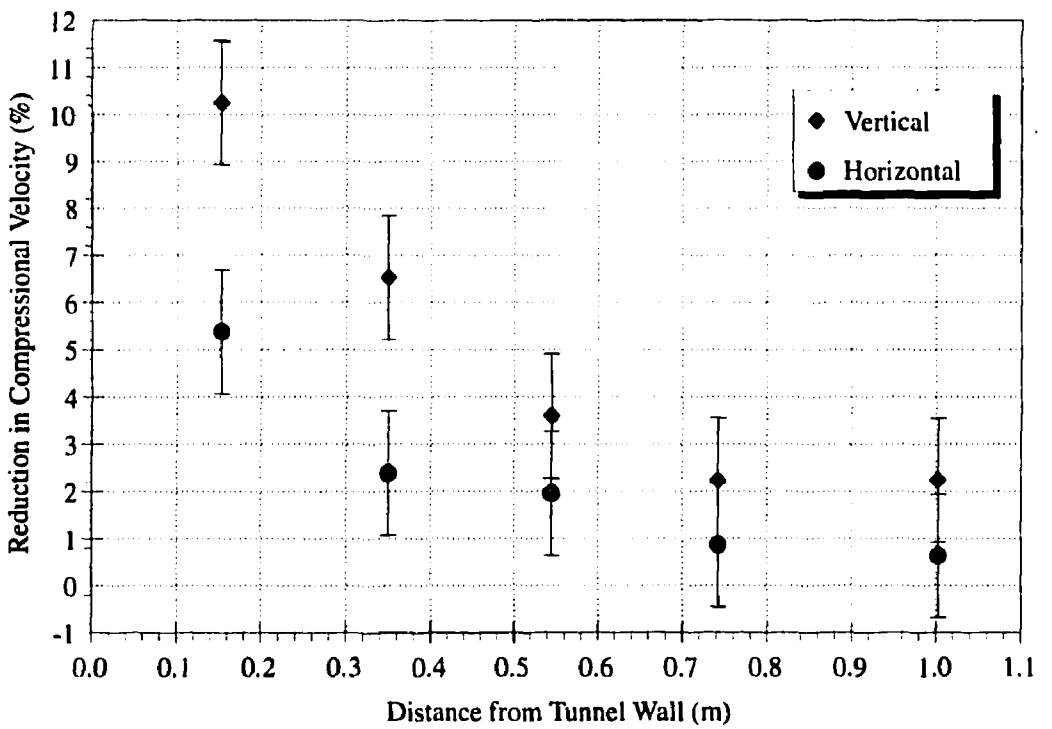

FIGURE 79: Results from ultrasonic velocity survey in sidewall of the test tunnel. Reduction in compressional velocity near the tunnel wall is more pronounced in vertical than in horizontal rays. Results indicate open crack porosity within about 0.5 m of the tunnel wall.

and towards the working face of the tunnel, with the most prominent cluster of activity just above the top borehole. Most of the events occurred within 0.8 m of the tunnel wall, with over two-thirds within the first 0.4 m (Figure 80). The mean 'event-to-free-surface' distance was 0.35 m. The strong concentration of events in the first 0.4 m of the tunnel wall is further evidence that open microcracks are concentrated near the tunnel wall.

Focal mechanism solutions were possible for 107 of the 199 events. Of the 107 solutions, 27 were tensile, 76 were shear and only 4 were compressive mechanisms. The recorded sequence of AE events (Carlson and Young 1993) suggests that the tensile events are a result of tunnel advance, which increases tensile stresses in the sidewall region. The other events tend to occur during periods where the face position is constant, and are related to stress redistribution resulting, in part, from the tensile microcracking. This sequence of tensile events followed by shear events is most notable in Round 18, but also occurs in Rounds 19 and 20. Round 17 shows primarily shear events because the AE array was installed after the initial advance of the round, and the tensile events related to the face advance were therefore not recorded. In addition, the tangential stress in the centre of Round 17 is close to the transition from compression to tension.

The spatial distribution of events (Figure 81) shows that the tensile events align with the *far-field* σ_1 direction, and cluster in the region where macroscopic tensile cracking is expected, given that the ratio of principal stresses in the cross-sectional plane is significantly greater than 3:1. In this region, σ_3 is tensile and approximately tangential to the tunnel wall, σ_2 is radial and tensile over a small distance from the tunnel wall, and σ_1 is axial and compressive. The shear events tend to occur on the flanks of the tensile region near the

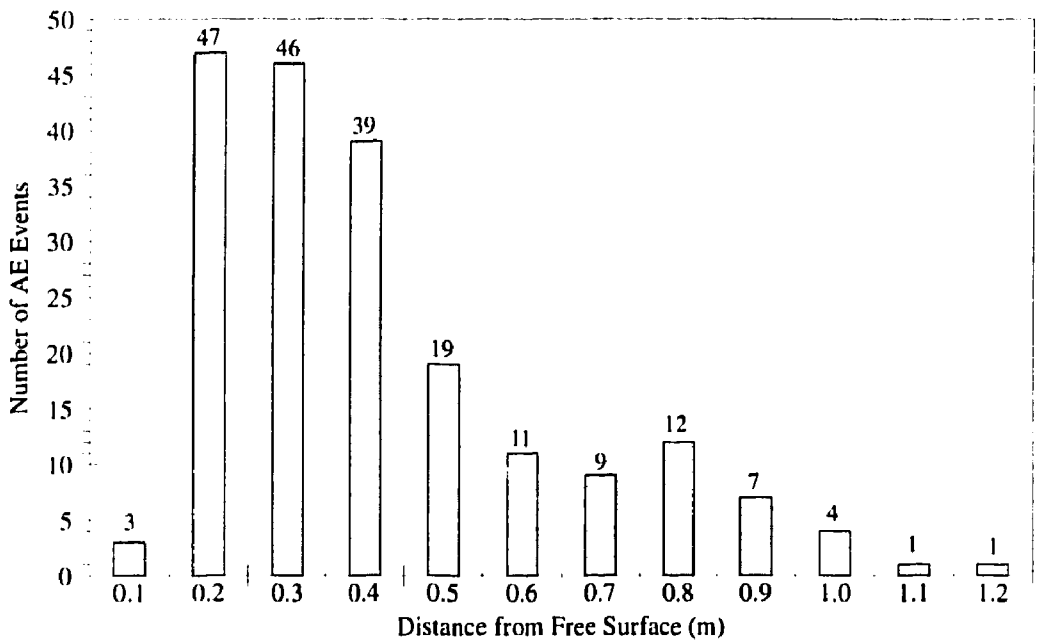

FIGURE 80: Number of AE events with distance from the sidewall surface. The total number of events is 199.

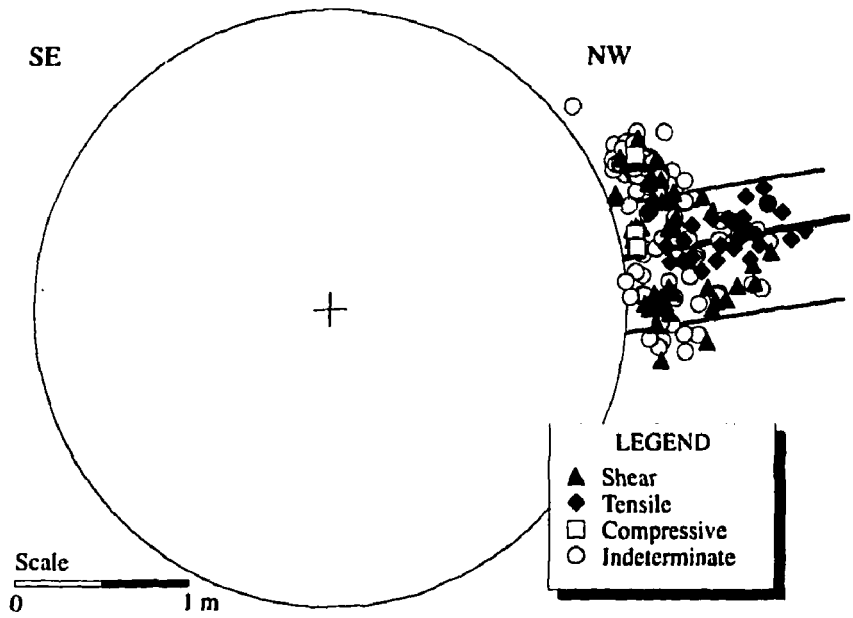

FIGURE 81: All AE locations within 0.75 m of the array centre. Note how the tensile events align with the *far-field* σ_1 direction.

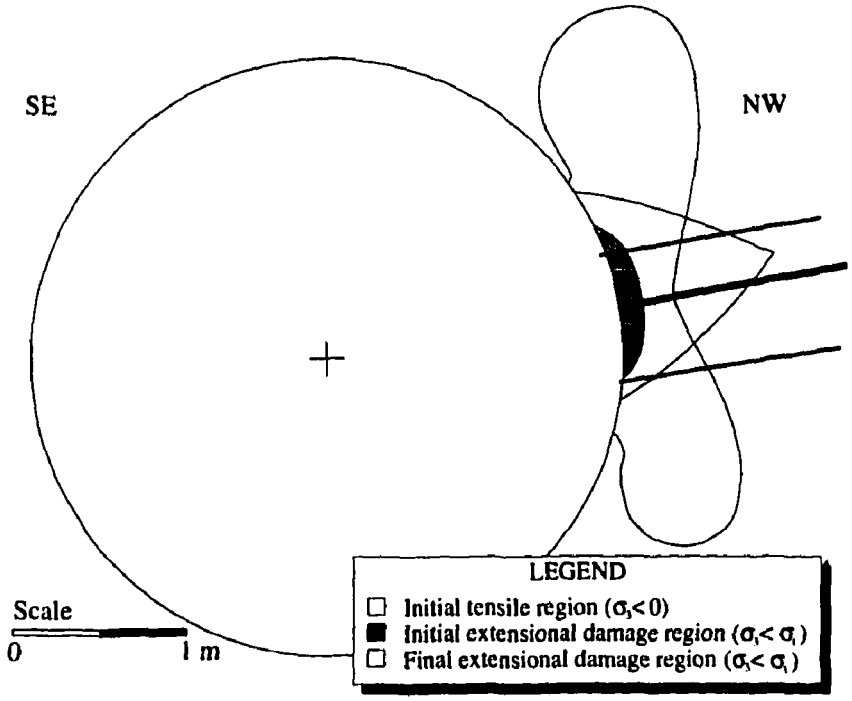

FIGURE 82: Extent of initial and final region where extensional cracking is expected for the Mine-by test tunnel. The initial region is based on the stress distribution around the tunnel related to Round 18.

opening. The compressive events are also located close to the tunnel wall. As described in Section 4.3.4, Read (1994) tracked the development of extensional damage in the sidewall region using an iterative finite difference analysis, substituting oriented ubiquitous joint elements for elastic elements that had failed in tension. The analysis showed that the initial region where $\sigma_3 < \sigma_t$ for the Mine-by test tunnel is confined to within 0.14 m of the tunnel wall, but grows to 0.94 m from the wall as a result of stress redistribution caused by progressive extensional cracking (Figure 82). Although the analysis was limited in its scope, the shape and extent of the eventual zone of extensional damage is similar to that recorded by the AE system. These results suggest that the tensile region in the sidewall has sustained excavation-induced damage to about 1.0 m from the wall, with the most significant damage within about 0.5 m of the tunnel wall, and only very minor damage past 0.75 m.

4.3.2.3 Three-Dimensional Seismic Velocity Imaging

Standard seismic velocity surveys measure the travel time of a seismic ray between known source and receiver positions, from which an average or apparent velocity is calculated assuming a straight raypath. However, when conducted close to an underground opening, these types of surveys do not account for ray diffraction around the opening, or variations in velocity along a given raypath. Consequently, the calculated apparent velocities may not reflect the actual velocity structure of the rock mass close to the opening. These effects can be compensated for by using three-dimensional seismic velocity imaging (Maxwell and Young 1994).

A near-field seismic P-wave velocity calibration study (Maxwell and Young 1994) was performed by detonating small explosions in short holes down the length of the Mine-by test tunnel, and recording the travel times to the AE/MS monitoring sensors. Considering only rays that were not subject to diffraction, i.e., straight raypaths that did not intersect the tunnel, a composite stereoplot of velocities measured from different sources around the tunnel was compiled (Figure 83). The stereoplot shows two main clusters of low velocity (black areas), one subvertical and the other subhorizontal, approximately orthogonal to the test tunnel azimuth (225°). The subvertical cluster comprises two subsets of low velocity. From the results of the AE study in the sidewall of the test tunnel (Carlson and Young 1993) and *in situ* characterization, the low velocity clusters are associated with those raypaths that intersect the localized excavation-induced damage in the tunnel sidewalls. The apparent velocity and anisotropy patterns represented by Figure 83 are therefore not expected to be pervasive around the actual tunnel but, nonetheless, can be used as an initial starting model for the inversion.

From Figure 83, the composite seismic velocities in the horizontal plane are noticeably anisotropic (5900 to 5500 m/s), with the fast direction (base velocity) parallel to the test tunnel axis. Comparison of results from the near-field survey to those from a far-field survey in intact rock away from openings (Figure 84) illustrates a common base velocity oriented at azimuth 045° for horizontal rays in the two surveys. The figure also illustrates that the magnitude of the anisotropy for the intact rock (5900 to 5800 m/s) is less than the apparent anisotropy in the near-field survey. Therefore, excavation damage around the Mine-by test

tunnel significantly reduces apparent velocities on some raypaths between the tunnel and the microseismic array.

To address the issues of diffraction and velocity variation, three-dimensional seismic velocity imaging was carried out using results from the near-field seismic P-wave velocity calibration study (Maxwell and Young 1994). P-wave arrivals were significantly delayed due to diffraction of raypaths around the opening, which was accounted for using a finite difference technique. This technique followed the wavefront propagation from a specific source location and allowed the actual raypath lengths from source to receiver, including the effects of diffraction, to be computed. Using the improved raypaths, three-dimensional seismic velocity imaging was conducted to determine the near-field velocity variations around the test tunnel (Maxwell and Young 1994). A least-squares estimate of the anisotropy observed for all the raypaths, based on the velocity distribution shown in Figure 83, was used as the initial starting model for velocities and anisotropy throughout the rock mass. While this assumption did not account for the variable and position-dependent nature of velocities around the test tunnel, i.e., localized induced damage, the model provided a starting point against which to compare the computed velocity variations.

A damped least-squares inversion technique was employed to determine the velocity variations around the tunnel. A grid of points with a 1 m spacing was set up around the tunnel,

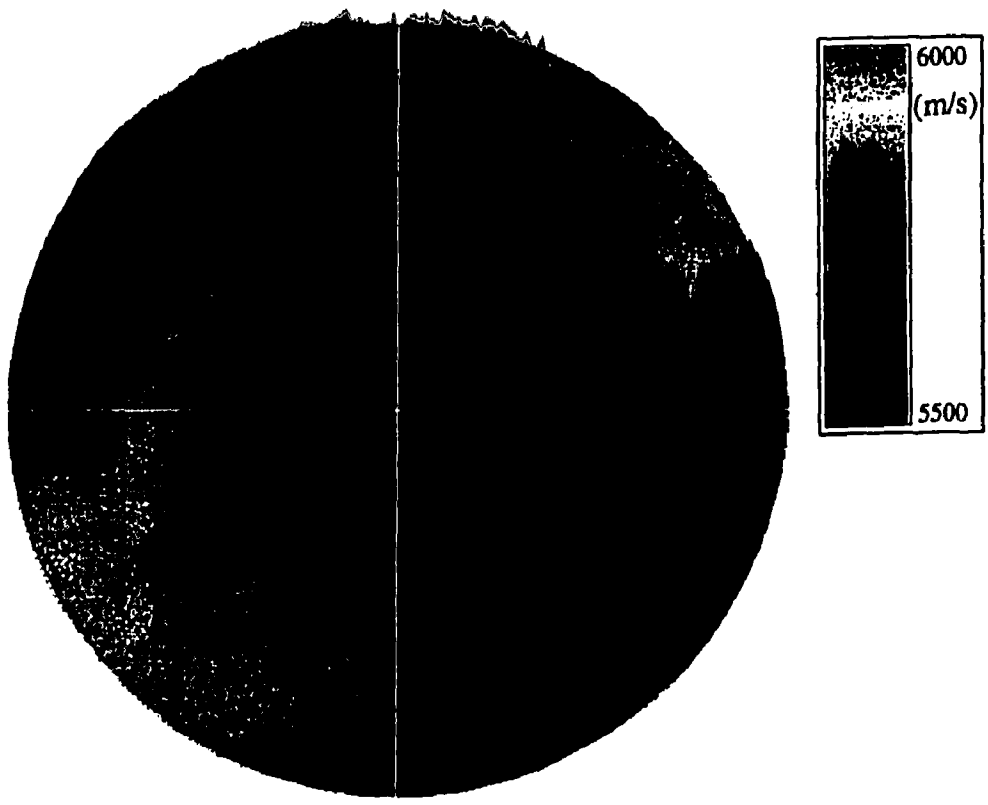

FIGURE 83: Contoured equal-area lower-hemisphere stereographic plot of apparent velocities (without diffraction effects) measured along raypaths originating at various points around the test tunnel perimeter.

and station corrections were used to account for heterogeneities outside of the image grid. The inversion included a parameter for the base velocity as well as anisotropy parameters to account for velocities along the unique anisotropy directions. However, because of numerical limitations related to the raypath coverage, it was not possible to resolve images of the velocity variations in the unique directions of the anisotropy. Instead, equivalent isotropic variations in velocity were computed. Consequently, there was no way to determine whether or not increases in velocity were related to an increase in the base velocity, or to a decrease in anisotropy relative to the initial starting model.

Results of the inversion showed a 250 m/s velocity increase in roof and floor regions of the tunnel, and a 150 m/s decrease in the sidewalls of the tunnel (Figure 85), relative to the velocities assumed in the starting model. Because there is evidence from other studies (e.g., Hayles et al. 1995; Everitt and McGregor 1995) to suggest that the base velocity does not increase above the background value of about 5900 m/s anywhere around the test tunnel, the regions of increased velocity in the roof and floor in Figure 85 most likely represent a reduction in the anisotropy assumed in the initial model (400 m/s) to about 150 m/s in these regions. This reduced anisotropy is similar to that measured in the far-field velocity survey for rock undisturbed by openings. This finding suggests that, in the roof and floor,

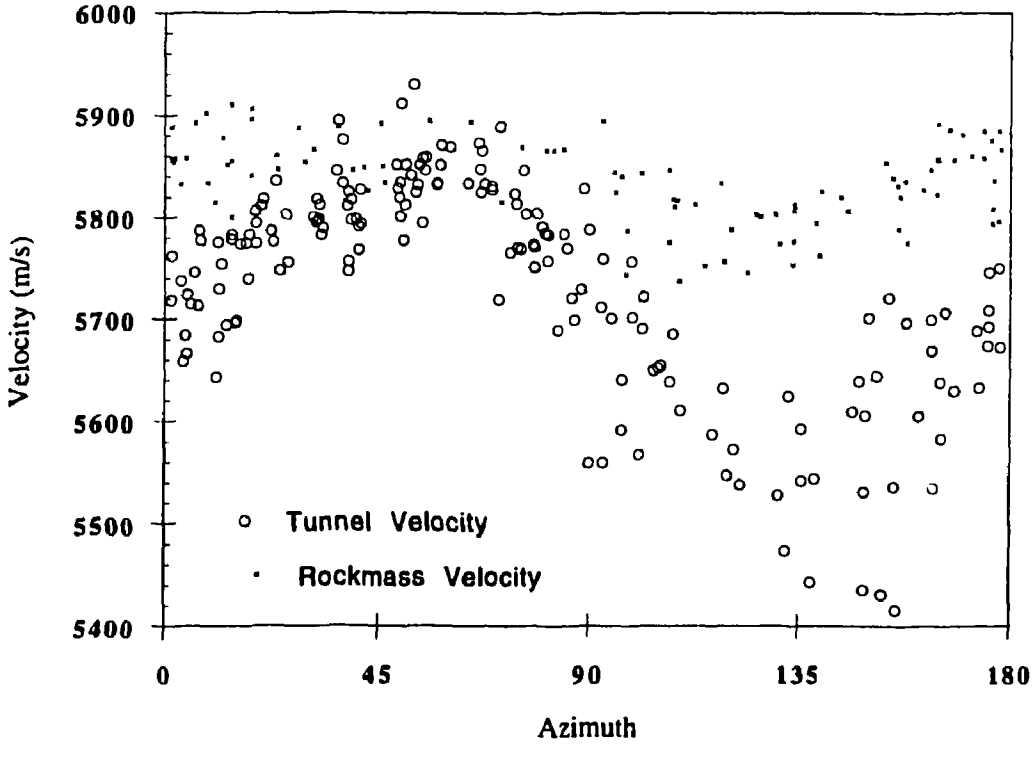

FIGURE 84: Apparent velocity versus azimuth for raypaths within 20° of horizontal for the tunnel survey and undisturbed rock survey. Results for the rock mass are pervasive, while those for the tunnel are dependent on position around the tunnel, i.e., roof versus sidewall.

there is little or no change in velocities or anisotropy compared to results from the far-field survey, i.e., the rock mass characteristics are relatively unaffected by tunnel excavation in these regions. In the sidewalls, the reduction in velocity of 150 m/s indicates that the equivalent isotropic velocity *in situ* close to the tunnel wall is lower than that assumed in the initial model. This finding is consistent with extensional damage localized in the tensile regions around the test tunnel.

Velocity images were also produced from the microseismic data using a simultaneous velocity-hypocentre inversion technique. A subset of microseismic events was selected from the centre of the tunnel, recorded over a 2 day interval. A 0.25 m spaced image grid was constructed in the region of the notch in the crown of the tunnel, and damped least-squares velocity perturbations were computed relative to the initial starting model described above. Figure 86 shows a wedge of decreased velocity (140 m/s) next to the tunnel, increasing in extent into the rock away from the tunnel face, above which there is a region of increased velocity (140 m/s). Compared to the far-field survey results, these findings suggest a net decrease in the equivalent isotropic velocity variations near the area of progressive failure in the roof. Another microseismic data subset was selected containing a significant number of events ahead of the tunnel face. Inversion results indicated a region of reduced velocity (200 m/s) generally corresponding to a tensile region.

These findings suggest that velocity imaging techniques, using both velocity calibration survey results and microseismic data, offer the possibility of analyzing the velocity variations in a specific region of interest at a particular instant in time. These techniques are particularly applicable in assessing excavation-induced damage around underground openings. However, in both velocity imaging techniques described above, the calculated velocity variations are changes relative to an initial starting model. In order to directly interpret these variations as *in situ* changes caused by tunnel excavation, the initial model must be representative of the undisturbed condition of the rock mass prior to tunnel excavation, and the back analysis technique must be sensitive to the initial starting model. Otherwise, only an indirect interpretation of *in situ* changes is possible.

4.3.3 Time-dependent Behaviour

Time-dependent behaviour, or creep, is characterized by a change in measured response over time under constant boundary conditions, e.g., static fatigue tests where the loading and environmental conditions are held constant. Responses measured during excavation of the Mine-by test tunnel typically reflected the advance of the tunnel in combination with changes in the tunnel geometry and in material behaviour caused by progressive failure. Effects caused by temperature variations, while minimized by the enthalpy control system, also contributed to the measured response. Consequently, in most circumstances, changes in the measured response with time were related primarily to changes in boundary conditions.

It was possible to separate out the effects of tunnel advance by observing changes in the measured response within a given excavation round during periods where there was no excavation activity. However, it was not as easy to isolate the effects of non-elastic material behaviour, i.e., creep, from those of tunnel geometry changes and temperature variations.

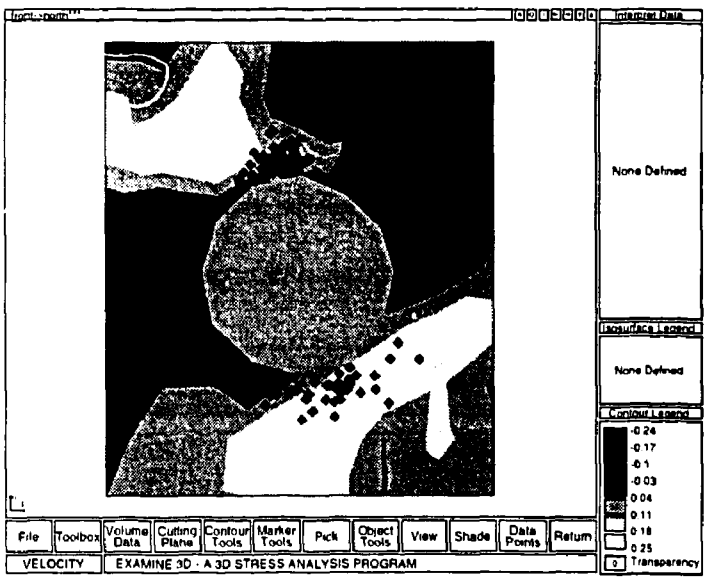

FIGURE 85: View normal to the tunnel axis of P-wave velocity variations, relative to the initial starting model, computed from controlled source data. Microseismic event locations and the tunnel outline are superimposed on the image.

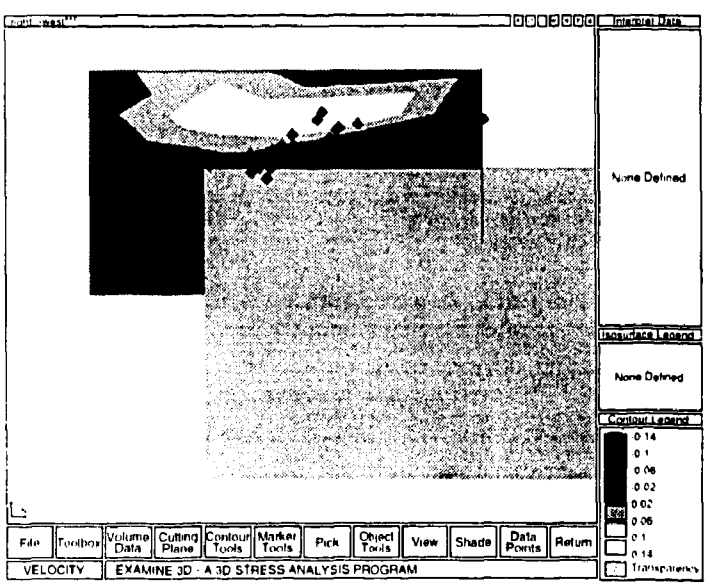

FIGURE 86: Vertical axial view of the tunnel with P-wave velocity variations relative to the initial starting model in the upper notch region computed from simultaneous velocity and hypocenter inversion of the microseismic data. Microseismic event locations and the tunnel outline are superimposed on the image.

During a 13-day period following the excavation of Round 17, changes were noted in the radial displacement responses around the Mine-by test tunnel. While there was no excavation activity in this period, there were ongoing construction and experimental activities involving drilling and instrument installation. Nevertheless, the position of the tunnel face did not change over this time interval. Tunnel profiles taken at the extensometer array near chainage 22+50, immediately behind the tunnel face, indicated that the geometry of the tunnel at this location changed only slightly due to minor spalling over the 13-day period. Therefore, the changes in radial displacement measured in this time interval were attributed mainly to changes in temperature and time-dependent behaviour.

The shapes of the individual radial displacement responses measured by the Bof-exs over this period were similar to the displacement responses measured during advancement of the test tunnel, showing an increase in divergence in the vertical extensometers, and an increase in convergence in the other extensometers. The radial displacement response measured by a horizontal extensometer (EXT11) and the associated downhole temperatures measured at six of the extensometer anchors are shown in Figure 87, along with the periods of activity in the test tunnel. Measurements at anchor 1, closest to the tunnel wall, reflect the air temperature in the test tunnel, while those at the other anchors reflect rock temperature.

As shown in Figure 87, temperature variations were held to less than 1.5°C at anchor 1, and to less than 0.3°C at anchor 3 and beyond. Changes in temperature were noticeable as far out as anchor 9, approximately 6.7 m from the tunnel wall. Martino (1995a) reported that rock-temperature variations of about 1°C around the URL shaft produced radial displacements of about 0.02 mm between Bof-ex anchors spaced 0.4 m apart. This spacing is similar to that between the first 4 anchors in EXT11. From March 12 to 19, a variation in temperature of 0.19°C was noted in EXT11 at anchor 3, and a change of 3.7 μm was recorded between anchors 2 and 3. Based on the results from the shaft, a thermally-induced change of 3.8 μm would be expected over this measurement interval. Consequently, the recorded changes in displacement after March 12 appear consistent with those expected from the small observed temperature variations. Therefore, there is no significant creep component in the measured response over this time interval.

For the period between March 7 and 9, there were only very minor temperature variations in EXT11. Nevertheless, the radial displacement response in Figure 87 shows relatively large changes, levelling off at anchors 2 to 10 by about noon on March 10. The change in displacements between March 7 and 9 is unrelated to temperature or underground activities, and therefore appears to be an indication of true time-dependent behaviour. However, this behaviour is fairly short-lived, spanning only 3.5 days following excavation of Round 17. This time frame is consistent with the period of microseismic activity typically observed within 1 m of the tunnel face after excavation of each round. For example, Figure 40 shows that the microseismicity associated with excavating Round 17 occurs within three days of completing excavation. Hence, the non-elastic displacement that occurs in this period is related to time-dependent damage development, and represents about 0.6% of the total displacement measured in EXT11. Similar non-elastic displacement was observed in the vertical extensometers, representing about 1.4% of the total measured displacement in this direction.

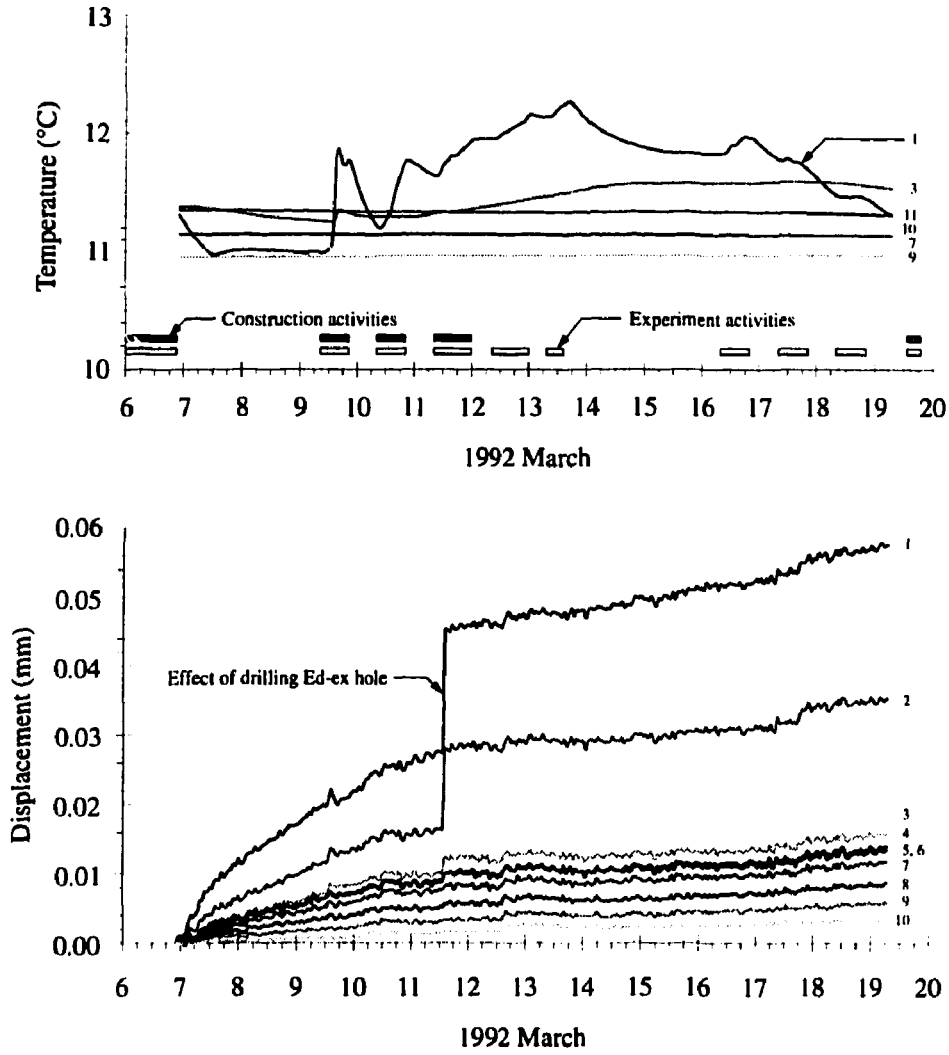

FIGURE 87: Changes in temperature (top) and radial displacement (bottom) in EXT11 for a constant tunnel face position over a 13-day period. Small numbers on the right indicate anchor numbers, anchor 1 being closest to the tunnel wall. The displacements shown are cumulative, i.e., referenced to the deepest anchor. Note that the large jump in displacement on March 11 is a result of drilling an Ed-ex hole adjacent to the Bof-ex borehole containing EXT11.

From Figure 87, it is apparent that the rock mass around the tunnel is very sensitive to small changes in boundary conditions. For instance, drilling of a 1-m-deep Ed-ex borehole near EXT11 caused a sharp increase in permanent deformation within about 1 m of the tunnel wall. Likewise, temperature variations in the tunnel, although cyclical, caused a monotonic increase in permanent deformation at anchor 1. Similar observations were made in Room 405, where very slight changes in temperature caused a small, but measurable, increase in breakout length in a 1.24-m-diameter vertical borehole. These observations suggest that even small changes in boundary conditions tend to promote the development of damage close to the tunnel wall, causing permanent non-elastic deformation. The displacements measured in EXT11 are consistent with the development of damage within about 1 m of the SE sidwall of the tunnel.

In summary, changes in measured responses over time can generally be attributed to changes in boundary conditions. However, there is evidence that true time-dependent behaviour occurs over a short period of about 3.5 days, in which microseismic activity is also observed, immediately behind the tunnel face following excavation advance. The permanent non-elastic deformation associated with this behaviour, however, is in the order of only about 1% of the total measured deformation, and is localized close to the tunnel wall.

4.3.4 Characteristics of the Damaged Zone

The extent and material behaviour of the damaged zone were determined by conducting a detailed *in situ* characterization of the test tunnel (Read 1994). This investigation used a series of slots and boreholes cut across the main notch area of the tunnel to identify any observable damage in these regions. Incorporating these observations into a two-dimensional finite difference model, the material behaviour around the tunnel in the damaged zone was then investigated, using the measured radial displacements from the experiment as a means of assessing model results (Read 1994).

4.3.4.1 Field Observations

From the post-excavation characterization program (Read 1994), it was determined that the only visible signs of damage to the rock mass occurred in the region of the notch tip in the roof and floor of the test tunnel. In the roof, the damage extends about 180 mm into the rock mass, and occurs up to about 500 mm either side of the notch tip in the flanks of the notch. In the floor, the damage extends to about 240 mm depth, dying out within 500 mm on the NW flank, and within 800 mm on the SE flank (Figure 88). The damaged zone comprises a series of closely spaced fractures that are parallel to the free surface. Consequently, the rock in the damaged zones has a much lower elastic modulus than the intact rock, and is therefore destressed. This view is supported by the fact that, in boreholes or slots drilled through these regions from within the tunnel, breakouts occur only in the sections beyond the observed damaged. Figure 89 shows the observable extent of excavation damage on a typical tunnel profile taken at chainage 20+40.

In the tensile sidewall regions of the test tunnel, there is no visible damage to the rock mass, i.e., no discrete tension cracks. However, as shown by the geophysics results, there

FIGURE 88: Damage in the floor slot drilled across the notch tip. Note that the fractures extend 200 mm into the rock mass, and show significant dilation. Fracturing diminishes on the flanks of the notch away from the apex.

is evidence for small-scale cracking in these regions as far as about 1 m from the opening, although the main region of damage is concentrated within about 0.35 m of the wall.

4.3.4.2 Back Analysis of Damaged Material Behaviour

A series of two-dimensional finite difference model simulations were conducted to investigate the material behaviour in the damaged zone around the tunnel. A staged approach was used in the numerical modelling exercise, starting with a simple elastic model, then progressively adding details consistent with observations from the *in situ* characterization of the test tunnel. Table 8 summarizes the various cases that were considered in the study. The main modifications made to the elastic model included: 1) a low modulus zone beyond the notch tips to account for observed *in situ* cracking in these regions; 2) a uniaxial tensile failure criterion using ubiquitous joints to simulate a unidirectional reduction in tensile strength in

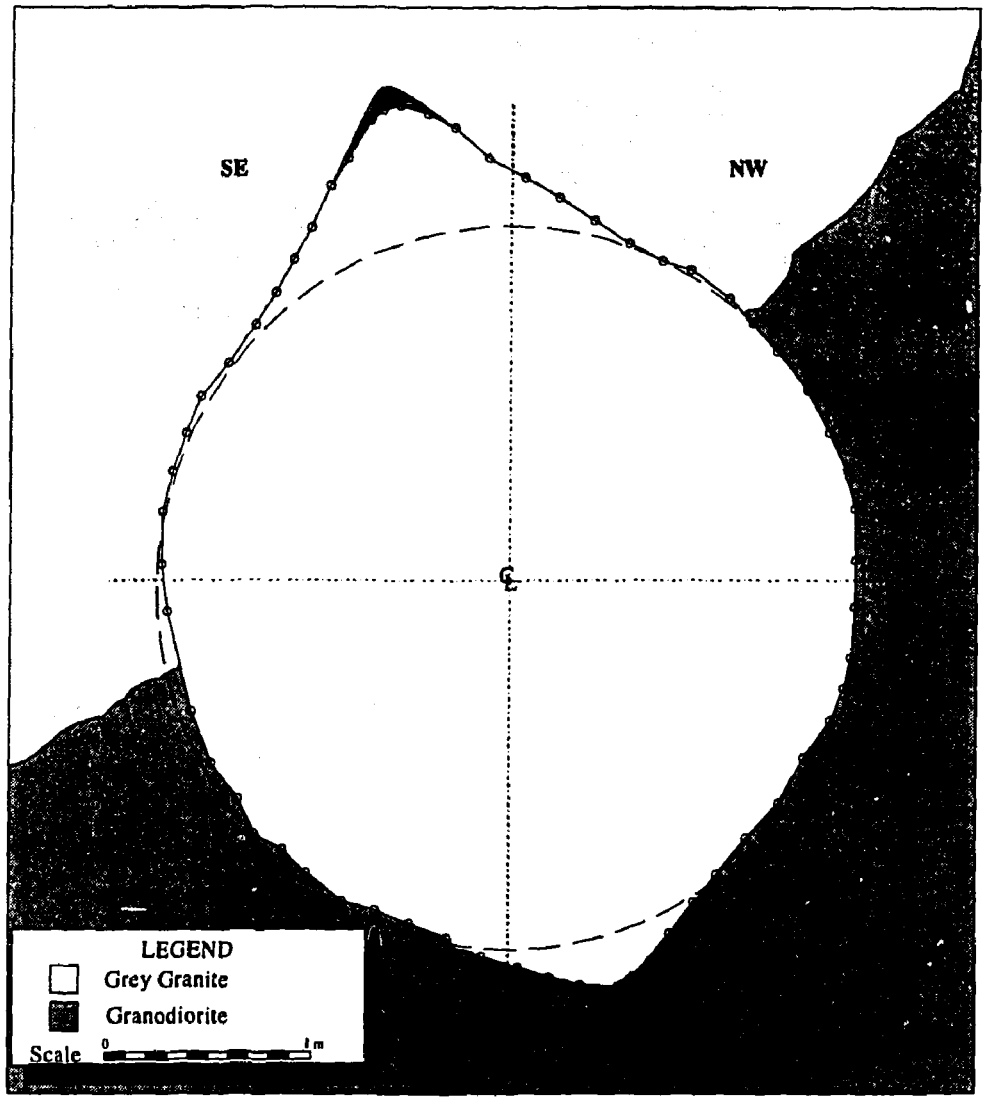

FIGURE 89: Typical tunnel profile at chainage 20+40 showing the extent of excavation-induced damage observable around Room 415. The damaged zone in the roof is about 180 mm thick, while that in the floor is 240 mm thick.

regions where $\sigma_3 < \sigma_t$; 3) a softening criterion to account for reduction of the shear modulus for regions where $\sigma_3 < \sigma_t$; and 4) two different material types, each with unique properties and failure characteristics, to account for the variations in geology near the extensometer arrays.

As a base case, the radial displacement responses versus normalized radial distance for a purely elastic model were generated for eight rotation angles (Figure 90). To assess the effect of the damage beyond the notch tip shown in Figure 89, zones of reduced elastic modulus were added to the model in these regions. The damaged modulus in these zones was arbitrarily taken as 10% and 1% of the intact modulus in separate simulations. The resulting radial displacement responses using a damaged modulus equal to 10% of the intact modulus are compared to the base elastic case in Figure 90. It is readily apparent from these plots that the damage observed *in situ* in the roof and floor of the tunnel has no significant effect on the radial displacement responses, producing only a marginal increase in displacement in the sidewalls. The same was true of the results using a damaged modulus equal to 1% of the intact modulus. The major role of the damage beyond the notch tip is to drive the point of maximum tangential stress into the rock mass away from the tunnel boundary, thus allowing sufficient confining stress to develop at that point to prevent further failure, i.e., the stresses at the point of maximum tangential stress would fall inside the failure envelope in principal stress space.

The measured radial displacement responses for the two extensometer arrays used in the Mine-by Experiment are shown in Figure 91. The responses represent the measured displacements at the end of Round 36, when the tunnel face was almost five tunnel diameters past the second instrument array. In comparison to the results in Figure 90, the measured displacement responses deviate from the elastic responses starting about one tunnel radius from the wall. The most notable differences are for instruments oriented at $\theta = 0$, 135, 180 and 315°. For the horizontal instruments, the gradient of the measured radial displacement responses is much steeper within one radius of the tunnel wall than for the elastic case. In the regions containing these instruments, the tangential stress near the tunnel is highly tensile, exceeding the tensile strength of the rock for distances within about 200 mm of the wall.

Martin (1993) showed that accumulated damage in the rock results in an increase in Poisson's ratio and a decrease in the Young's modulus, effectively reducing the shear modulus G of the damaged material. Comparing the results from the elastic model and the measured results, the difference in the horizontal responses is consistent with a reduction in the shear modulus in the zone within about one radius of the sidewalls. Likewise, the large increase in radial displacement in EXT12 in the upper SE quadrant of the tunnel indicates a similar change in the material properties in this region.

The studies by Hayles et al. (1995) and Carlson and Young (1993) support the idea of damage development in the tensile regions around the test tunnel, resulting in induced anisotropy, i.e., directional cracking, and reduced shear modulus. Several relatively simple models were used to simulate this process, and the resulting radial displacement responses. An elastic model, (case 4 in Table 8), using a softening criterion to reduce the shear modulus in zones where $\sigma_3 < \sigma_t$, produced only marginal changes in the radial displacement response,

TABLE 8

SUMMARY OF MODELS USED TO SIMULATE RADIAL DISPLACEMENT PATTERNS OBSERVED IN THE POSTERIOR DOMAIN OF THE TEST TUNNEL

Model	Material Model	Yield Criterion	Post-Yield Behaviour	Comments
1	Elastic	None	Elastic	Base case with notch geometry
2	Elastic	None	Elastic	Reduced E at notch tips
3	Elastic/ Ubiq/Mohr	Hoek-Brown	Non-associated plastic flow	Reduced E at notch tips
4	Elastic	Tension Cutoff	Elastic	Reduced E at notch tips, reduced G for $\sigma_3 < \sigma_t$
5	Elastic/ Ubiq	Tension Cutoff	Elastic	Reduced E at notch tips, reduced G for $\sigma_3 < \sigma_t$, uniaxial reduction in tensile strength
6	Elastic/ Ubiq	Tension Cutoff	Elastic	Reduced E at notch tips, reduced G for $\sigma_3 < \sigma_t$, uniaxial reduction in tensile strength, two material types

Note:
UBIQ - Ubiquitous Joint
MOHR - Mohr-Coulomb

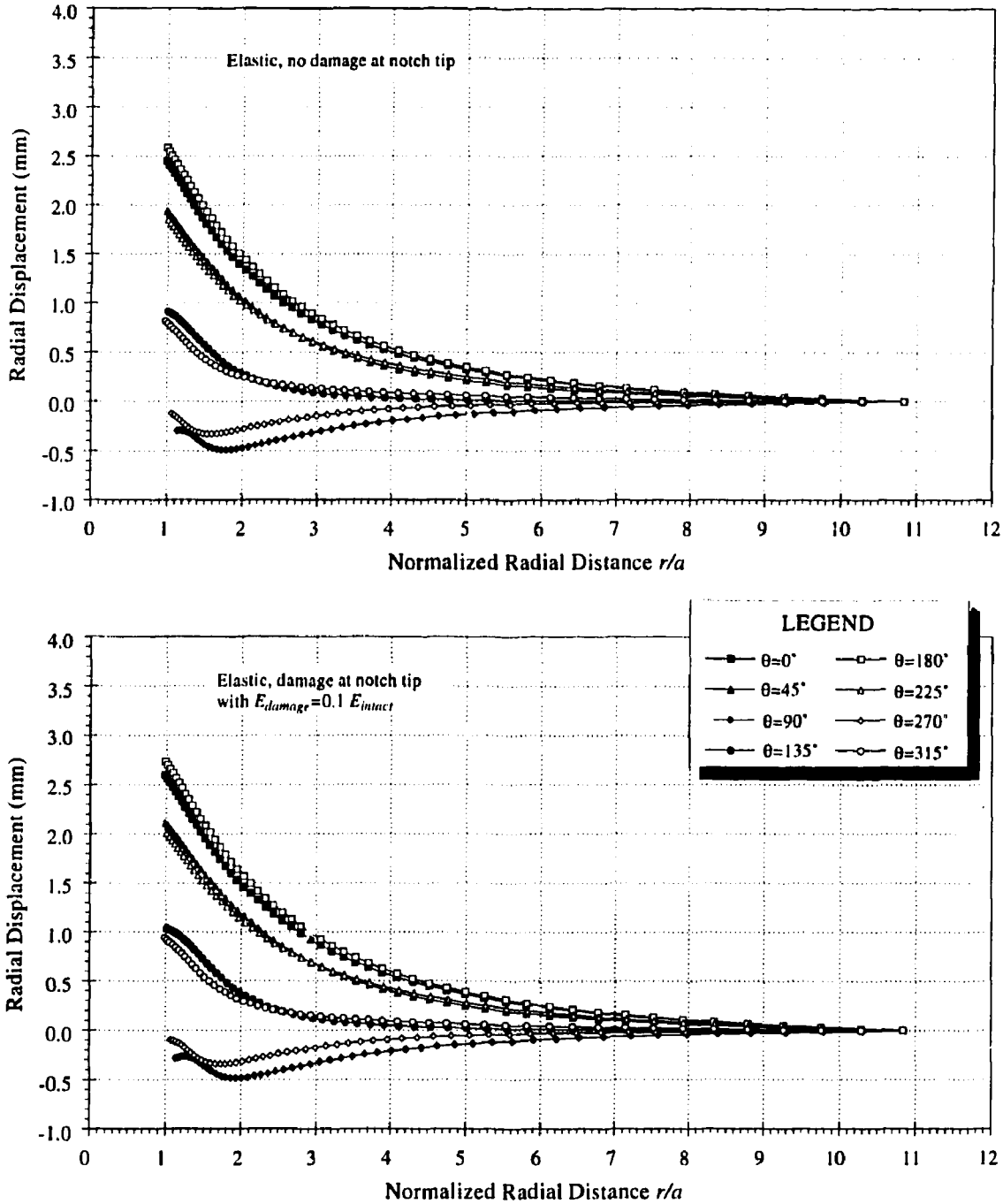

FIGURE 90: Radial displacement responses for elastic models excluding and including damage beyond the notch tip. Note that there is only a marginal difference in the responses resulting from the inclusion of additional damage at the notch tips.

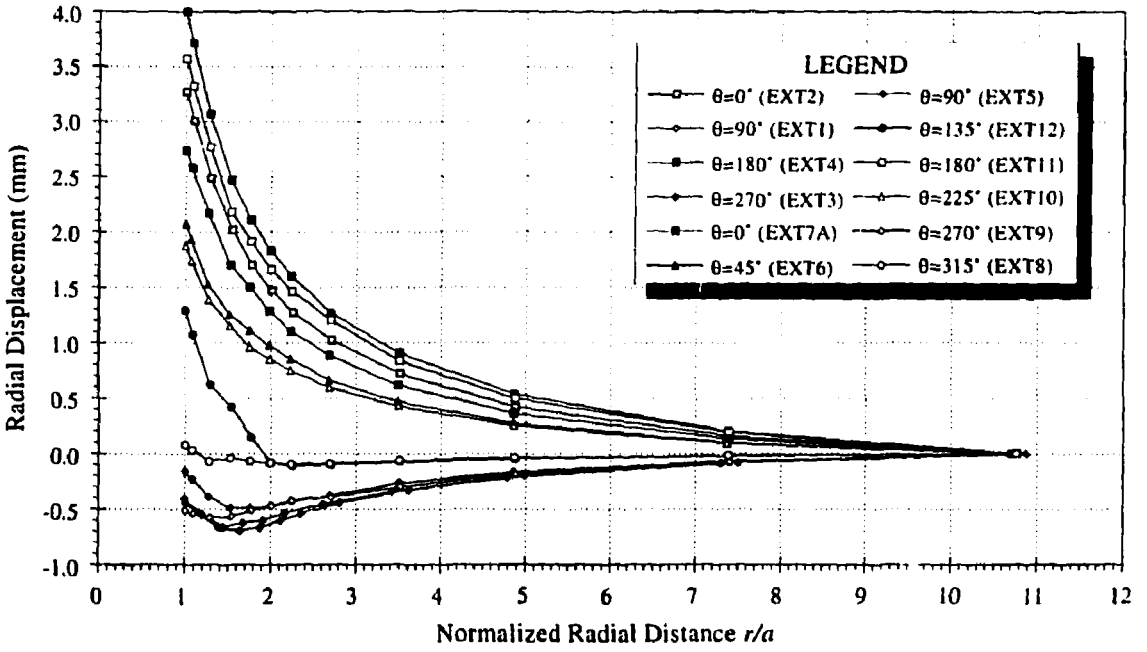

FIGURE 91: Radial displacement responses for the two extensometer arrays in the field study. Results from Array 1 are shaded in grey. Note the differences in these responses within one radius of the tunnel wall compared to the elastic case.

even when the shear modulus was reduced by an order of magnitude. To account for the reduction in tensile load-bearing capacity orthogonal to the induced cracking in the damaged material, ubiquitous joint elements were introduced into the zones where $\sigma_3 < \sigma_t$ (case 5). Stress redistribution associated with the reduction in tensile stresses near the tunnel wall was captured by iteratively checking for new zones where $\sigma_3 < \sigma_t$, substituting ubiquitous joint elements for those elastic elements that violated the tensile cutoff criterion, then allowing the model to equilibrate. In this way, the zone of damaged material propagated away from the tunnel wall until equilibrium was reached. Depending on the value selected for σ_t, the final extent of the zone of extensional damage could be significantly larger than the region that initially exceeded the tension cutoff. The tensile strength defined by the Hoek-Brown criterion is

$$\sigma_t = \frac{\sigma_c}{2}\left[m - \left(m^2 + 4s\right)^{\frac{1}{2}}\right] \tag{18}$$

The redistribution of stresses increased the radial displacement near the tunnel wall measured by the horizontal instruments. By incorporating a reduced shear modulus in the ubiquitous joint elements, the resulting displacement response from the model was very similar to the measured response.

Using this approach, it was found that differences in radial displacements between the two sides of the tunnel were more pronounced in the measured results than in the model results. As determined from *in situ* characterization of the test tunnel near extensometer array 2 (Everitt et al. 1993), the upper SE quadrant and part of the upper NW quadrant are primarily grey granite, while the other quadrants are granodiorite (Figure 89). The granite

typically shows more visible signs of cracking along grain boundaries than the granodiorite upon stress-relief, both *in situ* and in laboratory samples. The significance of lithology on excavation damage development is considered in Section 4.3.5. Lajtai et al. (1990) noted that, in tension, stresses at fracture nucleation and failure are assumed to be identical. The crack-damage stress for granite in tension was measured as 7.4 MPa from Brazilian tests, and as low as 1.5 MPa from direct tension tests on damaged samples from the 420 Level of the URL (Martin 1993). Recent Brazilian tests by Alexander (pers. comm.) have given tensile strengths of 6.5 ± 1.2 MPa for granite, and 10.0 ± 1.3 MPa for granodiorite from the 420 Level.

The elastic/ubiquitous joint model was modified to account for the two material types in the vicinity of the second extensometer array. A sensitivity study was then conducted, considering different tensile cutoff stresses and reduced shear moduli for the two rock types. As shown in Figure 92, reasonable agreement with the measured radial displacement response was obtained when tensile cutoff stresses of 6 and 11 MPa, and reduced shear moduli of 5 and 10 GPa, were used respectively for granite and granodiorite. The values of shear moduli represent reductions of 81 and 62% for granite and granodiorite, respectively. The extent of the zone of extensional damage is shown in Figure 93.

While this modelling approach appears to capture some of the mechanistic features observed *in situ*, it has several limitations. The most significant of these is that a tension cutoff in FLAC implies that, once a stress component falls below the tensile limit, it is cut to zero and cannot be tensile from that point on. In reality, the reduction in tensile strength related to the development of induced anisotropy as directional cracking along grain boundaries is directly related to the amount of damage sustained by the material (Martin 1993). Because the cracking is at the grain scale (Carlson and Young 1993), and the cracks are not necessarily connected, damaged material would still be able to sustain tensile loading, albeit at a reduced level. The tensile limit of the material would therefore increase towards the boundary of the tensile region, and, consequently, the stress redistribution *in situ* would be less extensive than suggested by the model. Nevertheless, the model illustrates that stress redistribution and a reduction in shear modulus resulting from induced cracking in the tensile region can account for the difference between the measured and modelled radial displacement responses.

4.3.5 Factors Controlling Excavation Damage Development

4.3.5.1 Effect of Geology

Extensive underground mapping (Everitt et al. 1993) and laboratory analyses of drill core samples from representative areas of the test tunnel were conducted as part of the post-excavation characterization. During the excavation of Room 415, six closed fractures were encountered, each with an areal extent on the order of 1 m^2. These types of fractures are interpreted as cooling fractures associated with the margins of a granodiorite dyke, and are tight with minor infillings of chlorite, serecite, hematite and carbonate (Everitt et al. 1993). They do not constitute paths of increased hydraulic conductivity because they are not connected, and are of very limited size.

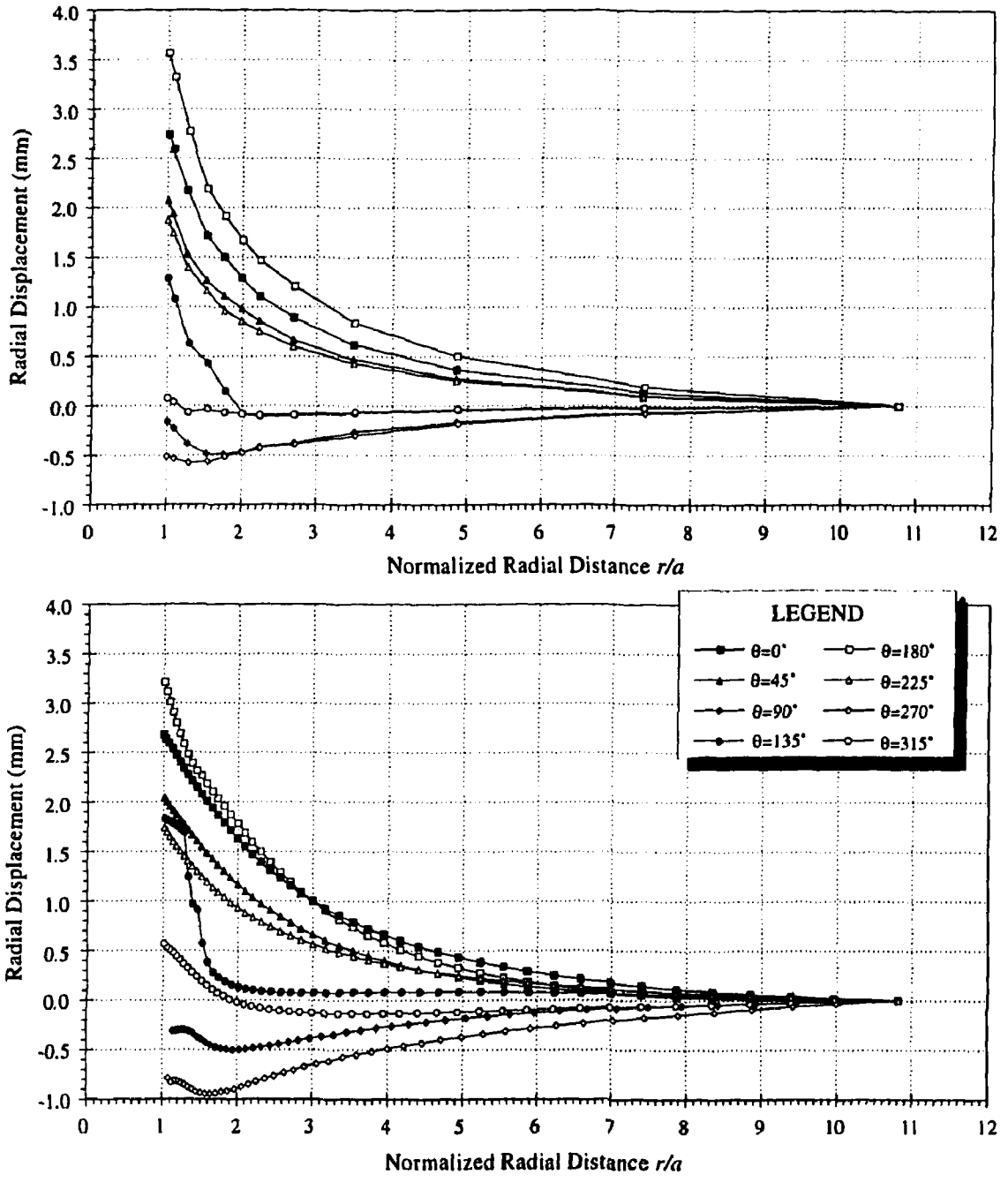

FIGURE 92: Radial displacement responses from the tension cutoff model (bottom) compared to measured results from extensometer array 2 (top).

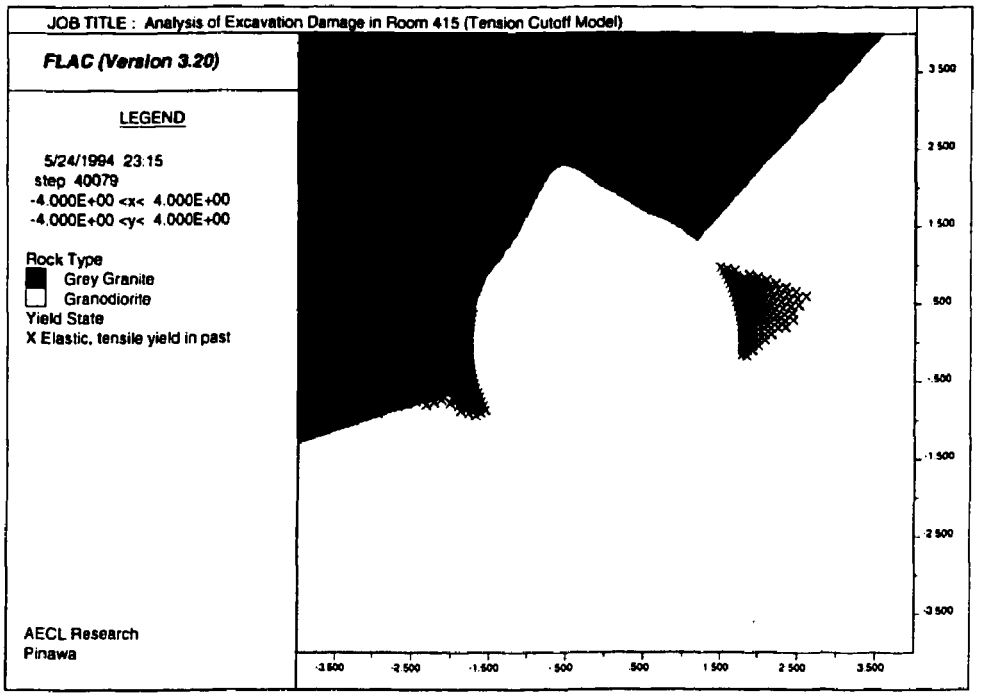

FIGURE 93: Extent of the zone of extensional damage in the tension cutoff model. Because of limitations in the model, the extent of the damaged region is overestimated.

As originally expected from exploratory drilling and excavation of the access tunnels for the Mine-by Experiment, the test tunnel was excavated in an area of mixed granite-granodiorite lithology. The distribution of grey granite and granodiorite is depicted on an unfolded perimeter map of the tunnel in Figure 94. Note that, with increasing chainage, the proportion of granodiorite increases to a maximum of 100% near chainage 30+00, then decreases again towards the end of the tunnel. In comparing the geology perimeter map to similar maps of overbreak contours and of microseismic activity occurring outside the design perimeter of the tunnel, it is clear that there is a correlation between geology, microseismic activity, and breakout development. Regions where granite was predominant showed more microseismic activity during excavation, and developed more pronounced breakouts as the tunnel advanced, than regions of granodiorite. This correlation is also apparent in tunnel profiles taken at various points in the test tunnel (Figure 95).

Petrographic analysis of nine samples carried out at Laurentian University (Kelly et al. 1993) showed that, although the rock types had previously been identified as granite and granodiorite, all rock types within the test tunnel volume fall within the International Union of Geological Sciences (IUGS) granite classification. However, to avoid confusion, the terms granite and granodiorite have been retained. The results of the petrographic analysis are summarized in Kelly et al. (1993).

Mineralogically, the samples are similar, with minor variations in mineral proportions. According to Kelly et al. (1993), the samples originally described as granodiorite contain

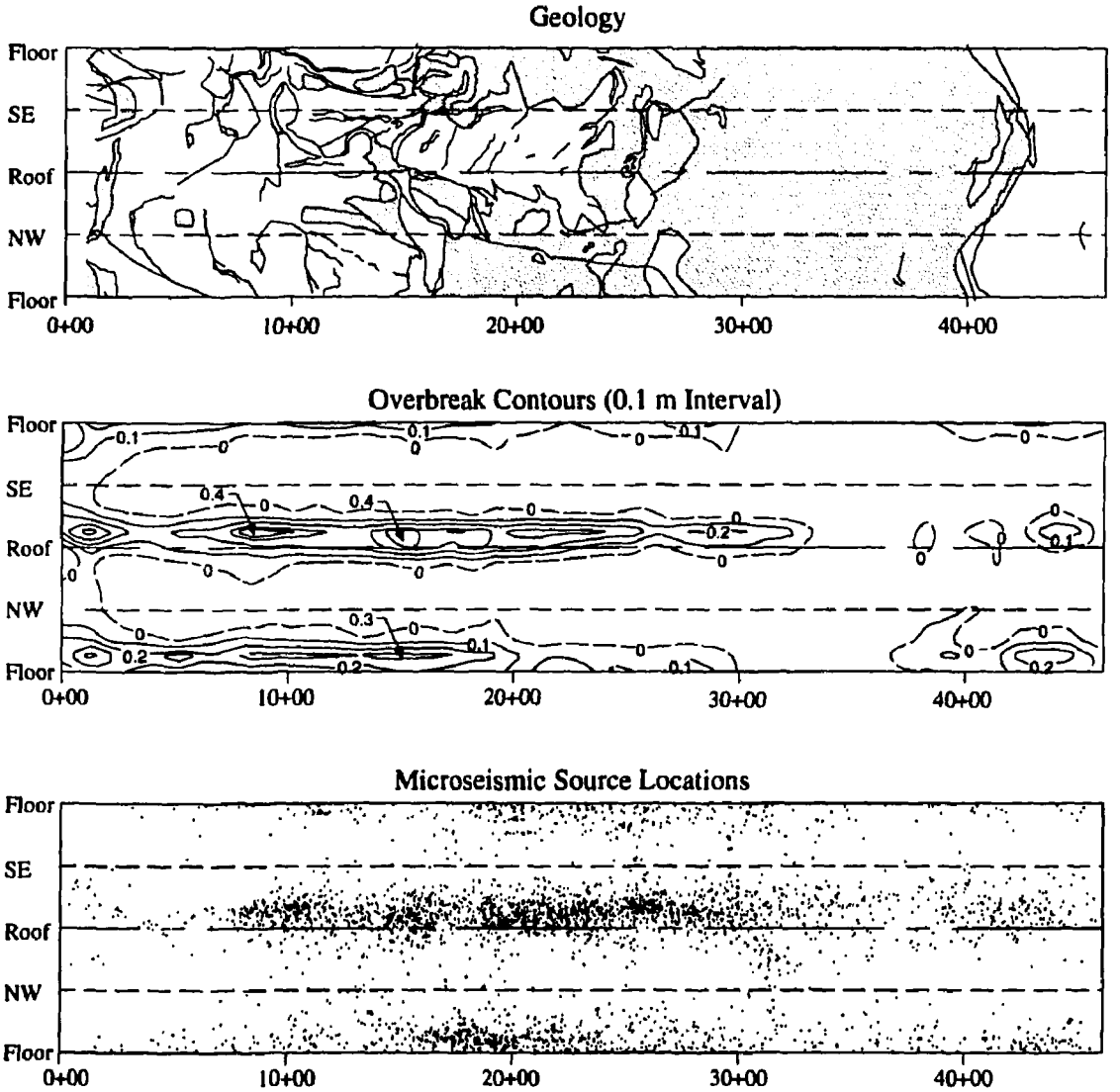

FIGURE 94: Perimeter maps of geology, overbreak and microseismic activity. Granite is shown as the light regions and granodiorite as the dark regions on the geology map. Note the correlation between areas of grey granite, overbreak and concentrated microseismic activity. Distance is shown as chainage (m) from the start of Room 415.

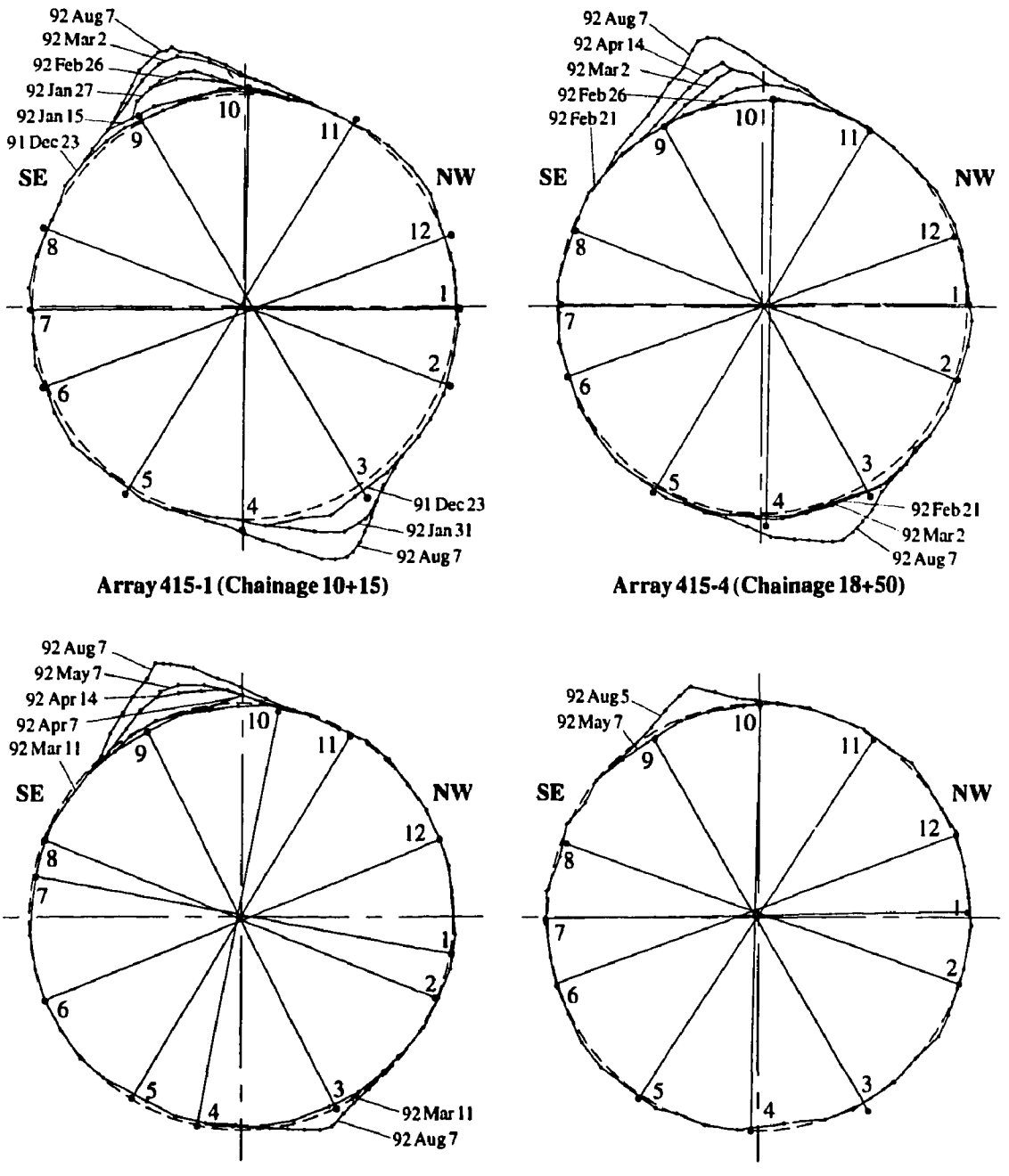

FIGURE 95: Comparison of tunnel profiles at convergence Arrays 415-1, 4, 5 and 8. These profiles represent a progression from a predominantly granite to a predominantly granodiorite region. Note that the extent of large-scale notch development is much less pronounced for Array 415-8 located completely in granodiorite.

TABLE 9

GRAIN SIZES OF THE MAIN MINERALS IN NINE SAMPLES FROM THE EXPERIMENT AREA

Mineral	Grain Size (mm)								
	AE1	AE2	AE3	AE4	AE5	AE6	AE7	AE8	AE9
Alkali Feldspar									
Min.	1.0	0.5	1.0	0.25	1.0	0.5	0.5	0.5	1.0
Max.	8.0	3.5	7.0	2.0	7.0	2.5	3.0	2.5	6.0
Mean	4.0	3.0	4.0	1.0	4.5	1.0	1.0	1.0	3.0
Plagioclase									
Min.	0.5	0.5	1.0	0.5	0.5	0.5	0.5	<0.5	2.0
Max.	6.0	6.0	5.0	2.0	4.0	2.0	2.5	1.5	5.0
Mean	4.0	3.5	3.0	1.5	2.0	1.0	1.0	1.0	3.0
Quartz									
Min.	0.5	0.25	0.25	<0.25	<0.25	<0.25	<0.25	<0.5	<0.25
Max.	4.0	3.0	4.0	1.0	4.0	1.5	1.5	1.5	3.0
Mean	2.0	1.5	2.5	0.75	2.0	0.5	0.75	0.75	0.75
Biotite									
Min.	0.25	<0.25	<0.25	<0.25	<0.25	<0.25	<0.25	<0.25	<0.25
Max.	2.0	2.0	2.0	1.0	2.5	0.5	1.5	2.0	2.0
Mean	1.0	0.75	1.0	0.25	1.0	0.5	0.5	1.0	0.75

Samples AE1, 2, 3, 5 and 9 are granite, the others granodiorite.
After Kelly et al. (1993).

between 7.6 and 13.2% biotite, while samples initially classified as grey granite contain between 1.8 and 7.8% biotite. This difference in biotite content accounts for the darker appearance of the granodiorite. Mineralogical alteration was found to be minor, and consistent throughout the sample set. Biotite was faintly to slightly altered to chlorite, and the feldspars were faintly sericitized. Minor abundances of epidote and carbonate were noted in the granodiorite samples.

As shown in the petrofabric analysis conducted by Kelly et al. (1993), the main difference between the two lithologic units is related to grain size and texture. The grey granite samples are generally coarsely crystalline, and inequigranular, containing large metamorphosed crystals of both alkali feldspar and plagioclase. The granodiorite is finely crystalline and equigranular by comparison. Table 9 presents the range and average grain sizes for the main minerals in each sample. The large feldspars characteristic of the grey granite were noted to be often significantly more fractured than finer-grained crystals, indicative of more brittle behaviour. It was concluded that differences in the rock mass characteristics of the two rock types are probably related to their grain size and textural characteristics rather than compositional differences (Kelly et al. 1993). Figure 96 shows core samples of granite (left) and granodiorite (right), illustrating the obvious differences in their grain structure.

The granite shows more visible signs of damage related to cracking of the larger feldspar crystals caused by stress relief during sampling.

As discussed in Section 3, Martin (1993) showed that the crack half-length is an important parameter in determining rock strength. Longer cracks imply more damage, and result in a greater reduction in the cohesion component of rock strength. He suggested that the crack half-length was related, in part, to the grain size of the rock. Work by Cundall (pers. comm.) using a particle flow code (PFC^{2D}) also suggests that inequigranular materials are more susceptible to cracking than equigranular materials. Owing to its inequigranular structure and the abundance of large feldspar crystals, the grey granite is expected to have a lower crack-initiation stress σ_{ci} and a lower crack-damage stress σ_{cd} than granodiorite. Based on the back-analyzed stress tensor, the *in situ* crack-initiation threshold for granite was found to be 73 MPa, similar to laboratory results from uniaxial compression tests conducted by Lajtai (1988). Results from laboratory tests on granodiorite samples suggest that the average crack-initiation threshold for granodiorite is about 100 MPa. Consequently, regions

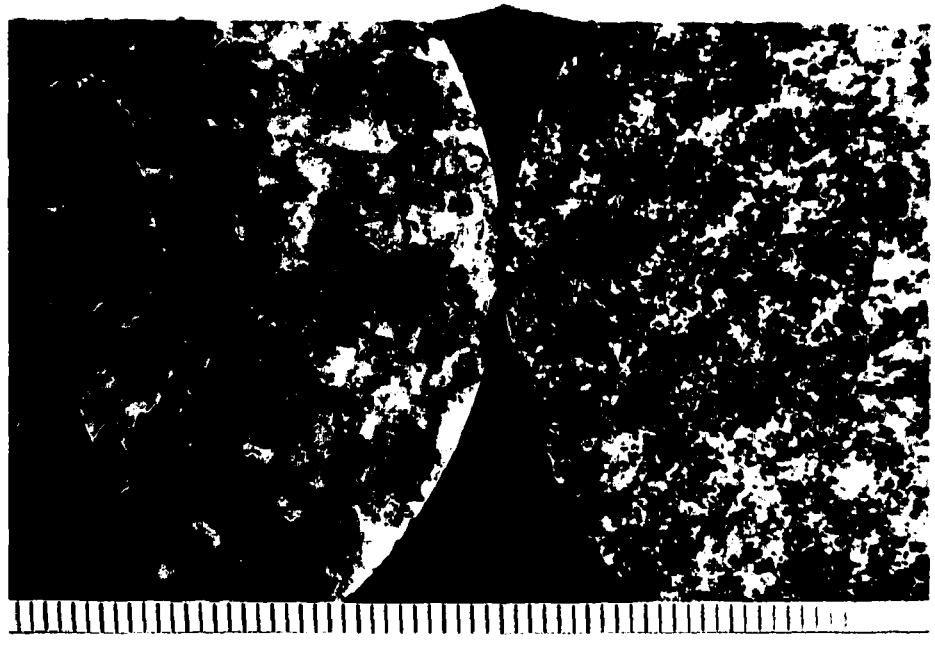

FIGURE 96: Core samples of grey granite (left) and granodiorite (right), illustrating the difference in petrofabric. Note the much larger crystals and inequigranular structure in the granite sample compared to the equigranular granodiorite sample. The small divisions at the bottom of the photograph are millimetres.

of granodiorite *in situ* would sustain less initial damage related to stress concentrations ahead of the advancing face, and would develop less pronounced breakouts behind the advancing face, than regions of granite under identical stress conditions. The same is true for the development of extensional damage in tensile regions, as discussed in Section 4.3.4.2.

4.3.5.2 Effect of Tunnel Orientation

In conjunction with the Mine-by Experiment, borehole breakouts have been studied extensively *in situ* at the URL (Martin et al. 1994; Read 1994; Read et al. 1995). In a series of boreholes with diameters ranging from 150 to 1240 mm, observed borehole breakouts did not form diametrically opposite one another in the plane orthogonal to the borehole axis. None of the boreholes were drilled parallel to a principal stress direction. The same observation was true of breakouts in the 3.5-m-diameter test tunnel for the Mine-by Experiment. This phenomenon is contrary to the idea that borehole breakouts initiate at the points of maximum tangential stress concentration around the borehole because, in an elastic medium subjected to an anisotropic stress field, these points are diametrically opposite one another on the borehole wall.

Read et al. (1995) showed that the distribution of maximum deviatoric stress ahead of the face is significantly affected by the orientation of the borehole relative to the principal directions (Figure 97). In conditions where the borehole is oriented parallel to a principal direction, the maximum deviatoric stress ahead of the face is distributed symmetrically with respect to the borehole axis. However, for situations where the borehole axis is not parallel to a principal direction, such as the Mine-by Experiment test tunnel, the distribution of the maximum deviatoric stress ahead of the face becomes asymmetric. Transforming the principal stress tensor to the cylindrical coordinate system of the borehole, this second situation has non-zero antiplane shear stress components, i.e., shear components in a plane containing the tunnel axis. Read (1994) has shown that these antiplane shear stresses are responsible for the asymmetric pattern of stresses ahead of the face of a cylindrical opening.

As described in Section 3, the combination of high deviatoric stresses and rotation of principal stresses ahead of the Mine-by test tunnel face generates local weakened zones that are eventually exposed at the tunnel perimeter as the tunnel advances. These zones are distributed asymmetrically with respect to the tunnel axis because the tunnel is not aligned with a principal direction. Consequently, even though the points of maximum tangential stress at the tunnel wall resulting from tunnel advance are distributed symmetrically with respect to the tunnel axis, breakouts develop asymmetrically, initiating in the regions of reduced strength.

Similar effects are also apparent in vertical boreholes at the URL. For example, a 1.24-m-diameter borehole was drilled to a depth of 5 m in the concrete-lined floor of Room 405. This horizontal room is horse-shoe-shaped, oriented towards azimuth 225°, and was excavated using a drill-and-blast technique. Excavation damage related to the development of the room, characterized by multiple subhorizontal fractures, was present to a depth of 0.76 m below the top of the concrete floor. Below this zone of damage, breakouts developed in the borehole during drilling, following the advancing face as the hole was deepened.

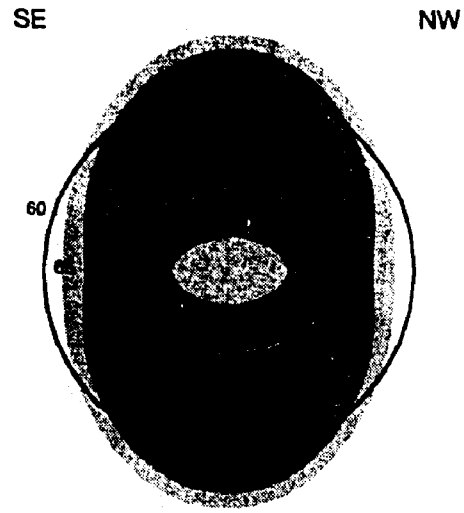

(a) Tunnel parallel to σ_2. Stress orientations (given as trend/plunge): σ_1 = 135°/0°, σ_2 = 225°/0° and σ_3 vertical.

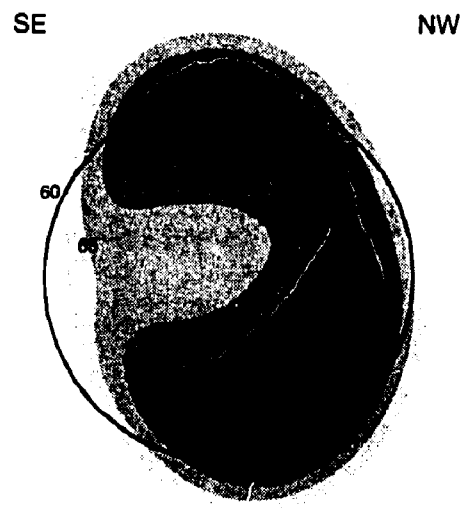

(b) Tunnel not aligned with a principal stress direction. Stress orientations: σ_1 = 145.4°/11.1°, σ_2 = 053.9°/07.7° and σ_3 = 289.8°/76.4°.

FIGURE 97: Pattern of maximum deviatoric stress from EXAMINE^{3D} in a plane 0.6 m ahead of a 3.5-m-diameter tunnel. The horizontal tunnel is oriented towards azimuth 225°. Principal stresses are 59.9, 44.3 and 9.4 MPa for σ_1, σ_2 and σ_3, respectively. Case (b) is typical of the Mine-by Experiment test tunnel.

As shown in Figure 98, the breakout pattern was asymmetrical in terms of the azimuths of the breakouts, and their depths of termination in the borehole. The azimuth of the SW breakout varied with depth away from Room 405, but near 2.0-m depth averaged 251°. The azimuth of the NE breakout, about 048°, was consistent with depth. At 2.0-m depth, the angular asymmetry, or offset from diametrically opposite positions, was 23°. In addition, the asymmetry in breakout lengths was 0.54 m, with the NE and SW breakouts extending to depths of 3.50 and 2.96 m, respectively. The hole was cylindrical and diamond-drilled vertically in homogeneous granite, thus ruling out the effects of gravity and excavation method that might contribute to asymmetry in the development of borehole breakouts.

A three-dimensional boundary element model of Room 405 and the 1.24-m-diameter borehole was constructed using EXAMINE^{3D} (Curran and Corkum 1993). Three borehole depths (2.3, 3.4 and 5.0 m) were chosen to assess the conditions ahead of the face during drilling at: 1) a point where the breakouts formed on both sides of the borehole, 2) a point

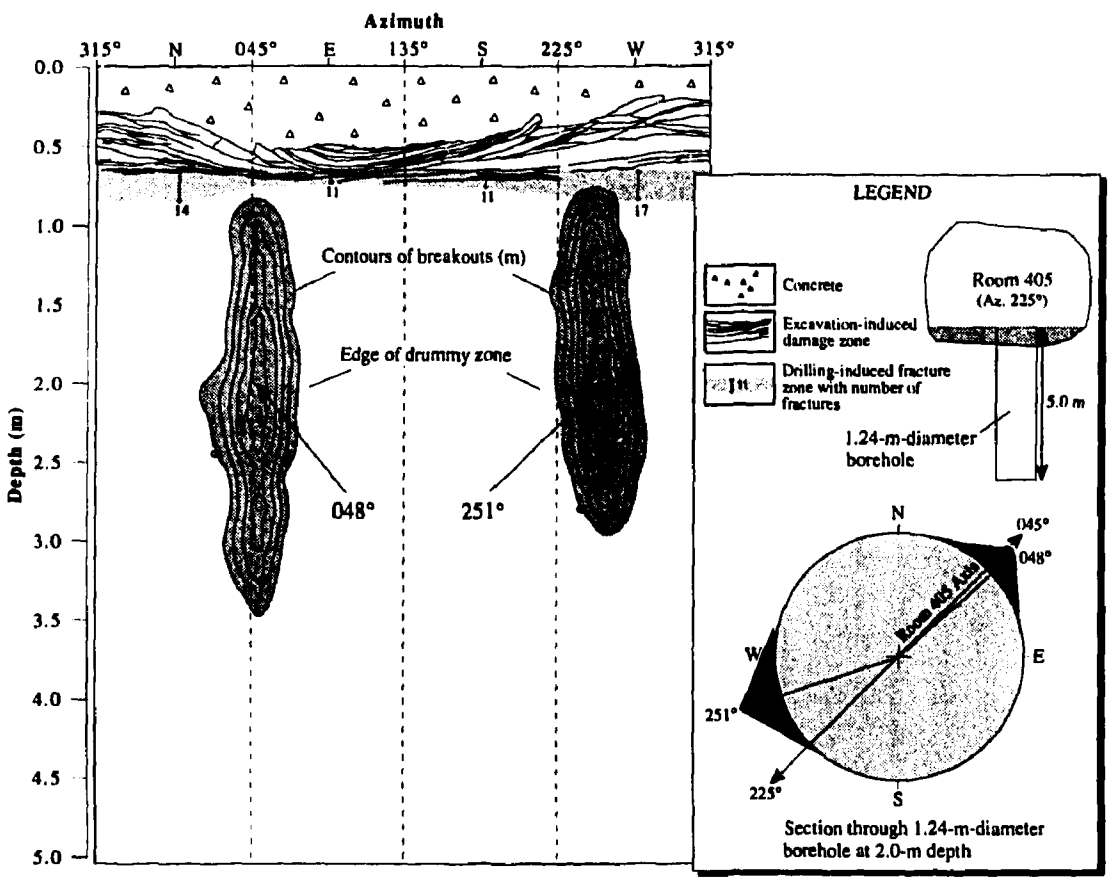

FIGURE 98: Perimeter map showing borehole breakouts in 1.24-m-diameter borehole in Room 405. Note the asymmetry in the azimuth and depth of breakouts on opposite sides of the borehole. The borehole location relative to Room 405 is shown in the inset.

where the borehole breakout occurred on one side only, and 3) a point where no breakouts were evident. Owing to the absence of breakouts in the excavation-induced damaged zone, it was inferred that the stresses within this zone had been shed to the adjacent intact rock. To account for this stress-relieved region, the floor of the room in the model was adjusted to coincide with the bottom of the damaged zone.

Stresses were determined at 0.1 diameters ahead of the face at the design perimeter. The maximum deviatoric stress was plotted versus azimuth to determine if the position of the peaks in the response correlated with the apex of each breakout (Figure 99). In addition, the magnitudes of the maximum deviatoric stress concentrations were compared with the crack-initiation threshold to determine if they were high enough to initiate damage ahead of the face, and if there was any asymmetry in their values.

As shown in Figure 99, the model produced a pattern of maximum deviatoric stress ahead of the face consistent with the observed pattern of breakouts, i.e., the azimuth of each breakout and the difference in their extent. At 2.3-m depth, where breakouts are present on both sides of the borehole, both peaks in the maximum deviatoric stress response ahead of the face exceed the threshold. At 3.4-m depth, where breakout occurs only on the NE side of the hole, the NE peak in the maximum deviatoric stress response exceeds the threshold, but the SW peak does not. At 5.0-m depth, there were no breakouts near the face. The peaks in the maximum deviatoric stress response ahead of the face confirm that, at this depth, the crack-initiation threshold is not exceeded at the design perimeter. In terms of azimuth, the positions of the peaks in the maximum deviatoric stress response at 0.1 borehole diameters ahead of the face correlate closely with those of the borehole breakouts.

Using a 600-mm-diameter borehole drilled parallel to the σ_3 direction, the asymmetry in the borehole breakouts was reduced from that in a vertical 1.24-m-diameter borehole, both in terms of the difference in breakout azimuths, and in breakout depths. The final breakouts extended to a depth of 2.29 m on the NE and 2.47 m on the SW side of the borehole. The

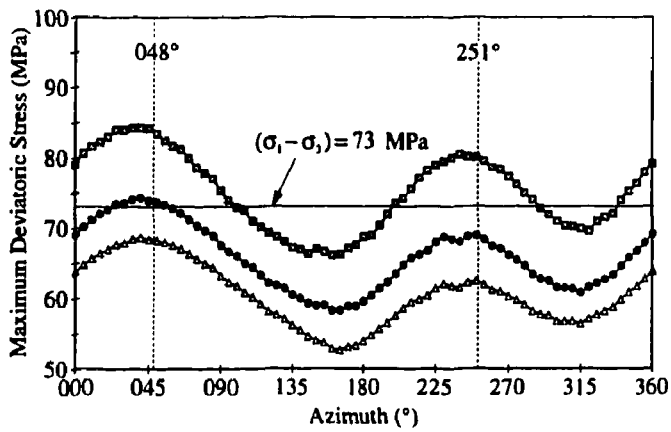

FIGURE 99: Maximum deviatoric stress pattern 0.1 diameters ahead of the 1.24-m-diameter borehole face at hole depths of 2.3 (upper), 3.4 (middle) and 5.0 m (bottom). Note the asymmetry of the peaks, both in magnitude and azimuth.

azimuths of the breakouts were 035° and 242° near the top of the hole, but approached 045° and 232° as the depth away from the room increased. Consequently, the amount of angular asymmetry near 2.0-m depth was reduced from 23° in the vertical 1.24-m-diameter borehole to 7° in the inclined 600-mm-diameter borehole. Likewise, the asymmetry in breakout length was reduced from 0.54 m to 0.18 m in the two holes, respectively. The orientations and magnitudes of the maximum deviatoric stress concentrations ahead of the borehole face are therefore consistent with field observations of breakouts in both the inclined and vertical borehole.

This study supports the notion that the complex loading path at the borehole face is responsible for initiating the damage which ultimately leads to the development of a breakout. It also confirms that the stress tensor predicted in Section 4.1.4 is consistent with observations of *in situ* breakouts. Read (1994) has shown that tunnel orientation relative to the principal stress directions is an important consideration in the interpretation of measured displacement responses.

4.3.5.3 Effect of Excavation Sequence

To determine whether or not excavation sequence was a contributing factor to the progressive failure process, the final 12 m section of the tunnel was excavated using a pilot-and-slash sequence. The rationale for this excavation approach was that, by first excavating a small full-face tunnel, the excavation damage associated with the three-dimensional face effects would be localized close to the pilot tunnel. By then slashing the small tunnel to a larger size, the excavation damage related to the pilot tunnel would be removed. In addition, because the slash would not involve a full-face excavation approach, the damage induced by the slash would be less than that associated with the pilot tunnel.

To assess the difference between the extent of breakouts associated with the pilot and the slash, the 2.5-m-diameter pilot tunnel was excavated with its floor at the same level as the main tunnel. The roof of the pilot tunnel was then slashed to increase its diameter to 3.5 m. In this way, breakout development in the floor would reflect the damage associated with the full-face pilot tunnel, and breakout development in the roof would reflect damage caused by the slash. Overall, the extent of excavation-induced damage was expected to be reduced from that caused by the full-face 3.5-m-diameter test tunnel owing to the initial smaller dimension of the pilot tunnel and the two-step approach to excavation.

Following excavation, the tunnel profile was surveyed to define the extent of breakouts. Although notch development in the roof of the tunnel initially appeared to be suppressed relative to development in the floor, the difference was less noticeable over time. In addition, it was difficult to draw any definite conclusions about the effect of excavation sequence owing to the presence of granodiorite in the test section, and the proximity of the test section to the end of the tunnel.

4.3.5.4 Effect of Artificial Support and Confinement

During excavation of the Mine-by test tunnel, it was necessary to install safety mesh to prevent loose material in the roof of the tunnel from falling (Keith and Onagi 1994). The mesh was held in place using 0.6-m-long mechanical rock bolts. However, the bolts were not tensioned, and were installed with rectangular wooden spacers, leaving approximately 100 mm between the rock and the bolt head. This arrangement provided protection in the event of large-scale spalling, but was specifically designed to avoid producing confining pressure in the region of the breakout notch.

In order to survey the tunnel profile, the rock bolts and mesh near the profile were periodically taken down, and any loose material was removed. During these periods, the extensometers close to the measured profile showed increased displacements, and there was evidence of increased AE/MS activity and subtle geometry changes in the roof notch. Similar observations were made in the floor of the tunnel when tunnel 'muck' used as rail ballast was removed. The differences between the patterns of microseismicity in the roof and in the floor are evident in Figure 40, which shows microseismic activity at 170 d related to removal of 'muck' from the tunnel floor. The temporary confinement provided by the spalled rock in the roof mesh, and by the tunnel 'muck' in the floor of the tunnel, therefore helped limit the progressive failure process, and reduced the development of excavation damage. These observations confirm that the progressive failure process and the development of excavation damage are very sensitive to small changes in confining pressure.

4.4 SUMMARY

Back analysis of displacement and strain measurements from the Mine-by Experiment provided confirmation that the *in situ* stress tensor used in the initial analysis of the experimental data was sufficient for the purposes of understanding the process of progressive failure and the development of excavation-induced damage. In addition, the back analysis improved the estimate of the stress orientations and the relative magnitudes of the various components within the tensor. Using the new tensor, it was shown that the orientation of the principal stresses relative to the tunnel axis can affect the pattern of excavation damage observed *in situ*, i.e., the development of asymmetric borehole breakouts. Variations in the relative magnitudes of the stress components were also shown to affect the absolute magnitudes of the stress concentrations around the tunnel, but did not change the overall pattern of stress concentrations or the interpretation of the experiment results.

Based on results from underground characterization, geophysics studies and numerical modelling, the excavation-induced damage around the Mine-by Experiment tunnel is concentrated in the regions of compressive stress concentrations in the roof and floor, and in the regions of tensile stress concentration in the sidewalls. The extent and characteristics of these damaged zones is shown schematically in Figure 100.

The damaged zone in the roof and floor comprises three distinct regions with different characteristics. The outer limit of damage is defined by the $\sigma_1 - \sigma_3 \approx 70$ MPa contour which extends approximately 0.7 m beyond the original tunnel perimeter. Within this

region, the rock mass has been damaged (weakened) as a result of high deviatoric stresses and stress rotation associated with the advancing tunnel face. The failed zone within this damaged region is v-shaped and extends to about 0.6 m beyond the original perimeter in the roof, and about 0.4 m in the floor. At the tip of each v-shaped notch is a localized process zone where the rock is crushed. Although the material in these zones is no longer part of the elastic continuum around the tunnel, it can be treated as a material that has been weakened and whose elastic modulus has been reduced (softened). The extent of the various regions in the compressive damaged zone varies depending on geology. AE/MS events recorded in these zones were typically in the 50 Hz to 10 kHz range.

In contrast, the damaged zone in the tensile sidewall regions of the tunnel is much more subtle than that in the roof and floor. The AE activity in this zone was typically in the 1 MHz range, indicating much smaller-scale cracking than in the compressive regions. Back analysis using extensometer results showed that the material behaviour in this zone can be characterized by softening of the shear modulus and anisotropic weakening (extensional cracking). In the NW sidewall (granodiorite), the AE activity indicates that most damage occurs within 0.35 m of the tunnel wall, and extends to about 1 m from the tunnel, dying out with distance from the sidewall. In granite, this zone of damage is more extensive, tending to expand into the tensile stress concentration lobes defined approximately by the

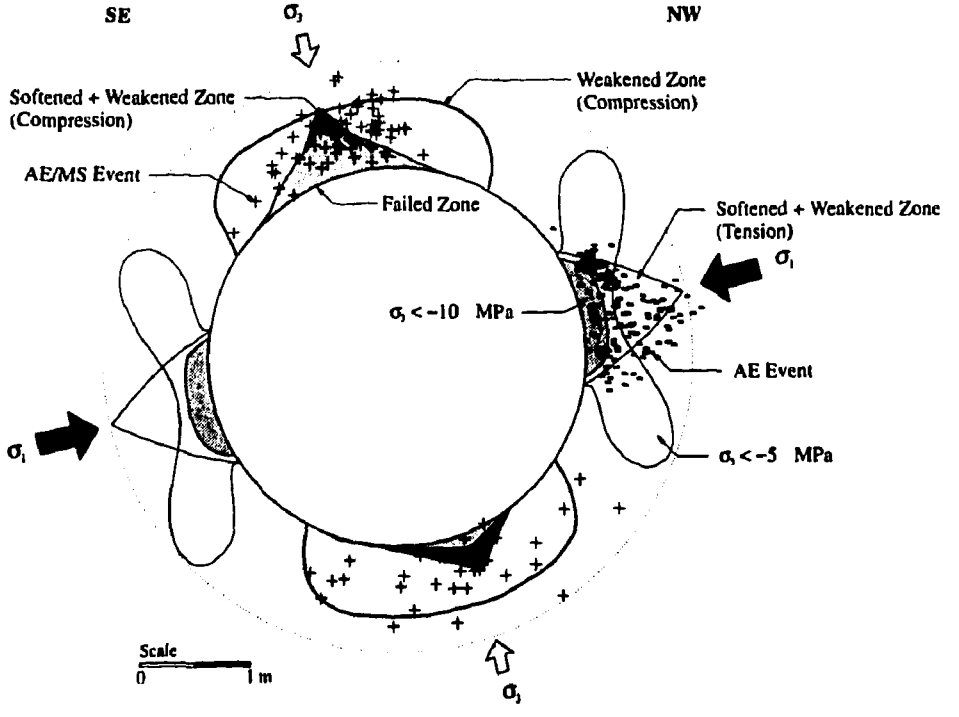

FIGURE 100: Schematic view of the extent and characteristics of excavation-induced damage around the Mine-by Experiment test tunnel. In the compressive regions, the damaged (weakened) zone is defined by $\sigma_1 - \sigma_3 \approx 70$ MPa and captures most of the AE/MS activity monitored in these regions. In the sidewalls, the damage initiates where $\sigma_3 < \sigma_t$, and migrates in a progressive fashion.

$\sigma_3 \approx -5$ MPa contour shown in Figure 100. The radial extent of the zone in granite, however, is similar to that in granodiorite. As with the compressive zones of damage, the extent of the damage zone in the tensile region is, in part, a function of geology.

In summary, the excavation-induced damage associated with the Mine-by Experiment test tunnel is limited to within about 1 m from the original tunnel perimeter. However, the characteristics of this damaged zone are variable around the tunnel, and are controlled or influenced by several factors. These factors include the nature of the stress concentration, i.e., compressive versus tensile; the mineralogy and grain size distribution of minerals within the various lithologic units; the *in situ* stress state, particularly the σ_1/σ_3 ratio; orientation of the principal stresses relative to the tunnel axis; excavation method and sequence; and confining pressure.

5. MODELLING PROGRESSIVE FAILURE

The philosophy adopted for numerical modelling of the Mine-by Experiment was that a staged approach was necessary to assess the state-of-the-art in numerical models and the ability of available models to predict the *in situ* rock mass behaviour. However, it was recognized early on in the Mine-by Experiment that none of the available numerical models was capable of simulating the complex processes involved in the progressive failure of brittle rock. Consequently, instead of comparing forward predictions with measured results, the emphasis of the numerical modelling component of the experiment was to improve our fundamental understanding of rock mass failure. It was hoped that, by advancing our understanding of the processes involved in progressive failure, numerical models could be developed which could later be used as predictive tools. Nonetheless, numerical modelling was an important element of the Mine-by Experiment, as it was an essential tool for scoping calculations and for back analyses of the measured results, e.g., see Sections 3 and 4.

Numerical modelling for the Mine-by Experiment was carried out using a variety of methods, as detailed in Table 10. The constitutive models used with the various numerical codes varied from linear elastic through to an extensive elastic-brittle-ductile (EBD) damage model developed by Ofoegbu and Curran (1991). The parameter values used in the EBD model were obtained from laboratory testing on representative samples of granite from the URL. However, none of the constitutive models used in the continuum models simulated the transition from a continuum to a discontinuum, an essential characteristic of progressive failure. Likewise, models using finite discrete fractures, and those based on a discontinuum, were also unable to adequately simulate the transition. Therefore, it is fair to say that the numerical modelling carried out during the course of the experiment was not successful in predicting *á priori* the extent and shape of failed region around the Mine-by test tunnel. In the following sections a brief overview is presented of the major findings from the modelling exercises conducted for the experiment.

TABLE 10

SUMMARY OF NUMERICAL MODELS USED IN THE MINE-BY EXPERIMENT

Model	Type	Use
Kirsch Solution	Analytical (2D)	Circular opening in an elastic continuum under plane strain conditions
EXAMINE^{2D}	Boundary element (2D)	Arbitrary 2D openings in an elastic continuum, explicit failure criteria
EXAMINE^{3D}	Boundary element (3D)	Arbitrary 3D openings in an elastic continuum, explicit failure criteria
MAP3D	Boundary element (3D)	Arbitrary 3D openings in an elastic continuum, multiple material types, displacement discontinuities, explicit failure criteria
FLAC	Finite difference (2D)	Arbitrary 2D openings in a continuum, multiple material types and constitutive models, explicit failure criteria
PHASES	Hybrid boundary element/finite element (2D)	Arbitrary 2D openings in an elastic continuum, multiple material types, explicit failure criteria
ABAQUS	Finite element (2D/3D)	Arbitrary 2 and 3D openings in a continuum, multiple material types, standard and custom constitutive models, explicit failure criteria
UDEC	Distinct element (2D)	Arbitrary 2D openings in an elastic discontinuum, multiple material types and constitutive models, explicit failure criteria
INSIGHT2D	Finite element (2D)	Arbitrary 2D openings in an elastic continuum, specialized meshing algorithm for finite discrete cracks, explicit failure criteria
EXAMINE^{FRAC}	Boundary element (2D)	Arbitrary 2D openings in an elastic continuum with discrete fractures, LEFM fracture propagation criterion

5.1 ELASTIC ANALYSES

Throughout the course of the experiment, it was demonstrated that relatively simple linear elastic models were illustrative of many aspects of the behaviour observed around the Mine-by test tunnel (Read 1991; Martin 1993). Elastic analyses were entirely adequate to predict the stresses and displacements around the test tunnel in regions that were not affected by the development of excavation-induced damage. Read (1994) successfully used elastic analyses to aid in back calculating the stress tensor at the 420 Level and to explain the occurrence of asymmetry in borehole breakouts, and Martin (1993) used elastic analyses to back-calculate the strength of Lac du Bonnet granite around the 420 Level tunnels. Elastic analyses were also routinely used to calculate the stress magnitude at which failure initiated, and to estimate the extent of the failed region based on the *in situ* crack-initiation stress (see Section 3).

In another study, Martin and Read (1992) showed that the slabbing process could be approximated using elastic analysis in conjunction with an elastic-brittle constitutive model. They simulated the failure process by performing iterative elastic analyses, removing slabs of rock next to the tunnel perimeter where the strength to stress ratio was 1 or less in each iteration. Their simulation started with the design profile and progressed through five steps (Figure 101). The analysis showed that the final excavated profile was stable except for a small region near the tip of the v-shaped notch (Figure 101). The numerical simulation used by Martin and Read (1992) is phenomenological, i.e., there is no attempt to follow the actual failure process. In addition, calibration of the unconfined compressive strength σ_c used in the model was required to match the observed behaviour. In this case, the unconfined strength used in the Hoek-Brown failure criterion was reduced from 157 to 100 MPa to obtain a reasonable match. This reduction in σ_c shifts the failure envelope downwards, and implies that the rock strength everywhere is reduced. From the microseismic data, it is clear that the rock strength is only locally damaged, and therefore the assumption that the rock strength everywhere is damaged is incorrect. This inherent assumption is one of the major drawbacks with analysis of this type, and can lead to pessimistic conclusions with regards to the rock strength *in situ*.

5.2 CONSTITUTIVE MODELS

In attempting to simulate the failure process in brittle rock, some form of strain-softening is generally used. In a strain-softening model, the elastic modulus and/or the strength of the rock is reduced as the load exceeds a critical value. By this process, load is redistributed from the region of failed material to other regions around the opening below the critical load.

Strain-softening behaviour around the Mine-by test tunnel was simulated by Khair and Chan (1994) using a two-dimensional finite element model. In their approach, iterative elastic analyses were performed, checking for material yield at each step. The yield criterion used was a Hoek-Brown envelope with $\sigma_c = 81.4$, $m = 16.4$ and $s = 1$. At each step, the Young's modulus of elements exceeding the yield limit was reduced by 20%. This reduction resulted in stress redistribution in successive steps, and was repeated until all elements were

below their yield limit. The equilibrium state at the end of the analysis showed only a very limited region of reduced modulus, i.e., yield, within the first row of elements next to the tunnel boundary. The modulus values in this region were reduced a maximum of 36%. The excavation-damaged zone predicted by the model was much smaller, and had a different shape, than that observed *in situ*. Read (1991) found similar results using FLAC.

In an attempt to simulate the slabbing process observed *in situ*, Read (1991) developed a routine within **FLAC** to conduct an iterative elastic analysis with explicit checks for tensile, compressive (shear) and slabbing failure based on a Hoek-Brown failure criterion with $\sigma_c = 100$, $m = 12$ and $s = 1$. A unidirectional tensile cutoff criterion was used in the case of tensile failure, which resulted in minor stress redistribution in the sidewalls of the tunnel. As in the previous analysis, compressive failure was noted close to the tunnel boundary in the roof and floor regions of the tunnel. Using a confining stress criterion in combination with a buckling criterion as a basis for removing elements at the free boundary, i.e., where the confinement was zero, Read (1991) found that the zone of removed material grew progressively, and was similar in shape to that observed *in situ*. He concluded that this type of modelling predicted responses for the instrumentation that were significantly different from those predicted by closed-form solutions for a circular hole in an infinite elastic medium. He also found that the shape of the predicted v-shaped notch was very dependent on the element removal scheme. Without the buckling constraint on the element removal scheme, Read (1991) found that the depth of the v-shaped notch approached $2a$ where a is the radius of the tunnel. However, with the buckling constraint, the depth of the v-shaped notch was reduced to $1.5a$ (Figure 102).

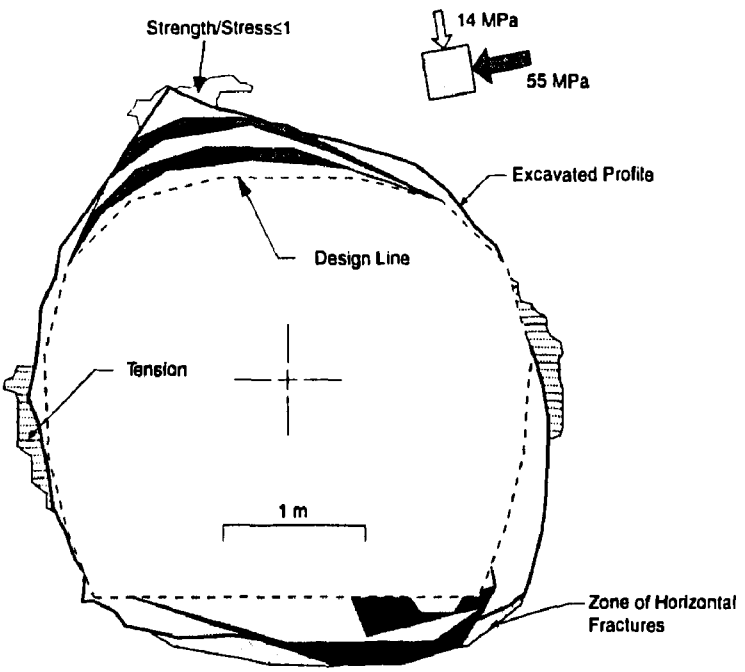

FIGURE 101: Numerical simulation of the slabbing process using elastic analyses and an elastic-brittle constitutive model.

The EBD model developed by Ofoegbu and Curran (1991) was implemented in the three-dimensional finite element program ABAQUS, and was used by Curran et al. (1992) to predict the stresses, displacements and damage around the Mine-by test tunnel. By comparing the results from linear elastic analyses and the EBD analyses, the zone of fracturing around the tunnel was predicted to extend to a depth of about 0.75 m, or about $1.4a$. These predictions were based on continuum analyses without accounting for progressive slabbing at the tunnel wall and changes in the excavation geometry. Thus, if the formation of the v-shaped notch had been accounted for in the analyses, the zone of fracturing would exceed 0.75 m. An example of the displacements predicted using the EBD model and the elastic model is presented in Figure 103. Note that both models predict very similar displacements. These results are similar to those of Read (1991) who also found that the inclusion of softened zones to represent failure did not significantly affect the predicted displacement response.

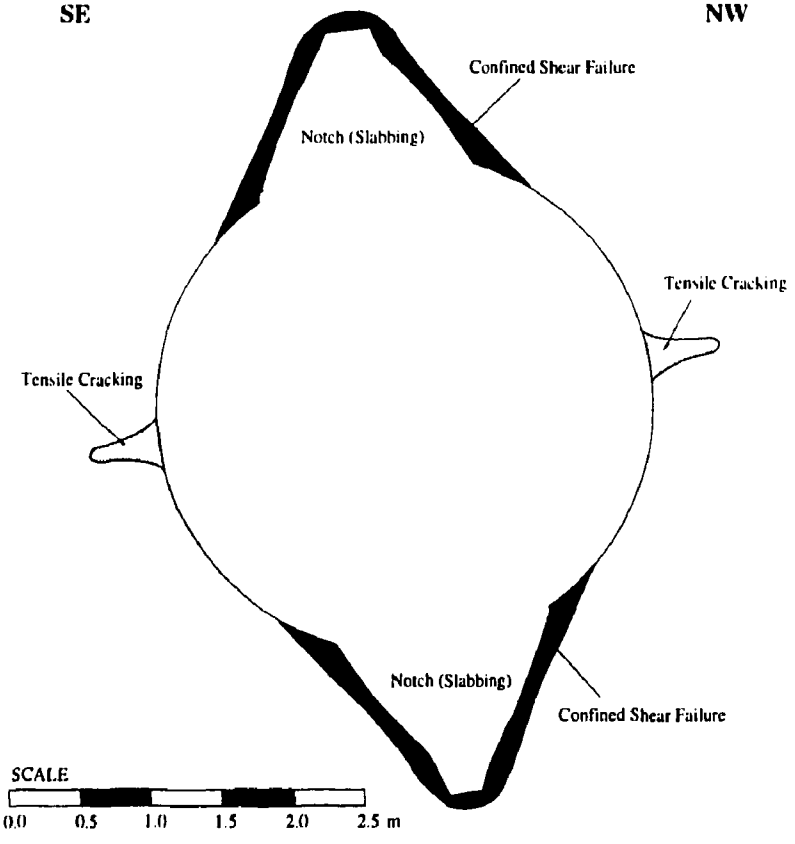

FIGURE 102: Predicted excavation damage around the Mine-by test tunnel, after Read (1991).

5.3 SUMMARY OF NUMERICAL MODELLING LIMITATIONS

The numerical modelling carried out during the course of the Mine-by Experiment showed that elastic analyses were adequate for interpreting the montoring results from the Mine-by test tunnel. However, both linear and nonlinear continuum analyses did not adequately predict the extent of damage around the Mine-by test tunnel, or the shape of the damaged zone. As discussed in Section 3, the process of progressive failure has several stages, starting with initiation at the boundary of the tunnel. This stage of the process can be predicted by continuum models, using an appropriate failure criterion. However, the stages following initiation, which involve dilation, slabbing and spalling, represent discontinuum-type behaviour. It is this behaviour that poses the major difficulty in using continuum models to predict the extent and shape of excavation damage. Until this limitation of the continuum models is overcome, current numerical models are of limited use in predicting the shape and extent of the failed region around the Mine-by test tunnel and similar underground openings. Despite this limitation, though, elastic modelling used in conjunction with the concepts developed in Section 3, are entirely adequate for engineering design purposes.

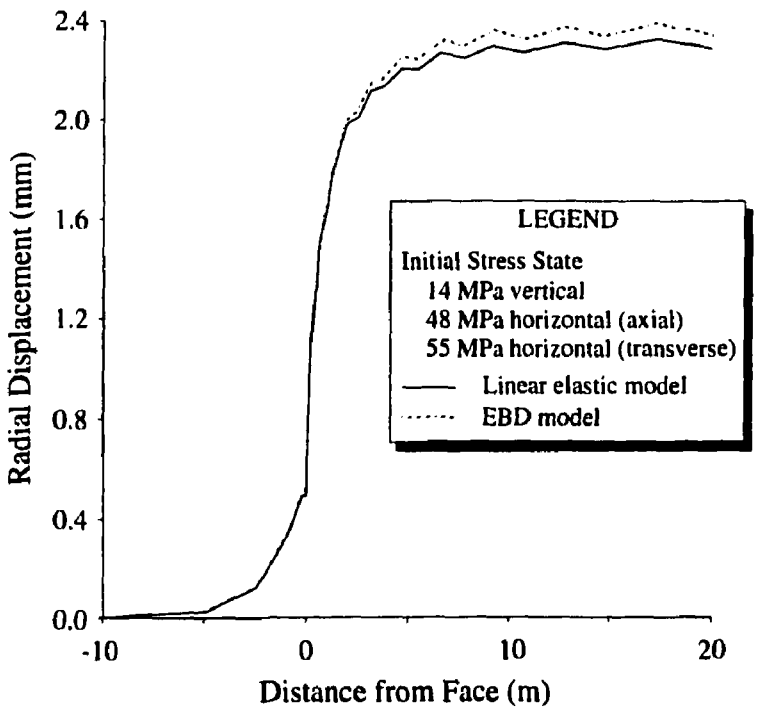

FIGURE 103: Predicted wall convergence around the Mine-by test tunnel at the sidewall ($\theta = 0°$), after Curran et al. (1992).

6. SUMMARY AND CONCLUSIONS

Phase 1 of the Mine-by Experiment was conducted at the 420 Level of the URL to investigate the response induced in the rock mass by excavating a 3.5-m-diameter circular test tunnel using a non-explosive technique. The main objectives of the experiment were to improve our fundamental understanding of *in situ* rock mass behaviour and failure mechanisms, and to evaluate the excavation damage created around underground openings. These two objectives were addressed in the investigations described in Sections 3 and 4, respectively. The findings from these investigations, and specifically the various studies using large-diameter boreholes in the floor of the underground openings, also contributed to the studies on the viability of the borehole alternative for emplacing nuclear fuel waste containers. The other two objectives, related to the development and evaluation of characterization methods and monitoring instrumentation, were addressed during the design and monitoring stages of the experiment. For example, characterization techniques and results of the characterization of the experiment area are detailed in Part 7 of the data summary reports for the experiment.

6.1 *IN SITU* ROCK MASS BEHAVIOUR AND FAILURE MECHANISMS

Back-analyses of tunnels excavated at the 420 Level of the URL showed that the *in situ* strength of Lac du Bonnet granite was less than that measured in short-term laboratory tests. However, because the tunnels were excavated in massive granite with no macroscopic discontinuities, the strength reduction could not be attributed to 'scale-effects'. Consequently, research into the role of the stress path on brittle rock strength was undertaken, comparing results from standard laboratory tests to those from *in situ* monitoring. In cylindrical laboratory samples, the sequence of events leading to failure is as follows:

- The failure process initiates with small cracks that form in the general direction of the maximum applied load. Stable crack growth starts at the crack-initiation stress, approximately 0.3 to 0.4 of the short-term peak strength of the sample.
- Stable crack growth continues until the density of cracks is sufficient to develop a macro failure zone. The stress level at which this occurs is about 0.7 to 0.8 of the short-term peak strength, and is referred to as unstable crack growth or crack-damage stress σ_{cd}.
- Once a macro failure zone is developed, the sample can no longer sustain the load and failure occurs.

In laboratory tests involving blocks with central boreholes, holes with diameters less than about 75 mm tend to show a marked scale/size effect, and require a maximum tangential stress of up to $2\sigma_c$ to initiate breakouts. For holes 75 mm or greater, this scale effect disappears, with tangential stress values approximately equal to σ_c at failure.

The sequence of events leading to failure around *in situ* openings is similar to that in the laboratory, but the stress level at failure is different. Based on results from the acoustic emission/microseismic (AE/MS) monitoring system used for the experiment:

- *In situ* crack initiation occurs at about 0.3 of the undisturbed laboratory strength.

- Spalling initiates when the tangential stress around the tunnel reaches about 100 to 120 MPa, i.e., 0.5 to 0.6 of the undamaged laboratory unconfined strength σ_c.
- Once failure initiates near the tunnel face, progressive development of a v-shaped notch occurs as the face advances. The failure process is controlled by a small process zone, consisting of highly strained/crushed rock at the tip of the notch. The failure process is multi-staged, involving crushing at the notch tip, dilation, then subsequent development of slabs, buckling and spalling. Development of the notch stops when the process zone is confined in a very small region at the notch tip, and the geometry of the notch is 'tear-drop' shaped.

Martin and Chandler (1994) showed that the measured σ_{cd} locus could be simulated using the Griffith sliding crack model proposed by Cook (1965). Using this model, they showed that stress/strain results from a laboratory compression test can be interpreted in terms of an interaction between friction and cohesion, in which the two components of strength are not mobilized at the same amount of damage. Initially, prior to any damage, the rock strength is composed of cohesion only, and can be described by

$$\sigma_1 - \sigma_3 = \text{ constant.} \tag{19}$$

The development of damage in a sample results in a rapid reduction in cohesion, and an associated increase in friction. Strength reduction of disturbed samples is thus related to cohesion loss.

The difference between the laboratory and *in situ* stress levels at which failure occurs is a result of the complex loading path around the advancing face of the tunnel *in situ*. As the tunnel advances, the principal stresses near the tunnel face change significantly in both magnitude and direction. Stress concentrations around the opening in excess of the crack-initiation stress, occurring at any period in the rock's loading history, result in a localized increase of damage to the rock and a corresponding loss of cohesion, i.e., weakening (see Section 3). The degree of damage is highest at the surface of the opening where confinement is zero and stress concentrations are greatest, and decreases with increasing distance into the rock.

Results from the AE/MS system showed that most microseismic activity is located within about 1 tunnel diameter of the face. Ahead of the tunnel face, the regions of microseismic activity correlate with the regions of compressive stress concentrations, which eventually result in breakout notches. This AE/MS activity is an indication of *in situ* damage development resulting from the complex loading path around the advancing face of the tunnel. Because of this loading path influence, the rock accumulates more crack damage for a given stress level than in laboratory tests, and undergoes more pronounced weakening. Consequently, failure *in situ* begins at lower compressive stress levels than in laboratory tests.

6.2 EXCAVATION DISTURBANCE AND DAMAGE

Numerical modelling and *in situ* characterization studies were conducted to establish the extent and characteristics of the damaged zone around the test tunnel. Back analyses of measured displacements and strains allowed the *in situ* stresses and material properties to

be deduced, leading to an improved estimate of the principal stress tensor at the 420 Level of the URL. This indicated that:

- The orientation of the principal stresses relative to the tunnel axis can affect the pattern of excavation damage observed *in situ*, in that borehole breakouts develop asymmetrically. The patterns of breakouts observed *in situ* were consistent with the new estimate of the stress tensor.
- Although the new estimate of the stress tensor changed the relative magnitudes of the stress components and the absolute magnitudes of the stress concentrations around the tunnel, it did not change the overall pattern of stress concentrations or the interpretation of the experiment results obtained using the previous estimate of the stress tensor.
- The complete *in situ* stress tensor can be determined u ing radial displacement measurements taken within 1-tunnel diameter of the face, using extensometers installed ahead of the face.
- Back analysis using a flat-faced cylinder model of the tunnel produced the lowest variability in the estimated tensor. External openings and small changes in Poisson's ratio had no significant effect on the results of the back analysis.

Results from underground characterization, geophysics studies and numerical modelling showed that the excavation-induced damage around the Mine-by Experiment tunnel is concentrated in the regions of compressive stress concentrations in the roof and floor, and in the regions of tensile stress concentration in the sidewalls. The damaged zone in the roof and floor comprises the following three distinct regions with different characteristics:

1. The outer limit of damage is defined by the $\sigma_1 - \sigma_3 \approx 70$ MPa contour which extends approximately 0.7 m beyond the original tunnel perimeter. Within this region, the rock mass has been damaged (weakened) as a result of high deviatoric stresses and stress rotation associated with the advancing tunnel face.
2. The failed zone within this damaged region is v-shaped and extends to about 0.6 m beyond the original tunnel perimeter in the roof, and about 0.4 m in the floor.
3. At the tip of each v-shaped notch is a localized process zone where the rock is crushed. Although the material in these zones is no longer part of the elastic continuum around the tunnel, it can be treated as a material that has been weakened, with a correspondingly reduced elastic modulus.

AE/MS events recorded in these three zones were in the 50 Hz to 10 kHz range.

The damaged zone in the tensile sidewall regions of the tunnel is much more subtle than that in the roof and floor. Thus,

- The AE events in this zone were typically in the 1 MHz range, indicating much smaller-scale cracking than in the compressive regions.
- Back analysis using extensometer results showed that the material behaviour in this zone can be characterized by softening of the shear modulus and anisotropic weakening (extensional cracking).

- In the NW sidewall, consisting primarily of granodiorite, the AE activity indicates that most damage occurs within 0.35 m of the tunnel wall. This activity extends to about 1 m from the tunnel, decreasing with distance from the sidewall. In granite, this zone of damage is more extensive.

Results of *in situ* characterization and numerical modelling showed that the excavation-induced damage associated with the Mine-by Experiment test tunnel occurs within about 1 m from the original tunnel perimeter. Within this region, however, the damage characteristics are highly variable around the tunnel, and are controlled or influenced by

- the nature of the stress concentration, i.e., compressive versus tensile;
- the geology of the rock mass, specifically the grain size distribution of minerals within the various lithologic units;
- the *in situ* stress state, particularly the σ_1/σ_3 ratio and the orientation of the principal stresses relative to the tunnel axis;
- excavation method and sequence, although the full influence of this factor was not quantified; and
- confining pressure.

Time-dependent behaviour was observed to occur immediately behind the tunnel face, typically over a period of about 3.5 days. However, the amount of non-elastic deformation was small, representing about 1% of the total deformation, and was localized close to the tunnel wall in the damaged zone.

6.3 NUMERICAL MODELLING

As described in Section 5, a thorough review of available numerical models showed that none was capable of simulating the transition from continuum to discontinuum behaviour, an essential feature in the progressive failure process. Consequently, the numerical modelling conducted for the Mine-by Experiment focused on improving our understanding of rock mass failure rather than conducting forward predictions and comparison with measured responses. Numerical models were used extensively in back analyses, as detailed in Section 4.

6.4 CONCLUDING REMARKS

In conclusion, the technical findings from the first phase of the Mine-by Experiment have improved our understanding of the processes involved in progressive failure and damage development. The most significant finding, from a practical viewpoint, is that the rock strength immediately around the test tunnel is only about 50% of the unconfined strength obtained in laboratory tests. This strength reduction occurs at very small levels of damage, and is related to cohesion loss. In addition, the development of damage *in situ* around the test tunnel was found to follow a complex path caused by effects of stress changes at the tunnel face. The rock underground undergoes stress changes from an initially loaded condition, whereas laboratory tests usually follow much different paths, starting from an

initially unloaded condition. Interpretation of laboratory test results assumes plane strain conditions in two-dimensions.

The findings from the Mine-by Experiment demonstrate the value in performing large-scale *in situ* experiments in combination with laboratory and numerical modelling studies in order to develop an understanding of the fundamental processes involved in the rock mass response to excavation.

ACKNOWLEDGEMENTS

The Mine-by Experiment is an activity within the Canadian Nuclear Fuel Waste Management Program, which is jointly funded by AECL and Ontario Hydro under the auspices of the CANDU Owners Group. The authors wish to thank Prof. Charles Fairhurst, Prof. Peter Kaiser, Prof. R. Paul Young, Prof. John Curran and Dr. Kam Tsui for their involvement in the Mine-by Experiment, and their technical review of this report.

REFERENCES

Barlow, J. P. (1986). Interpretation of tunnel convergence measurements. Master's thesis, Department of Civil Engineering, University of Alberta, Edmonton, AB.

Bieniawski, Z. T. (1967). Mechanism of brittle fracture of rock, Parts I, II and III. *Int. J. Rock Mech. Min. Sci. & Geomech. Abstr. 4*(4), 395–430.

Brace, W. F. and J. D. Byerlee (1968). Recent experimental studies of brittle fracture of rocks. In C. Fairhurst (Ed.), *Proc. 8th U.S. Symp. on Rock Mechanics, Minneapolis*, pp. 58–81. American Institute of Mining Engineers.

Brace, W. F., B. Paulding, and C. Scholz (1966). Dilatancy in the fracture of crystalline rocks. *J. Geophys. Res. 71*, 3939–3953.

Brown, A., N. M. Soonawala, R. A. Everitt, and D. C. Kamineni (1989). Geology and geophysics of the Underground Research Laboratory site, Lac du Bonnet Batholith, Manitoba. *Can. J. Earth Sci. 26*, 404–425.

Brown, E. T. (Ed.) (1981). *Rock characterization testing and monitoring, ISRM suggested methods*, pp. 107–127. Pergamon Press, Oxford.

Brown, E. T., J. W. Bray, B. Ladanyi, and E. Hoek (1983). Ground response curves for rock tunnels. *J. Geotech. Engng. Div. ASCE 109*(1), 15–39.

Brune, J. N. (1970). Tectonic stress and the spectra of seismic shear waves from earthquakes. *J. Geophys. Res. 75*, 4997–5009.

Carlson, S. R. and R. P. Young (1993). Acoustic emission and ultrasonic velocity study of excavation-induced microcrack damage at the Underground Research Laboratory. *Int. J. Rock Mech. Min. Sci. & Geomech. Abstr. 30*(7), 901–907.

Carter, B. J. (1992). Size and stress gradients effects on fracture around cavities. *Rock Mech. and Rock Engin. 25*(3), 167–186.

Chandler, N. A. and C. D. Martin (1994). The influence of near surface faults on in situ stresses in the Canadian Shield. In *Proc. 1st North American Rock Mech. Symp., Austin*, pp.369–376. Balkema, Rotterdam.

Chandler, N. A. (1993). Bored raise overcoring for in situ stress determination at the Underground Research Laboratory. *Int. J. Rock Mech. Min. Sci. & Geomech. Abstr. 30*(7), 989–992.

Chow, T., S. D. Falls, S. R. Carlson, and R. P. Young (1990). Ultrasonic imaging and acoustic emission monitoring of laboratory hydraulic fracturing experiments in Lac du Bonnet grey granite from AECL's Underground Research Laboratory. Contractor's Report to AECL Research, Contract No. WS-29J-54491, RP008AECL, Queen's University.

Collins, D. S., C. Baker, and R. P. Young (1994). Source parameters of excavation-induced seismicity from the Mine-by tunnel. Report to Atomic Energy of Canada Ltd. RP028AECL, Applied Seismology and Rock Physics Laboratory, Keele University, Staffordshire, U.K.

Collins, D. S. and R. P. Young (1992). Monitoring and source location of microseismicity induced by excavation of the Mine-by Test Tunnel: Preliminary analysis. Report to Atomic Energy of Canada Ltd. RP013AECL, Engineering Seismology Laboratory, Queen's University, Kingston, Canada.

Collins, D. S. and R. P. Young (1993). The spatial and temporal distribution of microseismicity recorded in Round 17 of the Mine-by tunnel. Report to Atomic Energy of Canada Ltd. RP023AECL, Applied Seismology and Rock Physics Laboratory, Keele University, Staffordshire, U.K.

Cook, N. G. W. (1965). The failure of rock. *Int. J. Rock Mech. Min. Sci. & Geomech. Abstr. 2*, 389–403.

Corthésy, R. and D. Gill (1992). Doorstopper stress measurements at the 420 Level of the URL. Final Report to AECL Research, le Centre de Développement Technologique de l'École Polytechnique de Montréal.

Curran, J. H. and B. T. Corkum (1993). *EXAMINE^{3D} - Three-Dimensional Excavation Analysis for Mines, Version 2.0.* Data Visualization Laboratory, Department of Civil Engineering, University of Toronto.

Curran, J. H., G. I. Ofoegbu, and M. W. Grabinsky (1992). Three dimensional finite element analyses of the URL Mine-by test tunnel. Contractor's Report to AECL Research, Contract No. WS-29J-54421 92-01, Data Visualization Laboratory, University of Toronto.

Davison, C. C., A. Brown, and N. M. Soonawala (1982). Preconstruction site evaluation program at the Canadian Underground Research Laboratory. In *Proc. 14th Information Meeting Nuclear Fuel Waste Management Program (1982 General Meeting).* Also Atomic Energy of Canada Limited Technical Record, TR-207, pages 162-187.

Doe, T. (1989). Hydraulic-fracturing stress measurements in horizontal holes at the 240- and 420-m Levels of the Underground Research Laboratory. Consulting Report to AECL Research 893-1002, Golder Associates.

Dusseault, M. B. and N. R. Morgenstern (1979). Locked sands. *Quarterly J. Engineering Geology 12*, 117–131.

Eissa, E. A. and A. Kazi (1988). Technical note - Relation between static and dynamic Young's moduli of rocks. *Int. J. Rock Mech. Min. Sci. & Geomech. Abstr. 25*(6), 479–482.

Everitt, R. A. and A. Brown (1986). Subsurface geology of the Underground Research Laboratory: An overview of recent developments. In *Proc. 20th Information Meeting Can. Nuclear Fuel Waste Management Program (1985 General Meeting), Vol. 1*, pp. 146–181. Also Atomic Energy of Canada Limited Technical Record, TR-375.

Everitt, R. A., A. Brown, C. C. Davison, M. Gascoyne, and C. D. Martin (1990a). Regional and local setting of the Underground Research Laboratory. In R. Sinha (Ed.), *Proc. Int. Symp. on Unique Underground Structures, Vol. 2, Denver, Colorado*, pp. 64:1–23. CSM Press, Denver.

Everitt, R. A., P. Chernis, D. Good, and A. Grogan (1989). Mapping of the excavation damage zone around the circular access shaft at Atomic Energy of Canada Limited's Underground Research Laboratory. In *Excavation Response in Geological Repositories for Radioactive Waste, Proc. NEA Workshop, Winnipeg, MB, 1988 April*, pp. 271 -282.

Everitt, R. A., P. Gann, and D. M. Boychuk (1993). Mine-by Experiment data summary: Part 7 - Geological setting and general geology. Report RC-1080, COG-93-251, Atomic Energy of Canada Limited.

Everitt, R. A. and C. McGregor (1996). Natural microcrack orientations as indicators of macro-scale fracture orientations and in situ stress orientations at AECL's Underground Research Laboratory. Submitted to *Can. J. Earth Sci.*

Everitt, R. A., D. Woodcock, P. Gann, and D. Robinson (1990). Geology of the 420 Level of the Underground Research Laboratory. Technical Record TR-529, Atomic Energy of Canada Limited.

Ewy, R. T. and N. G. W. Cook (1990). Deformation and fracture around cylindrical openings in rock, Parts I and II. *Int. J. Rock Mech. Min. Sci. & Geomech. Abstr. 27*, 387–427.

Feignier, B. and R. P. Young (1993). Moment tensor inversion of induced microseismic events: evidence of non-shear failures in the $-4 < M < -2$ moment magnitude range. *Geophys. Res. Lett. 19*(14), 1503–1506.

Filon, L. N. G. (1937). On antiplane stress in an elastic solid. *Proc. R. Soc. London A160*, 137–154.

Gladwin, M. T. and F. D. Stacey (1974). Ultrasonic pulse velocity as a rock stress sensor. *Tectonophysics 21*, 39–45.

Goodman, R. E. (1989). *Introduction to rock mechanics.* John Wiley and Sons, NY.

Grabinsky, M. W. and J. H. Curran (1993). Harmonic finite element analysis of a cylindrical excavation in an infinite medium. Contractor's Report to AECL Research, Contract No. W108113 Publication 93-02, Rock Engineering Group, Department of Civil Engineering, University of Toronto.

Gyenge, M., R. Jackson, and B. Gorski (1991). Residual strength envelopes using the confined shear test method. In J.-C. Roegiers (Ed.), *Proc. 32th U.S.Symposium on Rock Mechanics, Norman*, pp. 629-635. A.A. Balkema, Rotterdam.

Haimson, B., M. Lee, N. Chandler, and C. D. Martin (1993). Estimating the state of stress from subhorizontal hydraulic fractures at the Underground Research Laboratory, Manitoba. *Int. J. Rock Mech. Min. Sci. & Geomech. Abstr. 30*(7), 959-964.

Haimson, B. C. and C. G. Herrick (1989). Borehole breakouts and *in situ* stress. In *Proc. 12th Annual Energy-Sources Technology Cof. & Exhibition, Drilling Symp.*, pp. 17-22. American Society Mechanical Engineers, New York.

Hayles, J. G., M. H. Serzu, and G. S. Lodha (1995). Cross-hole seismic tomography surveys for the Mine-by Experiment. Technical Record TR-678, COG-95-021, Atomic Energy of Canada Limited.

Hayles, J. G., K. M. Stevens, M. H. Serzu, and G. S. Lodha (1992). Developments in the mini-CHARTS system and field trial results for excavation damage assessment in granite. In *Proc. Fourth Int. Symp. on Borehole Geophysics for Minerals, Geotechnical and Groundwater Applications, Toronto, Canada, August 18-23, 1991.*

Herget, G. (1988). *Stresses in rock*. A. A. Balkema, Rotterdam.

Hiramatsu, Y. and Y. Oka (1968). Determination of the stresses in rock unaffected by boreholes or drifts, from measured strains or deformations. *Int. J. Rock Mech. Min. Sci. 5*(4), 337-353.

Hock, E. (1965). Rock fracture under static stress conditions. CSIR Report MEG 383, National Mechanical Engineering Research Institute, Council for Scientific and Industrial Research, Pretoria, South Africa.

Hock, E. and E. T. Brown (1980). *Underground excavations in rock*. Inst. Min. Metall., London.

Hoskins, E. R. (1968). Strain rosette relief measurements in hemispherically ended boreholes. *Int. J. Rock Mech. Min. Sci. 5*(6), 551-559.

ISS (1994). *Guide to seismic monitoring in mines*. Welkom, South Africa: ISS International Limited.

Jackson, R., J. S. O. Lau, and A. Annor (1989). Mechanical, thermo-mechanical and joint properties of rock samples from the site of AECL's Underground Research Laboratory, Lac du Bonnet, Manitoba. In *Proc. 42nd Canadian Geotechnical Conference, Winnipeg, MB*, pp. 41-49.

Jaeger, J. C. and N. G. W. Cook (1979). *Fundamentals of rock mechanics* (Third ed.). Chapman and Hall, London.

Kaiser, P. K., T. D. Wiles, and D. Zou (1991). Two- and three-dimensional stress back-analysis. Report to Atomic Energy of Canada Limited under contract WS-29J-54460, Laurentian University.

Keilis-Borok, V. I. (1959). The study of earthquake mechanism. In J. H. Hodgson (Ed.), *The mechanics of faulting with special reference to the fault-plane work*, pp. 279. Dominion Observatory, Ottawa.

Keith, S. G. and D. P. Onagi (1994). Mine-by Experiment data summary: Part 8 - Construction summary. Report COG-93-252, Atomic Energy of Canada Limited.

Kelly, D., D. C. Peck, and R. S. James (1993). Petrography of granitic rock samples from the 420 m Level of the Underground Research Laboratory, Pinawa, Manitoba. Contractor's report to AECL Research, Laurentian University.

Khair, K. R. and T. Chan (1994). Finite element modelling of the geomechanical responses of the Mine-by Experiment. Technical Record TR-610, COG-93-242, Atomic Energy of Canada Limited.

Kobayashi, S., N. Nishimura, and K. Matsumoto (1988). Displacements and strains around a non-flat-end borehole. In *Proc. 2nd Int. Symp. on Field Measurements in Geomechanics*, pp. 1079–1084.

Lajtai, E. Z. (1972). Effect of tensile stress gradient on brittle fracture initiation. *Int. J. Rock Mech. Min. Sci. & Geomech. Abstr. 9*, 569–578.

Lajtai, E. Z. (1982). The fracture of Lac du Bonnet granite. Office of Industrial Research report TR-M-00007, University of Manitoba, Geological Engineering Department.

Lajtai, E. Z. (1988). The deformation, fracture and strength of Lac du Bonnet granite. Research report 19, University of Manitoba, Geological Engineering Department.

Lajtai, E. Z. and L. P. Bielus (1986). Stress corrosion cracking of Lac du Bonnet granite in tension and compression. *Rock Mech. Rock Engng. 19*, 71–87.

Lajtai, E. Z., B. J. Carter, and M. L. Ayari (1990). Criteria for brittle fracture in compression. *Eng. Frac. Mech. 37*(1), 59–74.

Lajtai, E. Z., B. J. Carter, and E. J. S. Duncan (1991). Mapping the state of fracture around cavities. *Engineering Geology 31*, 277–289.

Lajtai, E. Z. and A. M. Gadi (1989). Friction on a granite to granite interface. *Rock Mech. and Rock Engin. 22*, 25–49.

Lajtai, E. Z. and R. H. Schmidtke (1986). Delayed failure in rock loaded in uniaxial compression. *Rock Mech. Rock Engng. 19*, 11–25.

Lee, M. Y. and B. C. Haimson (1993). Laboratory study of borehole breakouts in Lac du Bonnet granite: A case of extensile failure mechanism. *Int. J. Rock Mech. Min. Sci. & Geomech. Abstr. 30*(7), 1039–1045.

Livesley, R. K. (1989). *Mathematical methods for engineers*. Ellis Horwood Limited, Chichester, 1st edition.

Martin, C. D. (1993). *The strength of massive Lac du Bonnet granite around underground openings*. Ph. D. thesis, Department of Civil and Geological Engineering, University of Manitoba, Winnipeg, MB.

Martin, C. D. and N. A. Chandler (1993). Stress heterogeneity and geological structures. *Int. J. Rock Mech. Min. Sci. & Geomech. Abstr. 30*(7), 993–999.

Martin, C. D. and N. A. Chandler (1994). The progressive fracture of Lac du Bonnet granite. *Int. J. Rock Mech. Min. Sci. & Geomech. Abstr. 31*(6), 643–659.

Martin, C. D., N. A. Chandler, and R. S. Read (1994). The role of convergence measurements in characterizing a rock mass. In *47th Canadian Geotechnical Conference, Halifax, NS.*

Martin, C. D., J. B. Martino, and E. J. Dzik (1994). Comparison of borehole breakouts from laboratory and field tests. In *Proc. EUROCK'94, SPE/ISRM Rock Mechanics in Petroleum Engineering Delft*, pp. 183–190. A.A. Balkema, Rotterdam.

Martin, C. D. and R. S. Read (1992). The *in situ* strength of massive granite around excavations. In *Proc. 16th Can. Rock Mech. Conf., Sudbury*, pp. 1–10.

Martin, C. D. and B. Stimpson (1994). The effect of sample disturbance on laboratory properties of Lac du Bonnet granite. *Can. Geotech. J. 31*(5), 692–702.

Martin, C. D., R. P. Young, and D. S. Collins (1995). Monitoring progressive failure around a tunnel in massive granite. In *Proc. 8th ISRM Congress on Rock Mechanics, Tokyo.* A.A. Balkema, Rotterdam.

Martino, J. B. (1989). Distometer convergence readings in the shaft extension of Atomic Energy of Canada Limited's Underground Research Laboratory. Technical Record TR-482, Atomic Energy of Canada Limited.

Martino, J. B. (1996). A guide to information archiving and retrieving for the Mine-by Experiment Excavation Response Phase. Technical Record in preparation, Atomic Energy of Canada Limited.

Martino, J. B. (1995a). Long-term shaft excavation response recorded by Bof-ex extensometers from 1988 to 1993 at the 324 and 384 instrumentation arrays. Technical Record TR-680, Atomic Energy of Canada Limited.

Martino, J. B., R. S. Read, and D. Collins (1993). Mine-by Experiment data summary report: Part 6 - Acoustic emission/ microseismic results. Technical Record TR-597, COG-93-185, Atomic Energy of Canada Limited.

Martino, J. B., R. S. Read, and S. G. Keith (1994). Mine-by Experiment data summary report: Part 9 - Observations. Report COG-93-347, Atomic Energy of Canada Limited.

Martino, J. B., R. S. Read, and J. H. Mitchell (1993a). Mine-by Experiment data summary report: Part 5 - Thermistor results. Technical Report RC-1079, COG-93-233, Atomic Energy of Canada Limited.

Mastin, L. (1984). The development of borehole breakouts in sandstone. Master's thesis, Stanford University, Berkley, Calfornia.

Maxwell, S. C. and R. P. Young (1994). Wave propagation effects of an underground opening. Contractor's Report to Atomic Energy of Canada Limited RP025AECL, Keele University.

McGarr, A. (1994). Some comparisons between mining-induced and laboratory earthquakes. *PAGEOPH 142*(3/4), 467–489.

Myrvang, A. M. (1991). Estimation of *in situ* compressive strength of rocks from *in situ* stress measurements in highly stressed rock structures. In W. Wittke (Ed.), *Proc. 7th ISRM Congress on Rock mechanics, Aachen*, pp. 573–575. A.A. Balkema, Rotterdam.

Niwa, Y., S. Kobayashi, and T. Fukui (1979). Stresses and displacements around an advancing face of a tunnel. In *Proc. 4th Int. Congr. Rock Mech., Vol. 1, Montreux*, pp. 703–710.

Ofoegbu, G. I. and J. H. Curran (1991). Development and numerical implementation of an elastic-brittle-ductile constitutive model. Contractor's Report to Atomic Energy of Canada Limited, Department of Civil Engineering, University of Toronto.

Onagi, D. P., S. G. Keith, and G. W. Kuzyk (1992). Non-explosive excavation technique developed for the excavation of AECL's Mine-by Experiment test tunnel at the Underground Research Laboratory. In *Proc. 10th Annual Tunnelling Assoc. of Canada Conf., Banff, AB.*

Panet, M. and A. Guenot (1982). Analysis of convergence behind the face of a tunnel. In *Proc. 3rd Int. Symp. on Tunnelling, Brighton, England*, pp. 197–204.

Paulsson, B. N. P. (1983). *Seismic velocities and attenuation in a heated underground granitic repository.* Ph. D. thesis, University of California, Berkeley, CA.

Paulsson, B. N. P. and M. S. King (1980). Between-hole acoustic surveying and monitoring of a granite rock mass. *Int. J. Rock Mech. Min. Sci. & Geomech. Abstr. 17*, 317–367.

Pelli, F. (1987). *The influence of near face behaviour on monitoring of deep tunnels.* Ph.D. thesis, Department of Civil Engineering, University of Alberta, Edmonton, AB.

Pelli, F., P. K. Kaiser, and N. R. Morgenstern (1991). An interpretation of ground movements recorded during construction of the Donkin-Morien tunnel. *Can. Geotech. J. 28*(2), 239–254.

Pusch, R. and R. Stanfors (1992). The zone of disturbance around blasted tunnels at depth. *Int. J. Rock Mech. Min. Sci. & Geomech. Abstr. 29*(5), 447–456.

Read, R. S. (1991). Mine-by Experiment - prediction of excavation-induced rock mass response. Technical Memorandum URL-EXP-022-M048, Atomic Energy of Canada Limited.

Read, R. S. (1994). *Interpreting excavation-induced displacements around a tunnel in highly stressed granite.* Ph. D. thesis, Department of Civil and Geological Engineering, University of Manitoba, Winnipeg, MB.

Read, R. S. and C. D. Martin (1991a). Mine-by Experiment final design report. Report AECL-10430, Atomic Energy of Canada Limited.

Read, R. S. and C. D. Martin (1991b). The Underground Research Laboratory Mine-by Experiment - a research perspective on tunnel design. *Canadian Tunnelling 7*, 75–88.

Read, R. S. and C. D. Martin (1992). Monitoring the excavation-induced response of granite. In *Proc. 33rd U.S. Symp. on Rock Mech., Santa Fe*, pp. 201–210. Balkema:Rotterdam.

Read, R. S. and C. D. Martin (1993). Mine-by Experiment plan, Underground Research Laboratory - Addendum 1: Mine-by Experiment heated failure tests. Quality Assurance Document DE010.086, Atomic Energy of Canada Limited.

Read, R. S., C. D. Martin, and E. J. Dzik (1995). Asymmetric borehole breakouts at the URL. In *Proc. 35th US Rock Mech. Symp., Lake Tahoe*, pp. 879-884. Balkema:Rotterdam.

Read, R. S., J. B. Martino, G. R. Karklin, E. Jacobs, and G. Hiltz (1994). Mine-by Experiment data summary: Part 1 - Survey results. Report COG-93-290, Atomic Energy of Canada Limited.

Read, R. S., J. B. Martino, and J. H. Mitchell (1993b). Mine-by Experiment data summary: Part 4 - Convergence results. Technical Record TR-595, COG-93-177, Atomic Energy of Canada Limited.

Read, R. S., J. B. Martino, and J. H. Mitchell (1994b). Mine-by Experiment data summary: Part 2 - Triaxial strain cell results. Report COG-93-353, Atomic Energy of Canada Limited.

Read, R. S., J. B. Martino, J. H. Mitchell, and M. H. Spinney (1994a). Mine-by Experiment data summary: Part 3 - Extensometer results. Report COG-93-354, Atomic Energy of Canada Limited.

Saleh, K., A.-P. Bois, and G. Ballivy (1992). Instrumentation des parios rocheuses à l'aide des Cylindres Instrumentés de l'Université de Sherbrooke. 2nd Progress Report GR-92-09-1, Laboratoire de mécanique des roches et de géologie appliquée, Département de génie civil, Faculté des sciences appliquées, Université de Sherbrooke, Québec, Canada.

Simmons, G. R. (1990). Operating phase experiments planned for Atomic Energy of Canada Limited's Underground Research Laboratory. In R. S. Sinha (Ed.), *Proc. Int. Symp. on Unique Underground Structures, Denver*, Volume 2, pp. 67:1-19. CSM Press, Denver.

Snider, G. R., P. A. Lang, and P. M. Thompson (1989). Procedures used for installing and monitoring geomechanical instrumentation during sinking of the URL shaft. Technical Record TR-486, Atomic Energy of Canada Limited.

Stacey, T. R. (1981). A simple extension strain criterion for fracture of brittle rock. *Int. J. Rock Mech. Min. Sci. & Geomech. Abstr. 18*(6), 469-474.

Stesky, R. M. (1980). Elastic properties and strain measurements of rock cores from Atomic Energy of Canada Ltd. Chalk River, Ontario and Whiteshell, Manitoba test areas. Contractor's Report DSS File No. 17ST.23233-8-1344, Atomic Energy of Canada Limited. Available from the AECL Records Management Office, Whiteshell Laboratories, Pinawa, Manitoba.

Stesky, R. M. (1985). Characterization of microcrack properties of deep granite samples through analysis of elastic properties. Contractor's Report DSS File No. 20SU.23233-2-1480, Atomic Energy of Canada Limited. Available from the AECL Records Management Office, Whiteshell Laboratories, Pinawa, Manitoba.

Stimpson, B. and R. Chen (1991). A new technique for measuring the bimodularity of rock. In *Proc. Canadian Conf. on Appl. Mechanics, Winnipeg, MB.*

Sugawara, K. and Y. Obara (1986). Measurement of in-situ rock stress by hemispherical-ended borehole technique. *Min. Sci. Technol. 3*, 287-300.

Talebi, S. and R. P. Young (1990). Design of a microseismic system for the URL Mine-by Experiment. Contractor's Report to AECL Research, Contract No. WS-30J-54474 RP006AECL, Queen's University.

Talebi, S. and R. P. Young (1992). Microseismic monitoring in highly stressed granite: relation between shaft-wall cracking and *in situ* stress. *Int. J. Rock Mech. Min. Sci. & Geomech. Abstr. 29*(1), 25–34.

Thompson, P. M., E. T. Kozak, and C. D. Martin (1989). Rock displacement instrumentation and coupled hydraulic pressure/rock displacement instrumentation for use in stiff crystalline rock. In *Excavation Response in Geological Repositories for Radioactive Waste, Proceedings of a NEA Workshop, Winnipeg, MB, 1988 April*, pp. 257–270.

Thompson, P. M., J. B. Martino, and M. H. Spinney (1993). Detailed measurements of deformation in the excavation disturbed zone. In *Proc. 34th U.S. Symposium on Rock Mechanics, 1993 June 27-30, Madison, Vol. 2*, pp. 757–760.

van Heerden, W. L. (1969). Potential fracture zones around boreholes with flat and spherical ends. *Int. J. Rock Mech. Min. Sci. 6*(5), 453–463.

Walker, J. R., C. D. Martin, and E. J. Dzik (1990). Technical note - Confidence intervals for in situ stress measurements. *Int. J. Rock Mech. Min. Sci. & Geomech. Abstr. 27*(2), 139–141.

Wiles, T. (1992). *Direct Boundary Element Method in 3-Dimensions.* Laurentian University, Sudbury, Canada: Geomechanics Research Centre.

Wiles, T. D. (1995). Back analysis of the Mine-by Experiment using the direct boundary element method. Contractor's report to Atomic Energy of Canada Limited, Mine Modelling Ltd.

Wiles, T. D. and P. K. Kaiser (1992). Under excavation method incremental analysis of 420 Level vent raise and Room 209 data. Contractor's report to Atomic Energy of Canada Limited, Laurentian University.

Wiles, T. D. and P. K. Kaiser (1994a). In situ stress determination using the under-excavation technique – Part 1: Theory. *Int. J. Rock Mech. Min. Sci. & Geomech. Abstr. 31*(5), 439–446.

Wiles, T. D. and P. K. Kaiser (1994b). In situ stress determination using the under-excavation technique – Part 2: Application. *Int. J. Rock Mech. Min. Sci. & Geomech. Abstr. 31*(5), 447–456.

Wong, J., N. Bregman, G. F. West, and P. Hurley (1987). Cross-hole seismic scanning and tomography. *Geophysics - The Leading Edge*, 36–41.

Woodcock, D. R. (1994). Geological data summary for the CSIRO-series boreholes drilled for the Mine-by Experiment at the Underground Research Laboratory. Technical Report COG-94-282, Atomic Energy of Canada Limited. Protected.

Worotnicki, G. and R. J. Walton (1976). Triaxial "hollow inclusion" gauges for the determination of rock stresses in situ. In *Proc. Symp. on Investigation of Stresses in Rock and Advances in Stress Measurement, supplement*, pp. 108.

Wu, H. and D. D. Pollard (1992). Possible secondary fracture patterns due to a change in the direction of loading. In *Preprints Conf. on Fractured and Jointed Rock Masses, Lake Tahoe*, Volume 2, pp. 505–512. US Dept of Energy.

Zheng, Z., J. Kemeny, and N. Cook (1989). Analysis of borehole breakouts. *J. Geophys. Res. 94*(B6), 7171–7182.

APPENDIX A

COMPLETED EXPERIMENT SCHEDULE

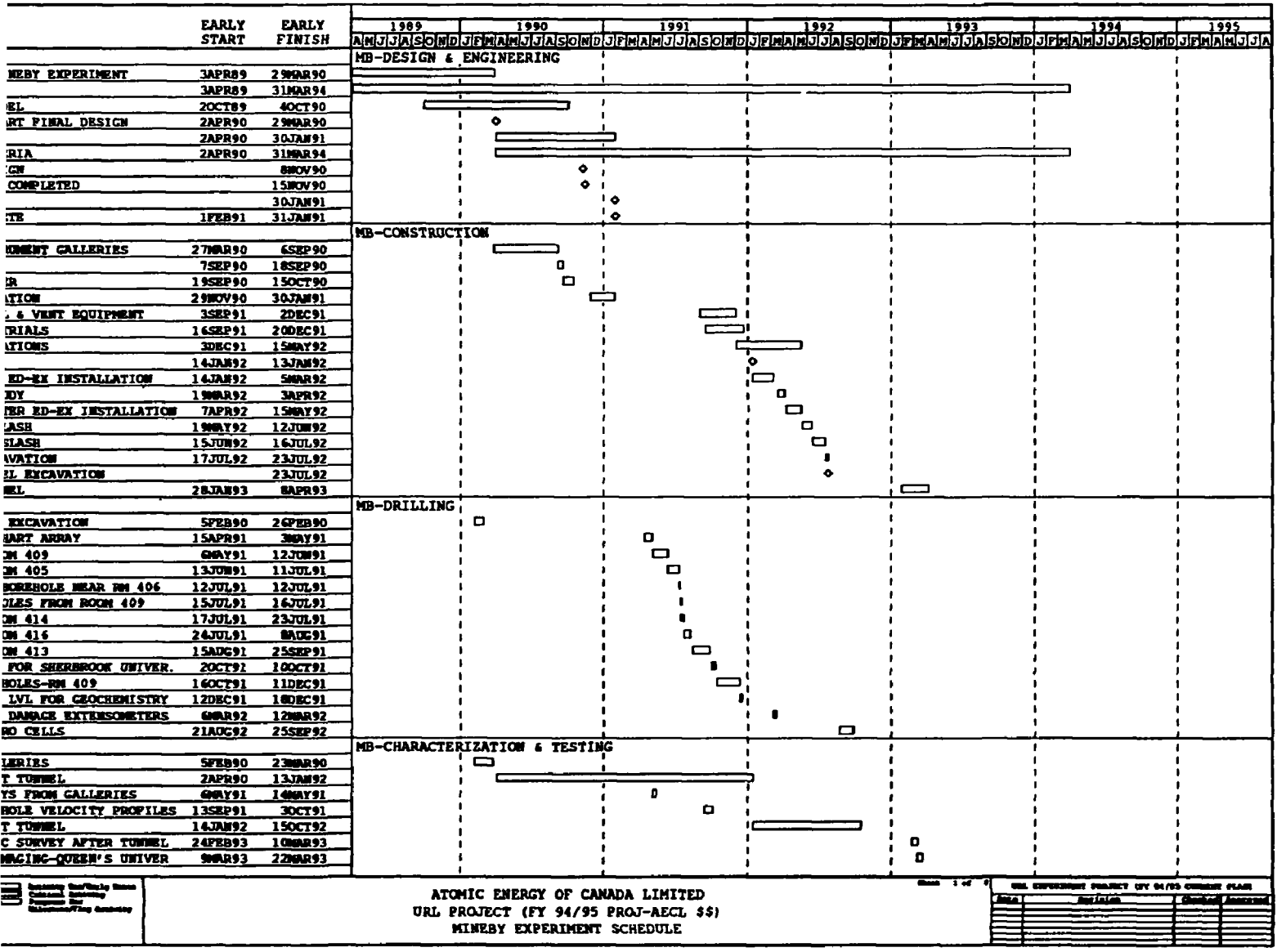

ATOMIC ENERGY OF CANADA LIMITED
URL PROJECT (FY 94/95 PROJ-AECL $$)
MINEBY EXPERIMENT SCHEDULE

ACTIVITY DESCRIPTION	EARLY START	EARLY FINISH
MB-PROCURE AE/MS INSTRUMENTS	9NOV90	5APR91
MB-PROCURE EXCAVATION RESPONSE INSTRUMENTS	1FEB91	24JUL91
MB-PROCURE VENT/ENTHALPY EQUIPMENT	1FEB91	30AUG91
MB-INSTALL AE/MS	17JUL91	15AUG91
MB-AE/MS SYSTEM INSTALLATION COMPLETE	16AUG91	15AUG91
MB-INSTALL EXCAVATION RESPONSE INSTRUMENTS	4OCT91	1NOV91
MB-INSTALL CONCRETE CYLINDERS UNIV OF SHERBROOKE	13JAN92	17JAN92
MB-INSTALL & MONITOR CONVERGENCE ARRAYS	14JAN92	23JUL92
MB-AE ARRAY INSTALLATION	13MAR92	17MAR92
MB-INSTALL EXCAVATION DAMAGE EXTENSOMETERS	13MAR92	18MAR92
MB-RETRIEVE INSTRUMENTS AFTER TEST TUNNEL	3SEP92	2OCT92
MB-START MINEBY EXPERIMENT	3APR89	
MB-MONITOR AE/MS SYSTEM	16AUG91	23JUL92
MB-MONITOR INSTRUMENTS B4 TEST TUNNEL	4NOV91	13JAN92
MB-MONITOR INSTRUMENTS DURING TEST TUNNEL	13JAN92	23JUL92
MB-MONITOR AE ARRAY DURING STUDY	18MAR92	6APR92
MB-FINISH MINE-BY EXPERIMENT		2NOV95
MB-MODELLING PREDICTIONS	5OCT90	4OCT91
MB-ANALYSIS & REPORTING OF AE/MS RESULTS	16AUG91	31MAR94
MB-REFINE MODELLING PREDICTIONS	7OCT91	30SEP92
MB-PRELIMINARY ANALYSIS	4NOV91	19AUG92
MB-MINEBY CONSTRUCTION COMPLETION REPORT	24JUL92	30SEP92
MB-DATA SUMMARY REPORTS	24JUL92	31MAR94
MB-EXCAVATION RESPONSE ANALYSIS	28SEP92	31OCT94
MB-FRACTURE CODE MODEL DEVELOPMENT	1APR93	30SEP93
MB-PUBLISH DATA REPORTS		31MAR94
MB-SUMMARY REPORT FOR PHASE 1	1APR94	30NOV94
MB-BACK ANALYSIS OF STRAINS	3OCT94	30MAR95
MB-COMMITTEE SUMMARY REPORT	1DEC94	30MAR95

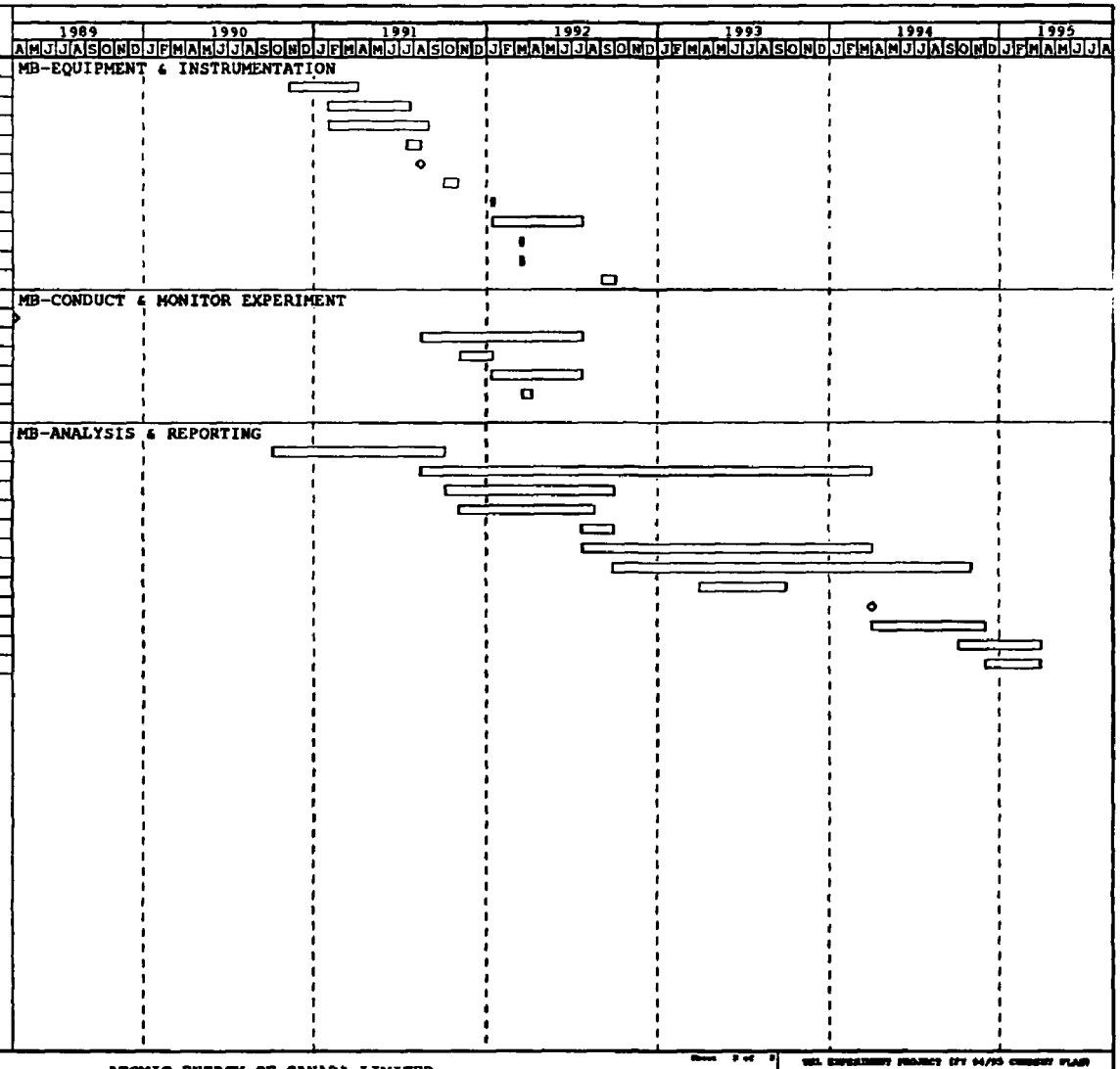

ATOMIC ENERGY OF CANADA LIMITED
URL PROJECT (FY 94/95 PROJ-AECL $$)
MINEBY EXPERIMENT SCHEDULE

APPENDIX B

DETAILS OF DISPLACEMENT BACK ANALYSIS METHOD

B.1 NOMENCLATURE

a = tunnel radius
D = tunnel diameter
r = radial distance from the tunnel centre
σ_{ij} = Components of partitioned stress tensor
σ_1 = Maximum principal stress
σ_2 = Intermediate principal stress
σ_3 = Minimum principal stress
G = shear modulus
E = Young's modulus
ν = Poisson's ratio
θ = rotation angle measured CCW from point on right sidewall at height of centreline
x, y, z = rectangular cartesion coordinates with tunnel axis parallel to x
r, θ, x = cylindrical coordinates with tunnel axis parallel to x
x_f = axial position of tunnel face
x_i = axial position of instrument
X = face position $x_f - x_i$
R = normalized radial position r/a
U_r = radial displacement
U_{r_o} = radial displacement at the tunnel face
$U_{r_{max}}$ = normalizing factor $a(1-\nu)/G$
K_{max} = stress ratio σ_{11}/σ_{33}
K_{axial} = stress ratio σ_{22}/σ_{33}
K_{min} = stress ratio σ_{22}/σ_{33}
$K_{a,b,c}$ = stress ratios relative to σ_{33}
D_l = radial displacement at $X = 0$ in the *spliced logistic function*
λ = scaling factor in the *spliced logistic function*
E_l = radial displacement at $X = +\infty$ in the *spliced logistic function*
for the posterior domain, and at $X = -\infty$ in the anterior domain
F = $(E_l - D_l)$ in the posterior domain and $(D_l - E_l)$ in the anterior domain
A = abscissa of pivot point controlling the shape of the *spliced logistic function*
B = slope parameter in the *spliced logistic function*
α = mean displacement response
β = amplitude about the mean of the harmonic component of the displacement response

ψ = phase constant

A_i = shape parameter in the inverse polynomial series approximating function

$$sign\,(x) = \begin{cases} 1 & x > 0 \\ 0 & x = 0 \\ -1 & x < 0 \end{cases}$$

B.2 APPROXIMATING AND PARAMETRIC FUNCTIONS

B.2.1 Approximating Functions

Spliced Logistic Function

Function to describe surface U_r vs. θ,X/D at $R = 1$

$$U_r\,(x) = y + \lambda \frac{d^2y}{dx^2}$$

where

$$y = D_l + sign\,(x)\,F\left[1 + \left|\frac{x}{A}\right|^B\right]^{\frac{1}{B}}$$

$$\frac{d^2y}{dx^2} = sign\,(x)\,\frac{F\,(B-1)}{|A|^B}\left\{\left[1 + \left|\frac{x}{A}\right|^B\right]^{\left(\frac{1}{B}-1\right)} |x|^{(B-2)}\right\} -$$

$$sign\,(x)\,\frac{F\,(B-1)}{|A|^{2B}}\left\{\left[1 + \left|\frac{x}{A}\right|^B\right]^{\left(\frac{1}{B}-2\right)} |x|^{2(B-1)}\right\}$$

When used to describe α and β parameters in the parametric functions, $\lambda = 0$.

Inverse Polynomial Series

Function to describe surface U_r vs. θ,R at $-0.4 \leq X/D \leq 0.4$

$$\frac{U_r}{U_{r_{max}}} = \sum_{i=1}^{3} \frac{A_i}{R^i} \text{ where } 1 \leq R \leq +\infty$$

Outside this region up to 5 diameters from the face, two additional terms are required for approximating purposes.

B.2.2 Parametric Functions

Examples of parametric functions describing the surface U_r vs. θ,X/D at $R = 1$, showing an application of the *spliced logistic function*. For characteristic surfaces U_r vs. θ,r/a, the parameters α and β are of the form given by the inverse polynomial series approximating function.

Plane normal components

$$\frac{U_r}{U_{r_{max}}} = \alpha_{11} + \beta_{11} \cos\left[2\,(\theta - \psi)\right]$$

where

$$\alpha_{11} = D_\alpha + sign\,(x)\,F_\alpha \left[1 + \left|\frac{x}{A_\alpha}\right|^{B_\alpha}\right]^{\frac{1}{n_\alpha}}$$

$$\beta_{11} = D_\beta + sign\,(x)\,F_\beta \left[1 + \left|\frac{x}{A_\beta}\right|^{B_\beta}\right]^{\frac{1}{n_\beta}}$$

and

$\psi = 0°$ for σ_{11}, $90°$ for σ_{33}

Plane shear component

$$\frac{U_r}{U_{r_{max}}} = 2\beta_{11} \sin(2\theta)$$

Antiplane normal component

$$\frac{U_r}{U_{r_{max}}} = \alpha_1 + \alpha_2 + \alpha_3$$

where

$$\alpha_1 = D_{\alpha_1} + sign\,(x)\,F_{\alpha_1} \left[1 + \left|\frac{x}{A_{\alpha_1}}\right|^{B_{\alpha_1}}\right]^{\frac{1}{n_{\alpha_1}}}$$

$$\alpha_2 = D_{\alpha_2} + sign\,(x)\,F_{\alpha_2} \left[1 + \left|\frac{x}{A_{\alpha_2}}\right|^{B_{\alpha_2}}\right]^{\frac{1}{n_{\alpha_2}}}$$

$$\alpha_3 = D_{\alpha_3} + sign\,(x)\,F_{\alpha_3} \left[1 + \left|\frac{x}{A_{\alpha_3}}\right|^{B_{\alpha_3}}\right]^{\frac{1}{n_{\alpha_3}}}$$

Antiplane shear components

$$\frac{U_r}{U_{r_{max}}} = \beta_{12} \cos(\theta - \psi)$$

where

$$\beta_{12} = D_\beta + sign\,(x)\,F_\beta \left[1 + \left|\frac{x}{A_\beta}\right|^{B_\beta}\right]^{\frac{1}{n_\beta}}$$

and

$\psi = 0°$ for σ_{12}, $90°$ for σ_{23}

B.2.3 Tables of Coefficients

TABLE 11

COEFFICIENTS FOR PARAMETRIC EQUATION DESCRIBING THE σ_{11} *CHARACTERISTIC RADIAL DISPLACEMENT SURFACE*

Mean Radial Displacement Component α			Harmonic Radial Displacement Component β		
Parameter	Anterior Domain	Posterior Domain	Parameter	Anterior Domain	Posterior Domain
A_α	0.1615	0.2182	A_β	0.2494	0.3241
B_α	-1.5602	-1.3371	B_β	-1.4120	-1.3072
D_α	0.1037	0.1037	D_β	0.2063	0.2063
E_α	0.0	0.3333	E_β	0.0	0.6667
F_α	0.1037	0.2296	F_β	0.2063	0.4603

Note that, for the σ_{11} tensor, the phase shift $\psi = 0$.
The coefficient of determination $r^2 = 0.9999$.

TABLE 12

COEFFICIENTS FOR PARAMETRIC EQUATION DESCRIBING THE σ_{22} *CHARACTERISTIC RADIAL DISPLACEMENT SURFACE*

Parameter	Radial Displacement Component		
	α_1 $X/D > 0$	α_2 $X/D < 0$	α_3 $X/D < 0$
A_α	0.7032	0.9592	0.1622
B_α	-1.5660	-1.9329	-1.2281
D_α	-0.0507	0.1417	-0.1924
E_α	0.0	0.0	0.0
F_α	0.0507	0.1417	-0.1924

The coefficient of determination $r^2 = 0.9993$.

TABLE 13

COEFFICIENTS FOR PARAMETRIC EQUATION DESCRIBING THE σ_{12} *CHARACTERISTIC RADIAL DISPLACEMENT SURFACE*

	Harmonic Radial Displacement Component β	
Parameter	Anterior Domain	Posterior Domain
A_β	0.6855	0.2846
B_β	-1.7715	-1.1961
D_β	0.6542	0.6542
E_β	0.0	0.0
F_β	0.6542	-0.6542

Note that, for the σ_{12} tensor, the phase shift $\psi = 0$.
The coefficient of determination $r^2 = 0.9996$.

TABLE 14

COEFFICIENTS FOR RADIAL DISPLACEMENT VERSUS RADIAL DISTANCE RELATIONSHIP AT FIVE FACE POSITIONS

X/D	Stress Component	Coefficient					
		A_{1_α}	A_{2_α}	A_{3_α}	A_{1_β}	A_{2_β}	A_{3_β}
-0.4	σ_{11}	0.16398	-0.31322	0.16253	0.47221	- 0.78082	0.36698
	σ_{22}	-0.03828	0.20895	-0.12166	-	-	-
	σ_{12}	-	-	-	0.62975	-0.13572	-0.17374
-0.1	σ_{11}	0.16940	-0.13616	0.01981	0.48948	- 0.40147	0.04170
	σ_{22}	-0.00979	-0.02801	0.05548	-	-	-
	σ_{12}	-	-	-	0.51860	0.38300	-0.32683
0.0	σ_{11}	0.16343	-0.05508	-0.00394	0.47141	- 0.18398	-0.08200
	σ_{22}	-0.02103	0.01009	-0.03731	-	-	-
	σ_{12}	-	-	-	0.57078	0.12493	-0.04398
0.1	σ_{11}	0.17067	-0.04119	0.05548	0.47115	- 0.06017	-0.08213
	σ_{22}	0.00722	-0.14289	0.08844	-	-	-
	σ_{12}	-	-	-	0.50707	0.43688	-0.47057
0.4	σ_{11}	0.15446	0.22335	-0.09864	0.43503	0.55103	-0.48399
	σ_{22}	-0.02745	-0.09091	0.09422	-	-	-
	σ_{12}	-	-	-	0.67066	-0.42177	-0.02677

APPENDIX C

LIST OF RELATED REPORTS AND PUBLICATIONS

C.1 DESIGN & ENGINEERING

- Mine-by Preliminary Design Report (URL-EXP-022-M044, Read and Martin 1990)†
- Mine-by Preliminary Scoping Calculations (URL-EXP-022-M045, Read 1990)†
- 3D Scoping Interaction of Adjacent Openings in Terms of Stress (Wiles 1990a)†
- AECL Mine-by Experiment Instrument Sensitivity Evaluation (Wiles 1990b)†
- Mine-by Experiment Plan - Underground Research Laboratory (DE010-011, Martin 1991)†
- Mine-by Experiment Final Design Report (AECL-10430, Read and Martin 1991)
- Mechanical Excavation of URL-Excavation Response Experiment Conceptual Engineering (Dynatec Engineering 1989)†
- Conceptual Design Report for: 1). Enthalpy Control System, 2). 420 Level Development 3). Electrical & Mechanical Services (Kuzyk 1990)†
- Conceptual Design Report for Enthalpy Control System Mine-by (MB) Experiment, Underground Research Laboratory, Depth 420 m (McCormac et al. 1990)†
- Underground Research Laboratory 420 Level Development and Mine-by Experiment Mechanical and Electrical Furnishings (Wardrop Engineering 1990)†

C.2 CHARACTERIZATION & EXPERIMENT MONITORING

Progress Reports

- Report 1 (URL-EXP-022-M050, Read et al. 1991)†
- Report 2 (URL-EXP-022-M051, Read et al. 1992)†
- Report 3 (URL-EXP-022-M052, Read et al. 1992)†
- Report 4 (URL-EXP-022-M053, Read et al. 1992)†
- Report 5 (URL-EXP-022-M054, Read et al. 1992)†
- Report 6 (URL-EXP-022-M055, Read et al. 1992)†
- Report 7 (URL-EXP-022-M056, Read et al. 1992)†

Data Summary Reports

- Part 1 - Survey Information (COG-93-290, Read et al. 1994)‡
- Part 2 - Triaxial Strain Cell Results (COG-93-353, Read et al. 1994b)‡
- Part 3 - Extensometer Results (COG-93-354, Read et al. 1994a)‡
- Part 4 - Convergence Results (TR-595, COG-93-177, Read et al. 1993b)
- Part 5 - Thermistor Results (RC-1079, COG-93-233, Martino et al. 1993a)
- Part 6 - Acoustic Emission/Microseismic Results (TR-597, COG-93-185, Martino et al. 1993)
- Part 7 - Geological Setting and General Geology (RC-1080, COG-93-251, Everitt et al. 1993)‡
- Part 8 - Construction Summary (COG-93-252, Keith and Onagi 1994)‡
- Part 9 - Observations (COG-93-347, Martino et al. 1994)‡

Corelogging Reports

- Geological Data Summary for the MB-Series Boreholes Drilled for the Mine-by Experiment at the Underground Research Laboratory (TR-577-9, COG-92-433, Woodcock 1993)
- Geological Data Summary for the GP-Series and MBW-Series Boreholes Drilled for the Mine-by Experiment at the Underground Research Laboratory (TR-577-10, COG-93-91, Woodcock 1993)
- Geological Data Summary for the AE/MS Series Boreholes Drilled for the Mine-by Experiment at the Underground Research Laboratory (RC-1080-11, COG-93-92, Woodcock 1993)‡
- Geological Data Summary for the Bof-Ex Extensometer-Series Boreholes Drilled for the Mine-by Experiment at the Underground Research Laboratory (RC-1080-12, COG-93-93, Woodcock, In review)‡
- Geological Data Summary for the CSIRO-Series Boreholes Drilled for the Mine-by Experiment at the Underground Research Laboratory (RC-1080-13, COG-94-282, Woodcock 1994)‡
- Geological Data Summary for the Microseismic Calibration-Series Boreholes Drilled for the Mine-by Experiment at the Underground Research Laboratory (RC-1080-14, COG-94-283, Woodcock, In review)‡
- Geological Data Summary for the Excavation Damage Assessment Series and the Acoustic Emission Series Boreholes Drilled for the Mine-by Experiment at the Underground Research Laboratory (RC-1080-15, COG-94-284, Woodcock, In review)‡
- Geological Data Summary for the Scale Effects Boreholes Drilled for the Mine-by Experiment at the Underground Research Laboratory (RC-1080-16, COG-94-285, Woodcock, In prep.)‡

General Characterization Reports

- Doorstoppers Stress Measurements at the 420 Level of the URL (Corthésy et al. 1993)†
- Instrumentation des parios rocheuses a l'aide des Cylindres Instrumentes de l'Universitè de Sherbrooke (Saleh et al. 1992)†
- Assessment of Rock Burst Risk in the URL Pinawa Manitoba Canada (Steffan et al. 1992)†
- Petrography of Granitic Rock Samples from the 420 Level of the Underground Research Laboratory, Pinawa, Manitoba (Kelly et al. 1993)†
- Orientation and Distribution of Inclusion Bearing Microcracks in Core from the 420 Level of the Underground Research Laboratory, Pinawa, Manitoba (Rousell 1993)†
- Petrofabric analysis of natural microfractures in quartz of the Lac du Bonnet Batholith (McArthur 1994)†
- Geology of the Mine-by Experiment Connected Permeability Phase Floor Slot (RC-1080-2, URL-EXP-022-R29, Gann and Everitt 1994)‡
- Geology of the Mine-by Experiment Test Tunnel Expansion (RC-1080-3, COG-94-227, URL-EXP-022-R30, Gann and Everitt 1994)‡
- Geology of the Observation Slot at the 420 Level of the Underground Research Laboratory, (RC-1080-4, COG-93-319, URL-EXP-022-R31, Gann and Everitt 1994)‡
- Block Sample Testing to Study the Effect of Stress Rotation on Rock Strength (Lau et al. 1994)†
- Cross-hole seismic tomography surveys for the Mine-by Experiment (TR-678, COG-95-021, Hayles et al. 1995)

AE/MS and Geophysics Reports (Queen's University and Keele University)

- Microseismic Monitoring and Excavation Damage Assessment at Atomic Energy of Canada Limited's Underground Research Laboratory (RP001AECL, Young and Talebi 1988)†
- Manual source locations of microseismic events induced by shaft extension at the Underground Research Laboratory (RP002AECL, Young and Talebi 1989)†
- Final Report on Source Location of Microseismic Events Induced by Shaft Excavation at the Underground Research Laboratory (RP003AECL, Talebi and Young 1989)†
- In Situ Measurements of P & S Wave Velocities at the Underground Research Laboratory (RP004AECL, Talebi and Young 1989)†
- Borehole Breakouts: A review of the Theory and a Discussion of their Investigation using Seismic Methods (RP005AECL, Rawlence 1990)†

- Design of a Microseismic System for the URL Mine-by Experiment (RP006AECL, Talebi and Young 1990)†
- Seismic and Radar Characterization at the 240-m Level of the Underground Research Laboratory (RP007AECL, Talebi and Young 1990)†
- Ultrasonic Imaging and Acoustic Emission Monitoring of Laboratory Hydraulic Fracturing Experiments in Lac du Bonnet Grey Granite from AECL'S Underground Research Laboratory (RP008AECL, Chow et al. 1990)†
- Analysis of the Microseismicity Induced by the 420 Level Development at the Underground Research Laboratory (RP009AECL, Talebi et al. 1991)†
- Calibration of the Queen's microseismic system at the Underground Research Laboratory (RP010AECL, Feustel and Young 1992)†
- In Situ Velocity Measurements for the Mine-by Experiment. (RP011AECL, Talebi and Young 1992)†
- Preliminary AE/MS results from the Mine-by Experiment (RP012AECL, Talebi and Young 1992)†
- Monitoring and Source Location of Microseismicity Induced by Excavation of the Mine-by Experiment Tunnel: Preliminary Analysis (RP013AECL, Collins and Young, 1992)†
- Uniaxial compression testing of large samples of Lac du Bonnet granite at low strain rates, Part 1: Studies of Acoustic emission rate (RP014AECL, Falls and Young 1992)†
- Acoustic Emission and Ultrasonic Velocity Study of Excavation-Induced Microcrack Damage in the Mine-by Tunnel at the Underground Research Laboratory (RP015AECL, Carlson and Young 1992)†
- AE/MS Source Location Calibration and Velocity Results: Two Surveys Performed After the Mine-by Tunnel Excavation (RP016AECL, Collins and Young 1993)†
- The Spatial and Temporal Distribution of AE/MS Source Locations Following the Mine-by Tunnel Excavation of Round 17 (RP017AECL, Young and Collins 1993)†
- Ultrasonic Imaging of Damage Induced by Cyclic Loading of Lac du Bonnet Granite (RP018AECL, Chow et al. 1993)†
- AE Monitoring During Loading of Lac du Bonnet Granite Blocks Containing Central Holes (RP019AECL, Meglis et al. 1993)†
- Thermally Induced Fracturing of Lac du Bonnet Granite (RP020AECL, Carlson et al. 1993)†
- Source Mechanism Studies at the Underground Research Laboratory (RP021AECL, Feignier and Young 1993)†

- Attenuation Analysis at the AECL Underground Research Laboratory Using the Spectral Ratio Method; Preliminary Results (RP022AECL, Feustal and Young 1993)†
- The spatial and temporal distribution of microseismicity recorded in Round 17 of the Mine-by Tunnel (RP023AECL, Collins and Young 1993)†
- Initial Progress Report on Acoustic Emission Monitoring of Stage 1 of the Mine-by Heated-Failure Tests (RP024AECL, Falls and Young 1994)†
- Wave Propagation Effects of an Underground Opening (RP025AECL, Maxwell and Young 1994)†
- Comparison of the excavation-induced microseismicity from the granite and granodiorite sections of the Mine-by Tunnel (RP026AECL, Collins and Young 1994)†
- Acoustic Emission and Ultrasonic Velocity Studies of the Mine-by Heated Failure Test - Phase 1 (RP027AECL, Falls and Young 1994)†
- Source Parameters of Excavation Induced Seismicity from the Mine-by Tunnel (RP028AECL, Collins et al. 1994)†

C.3 NUMERICAL MODELLING AND ANALYSIS

- Finite-Element Modelling of the Geomechanical Responses of the Mine-by Experiment (TR-610, COG-93-242, Khair and Chan 1991)
- Mine-By Experiment - Prediction of Excavation Induced Rock Mass Response Using UDEC (URL-EXP-009-M003, Martino 1991)†
- Mine-by Experiment - Prediction of Excavation Induced Rock Mass Response (URL-EXP-022-M048, Read 1991)†
- Rock Fracture Around Underground Openings for Nuclear Waste Disposal (WS-31J-98299, Ayari and DeClaire 1993)†
- Development and Numerical Implementation of an Elastic-Brittle-Ductile Constitutive Model (WS-29J-54421, Ofoegbu and Curran 1991)†
- URL Mine-by Experiment Rock Mass Response Predictions (WS-29J-54421, Curran et al. 1991)†
- Three Dimensional Finite Element Analyses of the URL Mine-by Test Tunnel (WS-29J-54421, Curran et al. 1992)†
- Harmonic Finite Element Analysis of a Cylindrical Excavation in an Infinite Medium (Grabinsky and Curran, 1993)†
- Two-dimensional Fracture Propagation Modelling of the URL Mine-by Test Tunnel (Curran et al. 1994)†
- Numerical Analysis of the AECL Mine-by Experiment (Post-construction Phase) Part 2a - Triaxial Strain Cell Results for a Circular Excavation (Curran et al. 1994)†

- Numerical Analysis of the AECL Mine-by Experiment (Post-construction Phase) Part 3a - Extensometer Results for a Circular Excavation (Curran et al. 1994)†
- Numerical Analysis of the AECL Mine-by Experiment (Post-construction Phase) Part 4a - Convergence Results for a Circular Excavation (Curran et al. 1994)†

C.4 PUBLISHED PAPERS RELATED TO THE MINE-BY EXPERIMENT

- AECL's Mine-by Experiment - From Concept to Construction (Onagi et al.1991)
- Design and Construction of Two Major Experiments at the URL (Thompson et al. 1992)
- Developments in the Mini-CHARTS System and Field Trial Results in Measuring Excavation Damage in Granite (Hayles et al. 1992)
- Preliminary analysis of shear-wave splitting in granite at the Underground Research Laboratory, Manitoba (Holmes et al. 1992)
- Acoustic emission and ultrasonic velocity study of excavation-induced microcrack damage at the Underground Research Laboratory (Carlson and Young 1993)
- An analysis of laboratory and long-term rock strength using a sliding crack model (Chandler and Martin 1995)
- The influence of near surface faults on *in situ* stresses (Chandler and Martin 1994)
- Numerical modelling of discrete fracture in granite (Dzik et al. 1994)
- Ultrasonic imaging and acoustic emission monitoring of thermally induced microcracks in Lac du Bonnet granite (Jansen et al. 1993)
- Near-face cracking and strength around underground openings (Martin et al. 1995)
- Brittle failure: Laboratory and *in situ* (Martin 1995)
- Monitoring progressive failure around a tunnel in massive granite (Martin et al. 1995)
- The progressive fracture of Lac du Bonnet granite (Martin and Chandler 1994)
- The effect of sample disturbance on laboratory properties of Lac du Bonnet granite (Martin and Stimpson 1994)
- Comparison of borehole breakouts from laboratory and field tests (Martin et al. 1994)
- Quantifying drilling-induced damage in samples of Lac du Bonnet granite (Martin 1994)
- The role of convergence measurements in characterizing a rock mass (Martin et al. 1994)
- The Underground Research Laboratory: an opportunity for basic rock mechanics (Martin and Simmons 1993)
- The effect of excavation-induced seismicity on the strength of Lac du Bonnet granite (Martin and Young 1993)

- Crack damage in the post-peak region (Martin and Lajtai, In prep.)
- The *in situ* strength of massive granite around excavations (Martin and Read 1992)
- Asymmetric borehole breakouts at the URL (Read et al. 1995)
- Monitoring the excavation-induced response of granite (Read and Martin 1992)
- The Underground Research Laboratory Mine-by Experiment - a research perspective on tunnel design (Read and Martin 1990)
- Potential role of acoustic emission/microseismicity investigations in the site characterization and performance monitoring of nuclear waste repositories (Young and Martin 1993)

C.5 REFERENCES

Ayari, M. L. and M. DeClaire (1993). Rock fracture around underground openings for nuclear waste disposals. Department of Mechanical and Industrial Engineering, University of Manitoba, Winnipeg, MB.†

Carlson, S. R. and R. P. Young (1992). Acoustic emission and ultrasonic velocity study of excavation-induced microcrack damage in the Mine-by Tunnel at the Underground Research Laboratory. Report to Atomic Energy of Canada Limited RP015AECL, Queen's University, Kingston, ON.†

Carlson, S. R. and R. P. Young (1993). Acoustic emission and ultrasonic velocity study of excavation-induced microcrack damage at the Underground Research Laboratory. *Int. J. Rock Mech. Min. Sci. & Geomech. Abstr.*, 30(7):901–907.

Carlson, S. R., D. P. Jansen and R. P. Young (1993). Thermally induced fracturing of Lac du Bonnet Granite. Report to Atomic Energy of Canada Limited RP020AECL, Queen's University, Kingston, ON.†

Chandler, N. A. and C. D. Martin (1995). An analysis of laboratory and long-term rock strength using a sliding crack model. In J. Daemen and R. Schultz, editors, *Proc. 35th U.S. Rock Mechanics Symposium, Lake Tahoe.* A.A. Balkema, Rotterdam.

Chandler, N. A. and C. D. Martin (1994). The influence of near surface faults on *in situ* stresses. In P. P. Nelson and S. E. Laubach, editors, *Proc. 1st North American Rock Mechanics Symposium, Austin*, pages 369–376. A.A. Balkema, Rotterdam.

Chow, T., S. D. Falls, S. R. Carlson and R. P. Young (1990). Ultrasonic imaging and acoustic emission monitoring of laboratory hydraulic fracturing experiments in Lac du Bonnet grey granite from AECL's Underground Research Laboratory. Report to Atomic Energy of Canada Limited RP008AECL, Queen's University, Kingston, ON.†

Chow, T., I. Meglis and R. P. Young (1993). Ultrasonic imaging of damage induced by cyclic loading of Lac du Bonnet granite. Report to Atomic Energy of Canada Limited RP018AECL, Queen's University, Kingston, ON.†

Collins, D. S. and R. P. Young (1992). Monitoring and source location of microseismicity induced by excavation of the Mine-by Experiment tunnel: preliminary analysis. Report to Atomic Energy of Canada Limited RP013AECL, Queen's University, Kingston, ON.†

Collins, D. S. and R. P. Young (1993). AE/MS source location calibration and velocity results: two surveys performed after the Mine-by Tunnel excavation. Report to Atomic Energy of Canada Limited RP016AECL, Queen's University, Kingston, ON.†

Collins, D. S. and R. P. Young (1994). The spatial and temporal distribution of microseismicity recorded in Round 17 of the Mine-by Tunnel. Report to Atomic Energy of Canada Limited RP023AECL, University of Keele.†

Collins, D. S. and R. P. Young (1994). Comparison of the excavation-induced microseismicity from the granite and granodiorite sections of the Mine-by Tunnel. Report to Atomic Energy of Canada Limited RP026AECL, University of Keele.†

Collins, D. S., C. Baker and R. P. Young (1994). Source parameters of excavation induced seismicity from the Mine-by Tunnel. Report to Atomic Energy of Canada Limited RP028AECL, University of Keele.†

Corthésy, R., D. E. Gill and M. H. Leite (1993). Doorstopper stress measurements at the 420 Level of the URL. C.D.T. Project P1596, l'Ecole Polytechnique de Montréal.†

Curran, J. H., G. I. Ofoegbu and M. W. Grabinsky (1991). URL Mine-by Experiment rock mass response predictions. Department of Civil Engineering, University of Toronto.†

Curran, J. H., G. I. Ofoegbu and M. W. Grabinsky (1992). Three dimensional finite element analyses of the URL Mine-by Test Tunnel. Department of Civil Engineering, University of Toronto.†

Curran, J. H., M. W. Grabinsky and B. T. Corkum (1994). Two-dimensional fracture propagation modelling of the URL Mine-by test tunnel. Department of Civil Engineering, University of Toronto.†

Curran, J. H., M. W. Grabinsky and B. T. Corkum (1994). Numerical analysis of the AECL Mine-by Experiment (Post-construction Phase) Part 2a - triaxial strain cell results for a circular excavation. Department of Civil Engineering, University of Toronto.†

Curran, J. H., M. W. Grabinsky and B. T. Corkum (1994). Numerical analysis of the AECL Mine-by Experiment (Post-construction Phase) Part 3a - extensometer results for a circular excavation. Department of Civil Engineering, University of Toronto.†

Curran, J. H., M. W. Grabinsky and B. T. Corkum (1994). Numerical analysis of the AECL Mine-by Experiment (Post-construction Phase) Part 4a - Convergence results for a circular excavation. Department of Civil Engineering, University of Toronto.†

Dynatec Engineering Inc. (1989). Mechanical excavation of URL-Excavation Response Experiment conceptual engineering. Project E238.R. Richmond Hill, ON.†

Dzik, E. J., E. Z. Lajtai and C. D. Martin (1994). Numerical modelling of discrete fracture in granite. In H.J. Siriwardane, editor, *Proc. 8th Int. Conf. on Computer Methods and Advances in Geomechanics (IACMAG94), Morgantown, West Virginia*, Volume 3. A.A. Balkema, Rotterdam.

Everitt, R. A., P. Gann and D. M. Boychuk (1993). Mine-by Experiment data summary: Part 7 - General Geology and Geological Setting. Atomic Energy of Canada Limited Report, RC-1080, COG-93-251.‡

Falls, S. D. and R. P. Young (1994). Uniaxial compression testing of large samples of Lac du Bonnet granite at low strain rates, Part 1: Studies of Acoustic emission rate. Report to Atomic Energy of Canada Limited RP014AECL, University of Keele.†

Falls, S. D. and R. P. Young (1994). Initial progress report on acoustic emission monitoring of Stage 1 of the Mine-by Heated-Failure Tests. Report to Atomic Energy of Canada Limited RP024AECL, University of Keele.†

Falls, S. D. and R. P. Young (1994). Acoustic emission and ultrasonic velocity studies of the Mine-by Heated Failure Test - Phase 1. Report to Atomic Energy of Canada Limited RP027AECL, University of Keele.†

Feigner, B. and R. P. Young (1993). Source mechanism studies at the Underground Research Laboratory. Report to Atomic Energy of Canada Limited RP021AECL, Queen's University, Kingston, ON.†

Feustel, A. J. and R. P. Young (1993). Attenuation analysis at the AECL Underground Research Laboratory using the spectral ratio method; preliminary results. Report to Atomic Energy of Canada Limited RP022AECL, Queen's University, Kingston, ON.†

Gann, P. and R. A. Everitt (1994). Geology of the Mine-by Experiment Connected Permeability Phase floor slot. Atomic Energy of Canada Limited Report RC-1080-2, URL-EXP-022-R29.‡

Gann, P. and R. A. Everitt (1994). Geology of the Mine-by Experiment Test Tunnel Expansion. Atomic Energy of Canada Limited Report RC-1080-3, COG-94-227, URL-EXP-022-R30.‡

Gann, P. and R. A. Everitt (1994). Geology of the observation slot at the 420 Level of the Underground Research Laboratory. Atomic Energy of Canada Limited Report RC-1080-4, COG-93-319, URL-EXP-022-R31.‡

Grabinsky, M. W. and J. H. Curran (1993). Harmonic finite element analysis of a cylindrical excavation in an infinite medium. Department of Civil Engineering, University of Toronto, 93-2.†

Hayles, J. G., M. H. Serzu, and G. S. Lodha (1995). Cross-hole seismic tomography surveys for the Mine-by Experiment. Atomic Energy of Canada Limited Technical Record TR-678. COG-95-021.

Hayles, J. G., K. M. Stevens, M. H. Serzu and G. S. Lodha (1992). Developments in the mini-CHARTS system and field trial results in measuring excavation damage in granite. In *Proc. 4th International MGLS/EGS Symposium on Borehole Geophysics for Minerals, Geotechnical and Groundwater Applications; Toronto*, 18-22 August 1991.

Holmes, G. M., S. Crampin and R. P. Young (1992). Preliminary analysis of shear-wave splitting in granite at the Underground Research Laboratory, Manitoba. In *Proc. Fifth International Workshop on Seismic Anisotropy, Banff*, 17-22 May.

Jansen, D. P., S. R. Carlson, R. P. Young, and D. A. Hutchins (1993). Ultrasonic imaging and acoustic emission monitoring of thermally induced microcracks in Lac du Bonnet Granite. *J. Geophysical Research*, 98(B12):22231-22243.

Keith, S. G. and D. P. Onagi (1994). Mine-by Experiment data summary: Part 8 - Construction summary. Atomic Energy of Canada Limited Report COG-93-252.‡

Kelly, D., D. C. Peck and R. S. James (1993). Petrography of granitic rock samples from the 420 Level of the Underground Research Laboratory, Pinawa, Manitoba. Laurentian University, Sudbury, Ontario.†

Khair, K. R. and T. Chan (1994). Finite-element modelling of the geomechanical responses of the Mine-by Experiment. Atomic Energy of Canada Limited Technical Record TR-610, COG-93-242.

Kuzyk, G. W. (1990). Conceptual design report for: 1. Enthalpy Control System 2. 420 Level Development 3. Electrical & Mechanical Services. Atomic Energy of Canada Design Report†

Lau, J. S. O., B. Gorski, B. Conlon, L. Butler and J. Folta (1994). Block sample testing to study the effect of stress rotation on rock strength. Canada Centre for Mineral and Energy Technology, MRL 94-004(CL).†

Martin, C. D., R. S. Read, and E. J. Dzik (1995). Near-face cracking and strength around underground openings. In H. P. Rossmanith, editor, *Proc. 2nd, Int. Conf. on Mechanics of Jointed and Faulted Rock*, pages 747–752. A.A. Balkema, Rotterdam.

Martin, C. D. (1995). Brittle failure: Laboratory and *in situ*. In *Proc. 8th, ISRM Congress on Rock Mechanics, Tokyo*. A.A. Balkema, Rotterdam.

Martin, C. D., R. P. Young, and D. S. Collins (1995). Monitoring progressive failure around a tunnel in massive granite. In *Proc. 8th ISRM Congress on Rock Mechanics, Tokyo*. A.A. Balkema, Rotterdam.

Martin, C. D. and N. A. Chandler (1994). The progressive fracture of Lac du Bonnet granite. *Int. J. Rock Mech. Min. Sci. & Geomech. Abstr.*, 31(6):643–659.

Martin, C. D. and B. Stimpson (1994). The effect of sample disturbance on laboratory properties of Lac du Bonnet granite. *Can. Geotech. J.*, 31(5):692–702.

Martin, C. D., J. B. Martino, and E. J. Dzik (1994). Comparison of borehole breakouts from laboratory and field tests. In *Proc. EUROCK'94, SPE/ISRM Rock Mechanics in Petroleum Engineering Delft*, pages 183–190. A.A. Balkema, Rotterdam.

Martin, C. D. (1994). Quantifying drilling-induced damage in samples of Lac du Bonnet granite. In P. P. Nelson and S. E. Laubach, editors, *Proc. 1st North American Rock Mechanics Symposium, Austin*, pages 419–426. A.A. Balkema, Rotterdam.

Martin, C. D., N. A. Chandler, and R. S. Read (1994). The role of convergence measurements in characterizing a rock mass. In *Proc. 47th Canadian Geotechnical Conference, Halifax.*

Martin, C. D. and G. R. Simmons (1992). The Underground Research Laboratory: an opportunity for basic rock mechanics. *ISRM News Journal*, 1(1):2–8.

Martin, C. D. and R. P Young (1993). The effect of excavation-induced seismicity on the strength of Lac du Bonnet granite. In R. P. Young, editor, *Proc. 3rd Int. Symp. on Rockbursts and Seismicity in Mines, Kingston*, pages 367–371. A.A. Balkema, Rotterdam.

Martin, C. D. and E. Z. Lajtai (In prep.). Crack damage in the post-peak region. *Int. J. Rock Mech. Min. Sci. & Geomech. Abstr.*.

Martin, C. D. and R. S. Read (1992). The *in situ* strength of massive granite around excavations. In P.K. Kaiser and D. McCreath, editors, *Proc. 16th Canadian Rock Mechanics Conference, Sudbury*, pages 1–10.

Martin, C.D. (1991). Mine-by experiment plan -Underground Research Laboratory. DE010-011. Atomic Energy of Canada Limited Disposal Technology Division Quality Assurance Document.†

Martino, J. B., R. S. Read, and J. H. Mitchell (1993a). Mine-by Experiment data summary: Part 5 – Thermistor results. Atomic Energy of Canada Limited Report RC-1079, COG-93-233.‡

Martino, J. B., R. S. Read, and D. Collins (1993). Mine-by Experiment data summary: Part 6 – Acoustic Emission/Microseismic results. Atomic Energy of Canada Limited Technical Record, TR-597, COG-93-185.‡

Martino J. B., R. S. Read and S. G. Keith (1994). Mine-by Experiment data summary: Part 9 – Observations. Atomic Energy of Canada Limited Report, COG-93-347.‡

Maxwell, S. C. and R. P. Young (1994). Wave propagation effects of an underground opening. Report to Atomic Energy of Canada Limited RP025AECL, University of Keele.†

McArthur, J. R. (1994). Petrofabric analysis of natural microfractures in quartz of the Lac du Bonnet Batholith. Report to Atomic Energy of Canada Limited.†

McCormac, D. D., E. L. Schatzlein, and D. T. K. Au (1990). Conceptual design report for Enthalpy Control System Mine-by (MB) Experiment Underground Research Laboratory depth 420 m. Atomic Energy of Canada Limited Design Report.†

Meglis, I. L., T. Chow and R. P. Young (1993). AE monitoring during loading of Lac du Bonnet granite blocks containing central holes. Report to Atomic Energy of Canada Limited RP019AECL, Queen's University, Kingston, ON.†

Ofoegbu, G. I. and J. H. Curran (1991). Development and numerical implementation of an elastic-brittle-ductile constitutive model. Department of Civil Engineering, University of Toronto.†

Onagi, D. P., R. S. Read and G. W. Kuzyk (1991). AECL's Mine-by Experiment - From concept to construction. In *Proc. Society for Mining, Metallurgy and Exploration Inc. Annual Meeting, Denver, CO*, 1991 February 25-28.

Rawlence, L. (1990). Borehole breakouts: a review of the theory and a discussion of their investigation using seismic methods. Report to Atomic Energy of Canada Limited RP005AECL, Queen's University, Kingston, ON.†

Read, R. S. (1990). Mine-by experiment preliminary scoping calculations. Atomic Energy of Canada Limited Technical Memorandum URL-EXP-022-M045.†

Read, R. S. and C. D. Martin (1990). Mine-by Experiment preliminary design report. Atomic Energy of Canada Limited Technical Memorandum URL-EXP-022-M044.†

Read, R. S. and C. D. Martin (1991). Mine-by Experiment final design report. Atomic Energy of Canada Limited Report AECL-10430.

Read, R. S., J. B. Martino, G. R. Karklin, E. Jacobs and G. Hiltz (1994). Mine-by Experiment data summary: Part 1 - Survey information. Atomic Energy of Canada Limited Report RC-1076, COG-93-290.‡

Read, R. S., J. B. Martino, and J. H. Mitchell (1994b). Mine-by Experiment data summary: Part 2 Triaxial strain cell results. Atomic Energy of Canada Limited Report RC-1077, COG-93-353.‡

Read, R. S., J. B. Martino, J. H. Mitchell and M.H. Spinney (1994). Mine-by Experiment data summary: Part 3 - Extensometer results. Atomic Energy of Canada Limited Report RC-1078, COG-93-354.‡

Read, R. S., J. B. Martino, J. H. Mitchell (1993b). Mine-by Experiment data summary: Part 4 - Convergence results. Atomic Energy of Canada Limited Technical Record TR-595, COG-93-177.‡

Read, R. S., C. D. Martin, and E. J. Dzik (1995). Asymmetric borehole breakouts at the URL. In J. Daemen and R. Schultz, editors, *Proc. 35th U.S. Rock Mechanics Symposium, Lake Tahoe*, pages 879-884. A.A. Balkema, Rotterdam.

Read, R. S. and C. D. Martin (1992). Monitoring the excavation-induced response of granite. In J.A. Tillerson and W.R. Wawersik, editors, *Proc. 33rd U.S. Symp. on Rock Mechanics, Santa Fe*, pages 201-210. A.A. Balkema, Rotterdam.

Read, R. S. and C. D. Martin (1990). The Underground Research Laboratory Mine-by Experiment - a research perspective on tunnel design. In *Proc. 8th Canadian Tunnelling Conference, Vancouver*, pages 213-226. BiTech Publishers Ltd, Vancouver. Also In *Canadian Tunnelling* (1991), pp. 75-88.

Rousell, D. H. (1993). Orientation and distribution of inclusion bearing microcracks in core from the 420 Level of the Underground Research Laboratory, Pinawa, Manitoba. Report to Atomic Energy of Canada Limited, Laurentian University, Sudbury, Ontario.†

Saleh, K., A-P. Bois, G. Ballivy (1992). Instrumentation des parios rocheuses à l'aide des Cylindres Instrumentés de l'Université de Sherbrooke. Laboratoire de méchanique des roches et de géologie appliquée, Département de génie civil, Faculté des sciences appliquées, Université de Sherbrooke, Québec, Canada.†

Talebi, S. and R. P. Young (1989). Final report on source location of microseismic events induced by shaft excavation at the Underground Research Laboratory. Report to Atomic Energy of Canada Limited RP003AECL, Queen's University, Kingston, ON.†

Talebi, S. and R. P. Young (1989). In situ measurements of P & S wave velocities at the Underground Research Laboratory. Report to Atomic Energy of Canada Limited RP004AECL. Queen's University, Kingston, ON.†

Talebi, S. and R. P. Young (1990). Design of a microseismic system for the URL Mine-by Experiment. Report to Atomic Energy of Canada Limited RP006AECL, Queen's University, Kingston, ON.†

Talebi, S. and R. P. Young (1990). Seismic and radar characterization at the 240 m level of the Underground Research Laboratory. Report to Atomic Energy of Canada Limited RP007AECL, Queen's University, Kingston, ON.†

Talebi, S., B. Feigner and R. P. Young (1991). Analysis of the microseismicity induced by the 420 Level development at the Underground Research Laboratory. Report to Atomic Energy of Canada Limited RP009AECL, Queen's University, Kingston, ON.†

Talebi, S. and R. P. Young (1992). In situ velocity measurements for the Mine-by Experiment. Report to Atomic Energy of Canada Limited RP011AECL, Queen's University, Kingston, ON.†

Talebi, S. and R. P. Young (1992). Preliminary AE/MS results from the Mine-by experiment. Report to Atomic Energy of Canada Limited RP012AECL, Queen's University, Kingston, ON.†

Thompson, P. M., B. H. Kjartanson and R. S. Read (1992). Design and construction of two major experiments at the URL. In *Proc. 1992 International High-Level Radioactive Waste Management Conference, Las Vegas, NV, Vol. 1*, pages 1082-1089, 1992.

Wardrop Engineering Inc. (1990). Underground Research Laboratory 420 Level development and Mine-by Experiment mechanical and electrical furnishings. Project No. 890025-02-00. Winnipeg, MB.†

Wiles, T. D. (1990a). 3D scoping interaction of adjacent openings in terms of stress. Final Technical Report Phase 1. Geomechanics Research Centre, Laurentian University, Sudbury, ON.†

Wiles, T. D. (1990b). AECL Mine-by Experient instrument sensitivity evaluation. Final Technical Report Phase 2. Mine Modelling Limited, Copper Cliff, ON.†

Woodcock, D. R. (1993). Geological data summary for the MB-series boreholes drilled for the Mine-by Experiment at the Underground Research Laboratory. Atomic Energy of Canada Limited Technical Record TR-577-9, COG-92-433.

Woodcock, D. R. (1993). Geological data summary for the GP-series and MBW-series boreholes drilled for the Mine-by Experiment at the Underground Research Laboratory. Atomic Energy of Canada Limited Technical Record TR-577-10, COG-93-91.

Woodcock, D. R. (1993). Geological data summary for the AE/MS series boreholes drilled for the Mine-by Experiment at the Underground Research Laboratory. Atomic Energy of Canada Limited Report RC-1080-11, COG-93-92.‡

Woodcock, D. R. (In review). Geological data summary for the Bof-ex extensometer-series boreholes drilled for the Mine-by Experiment at the Underground Research Laboratory. Atomic Energy of Canada Limited Report RC-1080-12, COG-93-93.‡

Woodcock, D. R. (1994). Geological data summary for the CSIRO-series boreholes drilled for the Mine-by Experiment at the Underground Research Laboratory. Atomic Energy of Canada Limited Report RC-1080-13, COG-94-282.‡

Woodcock, D. R. (In review). Geological data summary for the microseismic calibration-series boreholes drilled for the Mine-by Experiment at the Underground Research Laboratory. Atomic Energy of Canada Limited Report RC-1080-14, COG-94-283.‡

Woodcock, D. R. (In review). Geological data summary for the excavation damage assessment series and the acoustic emission series boreholes drilled for the Mine-by Experiment at the Underground Research Laboratory. Atomic Energy of Canada Limited Report RC-1080-15, COG-94-284.‡

Woodcock, D. R. (In prep.). Geological data summary for the scale effects boreholes drilled for the Mine-by Experiment at the Underground Research Laboratory. Atomic Energy of Canada Limited Report RC-1080-16, COG-94-285.‡

Young, R. P. and D. S. Collins (1993). The spatial and temporal distribution of AE/MS source locations following the Mine-by Tunnel excavation of Round 17. Report to Atomic Energy of Canada Limited RP017AECL, Queen's University, Kingston, ON.†

Young, R. P. and C. D. Martin (1993). Potential role of acoustic emission/microseismicity investigations in the site characterization and performance monitoring of nuclear waste repositories. *Int. J. Rock Mech. Min. Sci. & Geomech. Abstr.*, 30(7):797-803.

Young, R. P. and S. Talebi (1988). Microseismic monitoring and excavation damage assessment at Atomic Energy of Canada Limited's Underground Research Laboratory. Report to Atomic Energy of Canada Limited RP001AECL, Queen's University, Kingston, ON. †

Young, R. P. and S. Talebi (1989). Manual source locations of microseismic events induced by shaft extension at the Underground Research Laboratory. Report to Atomic Energy of Canada Limited RP002AECL, Queen's University, Kingston, ON.†

---

† Unpublished
‡ Protected

Cat. No. / N° de cat.: CC2-11311E
ISBN 0-660-16394-2
ISSN 0067-0367

To identify individual documents in the series, we have assigned an AECL- number to each. Please refer to the AECL- number when requesting additional copies of this document from

Scientific Document Distribution Office (SDDO)
AECL
Chalk River, Ontario
Canada K0J 1J0

Fax: (613) 584-1745 Tel.: (613) 584-3311
ext. 4623

Price: D

Pour identifier les rapports individuels faisant partie de cette série, nous avons affecté un numéro AECL- à chacun d'eux. Veuillez indiquer le numéro AECL- lorsque vous demandez d'autres exemplaires de ce rapport au

Service de Distribution des documents officiels (SDDO)
EACL
Chalk River (Ontario)
Canada K0J 1J0

Fax: (613) 584-1745 Tél.: (613) 584-3311
poste 4623

Prix: D